Rotation, magnétisme et turbulence dans les étoiles

François Lignières

Habilitation à diriger les recherches

Délivrée par : l'Université Toulouse 3 - Paul Sabatier

Soutenue par : François Lignières

Le 14/10/2010

Rotation, magnétisme et turbulence dans les étoiles

Jury

Dr. Claude CATALA (Examinateur)

Pr. Jorgen CRISTENSEN-DALSGAARD (Rapporteur)

Dr. Marie-Jo GOUPIL (Examinateur)

Dr. Frédéric THEVENIN (Examinateur)

Pr. Michel RIEUTORD (Dir. de thèse)

Pr. Ian ROXBURGH (Rapporteur)

Dr. Jean-Paul ZAHN (Rapporteur)

Ecole doctorale : Sciences de l'Univers, de l'Environnement et de l'Espace

Unité de Recherche : Laboratoire d'Astrophysique de Toulouse et Tarbes

Résumé

Ce travail de thèse concerne à la fois la modélisation des processus magnétohydrodynamiques dans les étoiles et l'obtention de contraintes observationnelles sur ces processus. Une partie importante du mémoire est consacrée à l'étude des effets de la rotation sur les modes propres d'oscillation des étoiles. La méconnaissance de ces effets est depuis longtemps identifiée comme l'un des principaux obstacles à l'interprétation des fréquences d'oscillations observées dans les étoiles massives et de masse intermédiaire. Je décris ici la mise au point d'un code d'oscillation tenant compte des effets de la rotation, l'exploration des nouvelles propriétés des modes au moyen de ce code, l'interprétation de ces propriétés dans le cadre d'une théorie asymptotique et comment elles peuvent être utilisées pour interpréter les spectres de fréquences observés. Pour construire la théorie asymptotique, j'ai été amené à m'intéresser au chaos quantique (ou chaos d'onde), une thématique qui est issue de l'étude des propriétés semi-classiques des systèmes quantiques mais qui concerne en fait la physique des ondes en général. La deuxième thématique concerne le magnétisme des étoiles de masse intermédiaire (de type B tardif et de type A) de la séquence principale. C'est un sujet relié mais distinct de celui de ma thèse de doctorat qui était consacré à la modélisation de l'évolution du moment cinétique de ces étoiles dans leur phase pré-séquence-principale. Il s'agit ici d'observations spectropolarimétriques qui renouvellent assez largement notre vision du magnétisme de ces étoiles. D'abord, la mise en évidence d'une limite inférieure à l'intensité du champ des étoiles Ap/Bp a permis de proposer un nouveau scénario pour expliquer l'origine de cette classe d'étoiles, la seule classe d'étoiles magnétiques connue jusqu'alors dans ce domaine du diagramme HR. Puis, la découverte d'un champ magnétique de très faible amplitude à la surface de Véga a montré l'existence d'un nouveau type de magnétisme dans ce domaine. La troisième thématique concerne l'étude des mouvements turbulents dans les intérieurs stellaires, d'une part la modélisation de leur contribution au transport des éléments chimiques dans les zones radiatives d'étoile et d'autre part l'origine des structures cohérentes

de la convection turbulente observées à la surface du Soleil.

Table des matières

Articles reproduits

A1. **Lignières F.**, Rieutord M., Reese D., "Acoustic oscillations in rapidly rotating polytropic stars ; I. Effects of the centrifugal distortion", A&A 455, pp. 607-620, 2006

A2. Reese D., **Lignières F.** and Rieutord M., "Acoustic oscillations in rapidly rotating polytropic stars ; II. Effects of the Coriolis and centrifugal accelerations", A&A 455, 621-637, 2006

A3. Ballot, J., **Lignières F.**, Reese D., Rieutord M., "Gravity modes in rapidly rotating stars. Limits of perturbative methods", accepté pour publication dans A&A, 2010 (preprint arXiv :1005.0275)

A4. Reese D., **Lignières F.** and Rieutord M., "Regular patterns in the acoustic spectrum of rapidly rotating stars", A&A 481, 449-452, 2008

A5. **Lignières F.**, "Asymptotic theory of stellar oscillations based on ray dynamics", Lectures Notes in Physics, Berlin : Spinger, sous presse

A6. **Lignières F.** and Georgeot B., "Wave chaos in rapidly rotating stars", Phys. Rev. E. 78, 016215-016219, 2008

A7. **Lignières F.** and Georgeot B., "Asymptotic analysis of high-frequency acoustic modes in rapidly rotating stars", A&A 500, 1173-1192, 2009

A8. Aurière M., Wade G. A., Silvester J., **Lignières F.** et al., "Weak magnetic fields in Ap/Bp stars. Evidence for a dipole field lower limit and a tentative interpretation of the magnetic dichotomy", A&A 475, 1053-1065, 2007

A9. Aurière M., Wade G. A., **Lignières F.** et al., "No detection of large-scale magnetic fields at the surfaces of Am and HgMn stars", sousmis à la revue A&A

A10. **Lignières F.**, Petit P., Bohm T., Aurière M. 2009, "First evidence of a magnetic field on Vega. Towards a new class of magnetic A-type stars", A&A 500, L41-L44, 2009

A11. Toqué N., **Lignières F.**, Vincent A., "Reduction of the vertical transport in two-dimensional stably stratified forced shear flows", Geophys. and Astrophys. Fluid Dynamics 100, 85-105, 2006.

A12. Roudier Th., **Lignières F.**, Rieutord M., Brandt P.N., Malherbe J.M., "Families of fragmenting granules and their relation to meso and supergranular flow fields", A&A 409, 299-308, 2003.

A13. Rincon F., **Lignières F.**, Rieutord M., "Mesoscale flows in large aspect ratio simulations of turbulent compressible convection", A&A 430, L57-L60, 2005.

Chapitre 1

Introduction

Après une présentation du contexte astrophysique de la thèse, les différents thèmes de recherche abordés et l'organisation du document sont précisés dans la partie "contenu de la thèse".

1.1 Motivations astrophysiques

Les mouvements macroscopiques du plasma dans les intérieurs stellaires ont un effet important et pourtant largement incompris sur l'évolution des étoiles. Dans le cadre du modèle standard d'évolution stellaire, ils sont entièrement négligés dans les zones radiatives alors qu'ils sont modélisés de façon trop simplifiée dans les zones convectives. Mieux comprendre et modéliser l'influence de ces processus magnétohydrodynamiques sur l'évolution des étoiles est aujourd'hui un défi majeur de la physique stellaire, tout en sachant que, les étoiles constituant les briques de base de l'univers, les progrès de la théorie de l'évolution stellaire rejaillissent immanquablement sur notre compréhension de l'univers, des galaxies aux exoplanètes.

Bien que les lois de la physique régissant les mouvements du plasma dans les intérieurs stellaires soient bien connues, on ne sait pas résoudre, analytiquement ou numériquement, les équations associées dans des conditions stellaires réalistes. Cette difficulté limite nécessairement les capacités prédictives des modèles décrivant ces mouvements. Ceux-ci font alors généralement appel à des paramètres libres qui ne peuvent être fixés qu'empiriquement. Il n'est donc pas possible de modéliser les processus magnétohydrodynamiques internes aux étoiles sans contraintes observationnelles. C'est ce lien fort entre modélisation et observation que nous chercherons à illustrer dans cette introduction. Nous verrons ensuite que

le travail présenté dans cette thèse concerne à la fois la modélisation des processus hydrodynamiques et l'obtention de contraintes observationnelles sur ces processus.

Au delà du modèle standard

Pour le modèle standard d'évolution stellaire, une étoile est un gaz auto-gravitant en équilibre hydrostatique où la chaleur engendrée au centre par les réactions nucléaires est transportée vers la surface soit par le rayonnement seul, soit par le rayonnement et les mouvements de convection thermique si le transport radiatif n'est pas assez efficace. Les succès de ce modèle pour décrire les grandes lignes de l'évolution stellaire et l'intérieur du Soleil (confronté aux données de l'héliosismologie) indiquent que ses ingrédients de physique microscopique, les taux de réactions nucléaires, les opacités radiatives, les équations d'état, sont relativement bien connus. Pourtant les limites du modèle standard sont elles-aussi bien connues : l'héliosismologie a fourni des informations suffisamment détaillées sur le Soleil interne pour montrer à la fois notre méconnaissance de la convection thermique de surface et la nécessité d'invoquer des processus de transport non-standard des éléments chimiques sous la zone convective (Christensen-Dalsgaard 2002). L'étude des abondances chimiques au travers du diagramme HR a également mis en évidence que des processus de transport hydrodynamique sont à l'oeuvre dans les intérieurs stellaires (Pinsonneault 1997). Notamment, l'étude de l'abondance du lithium des étoiles de type solaire a fourni des contraintes assez précises sur l'étendue des couches mélangées sous l'enveloppe convective de ces étoiles. De même, les anomalies d'abondance dans les étoiles massives, notamment les excès d'azote et d'hélium, indiquent un certain transport des éléments chimiques entre les couches profondes de l'étoile et la surface (Maeder & Meynet 2000). Même dans les étoiles de masse intermédiaire de type Am, où l'atmosphère est suffisamment stable pour que les processus de triage gravitationnel créent des anomalies d'abondance observées, un mélange non-standard doit aussi être invoqué pour reproduire les observations (Michaud 2004). Le modèle standard n'explique pas non plus l'origine des champs magnétiques stellaires et des phénomènes d'activité associés. Pourtant le champ magnétique influence l'évolution stellaire notamment de façon indirecte puisque son effet sur l'évolution du moment cinétique des étoiles (freinage par vent magnétique, transport du moment cinétique interne) modifie le mélange induit par la rotation. Ces limites du modèle standard se traduisent par des incertitudes importantes sur l'évolution des étoiles et par conséquent sur l'ensemble des domaines de l'astrophysique qui en dépendent (comme par exemple l'évolution chimique de l'univers, la formation et l'évolution des galaxies ou l'étude des systèmes stellaires - étoiles + exoplanètes).

Modéliser les processus magnéto-hydrodynamiques

Pour reproduire les observations à partir de modèles physiques, il faut améliorer la description des mouvements macroscopiques et surtout de leur effet sur la structure interne de l'étoile. Ces mouvements peuvent être induits par la rotation de l'étoile, le champ magnétique et des instabilités de la structure hydrostatique comme par exemple la convection thermique, la convection double-diffusive ou le κ mécanisme. C'est un défi majeur car la modélisation des processus magnéto-hydrodynamiques dans des systèmes naturels de grande dimension est notoirement complexe, la principale difficulté, également rencontrée dans d'autres branches de la physique, provenant du caractère non-linéaire des équations aux dérivées partielles de la mécanique des fluides. Par exemple, ces non-linéarités donnent lieu à la turbulence qui opère sur une très large gamme d'échelles spatiales et temporelles. Pour appréhender ce type de phénomènes, la simulation numérique multidimensionnelle s'est avérée un outil privilégié de modélisation que ce soit pour les écoulements géophysiques, astrophysiques ou de laboratoire. Néanmoins, même si les capacités grandissantes des ordinateurs permettent de tenir compte d'un nombre croissant d'échelles de temps et d'espace dans les simulations, la résolution directe des équations fluides avec des paramètres réalistes n'est envisageable ni à court terme ni à moyen terme. D'après la loi de Moore qui décrit la croissance exponentielle de la puissance de calcul, il faudra attendre 2070 pour résoudre toute les échelles dynamiques d'un écoulement à nombre de Reynolds de $Re = UL/\nu = 10^8$, typique de la couche limite planétaire, et 2120 pour la convection solaire à Re=10^{14} (Voller & Porté-Agel 2002) ! Que faire en attendant ? Si on prend l'exemple des modèles météorologiques ou, sur des échelles de temps plus longues, des modèles d'évolution des climats, la simulations numérique ne permet de considérer que les plus grandes échelles du mouvements (supérieures à $\sim$ 100 km pour les modèles météorologiques globaux) alors que les phénomènes qui ont lieu aux échelles inférieures à la résolution numérique sont décrits par des modèles qui prennent la forme de termes supplémentaires dans les équations de l'hydrodynamique. La modélisation de ces phénomènes dits de sous-maille est très difficile et contient des paramètres libres qui doivent être calibrés par comparaison avec, soit des observations des systèmes naturels étudiés, soit des expériences de laboratoires ou des simulations numériques dédiées. Par conséquent, en l'absence de théorie des phénomènes non-linéaires dans les fluides et du fait des limitations des simulations numériques, les modèles de transport hydrodynamique, aussi sophistiqués soient-ils, doivent s'appuyer sur des contraintes empiriques. À l'intérieur des étoiles, l'exemple le plus évident est celui du transport de la chaleur dans les zones convectives où la longueur de mélange est un paramètre libre qui a

d'abord été calibré sur le Soleil. La situation est d'ailleurs identique pour les écoulements turbulents les plus simples puisque le transport de quantité de mouvement entre les deux parois d'un canal où de l'eau s'écoule à grande vitesse fait aussi appel à une calibration empirique. Une caractéristique essentielle de la modélisation des processus de transport magnéto-hydrodynamique dans les étoiles est donc qu'elle est largement tributaire des contraintes observationnelles disponibles.

En principe, la démarche à suivre serait la suivante : (i) modéliser les processus magnéto-hydrodynamique, cette modélisation étant basée autant que possible sur une compréhension physique profonde des phénomènes, (ii) intégrer la modélisation de ces phénomènes dans un modèle de structure interne et d'évolution des étoiles destiné à être comparé aux observations, ce modèle pouvant être 1D ou 2D, (iii) obtenir des contraintes observationnelles suffisamment précises pour tester et calibrer la modélisation des processus magnéto-hydrodynamiques.

Nouvelles contraintes observationnelles

Même si les observables traditionnelles des étoiles, que sont la luminosité apparente, la parallaxe, la gravité de surface, la température effective, la composition chimique de surface et la vitesse équatoriale projetée sur l'axe de visée, ont permis de construire puis de mettre en évidence les faiblesses du modèle standard, elles ne fournissent que des informations globales sur les processus hydrodynamiques. De ce point de vue, la détection des oscillations à 5 minutes du Soleil a été le début d'une révolution. En effet, ces oscillations se sont révélées correspondre à des modes propres d'oscillation acoustique du Soleil dont la fréquence dépend directement des propriétés du fluide stellaire dans la région de propagation du mode. L'héliosismologie a ainsi permis d'extraire de ces fréquences (et des dizaines de milliers de fréquences détectées depuis) une information détaillée sur les processus hydrodynamiques à l'intérieur du Soleil (notamment les vitesses de rotation interne). Les étoiles pulsantes couvrant les différentes régions du diagramme HR, la sismologie stellaire est donc naturellement apparu comme l'instrument privilégié pour étudier l'influence de ces processus sur l'évolution stellaire. L'expérience spatiale COROT a été proposée dans cette optique (rappelons que l'acronyme original de Corot - était COnvection et ROTation) avant d'inclure la recherche d'exoplanètes par transit qui est aujourd'hui l'objectif principal des missions spatiales KEPLER et PLATO. Ces missions alliant haute sensibilité photométrique et longue base de temps fournissent des données d'une qualité inégalée sur les fréquences d'oscillations des étoiles.

Le champ magnétique, qui est un ingrédient essentiel de la dynamique du fluide stellaire, n'est pas directement contraint par la sismologie stellaire. Mais la spectropolarimétrie stellaire qui s'est également

fortement développée ces dernières années (NARVAL, ESPADONS) a permis d'étudier la topologie et l'intensité du champ magnétique à la surface de nombreuses étoiles (Donati & Landstreet 2009). Basée sur la modulation rotationnelle des raies spectrales, l'imagerie Doppler et Zeeman-Doppler (Brown et al. 1991) fournit en plus des contraintes sur les processus dynamiques de surface (rotation, rotation différentielle).

L'interférométrie a également montré qu'elle peut apporter des contraintes originales sur la rotation des étoiles les plus proches en déterminant l'aplatissement et éventuellement les écarts de température pole-équateur induits par la force centrifuge (Domiciano de Souza et al. 2003; Peterson et al. 2006). Dans ce panorama des nouveaux moyens d'observations susceptibles de contraindre les processus hydrodynamiques dans les étoiles, la mission Gaia jouera également un rôle essentiel car elle précisera les paramètres fondamentaux d'une très grande quantité d'étoiles et permettra une étude détaillée du diagramme HR (Lebreton 2000).

Nouveaux outils de modélisation

Les efforts de modélisation sont stimulés par ces nouvelles contraintes observationnelles. Ils le sont aussi par le développement des simulations numériques, cet outil ouvrant des perspectives de recherches originales. Nous avons déjà mentionné les limites des simulations numériques d'écoulements naturels liées aux valeurs extrêmes des nombres sans dimension mesurant l'importance des termes non-linéaires. Les simulations numériques sont donc toujours réalisées dans un régime de paramètres irréaliste et la comparaison directe entre leurs résultats et les observations est donc toujours sujette à caution. Un exemple de ce type de situation est fourni par l'étude numérique du transport du moment cinétique dans la zone convective solaire (Brun & Toomre 2002). En augmentant le nombre de Reynolds des simulations, l'accord entre les résultats des simulations et les profils internes de rotation issus de l'héliosismologie s'améliore dans un premier temps puis se dégrade à nouveau pour les simulations à plus haut nombre de Reynolds. Une exception notable concerne les simulations numériques locales de la convection thermique à la surface du Soleil. Alors que les profils de raies en absorption du spectre solaire n'étaient pas reproduits en détail par les modèles d'atmosphère 1D (malgré l'utilisation de deux paramètres libres), un accord très satisfaisant a pu être obtenu grâce à ces simulations. Même si le nombre de Reynolds de ces simulations est aussi très irréaliste, ce succès doit probablement être attribué au fait que le spectre n'est pas sensible aux aspects de la dynamique qui sont mal décrits dans ces simulations (Nordlund et al. 2009). Cela concerne évidemment les échelles de sous-maille mais aussi d'autres aspects que l'on peut mettre en

évidence en comparant ces simulations à l'analyse détaillée des images de la photosphère, par exemple la dynamique des familles de granules et le transport horizontal d'un scalaire passif (Roudier 2004).

En règle générale, il est donc plus approprié de parler d'expérience numérique dont le principal intérêt est de tester des modèles existants ou d'en construire de nouveaux. Les modèles phénoménologiques de transport hydrodynamique sont basés sur des hypothèses qui doivent être vérifiées (description diffusive du transport turbulent, description de la force électromotrice turbulente par l'effet α, ...) et ils dépendent de paramètres libres qui doivent être calibrés empiriquement (prescription de la viscosité ou de la diffusivité turbulente, de la valeur de α). Vu sous cet angle, les simulations numériques ne cherchent plus à simuler l'étoile dans son ensemble sur des temps d'évolution nucléaire mais sont au contraire configurées pour tester tel ou tel aspect particulier d'un modèle. Par exemple pour reproduire les profils d'absorption du spectre solaire, un domaine cartésien, comprenant la photosphère et un nombre raisonnable de granules, apparaît suffisant. Les simulations numériques présentent également certains avantages vis à vis des expériences de laboratoire, puisque certaines particularités du fluide stellaire, telles que les valeurs très élevées de sa diffusion thermique et de sa conductivité électrique, ne peuvent pas être reproduites en laboratoire alors qu'elles sont accessibles, au moins en principe, aux simulations numériques.

1.2 Contenu de la thèse

Le travail présenté dans cette thèse concerne à la fois la modélisation des processus hydrodynamiques et l'obtention de contraintes observationnelles sur ces processus. Il fait largement appel aux nouveaux moyens, théoriques et observationnels mentionnés ci-dessus. Les trois thématiques abordées sont :

- les effets de la rotation sur les modes propres d'oscillation des étoiles
- l'origine du champ magnétique des étoiles massives et de masse intermédiaire
- l'étude des mouvements turbulents dans les intérieurs stellaires.

Elles correspondent aux trois chapitres du mémoire.

La méconnaissance des effets de la rotation sur les oscillations stellaires est depuis longtemps identifiée comme l'un des principaux obstacles à l'interprétation des fréquences d'oscillations observées dans les étoiles massives et de masse intermédiaire. Je me suis intéressé à ce sujet dans le cadre de la préparation de la mission Corot et c'est depuis mon recrutement au LATT fin 2000 mon sujet de recherche principal et celui pour lequel j'ai obtenu mes résultats les plus significatifs. Dans la partie qui lui est consacrée, je

décris la mise au point d'un code d'oscillation tenant compte des effets de la rotation, l'exploration des nouvelles propriétés des modes au moyen de ce code et l'interprétation de ces propriétés dans le cadre d'une théorie asymptotique que nous avons développée. Dans la partie projet de recherche, je décrirai comment ces avancées peuvent être mise à profit pour développer des méthodes d'interpétation des spectres de fréquences observées. Pour construire la théorie asymptotique, j'ai été amené à m'intéresser à un sujet, le chaos d'onde, qui concerne la physique des ondes en général. Les ondes peuvent être décrites par des rayons dans la limite des petites longueurs d'onde (approximation WKB pour Wentzel, Kramers, Brillouin) et les trajectoires de ces rayons peuvent être décrites comme un système dynamique Hamiltonien. Le chaos d'onde désigne alors l'étude des propriétés des ondes dont la dynamique des rayons est chaotique. Jusqu'à présent cette étude a été menée essentiellement pour les systèmes quantiques sous le nom de chaos quantique. Nous montrons ici par le calcul que les oscillations des étoiles en rotation rapide possèdent certaines propriétés génériques de ces systèmes, ouvrant ainsi la voie à une première mise en évidence observationnelle du chaos d'onde dans un système naturel à grande échelle.

La deuxième thématique concerne le magnétisme des étoiles de masse intermédiaire (de type B tardif et de type A) de la séquence principale. C'est un sujet relié mais distinct de celui de ma thèse de doctorat qui était consacré à la modélisation de l'évolution du moment cinétique de ces étoiles dans leur phase pré-séquence-principale. Il s'agit ici d'observations spectropolarimétriques qui, comme on le verra, renouvellent assez largement notre vision du magnétisme de ces étoiles. D'abord, la mise en évidence d'une limite inférieure à l'intensité du champ des étoiles Ap/Bp a permis de proposer un nouveau scénario pour expliquer l'origine de cette classe d'étoile, la seule classe d'étoile magnétique connue jusqu'alors dans ce domaine du diagramme HR. Puis, la découverte d'un champ magnétique de très faible amplitude à la surface de Véga (et peut-être également à la surface de Sirius) montre l'existence d'un nouveau type de magnétisme dans ce domaine.

La troisième thématique concerne l'étude des mouvements turbulents dans les intérieurs stellaires. Une première partie sera consacrée à la modélisation des processus de transport turbulent dans les zones radiatives d'étoiles. La turbulence est ici affectée par la force d'Archimède qui agit comme une force de rappel sur les mouvements verticaux et par la diffusivité thermique qui tend à la fois à diminuer l'intensité de la force d'Archimède et à dissiper de l'énergie cinétique. Je présenterai une étude de ces effets sur le transport turbulent des éléments chimiques. La deuxième partie concerne l'étude des mouvements de convection à la surface du Soleil. Je me suis en particulier intéressé aux structures cohérentes observées

dans cet écoulement turbulent, en contribuant à l'analyse des images de la surface ainsi qu'à la mise en oeuvre et l'interprétation de simulations numériques de convection turbulente.

Dans la partie projet de recherche, j'indiquerai les directions dans lesquelles je compte développer ces trois thématiques.

Chapitre 2

Sismologie des étoiles en rotation rapide

Comme la sismologie terrestre, la sismologie stellaire étudie la structure interne des étoiles en se servant des ondes qui s'y propagent. Sur la Terre, on s'intéresse essentiellement aux ondes progressives émises par les séismes, la mesure du temps d'arrivée au sismographe permettant de remonter aux propriétés du milieu traversé par l'onde. Ce type d'analyse est également possible à la surface du Soleil dont la surface est résolue. La situation est un peu différente en sismologie stellaire, puisqu'au lieu des ondes progressives, on utilise les modes propres d'oscillation de l'étoile dont on mesure les fréquences.

Un mode propre est une solution harmonique en temps (i.e. $\propto \exp -i\omega t$) des équations linéaires régissant l'évolution des perturbations de faible amplitude d'une solution d'équilibre (ou stationnaire) d'un système (on parle également de mode normal). Physiquement, il peut être vu comme une onde progressive confinée dans une cavité et interférant positivement avec elle-même pour donner lieu à une onde stationnaire[1]. La fréquence du mode propre ω dépend alors des propriétés du fluide contenu à l'intérieur de cette cavité.

Donc, si on parvient à mesurer une fréquence de pulsation et à identifier le mode propre qui lui correspond, on disposera d'une information sur le fluide contenu à l'intérieur la cavité du mode. Cette phrase souligne à la fois l'énorme potentiel et l'une des principales difficultés de la sismologie stellaire. En effet, chaque fréquence identifiée apportant une nouvelle contrainte sur le modèle d'étoile, on voit comment la sismologie peut augmenter très significativement le nombre d'observable par rapport aux observables classiques que sont la luminosité apparente, la parallaxe, la gravité de surface, la température

[1] si la solution n'est pas axisymétrique, l'onde n'est en fait stationnaire que dans un plan méridien puisqu'elle peut se propager dans la direction azimutale ; cette situation est similaire à celle d'un guide d'onde

effective et la composition chimique. En particulier, on comprend pourquoi les dizaines de milliers de fréquences mesurées à la surface du Soleil puis identifiées ont pu révolutionner notre connaissance de l'intérieur du Soleil. Mais on voit aussi que, si on ne parvient pas à identifier la fréquence observée avec son mode propre d'oscillation, ou pire, si on l'identifie mais avec un mauvais mode, l'information sur l'étoile sera soit inexistante soit erronée[2].

Pour le Soleil, la possibilité de résoudre la surface visible facilite grandement l'identification puisque les images de la surface peuvent être décomposées sur la base des modes propres. Mais, l'identification des fréquences observées est également relativement aisée si l'on considère les données intégrées sur la surface visible, c'est-à-dire le Soleil vu comme une étoile. Dans ce cas, quatre propriétés essentielles contribuent à la réussite du processus d'identification : (i) les paramètres fondamentaux du Soleil (masse, rayon, température effective, métallicité, inclinaison) sont connus avec précision ; en conséquence, la gamme de modèles de structure interne du Soleil compatibles avec ces contraintes globales est déjà relativement restreinte, (ii) dans l'intervalle des fréquences observées, le nombre de modes propres que l'on s'attend à détecter d'après les calculs théoriques correspond au nombre de fréquences observées, (iii) le calcul des modes et fréquences propres d'un modèle de Soleil donné peut être effectué avec une précision suffisante ; dans la phase d'identification des modes, il faut s'assurer que les erreurs sur les fréquences théoriques n'induisent pas d'erreur sur l'identification des modes. Après la phase d'identification, lorsque l'on cherche le modèle d'étoile qui reproduit le mieux les fréquences, la précision des calculs théoriques doit être significativement supérieure à celle de la détermination observationnelle des fréquences (qui peut être très élevée). On peut ainsi attribuer toute différence entre fréquence calculée et observée au modèle d'étoile et non aux erreurs du calcul d'oscillations. (iv) l'organisation du spectre des fréquences est régulière et bien décrite par une théorie asymptotique des modes propres acoustiques (Tassoul 1980). Cette propriété est essentielle car elle permet de contraindre l'identification des modes directement à partir du spectre de fréquences observé, sans faire appel à des modèles de la structure interne du Soleil. En effet, les espacements réguliers entre les fréquences de modes acoustiques solaires de même degré ou appartenant à un même multiplet permettent d'identifier sans calcul le degré et le nombre azimutal des fréquences observées.

La situation est toujours moins favorable pour les autres étoiles ne serait-ce que parce que leurs

[2] le terme inexistant est un peu exagéré puisque, si l'on comprend bien le mécanisme d'excitation des modes, la simple présence de fréquences de pulsation peut apporter des contraintes sur l'intérieur de l'étoile

paramètres fondamentaux sont moins bien connus. À ce manque de contrainte sur le modèle d'étoile peut s'ajouter le fait que le spectre de fréquence observé est incomplet (on dit aussi lacunaire) dans le sens où le nombre de modes d'oscillation possibles d'après les modèles théoriques dépasse (parfois largement) le nombre de fréquences observées. Le problème de l'identification est alors sous-contraint ce qui conduit à plusieurs identifications possibles. En ce qui concerne la précision du calcul des modes et fréquences propres, le cas d'une étoile isolée sans rotation ni champ magnétique ne pose pas de problèmes (Christensen-Dalsgaard & Mullan 1994). De même, si les effets qui brisent la symétrie sphérique du système (la rotation, le champ magnétique, la binarité) sont suffisamment faibles, les méthodes perturbatives permettent d'obtenir des calculs suffisamment précis. Cela vaut pour le Soleil, les étoiles de type solaire en rotation lente et généralement aussi pour les SdB, les Céphéides, les naines blanches. Néanmoins, la limite de validité des méthodes perturbatives n'étant pas connue, on ne sait pas jusqu'où, c'est-à-dire jusqu'à quelle valeur de la rotation, du champ magnétique, on peut utiliser ces méthodes pour l'identification des fréquences ou la détermination du meilleur modèle d'étoile. Il en va de même pour l'organisation asymptotique du spectre de fréquence (à haute fréquence pour les modes acoustiques et à basse fréquence pour les modes de gravité) qui n'avait été déterminée que pour un système à symétrie sphérique.

Dans ce contexte, les étoiles de type solaire sont des cibles favorables parce qu'elles pulsent dans le régime asymptotique des hautes fréquences acoustiques, les spectres observés ne sont pas lacunaires et les écarts à la symétrie sphérique sont relativement faibles. Et, de fait, des identifications plausibles de fréquences observées sur ce type d'étoile (notamment par Corot) ont été obtenues (Benomar et al. 2009; Deheuvels et al. 2010). Dans un tout autre domaine du diagramme HR, celui des naines blanches, il est possible d'identifier partiellement les fréquences (degré et nombre azimutal) car ces étoiles pulsent dans le régime asymptotique des modes de gravité (Winget et al. 1991).

En revanche, dans le domaine des étoiles massives et de masse intermédiaire de la séquence principale, les exemples convaincants d'identification sont rares et correspondent à des situations particulières plutôt que génériques. En effet, la lacunarité des spectres de fréquence observés (avant Corot !) et les incertitudes sur l'importance des effets non perturbatifs, dus à la rotation ou au champ magnétique, ont empêché une identification fiable de la plupart des fréquences détectées dans ce domaine du diagramme HR. Les exceptions concernent essentiellement des étoiles à faibles $v \sin i$ pour lesquels des contraintes observationnelles supplémentaires sur les modes ont été obtenues par spectroscopie ou photométrie multi-

couleur (Desmet et al. 2009; Dupret et al. 2004; Aerts et al. 2003; Thoul et al. 2003). La spectroscopie permet en effet de contraindre le degré et le nombre azimutal des modes en analysant les déformations des profils de raie d'absorption provoquées par les perturbations de vitesses photosphériques associées aux modes (Kennelly 1994; Zima 2006). La photométrie multi-couleur est basée sur le fait que l'amplitude et la phase des perturbations de luminosité dépendent de la longueur d'onde et que cette dépendance est spécifique au type de mode considéré (Dupret et al. 2003). Ces deux méthodes ont été pour l'instant appliquées en supposant que les écarts à la symétrie sphérique sont faibles et donc que la distribution de surface des modes est représentée par une harmonique sphérique. Plus récemment des régularités dans l'espacement de fréquence ou de période, symptomatiques d'un comportement asymptotique, ont été détectées dans des spectres d'étoile massives et de masse intermédiaire par Corot (García Hernández et al. 2009; Degroote et al. 2010). De nouveau, l'interprétation de ces régularités par les théories asymptotiques existantes n'est valable que si l'écart à la symétrie sphérique est "suffisamment" faible.

La sensibilité photométrique et la durée des observations de Corot ont considérablement modifié notre perception des spectres de ce type d'étoile. Le cas le plus spectaculaire est celui des δ Scuti où jusqu'à 2000 pics de fréquences ont été détectées sur HD18155 dans le transformée de Fourier de la courbe de lumière. Du sol, le précédent record pour les δ Scuti était tenu par les 75 fréquences de FG Vir obtenues grâce à des décennies de campagnes d'observation (Breger et al. 2005). Pour ce type d'étoile, la lacunarité des spectres observés depuis le sol semble donc être simplement un effet de seuil de détection. Les spectres de Corot semblent maintenant trop denses par rapport à ce qui était attendu et la possibilité qu'une partie du signal soit en fait engendrée par des mouvements de convection thermique est actuellement envisagée (Kallinger & Matthews 2010). On notera qu'une telle concentration de fréquence d'oscillation pose également un problème dans l'interprétation des données spectroscopiques ; en effet, la durée et la couverture temporelle des observations ne sont pas suffisantes pour isoler une seule fréquence et donc pour isoler les perturbations du profil d'absorption induites par un seul mode.

Restent les effets non perturbatifs de la rotation qui sont potentiellement importants pour la grande majorité des étoiles massives et de masse intermédiaire, les γ Dor, δ Scuti, Slowly Pulsating B stars, β Cephei, ζ Oph, alors que le champ magnétique joue un rôle significatif pour les roAp, une classe d'étoiles pulsantes faisant partie du groupe des Ap/Bp, étoiles chimiquement particulières à champ fort. À ce stade, il est utile de différencier les deux effets distincts de la rotation sur l'identification des modes. La rotation agit d'une part sur le modèle stationnaire d'étoile et d'autre part sur les modes propres

d'oscillation de ce modèle. On pourrait se dire qu'une modélisation fine de l'effet de la rotation sur la structure de l'étoile n'est pas cruciale car le but de la sismologie est justement d'apporter des contraintes à cette modélisation. Cet argument est valable en principe, mais en pratique il faut d'abord identifier les modes et pour y parvenir un certain niveau de réalisme du modèle d'étoile est nécessaire.

Décrire les effets de la rotation sur les oscillations est évidemment un élément essentiel pour identifier et interpréter les fréquences observées. Lorsque j'ai commencé à travailler sur ce sujet fin 2000, les effets de la rotation avaient été presqu'exclusivement étudiés par des méthodes perturbatives au premier et deuxième ordre en Ω/ω ou dans le cadre de l'approximation traditionnelle, une forme simplifiée des équations pour les modes basse-fréquence qui approxime l'effet de la force de Coriolis (et ne tient pas compte de la force centrifuge). Une première exception concernait les travaux de Clément (une série de 5 articles de 1981 à 1998, Clement (1981, 1984, 1986, 1989, 1998)) qui a cherché à mettre au point un code de calcul de modes propres prenant pleinement en compte les effets de la rotation. L'auteur insiste beaucoup sur les difficultés d'ordre numérique qui ne lui ont pas permis d'obtenir des résultats précis. Néanmoins nous avons retrouvé certains résultats qualitatifs de Clément, notamment sur la concentration des modes p vers l'équateur. La deuxième exception concerne les travaux de Dintrans & Rieutord (2000) qui ont développé un code basé sur des méthodes spectrales qui leur a permis de calculer avec précision l'effet de la force de Coriolis sur des modes de gravité (en négligeant la déformation centrifuge, les effets de compressibilité sur les perturbations et les perturbations de la gravité). Ils ont centré leur étude sur la mise en évidence d'un nouveau type de mode, les modes singuliers, qui bien que n'étant pas directement observables, pourraient jouer un rôle important dans les processus de transport du moment cinétique.

Dans la suite, je vais décrire mes travaux sur (i) la mise au point d'un code de calcul des modes tenant pleinement compte des effets de la rotation, (ii) l'exploration des propriétés des modes calculés numériquement, (iii) une analyse asymptotique des modes acoustiques de haute fréquence basée sur la dynamique des rayons. Une section sera également consacrée au chaos d'onde et à la recherche de pulsations sur Véga, une thématique issue des résultats de la théorie asymptotique.

2.1 Un code d'oscillation pour les étoiles en rotation rapide

Le calcul numérique des modes d'oscillation d'étoile en rotation rapide a été abordé de trois façons différentes (i) la résolution directe du problème aux valeurs propres correspondant à la recherche des

modes normaux, (ii) une méthode basée sur le principe variationnel, (iii) la recherche de solution résonante des équations d'évolution soumise à un forçage périodique. La deuxième méthode utilise le principe variationnel qui fait apparaître la fréquence propre comme un extremum d'une fonctionnelle de l'écoulement. Sa mise en oeuvre par Clement (1984) pour les étoiles non-dégénérées et par Ipser & Lindblom (1990) dans le contexte de la stabilité des étoiles à neutrons suggère cependant qu'il est difficile d'atteindre une précision importante dans le calcul numérique des modes propres. Comme nous le verrons dans la suite, le principe variationnel peut aussi servir à contrôler la validité d'une solution obtenue par une autre méthode. La troisième méthode est a priori plus lourde à mettre en place puisqu'elle nécessite la résolution des équations d'évolution en temps ; elle a notamment été utilisée pour étudier des modes p de bas ordre et des modes f d'étoiles à neutrons (Font et al. 2000).

Nous avons choisi la première méthode qui, après discrétisation, se ramène à la recherche des éléments propres, vecteurs propres et valeurs propres, d'une matrice. Comme les solutions sont non-séparables dans deux directions spatiales, la matrice résultante est de grande taille, $(N \times N)$ où N est égal au nombre de points de discrétisation nécessaire pour représenter le mode dans un plan méridien de l'étoile. C'est un problème numérique classique mais exigeant si l'on veut des solutions dont on maîtrise la précision et qui puissent être obtenues dans un temps raisonnable. D'autant que la précision des fréquences obtenues par des observations spatiales quasi-continues sur des temps de l'ordre de l'année impose des contraintes fortes sur la précision du calcul numérique. Pour des fréquences typiques de modes acoustiques d'une étoile δ Scuti ($\nu = 400 \mu Hz$) observée pendant $T = 150$ jours, la précision relative $\delta\nu/\nu$ des fréquences observées est 8×10^{-5} (où $\delta\nu = 1/T$). On doit donc viser une précision du calcul numérique significativement supérieure pour que les erreurs numériques n'aient pas d'influence sur l'interprétation physique du spectre d'oscillation.

Une difficulté supplémentaire est liée à la géométrie sphéroïdale du modèle d'étoile qui n'est adaptée ni aux coordonnées sphériques ni aux coordonnées ellipsoïdales. Nous avons travaillé dans un système de coordonnées qui épouse la surface de l'étoile, mais le prix à payer est que l'écriture des opérateurs différentiels usuels dans un système de coordonnées non-orthogonales n'est plus standard (et peut même se compliquer sérieusement).

Quand j'ai commencé ce travail, il y avait aussi une part importante d'inconnu puisque la difficulté du calcul numérique est en définitive liée à la nature des modes et que l'on n'avait pas d'information sur ces modes à forte rotation. On savait néanmoins, par la série d'article de Clément sur le sujet, qu'il

s'agissait d'un problème numérique difficile !

On comprend donc que la mise au point d'un code de calcul des oscillations d'étoile en rotation rapide est complexe et que pour obtenir des fréquences et des modes propres précis et reproductibles par d'autres équipes, une certaine méthodologie était nécessaire. Nous avons donc procédé par étapes, en ajoutant progressivement les ingrédients physiques (mode acoustique : déformation centrifuge, inhomogénéité de la vitesse du son, force de Coriolis, modèles réalistes d'étoiles ; modes de gravité ; non-adiabaticité) ce qui nous a également aidé dans l'interprétation physique des résultats.

Dans la suite, nous décrivons plus en détail le problème aux valeurs propres (Sect. 2.1.1) et le choix des méthodes numériques employées (Sect. 2.1.2), puis nous rappelons les différentes étapes de la mise au point et les tests effectués sur le code d'oscillation (Sect. 2.1.3).

2.1.1 Un problème aux valeurs propres bidimensionnel

Les équations régissant l'évolution linéarisée de petites perturbations adiabatiques autour d'un modèle d'étoile en rotation uniforme Ω s'écrivent :

$$\partial_t \rho + \vec{\nabla} \cdot (\rho_0 \vec{u}) = 0, \tag{2.1}$$

$$\rho_0 \partial_t \vec{u} + 2\rho_0 \vec{\Omega} \wedge \vec{u} = -\vec{\nabla} P + \rho \vec{g}_0 - \rho_0 \vec{\nabla} \Psi, \tag{2.2}$$

$$\partial_t P + \vec{u} \cdot \vec{\nabla} P_0 = c_s^2 \left(\partial_t \rho + \vec{u} \cdot \vec{\nabla} \rho_0 \right), \tag{2.3}$$

$$\Delta \psi = 4\pi G \rho \tag{2.4}$$

où les quantités qui caractérisent le modèle d'étoile sont P_0, la pression, ρ_0, la densité, c_s, la vitesse du son, et $\vec{g}_0 = -\vec{\nabla}\left(\psi_0 - \Omega^2 w^2/2\right)$, la gravité effective qui dérive de la somme du potentiel gravitationnel ψ_0 et du potentiel associé à l'accélération centrifuge où w est la distance à l'axe de rotation. Les perturbations sont décrites par six variables dépendantes $\vec{u}$, ρ, P, Ψ qui désignent respectivement les perturbations eulérienne de vitesse, de densité, de pression et du potentiel gravitationnel.

L'accélération centrifuge et l'accélération de Coriolis brisent la symétrie sphérique du problème consis-

tant à rechercher les modes propres d'oscillation d'une d'étoile. La symétrie axiale étant conservée, on peut tout de même décomposer la solution recherchée comme le produit d'une fonction dépendant de l'angle azimutal ϕ, $\exp(im\phi)$, et d'une fonction définie dans un plan méridien, $\mathbf{f}(\mathbf{x_M})$; on se ramène ainsi, pour chaque valeur entière du nombre quantique azimuthal m, à un problème aux valeurs propres bidimensionnel. Il peut en particulier se mettre sous la forme :

$$\mathcal{A}\mathbf{f} = \lambda\mathcal{B}\mathbf{f} + \text{Conditions aux limites} \tag{2.5}$$

où $\mathcal{A}$ and $\mathcal{B}$ sont des opérateurs linéaires, et la valeur de λ est directement reliée à la fréquence de pulsation. En effet, dans leur forme habituelle (2.1), (2.2), (2.3), (2.4), les équations qui régissent l'évolution des petites perturbations sont du type $\partial_t X = ...$; on voit donc que la recherche des modes normaux $\propto \exp -i\omega t$ se met facilement sous la forme 2.5 avec $\lambda = -i\omega$ et $\mathbf{f} = \left(\hat{\rho}, \vec{\hat{u}}, \hat{P}, \hat{\Psi}\right)$, où les amplitudes complexes des variables, $\hat{\rho}$ ..., sont définies par $\rho = \Re\{\hat{\rho}(\mathbf{x_M})\exp(-i\omega t)\}$.

Le problème aux valeurs propres peut évidemment s'écrire sous d'autres formes, notamment si on cherche à réduire au maximum le nombre de variables dépendantes. On obtient alors, dans le cas général, un système du type $\mathcal{P}(\omega)\mathbf{g} = 0$ où $\mathcal{P}$ est un opérateur linéaire agissant sur une nouvelle variable $\mathbf{g}$, mais où la dépendance de $\mathcal{P}$ en fonction de ω n'est plus nécessairement linéaire. On trouvera d'ailleurs des exemples de tels systèmes dans l'annexe (A), où différentes formes des équations régissant les petites perturbations d'un étoile en rotation rapide sont explicitées. Cependant, pour le calcul numérique des modes propres, nous avons toujours mis les équations sous la forme 2.5 car elle est adaptée à la méthode de résolution numérique que nous avons utilisée.

Après discrétisation, le problème aux valeurs propres devient algébrique et s'écrit :

$$AF = \lambda BF + \text{Conditions aux limites} \tag{2.6}$$

où A et B sont des matrices $(N_V N_1 N_2) \times (N_V N_1 N_2)$, F un vecteur colonne de $(N_V N_1 N_2)$ composantes, N_1 et N_2 sont le nombre de point de discrétisation pour chacune des deux coordonnées du plan méridien, et N_V est le nombre de variables dépendantes.

À titre d'exemple, pour calculer le mode montré à la Figure 2.1, les matrices A et B sont 37500×37500 (le nombre de variable pour ce calcul est $N_V = 5$, le nombre de point de grille effectif (ici des points

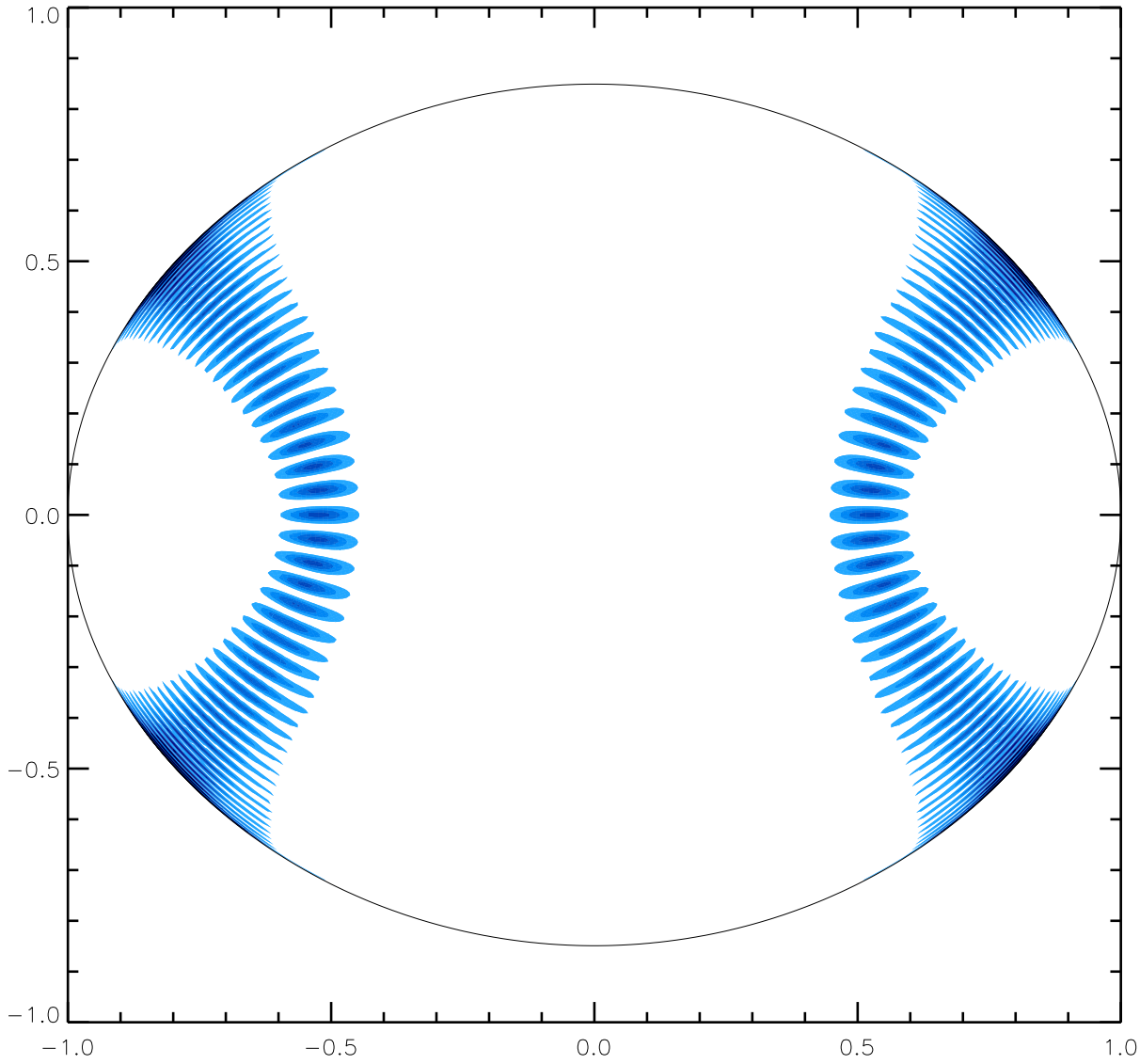

FIG. 2.1 – Distribution spatiale d'un mode acoustique axisymétrique dans un plan méridien. Il a été obtenu en suivant un mode $\ell = 1$, $n = 25$ de $\Omega = 0$ jusqu'à $\Omega/\Omega_K = 0.59$ où $\Omega_K = (GM/R_e^3)^{1/2}$ et R_e est le rayon équatorial.

de collocation associés à des méthodes spectrales) est 100×75). Le stockage mémoire de ces matrices nécessite 15 Go et le temps de calcul pour ce mode a été $\sim 3h$ sur un calculateur Altix 3700 équipé d'un processeur Itanium II à 1,5 Ghz. On voit donc qu'on a intérêt à choisir des méthodes efficaces, c'est-à-dire des méthodes qui, pour une précision donnée sur la fréquence ou sur le mode, minimisent le temps de calcul.

2.1.2 Discussion sur le choix des méthodes numériques

Pour développer un code d'oscillation, il faut choisir (i) une formulation des équations (nombre et choix des variables dépendantes), (ii) un système de coordonnées et une base de vecteur associée, (iii) une méthode de discrétisation, (iv) un algorithme de résolution du problème aux valeurs propres algébrique. Chacun de ces choix a une influence sur l'efficacité globale du code ; nous donnons ici les arguments qui nous ont guidés dans nos choix même si, comme souvent en numérique, il n'est pas possible d'établir à l'avance et de façon certaine la meilleure méthode.

L'efficacité des algorithmes de recherche des éléments propres d'une matrice va d'abord dépendre de la taille et de la structure de la matrice. Une structure simple (matrices symétriques, matrices à bandes, matrices creuses) permettra de simplifier considérablement l'algorithme de résolution. De la structure de la matrice va aussi dépendre son conditionnement, une propriété qui joue un rôle important dans la précision du calcul. En effet, même si, pour une matrice donnée, les algorithmes peuvent déterminer les valeurs propres avec une très grande précision, les coefficients de la matrice ne sont en fait connus qu'aux erreurs d'arrondi près (du fait de la représentation fini des nombres réels dans un ordinateur). Or, la détermination des éléments propres peut être très sensible à ces erreurs ; cela dépend de la structure de la matrice ou plus exactement de son conditionnement.

Le choix de la méthode de discrétisation va avoir une influence directe sur la taille et la structure des matrices A et B. Concernant la taille des matrices, on voit bien qu'une méthode de discrétisation qui minimisera le nombre de points nécessaires pour représenter le mode que l'on veut calculer (avec une précision donnée), minimisera le produit $N_1 N_2$. Cet argument plaide en faveur des méthodes de discrétisation d'ordre élevé en général et des méthodes spectrales en particulier puisque l'erreur de discrétisation des méthodes spectrales décroît exponentiellement avec le nombre de points de collocation (si la fonction que l'on veut représenter est infiniment dérivable). Cela permet d'être économe en nombre de point de calcul par rapport aux méthodes aux différences finies dont l'erreur décroît comme une

puissance du nombre de point.

Concernant la structure des matrices A et B, on sait qu'elles comportent toujours de nombreux termes nuls mais ceux-ci sont répartis plus ou moins régulièrement suivant le problème considéré et la méthode de discrétisation. Par exemple, si on néglige l'accélération centrifuge et que la discrétisation en latitude utilise un développement en harmonique sphérique, l'accélération de Coriolis couplera les coefficients du développement en harmonique sphérique à leur plus proche voisin de même parité (l'équation vérifiée par le coefficient C_ℓ de l'harmonique sphérique Y_ℓ^m, fera donc intervenir $C_{\ell+2}$ et $C_{\ell-2}$). Dans ce cas, il est possible de construire une matrice A à bandes. Lorsque l'étoile est déformée par la force centrifuge, les coefficients du développement en harmonique sphérique sont tous couplés entre eux (tout le moins ceux qui sont associés à des harmoniques sphériques de même parité vis à vis de l'équateur). Cela est du au fait que les termes caractérisant la structure de l'étoile, comme par exemple la vitesse du son ou la fréquence de Brunt-Väisälä, ne sont plus des fonctions triviales de la latitude. Il est encore possible de construire une matrice à bande dans ce cas, si on utilise une méthode aux différences finies dans la direction radiale. En effet, l'équation discrétisée au point i ne fera intervenir que les points adjacents car la méthode de discrétisation est locale. En revanche, si on utilise des méthodes globales dans les deux directions spatiales (comme par exemple les méthodes spectrales basées sur les polynômes de Legendre et de Chebyshev), la matrice n'est plus à bande. Un exemple de la structure d'une telle matrice est est montré dans la thèse de D. Reese (Figure 4.1, p 53).

La géométrie sphéroïdale du modèle d'étoile n'est adaptée ni aux coordonnées sphériques ni aux coordonnées ellipsoïdales (ces coordonnées sont telles que les surfaces de coordonnées sont des ellipsoïdes de mêmes foyers). Si on choisit malgré tout ces coordonnées usuelles, la surface de l'étoile n'est plus une surface de coordonnées et pour fixer les conditions aux limites à cette surface, une méthode spécifique doit être implémentée et testée. On s'attend alors à ce que les interpolations introduites par cette méthode provoquent des erreurs dans le calcul des modes et fréquences propres. Pour éviter ce problème, on peut choisir un système de coordonnées adapté à la forme de la surface de l'étoile ; la difficulté devient alors de nature mathématique (ou calculatoire) puisqu'il faut écrire les opérateurs différentiels usuels dans ce nouveau système de coordonnées.

Différentes formulations des équations des petites perturbations sont possibles (voir l'annexe (A)). On peut notamment chercher à diminuer le nombre de variable dépendante ce qui aura pour effet de réduire la taille des matrices. Un possible effet négatif de cette procédure est d'introduire des dérivées

d'ordre plus élevées des variables dépendantes mais aussi des termes de structure de l'étoile. Cela aura tendance à augmenter l'amplitude des erreurs de troncature.

Sur la base de ces considérations, nous avons choisi les méthodes suivantes : pour l'algorithme de résolution du problème aux valeurs propres algébrique, nous utilisons la méthode itérative d'Arnoldi avec une accélération de convergence de type Chebyshev. Cette méthode décrite dans Saad (1992) est adaptée pour les matrices creuses et elle avait déjà donné de bons résultats pour les calculs des modes gravito-inertiels (Dintrans et al. 1999). Le système de coordonnées choisi épouse la surface de l'étoile en introduisant, en plus des coordonnées sphériques angulaires θ et ϕ, une coordonnée pseudo-radiale ζ définie par $r = f(\zeta, \theta)$ et telle que $\zeta = 1$ décrit la surface. La base naturelle associée à ces coordonnées, définie par $(\vec{E}_\zeta = \partial\vec{OM}/\partial\zeta, \vec{E}_\theta = \partial\vec{OM}/\partial\theta, \vec{E}_\phi = \partial\vec{OM}/\partial\phi)$, permet d'exprimer relativement simplement les opérateurs vectoriels dans ce système de coordonnées non-orthogonales. La méthode de discrétisation est une méthode spectrale basée sur les harmoniques sphériques en θ et ϕ et sur les polynômes de Chebyshev dans la direction pseudo-radiale. D. Reese a également développé une version du code qui utilise des méthodes aux différences finies dans cette direction. Les équations sont mises sous la forme Eq. (2.5) et les variables dépendantes sont choisies de telle sorte qu'elles aient un comportement régulier au voisinage de la surface de l'étoile (ce point est considéré en détail dans Reese (2006)).

2.1.3 Développement, tests et précision du code

Développement et tests

Le code a été développé par étapes, en testant systématiquement les nouveaux éléments introduits. Les différentes étapes ont été les suivantes :

1. ***Modes acoustiques adiabatiques d'un ellipsoïde de densité constante (Lignières et al. 2001) :***

   L'intérêt de cette configuration est que le problème aux valeurs propres est séparable dans les coordonnées ellipsoïdales. Nous avons résolu numériquement le problème séparable et avons comparé la solution à celle obtenue par le code. Nous avons de plus dérivé une formule analytique pour les faibles aplatissements que nous avons également comparée aux résultats numériques. Ce test nous a donné une certaine confiance dans le traitement de la déformation par la combinaison des

méthodes spectrales et du système de coordonnées qui s'adapte à la surface.

2. ***Modes acoustiques adiabatiques d'un modèle polytropique d'étoile en l'absence de force de Coriolis (Lignières & Rieutord 2004; Lignières et al. 2006,A1) :***

   Physiquement, on rajoute ici essentiellement l'effet de l'inhomogénéité de la vitesse du son. Les équations primitives ont été transformées pour minimiser le nombre de variables dépendantes à trois : la divergence des vitesses, la pression et la perturbation du potentiel gravitationnel (voir l'annexe (A)). Écrire le système d'équations dans les coordonnées sphéroïdales demande alors de longs calculs analytiques. Dans un premier temps, le code numérique associé n'a pu être testé que vis-à-vis de la rotation nulle. Mais, l'étape suivante a permis de s'assurer de sa validité.

3. ***Modes acoustiques adiabatiques d'un modèle polytropique d'étoile (Reese et al. 2006,A2) :***

   Les effets de la force de Coriolis ont été ajoutés dans le cadre de la thèse de D. Reese (2003-2006). L'introduction de cette force dans les équations ne permet plus de réduire le nombre de variables dépendantes tout en conservant la forme (2.5) du problème aux valeurs propres. Le système d'équations codé par D. Reese au cours de sa thèse était donc de nature différente à celui que j'avais codé en l'absence de force de Coriolis. En supprimant la force de Coriolis du nouveau code, on obtenait ainsi un calcul indépendant qui pouvait être comparé aux résultats de l'étape précédente. Cette possibilité a joué un rôle important dans le développement du code puisque cela a d'abord permis de déboguer les premières versions du nouveau code et surtout, lorsque les deux codes ont donné les mêmes fréquences à 10^{-7} près (Reese 2006), on a pu considérer que les calculs sans force de Coriolis étaient très probablement justes. Pour les calculs avec force de Coriolis, D. Reese a introduit un test basé sur la formulation variationnelle des équations.

4. ***Modes acoustiques adiabatiques d'un modèle réaliste d'étoile (Reese et al. 2009) :***

   D. Reese a depuis développé une version du code (appelée TOP) capable de s'adapter à des modèles plus réalistes d'étoiles en rotation rapide. En particulier, dans la direction radiale, il est maintenant possible d'utiliser une méthode aux différences finies ou une méthode basée sur des fonctions polynomiales par morceaux (les splines). Ce nouveau code peut également tenir compte d'une rotation différentielle. Les tests effectués montrent notamment que si le modèle d'étoile n'est pas calculé avec une précision suffisante, le test basé sur la formulation variationnelle des équations est moins fiable.

5. ***Modes de gravité non-adiabatiques d'un modèle polytropique d'étoile (Ballot et al. 2010,A3) :***

   Dans le cadre d'un postdoc à Toulouse, J. Ballot a introduit l'effet de la diffusivité thermique dans le code TOP afin d'une part d'utiliser le plan complexe pour séparer plus facilement les fréquences des modes gravito-inertiels et d'autre part de préparer l'étude des mécanismes d'excitation de type saut d'opacité. Des tests ont été effectués pour les modes de gravité à rotation nulle.

Précision du code

La précision du code a été évaluée en testant l'influence des différents paramètres numériques sur la détermination des fréquences (Lignières et al. 2006, **A1**), (Reese et al. 2006, **A2**), (Ballot et al. 2010, **A3**). Considérons que le modèle d'étoile est donné et ne comporte pas d'erreur. Les deux principaux paramètres numériques pour le calcul des modes sont alors le nombre d'harmonique sphérique et le nombre de polynômes de Chebyshev utilisés pour représenter le mode. Pour étudier, par exemple, l'influence du nombre L_{max} d'harmoniques sphériques, on utilise comme référence la fréquence obtenue pour le calcul le plus résolu ω_{ref} et on détermine l'évolution de $\frac{\omega(L_{max})-\omega_{ref}}{\omega_{ref}}$. Cette quantité atteint en général un plateau qui indique que l'on ne peut plus améliorer la précision sur la fréquence en augmentant la résolution spatiale. Le niveau du plateau est lié aux erreurs d'arrondi dans la détermination des coefficients des matrices A et B et à leur effet sur la détermination des éléments propres. Comme nous l'avons mentionné plus haut, cet effet dépend du conditionnement de la matrice. Il est possible d'en calculer l'amplitude de façon théorique pour une matrice donnée mais le calcul est très long et très coûteux. Nous avons plutôt utilisé une méthode alternative validée par Valdettaro et al. (2007). Elle consiste à effectuer une série de calculs en faisant varier la valeur initiale de l'algorithme itératif d'Arnoldi-Chebyshev autour de la valeur propre ; l'écart-type de la distribution (gaussienne) des valeurs obtenues donne une bonne estimation de cette erreur. En résumé, ces études nous ont montré que nous pouvions maîtriser l'erreur sur le calcul des fréquences et que cette erreur était généralement très inférieure à la précision des données.

Nous avons ainsi déterminé les fréquences propres de ~ 160 modes avec 7 chiffres significatifs pour 16 valeurs différentes de la rotation comprises entre $\Omega = 0$ et $\Omega/\Omega_K = 0.59$ où $\Omega_K = (GM/R_e^3)^{1/2}$, R_e étant le rayon équatorial de l'étoile (elles sont publiées en annexe de la thèse de Reese (2006)). Le modèle d'équilibre est un modèle d'étoile polytropique d'indice $\mu = 3$ en rotation solide dont la solution est connue et peut être reproduite sans grande difficulté. Dans ce calcul c'est en fait la précision avec

laquelle le modèle polytropique a été obtenu qui limite la précision relative sur les fréquences à 10^{-7}. Nous espérons que ces fréquences pourront servir de référence à d'autres groupes qui souhaitent développer et tester leur code d'oscillation. C'est d'ailleurs le cas avec le modèle qui est actuellement développé au LESIA dans le cadre de la thèse de R. Ouazzani.

2.2 Exploration du spectre d'oscillation par le calcul numérique

Nous avons calculé numériquement des modes propres et étudié l'évolution de leurs propriétés avec la rotation. Étudier les modes propres d'un système non séparable par le calcul numérique présente des difficultés spécifiques qui sont rappelées ci-dessous (Sect. 2.2.1). Ensuite, la méthode d'exploration du spectre d'oscillation que nous avons utilisée est décrite (Sect. 2.2.2) ; puis, les résultats obtenus sur la limite de validité des méthodes perturbatives et la découverte d'une nouvelle forme de régularité dans le spectre sont présentés (Sect. 2.2.3, Sect. 2.2.4).

2.2.1 Difficultés inhérentes à l'étude numérique d'un problème aux valeurs propres non-séparables

L'étude des modes propres dans le cas à symétrie sphérique entièrement séparable présentent plusieurs différences essentielles avec le cas 2D qui nous intéresse ici. En effet, à symétrie sphérique, la partie numérique du calcul des modes propres se réduit à la résolution d'un problème aux valeurs propres 1D qui donne à la fois la fréquence propre et la dépendance radiale $f(r)$ du mode pour des valeurs prédéfinies de ℓ et m. Une solution de ce problème est immédiatement classifiée par ℓ, m et le nombre quantique radial n que l'on détermine facilement (par exemple) en comptant le nombre de noeuds radiaux de la fonction $f(r)$. Par ailleurs, le calcul du spectre de fréquences est facilité par le fait que les fréquences propres sont généralement régulièrement réparties sur la droite réel, l'écart entre deux fréquences propres consécutives étant appelé la grande différence. La situation est radicalement différente dans une étoile en rotation rapide. En premier lieu, une solution du problème aux valeurs propres ne donne plus le mode propre le long d'un rayon de l'étoile mais dans un plan méridien. Cela complique sérieusement l'analyse du résultat car il n'y a pas de raison pour que la répartition spatiale du mode dans un plan méridien soit suffisamment régulière pour être classifiée simplement. En effet, à symétrie sphérique, le réseau des lignes nodales de $f(r,\theta)$ est régulier et peut être caractérisé par deux nombres entiers, n et

$\ell - |m|$ en l'occurrence, alors que, comme l'illustre la Figure 2.2, ce n'est plus nécessairement le cas à rotation rapide. En second lieu, le spectre est aussi beaucoup plus dense que dans le cas séparable. En effet, dans un intervalle de fréquence donné, le spectre contient un nombre de fréquences équivalent à toutes les fréquences $\omega_{n\ell}$ d'un modèle sphérique dans cet intervalle, alors que, dans le cas sphérique, ce nombre se réduisait aux fréquences ω_n contenues dans l'intervalle. Dans le domaine acoustique, la densité des fréquences (définie comme le nombre de mode par intervalle de fréquence) augmente avec ω ; dans le domaine des ondes gravito-inertiels, et dans le cadre de l'approximation adiabatique, le spectre est même dense au sens mathématique du terme. Une conséquence de la densité du spectre de fréquences propres est la coexistence dans un faible intervalle de fréquence de modes possédant des échelles spatiales très différentes. Comme l'algorithme de recherche des valeurs propres en fournit plusieurs (en général 4) autour d'une valeur cible, le nombre de modes effectivement résolus dépendra de la résolution numérique choisie. Le fait que le résultat d'un calcul numérique dépende de la résolution numérique choisie complique évidemment l'exploration du spectre.

Finalement, une autre source de difficulté vient du phénomène de croisement évité qui est lié au fait que deux modes d'une même classe de symétrie ne peuvent pas être dégénérés. Comme le montre la Figure 2.3, si les fréquences de deux de ces modes tendent à se croiser lorsque on augmente la rotation, il y a un croisement évité. Lorsque l'écart entre les deux fréquences est minimum, les modes sont mixtes dans le sens où ils combinent les caractéristiques des modes avant le croisement (voir la Figure 2.4). Cela posera un problème de résolution numérique dans le cas d'un croisement évité entre un mode résolu et un mode non résolu.

Pour l'ensemble de ces raisons, il était peu probable que l'on arrive à comprendre l'effet de la rotation sur les modes en effectuant par exemple une recherche de mode propre à une rotation donnée et pour une résolution numérique donnée. La méthode d'exploration que j'ai choisie consiste à partir d'un ensemble de modes calculés pour une étoile à rotation nulle et de suivre chacun de ces modes en augmentant progressivement la rotation. Cette méthode a l'avantage de pouvoir associer les modes à rotation non nulle à quelque chose de connu, c'est-à-dire, le mode correspondant à rotation nulle et ses nombres quantiques n, ℓ, m. Bien que longue et quelque peu fastidieuse, la méthode s'est avérée tout à fait adaptée pour comprendre les effets de la rotation sur les modes étudiés. Les modes que nous avons suivis sont les modes qui, à rotation nulle, sont les plus facilement détectables en sismologie stellaire, c'est-à-dire les modes de bas degré pour lesquels l'effet d'annulation dû à l'intégration des perturbations sur le

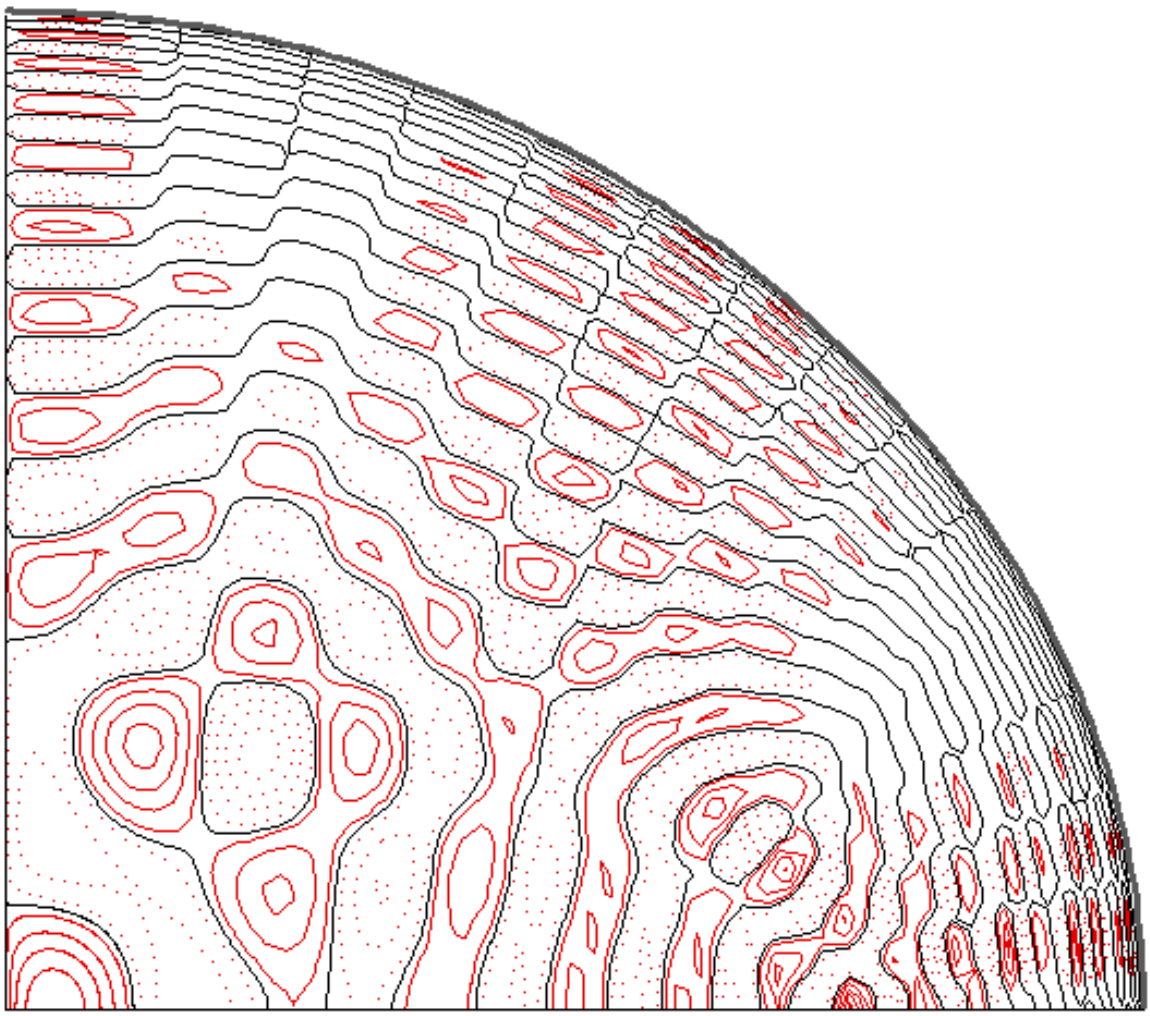

FIG. 2.2 – Distribution spatiale d'un mode acoustique axisymétrique dans le plan méridien d'un modèle d'étoile à une rotation de $\Omega/\Omega_K = 0.59$ où $\Omega_K = (GM/R_e^3)^{1/2}$ et R_e est le rayon équatorial. Des isocontours de l'amplitude de la perturbation eulérienne normalisée par la fonction α définie par Eq. (A.5) et la racine carré de la distance à l'axe de rotation sont représentés. Le réseau des lignes nodales (en noir) est irrégulier et ne permet pas, comme dans le cas sphérique, de caractériser la distribution spatiale du mode par deux nombres entiers bien définis.

disque stellaire est le plus faible. Il était en effet assez naturel de supposer que les modes les plus visibles à rotation nulle allaient rester les plus visibles à rotation plus élevée. Nous verrons néanmoins dans la suite que cette hypothèse ne s'est pas révélée exacte puisqu'à rotation élevée, les modes dits chaotiques, peuvent être aussi visibles alors qu'ils sont issus de modes de relativement haut degré à rotation nulle.

2.2.2 Suivi des modes

Le suivi individuel de mode depuis la rotation nulle a d'abord été effectué pour une gamme de mode acoustique de relativement bas degré $\ell = 0 - 7$, d'ordre radial inférieur à $n = 10$ et axisymétrique, pour un modèle d'étoile polytropique d'indice $\mu = 3$ et jusqu'à une rotation de $\Omega = 0.59\Omega_K$ en utilisant un code qui ne tient pas compte de la force de Coriolis (Lignières et al. 2006, **A1**). Un autre suivi a ensuite été réalisé par D. Reese d'abord pour les modes de bas degré $\ell = 0 - 3$, d'ordre radial inférieur à $n = 10$ et de nombre azimutal $m = -\ell, ..., \ell$ (Reese et al. 2006, **A2**), puis dans la gamme des hautes fréquences $n = 21 - 25$ (Reese et al. 2008, **A4**). Finalement, toujours pour les mêmes modèles d'étoile, un suivi des modes de gravité a été effectué par J. Ballot en partant des modes $\ell = 1$, $n = 1$–14, $m = -\ell, ..., \ell$ et des modes $\ell = 2$–3, $n = 1$–5, 16–20 , $m = -\ell, ..., \ell$ (Ballot et al. 2010, **A3**). Pour réaliser ce suivi, il faut pouvoir associer entre eux les modes calculés à deux rotations voisines. Pour ce faire, nous avons utilisé essentiellement des critères basés sur les degrés dominants dans le spectre de puissance de la décomposition en harmonique sphérique du mode (Lignières et al. 2006, **A1**), (Reese et al. 2006, **A2**), (Ballot et al. 2010, **A3**) mais aussi sur la fonction de corrélation des modes propres (Ballot et al. 2010, **A3**). Ces trois études ont montré que, au moins dans la gamme de paramètres considérée, le suivi des modes depuis la rotation nulle est possible. Ce résultat est illustré à la Figure 2.3 où l'on voit l'évolution avec la rotation de l'ensemble des fréquences $\ell = 0 - 7$, $n \leq 10$ (Lignières et al. 2006, **A1**).

La principale difficulté que nous avons rencontrée vient des croisements évités car, au moment où les modes ont un caractère mixte, un label ne peut pas leur être attribué sans ambiguïté (Figures (2.3)-(2.4)). Cette difficulté d'ordre théorique est la cause principale des défaillances des procédures de suivi automatiques mises en place dans Reese et al. (2006, **A2**) et Ballot et al. (2010, **A3**). Néanmoins, le nombre et l'intensité des croisements évités restent suffisamment limités pour permettre le suivi des modes de bas degré.

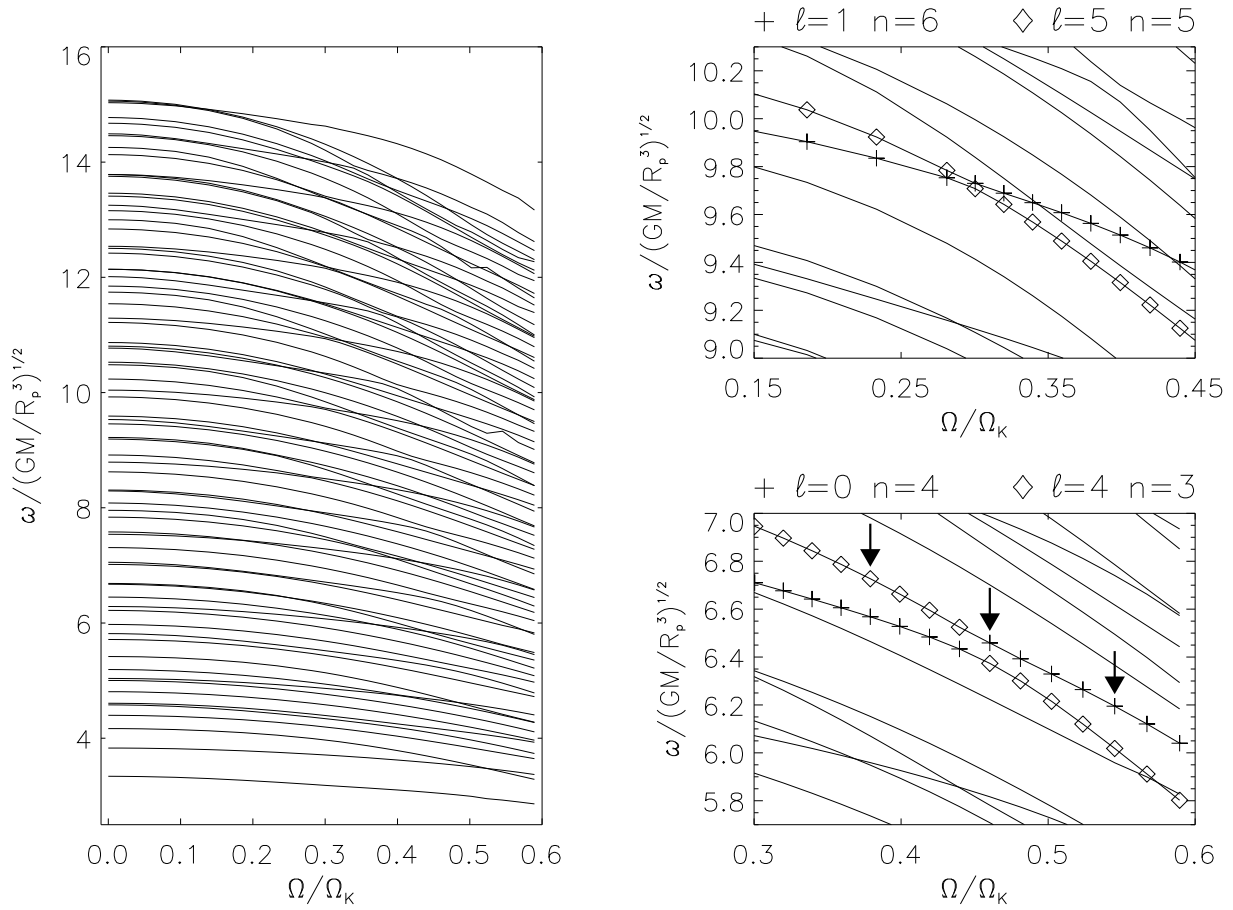

FIG. 2.3 – Suivi des modes acoustiques $\ell = 0 - 7$, $n \leq 10$, $m = 0$ en augmentant progressivement la rotation du modèle polytropique d'étoile de $\Omega = 0$ jusqu'à $\Omega/\Omega_K = 0.59$. La figure de gauche donne une vision globale de l'évolution des fréquences des modes en fonction de la rotation. Les figures de droite sont des agrandissements qui montrent le phénomène de croisement évité entre deux modes de la même classe de symétrie. La figure suivante montre l'évolution de la distribution spatiale des modes pendant le croisement entre les modes ($\ell = 0$ $n = 4$) et ($\ell = 4$ $n = 3$).

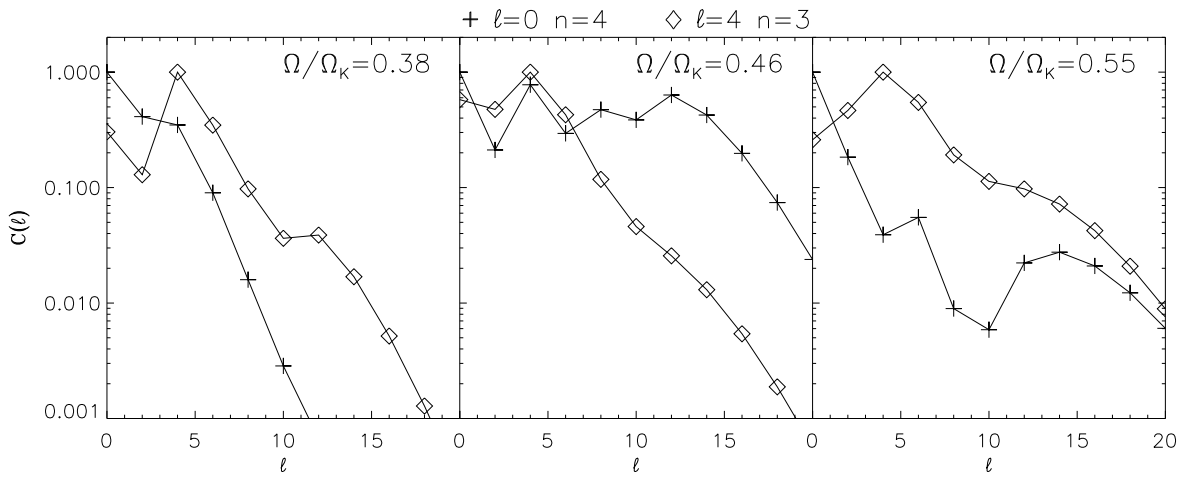

FIG. 2.4 – Coefficients de la décomposition en harmonique sphérique de deux modes au cours d'un croisement évité entre les modes ($\ell = 0 \quad n = 4$) et ($\ell = 4 \quad n = 3$) montré à la figure précédente. Les modes qui ont une identité claire avant et après le croisement évité sont mixtes lorsque la séparation entre les fréquences est minimale.

2.2.3 Domaine de validité des méthodes perturbatives

Ces méthodes de calcul des modes propres font l'hypothèse que les effets de la rotation sont suffisamment faibles pour être traités de façon perturbative. En l'absence de code prenant en compte complètement les effets de la rotation, elles ont été l'unique moyen d'aborder la sismologie des étoiles en rotation. Le problème majeur dans leur utilisation était que leur limite de validité n'était pas connue. Notre code de calcul des modes prenant pleinement en compte les effets de la rotation sur les modes a permis de déterminer cette limite pour la première fois, d'abord pour les modes acoustiques (Lignières et al. 2006, **A1**), (Reese et al. 2006, **A2**), (Reese et al. 2008, **A4**) puis pour les modes de gravité (Ballot et al. 2010, **A3**) de modèles polytropiques d'étoile. Les Figures (2.5)-(2.6) visualisent les limites des méthodes perturbatives.

Considérons d'abord les modes acoustiques d'une étoile de masse intermédiaire de type δ Scuti ($M = 1.9 M_\odot$ et de rayon $R = 2.3 R_\odot$). Pour les modes de bas degré et d'ordre radial inférieur à 10, nos résultats indiquent que l'erreur sur les fréquences calculées par des méthodes perturbatives jusqu'à l'ordre 3 devient supérieure à la précision des données Corot (0.08μ Hz) lorsque la vitesse équatoriale de l'étoile dépasse 50 km s^{-1}. Cela exclut la majorité des étoiles pulsantes de cette gamme de masse. En revanche, les méthodes perturbatives d'ordre 2 restent le plus souvent valides pour identifier les modes acoustiques des étoiles de type-solaire, ce qui est un résultat essentiel pour l'exploitation des données

de Corot et Kepler notamment. On s'aperçoit également que, pour les modes de bas degré considéré, la limite de validité diminue avec la fréquence (l'ordre radial). Ce comportement ne peut pas être du à la force de Coriolis car, en effectuant des calculs avec et sans force de Coriolis, nous avons montré que celle-ci jouait un rôle négligeable pour les ordres radiaux supérieurs à $4-5$. Cela se comprend car, pour des fréquences de mode croissantes, le temps caractéristique de la force de Coriolis, $1/(2\Omega)$, devient forcément beaucoup plus long que la période des oscillations. Cela veut donc dire que la qualité de l'approximation des effets géométriques de la force centrifuge par la méthode perturbative diminue avec la fréquence. Qualitativement, l'augmentation de l'erreur des méthodes perturbatives avec la fréquence peut s'interpréter simplement en utilisant l'analogie de la corde vibrante fixée entre deux murs. La relation qui donne les fréquences propres $\omega_n = n\pi c/L$ (où L est la distance entre les murs et $c = T/\mu_L$ s'exprime en fonction de la tension de la corde T et de sa densité linéaire μ_L) montre qu'une erreur $|\delta L|$ sur L produit une erreur sur la fréquence $|\delta\omega| = \omega|\delta L|/L$ qui croît avec fréquence. L'exemple de la corde vibrante montre ainsi qu'une erreur sur la géométrie de la cavité résonante induit une erreur sur la fréquence proportionnelle à la fréquence.

On verra à la Sect. 2.3 que la théorie asymptotique des modes acoustiques donne une vision plus fine des modifications dans la nature des modes provoquées par la déformation centrifuge. Mentionnons également que d'autres groupes (Charpinet et al. 2008; Ouazzani et al. 2009; Burke et al. 2010; Suàrez et al. 2010) utilisent aujourd'hui les fréquences calculées dans Reese et al. (2006, **A2**) pour déterminer les limites de l'approche perturbative dans différentes configurations spécifiques.

Pour les modes de gravité de bas degré, nous montrons que la validité des méthodes perturbatives dépend fortement du domaine de fréquence considéré (Ballot et al. 2010, **A3**). Pour les bas ordres radiaux c'est-à-dire les modes g de plus haute-fréquence, le domaine de validité est significativement plus étendu que pour les modes acoustiques. La méthode perturbative au second ordre est en effet valable jusqu'à 100 km/s pour une γ Doradus typique de masse $M = 1.55M_\odot$ et de rayon $R = 1.6R_\odot$, et jusqu'à 150 km/s pour une étoile B de masse $M = 4M_\odot$ et de rayon $R = 7R_\odot$. Cela veut dire que l'effet de la force centrifuge est moins important sur les modes g que sur les modes p. Un autre effet, qui va dans le même sens, est que l'énergie des modes g est concentrée dans les régions internes de l'étoile où la déformation centrifuge se fait moins sentir. La situation est différente dans la gamme des basses fréquences (ou des modes d'ordre radial élevé) car le domaine de validité des méthodes perturbatives se réduit fortement. Pour la même étoile γ Doradus, la méthode perturbative à l'ordre 2 n'est maintenant valide que jusqu'à

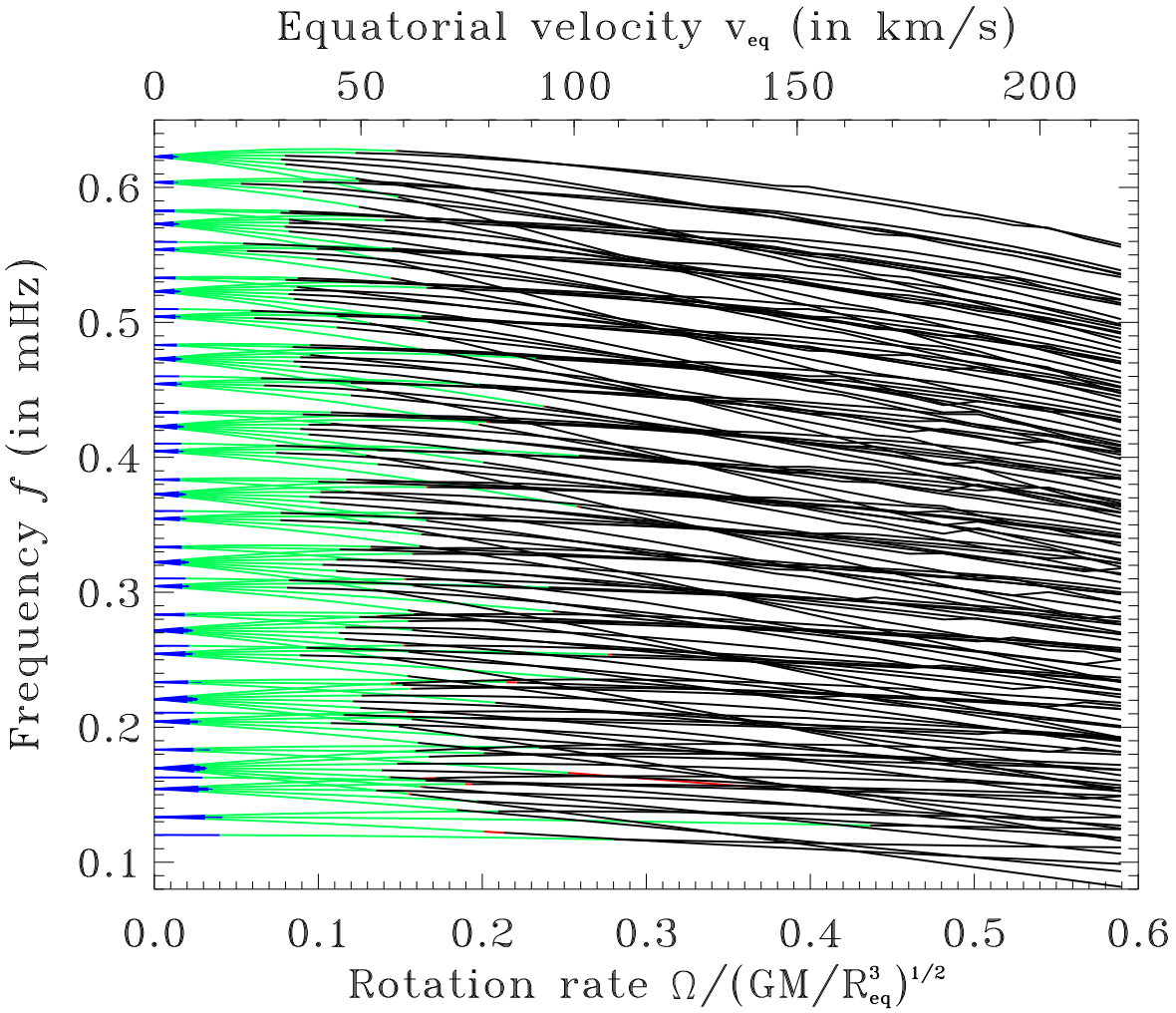

FIG. 2.5 – Domaine de validité des méthodes perturbatives au premier (bleu), deuxième (vert) et troisième (rouge) ordre pour le calcul des modes acoustiques avec une erreur correspondant à la précision de Corot (0.08 μHz) et une étoile de type δ Scuti ($M = 1.9M_\odot, R = 2.3R_\odot$). Les fréquences des modes acoustiques $\ell = 1 - 3, \quad n \leq 10, \quad m = -\ell, ..., +\ell$, ont été suivies depuis la rotation nulle jusqu'à $\Omega/\Omega_K = 0.59$.

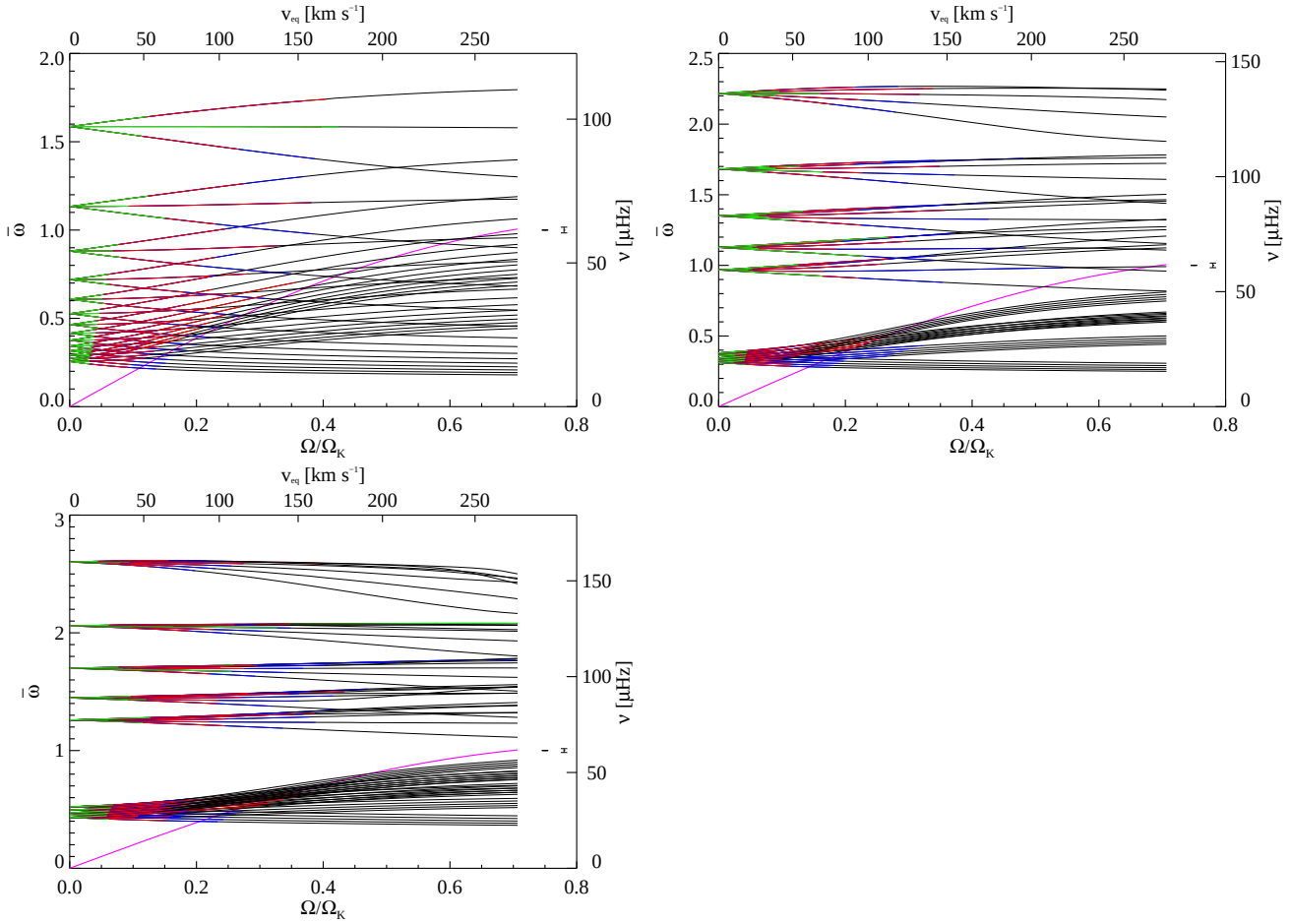

FIG. 2.6 – Domaine de validité des méthodes perturbatives au premier (vert), deuxième (rouge) et troisième (bleu) ordre pour le calcul des modes de gravité avec une erreur correspondant à la précision de Corot (0.1 μHz) et une étoile de type γ Doradus ($M = 1.55M_\odot, R = 1.6R_\odot$). Les fréquences des modes de gravité $\ell = 1$, $n =$ 1–14, $m = -\ell, ..., \ell$ (figure en haut à gauche), $\ell = 2$, $n =$ 1–5, 16–20, $m = -\ell, ..., \ell$ (figure en haut à droite) et $\ell = 3$, $n =$ 1–5, 16–20, $m = -\ell, ..., \ell$ (figure en bas à gauche) ont été suivies depuis la rotation nulle jusqu'à $\Omega/\Omega_K = 0.71$. La courbe $\omega = 2\Omega$ est représentée en magenta.

50 km s^{-1}. On observe en fait que les méthodes perturbatives sont systématiquement inopérantes pour des fréquences inférieures à 2Ω (comme le montre la courbe $\omega = 2\Omega$ sur la Figure 2.6). Cela est du au fait que les méthodes perturbatives ne prennent pas en compte la modification de la forme de la cavité résonante induite par la force de Coriolis sur les modes sub-inertiels ($\omega < 2\Omega$). On montre en effet, soit par la méthode des caractéristiques (Dintrans & Rieutord 2000), soit par l'approche WKB (Prat 2010), que ces modes sont confinés dans une région équatoriale de la forme $\theta > \theta_c = \arccos[\omega/(2\Omega)]$. Cette diminution du volume de la cavité résonante a un effet direct sur les fréquences, qui n'est apparemment pas pris en compte par la méthode perturbative.

2.2.4 Découverte d'une nouvelle organisation du spectre de fréquence

La structure du spectre des étoiles à faible rotation est caractérisée par des espacements réguliers entre fréquences (pour les modes acoustiques de haute-fréquence) ou entre périodes (pour les modes de gravité de basse fréquence). Ces régularités sont observées dans le spectre de modes-p du Soleil ou dans le spectre de modes-g des naines blanches. Elles sont également établies analytiquement par une approximation WKB de l'équation régissant la partie radiale du mode propre. Cette approximation consiste à chercher une solution de type onde $f(r) = A(r)\exp[i\Phi(r) - i\omega t]$ dans la limite où la longueur d'onde caractéristique de cette solution est très petite devant l'échelle des inhomogénéités du milieu (Gough 2007). En particulier, pour les modes acoustiques de bas degré, on obtient la formule dite de Tassoul :

$$\omega = \frac{\pi}{\int_0^R \frac{dr}{c_s}}(n + (\ell + 1/2)/2 + \alpha) + \mathcal{O}\left(\frac{1}{\omega}\right) \tag{2.7}$$

valable à l'ordre zéro en $1/\omega$ et où c_s désigne la vitesse du son et R le rayon de l'étoile.

La procédure de suivi des modes nous a permis de découvrir que cette structure du spectre étaient détruite par la rotation puis progressivement remplacés par un nouveau type de régularités de la forme :

$$\omega = \Delta_n\, n + \Delta_\ell\, \ell + \alpha \tag{2.8}$$

où $\Delta_n \neq \Delta_\ell/2$ (Lignières et al. 2006, **A1**). Des calculs à plus hautes fréquences ($20 < n < 30$), effectués pour une rotation donnée, ont ensuite confirmé le caractère asymptotique de ces régularités (Lignières & Georgeot 2008, **A6**). C'est important car si la propriété traduit un comportement asymptotique du

système, elle est généralisable à d'autres modèles d'étoile (tant que l'approximation WKB reste valable pour ces modèles). Puis, dans Reese et al. (2008, **A4**), ces résultats ont été étendus aux modes non-axisymétriques ; il a été montré à cette occasion que, comme on s'y attendait, la force de Coriolis et les perturbations du potentiel gravitationnel ne modifiaient pas les résultats. Finalement, dans Reese et al. (2009), ces résultats ont été confirmés pour des modèles d'étoile plus réalistes avec ou sans rotation différentielle. Par analogie avec le cas sans rotation, l'existence de ce nouveau type de régularités et son caractère asymptotique suggérait que la nouvelle organisation pouvait être obtenue à partir d'une théorie asymptotique, même si la façon de généraliser la théorie asymptotique de Tassoul au cas d'une étoile en rotation rapide n'était pas connue. La Sect. 2.3 décrit la construction d'une telle théorie à partir de l'étude de la dynamique des rayons (Lignières & Georgeot 2009, **A7**).

De même, nos travaux récents sur les modes de gravité montrent que la structure en période du spectre à rotation nulle est également détruite à rotation élevée (Ballot et al. 2009). Elle est remplacée par une nouvelle structure que nous sommes en train de caractériser. Nous avons néanmoins déjà observé que cette structure a une forme similaire quoique différente à celle que l'on trouve dans le cadre de l'approximation traditionnelle. Cela suggère de nouveau qu'une théorie asymptotique pourrait rendre compte de ce comportement, ce qui nous a conduit à démarrer une étude de la dynamique des rayons de gravité (voir Sect. 5.1.4).

Au delà de leur interprétation dans le cadre de la dynamique des rayons, ces régularités sont appelées à jouer un rôle essentiel dans la sismologie des étoiles en rotation rapide. Détectées dans un spectre de fréquences observées, elles fourniraient des informations a priori, cruciales pour l'identification des modes. Nous reviendrons sur ce point dans la Sect. 5.1.1 une fois que nous aurons une meilleure idée de la structure globale du spectre de fréquence.

2.3 Une théorie asymptotique basée sur la dynamique des rayons

Dans le cas à symétrie sphérique, l'approximation WKB appliquée à l'équation différentielle ordinaire vérifiée par la composante radiale du mode permet de trouver une solution analytique des modes propres. Nous allons voir que, appliquée au cas des étoiles en rotation rapide, l'approximation WKB mène naturellement à la dynamique des rayons. Nous cherchons donc une solution de type onde $A(\vec{x})\exp[i\Phi(\vec{x})-i\omega t]$ des équations des petites perturbations adiabatiques dans la limite où la longueur d'onde caractéristique

de cette solution $\lambda = 2\pi/|\vec{\nabla}\Phi(\vec{x})|$ est très petite devant l'échelle L des inhomogénéités de la structure de l'étoile. $\Phi(\vec{x})$ est ici une phase généralisée que l'on peut associer à un vecteur d'onde local $\vec{k} = \vec{\nabla}\Phi$. Un développement asymptotique en $\Lambda = L/\lambda$ de la solution sous la forme :

$$\Phi = \Lambda(\Phi_0 + \frac{1}{\Lambda}\Phi_1...) \qquad A = A_0 + \frac{1}{\Lambda}A_1... \tag{2.9}$$

conduit à l'ordre dominant à une équation sur Φ_0 uniquement (c'est l'équation iconale) et à l'ordre suivant à une équation reliant A_0 et Φ_0, et donc à une solution $A_0(\vec{x})\exp[i\Phi_0(\vec{x}) - i\omega t]$.

Dans le cas général l'équation iconale contient les différents types d'onde présentes dans le milieu à savoir, les ondes inertielles, les ondes de gravité et les ondes sonores (voir Sect. 5.1.4). Si on suppose que la fréquence ω est de l'ordre de Λ, on obtient alors une équation iconale pour les ondes sonores seules :

$$\omega^2 = c_s^2(\vec{\nabla}\Phi_0)^2 + \omega_c^2 \tag{2.10}$$

où ω_c, qui augmente fortement près de surface de l'étoile, permet de maintenir les ondes de fréquence $\omega < \omega_c$ à l'intérieur de l'étoile.

Plutôt que de chercher une solution de cette équation aux dérivées partielles directement valable dans tout l'espace, l'approche des rayons consiste à la résoudre le long de trajectoires particulières[3] $\vec{x}(t)$. La solution de Eq. (2.10) le long d'un chemin :

$$\frac{d\vec{x}}{ds} = \vec{k} \tag{2.11}$$

s'écrit :

$$\frac{d\vec{k}}{ds} = \vec{\nabla}\left(\frac{1}{2c_s^2}(\omega^2 - \omega_c^2)\right) \tag{2.12}$$

où s est relié à l'abscisse curviligne σ par $ds = c_s d\sigma/(\omega^2 - \omega_c^2)^{1/2}$. Une propriété essentielle, valable pour une équation iconale générale du type $D(\vec{x}, \vec{\nabla}\Phi, \omega) = 0$, est qu'il est toujours possible de choisir un chemin tel que les équations qui régissent l'évolution de $\vec{x}$ et $\vec{k} = \vec{\nabla}\Phi$ se mettent sous une forme Hamiltonienne (voir Ott (1993) ou Lignières (2010, **A5**) pour une démonstration). C'est déjà évident pour les équations ci-dessus puisque l'équation Eq. (2.12) a la forme de la seconde loi de Newton, où

[3] dans un vocabulaire mathématique, c'est une solution aux caractéristiques.

$W = -\frac{1}{2c_s^2}\left(\omega^2 - \omega_c^2\right)$ est le potentiel dont dérive la force. Il s'agit en l'occurrence d'un puits de potentiel qui permet de conserver les rayons à l'intérieur de l'étoile.

La procédure que nous venons de décrire est classique en physique des ondes puisque c'est elle qui permet de décrire les ondes électromagnétiques dans la limite de l'optique géométrique ou les systèmes quantiques dans leur limite classique. Mais il est important de se rappeler que nous cherchons des modes c'est-à-dire des ondes stationnaires et que l'étude des rayons, qui représentent des ondes progressives de petite longueur d'onde, ne va pas nous donner directement la réponse souhaitée. Il faudra trouver, et c'est là toute la difficulté de la théorie, un moyen d'obtenir ces modes à partir d'une ou plusieurs ondes progressives interférant constructivement. Comme nous le verrons dans la suite, nous avons profité du fait que cette question a été considérée dans le contexte de la mécanique quantique et de l'étude de son lien avec la mécanique classique.

Mais dans un premier temps, il nous faut déjà comprendre quel est l'effet de la rotation sur la dynamique des rayons acoustiques et nous utiliserons pour cela les ressources de la dynamique Hamiltonienne (Sect. 2.3.1). Nous présentons ensuite son interprétation en terme de propriétés des modes (Sect. 2.3.2) et finalement nous décrivons la confrontation de ces prédictions avec le calcul numérique des modes (Sect. 2.3.3). Ces sections résument les résultats des articles Lignières & Georgeot (2008, **A6**) et Lignières & Georgeot (2009, **A7**).

2.3.1 Dynamique des rayons dans une étoile en rotation rapide

Nous avons mis au point un code numérique pour résoudre le système d'équation Eqs. (2.11)-(2.12) et nous avons étudié les propriétés des rayons acoustiques pour des modèles polytropiques d'étoile de rotation croissante. Comme l'a montré l'étude des systèmes Hamiltoniens, la nature de la dynamique est caractérisée par la structure de l'espace des phases $(\vec{x}, \vec{k})$ et c'est donc cette structure et son évolution avec la rotation que nous avons étudiées.

Le moyen standard pour explorer la structure de l'espace des phases est la section de Poincaré. Elle est construite en déterminant l'intersection des trajectoires avec une hypersurface du type $x_1 = \text{cste}$ et, du fait de la conservation de l'énergie, a une dimension $2N-2$, où $2N$ est la dimension de l'espace des phases et N est le nombre de degré de liberté du système.

Notre espace des phases $(\vec{x}, \vec{k})$ a 6 dimensions (avec N=3) mais, grâce à la symétrie axiale du problème, $L_z = r\sin\theta\vec{k}\cdot\vec{e}_\phi$ la projection du moment cinétique, $\vec{L} = \vec{r}\wedge\vec{k}$, sur l'axe de rotation est un invariant,

et l'étude de la dynamique peut donc se ramener à celle d'un sous-système Hamiltonien dans un espace de dimension[4] 4. Pour chaque valeur de L_z, on peut donc facilement visualiser la structure de l'espace des phases car la section de Poincaré sera de dimension 2.

La Figure 2.7 illustre la définition de la section de Poincaré $r = r_P$, et les Figures (2.8)-(2.9) montrent l'évolution de la section de Poincaré avec la rotation dans le cas $L_z = 0$. Nous avons utilisé le vecteur d'onde normalisé par la fréquence, $\vec{k}_\theta/\omega$, car avec cette normalisation, et dans le régime de fréquence qui nous intéresse, la dynamique ne dépend pratiquement plus[5] de ω.

Pour "lire" ces surfaces de Poincaré, il faut savoir qu'il existe deux types de structures dans l'espace des phases, correspondant à deux type de trajectoires. Les trajectoires chaotiques, qui n'ont pas d'autres invariants que l'énergie, parcourent de façon ergodique des régions de dimension 3. Les trajectoires qui possèdent un invariant supplémentaire restent confinées dans des structures de dimension 2 que l'on appelle des tores invariants (car on peut montrer que ces structures ont la topologie d'un tore). La section de Poincaré étant une coupe de l'espace des phases, les tores invariants apparaissent comme des courbes sur la section de Poincaré alors que les zones chaotiques correspondent à des surfaces. Comme l'illustrent les Figures (2.8)-(2.9), les zones chaotiques et les tores invariants se distinguent ainsi clairement sur les sections de Poincaré.

On constate d'abord qu'à rotation nulle l'espace des phases n'est fait que de tores invariants. C'est la propriété caractéristique d'un système intégrable[6]. À faible rotation, on observe la formation de petites zones chaotiques et de nouveaux tores. La zone chaotique centrale devient de plus en grande au fur et à mesure que la rotation augmente, et dans le même temps, deux grandes structures associées à des tores approximativement concentriques émergent clairement. Pour les grandes valeurs de k_θ/ω, on observe des courbes ondulées qui sont la trace de tores qui s'apparentent aux tores du cas sans rotation.

Cette transition douce d'un système intégrable vers un système mixte où des trajectoires chaotiques coexistent avec des trajectoires régulières est caractéristique d'une transition de type KAM (d'après Kolmogorov, Arnold, Moser qui ont donné leur nom a un théorème qui décrit précisément cette transition

[4] Si $\vec{x}_M$ désigne la position du rayon dans un plan méridien tournant autour de l'axe de rotation à la vitesse angulaire $d\phi/ds = L_z/(r\sin\theta)^2$, et $\vec{k}_M = \vec{k} - (\vec{k}\cdot\vec{e}_\phi)\vec{e}_\phi$ est le vecteur d'onde projeté sur ce plan méridien, le problème se réduit à rechercher les solutions du système pour $(\vec{x}_M, \vec{k}_M)$, où le potentiel de l'Hamiltonien réduit est $W_r = \frac{L_z^2}{2(r\sin\theta)^2} - \frac{1}{2c_S^2}\left(\omega^2 - \omega_c^2\right)$.

[5] Cette propriété serait exacte si l'équation de dispersion se réduisait à $\omega = kc_s$, ce qui est le cas en dehors des régions proches de la surface de l'étoile. Elle est encore approximativement vérifiée pour $\omega^2 = k^2c_s^2 + \omega_c^2$ car, du fait de la croissance abrupte de ω_c près de la surface, ce terme agit comme une barrière de potentiel et la position du rebond dépend peu de ω.

[6] en plus de l'énergie et de L_z, la norme du moment cinétique $\vec{L}$ est le troisième invariant ; il est lié à la symétrie sphérique du système.

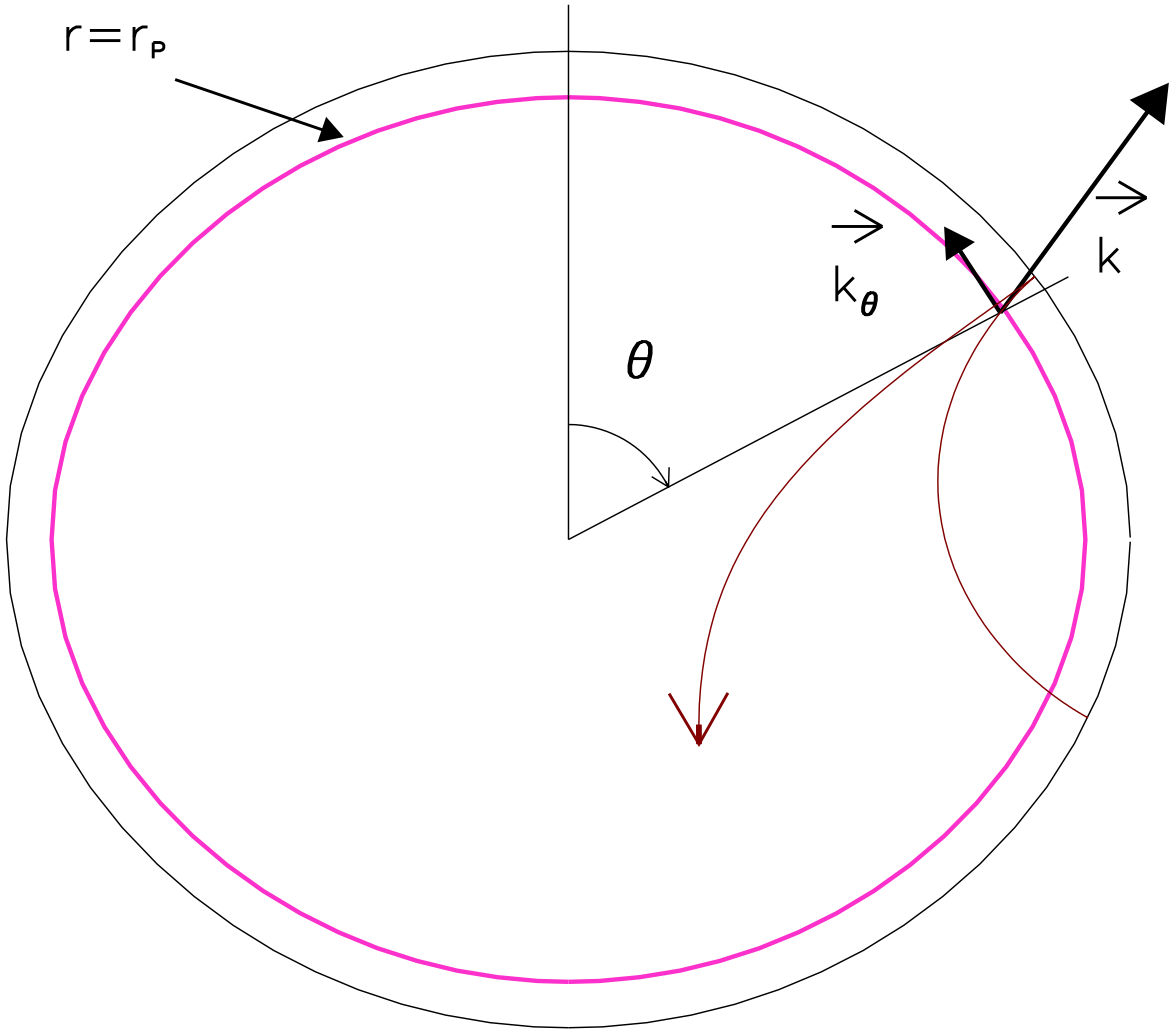

FIG. 2.7 – Intersection d'un rayon acoustique (en marron) avec la courbe $r = r_P(\theta)$ (en magenta). Le point correspondant sur la section de Poincaré est spécifié par la colatitude θ et une composante latitudinale du vecteur d'onde normalisée par la fréquence k_θ/ω.

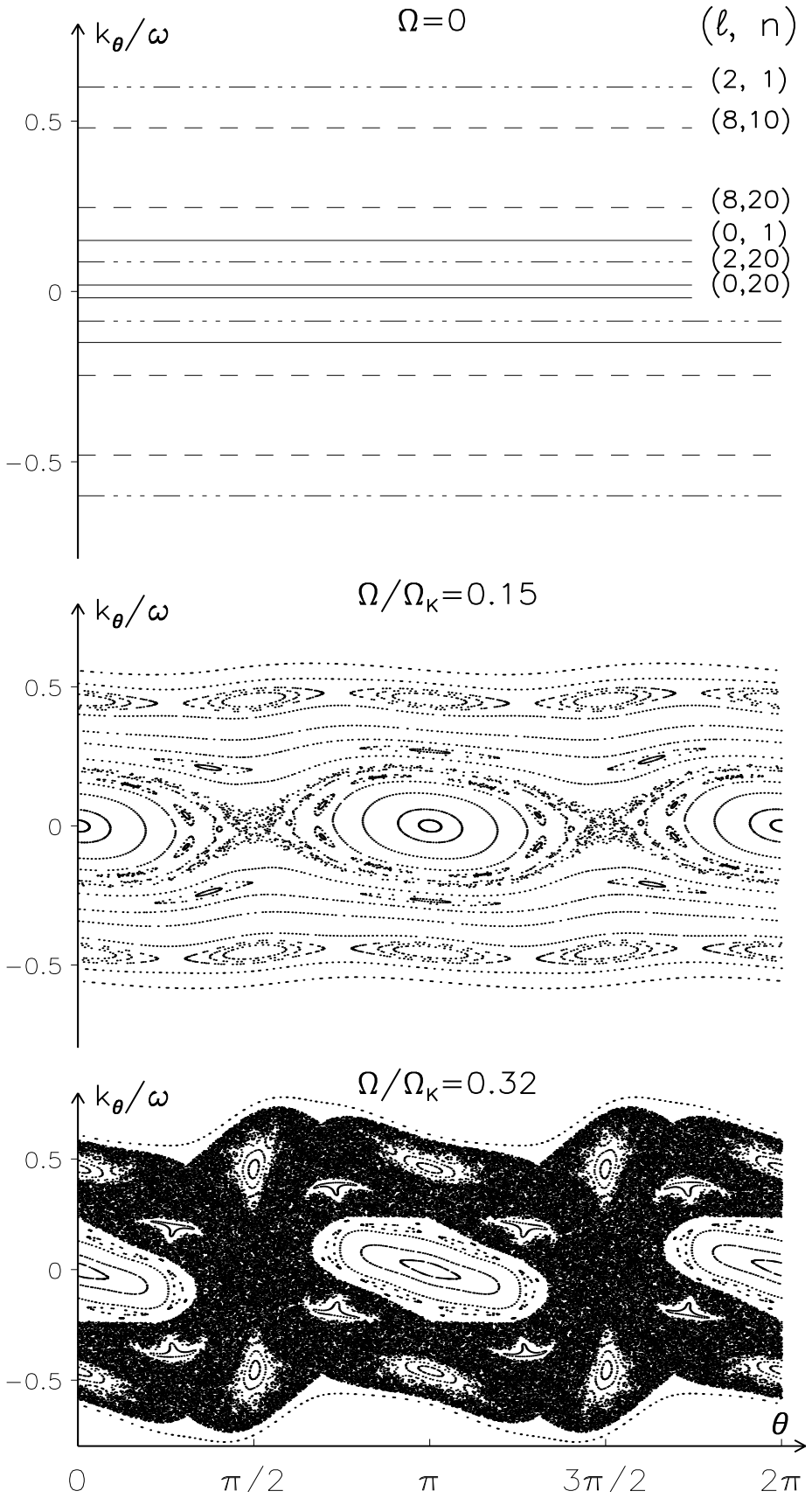

FIG. 2.8 – Trois sections de Poincaré pour des rotations relativement faibles montrant la transition vers le chaos de la dynamique des rayons acoustiques. L'unité de l'ordonnée est $(GM/R_p^3)^{-1/2}$ où R_p est le rayon polaire de l'étoile. À rotation nulle, la correspondance entre les tores et les modes est indiquée.

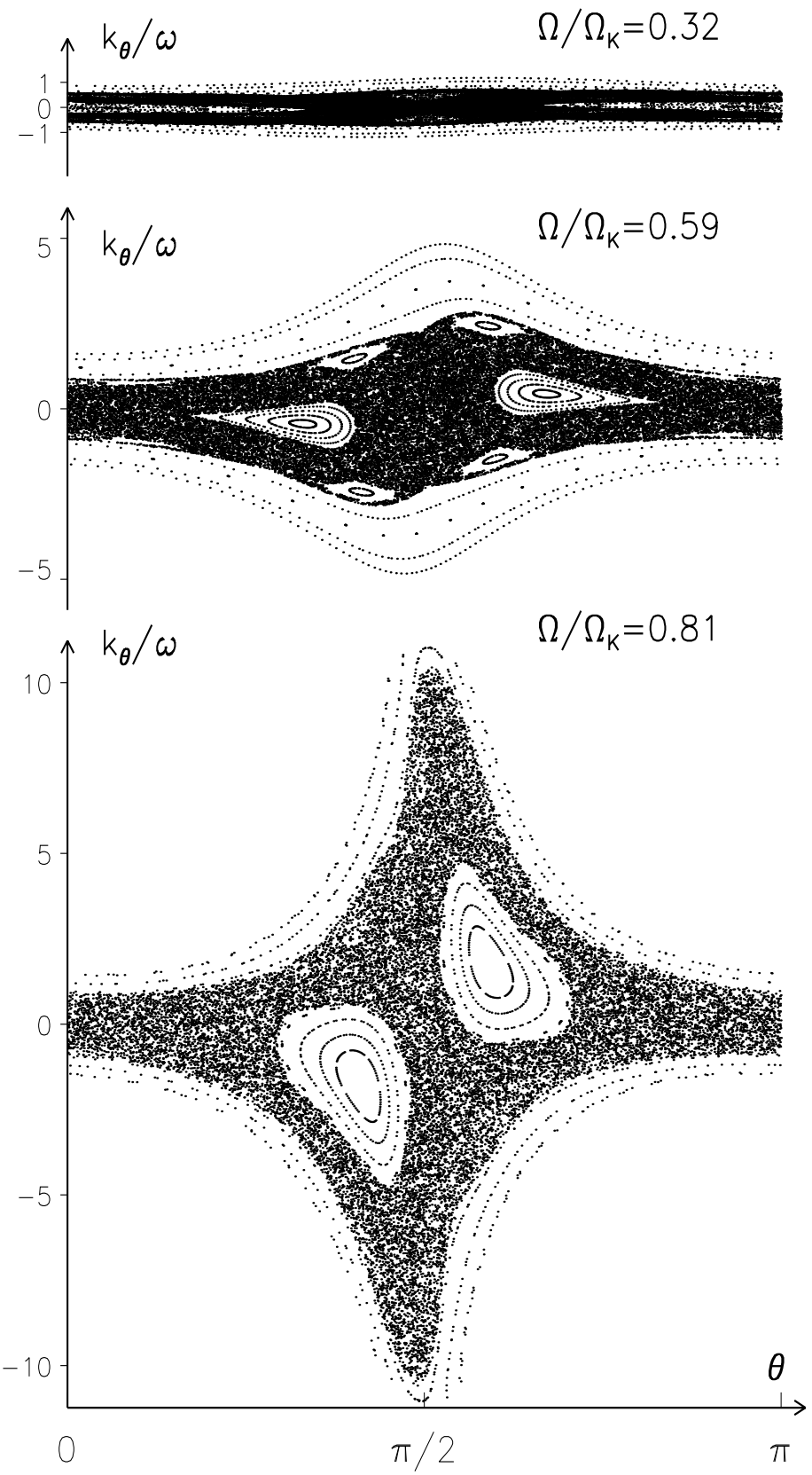

FIG. 2.9 – Trois sections de Poincaré pour des valeurs plus élevées de la rotation (on notera le changement d'échelle de l'ordonnée par rapport à la figure précédente). Les structures dominantes de l'espace des phases sont la chaîne d'îlot centrale formée autour de l'orbite stable de période 2 et une grande région chaotique.

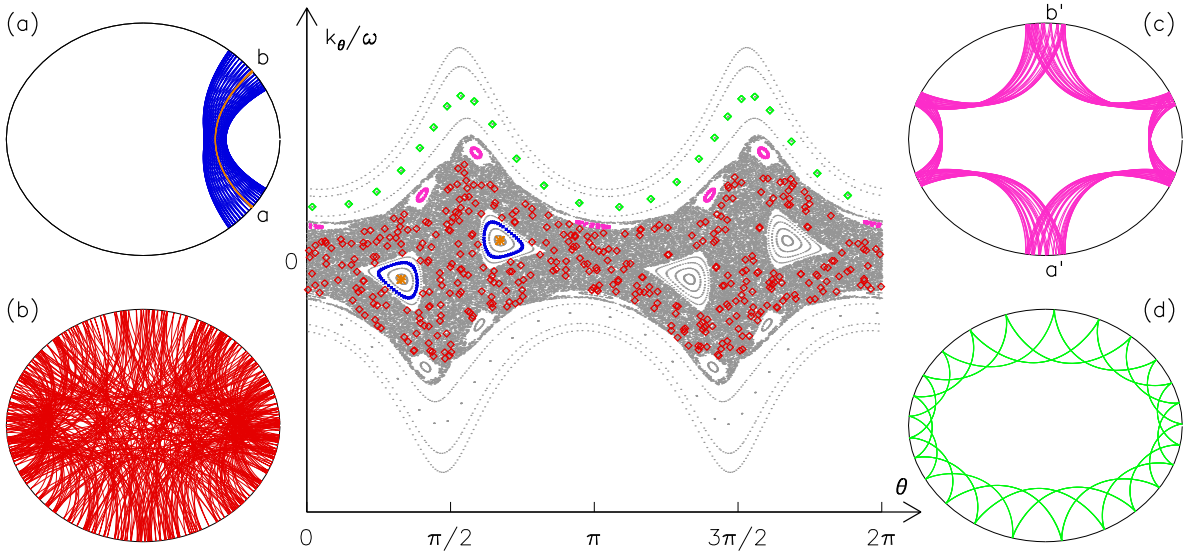

FIG. 2.10 – Section de Poincaré (au centre) et trajectoires de rayons acoustiques typiques à une rotation $\Omega/\Omega_K = 0.59$. Une trajectoire de type "whispering gallery" (vert), deux trajectoires associées à des chaînes d'îlot stable (bleu et magenta) et une trajectoire chaotique (rouge) sont montrées à la fois dans l'espace physique et sur la section de Poincaré. L'orbite stable de période 2, entre les points noté a et b, est aussi montrée en jaune. Un tel espace des phases est dit mixte car des zones chaotiques coexistent avec des tores invariants tels que ceux formés autour des orbites périodiques stables ou ceux associés aux trajectoires de type "whispering gallery".

dans le régime où les perturbations du système intégrable sont petites). Sur la Figure 2.10, on montre les différents types de trajectoires associées aux différentes régions de l'espace des phase. On observe en particulier que les tores concentriques que l'on appelle en fait des chaînes d'îlots stables se forment autour d'une orbite périodique (c'est-à-dire une trajectoire qui reboucle sur elle-même dans l'espace des phases). On voit également que les courbes à grand k_θ/ω correspondent à des trajectoires de type "whispering gallery", qui comme dans le cas à symétrie sphérique, ont une caustique interne bien définie[7].

2.3.2 Interpréter la dynamique des rayons en terme de propriétés des modes : les prédictions du chaos quantique

La construction de solution d'onde stationnaire à partir des rayons a d'abord été étudiée en physique quantique. Dans ce contexte, la limite WKB de l'équation de Schrödinger définit un système dynamique qui correspond à la limite classique du système quantique de départ. Depuis le modèle de Bohr de l'atome d'Hydrogène, de nombreux efforts ont été entrepris pour relier les propriétés classiques et quantiques des

[7] On trouvera plus de détails sur les propriétés de la dynamique dans Lignières & Georgeot (2009, **A7**).

systèmes quantiques et en particulier pour déterminer ses états propres et ses niveaux d'énergie à partir des trajectoires classiques. Les premiers travaux se sont limités au cas des systèmes intégrables et, dans ce cas, une procédure générale a été trouvée pour calculer les états propres et les niveaux d'énergie. Cette procédure est connue sous le nom de quantification semiclassique EBK (Einstein, Brillouin et Keller étant les trois principaux contributeurs). Elle montre que le spectre des niveaux d'énergie d'un système dont la dynamique sous-jacente est intégrable est régulier dans le sens où il est décrit par une fonction analytique de N entiers. Le cas des systèmes Hamiltoniens non-intégrables a été considéré au cours des trente dernières années ; il s'agissait en particulier d'étudier les signatures de la dynamique chaotique d'un système classique sur les propriétés du système quantique associé. Ce thème de recherche s'appelle le chaos quantique et a produit un certain nombre de résultats importants notamment concernant la statistique des niveaux d'énergie. Le spectre des niveaux d'énergie n'est pas régulier comme dans le cas intégrable mais il a été montré expérimentalement et numériquement pour différents systèmes entièrement chaotiques que la statistique des différences de niveaux d'énergie consécutif suit une loi générique, que l'on peut déduire à partir d'arguments heuristiques proposés par Wigner (1932). Cette loi a également été observée dans d'autres systèmes ondulatoires comme les résonateurs micro-ondes ou les blocs de quark, étendant ainsi la notion de chaos quantique à celle de chaos d'onde. Des détails sur le lien entre l'équation de Schrödinger stationnaire et les équations des ondes sonores (ou électromagnétiques), la dérivation de la dynamique Hamiltonienne des rayons et les résultats de l'approche semi-classique mentionnés ci-dessus (quantification EBK et chaos quantique) peuvent être trouvé dans la version écrite du cours que j'ai donné pour l'école de sismologie de Saint Flour (Lignières 2010, **A5**).

Nous avons vu dans la section précédente que la dynamique des rayons acoustiques dans une étoile en rotation rapide est mixte, des régions chaotiques et des régions quasi-intégrables (car structurées par des tores invariants) coexistant dans l'espace des phases. Pour ce type de système, Percival (1973) puis Berry & Robnik (1984) ont prédit que les différentes régions de l'espace des phases étaient quantifiées de façon indépendante de telle sorte que :

- Les sous-spectres de fréquence correspondant aux modes construits dans une région quasi-intégrable sont réguliers et peuvent donc être décrits par une fonction de deux entiers (trois si on compte le nombre azimutal $m = L_z$).
- Les sous-spectres de fréquence correspondant aux modes construits dans une région chaotique sont irréguliers, mais possèdent des propriétés statistiques spécifiques.

Autrement dit, la structure de l'espace des phases reflète la classification physique des modes et la structure du spectre de fréquence.

La structure asymptotique du spectre des oscillations acoustiques peut donc se "lire" sur les sections de Poincaré montrées plus haut. Prenons par exemple la section de Poincaré (Figure 2.10) correspondant à une rotation de $\Omega = 0.6\Omega_K$. On observe 4 principales régions dynamiquement indépendantes, la grande zone chaotique centrale, la chaîne d'îlots stables construite autour de l'orbite périodique $[a, b]$, la chaîne d'îlot stable construite autour de l'orbite périodique $[a', b']$, le domaine des grandes valeurs de k_θ/ω correspondant aux trajectoires de type "whispering gallery" et également structuré par des tores invariants. D'après la conjecture de Percival (1973), le spectre résultant est, dans la régime asymptotique, la superposition de trois sous-spectres réguliers associés aux trois régions quasi-intégrables et d'un sous-spectre irrégulier associé à la zone chaotique. Les sous-spectres réguliers peuvent être modélisés par la méthode de quantification semi-classique EBK. Les propriétés statistiques du sous-spectre associé à la région chaotique sont connues.

Une autre notion importante est la quantité de mode que l'on peut construire dans une région de l'espace des phase. D'après le théorème de Weyl, ce nombre dépend directement du volume occupé par la région. On peut comprendre cette propriété comme une conséquence du fait qu'un mode, comme toute fonction, ne peut être localisé à la fois dans l'espace physique et dans l'espace spectrale (de Fourier) ; il occupe donc un volume fini, de l'ordre de $(2\pi)^N$, dans l'espace des phases $(\vec{x}, \vec{k})$. Bien que la section de Poincaré ne nous montre pas des volumes mais des coupes de l'espace des phases, le rapport entre les surfaces donne semble-t-il une bonne idée des rapports les volumes, c'est du moins ce que nous avons constaté dans un cas particulier. De plus, les sections de Poincaré sont représentées avec la coordonnée normalisée k_θ/ω, ce qui veut dire que l'interprétation des surfaces en terme de nombre de mode dépend du domaine de fréquence considéré. Si on se place à haute fréquence, le volume de l'espace des phases $(\vec{x}, \vec{k})$ et donc le nombre de mode associé à une région donnée dans la section de Poincaré $(\theta, k_\theta/\omega)$ sera plus grand.

On dispose maintenant des outils nécessaires à l'interprétation des sections de Poincaré et de leur évolution avec la rotation : à faible rotation $\Omega = 0.15\Omega_K$, une nouvelle famille de mode apparaît, elle se construit autour d'une orbite périodique polaire. Le nombre de mode de ce type dépend du domaine de fréquence considéré. D'autres structures se forment également autour d'orbite périodique plus longue, et une mince zone chaotique apparaît, le nombre de modes dans ces structures étant beaucoup plus faible

car celles-ci n'occupent qu'un volume réduit de l'espace des phases. Lorsqu'on augmente la rotation le nombre de modes construits autour de l'orbite périodique la plus courte augmente progressivement. Dans le même temps, la zone chaotique centrale augmente également, occupant un volume de plus en plus important. Des structures de plus petites tailles peuvent être présentes à une rotation donnée mais elle ne survivent pas au delà d'une certaine rotation. En revanche, il existe toujours une zone correspondant aux grandes valeurs de k_θ/ω où des modes "whispering gallery" sont construits. Même si l'extension de la zone chaotique avec la rotation rotation tend à la confiner à des valeurs de plus en plus élevées de k_θ/ω.

L'étude des modes non-axisymétriques se fait de la même façon à partir du calcul et de l'interprétation des sections de Poincaré pour des rayons à $L_z \neq 0$ (voir un exemple dans Lignières & Georgeot (2009, **A7**)).

Quels sont les résultats quantitatifs de la théorie asymptotique ? En principe, toutes les zones quasi-intégrables de l'espace des phases peuvent être quantifiées par la méthode EBK. Cependant la procédure générale demande de nombreux calculs de rayons et surtout elle ne fournit pas nécessairement d'expression analytique du spectre. Pour les modes construits autour d'une orbite périodique, nous avons utilisé un formalisme similaire à celui qui permet de trouver les solutions stationnaires des ondes électromagnétiques dans une cavité laser (Lignières & Georgeot 2008, **A6**). La forme du spectre que nous obtenons est la suivante :

$$\omega_{n\ell} = n\delta_n + \ell\delta_\ell + \alpha, \tag{2.13}$$

avec

$$\delta_n = \frac{\pi}{\int_{\rm a}^{\rm b} d\sigma/c_s} \quad \text{and} \quad \delta_\ell = 2\frac{\int_{\rm a}^{\rm b} c_s d\sigma/w^2}{\int_{\rm a}^{\rm b} d\sigma/c_s} \tag{2.14}$$

où σ est l'abscisse curviligne le long de l'orbite périodique. La quantité δ_n peut être calculée facilement et correspond à l'inverse du temps sonore pour parcourir la distance $[a, b]$. En revanche, δ_ℓ s'exprime en fonction de $w(\sigma)$, l'élargissement du faisceau (laser), qui peut être calculé en résolvant le long de l'orbite une équation différentielle qui dépend de la vitesse du son et de sa dérivée seconde dans la direction transverse à l'orbite. La forme des modes associés est :

$$\Phi(\sigma, \xi) \propto H_\ell(\sqrt{2}\xi/w(\sigma)) \exp(-\xi^2/w(\sigma)^2) \exp(-i\phi(\sigma, \xi)) \tag{2.15}$$

où ξ est la coordonnée transverse à l'orbite périodique, H_ℓ est le polynôme d'Hermite de degré ℓ et la phase $\phi(\sigma, \xi)$ est donnée par :

$$\phi(\sigma, \xi) = \omega \int_0^\sigma d\sigma'/c_s - 2(\ell+1) \int_0^\sigma c_s d\sigma'/w^2 + \xi^2/(2c_s R). \tag{2.16}$$

où $R = w/(dw/d\sigma)$ est le rayon de courbure du front d'onde.

Une autre prédiction quantitative concerne la statistique des différences de fréquence consécutive pour les modes issues de la zone chaotique (voir Sect. 2.3.3). Finalement, le nombre de modes associés à chacune des régions de l'espace des phases peut être estimé en calculant leur volume. Nous l'avons fait pour la région des îlots stables et pour la région chaotique à $\Omega = 0.6\Omega_K$.

À ce stade, il me semble intéressant de faire remarquer que, au moment où nous avons construit la dynamique des rayons, le calcul numérique des modes ne nous avait montré "que" les modes associés à la chaîne d'îlots centrale. En effet, à cause des difficultés de l'exploration numérique, nous avions dû nous concentrer sur un nombre restreint de modes (que nous pensions être les plus visibles), ce qui nous avait fait "manqué" une bonne partie de la physique des oscillations d'une étoile à rotation rapide. En comparaison, la dynamique des rayons offre une vision globale de la classification des modes et de la structure du spectre !

2.3.3 Confrontation avec le calcul numérique d'un spectre haute-fréquence de modes acoustiques

Nous avons confronté les prédictions qualitatives et quantitatives de la théorie asymptotique aux calculs numériques des modes. Comme il s'agit d'une théorie asymptotique, l'un des principaux enjeux de cette confrontation est de savoir si les modes acoustiques des étoiles sont dans une gamme de fréquence où cette théorie est valable. De plus, la conjecture de Percival pour les systèmes mixtes peut être remise en cause par la présence de structures de l'espace des phases difficiles à repérer comme des barrières partielles dans la zone chaotique qui laissent passer les rayons mais pas les ondes ou encore par des comportements quasi-réguliers de modes construits dans les zones chaotiques autour d'orbites périodiques instables (connus sous le nom de "scars").

Cette confrontation a été faite en calculant un spectre de fréquences propres aussi complet que possible dans un intervalle de fréquences correspondant à des modes de type solaire (c'est-à-dire des

ordres radiaux allant de $n = 20$ à $n = 30$) pour une rotation donnée $\Omega = 0.6\Omega_K$. En fait, grâce à la structure de l'espace des phases, nous savons qu'au delà d'une certaine valeur de k_θ/ω tous les modes sont de type "whispering gallery". Donc, dans un intervalle de fréquence donné, si on choisit une résolution numérique qui permet de résoudre des modes "whispering gallery", on sait que l'on pourra résoudre tous les modes dans la région des plus petites valeurs de k_θ dans la même gamme de fréquence. De plus, les modes qui ne seront pas calculés avec cette résolution sont les modes "whispering gallery" correspondant à des plus grandes valeurs de k_θ donc à des plus petites longueurs d'onde en latitude. La résolution utilisée pour ces calculs a été $L_{max} = 150$ et $N_r = 100$.

Nous avons ainsi calculé de l'ordre de 300 modes axisymétriques. Dans certains cas la classification se fait sans difficulté en comparant la trajectoire au mode dans l'espace physique. Néanmoins, ce n'est pas toujours aussi évident et dans ce cas on peut utiliser des fonctionnelles qui donne une représentation du mode dans l'espace des phases. Nous avons utilisé la fonction de Husimi qui s'apparente à une projection du mode sur une base de paquets d'onde gaussien $\exp(-\|\vec{x}' - \vec{x}\|^2/(2\Delta_x^2))\exp(i\vec{k}\cdot\vec{x})$ répartis en chaque point $(\vec{x}, \vec{k})$ de l'espace des phases (on trouvera des détails dans Lignières & Georgeot (2009, **A7**)).

Cette classification a permis de déterminer 4 familles de modes dont les spectres sont représentés à la Figure 2.11. La régularité des trois spectres associés aux régions quasi-intégrables est évidente. De plus, la régularité des lignes nodales caractérisant la distribution spatiale de ces modes permet d'associer deux nombres entiers aux modes. Pour les modes d'îlots, un de ces nombres correspond au nombre de noeuds dans la direction perpendiculaire à l'orbite périodique et l'autre au nombre de noeuds le long de l'orbite périodique (voir un exemple de mode d'îlot Figure 2.1). Pour les modes "whispering gallery", il s'agit du nombre de noeud à la surface entre $\theta = 0$ et $\theta = \pi$ et du nombre de noeuds le long d'un rayon équatorial. La distribution spatiale des modes chaotiques ne peut pas être caractérisée par deux nombres entiers (voir la Figure 2.2). Le spectre des modes chaotiques ne présente pas non plus de régularité évidente mais, comme le montre la Figure 2.12, la statistique des différences consécutives (bien que réduite à un échantillon relativement limité de modes) est proche de la statistique de Wigner.

Comme prévu par la théorie asymptotique, le spectre total apparaît donc comme la superposition de spectres réguliers et d'un spectre irrégulier. Le spectre des modes issus des îlots centraux peut se mettre sous la forme $\omega_{n\ell} = \Delta_n\ n + \Delta_\ell\ \ell + \alpha$ où les nombres entiers ont n et ℓ sont les nombres de noeuds respectivement le long de l'orbite périodique et perpendiculairement à cette orbite. Nous avons comparé cette valeur de Δ_n issue du calcul numérique des modes à celle obtenue à partir de la quantification

semi-classique Eq. (2.13). Nous trouvons un accord à 2% près (Lignières & Georgeot 2008, **A6**). Il en va de même pour les modes associés à la deuxième chaîne d'îlot (Lignières & Georgeot 2009, **A7**). Une autre comparaison quantitative avec la théorie asymptotique a été obtenue en comparant le nombre de modes que nous avons associés avec une région de l'espace des phases avec l'estimation de ce nombre donnée par le volume de cette région. Dans la gamme de fréquence considéré, 276 modes calculés numériquement ont été classés comme appartenant à la région centrale de l'espace des phases délimitée par le domaine des modes "whispering gallery". Le calcul du volume de l'espace des phases correspondant donne 270 $\pm$ 8 modes (l'intervalle d'erreur est du au fait que nous avons utilisé une méthode probabiliste, une intégration de type Monte-Carlo, pour le calcul des volumes de l'espace à dimension 4). L'accord est très bon, meilleur que celui que l'on trouve en se restreignant à la chaîne d'îlot centrale puisque le volume de l'espace des phase donne 34 ± 2 modes alors que 50 modes ont été classés comme appartenant à cette structure (les possibles raisons de cette différence sont discutées dans (Lignières & Georgeot 2009, **A7**)).

Globalement il y a un très bon accord, qualitatif et quantitatif, entre la théorie asymptotique et le calcul numérique des modes pour le cas que nous avons considéré (domaine de fréquences de modes-p de type solaire, modèle polytropique d'étoile à la rotation $\Omega = 0.6\Omega_K$). Mais on peut se demander dans quelle mesure cet accord peut être étendu au delà du cas considéré. Concernant le domaine de fréquence, on ne s'attend pas à ce que la théorie asymptotique donne des résultats quantitatifs corrects pour les modes-p de plus basses fréquences. Mais l'étude numérique des modes d'îlot a néanmoins montré pour des ordres radiaux relativement faibles, compris entre $n = 5$ et $n = 10$, qu'une formule du type Eq. (2.13) reproduit le spectre avec une erreur limitée à quelques pour cent de la grande différence (Lignières et al. 2006, **A1**). De plus, même dans un domaine de fréquence où les résultats quantitatifs de la théorie asymptotique ne sont plus valables, on devrait toujours pouvoir l'utiliser pour la classification des modes.

Un des avantages du cas que nous avons considéré pour faire la comparaison avec la théorie asymptotique est que les principales structures de l'espace des phases occupent des volumes importants dans cette espace. En effet, si on se place dans un cas où les structures sont petites par rapport au volume occupé par un mode dans l'espace des phases, les effets de longueur d'onde finie dégraderont l'accord avec la théorie asymptotique. Par exemple, à rotation $\Omega = 0.32\Omega_K$ (voir Figure 2.8), les plus petites structures visibles dans la zone chaotique ne peuvent probablement pas contenir un mode pour la gamme de fréquence que nous avons considéré. Ces effets de longueur d'onde finie permettent également d'ex-

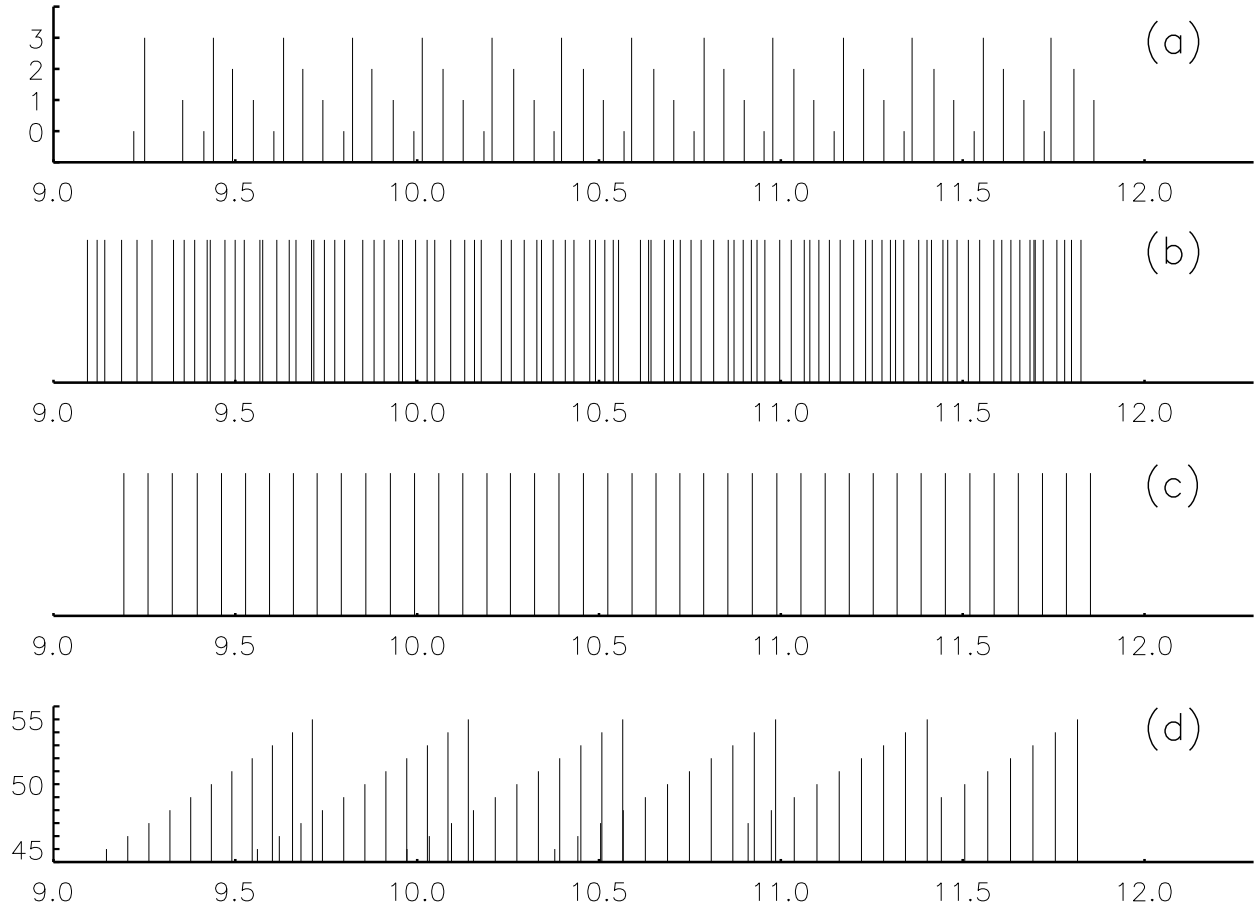

FIG. 2.11 – Sous-spectres de fréquences correspondant à quatre classes de modes : (a) les modes d'îlot formés autour de l'orbite stable de période 2, (b) les modes chaotiques antisymétriques par rapport à l'équateur, (c) les modes d'îlot formés autour de l'orbite stable de période 6, (d) des modes de type "whispering gallery". Pour les sous spectres (a) et (d) la hauteur de la barre verticale correspond à l'un des deux nombres quantiques qui caractérisent le mode. L'unité de fréquence est la fréquence acoustique fondamentale de l'étoile.

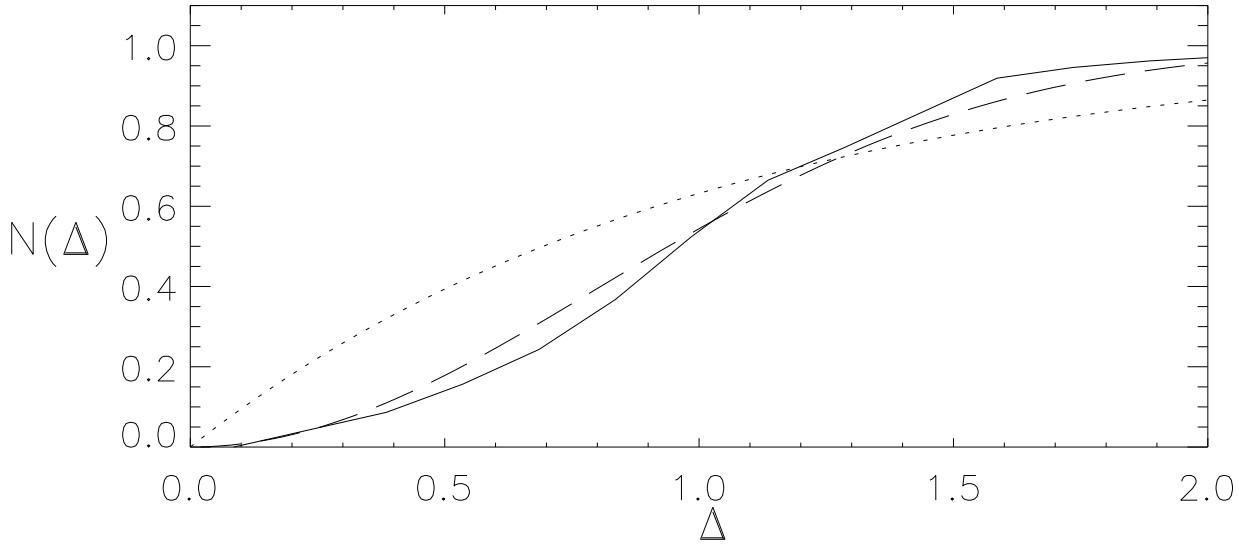

FIG. 2.12 – La distribution intégrée des écarts entre fréquences consécutives des modes acoustiques chaotiques (en trait noir) est comparée à la statistique de Wigner intégrée (traits interrompus) et à la statistique de Poisson intégrée (pointillés).

pliquer une apparente incohérence entre la dynamique des rayons et les propriétés des modes. En effet, à très faible rotation, par exemple pour une rotation solaire, la dynamique des rayons n'est déjà plus intégrable et des structures telle que des chaînes d'îlots stables ou des régions chaotiques autour de points hyperboliques se sont formées. Pourtant, ces propriétés de la dynamique ne se reflètent pas sur les modes qui sont alors très bien décrits par la méthode perturbative. Cela est dû au fait que ces structures existent à de toutes petites échelle dans l'espace des phases et qu'elles sont invisibles pour des modes de longueur d'onde finie (ou ici de fréquence finie).

On peut aussi questionner l'utilisation d'un modèle d'étoile polytropique pour cette comparaison. En fait, cela ne doit pas jouer de rôle tant que l'on reste dans le domaine de validité de l'approximation WKB, c'est-à-dire tant que la longueur d'onde caractéristique des modes est très petite devant l'échelle des inhomogénéités de la structure de l'étoile. Ce point est confirmé par le travail de Reese et al. (2009) où la classification entre modes d'îlots et modes chaotiques a pu être appliquée à des modes de modèles d'étoiles plus réalistes. En revanche, les forts gradients locaux engendrés au voisinage des zones d'ionisation ou des cœurs convectifs modifient effectivement les comportements asymptotiques si les ondes concernées les traversent. Néanmoins, on sait que, dans le cas sphérique, l'effet de ces gradients

n'est pas de détruire entièrement la régularité du spectre mais d'y ajouter une modulation périodique qui peut être modélisée (Vorontsov 1988; Gough 1990; Ballot et al. 2004).

Au final, même si elle n'est pas aussi simple que dans le cas des étoiles sphériques, la théorie asymptotique que nous avons développée est suffisamment complète pour comprendre, à partir du calcul de la dynamique des rayons, les principales propriétés des modes acoustiques dans une étoile en rotation (classification des modes, structure du spectre, régularités, statistique des fréquences ...). Il reste bien sûr de nombreux aspects à développer. Par exemple, le calcul de la quantification des modes d'îlots doit être mené à terme avec en particulier la détermination du terme Δ_ℓ par la dynamique des rayons et la dépendance de la formule de quantification avec le nombre azimutal. Une thèse que je co-dirige avec B. Georgeot a débuté à l'automne 2009 pour poursuivre le développement de la théorie asymptotique. Les premiers résultats obtenus par Mickaël Pasek indiquent que la détermination semi-classique du terme Δ_ℓ se compare bien avec les résultats du calcul numérique.

2.4 Chaos d'onde et recherche de pulsation sur Véga

Ce terme généralise le terme de chaos quantique à d'autres types d'onde que les ondes quantiques. En effet, les ondes peuvent génériquement être décrites par des rayons dans la limite des petites longueurs d'onde. Le chaos d'onde désigne alors l'étude des systèmes d'onde dont la dynamique des rayons est chaotique. Les propriétés spécifiques de ces systèmes ont d'abord été étudiées dans le cadre de la mécanique quantique (depuis les années 1970 Gutzwiller (1990); Ott (1993)). L'une des plus remarquables est que la statistique des niveaux d'énergie suit une loi générique, la distribution de Wigner, déduite des arguments heuristiques proposés par Wigner (1932). Cette loi a été observée expérimentalement pour la première fois en analysant les niveaux d'énergie nucléaires de noyaux d'atomes Haq et al. (1982).

Nous avons montré par le calcul que la statistique des fréquences acoustiques chaotiques (c'est-à-dire celles correspondant aux modes formés à partir des trajectoires des rayons chaotiques) des étoiles en rotation rapide est compatible avec la loi de Wigner (voir Figure 2.12). C'est la première fois qu'une manifestation du chaos d'onde est ainsi mise en évidence dans un système naturel à grande échelle (Lignières & Georgeot 2008, **A6**).

Au delà de ce résultat théorique, retrouver cette statistique à partir des observations des fréquences d'oscillation des étoiles après l'avoir obtenue expérimentalement pour des niveaux d'énergie nucléaire

serait une belle confirmation de son caractère universel. Néanmoins, pour cela, il faut pouvoir extraire du spectre observé un ensemble de fréquences consécutives associées à des modes chaotiques d'une même classe de symétrie (i.e. des modes de même nombre quantique azimutal, m, et de même symétrie par rapport à l'équateur). Dans cette optique, une configuration favorable est celle d'une étoile pulsante vue du pôle car, dans ce cas, seules deux classes de symétrie sont visibles (les modes $m = 0$ symétriques et antisymétriques par rapport à l'équateur). C'est ce raisonnement qui m'a conduit m'intéresser à l'étoile Véga puisque des mesures spectroscopiques, récemment confirmées par des mesures interférométriques, ont montré qu'elle était vue presque par le pôle ($i = 5 - 7°$).

Néanmoins, Véga n'étant pas connu comme une étoile pulsante et ne faisant pas partie d'une classe d'étoile pulsante, il fallait d'abord trouver un indice de variabilité avant de demander le temps de télescope nécessaire à une recherche approfondie de pulsations dans Véga. Dans le cadre d'un programme de recherche de champ magnétique sur les étoiles A (PI M. Aurière), nous avons obtenu 11 spectres de Véga et leur variabilité a été ensuite analysée en collaboration avec T. Böhm. La détection d'un faible niveau de variabilité spectrale nous a conduit à faire une demande d'observation de 5 nuits consécutives sur Véga. La présence de pulsations stellaires sur Véga serait intéressante à plusieurs titres. Tout d'abord, le mécanisme d'excitation des pulsations doit être nouveau puisque Véga est en dehors des bandes d'instabilité de cette région du diagramme HR. Ensuite, comme nous l'avons indiqué ci-dessus, la configuration quasi-polaire de Véga est particulièrement favorable pour l'identification des fréquences. Finalement, si les contraintes sismiques peuvent s'ajouter aux nombreuses informations dont nous disposons sur cette étoile, Véga pourrait devenir une étoile prototype pour comprendre les effets de la rotation rapide sur la structure stellaire.

Cette campagne a d'abord abouti à la détection d'un champ magnétique à la surface de Véga (voir Sect. 3.2). Puis l'analyse détaillée des quelques 300 spectres à haut rapport signal sur bruit a récemment permis d'obtenir la première évidence d'un mode d'oscillation sur cette étoile. Des observations plus récente de Véga obtenues par Espadons ont indiqué également la présence d'un autre mode d'oscillation (ces résultats ont été présentés au colloque Helas IV en Février 2010). Dans les prochains mois, nous chercherons à confirmer ces résultats par de nouvelles campagnes d'observation avec Harps ou Sophie.

Au delà du cas particulier de Véga, ces résultats nous incitent à poursuivre la recherche d'étoiles pulsantes en rotation rapide dans une configuration quasi-polaire, notamment pour trouver des signatures observationnelles du chaos d'onde. Le programme d'observation auquel nous avons pensé est décrit dans

la partie projet de ce mémoire (Sect. 5.4).

2.5 Articles A1-A7

2.5.1 A1 : Acoustic oscillations in rapidly rotating polytropic stars ; I. Effects of the centrifugal distortion

"Acoustic oscillations in rapidly rotating polytropic stars ; I. Effects of the centrifugal distortion"

Lignières F., Rieutord M., Reese D.

A&A 455, 607-620, 2006

A&A 455, 607–620 (2006)
DOI: 10.1051/0004-6361:20065015

Astronomy & Astrophysics

Acoustic oscillations of rapidly rotating polytropic stars

I. Effects of the centrifugal distortion⋆

F. Lignières, M. Rieutord, and D. Reese

Laboratoire d'Astrophysique de Toulouse et Tarbes, UMR 5572, Observatoire Midi-Pyrénées, Université Paul Sabatier – Toulouse 3, 14 avenue É. Belin, 31400 Toulouse, France
e-mail: francois.lignieres@ast.obs-mip.fr

Received 13 February 2006 / Accepted 31 March 2006

ABSTRACT

Aims. A new non-perturbative method to compute accurate oscillation modes in rapidly rotating stars is presented.
Methods. The effect of the centrifugal force is fully taken into account while the Coriolis force is neglected. This assumption is valid when the time scale of the oscillation is much shorter than the inverse of the rotation rate and is expected to be suitable for high radial order p-modes of δ Scuti stars. Axisymmetric p-modes have been computed in uniformly rotating polytropic models of stars.
Results. In the frequency and rotation range considered, we found that as rotation increases (i) the asymptotic structure of the non-rotating frequency spectrum is first destroyed then replaced by a new form of organization (ii) the mode amplitude tends to concentrate near the equator (iii) differences to perturbative methods become significant as soon as the rotation rate exceeds about fifteen percent of the Keplerian limit. The implications for the seismology of rapidly rotating stars are discussed.

Key words. stars: oscillations – stars: rotation

1. Introduction

Since helioseismology revolutionized our knowledge of the solar interior, great advances in stellar structure and evolution theory are expected from asteroseismology. Major efforts including space missions are under way to detect pulsation frequencies with unprecedented accuracy across the HR diagram (Catala et al. 1995; Walker et al. 2003). To draw information from the observed frequencies, seismology relies on the theoretical computation of eigenmodes for a given model of a star. Yet, except for slowly rotating stars, the effect of rotation on the gravito-acoustic modes is not fully taken into account in the present theoretical calculations (e.g. Rieutord 2001).

Rotational effects have been mostly studied through perturbative methods. In this framework, both Ω/ω, the ratio of the rotation rate Ω to the mode frequency ω, and $\Omega/\sqrt{GM/R^3}$, the square root of the ratio of the centrifugal force to the gravity at equator are assumed to be small and of the same order. Solutions valid up to the first, second, and even third order in Ω/ω have been obtained by Ledoux (1951), Saio (1981) and Soufi et al. (1998). The first order analysis proved fully adequate to match the observed acoustic frequency of the slowly rotating sun (Dziembowski & Goode 1992). At the other extreme, the perturbative methods are not expected to be correct for stars approaching the Keplerian limit $\Omega_K = \sqrt{GM/R_e^3}$, where R_e is the equatorial radius. Achernar is a spectacular example of such star since interferometric observations showed a very important distortion of its surface, the equatorial radius R_e being at least one and a half times larger than the polar radius R_p (Domiciano de Souza et al. 2003). In the context of Roche models, such a flattening occurs at the Keplerian limit Ω_K. For intermediate rotation rates, second or third order perturbative methods might be used, but the main problem is that the limit of validity of the perturbative methods is unknown. Departures from the perturbative results would impact the values of individual frequency but also other properties that are commonly used to analyze the spectrum of observed frequencies. This concerns in particular the rotational splitting, the asymptotic large and small frequency separations or the mode visibility.

New methods able to compute accurate eigenmodes in rotating stars are therefore needed to allow progress in the seismology of rapidly rotating stars. Such methods would also assess the limit of validity of perturbative analysis. The main difficulty comes from the fact that, except in the special cases of spherically symmetric media and uniform density ellipsoids, the eigenvalue problem of gravito-acoustic resonances in arbitrary axially symmetric cavities is not separable in the radial and meridional variables. For self-gravitating and rotating stars, a two-dimensional eigenvalue problem has to be solved.

Clement (1981, 1998) made the first attempts to solve this eigenvalue problem for gravito-acoustic modes, investigating various numerical schemes. However, the accuracy of his calculations is generally difficult to estimate. Moreover, the different numerical schemes could not converge for low frequency g-modes when Ω/ω exceeds about 0.5. Since then, eigenmodes in this frequency range have been successfully calculated by Dintrans & Rieutord (2000) using spectral methods. These authors however did not consider the effect of the centrifugal acceleration in their model. The search for unstable modes in neutron stars also triggered the development of numerical schemes able to solve the two-dimensional eigenvalue problem. But only surface gravity modes (f-modes) and some inertial modes (r-modes) have been determined in this context (Yoshida et al. 2005). Espinosa et al. (2004) reported calculations of adiabatic acoustic

⋆ Appendices A–C are only in electronic form at
http://www.edpsciences.org

modes in MacLaurin spheroids of uniform density neglecting the Coriolis force, the potential perturbation and the Brunt-Väisälä frequency.

In this paper, we present a new method to compute accurate eigenmodes in rotating stars. For the first application of the method, we only consider the effect of the centrifugal force through its impact on the equilibrium state of the star; we thus neglect the Coriolis force. This assumption is valid when the time scale of the oscillation is much shorter than the inverse of the rotation rate and is expected to be suitable for high radial order p-modes of δ Scuti stars. The problem is further simplified by using uniformly rotating polytropes as equilibrium models and assuming adiabatic perturbations as well as the Cowling approximation. Low frequency axisymmetric p-modes have been computed for rotation rates varying from $\Omega = 0$ up to $\Omega/\Omega_K = 0.59$, this ratio corresponding to a typical δ Scuti star ($M = 1.8\ M_\odot, R = 2\ R_\odot$) with an equatorial velocity of 240 km s^{-1}. The centrifugal force modifies the effective gravity in two ways: it makes it smaller and aspherical. Decreasing the effective gravity should affect sound waves by reducing the sound speed inside the star and by increasing the star's volume, thus potentially the volume of the resonant cavity. The physical consequences of the non-spherical geometry are unknown.

In the following, the formalism and the numerical method are presented along with accuracy tests. Then, the parameter range of the calculations is given together with the method used to label the eigenmodes. The structure of the frequency spectrum, some properties of the eigenfunctions and the differences with perturbative methods are further analyzed as a function of the rotation rate. These results are discussed in the last section.

2. Formalism

Accurate numerical solutions of 2D eigenvalue problems require a careful choice of the numerical method and the mathematical formalism. In this section we explain the choices that have been made for the variables, the coordinate system, the numerical discretization, and the method to solve the resulting algebraic eigenvalue problem. All play a role in the accuracy of the eigenfrequency determinations that will be presented at the end of this section.

2.1. Equilibrium model

The equilibrium model is a self-gravitating uniformly rotating polytrope. It is therefore governed by a polytropic relation, the hydrostatic equilibrium in a rotating frame, and Poisson's equation for the gravitational potential:

$$P_0 = K\rho_0^{1+1/N} \tag{1}$$

$$0 = -\boldsymbol{\nabla} P_0 - \rho_0 \boldsymbol{\nabla}\left(\psi_0 - \Omega^2 s^2/2\right) \tag{2}$$

$$\Delta\psi_0 = 4\pi G\rho_0 \tag{3}$$

where P_0 is the pressure, ρ_0 the density, K the polytropic constant, N the polytropic index, ψ_0 the gravitational potential, s the distance to the rotation axis and G the gravitational constant.

The polytropic relation and uniform rotation ensure that the fluid is barotropic. A pseudo-enthalpy can then be introduced $h_0 = \int \mathrm{d}P_0/\rho_0 = (1+N)P_0/\rho_0$ and the integration of the hydrostatic equation reads:

$$h_0 = h_c - (\psi_0 - \psi_c) + \frac{1}{2}\Omega^2 s^2 \tag{4}$$

where the subscript "c" denotes the value in the center of the polytropic model. Equation (4) is then inserted into Poisson's equation to yield:

$$\Delta\psi_o = 4\pi G\rho_c \left(1 - \frac{\psi_o - \psi_c}{h_c} + \frac{\Omega^2 s^2}{2h_c}\right)^N. \tag{5}$$

Equation (5) is solved numerically, using an iterative scheme. Since the shape of the star is not spherical, a system of coordinates (ζ, θ, ϕ) based on Bonazzola et al. (1998) is used, such that $\zeta = 1$ corresponds to the surface of the spheroid (more details on the coordinate system are given in Sect. 2.3). This enables the use of spectral methods both for the radial coordinate ζ and the angular ones. The numerical method is further detailed in Rieutord et al. (2005).

2.2. Perturbation equations and boundary conditions

Neglecting the Coriolis force, the linear equations governing the evolution of small amplitude adiabatic perturbations read:

$$\partial_t \rho + \boldsymbol{\nabla}\cdot(\rho_0 \boldsymbol{v}) = 0, \tag{6}$$

$$\rho_0 \partial_t \boldsymbol{v} = -\boldsymbol{\nabla} P + \rho \boldsymbol{g}_0 - \rho_0 \boldsymbol{\nabla}\psi, \tag{7}$$

$$\partial_t P + \boldsymbol{v}\cdot\boldsymbol{\nabla} P_0 = c_0^2\ (\partial_t \rho + \boldsymbol{v}\cdot\boldsymbol{\nabla}\rho_0), \tag{8}$$

$$\Delta\psi = 4\pi G\rho \tag{9}$$

where $\boldsymbol{v}$, ρ, P and ψ, are the perturbations of velocity, density, pressure and gravitational potential. The sound speed is $c_0 = \sqrt{\Gamma_{1,0} P_0/\rho_0}$, $\Gamma_{1,0}$ being the first adiabatic exponent of the gas, and the effective gravity $\boldsymbol{g}_0 = -\boldsymbol{\nabla}\left(\psi_0 - \Omega^2 s^2/2\right)$ has been introduced. In the framework of polytropic models of stars, the polytropic relation (1) is assumed to give a reasonably good approximation of the relation between the pressure and the density of the equilibrium state. As the first adiabatic exponent $\Gamma_{1,0}$ is obtained from the equation of state of the gas, $\Gamma_{1,0}$ is in general not equal to $1 + 1/N$.

We simplified Eqs. (6)–(9) following two constraints: first, the governing equations should be written for general coordinate systems because we shall use a surface-fitting non-orthogonal coordinate system. Second, they should take the form $\mathcal{M}\boldsymbol{X} = \lambda \boldsymbol{Q}\boldsymbol{X}$ where λ is the eigenvalue, $\boldsymbol{X}$ is the eigenfunction, and $\mathcal{M}$ and $\boldsymbol{Q}$ are linear differential operators. Indeed, the method that we shall use to solve the algebraic eigenvalue problem obtained after discretization works for problem reading $[M]X = \lambda[Q]X$, where X is the discretized eigenvector and, $[M]$ and $[Q]$ are matrices. Taking the time derivative of Eqs. (7) and (9) and using Eqs. (6) and (8) to eliminate the pressure and density perturbations, we obtain two equations for the velocity and the gravitational potential perturbation:

$$\partial_{tt}^2 \boldsymbol{v} = \boldsymbol{\nabla}\ \left(c_0^2 \chi + \boldsymbol{v}\cdot\boldsymbol{g}_0 - \partial_t\psi\right) - \chi \boldsymbol{A}_0 \tag{10}$$

$$\Delta\partial_t\psi = -4\pi G\ (\boldsymbol{v}\cdot\boldsymbol{\nabla}\rho_0 + \rho_0\chi) \tag{11}$$

where $\chi = \boldsymbol{\nabla}\cdot\boldsymbol{v}$ is the divergence of the velocity. The vector $\boldsymbol{A}_0$ characterizes the stratification of the equilibrium model:

$$\boldsymbol{A}_0 = c_0^2 \left(\frac{1}{\Gamma_{1,0}}\frac{\boldsymbol{\nabla} P_0}{P_0} - \frac{\boldsymbol{\nabla}\rho_0}{\rho_0}\right) = \frac{c_0^2 N_0^2}{\|\boldsymbol{g}_0\|}\boldsymbol{n}_0, \tag{12}$$

where N_0 is the Brunt-Väisälä frequency and $\boldsymbol{n}_0$ is the unit vector in the direction opposite to the effective gravity defined by:

$$\boldsymbol{g}_0 = -\|\boldsymbol{g}_0\|\boldsymbol{n}_0. \tag{13}$$

Note that the barotropicity of the fluid has been used to obtain (10).

In addition to the gravitational potential perturbation, the right hand sides of Eqs. (10) and (11) only involve the divergence of the velocity and the scalar product of the velocity with vectors parallel to gravity. Then, the scalar product of Eq. (10) with gravity,

$$\partial_{tt}^2 \boldsymbol{v}\cdot\boldsymbol{g}_0 = \boldsymbol{g}_0\cdot\boldsymbol{\nabla}\left(c_0^2\chi + \boldsymbol{v}\cdot\boldsymbol{g}_0 - \partial_t\psi\right) - \chi\boldsymbol{g}_0\cdot\boldsymbol{A}_0 \tag{14}$$

and the divergence of Eq. (10),

$$\partial_{tt}^2\chi = \Delta(c_0^2\chi + \boldsymbol{v}\cdot\boldsymbol{g}_0 - \partial_t\psi) - \boldsymbol{\nabla}\cdot(\chi\boldsymbol{A}_0) \tag{15}$$

yield, together with Eq. (11), a complete set of differential equations for the variables $\boldsymbol{v}\cdot\boldsymbol{g}_0, \chi$ and ψ. Pekeris (1938) who studied the oscillations of spherically symmetric polytropes considered similar variables but, instead of Eq. (10), used a combination of Eqs. (14) and (10) which does not involve second order derivative with respect to the radial coordinate. For general system of coordinate as well, the order of the differential system can be lowered replacing Eq. (10) by the following one:

$$\partial_{tt}^2\left[\chi - g^{11}\partial_1\left(\frac{\boldsymbol{v}\cdot\boldsymbol{g}_0}{g_0^1}\right)\right] = \mathcal{L}(c_0^2\chi + \boldsymbol{v}\cdot\boldsymbol{g}_0 - \partial_t\psi) - \boldsymbol{\nabla}\cdot(\chi\boldsymbol{A}_0) + g^{11}\partial_1\left(\frac{\chi\boldsymbol{g}_0\cdot\boldsymbol{A}_0}{g_0^1}\right) \tag{16}$$

where the linear operator $\mathcal{L}$, defined by,

$$\mathcal{L}(F) = \Delta F - g^{11}\partial_1\left(\frac{\boldsymbol{g}_0\cdot\boldsymbol{\nabla}F}{g_0^1}\right) \tag{17}$$

does not contain second order derivatives with respect to the first coordinate x^1. In this expression, g_0^1 is the first contravariant component of the gravity in the natural basis $(\boldsymbol{E}_1, \boldsymbol{E}_2, \boldsymbol{E}_3)$ defined by $\boldsymbol{E}_i = \partial\boldsymbol{OM}/\partial x^i$, and g^{11} is the first contravariant component of the metric tensor.

The equations are non-dimensionalized using the equatorial radius, R_e, as length unit, the density at the center of the polytrope, ρ_c, as density unit and $T_0 = (4\pi G\rho_\mathrm{c})^{-1/2}$ as time unit. As we look for harmonic solutions in time, the variable are written $F = \hat{F}\exp(i\omega t)$. Dropping the hat and denoting dimensionless quantities as previous dimensional ones, the governing equations read:

$$\lambda W = \boldsymbol{g}_0\cdot\boldsymbol{\nabla}\left(c_0^2\chi + W + \Psi\right) - c_0^2N_0^2\chi \tag{18}$$

$$\lambda\left[\chi - g^{11}\partial_1\left(\frac{W}{g_0^1}\right)\right] = \mathcal{L}(c_0^2\chi + W + \Psi) - \boldsymbol{\nabla}\cdot(\chi\boldsymbol{A}_0) + g^{11}\partial_1\left(\frac{c_0^2N_0^2\chi}{g_0^1}\right) \tag{19}$$

$$0 = \Delta\Psi - d_0W - \rho_0\chi \tag{20}$$

where $\lambda = -\omega^2$, $W = \boldsymbol{v}\cdot\boldsymbol{g}_0$, $\Psi = -i\omega\psi$ and d_0 denotes

$$d_0 = \frac{\|\boldsymbol{\nabla}\rho_0\|}{\|\boldsymbol{g}_0\|}. \tag{21}$$

Another form of these equations may be obtained replacing W by a new variable $U = c_0^2\chi + W + \Psi$. The set of equations then reads:

$$\boldsymbol{g}_0\cdot\boldsymbol{\nabla}U - c_0^2N_0^2\chi = \lambda(U - \Psi - c_0^2\chi) \tag{22}$$

$$\mathcal{L}(U) - \boldsymbol{\nabla}\cdot(\chi\boldsymbol{A}_0) + g^{11}\partial_1\left(\frac{c_0^2N_0^2\chi}{g_0^1}\right) = \lambda\left[-g^{11}\partial_1\left(\frac{U-\Psi}{g_0^1}\right) + \chi + g^{11}\partial_1\left(\frac{c_0^2\chi}{g_0^1}\right)\right] \tag{23}$$

$$-d_0U + (d_0c_0^2 - \rho_0)\chi + d_0\Psi + \Delta\Psi = 0. \tag{24}$$

As in Pekeris (1938), the boundary conditions are that the gravitational potential vanishes at infinity and that U and χ be regular everywhere.

2.3. Coordinates choice

The choice of the coordinate system has been guided by two considerations. First, for the accuracy of the numerical method, it seems preferable to apply the boundary conditions on a surface of coordinate. This imposes that the stellar surface is described by an equation $\zeta = \text{const.}$, where ζ is one of the coordinates. Second, when using spherical harmonic expansions, the regularity conditions at the center have a simple form for spherical coordinates only. Therefore, the coordinate system should become spherical near the center. If (r, θ, ϕ) denotes the usual spherical coordinates and $r = S(\theta)$ describes the surface, families of coordinates (ζ, θ', ϕ') verifying both conditions have been proposed by Bonazzola et al. (1998):

$$\begin{cases} r = r(\zeta, \theta') \\ \theta = \theta' \\ \phi = \phi', \end{cases} \tag{25}$$

where

$$r(\zeta, \theta) = \alpha\zeta + A(\zeta)\left[S(\theta) - \alpha\right]. \tag{26}$$

The polynomial $A(\zeta) = (5\zeta^3 - 3\zeta^5)/2$ ensures that $r \propto \zeta$ near the center and that $\zeta = 1$ describes the surface $r = S(\theta)$. The scalar α is chosen so that the transformation $(r, \theta, \phi) \mapsto (\zeta, \theta, \phi)$ is not singular and the numerical convergence is fast. We find that $\alpha = 1 - \epsilon$ is a convenient choice, $\epsilon = 1 - R_\mathrm{p}/R_\mathrm{e}$ being the flatness of the star surface. In the following, we shall refer to ζ as the pseudo-radial coordinate.

To express the governing equations in this non-orthogonal coordinate system, we use the covariant and contravariant components of the corresponding metric tensor. The non-vanishing components read:

$$\begin{array}{ll} g_{11} = r_\zeta^2 & g_{12} = g_{21} = r_\zeta r_\theta \\ g_{22} = r^2 + r_\theta^2 & g_{33} = r^2\sin^2\theta \\ g^{11} = (r^2 + r_\theta^2)/(r^2r_\zeta^2) & g^{12} = g^{21} = -r_\theta/(r^2r_\zeta) \\ g^{22} = 1/r^2 & g^{33} = 1/(r^2\sin^2\theta), \end{array} \tag{27}$$

and the square-root of the absolute value of the metric tensor determinant is:

$$\sqrt{|\,g\,|} = r^2r_\zeta\sin\,\theta. \tag{28}$$

In Appendix A, the linear operators involved in Eqs. (22)–(24) are expressed in terms of the partial derivatives of $r(\zeta, \theta)$. Note that, for vectorial operators, we used the natural basis defined above.

2.4. The numerical method

The method follows and generalizes the one presented in Rieutord & Valdettaro (1997). The numerical discretization is done with spectral methods, spherical harmonics for the angular coordinates θ and ϕ and Chebyshev polynomials for the pseudo-radial coordinate ζ. The variables U, Ψ and χ are expanded into spherical harmonics:

$$U(\zeta,\theta,\phi) = \sum_{\ell=0}^{L}\sum_{m=-\ell}^{+\ell} U_m^\ell(\zeta) Y_\ell^m(\theta,\phi), \tag{29}$$

and equivalent expressions for Ψ and χ, where ℓ and m are respectively the degree and the azimuthal number of the spherical harmonic $Y_\ell^m(\theta,\phi)$. Then, the governing equations are projected onto spherical harmonics to obtain a system of ordinary differential equations (ODE) of the variable ζ for the coefficients of the spherical harmonic expansion $U_m^\ell(\zeta), \chi_m^\ell(\zeta), \Psi_m^\ell(\zeta)$. This system is then discretized on the collocation points of a Gauss-Lobatto grid associated with Chebyshev polynomials. It results in an algebraic eigenvalue problem $[M]X = \lambda[Q]X$, where X is the eigenvector of $L \times N_r$ components and $[M]$ and $[Q]$ are square matrices of $L \times N_r$ lines, L and N_r being respectively the truncation orders on the spherical harmonics and Chebyshev basis. The algebraic eigenvalue problem is solved using either a QZ algorithm or an Arnoldi-Chebyshev algorithm. The QZ algorithm provides the whole spectrum of eigenvalues while the iterative calculation based on the Arnoldi-Chebyshev algorithm computes a few eigenvalues around a given value of the frequency.

Because of the symmetries of the equilibrium model with respect to the rotation axis and the equator, one obtains a separated eigenvalue problem for each absolute value of the azimuthal number $|\,m\,|$ and each parity with respect to the equator. Thus, for a given $m \geq 0$, we have two independent sets of ODE coupling the coefficients of the spherical harmonic expansion having respectively even and odd degree numbers, that is:

$$\begin{array}{llll} \hat{U}^+ = U_m^{m+2k}(\zeta) & \hat{\chi}^+ = \chi_m^{m+2k}(\zeta) & \hat{\Psi}^+ = \Psi_m^{m+2k}(\zeta) \\ \hat{U}^- = U_m^{m+2k+1}(\zeta) & \hat{\chi}^- = \chi_m^{m+2k+1}(\zeta) & \hat{\Psi}^- = \Psi_m^{m+2k+1}(\zeta), \end{array} \tag{30}$$

where $0 \leq k < +\infty$. The solutions of these two ODE systems are either symmetric or antisymmetric with respect to the equator.

The two sets of ODE can be written in the form:

$$\left(\mathcal{A}\frac{\mathrm{d}^2}{\mathrm{d}\zeta^2} + \mathcal{B}\frac{\mathrm{d}}{\mathrm{d}\zeta} + C\ \mathrm{Id}\right)\boldsymbol{\Xi} = \lambda\left(\mathcal{D}\frac{\mathrm{d}}{\mathrm{d}\zeta} + \mathcal{E}\right)\boldsymbol{\Xi}, \tag{31}$$

where $\boldsymbol{\Xi}$ denotes

$$\boldsymbol{\Xi}^+ = \begin{vmatrix} \hat{U}^+ \\ \hat{\chi}^+ \\ \hat{\Psi}^+ \end{vmatrix} \quad \text{or} \quad \boldsymbol{\Xi}^- = \begin{vmatrix} \hat{U}^- \\ \hat{\chi}^- \\ \hat{\Psi}^- \end{vmatrix} \tag{32}$$

and where the matrices are defined by blocks as follows:

$$\mathcal{A} = \begin{pmatrix} 0 & 0 & 0 \\ 0 & 0 & 0 \\ 0 & 0 & \mathrm{A}_{33} \end{pmatrix} \qquad \mathcal{B} = \begin{pmatrix} \mathrm{B}_{11} & 0 & 0 \\ \mathrm{B}_{21} & \mathrm{B}_{22} & 0 \\ 0 & 0 & \mathrm{B}_{33} \end{pmatrix} \tag{33}$$

$$C = \begin{pmatrix} \mathrm{C}_{11} & \mathrm{C}_{12} & 0 \\ \mathrm{C}_{21} & \mathrm{C}_{22} & 0 \\ \mathrm{C}_{31} & \mathrm{C}_{32} & \mathrm{C}_{33} \end{pmatrix} \tag{34}$$

$$\mathcal{D} = \begin{pmatrix} 0 & 0 & 0 \\ \mathrm{D}_{21} & \mathrm{D}_{22} & -\mathrm{D}_{21} \\ 0 & 0 & 0 \end{pmatrix} \qquad \mathcal{E} = \begin{pmatrix} \mathrm{E}_{11} & \mathrm{E}_{12} & -\mathrm{E}_{11} \\ \mathrm{E}_{21} & \mathrm{E}_{22} & -\mathrm{E}_{21} \\ 0 & 0 & 0 \end{pmatrix}. \tag{35}$$

Equivalently, one can write Eq. (31) as:

$$\begin{array}{l} \left(\mathrm{B}_{11}\frac{\mathrm{d}}{\mathrm{d}\zeta} + \mathrm{C}_{11}\right)\hat{U} + \mathrm{C}_{12}\hat{\chi} = \lambda\left[\mathrm{E}_{11}\ \left(\hat{U} - \hat{\Psi}\right) + \mathrm{E}_{12}\hat{\chi}\right] \\ \left(\mathrm{B}_{21}\frac{\mathrm{d}}{\mathrm{d}\zeta} + \mathrm{C}_{21}\right)\hat{U} + \ \left(\mathrm{B}_{22}\frac{\mathrm{d}}{\mathrm{d}\zeta} + \mathrm{C}_{22}\right)\hat{\chi} = \\ \lambda\left[\ \left(\mathrm{D}_{21}\frac{\mathrm{d}}{\mathrm{d}\zeta} + \mathrm{E}_{21}\right)\ \left(\hat{U} - \hat{\Psi}\right) + \ \left(\mathrm{D}_{22}\frac{\mathrm{d}}{\mathrm{d}\zeta} + \mathrm{E}_{22}\right)\hat{\chi}\right] \\ \mathrm{C}_{31}\hat{U} + \mathrm{C}_{32}\hat{\Psi} + \ \left(\mathrm{A}_{33}\frac{\mathrm{d}^2}{\mathrm{d}\zeta^2} + \mathrm{B}_{33}\frac{\mathrm{d}}{\mathrm{d}\zeta} + \mathrm{C}_{33}\right)\hat{\Psi} = 0. \end{array} \tag{36}$$

Each sub-matrices can be expressed in terms of the two following functionals:

$$\mathrm{I}_{\ell\ell'}^m(\mathrm{G}) = 2\pi\int_0^\pi \mathrm{G}(\zeta,\theta)\hat{Y}_\ell^m(\theta)\hat{Y}_{\ell'}^m(\theta)\sin\theta\mathrm{d}\theta \tag{37}$$

$$\mathrm{J}_{\ell\ell'}^m(\mathrm{G}) = 2\pi\int_0^\pi \mathrm{G}(\zeta,\theta)\hat{Y}_\ell^m(\theta)\frac{\partial\hat{Y}_{\ell'}^m}{\partial\theta}(\theta)\sin\theta\mathrm{d}\theta \tag{38}$$

where $\hat{Y}_\ell^m(\theta) = Y_\ell^m(\theta,\phi)\mathrm{e}^{-\mathrm{i}m\phi}$ is a normalized Legendre polynomial.

In Appendix B, all the coefficient of the sub-matrices are made explicit in terms of the function $r(\zeta,\theta)$ and its first and second order derivatives as well as in terms of the enthalpy of the equilibrium model, its first and second order derivatives.

In the following, we consider the Cowling approximation thus neglecting the gravitational potential perturbation. The ODE system (31) is simplified accordingly and in particular reduces to the first order.

3. Tests and accuracy

The formalism and the numerical method presented in the previous section have been tested and the accuracy of the frequency determinations has been estimated.

3.1. Tests

A first test of the method has been performed in the case of axisymmetric ellipsoids of uniform density. We choose this configuration because the eigenvalue problem is fully separable using the oblate spheroidal coordinates (ξ,η,ϕ) defined as ($x = a\cosh\xi\sin\eta\sin\phi$, $y = a\cosh\xi\sin\eta\cos\phi$, $z = a\sinh\xi\cos\eta$), where $0 \leq \xi < +\infty$, $0 \leq \eta \leq \pi$ et $0 \leq \phi \leq 2\pi$. The eigenfrequencies obtained with this method were compared with the eigenfrequencies computed with our general method, $S(\theta)$ describing an ellipse. We found the same frequencies with a high degree of accuracy for arbitrary values of the ellipsoid flatness between 0 and 0.5. Moreover, as the flatness goes to zero, the frequencies were found to converge towards the values given by a first order perturbative analysis in terms of flatness. More details about this test are given in Lignières et al. (2001) and Lignières & Rieutord (2004).

The frequencies of axisymmetric p-modes in a self-gravitating uniformly rotating $N = 3$ polytrope that will be presented in the following sections have been also tested. As shown in the previous section, the method involves lengthy analytical calculations of the coefficients of the ODE system (31). Terms involved in the non-rotating case have been tested by comparing our result with the p-modes frequencies in a non-rotating self-gravitating $N = 3$ polytrope published in Christensen-Dalsgaard & Mullan (1994). The relative error is smaller than 10^{-7} for the $\ell = 0$ to 3, $n = 1$ to 10 modes. In the rotating case, we compared our results with the ones obtained by solving the same problem but using a different form of the starting equations. This alternative system of equations aims at including the Coriolis

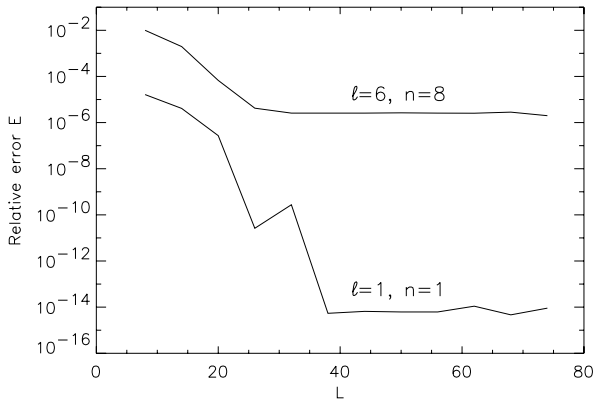

Fig. 1. Evolution of the frequency relative error, $E(L) = |\omega(L) - \omega(L^{\max})|/\omega(L^{\max})$, as the spatial resolution in latitude is increased. Two modes labeled ($\ell = 1,\ n = 1$) and ($\ell = 6,\ n = 8$) are considered at the rotation rate $\Omega/\Omega_{\rm K} = 0.46$ with $L^{\max} = 80$ and $N_r = 61$.

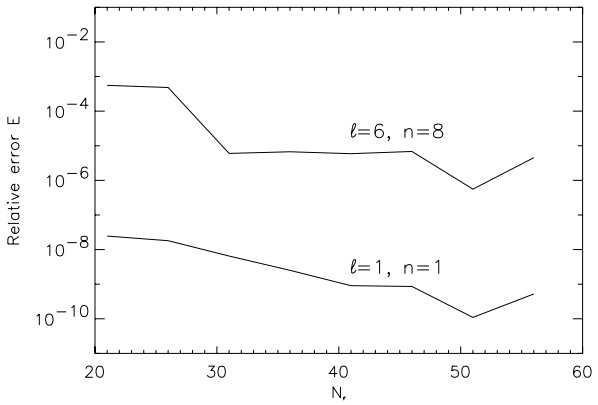

Fig. 2. Evolution of the frequency relative error, $E(N_r) = |\omega(N_r) - \omega(N_r^{\max})|/\omega(N_r^{\max})$ as the resolution in the radial coordinate is increased. Two modes labeled ($\ell = 1,\ n = 1$) and ($\ell = 6,\ n = 8$) are considered at a rotation rate $\Omega/\Omega_{\rm K} = 0.46$ with $N_r^{\max} = 61$ and $L = 62$.

force; thus the variables and the resulting ODE systems to be solved are different. We verified that when the terms involving the Coriolis force are omitted from the equations, eigenfrequencies presented in the next section are recovered with a very high precision (Reese et al. 2006a). For instance, the maximum relative error on the eigenfrequency for all the frequencies computed at $\Omega/\Omega_{\rm K} = 0.59$ has been found of the order of 10^{-6}, for a given set of numerical parameters. This last test gives us strong confidence in the method and its implementation.

3.2. Accuracy

As pointed out by Clement (1981, 1998), accurate numerical solutions of the 2D eigenvalue problem are not easy to obtain. It is therefore important to estimate the accuracy of our method. In the following we first investigate the influence of the spatial resolution on the eigenfrequencies and then consider other sources of errors.

A relative spectral error E is defined as the absolute value of the relative difference between the frequency computed at a given resolution and the frequency obtained at the maximum resolution considered. Let us first consider the effects of the angular resolution. Figure 1 displays $E(L) = |\omega(L) - \omega(L^{\max})|/\omega(L^{\max})$ as a function of L, the truncation order of the spherical harmonic expansion, for two axisymmetric modes labeled ($\ell = 1,\ n = 1$) and ($\ell = 6,\ n = 8$) whose spatial structures are dominated by large and small length scales, respectively (the labeling of the mode will be described in the next section). The maximum angular resolution is $L^{\max} = 80$, the resolution in the pseudo-radial coordinate is fixed to $N_r = 61$ and the rotation rate is $\Omega/\Omega_{\rm K} = 0.46$. In the same way, Fig. 2 illustrates the effects of the pseudo-radial resolution by showing $E(N_r) = |\omega(N_r) - \omega(N_r^{\max})|/\omega(N_r^{\max})$ as a function of N_r, the truncation order of the Chebyshev polynomial expansion, for the same modes and rotation rate. The maximum radial resolution is $N_r^{\max} = 61$ and the latitudinal resolution is fixed to $L = 62$. In both figures, we observe that the error first decreases and then reaches a plateau which means that a better approximation of the eigenfrequency cannot be obtained by increasing the spatial resolution. The plateau are significantly higher for the ($\ell = 6,\ n = 8$) mode than for the ($\ell = 1,\ n = 1$) mode. We verified that this difference is due to the presence of smaller radial length scales (rather than to smaller angular length scales).

Even when the spatial resolution is sufficient, two other sources of numerical errors can indeed limit the accuracy of eigenfrequency determination. First, the component of the matrix L and M being computed numerically, they are determined with a certain error. Second, even when this error is reduced to round-off errors, the accuracy of the algebraic eigenvalue solver, the Arnoldi-Chebyshev algorithm, remains limited.

Errors on the matrix component that arise from quadratures (see Eqs. (37) and (38)) can approach round-off errors using weighted Gauss-Lobatto quadratures. The other source of error in the matrix components comes from the computation of equilibrium quantities. Indeed, the accuracy of the enthalpy, its first and second derivatives and the surface shape, is at best limited by the effect of round-off errors on the convergence of the algorithm used to compute the polytropic stellar models. The effect of these errors on the eigenfrequencies have been investigated and appears to be smaller than the effect of the Arnoldi-Chebyshev algorithm itself which is now described.

As any solver in linear algebra, the Arnoldi-Chebyshev algorithm amplifies the round-off error that affect the matrix components. Thus, the error on the eigenvalue and the associated eigenvector is usually much larger than the round-off error of double precision arithmetic. The accuracy of the Arnoldi-Chebyshev algorithm has been studied in details by Valdettaro et al. (2006) in the context of inertial modes in a spherical shell where the matrix component are known analytically. Theoretically, it can be estimated by computing the spectral portrait of the eigenvalue problem $[M]X = \lambda[Q]X$, which shows how small variations of $[M]$ and $[Q]$ affects the determination of each eigenfrequencies. In fact, as the iterative Arnoldi-Chebyshev algorithm requires an initial guess of the eigenfrequency, a practical alternative to measure the accuracy of a frequency determination is to compute frequencies for slightly different values of the initial guess. This has been done for a large number (100) of initial guess values randomly distributed around the eigenfrequency of the ($\ell = 1,\ n = 1$) and ($\ell = 6,\ n = 8$) modes. The histogram in Fig. 3 shows the resulting frequencies distribution around a most probable mean eigenfrequency. The width of the histogram determined by the standard deviation of the distribution provides a measure of the algorithm accuracy. The standard deviation σ is equal to 5.6×10^{-6} for the ($\ell = 6,\ n = 8$) mode and to 6.2×10^{-10} for the ($\ell = 1,\ n = 1$) mode. The error thus grows with the radial order of the mode, this trend being general in our results (as in

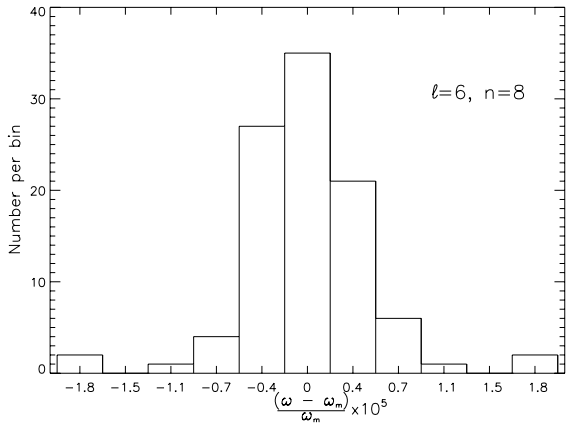

Fig. 3. Histogram of 100 frequencies obtained for 100 different values of the initial guess of the Arnoldi-Chebyshev algorithm randomly chosen in a small interval around $\omega_m = 12.0547$. The standard deviation of this frequency distribution $\sigma = 5.6 \times 10^{-6}$ measures the algorithm relative error on the frequency for this particular mode labeled ($\ell = 6,\ n = 8$). The spatial resolution is $N_r = 61$ and $L = 62$ and the rotation rate is $\Omega/\Omega_K = 0.46$.

Valdettaro et al. 2006). Moreover, the width of the histogram does not depend on the amplitude of the initial guess perturbation provided it is sufficiently small.

We also observe that, except for the dependence of the ($\ell = 1,\ n = 1$) frequency on the angular resolution, the levels of the plateau shown in Figs. 1 and 2 are of the same order as the error of the algorithm. It means that, in these cases, the changes in the matrix component and size associated with the modification of the resolution have a similar effect on the frequency as varying the initial guess of the algorithm. However, the convergence of the ($\ell = 1,\ n = 1$) frequency at a 10^{-14} level, much lower than the 6.2×10^{-10} accuracy of the algorithm, shows that it is not always true and that the spectral error can underestimate the true error.

Although it is too demanding to compute a global accuracy by repeating the statistical study on the initial guess for all eigenfrequencies, the relative accuracy on all tested frequencies is always better than 2×10^{-5} using double precision arithmetic.

Note that another potential source of error will be discussed below when describing avoided crossings between modes.

4. Results

The parameter range of the calculations is first presented. Then, we describe the method used to label the eigenmodes, the structure of the frequency spectrum, some properties of the eigenfunctions and the differences with perturbative methods.

4.1. Parameter range

Self-gravitating uniformly rotating polytropes of index $N = 3$ and specific heat ratio $\Gamma_{1,0} = 5/3$ have been computed for rotation rates varying from $\Omega = 0$ up to $\Omega/\Omega_K = 0.59$. In this range, the flatness of the star's surface $\epsilon = 1 - R_p/R_e$ increases from 0 to 0.15.

Low frequency axisymmetric p-modes have been computed for each polytropic model. We started with the non-rotating model and computed the $\ell = (0, ..., 7),\ n = (1, ..., n_{max})$ axisymmetric p-modes, the largest radial order depending on the degree ℓ: $n_{max} = 10$ for $\ell = (0, 1)$, $n_{max} = 9$ for $\ell = (2, 3, 4)$ and $n_{max} = 8$ for $\ell = (5, 6, 7)$. All these 71 modes were then calculated at higher rotation rates by progressively increasing the rotation of the polytropic model. In the next section, we explain how we could track and label them from zero rotation to $\Omega/\Omega_K = 0.59$.

4.2. Mode labeling

In the absence of rotation, modes are identified and classified by the three "quantum" numbers n, ℓ, m characterizing their radial, latitudinal and azimuthal structure respectively. Because of separability, independent 1D eigenvalue problems are solved for each pair (ℓ, m) and it is then an easy task to order the computed frequencies, the order n additionally indicating the number of radial nodes of the mode. By contrast, in the presence of rotation, independent 2D eigenvalue problems are solved for a given $|m|$ and a given equatorial parity. The computed modes are then obtained without a priori information about their latitudinal and radial structures. Therefore, an important issue is whether it is possible to define a meaningful classification of these modes. In this work, we investigate the possibility of associating unambiguously each mode with a non-rotating mode thus identifying it by the three quantum numbers n, ℓ, m of the non-rotating mode. Similarly, Clement (1986) followed some equatorially symmetric acoustic modes to high rotation rates but in a limited frequency range and using low spatial resolution calculations.

In practice, instead of backtracking modes towards zero rotation, we started at zero rotation with a mode we are interested in and tried to follow it by progressively increasing the rotation. We managed to track all the $\ell = (0, ..., 7),\ n = (1, ..., n_{max})$ axisymmetric p-modes from $\Omega = 0$ to $\Omega/\Omega_K = 0.59$, a global view of the eigenfrequencies evolution being displayed in Fig. 4 (left panel). As explained below, the main difficulty comes from avoided crossings between modes of the same equatorial parity.

Zooms in the $\omega - \Omega$ plane displayed in Fig. 4 (right panels) provide two examples of avoided crossings respectively between odd ($\ell = 1,\ n = 6$ and $\ell = 5,\ n = 5$) and even ($\ell = 0,\ n = 4$ and $\ell = 4,\ n = 3$) modes. Modes tends to cross because their frequencies are not affected in the same way by the centrifugal force but, as two eigenstates of the same parity cannot be degenerate, an avoided crossing takes place during which the two eigenfunctions exchange their characteristics. This exchange of property is illustrated in Fig. 5 in the case of the ($\ell = 0,\ n = 4$), ($\ell = 4,\ n = 3$) crossing. A mean Legendre spectrum is displayed before, near the closest frequency separation and after the avoided crossing. The mean Legendre spectrum of a field U is defined as $C(\ell) = \max_{n_r}|U(\ell, n_r)|/\max|U(\ell, n_r)|$, where $U(\ell, n_r)$ are the components of the Legendre/Chebyshev expansion, n_r being the degree of the Chebyshev polynomial. The quantity $C(\ell)$ thus represents the largest Chebyshev component for a given value of ℓ normalized by the maximum over all spectral components. The mean Legendre spectra peak at one characteristic degree before and after the avoided crossing, thus showing that the modes recover their original properties after the crossing and therefore can be unambiguously recognized. Up to the fastest rotation considered, the $\ell = 0{-}7,\ n = 1{-}10,\ m = 0$, p-modes undergo a limited number of avoided crossing and could be followed unambiguously.

It remains that near the crossing the labeling is somewhat ambiguous. First, it is difficult to define a criterion to assign a label. Here, we mostly use the degree at which the mean Legendre spectrum reaches a maximum. But it occurred that the two interacting modes peak at the same degree in which case we determined the location of the smallest frequency separation. Second,

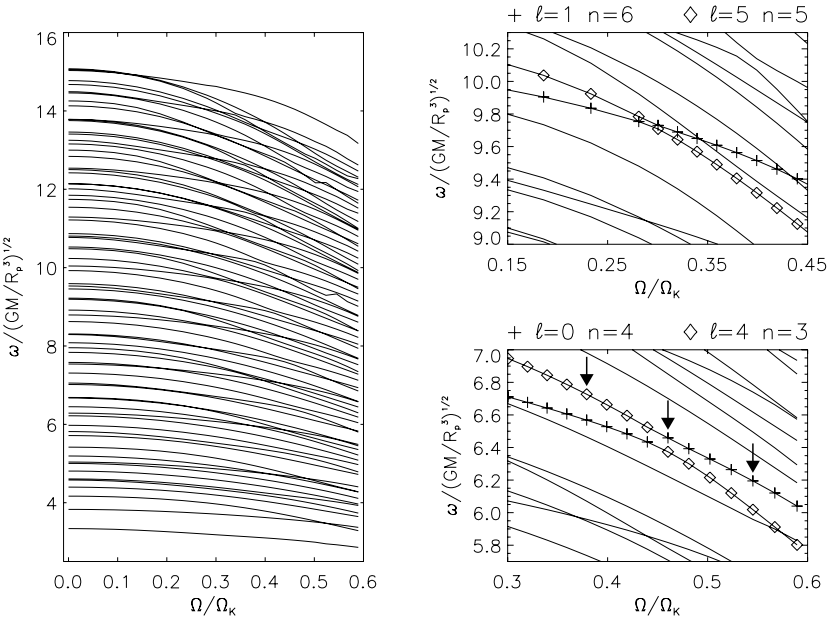

Fig. 4. Evolution of all the computed p-modes frequencies from $\Omega = 0$ to $\Omega/\Omega_K = 0.59$. The frequencies have been adimensionalized by $(GM/R_p^3)^{1/2}$ because we expect that the polar radius R_p does not change much as the rotation of the star increases. Non-rotating $\ell = (0, ..., 7)$, $n = (1, ..., n_{max})$ p-modes have been followed by progressively increasing the rotation. This mode tracking requires special care when an avoided crossing occurs between two modes of the same equatorial parity. The figure on the left shows an overview of the frequency evolution while the two right figures display zooms to illustrate avoided crossings between the $\ell = 1$, $n = 6$ and $\ell = 5$, $n = 5$ modes and the $\ell = 0$, $n = 4$ and $\ell = 4$, $n = 3$ modes, respectively. Although the two "interacting" modes have a mixed character near the closest frequency approach, their original properties are recovered after the crossing which enables to unambiguously follow and label the modes. This is illustrated in Fig. 5 by considering the spectra of Legendre expansion components of the $\ell = 0$, $n = 4$ and $\ell = 4$, $n = 3$ modes at the rotation rates marked by an arrow. Note that in the above figures crossings do occur between equatorially symmetric and anti-symmetric modes. In the global view, there are two examples of discontinuous frequency changes due to avoided crossing with modes which frequency is not represented on the figure. Actually, the $\ell = 8$, $n = (1, 2, 3)$ modes have been displayed in this view to avoid more discontinuous changes.

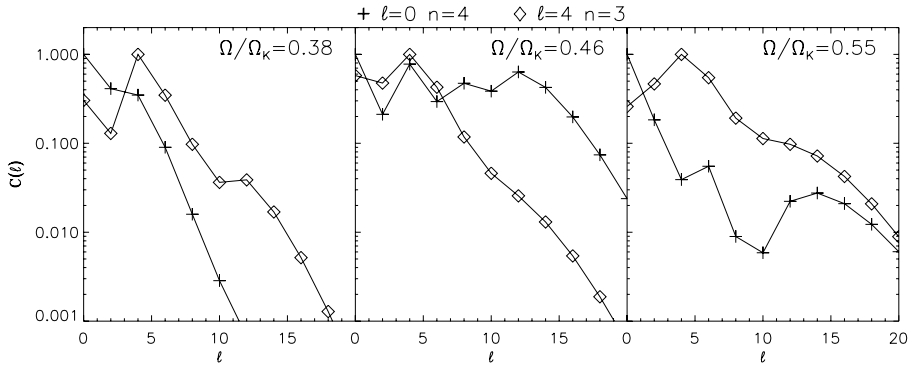

Fig. 5. Evolution of the Legendre components $C(\ell) = \max_{n_r}|U(\ell, n_r)|$ of the $\ell = 0$, $n = 4$ and $\ell = 4$, $n = 3$ modes during the avoided crossing shown in Fig. 4. Prior to ($\Omega/\Omega_K = 0.38$) and after ($\Omega/\Omega_K = 0.55$) the avoided crossing, the spectrum of Legendre components peaks at a given degree while, near the closest approach ($\Omega/\Omega_K = 0.46$), the double peaks of the spectra show the mixed character of the eigenmodes.

as shown by Fig. 5, a more fundamental problem is that a single label cannot reflect the mixed nature of the eigenfunction.

Another issue related to avoided crossings concerns their influence on the accuracy of the eigenfunction computation. Indeed, if a large-scale, well resolved eigenfunction undergoes an avoided crossing with a small-scale unresolved mode, the accuracy of the eigenfunction determination will be affected. The effect on the frequency accuracy should be small as the frequency gap induced by the avoided crossing of two modes of well separated length scales is small. But, at the closest approach, the eigenfunctions will be much affected. At zero rotation, the highest degree mode present in our frequency range is $\ell = 51, n = 1$. Thus, if one of the low degree modes that we computed undergoes an avoided crossing with a mode of such a high degree, the high degree mode should be resolved to ensure an accurate determination of the eigenfunction of the low degree mode.

4.3. The structure of the frequency spectrum

The effect of the centrifugal force on the acoustic frequency spectrum of axisymmetric modes is investigated. The mean modifications of the spectrum are discussed then we investigate how regularities in the frequency spacings evolve with rotation. Finally, differences between equatorially symmetric and anti-symmetric modes are outlined.

4.3.1. Global spectrum evolution

Figure 6 compares the frequency spectrum of the $\ell = 0$–$7, n = 1 - n_{max}, m = 0$ modes at $\Omega = 0$ (upper panel) and at $\Omega/\Omega_K = 0.59$ (lower panel), the height of the vertical bars corresponding to the degree ℓ of the mode. It appears that the centrifugal force induces a mean contraction of the frequency spectrum. This is expected as the decrease of the sound speed and the increase

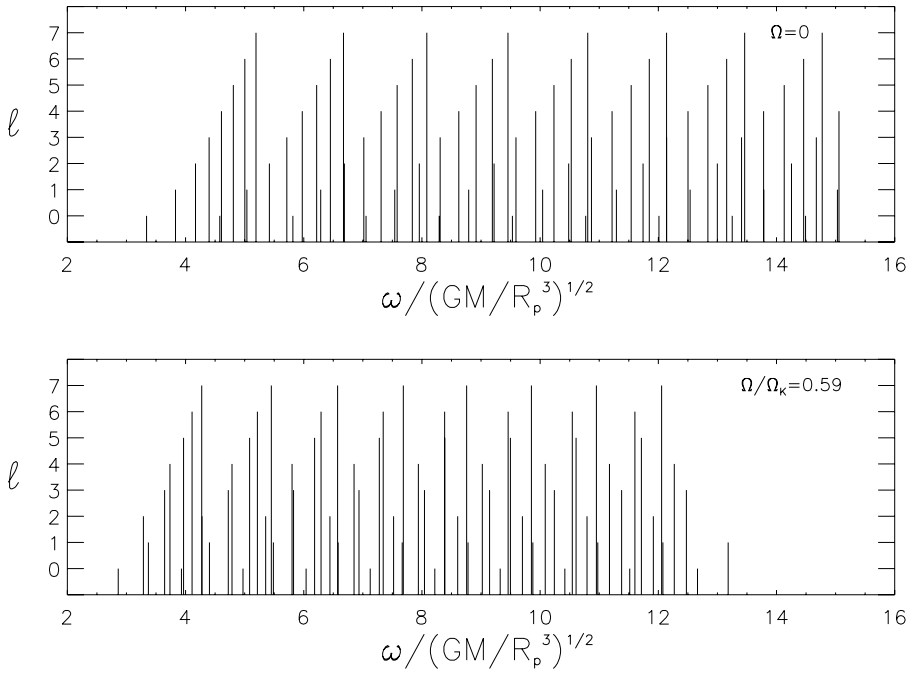

Fig. 6. Frequency spectrum of $\ell = 0$–7, $n = 1 - n_{\max}, m = 0$ modes at $\Omega = 0$ (*top panel*) and $\Omega/\Omega_{\rm K} = 0.59$ (*bottom panel*). The degree number ℓ associated with the frequency is shown by the height of the vertical bar.

of the star volume induced by the centrifugal force both tend to lessen the frequency of acoustic modes.

To illustrate this effect, consider a spherically symmetric decrease of the effective gravity. In a homologous series of spherical models of increased volume V, the decreasing rate of the frequencies $\Delta\omega/\omega$ is $-(1/2)(\Delta V/V)$, as the normalized frequencies $\omega/(GM/R^3)^{1/2}$ remain constant. For non-homologous spherically symmetric changes, $\Delta\omega/\omega$ is asymptotically equal to $-\Delta(\ln \int_0^{R_{\rm p}} {\rm d}r/c)$ for high order modes verifying the following asymptotic formula valid for low degree and high order p-modes (Tassoul 1980):

$$\omega = \frac{\pi}{\int_0^R \frac{{\rm d}r}{c}}(n + (\ell + 1/2)/2 + \alpha) \tag{39}$$

where $1/\int_0^R \frac{{\rm d}r}{c}$ is the sound travel time along a stellar radius and α is a constant. When, as in these two previous cases, $\Delta\omega/\omega$ does not depend on the frequency, the concentration of the frequency spectrum is homothetic.

This is clearly not the case here since the frequencies cross each other (see Fig. 4). But there is still an average contraction rate which is of the order of $-(1/2)(\Delta V/V)$, where now V is the volume of the centrifugally distorted star. In addition, the contraction rates of individual frequencies appears to be comprised between the logarithmic derivative of the sound travel times computed respectively along the polar and equatorial radii:

$$\partial_\Omega\left(\ln\int_0^{R_{\rm p}}\frac{{\rm d}r}{c}\right) \le -\partial_\Omega(\ln\omega) \le \partial_\Omega\left(\ln\int_0^{R_{\rm e}}\frac{{\rm d}r}{c}\right). \tag{40}$$

Another interesting property is that, at small rotation rates, say $\Omega/\Omega_K \le 0.05$, the contraction rate $\partial_\Omega(\ln\omega)$ tends to be independent of ℓ and n for the large degree modes $\ell \ge 3$. This suggests that an asymptotic regime exists for modes with horizontal wavelengths smaller than the dominant length scales of the centrifugal distortion. In this regime, the contraction rate has a constant value that is not equal to $-(1/2)(\Delta V/V)$. We already found such behaviour in the case of homogeneous ellipsoids (Lignières et al. 2001) where a perturbative analysis shows that the contraction rate of axisymmetric modes is constant for high ℓ and n and that it can be related to the increase of the ellipse perimeter.

Nevertheless, for the low degree modes $\ell \le 2$ below $\Omega/\Omega_K \approx 0.05$, and for all modes at higher rotation rates, $\partial_\Omega(\ln\omega)$ depends on ℓ and n. This differential effect modifies the structure of the frequency spectrum as the rotation increases.

4.3.2. Regular frequency spacings

In a non-rotating star, the frequency spectrum presents some regular frequency spacings which can be accounted for by an asymptotic theory in the high frequency limit $\omega \to \infty$. The asymptotic formula (39), valid for low degree and high order modes, shows that the large frequency separation between modes of consecutive order n, $\Delta_n = \omega_{n+1,\ell} - \omega_{n,\ell}$, does not depend on ℓ and n and is equal to $\pi/\int_0^R \frac{{\rm d}r}{c}$. A more detailed asymptotic analysis also shows how the so-called small frequency separation $\delta = \omega_{n+1,\ell} - \omega_{n,\ell+2}$ vanishes as a function of the frequency. Although our calculations are restricted to the low frequency part of the acoustic spectrum, we observe a clear tendency towards these asymptotic behaviors in the non-rotating case. We can therefore investigate whether these properties are modified by rotation.

Figure 7 presents the large frequency separation Δ_n and the frequency separation between consecutive modes of the same order and parity:

$$\Delta_{2,\ell} = \omega_{n,\ell+2} - \omega_{n,\ell}, \tag{41}$$

as a function of the radial order n for four different rotation rates, (a) $\Omega = 0$, (b) $\Omega/\Omega_{\rm K} = 0.32$, (c) $\Omega/\Omega_{\rm K} = 0.46$ and (d) $\Omega/\Omega_{\rm K} = 0.59$. As in the previous figures, the frequencies are adimensionalized by $(GM/R_{\rm p}^3)^{1/2}$. Continuous lines have been drawn between frequencies of the same degree ℓ. We first observe that the large frequency separation tends to be independent of n and ℓ at all rotation rates. In accordance with the mean contraction of the frequency spectrum mentioned above, the large

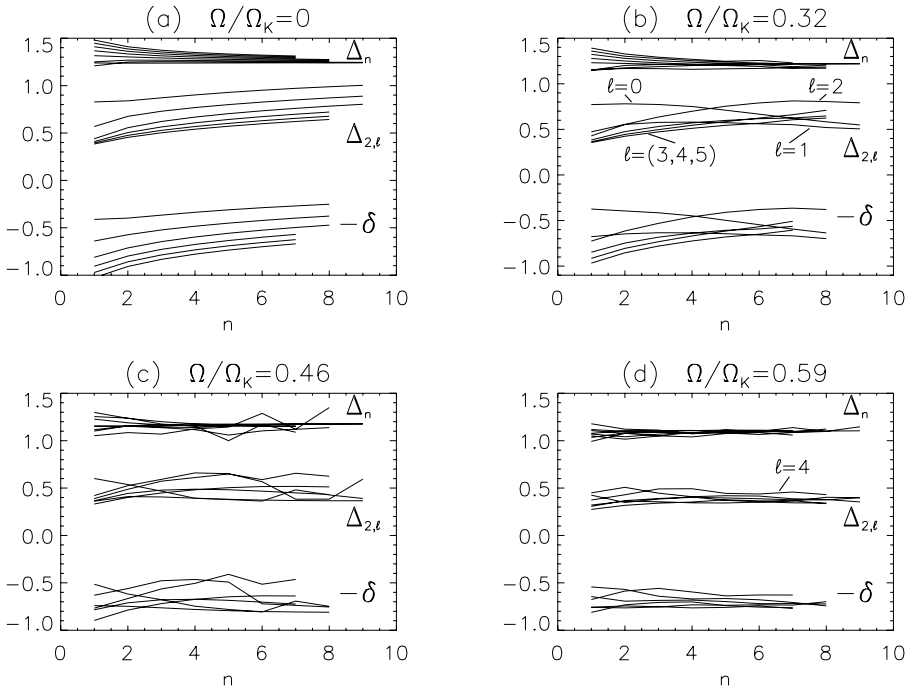

Fig. 7. Regularities in the frequency spacings of axisymmetric ($m = 0$) modes. The large frequency separation between modes of consecutive order $\Delta_n = \omega_{n\ell} - \omega_{n-1\ell}$, the frequency separation between $\ell + 2$ and ℓ modes, $\Delta_{2,\ell} = \omega_{n,\ell+2} - \omega_{n,\ell}$, and the small frequency separation $\delta = \Delta_n - \Delta_{2,\ell}$ are displayed as a function of the radial order n for four different rotation rates, **a)** $\Omega = 0$, **b)** $\Omega/\Omega_K = 0.32$, **c)** $\Omega/\Omega_K = 0.46$ and **d)** $\Omega/\Omega_K = 0.59$. We plotted the opposite of the small frequency separation $-\delta$ for clarity. Continuous lines have been drawn between frequencies of the same degree ℓ.

frequency separation decreases with rotation. It is always between $\pi/\int_0^{R_p} dr/c$ and $\pi/\int_0^{R_e} dr/c$.

The dispersion of the large frequency separations around their mean value also has an interesting evolution with rotation. In the non-rotating case, the dispersion reflects a regular departure from the asymptotic limit. It is larger for high degrees and monotonically decreases with frequency (see Fig. 7a). In the rotating cases, the dispersion is not as regular. The largest departures, some of which are most clearly visible in Fig. 7c, can be attributed to an ongoing avoided crossing. The residual dispersion is irregular and decreases with rotation. At $\Omega/\Omega_K = 0.59$, if we exclude all $n < 4$ values from our sample, the mean large frequency separation $\langle\Delta_n\rangle$ is equal to $1.095(GM/R_p^3)^{1/2}$ and its standard deviation is $0.017\langle\Delta_n\rangle$.

We now consider the small frequency separation $\delta = \Delta_n - \Delta_{2,\ell}$. As expected, in the absence of rotation the small frequency separation tends to vanish as n increases. But, at $\Omega/\Omega_K = 0.32$, the small frequency separation no longer decreases with n for some values of ℓ and for the higher rotation rates it becomes nearly constant. At the same time, the $\Delta_{2,\ell}$ separation becomes more and more uniform as rotation increases. As shown in Fig. 7b, $\Delta_{2,\ell}$ becomes approximatively constant with n first for low degree modes while it still increases with frequency for high degree modes. In addition, equatorially antisymmetric modes reach this new regime at a lower rotation rate than the equatorially symmetric modes of similar degree. This is illustrated in Fig. 7d by the $\Delta_{2,\ell=4}$ curve which still remains above the mean $\Delta_{2,\ell}$ value while the $\Delta_{2,\ell=5}$ separation collapses with the other curves. At $\Omega/\Omega_K = 0.59$, if we exclude all $n < 4$ values from our sample, the mean frequency separation $\Delta_{2,\ell}$ is equal to $0.387(GM/R_p^3)^{1/2}$ and its standard deviation is $0.033\langle\Delta_n\rangle$.

As a consequence of the near uniformity of Δ_n and $\Delta_{2,\ell}$, the frequencies of low degree and high order modes can be approximated by the following expressions:

$$\tilde{\omega}_{n\ell} = \begin{cases} n\delta_n + p\delta_\ell + \alpha^+ \text{ if } \ell = 2p \\ n\delta_n + p\delta_\ell + \alpha^- \text{ if } \ell = 2p+1 \end{cases} \quad (42)$$

where $\delta_n = \langle\Delta_n\rangle$, $\delta_\ell = \langle\Delta_{2,\ell}\rangle$, α^+ and α^- only depend on the equilibrium model. Using a reference frequency to determine the α constants (the $\ell = 0$, $n = 8$ frequency for α^+ and the $\ell = 1$, $n = 8$ frequency for α^-), we computed the root mean square error $\sqrt{1/N\sum(\tilde{\omega} - \omega)^2}$ and the maximum error made in using the approximate expressions (42). For a frequency subset containing the $n > 4$ and $\ell < 5$ modes, the rms error is $0.017\delta_n$ while the maximum error amounts to $0.05\delta_n$. Both errors are a very small fraction of the large separation which shows that Eq. (42) yields useful approximations of the frequency spectrum.

4.3.3. Equatorially symmetric versus anti-symmetric frequency spectra

We have seen that the regular frequency spacings Δ_n and $\Delta_{2,\ell}$ have similar values for symmetric and anti-symmetric modes with respect to the equator. The evolution of the equatorially symmetric and anti-symmetric frequency spectra are nevertheless quite different. Indeed, considering two modes of similar frequency but of opposite equatorial parity, the frequency of the symmetric mode generally decreases faster with rotation than the frequency of the antisymmetric modes. The consequence is that the frequency separation between modes of consecutive degree (and thus of opposite parity) $\Delta_l = \omega_{n,\ell+1} - \omega_{n,\ell}$ tends to increase when ℓ is even and to decrease when ℓ is odd. The frequency separation Δ_l can even become negative which implies that, contrary to the non-rotating case, frequencies of a given order n do not increase monotonically with the degree ℓ. This striking modification of the usual frequency ordering is apparent in Fig. 6 where the $(\ell = 2, n)$ frequencies are smaller than the $(\ell = 1, n)$ frequencies for all the order n that we calculated, that is $n = (1, ..., 10)$. In the same way, the $(\ell = 4, n)$ frequencies are smaller than the $(\ell = 3, n)$ frequencies if $n \geq 3$, and again the $(\ell = 6, n)$ frequencies are smaller than the $(\ell = 5, n)$ frequencies if $n \geq 5$.

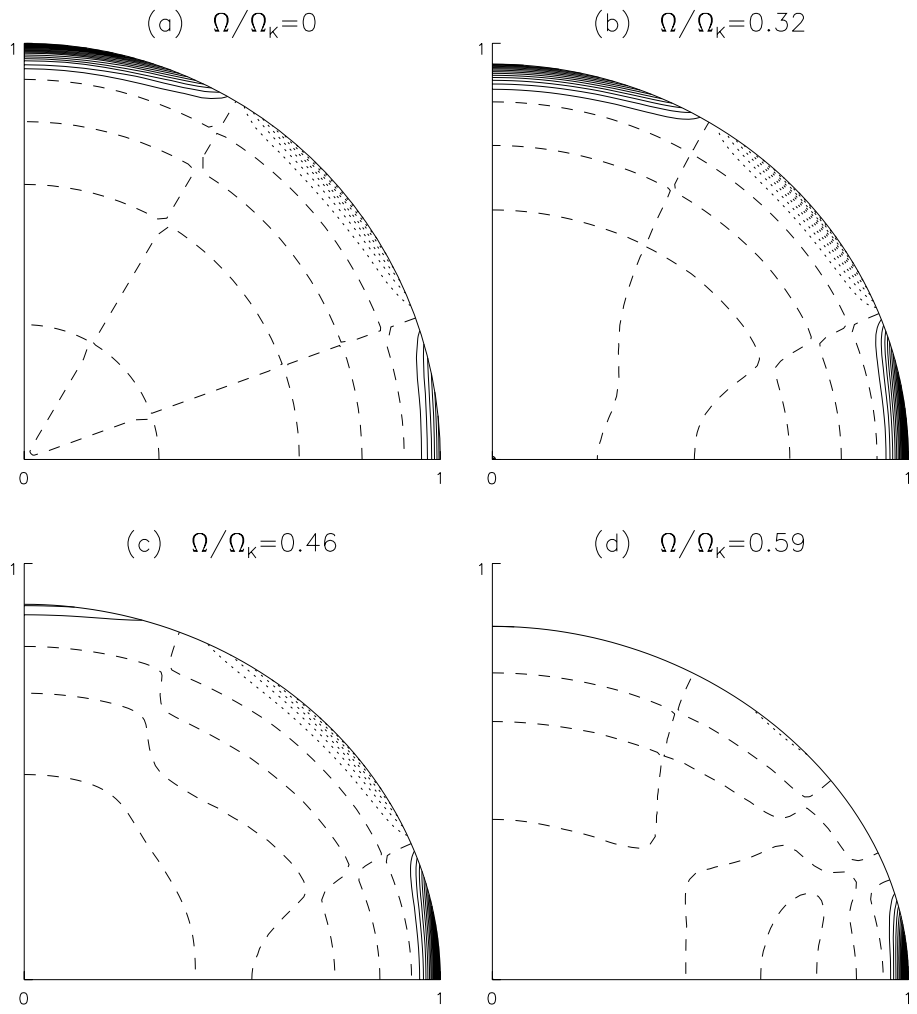

Fig. 8. Isocontours of the $\ell = 4, n = 4$ mode amplitude in a meridional plane as a function of the rotation **a)** $\Omega = 0$, **b)** $\Omega/\Omega_K = 0.32$, **c)** $\Omega/\Omega_K = 0.46$ and **d)** $\Omega/\Omega_K = 0.59$. The amplitude is normalized to the maximum of its absolute value. Continuous lines correspond to positive amplitudes, dashed lines to the zero amplitude and dotted lines to negative amplitudes. At zero rotation, the angular distribution is given by the $\hat{Y}_4^0(\theta)$ Legendre polynomial while the radial distribution is characterized by the surface concentration of the amplitude and the presence of $n = 4$ nodes in the inner part. For larger rotation rates, the largest amplitudes concentrates toward the equator. We also note that the number of radial nodes decreases along the polar radius while it increases along the equatorial radius.

4.4. Equatorial concentration

In this section, we focus on the most notable effect of the centrifugal force on the eigenmodes, namely the equatorial concentration and consider its consequences on the mode visibility. Note that Clement (1981) also reported an equatorial concentration of the equatorially symmetric modes that he calculated.

Figure 8 shows this effect on the ($\ell = 4, n = 4$) mode. Contours of the amplitude of the Lagrangian pressure perturbation are plotted in a meridional plane for increased rotation rates, (a) $\Omega = 0$, (b) $\Omega/\Omega_K = 0.32$, (c) $\Omega/\Omega_K = 0.46$ and (d) $\Omega/\Omega_K = 0.59$. We observe that the number of nodes increases along the equatorial radius and decreases along the polar one. Along the surface, the number of nodes remains equal to ℓ before $\Omega/\Omega_K = 0.59$ where additional nodes appear. The equatorial concentration is clearly seen in the outermost layers.

In Fig. 9, the equatorial concentration is shown for other modes including the lowest and highest degree modes of our sample as well as symmetric and anti-symmetric modes. The latitudinal variation of the mode amplitude is displayed at the surface for the following modes, (a) $\ell = 0, n = 1$, (b) $\ell = 1, n = 1$, (c) $\ell = 6, n = 8$, (d) $\ell = 7, n = 8$. In each case, the equatorial concentration grows with rotation. At the largest rotation rate, symmetric modes are maximal at the equator while anti-symmetric modes peak at small latitudes since they must vanish at the equator. The contrast between these maxima and the polar amplitude is strong.

The equatorial concentration reveals a modification of the resonant cavity of the acoustic waves. In particular, the reduction of the volume of the resonant cavity should tend to increase the frequency. The equatorial concentration seems also to be associated with the near-uniformity of the frequency separation $\Delta_{2,\ell}$. At low rotation rates, the concentration is not completed and $\Delta_{2,\ell}$ is clearly not constant. At the largest rotation rate, all modes are concentrated near the equator and $\Delta_{2,\ell}$ is nearly uniform.

Besides its effect on the frequency spectrum, the equatorial concentration of eigenmodes should induce a profound modification of the mode visibility as compared to the non-rotating case. The photometric mode visibility is determined by the integration over the visible part of the star's perturbed surface of the radiation intensity perturbations associated with a particular pulsation mode. Rigorous calculations of photometric visibilities are beyond the scope of the present paper as they require non-adiabatic calculations of the oscillation modes and stellar atmosphere models (e.g. Daszyńska-Daszkiewicz et al. 2002). But we can still determine the effects of averaging the perturbations over the visible surface which have a direct impact on the visibility. The disk-averaging factor is defined as:

$$D(i) = \frac{1}{\pi R_e^2 \delta T_0} \iint_{S_v} \delta T(\theta, \phi) \mathrm{d}\mathbf{S} \cdot \mathbf{e}_i \tag{43}$$

where i is the inclination angle between the line-of-sight and the rotation axis, $\mathbf{e}_i$ is a unit vector in the observer's direction and δT is the spatial part of the Lagrangian temperature perturbation at

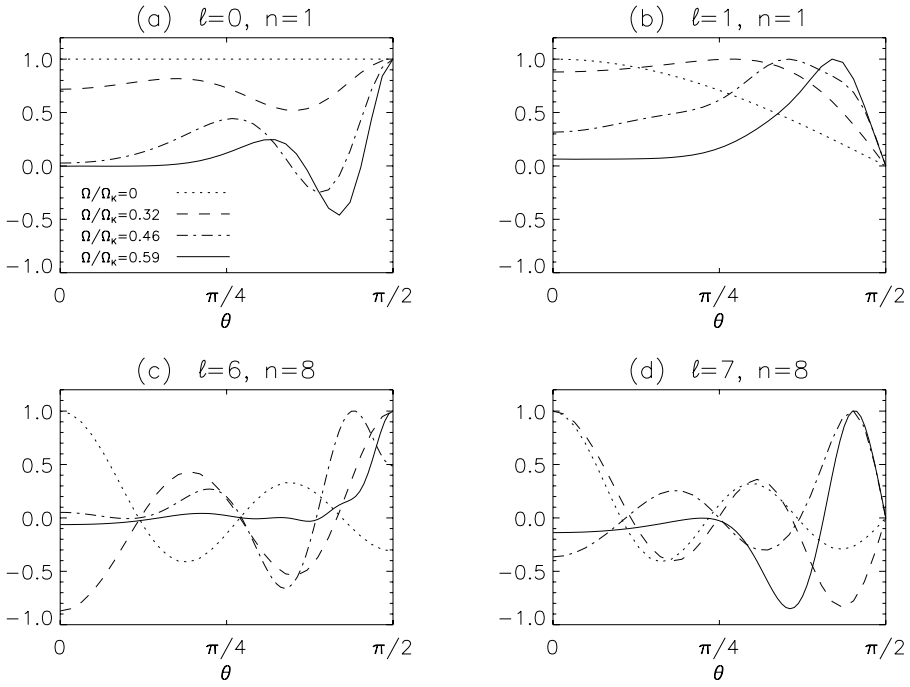

Fig. 9. The mode amplitude at the surface of the polytropic model as a function of the rotation rate **a)** $\ell = 0, n = 1$, **b)** $\ell = 1, n = 1$, **c)** $\ell = 6, n = 8$, **d)** $\ell = 7, n = 8$. The amplitude is normalized to the maximum of its absolute value. While the angular distribution is given by the corresponding Legendre polynomial $\hat{Y}_\ell^0(\theta)$ in the absence of rotation, the oscillation amplitude progressively concentrates towards the equator ($\theta = \pi/2$) as rotation increases.

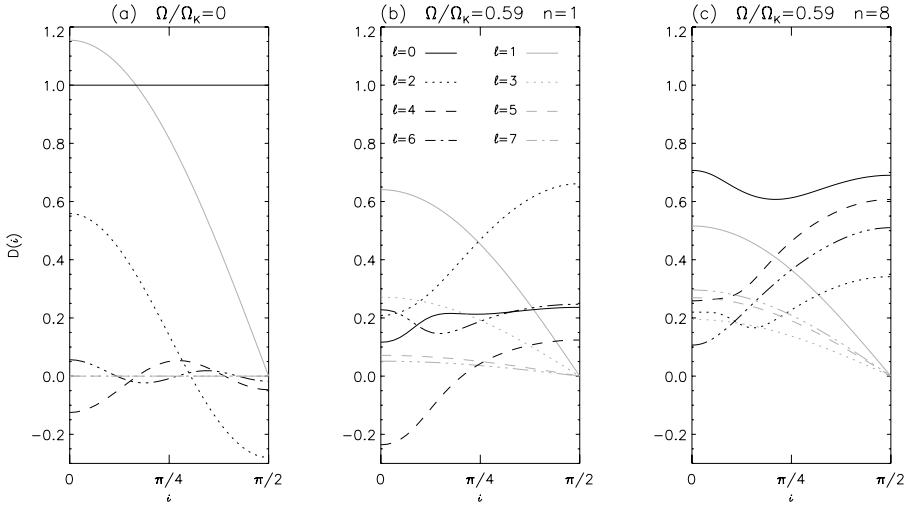

Fig. 10. The disk-averaging factor $D(i)$ is shown as a function of the inclination angle i for various axisymmetric modes at two different rotation rates $\Omega = 0$ **a)** and $\Omega/\Omega_K = 0.59$. The degree of the modes varies from $\ell = 0$ to $\ell = 7$. In the rotating case, the surface distribution also depends on the order of the mode. Two values $n = 1$ **b)** and $n = 8$ **c)** have been considered at $\Omega/\Omega_K = 0.59$.

the stellar surface, δT being proportional to the velocity divergence χ in the approximation of adiabatic perturbations. The mode amplitude is normalized by δT_0 the root mean square of the perturbation over the whole stellar surface

$$\delta T_0 = \left(\iint_S \delta T^2(\theta, \phi) \mathrm{d}S \right)^{1/2} \tag{44}$$

and the visible surface S_v has been normalized by πR_e^2, the visible surface of a star seen pole-on. With these normalizations the disk-averaging factor of a radial mode seen pole-on is unity.

In the absence of rotation, the surface distribution of modes is determined by a unique spherical harmonic and the disk-averaging factor takes a simple analytical form (Dziembowski 1977). For even degree and for $\ell = 1$, the disk-averaging factor varies with the inclination angle as the Legendre polynomial $\hat{Y}_\ell^m(i)$ while it vanishes altogether for odd degree $\ell \geq 3$. For rotating stars, the method of the calculation is detailed in Appendix C. Note that for modes that are equatorially antisymmetric and axisymmetric, the disk-averaging factor also has a simple dependency on the inclination angle as it is proportional to $\cos(i)$.

Figure 10 shows the disk-averaging factor of various axisymmetric modes as a function of the inclination angle. The non-rotating case is displayed in Fig. 10a where $\ell = 0$ to $\ell = 7$ modes are considered. We recall that, at $\Omega = 0$, modes of different radial orders but same ℓ and m have the same surface distribution. This is not true in the rotating case and, at $\Omega/\Omega_K = 0.59$, Figs. 10b and c present the disk-averaging factor for modes of the same degree numbers but for two different radial orders $n = 1$ and $n = 8$, respectively. Note also that the disk-averaging factor was allowed to take a negative value for clarity of the figure although it is its absolute value that is relevant for the mode's visibility. Figure 10 shows that rotation strongly modifies the dependency of the disk-averaging factor on the inclination angle as well as on the degree number.

Figure 10c shows that for all $n = 8$ equatorially symmetric modes the absolute value of the disk-averaging factor tends to increase with the inclination angle. This is due to the equatorial concentration of these modes (see for example the surface

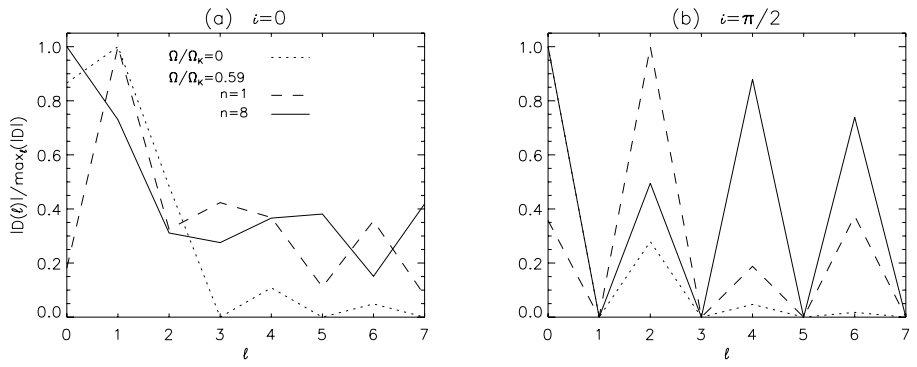

Fig. 11. The variation of the disk-averaging factor as a function of the degree ℓ is shown at two fixed values of the inclination angle ($i = 0$ and $i = \pi/2$). The three curves in each figure correspond to the non-rotating case and, at $\Omega/\Omega_K = 0.59$, to two different orders, $n = 1$ and $n = 8$. The absolute value of the disk-averaging factor has been rescaled by its maximum value among the different degree considered to outline its dependency on the degree number. In sharp contrast to the non-rotating case, the disk-averaging factor at $\Omega/\Omega_K = 0.59$ does not show a strong decrease with ℓ.

distribution of the ($\ell = 6, n = 8$) mode at $\Omega/\Omega_K = 0.59$ shown in Fig. 9c). This tendency is less pronounced for the $n = 1$ symmetric modes shown in Fig. 10b (except for the $\ell = 2$ mode) although these modes are also equatorially concentrated. This is due to a cancellation effect between positive and negative perturbations concentrated near the equator as illustrated by the surface distribution of the ($\ell = 0, n = 1$) mode in Fig. 9a. The non-rotating case strongly differs since the absolute value of the disk-averaging factor for even degree $\ell > 0$ modes does not vary monotonically with the inclination. Indeed, they have $\ell/2$ nodes between 0 and $\pi/2$. For odd ℓ modes, the disk-averaging factor is also modified by rotation since it no longer vanishes for $\ell \geq 3$. This occurs because the projected elementary surfaces $d\mathbf{S} \cdot \mathbf{e}_i$ are no longer symmetric with respect to the observer's direction and because the projection of the eigenmode surface distribution onto the Legendre polynomial $\hat{Y}_1^0$ is not zero for $\ell \geq 3$ modes.

In non-rotating stars, the cancellation effect between positive and negative perturbations results in a rapid decrease of the disk-averaging factor as the degree ℓ of the mode increases. Consequently, modes above a certain degree $\ell \geq 3$–4 are not expected to be detectable with photometry and are therefore not included when trying to identify the observed frequencies. As shown in Fig. 11, this property must be reconsidered for rapidly rotating stars. The absolute disk-averaging factor normalized by its maximum value over the degree considered $0 \leq \ell \leq 7$, $|D(i)|/\max_\ell |D(i)|$, is plotted as a function of ℓ for two fixed values of the inclination angle, $i = 0$ in Fig. 11a and $i = \pi/2$ in Fig. 11b. The three curves correspond to $\Omega = 0$ and to $\Omega/\Omega_K = 0.59$ for the $n = 1$ and $n = 8$ modes, respectively. In contrast to the non-rotating case, the disk-averaging factor has no tendency to decrease above $\ell = 2$. Again, this can be explained by the equatorial concentration as modes of different degree have a similar surface distribution.

4.5. Comparison with perturbative methods

According to the perturbative analysis, centrifugal effects appear at second order in Ω (Saio 1981). To determine the second-order perturbative coefficient from our complete calculations, we performed a series of calculations for small rotation rates ($\Omega = 0, 1.8 \times 10^{-3}$, 1.8×10^{-2}, 4.6×10^{-2}, 0.09×10^{-2}, ... in units of Ω_K). From them, we determined the second-order perturbative coefficient, denoted ω_1, as the limit of the ratio $(\omega(\Omega) - \omega_0)/\Omega^2$, where ω_0 denotes a non-rotating eigenfrequency. Thus the approximate frequencies valid up to the second order in Ω read $\omega_{\rm pert} = \omega_0 + \omega_1 \Omega^2$, where the frequencies are in units of $(GM/R_p^3)^{1/2}$ and the rotation is in units of Ω_K. To assess the range of validity of the second order perturbative approach, we compared these approximate frequencies to the "exact" frequencies. In Fig. 12, the relative differences between the two calculations, $(\omega - \omega_{\rm pert})/\omega$, is plotted as a function of the rotation rate for the $\ell = 0$–2, $n = 1$–10 modes. The departures computed for the other modes, $\ell = (3, ..., 7)$, $n = (1, ..., n_{\rm max})$, are smaller than the extremal differences shown in Fig. 12 and are not displayed for clarity. The relative differences are generally larger for low degree modes and, for small rotation rates, are a monotonic function of the radial order n (an increasing function for the $\ell = 0$–2 modes shown in Fig. 12). As mentioned before the low degree modes seem to be sensitive to the precise form of the distortion that occurs at similar lengthscales. As rotation increases, it appears that higher than second order effects are important to describe the effect of the centrifugal distortion on these modes. The second order approximation is much better for large ℓ modes which are sensitive to global distortion properties.

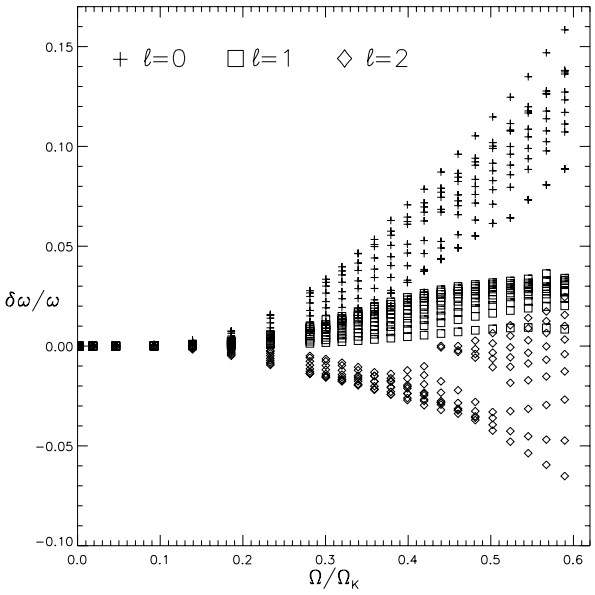

Fig. 12. The relative difference between exact frequencies and their second order perturbative approximation (second order in terms of the small parameter Ω/Ω_K), namely $\delta\omega/\omega$ where $\delta\omega = \omega - \omega_{\rm pert}$ is displayed as a function of the rotation rate for the $\ell = 0$–2, $n = 1$–10, $m = 0$ modes.

As compared to the observational uncertainties on the frequency determinations, the error made in using second order perturbative methods becomes rapidly significant as rotation increases. For a ratio $\Omega/\Omega_K = 0.24$, corresponding to a typical δ Scuti star with an equatorial velocity of 100 km s^{-1}, the maximum absolute difference is 11 μHz which is much larger than typical observational uncertainties.

The fact that in our frequency sample the absolute difference increases with frequency suggests that departure from the perturbative approach could be detectable for moderately rotating stars pulsating in high order modes. In our data limited to $n \leq 10$, the largest relative difference is 2.87×10^{-3} for a $\Omega/\Omega_K = 0.139$ rotation corresponding to a solar-type star with an equatorial velocity of 60 km s^{-1}. If we assume that the same relative difference holds for high order p-modes in the range of 2000 μHz generated in convective envelopes of these stars, the absolute difference is 5.7 μHz for a typical 2000 μHz frequency. This would be also easily detectable given the observational uncertainties (Bouchy et al. 2005). However, a firm conclusion should await a direct comparison between the perturbative approach and the complete calculation for p-modes generated in the convective envelope of rotating solar-type stars.

5. Discussion and conclusion

A new non-perturbative method to compute accurate oscillation modes in rotating stars was presented. The accuracy of the computed frequencies has been obtained by testing the effect of the different parameters of the numerical method. Then, the effects of the centrifugal force on low frequency axisymmetric acoustic oscillation modes were investigated in uniformly rotating polytropic models of stars. Seventy-one low degree $\ell \leq 7$ and low order $n \leq 10$ modes were first determined at zero rotation and then tracked at higher rotation rates up to $\Omega/\Omega_K = 0.59$.

In the frequency and rotation ranges considered in this paper, the zero rotation quantum numbers ℓ and n were used to label the modes. This labeling turned out to be meaningful since we found regular frequency spacings between modes of the same degree and consecutive orders, Δ_n, and, within the subsets of modes of the same equatorial parity, between modes of the same order and consecutive degree, $\Delta_{2,\ell}$. We noted however that near avoided crossings, when the eigenfunction is a mix of the two "interacting" modes, a unique label cannot reflect the actual eigenfunction structure. Although successful in the frequency and rotation ranges considered, it remains to be proved that this labeling can be performed in practice at higher rotation and at higher frequencies. Indeed, the main difficulty of the labeling procedure arises from the avoided crossing between modes of the same equatorial parity and such crossings will be more frequent as the eigenfrequency density increases with the frequency. The coupling between modes is also stronger at higher rotation rates. It might then be necessary to investigate tools other than the mean Legendre power spectrum to characterize the modes.

The study of the frequency spectrum showed a quite unexpected result, namely that, at the highest rotation rates, a new form of organization sets in after the zero rotation asymptotic structure of the spectrum has been destroyed. In the absence of rotation, the asymptotic theory is directly related to the spherical symmetry of the stars and ultimately to the integrability of the underlying ray dynamics. In the presence of rotation, the eigenvalue problem is not fully separable and the underlying acoustic ray dynamics is most probably not integrable. The regular spacings observed at high rotation rates were not expected. They might be the sign of a near-integrable ray dynamic rather than a chaotic system. These aspects will be investigated in a ray dynamic study of rotating polytropic models of stars.

Most importantly for asteroseismology, the existence of regular spacings in the spectrum can potentially provide tools for the mode identification in rapidly rotating pulsating stars. A complete acoustic frequency spectrum including $m \neq 0$ modes and the effects of the Coriolis acceleration should however be computed and analyzed to assess the practical relevance of these regular spacings.

Apparently, there is a relation between the new spectrum structure and the equatorial concentration of the mode amplitudes. A consequence would be that this spectrum structure does not apply to the whole spectrum. Indeed, sufficiently high degree modes should still be of the whispering gallery type (e.g. Rieutord 2001). Then, being so different from equatorially concentrated modes, they are not expected to follow the same regular spacings.

Another interesting issue is the difference between the modes of different equatorial symmetry. We have seen that although the structure of the symmetric and anti-symmetric spectra is similar, the frequency spectrum of the symmetric modes as a whole seems to evolve independently from the anti-symmetric spectrum. The equatorial symmetry also influences the "strength" of the avoided crossings measured by the frequency separation at the closest frequency approach. As illustrated in Fig. 4 (right panels), avoided crossings between symmetric modes are always stronger than avoided crossings between anti-symmetric modes since they remain further apart.

Modes undergoing an avoided crossing are particular because they have close frequencies and similar eigenfunctions. As a consequence, both can be excited to observable levels by some excitation mechanism. They are therefore good candidates to explain the occurrence of close frequencies in observed spectra (Breger & Pamyatnykh 2006) as well as the associated amplitude variations induced by beating between the two close frequencies.

The most striking effect of the centrifugal force on the eigenfunction is the equatorial concentration of the mode amplitude. Again, the study of the ray dynamics should help specify the conditions in which the sound waves stay focused in the equatorial region. As compared to the non-rotating case, the equatorial concentration strongly modifies the integrated light visibility and in particular its variation with respect to the mode degree and the inclination angle. Our results showing a global increase of the disk-integration factor as the star is seen equator-on are compatible with observations of δ Scuti pulsations which also suggest an increase of the pulsation amplitudes with i (Suárez et al. 2002). Another finding of practical interest is that, for rapidly rotating stars, the cancellation effect of the disk averaging no longer sharply decreases with the degree of the mode and also varies with the order of the mode. Realistic calculations of the mode visibility including non-adiabatic calculations of the oscillation modes, stellar atmosphere models as well as the gravity and limb darkening effect will however be needed to draw firm observational conclusions.

The omission of the Coriolis force did not allow a complete treatment of the rotational effects. However, the effect of the Coriolis force vanishes for sufficiently large frequency (as the time scale of the Coriolis acceleration $1/\Omega$ becomes much larger than the pulsation period) while the modification of the equilibrium model by the centrifugal force affects all frequencies. Therefore, the results presented here should be useful for the high frequency part of the acoustic spectrum in rotating stars. In a companion paper (Reese et al. 2006b), we extend the present results by taking into account the Coriolis acceleration which, among other things, allows us to specify the domain of validity of perturbative calculations.

Acknowledgements. We thank L. Valdettaro for his contribution to the numerical part of this work and B. Georgeot for fruitful discussions. We also thank the referee for constructive comments. Numerical simulations have been performed with the computing resources of Institut du Développement et des Ressources

en Informatique Scientifique (IDRIS, Orsay, France) and of CALcul en MIdi-Pyrénées (CALMIP, Toulouse, France) which are gratefully acknowledged.

References

Bonazzola, S., Gourgoulhon, E., & Marck, J. A. 1998, Phys. Rev. D, 58, 104020
Bouchy, F., Bazot, M., Santos, N. C., Vauclair, S., & Sosnowska, D. 2005, A&A, 440, 609
Breger, M., & Pamyatnykh, A. A. 2006, MNRAS, in press
Catala, C., Mangeney, A., Gautier, D., et al. 1995, GONG 1994. Helio- and Astro-Seismology from the Earth and Space, ed. R. K. Ulrich, E. J. Rhodes, & W. Dappen, ASP Conf. Ser., 76, 426
Christensen-Dalsgaard, J., & Mullan, D. J. 1994, MNRAS, 270, 921
Clement, M. J. 1981, ApJ, 249, 746
Clement, M. J. 1986, ApJ, 301, 185
Clement, M. J. 1998, ApJS, 116, 57
Daszyńska-Daszkiewicz, J., Dziembowski, W. A., Pamyatnykh, A. A., & Goupil, M.-J. 2002, A&A, 392, 151
Dintrans, B., & Rieutord, M. 2000, A&A, 354, 86
Domiciano de Souza, A., Kervella, P., Jankov, S., et al. 2003, A&A, 407, L47
Dziembowski, W. 1977, Acta Astronomica, 27, 203
Dziembowski, W. A., & Goode, P. R. 1992, ApJ, 394, 670
Edmonds, A. R. 1960, Angular Momentum in Quantum Mechanics, second edn. (Princeton Univ. Press)
Espinosa, F., Pérez Hernández, F., & Roca Cortès, T. 2004, Proceedings of the SOHO 14 GONG 2004 Workshop, ed. D. Danesy, ESA SP-559, 424
Ledoux, P. 1951, ApJ, 114, 373
Lignières, F., & Rieutord, M. 2004, IAU Symp., 215, 414
Lignières, F., Rieutord, M., & Valdettaro, L. 2001, in SF2A 2001: Semaine de l'Astrophysique Française (EDP Sciences), ed. F. Combes et al., 127
Pekeris, C. L. 1938, ApJ, 88, 189
Reese, D., Lignières, F., & Rieutord, M. 2006a, Commun. Asteroseismol., 147, 65
Reese, D., Lignières, F., & Rieutord, M. 2006b, A&A, 455, 621
Rieutord, M. 2001, in Stellar Astrophysical Fluid Dynamics, ed. M. J. Thompson, & J. Christensen-Dalsgaard (Cambridge Univ. Press), 99
Rieutord, M., & Valdettaro, L. 1997, J. Fluid Mech., 341, 77
Rieutord, M., Dintrans, B., Lignières, F., Corbard, T., & Pichon, B. 2005, in SF2A 2005: Semaine de l'Astrophysique Française (EDP Sciences), ed. F. Combes et al., 759
Saio, H. 1981, ApJ, 244, 299
Soufi, F., Goupil, M. J., & Dziembowski, W. A. 1998, A&A, 334, 911
Suárez, J. C., Michel, E., Pérez Hernández, F., et al. 2002, A&A, 390, 523
Tassoul, M. 1980, ApJS, 43, 469
Valdettaro, L., Rieutord, M., Braconnier, T., & Frayssé, V. 2006, [arXiv:physics/0604219]
Walker, G., Matthews, J., Kuschnig, R., et al. 2003, PASP, 115, 1023
Yoshida, S., Yoshida, S., & Eriguchi, Y. 2005, MNRAS, 356, 217

Online Material

Appendix A: Linear operators in spheroidal coordinates

Let us now express the linear operators involved in Eqs. (22)–(24), using the spheroidal coordinates given by Eq. (25). We need the general expression of the divergence

$$\boldsymbol{\nabla}\cdot\boldsymbol{V} = \frac{1}{\sqrt{|\,g\,|}}\partial_i\left(\sqrt{|\,g\,|}V^i\right) \tag{A.1}$$

and the Laplacian:

$$\Delta\Phi = \frac{1}{\sqrt{|\,g\,|}}\partial_i\left(\sqrt{|\,g\,|}g^{in}\partial_n\Phi\right) \tag{A.2}$$

where $\boldsymbol{V} = V^1\boldsymbol{E}_1+V^2\boldsymbol{E}_2+V^3\boldsymbol{E}_3 = V_1\boldsymbol{E}^1+V_2\boldsymbol{E}^2+V_3\boldsymbol{E}^3$ is written in the natural basis $\boldsymbol{E}_i = \partial\boldsymbol{OM}/\partial x^i$ or the conjugated basis $\boldsymbol{E}^i$ verifying $\boldsymbol{E}_i\cdot\boldsymbol{E}^j = \delta_{ij}$, g^{in} are the components of the metric tensor and $|g|$ is the absolute value of metric tensor determinant.

From these expressions, we derived the form of the following operators:

$$\boldsymbol{g}_0\cdot\boldsymbol{\nabla} \equiv (g_0^1\boldsymbol{E}_1 + g_0^2\boldsymbol{E}_2)\cdot\partial_i\,\boldsymbol{E}^i \equiv g_0^1\partial_\zeta + g_0^2\partial_\theta \tag{A.3}$$

$$r^2\Delta \equiv h_1\partial^2_{\zeta\zeta} - 2h_2\partial^2_{\theta\zeta} + h_4\partial_\zeta + \Delta_{\theta\phi} \tag{A.4}$$

$$r^2\mathcal{L} \equiv -\left(h_1\frac{g_0^2}{g_0^1}+2h_2\right)\partial^2_{\theta\zeta} + h_4\partial_\zeta - \left[h_1\partial_\zeta\left(\frac{g_0^2}{g_0^1}\right)\right]\partial_\theta + \Delta_{\theta\phi} \tag{A.5}$$

$$r^2\boldsymbol{\nabla}\cdot(\bullet\,\boldsymbol{A_0}) \equiv (r^2A_0^1)\partial_\zeta + (r^2A_0^2)\partial_\theta + r^2\boldsymbol{\nabla}\cdot\boldsymbol{A_0}[\mathrm{id}] \tag{A.6}$$

where $\Delta_{\theta\phi}$ represent the horizontal part of the Laplacian in spherical coordinates:

$$\Delta_{\theta\phi} \equiv \partial^2_{\theta\theta} + \cot\theta\partial_\theta + \frac{1}{\sin^2\theta}\partial^2_{\phi\phi}, \tag{A.7}$$

and

$$h_1 = \frac{r^2+r_\theta^2}{r_\zeta^2} \tag{A.8}$$

$$h_2 = \frac{r_\theta}{r_\zeta} \tag{A.9}$$

$$h_3 = \frac{r}{r_\zeta} \tag{A.10}$$

$$h_4 = \frac{1}{r_\zeta}\left[\partial_\zeta\left(\frac{r^2+r_\theta^2}{r_\zeta}\right) - \frac{1}{\sin\theta}\partial_\theta(r_\theta\sin\theta)\right]. \tag{A.11}$$

We recall that:

$$r = (1-\epsilon)\zeta + A(\zeta)\;\;(S(\theta) - 1 + \epsilon) \tag{A.12}$$

where $S(\theta)$ describes the stellar surface.

Appendix B: Coupling matrix

The components of the sub-matrices which define the ODE system (36) are specified below using the functionals $\mathrm{I}^m_{\ell\ell'}$ and $\mathrm{J}^m_{\ell\ell'}$ defined in Eqs. (37) and (38):

$$\mathrm{A}_{33} \quad \mathrm{I}^m_{\ell\ell'}(h_1) \tag{B.1}$$

$$\mathrm{B}_{11} \quad \mathrm{I}^m_{\ell\ell'}(r^2g_0^1) \tag{B.2}$$

$$\mathrm{B}_{21} \quad \mathrm{I}^m_{\ell\ell'}(h_4) - \mathrm{J}^m_{\ell\ell'}\left(2h_2 + h_1\frac{g_0^2}{g_0^1}\right) \tag{B.3}$$

$$\mathrm{B}_{22} \quad \mathrm{I}^m_{\ell\ell'}\left(h_1\frac{c_0^2N_0^2}{g_0^1} - r^2A_0^1\right) \tag{B.4}$$

$$\mathrm{B}_{33} \quad \mathrm{I}^m_{\ell\ell'}(h_4) - \mathrm{J}^m_{\ell\ell'}(2h_2) \tag{B.5}$$

$$\mathrm{C}_{11} \quad \mathrm{J}^m_{\ell\ell'}(r^2g_0^2) \tag{B.6}$$

$$\mathrm{C}_{12} \quad -\mathrm{I}^m_{\ell\ell'}(r^2c_0^2N_0^2) \tag{B.7}$$

$$\mathrm{C}_{21} \quad -\ell(\ell+1)\delta_{\ell\ell'} - \mathrm{J}^m_{\ell\ell'}\left[h_1\partial_\zeta\left(\frac{g_0^2}{g_0^1}\right)\right] \tag{B.8}$$

$$\mathrm{C}_{22} \quad \mathrm{I}^m_{\ell\ell'}\left[h_1\partial_\zeta\left(\frac{c_0^2N_0^2}{g_0^1}\right) - r^2\boldsymbol{\nabla}\cdot\boldsymbol{A}_0\right] - \mathrm{J}^m_{\ell\ell'}(r^2A_0^2) \tag{B.9}$$

$$\mathrm{C}_{31} \quad -\mathrm{I}^m_{\ell\ell'}(r^2d_0) \tag{B.10}$$

$$\mathrm{C}_{32} \quad \mathrm{I}^m_{\ell\ell'}\left[r^2(d_0c_0^2 - \rho_0)\right] \tag{B.11}$$

$$\mathrm{C}_{33} \quad -\ell(\ell+1)\delta_{\ell\ell'} + \mathrm{I}^m_{\ell\ell'}(r^2d_0) \tag{B.12}$$

$$\mathrm{D}_{21} \quad -\mathrm{I}^m_{\ell\ell'}\left(\frac{h_1}{g_0^1}\right) \tag{B.13}$$

$$\mathrm{D}_{22} \quad \mathrm{I}^m_{\ell\ell'}\left(\frac{h_1c_0^2}{g_0^1}\right) \tag{B.14}$$

$$\mathrm{E}_{11} \quad \mathrm{I}^m_{\ell\ell'}(r^2) \tag{B.15}$$

$$\mathrm{E}_{12} \quad -\mathrm{I}^m_{\ell\ell'}(r^2c_0^2) \tag{B.16}$$

$$\mathrm{E}_{21} \quad -\mathrm{I}^m_{\ell\ell'}\left[h_1\partial_\zeta\left(\frac{1}{g_0^1}\right)\right] \tag{B.17}$$

$$\mathrm{E}_{22} \quad \mathrm{I}^m_{\ell\ell'}\left[r^2 + h_1\partial_\zeta\left(\frac{c_0^2}{g_0^1}\right)\right] \tag{B.18}$$

where $\ell = m+2k$, $\ell' = m+2k'$ when applied to the $\boldsymbol{\Xi}^+_m$ vector and $\ell = m+2k+1$, $\ell' = m+2k'+1$ for $\boldsymbol{\Xi}^-_m$.

For a polytropic model of index N, the quantities describing the equilibrium can be expressed in terms of the dimensionless enthalpy H as follows:

$$\boldsymbol{g}_0 = \boldsymbol{\nabla}H \qquad \boldsymbol{A}_0 = \left(1 - \tfrac{N\Gamma_{1,0}}{N+1}\right)\boldsymbol{\nabla}H$$

$$c_0^2 = \tfrac{\Gamma_{1,0}}{N+1}H \quad c_0^2N_0^2 = \left(1 - \tfrac{N\Gamma_{1,0}}{N+1}\right)\|\boldsymbol{\nabla}H\|^2 \tag{B.19}$$

$$\rho_0 = \Lambda^N H^N \;\; d_0 = N\Lambda^N H^{N-1},$$

where Λ is such that

$$\Lambda = \frac{4\pi G\rho_c R_e^2}{h_c} \tag{B.20}$$

where h_c and ρ_c are the dimensional enthalpy and density at the center of the polytropic model.

The components of the ODE, given by Eqs. (B.1) to (B.18), can then be expressed in terms of the enthalpy and its derivatives,

$H_\zeta, H_\theta, H_{\zeta\zeta} H_{\theta\theta}$. This has been done in order to minimize the numerical error in the calculation of these components. The most useful expressions are:

$$g_0^1 = \frac{h_1 H_\zeta - h_2 H_\theta}{r^2} \tag{B.21}$$

$$g_0^2 = \frac{-h_2 H_\zeta + H_\theta}{r^2} \tag{B.22}$$

$$\|\boldsymbol{\nabla} H\|^2 = \frac{h_1 H_\zeta^2 - 2h_2 H_\zeta H_\theta + H_\theta^2}{r^2} \tag{B.23}$$

$$h_1 \frac{c_0^2 N_0^2}{g_0^1} - r^2 A_0^1 = \left(1 - \frac{N\Gamma_{1,0}}{N+1}\right) \frac{H_\theta^2}{r_\zeta^2 g_0^1} \tag{B.24}$$

$$\partial_\zeta \left(\frac{g_0^2}{g_0^1}\right) = \frac{1}{\left(r^2 g_0^1\right)^2} \Big[h_3^2 \left(H_{\zeta\theta} H_\zeta - H_{\zeta\zeta} H_\theta\right) + \left(h_2 \partial_\zeta h_1 - h_1 \partial_\zeta h_2\right) H_\zeta^2 - \partial_\zeta h_1 H_\zeta H_\theta + \partial_\zeta h_2 H_\theta^2\Big] \tag{B.25}$$

$$h_1 \partial_\zeta \left(\frac{c_0^2 N_0^2}{g_0^1}\right) - r^2 \boldsymbol{\nabla} \cdot \boldsymbol{A}_0 = -\left(1 - \frac{N\Gamma_{1,0}}{N+1}\right) r^2 \mathcal{L}(H) \tag{B.26}$$

$$r^2 \mathcal{L}(H) = -h_1 \left[\frac{g_0^2}{g_0^1} H_{\theta\zeta} + \partial_\zeta \left(\frac{g_0^2}{g_0^1}\right) H_\theta\right] - 2h_2 H_{\theta\zeta} + h_4 H_\zeta + \Delta_{\theta\phi} H \tag{B.27}$$

$$d_0 c_0^2 - \rho_0 = -\left(1 - \frac{N\Gamma_{1,0}}{N+1}\right) \Lambda^N H^N \tag{B.28}$$

$$\partial_\zeta \left(\frac{1}{g_0^1}\right) = -\frac{r^2}{\left(r^2 g_0^1\right)^2} \Big[h_1 H_{\zeta\zeta} - h_2 H_{\zeta\theta} + \left(\partial_\zeta h_1 - 2h_1/h_3\right) H_\zeta + \left(2h_2/h_3 - \partial_\zeta h_2\right) H_\theta\Big] \tag{B.29}$$

$$\partial_\zeta \left(\frac{c_0^2}{g_0^1}\right) = \frac{\Gamma_{1,0}}{N+1} \left[H \partial_\zeta \left(\frac{1}{g_0^1}\right) + \frac{H_\zeta}{g_0^1}\right] \tag{B.30}$$

where

$$\partial_\zeta h_1 = 2\left(\frac{r_{\theta\zeta}}{r_\zeta} h_2 - \frac{r_{\zeta\zeta}}{r_\zeta} h_1 + h_3\right) \tag{B.31}$$

$$\partial_\zeta h_2 = \frac{r_{\theta\zeta}}{r_\zeta} - \frac{r_{\zeta\zeta}}{r_\zeta} h_2 \tag{B.32}$$

Appendix C: Calculation of the disk-integration factor

According to the definition of the disk-integration factor, Eq. (43), we are led to calculate integrals of the following form:

$$I = \iint_{S_v} F(\theta,\phi) \mathrm{d}\mathbf{S} \cdot \mathbf{e}_i \tag{C.1}$$

$$= \iint_{S_v} G(\theta,\phi,i) \mathrm{d}\mu \mathrm{d}\phi \tag{C.2}$$

where $\mu = \cos(\theta)$ and $F(\theta,\phi)$ is the surface distribution of the eigenfunction obtained in the coordinate system (25) in which the polar axis is the rotation axis. The integral is most simply calculated in the coordinate system in which the polar axis is aligned with the direction of the observer. This coordinate system results from a rotation of angle i around the y axis of the original coordinate system, the new angular variables being denoted θ' and ϕ'. To express G in these coordinates, we use the formula relating the spherical harmonics in both systems:

$$Y_\ell^m(\theta,\phi) = \sum_{m'=-\ell}^{+\ell} d_{mm'}^\ell(i) Y_\ell^{m'}(\theta',\phi') \tag{C.3}$$

where $d_{mm'}^\ell(i)$ do not generally have a simple form (Edmonds 1960). Then, using the spherical harmonic expansion of G, we obtain:

$$G = \sum_{\ell=0}^{+\infty} \sum_{m=-\ell}^{+\ell} G_m^\ell(i) Y_\ell^m(\theta,\phi) \tag{C.4}$$

$$= \sum_{\ell=0}^{+\infty} \sum_{m=-\ell}^{+\ell} \sum_{m'=-\ell}^{+\ell} G_m^\ell(i) d_{mm'}^\ell(i) Y_\ell^{m'}(\theta',\phi'). \tag{C.5}$$

Then, integrating over the longitude ϕ', from 0 to 2π, the terms involving $Y_\ell^{m'}(\theta',\phi')$ vanish if $m' \neq 0$. It follows that

$$I = 2\pi \sum_{\ell=0}^{+\infty} \sum_{m=-\ell}^{+\ell} J_\ell G_m^\ell(i) \hat{Y}_\ell^m(i) \tag{C.6}$$

where we used the following relations,

$$d_{m0}^\ell(i) = \sqrt{\frac{4\pi}{2\ell+1}} \hat{Y}_\ell^m(i) \tag{C.7}$$

$$\mathrm{d}\mu \mathrm{d}\phi = \mathrm{d}\mu' \mathrm{d}\phi' \quad \text{where } \mu' = \cos\theta' \tag{C.8}$$

and defined J_ℓ as,

$$J_\ell = \sqrt{\frac{4\pi}{2\ell+1}} \int_0^1 \hat{Y}_\ell^0(\mu') \mathrm{d}\mu' \tag{C.9}$$

$$= \begin{cases} 0 & \text{if } \ell \text{ is even and } \ell \neq 0, \\ 1 & \text{if } \ell = 0, \\ (-1)^{\frac{\ell-1}{2}} \frac{1.3\ldots(\ell-2)}{2.4\ldots(\ell+1)} & \text{if } \ell \text{ is odd and } \ell \neq 1, \\ \frac{1}{2} & \text{if } \ell = 1. \end{cases} \tag{C.10}$$

Because of axial axial symmetry, the function to integrate reads

$$F(\theta,\phi) = W(\theta) \mathrm{e}^{\mathrm{i}m\phi}. \tag{C.11}$$

Then, from the expression of the vector $\mathrm{d}\boldsymbol{S}$ at the star's surface:

$$\mathrm{d}\boldsymbol{S} = \partial_\theta \boldsymbol{OM} \times \partial_\phi \boldsymbol{OM} \mathrm{d}\theta \mathrm{d}\phi = \boldsymbol{E}_2 \times \boldsymbol{E}_3 \mathrm{d}\theta \mathrm{d}\phi = \sqrt{g} \boldsymbol{E}^1 \mathrm{d}\theta \mathrm{d}\phi \tag{C.12}$$

we deduce that

$$G = rA(\theta,\phi,i) W(\theta) \mathrm{e}^{\mathrm{i}m\phi} \tag{C.13}$$

where

$$A(\theta,\phi,i) = r r_\zeta \boldsymbol{E}^{\mathbf{1}} \cdot \boldsymbol{e}_i = \sqrt{r^2 + r_\theta^2} \boldsymbol{e}^s \cdot \boldsymbol{e}_i \tag{C.14}$$

$$= r\ (\sin\theta\cos\phi\sin i + \cos\theta\cos i) + r_\theta\ (\sin\theta\cos i - \cos\theta\cos\phi\sin i) \tag{C.15}$$

$$= \cos i \frac{\mathrm{d}}{\mathrm{d}\theta}\ (r\sin\theta) - \sin i\cos\phi \frac{\mathrm{d}}{\mathrm{d}\theta}\ (r\cos\theta) \tag{C.16}$$

where $\boldsymbol{e}^s$ denotes the unit vector perpendicular to the surface, r and r_θ are calculated at the star surface $\zeta = 1$. Thus the dependency of G on i, ϕ and θ can be specified as follows:

$$G = A(\theta)\cos i e^{\mathrm{i}m\phi} - B(\theta)\sin i\cos\phi e^{\mathrm{i}m\phi} \tag{C.17}$$

where

$$A = r\frac{\mathrm{d}}{\mathrm{d}\theta}\ (r\sin\theta)\,W(\theta) \tag{C.18}$$

$$B = r\frac{\mathrm{d}}{\mathrm{d}\theta}\ (r\cos\theta)\,W(\theta). \tag{C.19}$$

It follows that

$$G_k^\ell = 0 \ \text{ if } k \neq m-1, m, m+1 \tag{C.20}$$

so that the integral now reads:

$$I/2\pi = I_{m-1} + I_m + I_{m+1} \ \text{ where} \tag{C.21}$$

$$I_m = \cos i\hat{A}_m(i) \tag{C.22}$$

$$I_{m-1} = -\frac{\sin i}{2}\hat{B}_{m-1}(i) \tag{C.23}$$

$$I_{m+1} = -\frac{\sin i}{2}\hat{B}_{m+1}(i) \tag{C.24}$$

where $\hat{A}_m$ denotes:

$$\hat{A}_m(i) = \sum_{\ell=|m|}^{+\infty} J_\ell A_m^\ell \hat{Y}_\ell^m(i) \tag{C.25}$$

$$A_m^\ell = 2\pi\int_0^\pi A(\theta)\hat{Y}_\ell^m(\theta)\sin\theta\mathrm{d}\theta \tag{C.26}$$

the $\hat{B}_m$ terms being defined accordingly.

Note that for modes which are equatorially anti-symmetric and axisymmetric ($m = 0$), $\hat{A}_0(i) = J_0 A_0^0 \hat{Y}_0^0(i)$ and $\hat{A}_1(i) = \hat{A}_{-1}(i) = 0$, thus the integral I reduces to:

$$I = 4\pi\sqrt{\pi}A_0^0\cos(i). \tag{C.27}$$

2.5.2 A2 : Acoustic oscillations in rapidly rotating polytropic stars ; II. Effects of the Coriolis and centrifugal accelerations

"Acoustic oscillations in rapidly rotating polytropic stars ; II. Effects of the Coriolis and centrifugal accelerations"

Reese D., Lignières F and Rieutord M.

A&A 455, 621-637, 2006

A&A 455, 621–637 (2006)
DOI: 10.1051/0004-6361:20065269

Astronomy & Astrophysics

Acoustic oscillations of rapidly rotating polytropic stars

II. Effects of the Coriolis and centrifugal accelerations⋆

D. Reese, F. Lignières, and M. Rieutord

Laboratoire d'Astrophysique de Toulouse et Tarbes, UMR 5572, Université Paul Sabatier Toulouse 3, Observatoire Midi-Pyrénées, 14 avenue É. Belin, 31400 Toulouse, France
e-mail: daniel.reese@ast.obs-mip.fr

Received 24 March 2006 / Accepted 12 May 2006

ABSTRACT

Context. With the launch of space missions devoted to asteroseismology (like COROT), the scientific community will soon have accurate measurements of pulsation frequencies in many rapidly rotating stars.
Aims. The present work focuses on the effects of rotation on pulsations of rapidly rotating stars when both the Coriolis and centrifugal accelerations require a non-perturbative treatment.
Methods. We develop a 2-dimensional spectral numerical approach which allows us to compute acoustic modes in centrifugally distorted polytropes including the full influence of the Coriolis force. This method is validated through comparisons with previous studies, and the results are shown to be highly accurate.
Results. In the frequency range considered and with COROT's accuracy, we establish a domain of validity for perturbative methods, thus showing the need for complete calculations beyond $v \sin i = 50\,\mathrm{km\,s^{-1}}$ for a $R = 2.3\,R_\odot$, $M = 1.9\,M_\odot$ polytropic star. Furthermore, it is shown that the main differences between complete and perturbative calculations come essentially from the centrifugal distortion.

Key words. stars: oscillations – stars: rotation

1. Introduction

The study of rapidly rotating stars is a field in which there are many unresolved questions. The structure of these stars, the rotation profile, the angular momentum transport and many other aspects are not well understood. In order to answer some of these questions, many different theoretical and observational methods have been developed over the years. For instance, interferometry is starting to give clues as to the shape of these stars and effects such as gravitational darkening (e.g. Domiciano de Souza et al. 2003, 2005; Peterson et al. 2006). On the theoretical side, there exists a number of numerical models which are progressively becoming more realistic (e.g. Roxburgh 2004; Jackson et al. 2005; Rieutord et al. 2005; Rieutord 2006). These models can then be supplemented with asteroseismology which relates the internal structure to observable stellar pulsations. In order to fully exploit these pulsations, it is necessary to accurately quantify how they are affected by rotation. In the present work, we will show how this can be done for acoustic pulsations in uniformly rotating polytropic stellar models.

Rotation has several effects on stars and their pulsations. These result from the apparition of two inertial forces, namely the centrifugal and the Coriolis forces. The centrifugal force distorts the shape of the star and modifies its equilibrium structure. The Coriolis force intervenes directly in the oscillatory motions. Neither of these effects respect spherical geometry, which means that the radial coordinate r and the colatitude θ are no longer separable. As a result, pulsation modes cannot be described by a single spherical harmonic as was the case for non-rotating stars. In order to tackle this problem, two basic approaches have been developed. The first one is the perturbative approach and applies to small rotation rates. In this approach, both the equilibrium structure and the pulsation mode are the sum of a spherical solution (or a single spherical harmonic), a perturbation, and a remainder which is neglected. The second approach consists in solving directly the 2-dimensional eigenvalue problem fully including the effects of rotation.

Historically, the perturbative method has been applied to first, second and third order. Previous studies include Saio (1981); Gough & Thompson (1990), and Dziembowski & Goode (1992) for second order methods and Soufi et al. (1998) and Karami et al. (2005) for third order methods. These have been applied to polytropic models (Saio 1981) and then to more realistic models. There have also been some studies based on the non-perturbative approach. Most non-perturbative calculations have focused on the stability of neutron stars, r-modes and f-modes rather than on p-modes. Some exceptions are Clement (1981, 1984, 1986, 1989, 1998), Yoshida & Eriguchi (2001) and Espinosa et al. (2004).

The present work aims at accurately taking into account the effects of rotation on stellar acoustic pulsations, so as to be able to deduce asteroseismological information from rapidly rotating stars. Previous results are either inaccurate or not valid for high enough rotation rates. In order to achieve a sufficient degree of precision, we used numerical methods which have already proved to be highly accurate for other similar problems. The present method is a further development of the numerical method of Lignières et al. (2006b) and Lignières et al. (2006a, hereafter Paper I) who used a spectral method (Canuto et al. 1988) with a surface-fitting spheroidal

⋆ Appendices A–C are only available in electronic form at http://www.edpsciences.org

coordinate system based on Bonazzola et al. (1998). The spectral method itself has already been used for calculating inertial waves in spherical shells (Rieutord & Valdettaro 1997) and gravito-inertial modes in a 1.5 $M_\odot$ ZAMS star (Dintrans & Rieutord 2000) both of which involve the non-perturbative effects of the Coriolis force. Achieving high precision is of great importance for interpreting present and future measurements of stellar pulsations. Furthermore, it provides a means to establish the domain of validity of perturbative methods. Finally, this work can then be used as a reference to validate future methods.

The organisation of the paper is as follows: in the next section, the numerical method is described in detail. This section is followed by a series of comparisons and tests which establish the accuracy of the results. We then proceed to discuss perturbative methods and their validity. A conclusion and outlooks follow.

2. Formalism

The calculation of oscillation modes of rotating polytropes takes place in two steps. Firstly, an equilibrium model must be determined. Secondly, this model needs to be perturbed so as to give the eigenoscillations.

2.1. Equilibrium model

The equilibrium model is a self-gravitating uniformly rotating polytrope described by the following equations in the rotating frame:

$$P_\mathrm{o} = K\rho_\mathrm{o}^\gamma, \tag{1}$$

$$0 = -\boldsymbol{\nabla} P_\mathrm{o} - \rho_\mathrm{o}\boldsymbol{\nabla}\left(\Psi_\mathrm{o} - \frac{1}{2}\Omega^2 s^2\right), \tag{2}$$

$$\Delta\Psi_\mathrm{o} = 4\pi G\rho_\mathrm{o}, \tag{3}$$

where P_o is the pressure, ρ_o the density, K the polytropic constant, γ the polytropic exponent, Ψ_o the gravitational potential, s the distance to the rotation axis and G the gravitational constant. One can also introduce the polytropic index $N = 1/(\gamma - 1)$ and a (pseudo-)enthalpy $h = \int \mathrm{d}P/\rho = (1+N)P_\mathrm{o}/\rho_\mathrm{o}$. The pressure and density profiles are then proportional to powers of this enthalpy: $P_\mathrm{o} \propto h^{N+1}$, and $\rho_\mathrm{o} \propto h^N$. A number of non-dimensional parameters also intervene and characterise the polytropic model:

$$\Lambda = \frac{4\pi G\rho_\mathrm{c} R_\mathrm{eq}^2}{h_\mathrm{c}}, \qquad \Omega_\star = \frac{\Omega R_\mathrm{eq}}{\sqrt{h_\mathrm{c}}}, \qquad \alpha = \frac{\rho_\mathrm{c}}{\langle\rho\rangle}, \qquad \varepsilon = 1 - \frac{R_\mathrm{pol}}{R_\mathrm{eq}}, \tag{4}$$

where quantities with the subscript "c" denote the equilibrium value at the centre of the polytrope, R_eq and R_pol are the equatorial and polar radii, resp., and $\langle\rho\rangle = 3M/4\pi R_\mathrm{eq}^3$ a pseudo-mean density. The method used to compute the equilibrium model is described in Paper I.

2.2. Perturbation equations

We calculate adiabatic, inviscid oscillation modes using Eulerian perturbations to the equilibrium quantities[1]. The linearised equations in the rotating frame read:

$$\partial_\mathrm{t}\rho = -\boldsymbol{\nabla}\cdot(\rho_\mathrm{o}\boldsymbol{v}), \tag{5}$$

$$\rho_\mathrm{o}\partial_\mathrm{t}\boldsymbol{v} = -\boldsymbol{\nabla}p + \rho\boldsymbol{g}_\mathrm{o} - \rho_\mathrm{o}\boldsymbol{\nabla}\Psi - 2\rho_\mathrm{o}\boldsymbol{\Omega}\times\boldsymbol{v}, \tag{6}$$

$$\partial_\mathrm{t}p - c_\mathrm{o}^2\partial_\mathrm{t}\rho = \frac{\rho_\mathrm{o}N_\mathrm{o}^2 c_\mathrm{o}^2}{\|\boldsymbol{g_\mathrm{o}}\|^2}\boldsymbol{v}\cdot\boldsymbol{g}_\mathrm{o}, \tag{7}$$

$$0 = \Delta\Psi - 4\pi G\rho, \tag{8}$$

where quantities with the subscript "o" denote equilibrium quantities and those without any subscript Eulerian perturbations. $\boldsymbol{g}_\mathrm{o}$ is the effective gravity, c_o is the speed of sound, Γ_1 the adiabatic exponent and N_o the Brunt-Väisälä frequency. These are given by the following formulas:

$$\boldsymbol{g}_\mathrm{o} = -\boldsymbol{\nabla}\left(\Psi_\mathrm{o} - \frac{1}{2}\Omega^2 s^2\right), \tag{9}$$

$$c_\mathrm{o}^2 = \Gamma_1 P_\mathrm{o}/\rho_\mathrm{o}, \tag{10}$$

$$\Gamma_1 = \left(\frac{\partial\ln p}{\partial\ln\rho}\right)_\mathrm{ad}, \tag{11}$$

$$N_\mathrm{o}^2 = \boldsymbol{g_\mathrm{o}}\cdot\left(-\frac{1}{\Gamma_1}\frac{\boldsymbol{\nabla}P_\mathrm{o}}{P_\mathrm{o}} + \frac{\boldsymbol{\nabla}\rho_\mathrm{o}}{\rho_\mathrm{o}}\right). \tag{12}$$

It is worth noting that we have used the fluid's barotropicity in the definition of N_o.

[1] The term "perturbation", which means a small departure from equilibrium in this context, is not to be confused with perturbation from the perturbative method, where it means a small departure from the spherical case.

We can then put these equations in non-dimensional form using the following transformations:

$$\begin{array}{llllll} t = T_{\rm r}\underline{t}, & \rho = \rho_{\rm c}\underline{\rho}, & \boldsymbol{r} = R_{\rm eq}\underline{\boldsymbol{r}}, & \boldsymbol{g} = g_{\rm r}\underline{\boldsymbol{g}}, & \boldsymbol{v} = V_{\rm r}\underline{\boldsymbol{v}}, \\ p = P_{\rm r}\underline{p}, & \Omega = \omega_{\rm r}\underline{\Omega}, & c_{\rm o} = V_{\rm r}\underline{c}_{\rm o}, & N_{\rm o} = \omega_{\rm r}\underline{N}_{\rm o}, & \end{array} \tag{13}$$

where:

$$\omega_{\rm r} = T_{\rm r}^{-1} = (4\pi G\rho_{\rm c})^{1/2}, \qquad V_{\rm r} = \frac{R_{\rm eq}}{T_{\rm r}}, \qquad g_{\rm r} = \frac{R_{\rm eq}}{T_{\rm r}^2} = 4\pi G, R_{\rm eq}\rho_{\rm c} \qquad P_{\rm r} = \frac{\rho_{\rm c}R_{\rm eq}^2}{T_{\rm r}^2}\cdot \tag{14}$$

It is important to note that $\Omega_\star$ and $\underline{\Omega}$ correspond to two different dimensionless expressions of the rotation rate. In order to go from one expression to the other, one can use the following formula:

$$\Omega_\star = \underline{\Omega}\sqrt{\Lambda}, \tag{15}$$

where Λ is given by Eq. (4).

If we assume a time dependence of the form $\exp(\lambda\underline{t})$, the following generalised eigenvalue problem is obtained (we have dropped the underlined notation):

$$\lambda\rho = -\boldsymbol{v}\cdot\boldsymbol{\nabla}\rho_{\rm o} - \rho_{\rm o}\boldsymbol{\nabla}\cdot\boldsymbol{v}, \tag{16}$$

$$\lambda\rho_{\rm o}\boldsymbol{v} = -\boldsymbol{\nabla}p + \rho\boldsymbol{g}_{\rm o} - \rho_{\rm o}\boldsymbol{\nabla}\Psi - 2\rho_{\rm o}\Omega\boldsymbol{e}_z\times\boldsymbol{v}, \tag{17}$$

$$\lambda p - \lambda c_{\rm o}^2\rho = \frac{\rho_{\rm o}N_{\rm o}^2c_{\rm o}^2}{\|\boldsymbol{g}_{\rm o}\|^2}\boldsymbol{v}\cdot\boldsymbol{g}_{\rm o}, \tag{18}$$

$$0 = \Delta\Psi - \rho. \tag{19}$$

2.3. Change of variables

In order to have solutions with a good numerical behaviour on the surface of the star, we use the following variables:

$$\Pi = \frac{p}{H^N}, \qquad b = \frac{\rho}{H^{N-1}}, \tag{20}$$

where $H = h_{\rm o}/h_{\rm c}$ is a non-dimensional form of the enthalpy. These choices result from an analysis of the behaviour of the solution near the surface, based on a "generalised" Frobenius study of the system of equations. Although not fully proved, this study gives the correct results in the spherical case (see Appendix A). It also leads to the following boundary condition on the stellar surface:

$$\delta p/\rho_{\rm o} = 0, \tag{21}$$

where δp is the Lagrangian pressure perturbation. Not only is this result in agreement with previous results, but it also specifies how fast δp goes to zero near the stellar surface. More details on this method are given in Appendix A. This new choice of variables leads to the following set of equations:

$$\lambda b = -N\boldsymbol{v}\cdot\boldsymbol{\nabla}H - H\boldsymbol{\nabla}\cdot\boldsymbol{v}, \tag{22}$$

$$\lambda H\boldsymbol{v} = -H\left(\boldsymbol{\nabla}\Pi + \boldsymbol{\nabla}\Psi\right) + \boldsymbol{\nabla}H\left(-N\Pi + \frac{b}{\Lambda}\right) - 2\Omega H\boldsymbol{e}_z\times\boldsymbol{v}, \tag{23}$$

$$\lambda\Pi - \lambda\frac{\Gamma_1}{(N+1)\Lambda}b = \left(\frac{\Gamma_1}{\gamma} - 1\right)\frac{\boldsymbol{v}\cdot\boldsymbol{\nabla}H}{\Lambda}, \tag{24}$$

$$0 = \Delta\Psi - H^{N-1}b. \tag{25}$$

If $\Gamma_1 = \gamma$ then $N_{\rm o}^2 = 0$ and the above system reduces to:

$$\lambda N\Lambda\Pi = -N\boldsymbol{v}\cdot\boldsymbol{\nabla}H - H\boldsymbol{\nabla}\cdot\boldsymbol{v}, \tag{26}$$

$$\lambda\boldsymbol{v} = -\boldsymbol{\nabla}\Pi - \boldsymbol{\nabla}\Psi - 2\Omega\boldsymbol{e}_z\times\boldsymbol{v}, \tag{27}$$

$$0 = \Delta\Psi - N\Lambda H^{N-1}\Pi. \tag{28}$$

This simplification occurs when the polytropic relation (1) is also the equation of state, a situation typical of white dwarfs or neutron stars. Furthermore, both Π and b become proportional to the Eulerian perturbation of the enthalpy, thus justifying a posteriori the choice of these variables. As a result, apart from a few multiplicative factors, and the lack of a dissipative force, this second set of equations corresponds to those obtained by Yoshida & Eriguchi (1995).

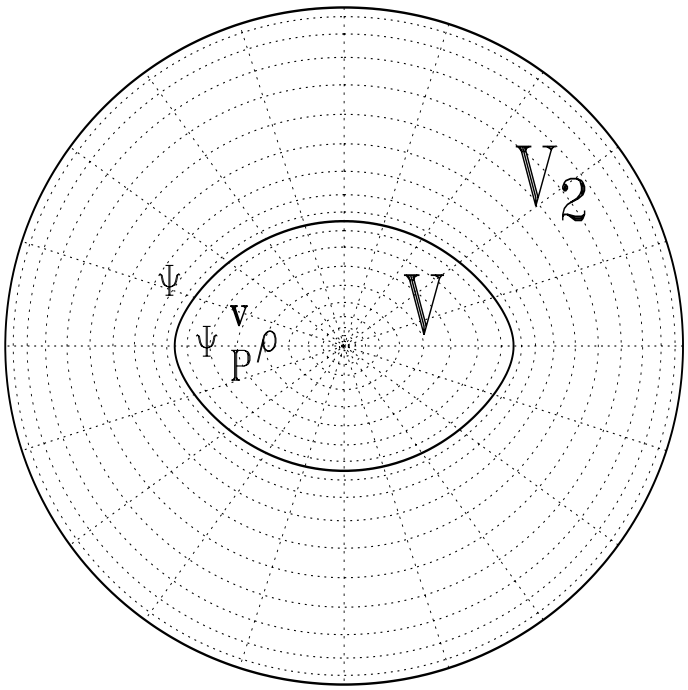

Fig. 1. Coordinate system used in computing the equilibrium model of the star and the pulsation modes. The domain V corresponds to the star itself (which in this case is a $N = 3$ polytrope at 84% of the breakup rotation rate). The domain V_2 encompasses the star, its outer limit being a sphere of radius $r = 2$ (twice the equatorial radius). The dotted lines correspond to $\zeta = 0.1,\ 0.2 ... 0.9$ in the domain V, $\zeta = 1.1,\ 1.2 ... 1.9$ in the domain V_2 and $\theta = 0°,\ 18°,\ ...342°$. The centre of the star corresponds to $\zeta = 0$, the star's surface (the boundary between V and V_2) to $\zeta = 1$, and the outer boundary to $\zeta = 2$. The continuity equation, Euler's equation, the energy equation and Poisson's equation are solved in the first domain. The letters Ψ, $\boldsymbol{v}$, P and ρ in the domain V show that these variables intervene in the first domain. In the second domain, only Poisson's equation is solved, and only the perturbation of the gravity potential Ψ intervenes. This is represented by the letter Ψ in the domain V_2.

2.4. Domains and boundary/interface conditions

In order to complete the eigenvalue problem given by Eqs. (22)−(25), it is necessary to specify a number of boundary conditions. The basic requirements are that the solutions remain bounded at the surface and at the centre of the star, and that the gravity potential goes to zero at infinity.

At the centre of the star, the regularity conditions are classically expressed in terms of spherical harmonics (see Eqs. (53) and (54)). By using the variables Π and b from the generalised Frobenius study, the solution is naturally bounded on the star's surface. However, the use of these variables leads to a degeneracy between Eqs. (22), (24) and the radial component of Eq. (23) on the surface of the star. This problem is remedied by replacing the radial component of Eq. (23) with its radial derivative on the surface.

It is also necessary to impose a boundary condition on the perturbation to the gravity potential Ψ, in order to ensure that the potential goes to zero at infinity. Traditionally, this is done by doing a harmonic decomposition of Ψ and imposing the correct condition on each component. However, such a procedure becomes complicated on a spheroidal surface, and it is not certain whether the decomposition of Ψ will converge for highly flattened configurations (Hachisu et al. 1982). We therefore employ a different method based on Bonazzola et al. (1998). It consists in adding a second domain V_2 which is bounded on the inside by the star's surface and on the outside by a sphere of radius $r = 2$ (which is twice the equatorial radius). We solve Poisson's equation in this domain and impose the correct boundary condition on its outer boundary (where we can safely apply a harmonic decomposition). On the inner boundary, it is necessary to use interface conditions which ensure the continuity of Ψ and its radial derivative across the stellar surface.

2.5. Spheroidal geometry

The next step in the calculations is the choice of a coordinate system based on Bonazzola et al. (1998) for each domain. In order to preserve spectral accuracy, the system of coordinates in the first domain needs to fit the surface of the star, and provide a non-singular transformation in the centre. As in Paper I and Rieutord et al. (2005), we choose the following definition for the radial coordinate ζ, which ensures a good convergence of the numerical method:

$$r(\zeta,\theta) = (1-\varepsilon)\zeta + \frac{5\zeta^3 - 3\zeta^5}{2}\left(R_{\rm s}(\theta) - 1 + \varepsilon\right), \tag{29}$$

where ε is the flatness given by Eq. (4), $(r(\zeta,\theta),\theta,\phi)$ are the spherical coordinates corresponding to the point (ζ,θ,ϕ), and $R_{\rm s}(\theta)$ is the surface of the star. By setting $\zeta = 1$, one obtains $r(1,\theta) = R_{\rm s}(\theta)$, and the centre $r = 0$ is given by $\zeta = 0$.

In second domain, we used the following definition:

$$r(\zeta,\theta) = 2\varepsilon + (1-\varepsilon)\zeta + \left(2\zeta^3 - 9\zeta^2 + 12\zeta - 4\right)\left(R_{\rm s}(\theta) - 1 - \varepsilon\right), \tag{30}$$

where $\zeta \in [1,2]$. This mapping is chosen so as to insure the continuity of r and r_ζ across the boundary $\zeta = 1$, and so that the surface given by $\zeta = 2$ corresponds to the sphere $r = 2$ (r_ζ denotes $\partial_\zeta r$).

Once the coordinate system has been established, it is also necessary to choose a set of vectors as a basis. We define the following vectors, which are derived from the natural covariant basis $(\boldsymbol{E}_\zeta, \boldsymbol{E}_\theta, \boldsymbol{E}_\phi)$ (defined as $\boldsymbol{E}_i = \partial_i \boldsymbol{r}$):

$$\begin{aligned}
\boldsymbol{a}_\zeta &= \frac{\zeta^2}{r^2 r_\zeta}\boldsymbol{E}_\zeta &&= \frac{\zeta^2}{r^2}\boldsymbol{e}_r,\\
\boldsymbol{a}_\theta &= \frac{\zeta}{r^2 r_\zeta}\boldsymbol{E}_\theta &&= \frac{\zeta}{r^2 r_\zeta}\left(r_\theta \boldsymbol{e}_r + r\boldsymbol{e}_\theta\right),\\
\boldsymbol{a}_\phi &= \frac{\zeta}{r^2 r_\zeta \sin\theta}\boldsymbol{E}_\phi &&= \frac{\zeta}{r r_\zeta}\boldsymbol{e}_\phi,
\end{aligned} \tag{31}$$

where $(\boldsymbol{e}_r, \boldsymbol{e}_\theta, \boldsymbol{e}_\phi)$ are the usual spherical vectors. The vectors $(\boldsymbol{a}_\zeta, \boldsymbol{a}_\theta, \boldsymbol{a}_\phi)$ have been chosen so that they become $(\boldsymbol{e}_r, \boldsymbol{e}_\theta, \boldsymbol{e}_\phi)$ in the spherical limit. Using this base of vectors, we can then express the velocity field as follows:

$$\boldsymbol{v} = u^\zeta \boldsymbol{a}_\zeta + u^\theta \boldsymbol{a}_\theta + u^\phi \boldsymbol{a}_\phi. \tag{32}$$

With these definitions, it is now possible to give an explicit expression of the oscillation equations:

$$\lambda b = -\frac{N\zeta^2}{r^2 r_\zeta}\left[H_\zeta u^\zeta + \frac{H_\theta u^\theta}{\zeta}\right] - \frac{\zeta^2 H}{r^2 r_\zeta}\left[\partial_\zeta u^\zeta + \frac{2u^\zeta}{\zeta} + \frac{\partial_\theta u^\theta}{\zeta} + \frac{\cot\theta u^\theta}{\zeta} + \frac{\partial_\phi u^\phi}{\zeta\sin\theta}\right], \tag{33}$$

$$\lambda\left[\frac{\zeta^2 H r_\zeta u^\zeta}{r^2} + \frac{\zeta H r_\theta u^\theta}{r^2}\right] = \frac{2\Omega H\zeta\sin\theta u^\phi}{r} - H\left(\partial_\zeta\Pi + \partial_\zeta\Psi\right) + H_\zeta\left(\frac{b}{\Lambda} - N\Pi\right), \tag{34}$$

$$\lambda\left[\frac{\zeta^2 r_\theta u^\zeta}{r^2} + \frac{\zeta(r^2 + r_\theta^2)u^\theta}{r^2 r_\zeta}\right] = \frac{2\Omega\zeta(r_\theta\sin\theta + r\cos\theta)u^\phi}{r r_\zeta} - \partial_\theta\Pi - \partial_\theta\Psi + \frac{H_\theta}{H}\left(\frac{b}{\Lambda} - N\Pi\right), \tag{35}$$

$$\lambda\frac{\zeta u^\phi}{r_\zeta} = -\frac{2\Omega\zeta^2\sin\theta u^\zeta}{r} - \frac{2\Omega\zeta(r_\theta\sin\theta + r\cos\theta)u^\theta}{r r_\zeta} - \frac{\partial_\phi\Pi}{\sin\theta} - \frac{\partial_\phi\Psi}{\sin\theta}, \tag{36}$$

$$\lambda\left(\Pi - \frac{\Gamma_1 b}{(N+1)\Lambda}\right) = \frac{\zeta^2}{\Lambda r^2 r_\zeta}\left(\frac{\Gamma_1}{\gamma} - 1\right)\left[H_\zeta u^\zeta + \frac{H_\theta u^\theta}{\zeta}\right], \tag{37}$$

$$0 = \frac{r^2 + r_\theta^2}{r^2 r_\zeta^2}\partial^2_{\zeta\zeta}\Psi + c_\zeta\partial_\zeta\Psi - \frac{2r_\theta}{r^2 r_\zeta}\partial^2_{\zeta\theta}\Psi + \frac{1}{r^2}\Delta_{\theta\phi}\Psi - H^{N-1}b, \tag{38}$$

where:

$$c_\zeta = \frac{1}{r^2 r_\zeta^3}\left(2r_\zeta r_\theta r_{\zeta\theta} - r^2 r_{\zeta\zeta} - r_\zeta^2 r_{\theta\theta} + 2r r_\zeta^2 - r_\theta^2 r_{\zeta\zeta} - r_\zeta^2 r_\theta\cot\theta\right), \tag{39}$$

$$\Delta_{\theta\phi} = \partial^2_{\theta\theta} + \cot\theta\partial_\theta + \frac{1}{\sin^2\theta}\partial^2_{\phi\phi}. \tag{40}$$

Equation (33) is the continuity equation, Eqs. (34)−(36) are Euler's equations, Eq. (37) corresponds to the adiabatic energy equation and Eq. (38) is Poisson's equation. Euler's equations have been used in their covariant rather than contravariant form, as it is advantageous from a numerical point of view. In order to understand this, it is helpful to bear in mind that H_θ/H converges towards $H_{\zeta\theta}/H_\zeta$ on the stellar surface, whereas H_ζ/H is unbounded (since $H_\zeta \neq 0$ on the surface). As a result, the radial component of Euler's equation reduces to $b = \Lambda N\Pi$ on the surface (which incidentally is already implied by a linear combination of the energy and continuity equations), whereas the two other components retain useful information on the surface. If the equations where in their contravariant form, than the θ component of Euler's equation would also reduce to $b = \Lambda N\Pi$ on the stellar surface since H_ζ would appear in this equation, thus preventing the possibility of dividing by H. It would then be necessary to also replace this equation by a supplementary boundary condition which would provide the information already contained in the covariant form. This system of equations applies in the first domain, except for Poisson's equation which is used in both domains (of course, the density perturbation no longer appears in the second domain).

2.6. Numerical method

In order to solve Eqs. (33)−(38), we project these equations onto the spherical harmonics (Rieutord 1987). This is done in two steps (cf. Paper I). First of all, the different unknowns are expressed in terms of a sum over the spherical harmonics. Explicitly, we obtain:

$$b = \sum_{\ell'=|m|}^{\infty} b_m^{\ell'} Y_{\ell'}^m, \tag{41}$$

$$\Pi = \sum_{\ell'=|m|}^{\infty} \Pi_m^{\ell'} Y_{\ell'}^m, \tag{42}$$

$$\Psi = \sum_{\ell'=|m|}^{\infty} \Psi_m^{\ell'} Y_{\ell'}^m, \tag{43}$$

$$\boldsymbol{v} = \sum_{\ell'=|m|}^{\infty} u_m^{\ell'} \boldsymbol{R}_{\ell'}^m + v_m^{\ell'} \boldsymbol{S}_{\ell'}^m + w_m^{\ell'} \boldsymbol{T}_{\ell'}^m, \tag{44}$$

where $Y_{\ell'}^m$ is the spherical harmonic of degree ℓ' and azimuthal order m and $b_m^{\ell'}$, $\Pi_m^{\ell'}$ etc. are radial functions that need to be determined, and which only depend on ζ. The equilibrium model is axisymmetric meaning that the variable ϕ is not coupled to the two others variables. Therefore, there is no summation over the azimuthal order m in these expressions. However, ζ and θ are not separable since the star does not respect spherical symmetry. As a result, it is necessary to sum over the harmonic degree ℓ'.

$\boldsymbol{R}_{\ell'}^m$, $\boldsymbol{S}_{\ell'}^m$, and $\boldsymbol{T}_{\ell'}^m$ are defined as follows:

$$\boldsymbol{R}_{\ell'}^m = Y_{\ell'}^m \boldsymbol{a}_\zeta, \tag{45}$$

$$\boldsymbol{S}_{\ell'}^m = \partial_\theta Y_{\ell'}^m \boldsymbol{a}_\theta + \mathrm{D}_\phi Y_{\ell'}^m \boldsymbol{a}_\phi, \tag{46}$$

$$\boldsymbol{T}_{\ell'}^m = \mathrm{D}_\phi Y_{\ell'}^m \boldsymbol{a}_\theta - \partial_\theta Y_{\ell'}^m \boldsymbol{a}_\phi, \tag{47}$$

$$\mathrm{D}_\phi \equiv \frac{\partial_\phi}{\sin\theta}. \tag{48}$$

It is worth noting that $\boldsymbol{R}_{\ell'}^m$, $\boldsymbol{S}_{\ell'}^m$, and $\boldsymbol{T}_{\ell'}^m$ are *not* the usual vectorial spherical harmonics because $(\boldsymbol{a}_\zeta, \boldsymbol{a}_\theta, \boldsymbol{a}_\phi)$ is not the same as $(\boldsymbol{e}_r, \boldsymbol{e}_\theta, \boldsymbol{e}_\phi)$. However, in the spherical limit, they will become the usual spherical harmonics. An explicit expression for each component of the velocity reads:

$$u^\zeta = \sum_{\ell'=|m|}^{\infty} Y_{\ell'}^m u_m^{\ell'}, \tag{49}$$

$$u^\theta = \sum_{\ell'=|m|}^{\infty} \partial_\theta Y_{\ell'}^m v_m^{\ell'} + \mathrm{D}_\phi Y_{\ell'}^m w_m^{\ell'}, \tag{50}$$

$$u^\phi = \sum_{\ell'=|m|}^{\infty} \mathrm{D}_\phi Y_{\ell'}^m v_m^{\ell'} - \partial_\theta Y_{\ell'}^m w_m^{\ell'}. \tag{51}$$

Once the unknown quantities have been expressed this way, the next step is to project the equations themselves onto the spherical harmonic basis. Eqs. (33), (34), (37) and (38) are multiplied by $\left\{Y_\ell^m\right\}^*$ and integrated over 4π steradians. For each harmonic degree ℓ of $\left\{Y_\ell^m\right\}^*$, a different equation is obtained. The remaining equations are obtained from Eqs. (35) and (36) in a more complicated manner. We compute the integral over 4π radians of $\{\text{Eq. (35)}\}\left\{\partial_\theta Y_\ell^m\right\}^* + \{\text{Eq. (36)}\}\left\{\mathrm{D}_\phi Y_\ell^m\right\}^*$ and $\{\text{Eq. (35)}\}\left\{\mathrm{D}_\phi Y_\ell^m\right\}^* - \{\text{Eq. (36)}\}\left\{\partial_\theta Y_\ell^m\right\}^*$. This operation corresponds to what would be done in the spherical case (i.e. a projection onto the vectorial spherical harmonics). As a result, the system thus obtained reduces to the classical uncoupled system of equations in the spherical limit. In general, however, this set of equations is a highly coupled system of ordinary differential equations in terms of the radial coordinate ζ, the solution of which gives the unknown radial functions (see Appendix B).

In order to solve this system numerically, we first begin by using a finite number of spherical harmonics $L_{\max}$. The equations are then discretised onto a Gauss-Lobatto collocation grid of $N_r + 1$ points, based on the Chebyshev polynomials. This results in an algebraic system of the form $\mathcal{A}v = \lambda\mathcal{B}v$ in which $\mathcal{A}$ and $\mathcal{B}$ are numerically determined square matrices. The eigensolutions (λ, v) of this system correspond to the frequencies and pulsation modes of the star. They are determined iteratively through the Arnoldi-Chebyshev algorithm (e.g. Chatelin 1988). The coefficients of matrices $\mathcal{A}$ and $\mathcal{B}$ are computed using an equilibrium model with a harmonic resolution L_{mod} and a Chebyshev (radial) resolution of $N_r + 1$. They are calculated using the coupling integrals given in Appendix B. This is achieved through Gauss' quadrature method with L_{res} points. Typical values for the different resolutions are: $N_r = 60$, $L_{\mathrm{mod}} = 50$, $L_{\max} = 80$, $L_{\mathrm{res}} = 230$.

At this point, we can write the boundary condition on the gravitational potential and the regularity conditions at the centre. The boundary condition is applied along the surface $r_{\mathrm{ext}} = 2$ (or $\zeta = 2$) on each harmonic component of the gravitational potential perturbation (Hurley et al. 1966):

$$\frac{1}{1-\varepsilon}\frac{\mathrm{d}\Psi_m^\ell}{\mathrm{d}\zeta} + \frac{\ell+1}{r_{\mathrm{ext}}}\Psi_m^\ell = 0. \tag{52}$$

The regularity condition depends on the parity of ℓ in a solution. Thanks to star's equatorial symmetry, modes will either be described by a sum of spherical harmonics with even degrees or odd degrees[2] (see Sect. 2.7). For modes with even harmonics, we apply the following condition at $r = 0$ (or $\zeta = 0$):

$$\frac{\mathrm{d}\Psi_m^\ell}{\mathrm{d}\zeta} = 0, \qquad \frac{\mathrm{d}\Pi_m^\ell}{\mathrm{d}\zeta} = 0, \qquad \frac{\mathrm{d}b_m^\ell}{\mathrm{d}\zeta} = 0, \qquad u_m^\ell = 0, \qquad v_m^\ell = 0, \qquad w_m^\ell = 0. \tag{53}$$

[2] The toroidal components w_m^ℓ have the opposite parity with respect to the other components.

The other modes follow the condition:

$$\Psi_m^\ell = 0, \qquad \Pi_m^\ell = 0, \qquad b_m^\ell = 0, \qquad \frac{\mathrm{d}u_m^\ell}{\mathrm{d}\zeta} = 0, \qquad \frac{\mathrm{d}v_m^\ell}{\mathrm{d}\zeta} = 0, \qquad \frac{\mathrm{d}w_m^\ell}{\mathrm{d}\zeta} = 0. \tag{54}$$

2.7. Mode classification and symmetries

A number of useful pieces of information can be deduced from the various symmetries present in the system. These help with mode classification, reduce numerical demand and explain certain properties which were observed in perturbative calculations.

The first and most obvious symmetry stems from the fact that the equilibrium model is axisymmetric. This implies that modes will have a well defined azimuthal order m (as explained earlier on). A second equally obvious symmetry results from the star being symmetric with respect to the equatorial plane. This leads to oscillation modes which are either symmetric or antisymmetric with respect to the equatorial plane and which are called even or odd, respectively. In terms of spherical harmonics, even modes are made up of harmonic components such that $\ell + m$ is even, except for the toroidal component of the velocity field in which $\ell + m$ is odd. Odd modes correspond to the opposite situation. From a numerical point of view, eigensolutions are described with half as many components as solutions with no particular parity.

There are two more symmetries which are a little more subtle than the previous ones. The first one only applies if the Coriolis force is neglected and only shows up in the rotating frame. In this situation, only even powers of the rotation rate show up in the equilibrium and pulsation equations. As a result, a given mode will also only depend on Ω^2 and will be a solution for the rotation rates Ω and $-\Omega$. When this symmetry is combined with the next one, then for a given multiplet, modes with azimuthal orders m and $-m$ have the same frequency, as was already pointed out in Paper I.

The last symmetry applies even with the Coriolis force and for both rotating and non-rotating frames. Let us consider a solution $(\omega, \rho, P, \boldsymbol{v}, \Psi, \Omega, m)$ (we include the rotation rate and the azimuthal order for the sake of clarity) and denote by $\mathcal{S}$ the operator which gives the mirror image with respect to the meridian passing through $\phi = 0$[3]. We then find that $(\omega, \mathcal{S}\rho, \mathcal{S}P, \mathcal{S}\boldsymbol{v}, \mathcal{S}\Psi, -\Omega, -m)$ is also a solution (this is not to be confused with the previous symmetry for which $(\omega, \rho, P, \boldsymbol{v}, \Psi, -\Omega, m)$ was the corresponding solution). This symmetry was pointed out by Clement (1989), however some of its consequences on perturbative calculations were not fully appreciated at the time. Let us consider a perturbative description of two frequencies with the same radial order and harmonic degree but with opposite azimuthal orders. We will obtain expressions of the following form:

$$\omega_{n,\ell,m}(\Omega) = \omega^0_{n,\ell,m} + \omega^1_{n,\ell,m}\Omega + \omega^2_{n,\ell,m}\Omega^2 + ... + O\left(\Omega^k\right), \tag{55}$$

$$\omega_{n,\ell,-m}(\Omega) = \omega^0_{n,\ell,-m} + \omega^1_{n,\ell,-m}\Omega + \omega^2_{n,\ell,-m}\Omega^2 + ... + O\left(\Omega^k\right), \tag{56}$$

where $\omega^j_{n,\ell,m}$ is the jth perturbative coefficient of $\omega_{n,\ell,m}(\Omega)$. If we apply the symmetry, we find that $\omega_{n,\ell,m}(\Omega) = \omega_{n,\ell,-m}(-\Omega)$. By equating like powers of $\omega_{n,\ell,-m}(-\Omega)$ with $\omega_{n,\ell,m}(\Omega)$, we find that $\omega^j_{n,\ell,m} = (-1)^j\omega^j_{n,\ell,-m}$. Therefore $\omega^j_{n,\ell,m}$ will be an even function of m when j is even and an odd function of m when j is odd. This explains why the second order coefficients of Dziembowski & Goode (1992) were polynomials in m^2, and is also found at third order (Goupil, private communication). This symmetry can also be used to increase the accuracy of least squares estimates of the coefficients based on non-perturbative calculations (see Sect. 4.1.1).

3. Analysis of the accuracy of the results

In order to check whether the results presented here are correct, it is important to do a number of internal tests and comparisons with previous studies. We first begin by discussing the accuracy of the underlying polytropic models. This is then followed by a series of comparisons with other studies. In the two first comparisons, the previous results have a limited accuracy, therefore only allowing a qualitative evaluation. The next two comparisons are with very accurate results, thus allowing a quantitative evaluation of the precision of the present results. These are then followed by a test based on the variational principle and an analysis of the sensitivity of the results to the parameters used in the numerical method. Finally, we conclude by estimating the overall accuracy of the results.

3.1. Accuracy of the polytropic models

There are several different tests which give an idea of the accuracy of the polytropic models. One way is by looking at the effects of different input parameters, such as the radial or harmonic resolution, on various non-dimensional parameters like those in Eq. (4). For non-rotating models, these non-dimensional parameters can be compared with those given in Seidov (2004). In Table 1, we give such a comparison, which shows that it is possible to correctly obtain 6 digits after the decimal point. Table 2 contains α and Λ for an $N = 3$ polytrope rotating at 0.59 Ω_K. This table shows the strong influence of N_r and the need for a sufficient radial resolution. It also suggests a precision of 6 digits after the decimal point, if we compare the values for $N_\mathrm{r} = 50$ and $N_\mathrm{r} = 60$.

In addition to the previous test, it is also possible to apply the virial theorem to obtain a measure of the accuracy of the model's structure. In what follows we use the following formulation of the theorem:

$$0 = \int_V \rho_\mathrm{o}\Omega_\star^2 r^2 \sin^2\theta \mathrm{d}V + \frac{1}{2}\int_V \rho_\mathrm{o}\Psi_\mathrm{o}\mathrm{d}V + \frac{3}{N+1}\int_V P_\mathrm{o}\mathrm{d}V, \tag{57}$$

[3] In spherical coordinates, $\mathcal{S}$ is defined as follows for a scalar quantity: $\mathcal{S}A(r,\theta,\phi) = A(r,\theta,-\phi)$. For a vector field it takes on the definition: $\mathcal{S}\boldsymbol{V}(r,\theta,\phi) = V_\mathrm{r}(r,\theta,-\phi)\boldsymbol{e}_r + V_\theta(r,\theta,-\phi)\boldsymbol{e}_\theta - V_\phi(r,\theta,-\phi)\boldsymbol{e}_\phi$.

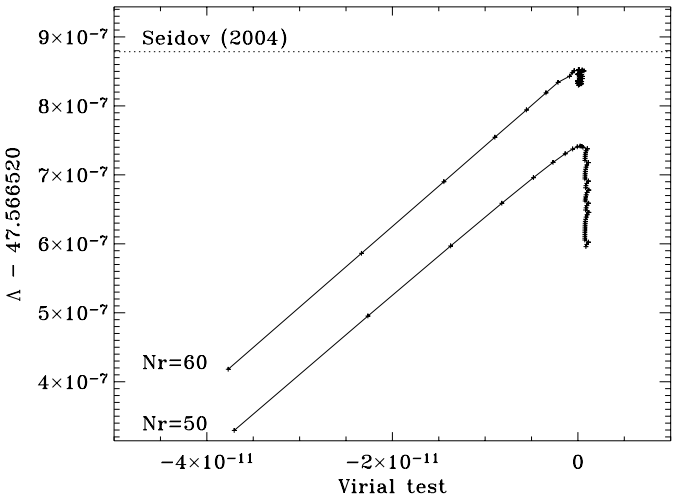

Fig. 2. A plot of the value of Λ as a function of the virial error. Each iteration is marked by a plus "+" and connected consecutively. As shown in the figure, the iterated models reach a point of closest approach to the mathematical solution, and then slowly drift towards less accurate models.

Table 1. Non-dimensional parameters of a non-rotating $N = 3$ polytrope. $L_{\max} = 50$ for all the calculations. It is difficult to accurately obtain the 7^{th} digit after the decimal point, in comparison with the values of Seidov (2004).

$N_{\rm r}$	α	Λ
50	54.182 480 87	47.566 520 74
60	54.182 481 06	47.566 520 85
100	54.182 480 87	47.566 520 74
Seidov (2004)	54.182 481 11	47.566 520 88

Table 2. Same as Table 1 but for an $N = 3$ polytrope rotating at 0.59 Ω_K. The radial resolution $N_{\rm r}$ has a stronger effect on the values of α and Λ than the harmonic resolution $L_{\max}$.

$N_{\rm r}$	$L_{\max}$	α	Λ
50	16	81.108 265 69	63.025 583 86
20	50	81.108 444 82	63.025 591 55
50	50	81.108 249 13	63.025 575 39
50	60	81.108 249 08	63.025 575 36
60	50	81.108 249 38	63.025 575 52
60	60	81.108 249 38	63.025 575 52

where $\rho_{\rm o} = H^N$, $P_{\rm o} = H^{N+1}$ and $\Psi_{\rm o} = \psi_{\rm o}/h_{\rm c}$. For a sufficient number of iterations, it is possible to attain a precision of 10^{-13} on the virial test. Beyond this point, successive iterations are useless and can actually decrease the accuracy of the model. In Fig. 2, we follow the evolution of Λ and the virial error with each iteration. As can be seen in the figure, there are two phases: a first phase in which the model is approaching the mathematical solution to the problem, and a second phase in which the maximum precision has been attained and the model is slowly drifting towards less accurate solutions. For some of the rotating configurations and with a well adjusted resolution, this second phase does not contain a slow drift but remains close to a fixed point. Either way, the best point at which to stop the iterative scheme is at the transition between the two phases.

The models on which are based the pulsation frequencies do not attain as high a precision, because the iterative scheme was stopped before the transition between the two phases. This is because we use a small parameter called ϵ which controls the relative error on the enthalpy and serves as a stopping criteria. If the value of ϵ is too low, than the iterative program never reaches this precision on the enthalpy and therefore does not output the stellar model. We therefore set $\epsilon = 10^{-8}$ in most calculations, which ensures successful convergence but reduces the accuracy of the model. As a result, the virial test typically attains a precision of 4×10^{-10}. For the non-rotating model, α takes on a value around 54.182473, which starts differing at the 5^{th} digit after the decimal point from the value given in Seidov (2004) and corresponds to a relative precision of $\sim 10^{-7}$.

3.2. Comparison with Saio (1981)

Saio (1981) gives second order perturbative calculations for polytropic models. Based on his coefficients, it is possible to obtain pulsation frequencies via the following formula:

$$\omega = \omega_0 - (1 - C_1)\, m\Omega + \left\{(X_1 + X_2 + Z) + m^2\,(Y_1 + Y_2)\right\} \frac{\Omega^2}{\omega_0}. \tag{58}$$

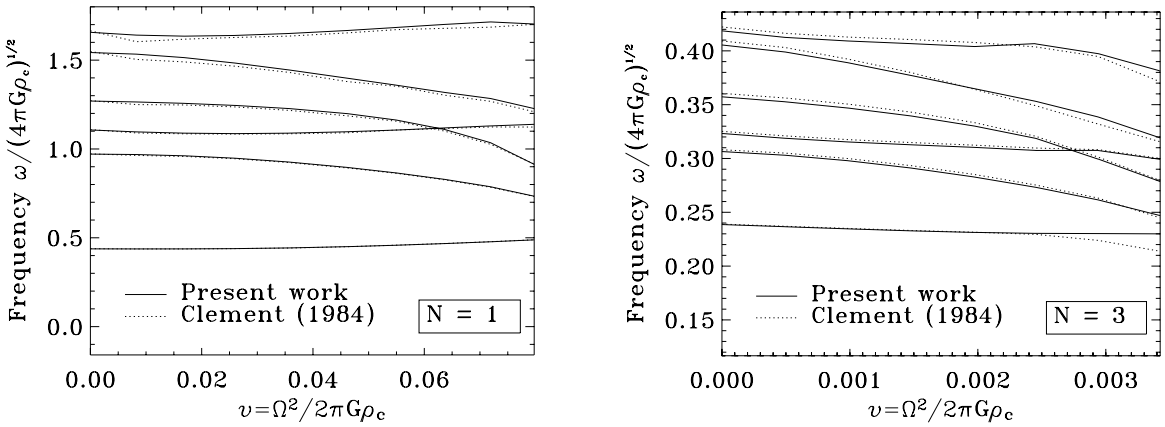

Fig. 3. A plot showing the frequencies in Clement (1984) and our calculations of the same frequencies.

In order to compare our results with his, it is necessary to extract perturbative coefficients from our own results. The procedure used to find these coefficients is fully described in Sect. 4.1.1. Before applying this procedure, we first had to express our results in the same units as Saio (1981) via the following conversion rule:

$$\omega_{S81} = \sqrt{3\alpha_{\rm nr}}\omega, \tag{59}$$

$$\Omega_{S81} = \sqrt{\frac{3\alpha_{\rm nr}}{\Lambda}}\Omega_\star, \tag{60}$$

where the subscript "nr" means "non-rotating" (i.e. the value of the parameter for the non-rotating polytrope) and the subscript "S81" means that the quantity is in Saio's units. It turns out that in Saio's units, the mass of the polytrope depends on the rotation rate. A comparison between his coefficients $\left(\omega_0^2, C_1, X_1 + X_2 + Z, Y_1 + Y_2\right)$ and ours showed a qualitative agreement between the two (to within 2%). This reduces the possibility of programming errors affecting our results.

3.3. Comparison with Clement (1984)

Further comparisons can be done with Clement (1984), who applied non-perturbative techniques to calculate pulsation frequencies for $N = 1$ and $N = 3$ polytropes. His frequencies are given in the same units as ours and no conversion is needed. However, Clement (1984) used a rotational parameter which he called "α" (denoted here as α_{C84} so as to avoid confusion with α from Eq. (4)) and which is "neither dimensionless nor scale-free". Therefore, based on the conversion given in Tables 1 and 2 of Clement (1984) and following his recommendations, we used the parameter $\upsilon = \Omega^2/2\pi G\rho_c$ instead. We allowed for uncertainties in the last digit of υ and therefore calculated a corresponding range of frequencies. For example, if $\upsilon = 1.69 \times 10^{-2}$ we would calculate the frequencies corresponding to $\upsilon = 1.69 \times 10^{-2} \pm 5 \times 10^{-5}$. The results are presented in Fig. 3.

As can be seen from Fig. 3 the two sets of results qualitatively agree, which once more makes numerical programming mistakes unlikely in our calculations. However, Clement's results usually do not lie in the frequency intervals we calculated (this would require a 4-digit accuracy). This is partially due to the fact that it is difficult to accurately reproduce the polytropic models he used. In order to illustrate this, we can use the different parameters (υ, $\rho_c/\underline{\rho}$, $R_{\rm eq}/R_{\rm pol}$, g_e/g_p) provided in Tables 1 and 2 of Clement (1984), allow for uncertainties in the last digit, and calculate the corresponding ranges for $\Omega_\star$. For a given rotation rate, if all the digits in the four parameters are accurate, then the four different ranges for $\Omega_\star$ should overlap and give a more precise idea as to the underlying model. However, it was only possible to obtain at most three overlapping ranges, and not four. A typical example for the $N = 1$ polytrope (with $\alpha_{C84} = 0.004$) is:

$$\begin{aligned}
\upsilon &= 3.57 \times 10^{-2} \pm 5 \times 10^{-5} &\Rightarrow\ \Omega_\star &= 0.4615 \pm 4 \times 10^{-4},\\
\rho_c/\underline{\rho} &= 3.40 \pm 5 \times 10^{-3} &\Rightarrow\ \Omega_\star &= 0.4580 \pm 9.4 \times 10^{-3},\\
R_{\rm eq}/R_{\rm pol} &= 1.162 \pm 5 \times 10^{-4} &\Rightarrow\ \Omega_\star &= 0.4590 \pm 7 \times 10^{-4},\\
g_e/g_p &= 0.686 \pm 5 \times 10^{-4} &\Rightarrow\ \Omega_\star &= 0.4621 \pm 4 \times 10^{-4}.
\end{aligned} \tag{61}$$

This shows that the error bars we used on Clement's parameters are too small and that the uncertainties on his models are larger. Nonetheless, these uncertainties do not fully account for the discrepancies between our frequencies and his. This can be shown by the fact that even for non-rotating configurations (where there is no ambiguity on the underlying model) the differences are still of the same order of magnitude.

In general, a quantitative comparison between our results and those of Saio (1981) and Clement (1984) showed an agreement to 2 or 3 significant digits. While providing a correct qualitative picture, the precision of these studies is insufficient for future missions such as COROT. COROT will observe pulsation frequencies within the range of 0.1−10 mHz with an accuracy of 0.6 μHz for the 20 day runs and 0.08 μHz for the 150 day runs (e.g. Baglin et al. 2002), meaning that an accuracy of 3 to 5 digits is required. Therefore, it is important to show that our results meet up to this requirement through other more constraining tests and comparisons.

3.4. Comparison with Christensen-Dalsgaard & Mullan (1994)

Christensen-Dalsgaard & Mullan (1994) give very accurate frequencies for several *non-rotating* polytropic models. Comparing our results with theirs provides a robust test for accuracy. In order to convert our frequencies ω into their units, we apply the following conversion rule:

$$\nu_{\rm CDM} = \nu_{\rm g} \sqrt{3\alpha}\omega, \tag{62}$$

where $\nu_{\rm CDM}$ is our frequency in their units, $\nu_{\rm g} = 99.855377\,\mu$Hz, and α is given by Eq. (4). A comparison between their frequencies and ours revealed a very good agreement ($\Delta\omega/\omega \sim 10^{-7}$ for a $N = 3$ polytrope and $\Delta\omega/\omega \sim 10^{-8}$ for a $N = 1.5$ polytrope at $\Omega = 0$). The modes which were compared are: $\ell = 0$ to 3, $n = 1$ to 10 for $N = 3$ and $n = 15$ to 25 for $N = 1.5$. The differences come from round-off errors in the last digit (if we keep the same number of significant digits).

3.5. Comparison with Paper I

We finally compared our results with those of Paper I. In order to do this comparison, it is necessary to remove the Coriolis force and to make the Cowling approximation. No conversion rule is necessary since both sets of results are given in the same units. The two sets of frequencies agree quite well, even at large rotation rates ($\Delta\omega/\omega \sim 10^{-7}$). This result is significant due to the fact that the set of equations used in Paper I is entirely different than the one used here.

3.6. Variational test

The variational principle provides an integral formula which relates a pulsation frequency to the structure of the corresponding mode (e.g. Lynden-Bell & Ostriker 1967). It is therefore possible to apply this formula to a numerically calculated eigenmode to obtain a "variational frequency". The error on this frequency is quadratic in the error of the eigenfunction (cf. Christensen-Dalsgaard & Mullan 1994). By comparing this frequency with the one obtained directly, it is possible to estimate the accuracy of the results. We used the following non-dimensional formulation of the variational principle:

$$\omega^2 \int_V \rho_{\rm o}|\boldsymbol{v}|^2 {\rm d}V - |\omega|^2 \left(\int_V \frac{|p|^2 {\rm d}V}{\rho_{\rm o} c_{\rm o}^2} - \int_{V_\infty} |\boldsymbol{\nabla}\Psi|^2 \, {\rm d}V \right) + 2{\rm i}\omega \int_V \rho_{\rm o} \boldsymbol{\Omega} \cdot (\boldsymbol{v}^* \times \boldsymbol{v}) \, {\rm d}V - \int_V \rho_{\rm o} N_{\rm o}^2 \left| \boldsymbol{v} \cdot \boldsymbol{e}_{\rm g} \right|^2 {\rm d}V = 0, \tag{63}$$

where V is the volume of the star, V_∞ is infinite space, and $\boldsymbol{e}_{\rm g}$ the unit vector in the same direction as the gravity vector. The pressure is replaced by $H^N\Pi$ and the different integrals are performed numerically[4] which gives a second degree equation in ω. Solving this equation gives the variational frequency which can then be compared with the direct calculation of ω. Generally, we find differences $\Delta\omega/\omega \sim 10^{-8}$ or better between the two. This can be compared with the results of Ipser & Lindblom (1990) who found differences of 10^{-3} when they applied the variational principle to their calculations. An explicit formulation of the variational principle in spheroidal geometry is given in Appendix C.

3.7. Influence of the parameters from the numerical method

A final test consists in modifying different input parameters and seeing the effect it has on the results. We have therefore applied this test to a few modes which are representative of all the modes that have been calculated. The parameters that were modified are the radial resolution $N_{\rm r}$ (which is the same for the equilibrium model and the pulsation mode), the harmonic resolution of the model $L_{\rm mod}$, the harmonic resolution of the pulsation mode $L_{\rm max}$, the shift σ used in the Arnoldi-Chebyshev algorithm[5], and ϵ which controls the relative error of the enthalpy in the equilibrium model. Table 3 lists the values used for the different parameters and the induced frequency variations. For a given parameter, we used the frequency obtained at highest resolution (or lowest value for ϵ) as a reference. In most cases, we obtained a rough plateau at the different levels given in Table 3. In some cases however, there was a definite decrease of the error. For instance, for those modes in which it was tested, the error was roughly proportional to ϵ. Also, for high frequency modes, the error strongly decreased as $N_{\rm r}$ increased, as could be expected for high radial orders. In the table, we put the lower/final values of the error for both of these parameters. The information on the shift is slightly different. The line "Values" gives the amplitude of the variation on the value of the shift. The next two lines contain the standard deviation of the results.

The results on ϵ are not representative of the calculated frequencies. As was pointed out in Sect. 3.1, the number iterations was usually less than optimal because of a large value of ϵ (10^{-8} instead of 10^{-10}), thus resulting in a decreased accuracy. The relative error on low frequency modes is 10^{-8} and that of high frequency modes 10^{-7}.

3.8. Discussion

Overall, the main source of error in the present calculations is the uncertainties on the equilibrium model. This is because we chose a convergence criteria which was sure to be met, but which lead to a number of iterations less than optimal. This therefore leads to a global accuracy of 7 digits after the decimal point (in units of $\sqrt{4\pi G\rho_{\rm c}}$), the last digit being uncertain. Table 3 however

[4] The numerical integration was based on Gauss' quadrature method and a spectral expansion, using a radial resolution of 101 points and an angular resolution of 200 points.

[5] The shift comes from shift-and-invert methods and corresponds to a trial value around which the Arnoldi-Chebyshev algorithm looks for frequencies. See Valdettaro et al. (2006) for an extensive discussion on the role of the shift in numerical errors.

Table 3. Frequencies variations in terms of different parameters. $L_{\max}$ is the harmonic resolution of the pulsation modes, L_{mod} the harmonic resolution of the models and N_{r} the radial resolution. The line "Values" gives the different values that were used for the resolutions, ϵ and the width giving the variation of the shift. The two following lines give the order of magnitude of the induced frequency variations (in units of $\sqrt{4\pi G\rho_{\mathrm{c}}}$).

	$L_{\max}$	L_{mod}	N_{r}	Shift	ϵ
Values	40, 44 ... 80	30, 34 ... 70	32, 36 ... 60	$2\text{–}5\times10^{-4}$	$10^{-8}...10^{-10}$
Low frequency modes	$<10^{-15}$	10^{-10}	10^{-10}	10^{-13}	10^{-10}
High frequency modes	10^{-14}	10^{-9}	10^{-10}	10^{-11}	10^{-9}

shows that these calculations could potentially be made more accurate. The present accuracy is nonetheless largely sufficient for the requirements of COROT, which will be at most 5 significant digits.

4. Results

We now proceed to present the results themselves. We followed acoustic adiabatic pulsation modes (with $\Gamma_1 = 5/3$) from a zero rotation rate to $0.59\Omega_K$ (where $\Omega_K = \sqrt{GM/R_{\mathrm{eq}}^3}$ is the Keplerian break-up rotation rate), using the same procedure as in Paper I. This involves identifying the frequencies at $\Omega = 0$, following their evolution while progressively increasing the rotation rate, and working through a number of avoided crossings. The underlying polytropic models have an index $N = 3$ which gives a polytropic exponent $\gamma = 4/3$. The modes that were calculated are: $\ell = 0$ to 3, $n = 1$ to 10 and $m = -\ell$ to ℓ both with and without the Coriolis force.

4.1. Comparison with perturbative methods

In this section, we compare complete and perturbative calculations so as to determine the range of validity of perturbative methods.

4.1.1. Perturbative coefficients

In order to compare perturbative calculations with complete ones, it proved necessary to compute our own perturbative coefficients, since we were unable to find perturbative coefficients for polytropic models with a sufficient accuracy in the literature. Instead of using the traditional method of perturbing the fluid equations and finding corrections of various orders on the frequencies (see Soufi et al. 1998 for a complete description), we did a series of complete calculations for small rotation rates ($(\Omega_\star)_i = 0$, 10^{-6}, 10^{-5}, 10^{-4}, 10^{-3}, 0.002, 0.004 ... 0.018) and applied a least squares fit to the results. In order to increase the accuracy of such calculations, we made use of Eq. (55) and separated even and odd powers of the rotation rate:

$$\frac{\omega_{n,l,m}+\omega_{n,l,-m}}{2} = \omega^0_{n,l,m} + \omega^2_{n,l,m}\Omega^2 + \omega^4_{n,l,m}\Omega^4 + O(\Omega^6), \tag{64}$$

$$\frac{\omega_{n,l,m}-\omega_{n,l,-m}}{2} = \omega^1_{n,l,m}\Omega + \omega^3_{n,l,m}\Omega^3 + \omega^5_{n,l,m}\Omega^5 + O(\Omega^7). \tag{65}$$

By fitting $(\omega_{n,l,m}+\omega_{n,l,-m})/2$ and $(\omega_{n,l,m}-\omega_{n,l,-m})/2$ the number of unknowns is reduced to three and the residues are smaller. It is necessary to include the fourth and fifth powers of the rotation rate so as to ensure that the second and third order coefficients are reasonably accurate. The results are given in Table 4 for frequencies and rotation rates in units of $\left(GM/R^3_{\mathrm{pol}}\right)$. From these coefficients the frequencies are given through the following formula:

$$\omega = \omega_0 - m(1-C)\Omega + \left(D_1 + m^2 D_2\right)\Omega^2 + m\left(T_1 + m^2 T_2\right)\Omega^3 + O\left(\Omega^4\right). \tag{66}$$

The form of the second degree coefficients was obtained from Saio (1981) and that of the third degree coefficients from Goupil (private communication). In order to express these results in units of Ω_K instead, one can use the following perturbative formula:

$$\left(\frac{\Omega}{\Omega_K}\right) = \left(\frac{\Omega}{\Omega_K^{\mathrm{pol}}}\right) + A\left(\frac{\Omega}{\Omega_K^{\mathrm{pol}}}\right)^3 + O\left\{\left(\frac{\Omega}{\Omega_K^{\mathrm{pol}}}\right)^5\right\}, \tag{67}$$

where $\Omega_K^{\mathrm{pol}} = \left(GM/R^3_{\mathrm{pol}}\right)$ and $A \simeq 0.77166$.

In order to estimate the accuracy of these perturbative coefficients, there are a number of tests that can be done. First of all, the zeroth order coefficients are simply the pulsation frequencies without rotation but are treated as unknowns in the least squares development. The frequencies without rotation are recovered in the least squares fit to an accuracy of at least 5.4×10^{-8} in the units of Table 4. The first order coefficient C, can be calculated via integrals based on the zeroth order solution (Ledoux 1951). This alternate way of calculating the coefficients agrees to within 1.4×10^{-9} (this does not necessarily mean that the coefficients are accurate to that precision but does show a high degree of internal coherence). For the second and third degree coefficients, we checked to see if they satisfied the forms given in Eq. (66); the number of significant digits in Table 4 has been adjusted accordingly. These forms were a constraint only on the $\ell = 2$ and 3 second order coefficients and on the $\ell = 3$ third order coefficients. Another test we did consisted in applying the least squares fit to a subset of the results used in the first fit and seeing whether the coefficients were altered. This test indicates roughly the same accuracy as the other tests.

Table 4. Perturbative coefficients for a $N = 3$ polytrope, deduced from complete calculations. The frequencies and the rotation rate are expressed in units of $\left(GM/R_{\rm pol}^3\right)^{1/2}$.

ω_0	C	D_1	D_2	T_1
		$\ell = 0$		
3.042155	...	–1.194	...	...
4.121230	...	–2.315	...	...
5.336900	...	–3.439	...	...
6.591212	...	–4.484	...	...
7.855027	...	–5.484	...	...
9.120432	...	–6.459	...	...
10.384948	...	–7.416	...	...
11.647767	...	–8.361	...	...
12.908679	...	–9.298	...	...
14.167704	...	–10.228	...	...
		$\ell = 1$		
3.377036	0.0295367	–1.072	–1.030	–0.04612
4.642432	0.0342809	–1.760	–1.699	–0.04204
5.909240	0.0335303	–2.402	–2.315	–0.02715
7.176668	0.0305143	–3.019	–2.901	–0.01634
8.443277	0.0270732	–3.621	–3.470	–0.00951
9.708372	0.0238467	–4.213	–4.028	–0.00524
10.971700	0.0210064	–4.797	–4.578	–0.00254
12.233222	0.0185621	–5.375	–5.122	–0.00080
13.492998	0.0164731	–5.950	–5.662	0.00034
14.751133	0.0146882	–6.521	–6.198	0.00108

ω_0	C	D_1	D_2	T_1	T_2
			$\ell = 2$		
3.906874	0.1538359	–1.578	–0.294	0.02344	0.00527
5.169469	0.0818188	–2.396	–0.459	0.00493	0.00477
6.439990	0.0544285	–3.146	–0.606	0.00020	0.00307
7.708951	0.0403695	–3.867	–0.745	–0.00087	0.00218
8.975891	0.0318248	–4.572	–0.880	–0.00094	0.00169
10.240946	0.0260651	–5.267	–1.013	–0.00074	0.00139
11.504260	0.0219090	–5.955	–1.144	–0.00049	0.00119
12.765953	0.0187647	–6.636	–1.273	–0.00025	0.00105
14.026134	0.0163027	–7.314	–1.402	–0.00006	0.00094
15.284901	0.0143246	–7.987	–1.530	0.00010	0.00086
			$\ell = 3$		
4.294602	0.1193654	–1.898	–0.169	–0.01155	0.00041
5.591067	0.0742468	–2.728	–0.240	–0.00113	0.00157
6.878680	0.0517251	–3.496	–0.307	0.00015	0.00140
8.158826	0.0387755	–4.236	–0.371	0.00038	0.00113
9.433911	0.0305232	–4.960	–0.434	0.00043	0.00091
10.705348	0.0248710	–5.674	–0.496	0.00044	0.00076
11.973956	0.0207887	–6.380	–0.557	0.00046	0.00064
13.240238	0.0177183	–7.081	–0.618	0.00048	0.00055
14.504529	0.0153345	–7.777	–0.678	0.00050	0.00048
15.767068	0.0134359	–8.470	–0.738	0.00051	0.00042

4.1.2. Comparison

Based on these coefficients, it is possible to calculate perturbative frequencies which can then be compared to the complete calculations, thereby establishing a domain of validity for perturbative methods. In Fig. 4, we show two such domains for 3rd order methods, one for each of COROT's error bars (0.6 μHz for the 20 runs and 0.08 μHz for the 150 day runs). The underlying polytropic models have a fixed mass of 1.9 $M_\odot$ and a fixed polar radius of 2.3 $R_\odot$, both of which are typical of δ Scuti pulsators. When the distance between the perturbative frequency and the complete one exceeds COROT's error bars, the frequency is shown in black. Otherwise, it is shown in grey. From these figures, it is clear that complete methods are required beyond $v \sin i = 75\,{\rm km\,s^{-1}}$ for COROT's 20 day programs and $v \sin i = 50\,{\rm km\,s^{-1}}$ for COROT's 150 day programs.

It is important to bear in mind that the domain of validity obtained for perturbative methods depends on the choice of rotational variable used in the development. In order to illustrate this, suppose we develop a frequency in terms of two different rotational parameters X and Y: $\omega = a_0 + a_1 X + a_2 X^2 + a_3 X^3 + O(X^4) = b_0 + b_1 Y + a_2 Y^2 + a_3 Y^3 + O(Y^4)$. When the relationship between X and Y is more complex than a simple proportionality, the neglected terms, $O(X^4)$ and $O(Y^4)$, are not the same. As a result, a 3rd order development in terms of X or Y will give different values for ω, thus modifying the corresponding domain of validity. Therefore, we decided to compute the domain of validity associated with the variables Ω/Ω_K and $\Omega/(GM/R_{\rm pol}^3)^{1/2}$ to see if there was a substantial difference between the two. For individual frequencies, there can be large differences, but when all the frequencies are considered, the global result is roughly the same.

In Fig. 5, we show the differences between complete frequencies and perturbative ones at $0.59\Omega_K$. We have kept the same parameters for the equilibrium model as in Fig. 4. As can be seen from the figure, differences between the two sets of calculations are substantial and comparable to the large frequency separation (which seems to survive rotation). The order of frequencies is not the same between the two sets of calculations. As a result, it is necessary to use complete calculations in order to correctly interpret a pulsating star rotating at such a high rotation rate.

Recently, Suárez et al. (2005) attempted to model Altair through asteroseismology. The effects of rotation were included in the pulsation modes using 2nd order perturbative methods. Later interferometric studies suggested an equatorial velocity of 280 km s^{-1} (Domiciano de Souza et al. 2005), which is above 216 km s^{-1}, the equatorial velocity corresponding to Fig. 5 (if we use a mass of $M = 1.8\,M_\odot$ and a polar radius $R_{\rm pol} = 1.7\,R_\odot$ instead, we obtain $v_{\rm eq} = 244\,{\rm km\,s^{-1}}$). As a result, it is pretty obvious that what is required in Suárez et al. (2005) is complete calculations of the effects of rotation before being able to interpret Altair's oscillation spectrum (not to mention complete models of rapidly rotating stars).

4.1.3. Relative importance of the Coriolis and centrifugal forces

It is then interesting to analyse what is the main source of differences between perturbative calculations and complete ones. In Fig. 6 we show three different graphs which give the relative errors associated with different calculations:

$$\left(\frac{\delta\omega}{\omega}\right)_{(a)} = \frac{\omega_{\rm pert.} - \omega}{\omega}, \tag{68}$$

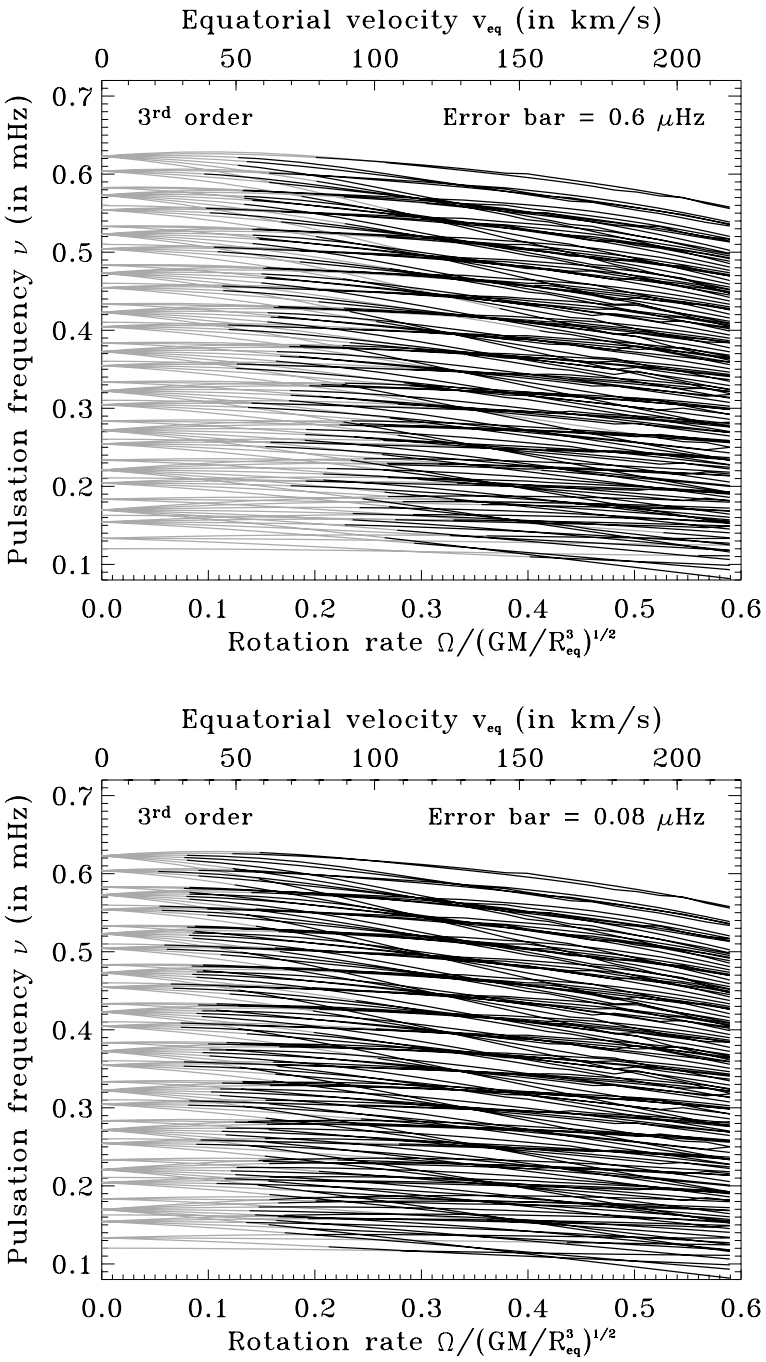

Fig. 4. Plots of the evolution of pulsation cyclic frequencies ($\nu = \omega/2\pi$) as a function of the rotation rate. The frequencies are followed from the non-rotating case to $0.59\,\Omega_K$ using the procedure described in Paper I. At small rotation rates, it is easy to recognise the usual multiplet structure as predicted from perturbative methods. Once the rotation rate is sufficient large, the multiplets are less regular and overlap, which greatly complicates the interpretation of the oscillation spectrum. Superimposed is the domain of validity of 3rd order perturbative methods using COROT's error bars of $0.6\,\mu$Hz (upper panel) and $0.08\,\mu$Hz (lower panel). The calculations were done with $N = 3$ polytropic models with $R_{\rm pol} = 2.3\ R_\odot$ and $M = 1.9\ M_\odot$.

$$\left(\frac{\delta\omega}{\omega}\right)_{(b)} = \frac{\omega^{\text{no Cor.}}_{\text{pert.}} - \omega^{\text{no Cor.}}}{\omega^{\text{no Cor.}}}, \tag{69}$$

$$\left(\frac{\delta\omega}{\omega}\right)_{(c)} = \frac{\omega^{\text{no Cor.}} - \omega}{\omega}, \tag{70}$$

where the subscripts (a), (b) and (c) correspond to the different panels in Fig. 6, the subscript "pert." to 3rd order perturbative calculations and the superscript "no Cor." to calculations done without the Coriolis force. From these panels, it is possible to deduce the dominant role of the centrifugal force in the differences between perturbative and complete calculations. Panels (a) and (b) are very similar, yet the first one includes the Coriolis force and the second one excludes it. Panel (c) shows the errors which come from excluding the Coriolis force. These errors are at least ten times smaller than in cases (a) and (b) and decrease with the radial order. This decrease is expected because as the radial order n of the mode increases, the time scale of the oscillations decreases and becomes much shorter than the $1/\Omega$ time scale associated with the Coriolis force. As a result high order modes are less affected by the Coriolis force.

The effects of the centrifugal force, on the other hand, increase with radial order. The reason for this, as explained in Paper I, is that changes in the stellar structure and the sound velocity profile causes modifications which are roughly proportional to the

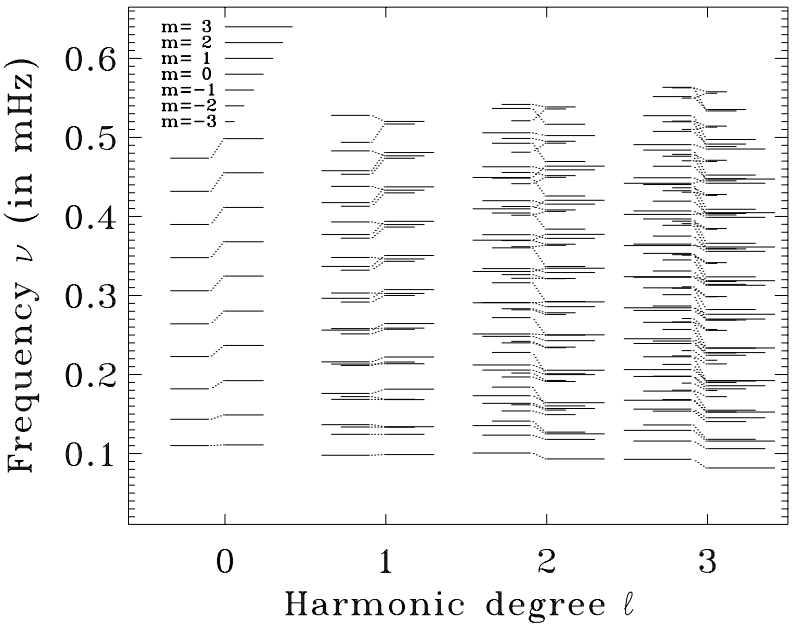

Fig. 5. This figure shows a comparison between perturbative cyclic frequencies and complete ones at $0.59\Omega_K$. The equilibrium model is the same as in Fig. 4. The complete calculations are represented by the bars that go to the right and the perturbative ones by the bars going to the left. The length of the bars gives the azimuthal order. Complete and perturbative calculations are connected by dotted lines (the correspondence is based on mode labelling as described in Paper I). It is clear from this figure that perturbative calculations lead to substantial error at high rotation rates, and cannot correctly anticipate the order of the modes. Even if the perturbative frequencies were multiplied by a global corrective factor, the agreement remains poor.

frequencies. For spherically symmetric changes in a star's structure, we have $\Delta \ln \omega = -\Delta \ln \int_0^R \mathrm{d}r/c$ (where Δ means the variations due to the change in stellar structure), based on Tassoul's asymptotic formula (Tassoul 1980). The same principle applies for more complicated changes in the structure, such as those provoked by the centrifugal force, but will have a more complicated mathematical formulation. One way of illustrating this is by plotting the ratios D_1/ω_0 (see Eq. (66)), which correspond to $\partial \ln \omega/\partial\Omega^2$ calculated at $\Omega = 0$ for $m = 0$ modes. We take the derivative with respect to Ω^2 since the effects of the centrifugal force begin at 2nd order in Ω. In Fig. 7, we can see that these ratios approach constant values as n increases for a given ℓ. Furthermore, we have plotted these ratios both with and without the Coriolis force, thereby demonstrating that this effect is entirely due to the centrifugal force. For non-axisymmetric modes, the relevant ratios $(D_1 + m^2 D_2)/\omega_0$ also show the same behaviour. This shows that the effects of the centrifugal distortion is roughly proportional to the frequency.

It can then be expected that making errors on the effects of the centrifugal force will also lead to differences proportional to the frequencies. If we look at panel (b) of Fig. 6 in which the Coriolis force has been suppressed, we can see that the relative differences between perturbative and complete calculations $\delta\omega/\omega$ actually increase with radial order (at least for lower and moderate rotation rates). It is an open question whether or not these relative differences will approach an asymptotic limit as the radial order increases like in Fig. 7.

The increase of perturbative errors with radial order may have important implications for stars which pulsate in high radial overtones. Examples of these are solar type stars which typically pulsate with radial orders between 15 and 25. If we assume that perturbative errors scale with frequency and frequency with radial order, we can estimate at what point complete methods will be necessary to calculate the effects of rotation on such modes. The average limit for $n = 25$ pulsation modes in $M = 1\,M_\odot$, $R_{\rm pol} = 1\,R_\odot$ stars would be $v_{\rm eq} = 25\,\mathrm{km\,s^{-1}}$ ($45\,\mathrm{km\,s^{-1}}$) for COROT's primary (secondary, resp.) program. This implies that non-perturbative effects of rotation could be visible for moderate rotation rates. Nonetheless, direct comparisons between perturbative and complete calculations for high order modes are necessary to confirm this conclusion.

In order to further understand the role of the centrifugal force in perturbative errors, it is helpful to bear in mind the approximations which result from applying perturbative methods. First of all, the frequencies, the stellar structure and the mode structure are all described by low degree polynomials in Ω. This then leads to the following effects: the equilibrium structure is only described by $\ell = 0$ and $\ell = 2$ spherical harmonics (for 2nd and 3rd order methods) and the pulsation mode structure is also limited to a few spherical harmonics. In order to analyse the effects of using only a few spherical, we did highly truncated numerical calculations, in which the equilibrium model has been reduced to 2 spherical harmonics and the pulsation modes to 4 spherical harmonics (2 poloidal + 2 toroidal). In Fig. 8, the black lines represent the relative differences between these truncated calculations and complete ones. These differences are significant, thus showing the need for more spherical harmonics. Nonetheless, we also plot in Fig. 8 the perturbative errors which are higher than the truncated calculations. This shows that including higher order terms in Ω in the contribution of even the lowest degree spherical harmonics can improve results.

4.2. Discussion

As can be seen from previous sections, differences between perturbative calculations and complete ones can be quite substantial. This is problematic because obtaining accurate results is crucial in asteroseismology. Differences between theoretical calculations and observed frequencies need to come from differences between the stellar model and the star's actual structure rather than from an approximate treatment of the effects of rotation. Otherwise, modifying the stellar structure so as to match the observed frequencies will end up compensating errors in the calculation of frequencies instead of improving the stellar model. Moreover, large errors on frequency calculations can lead to erroneous mode identifications, especially if proximity between observed and theoretical

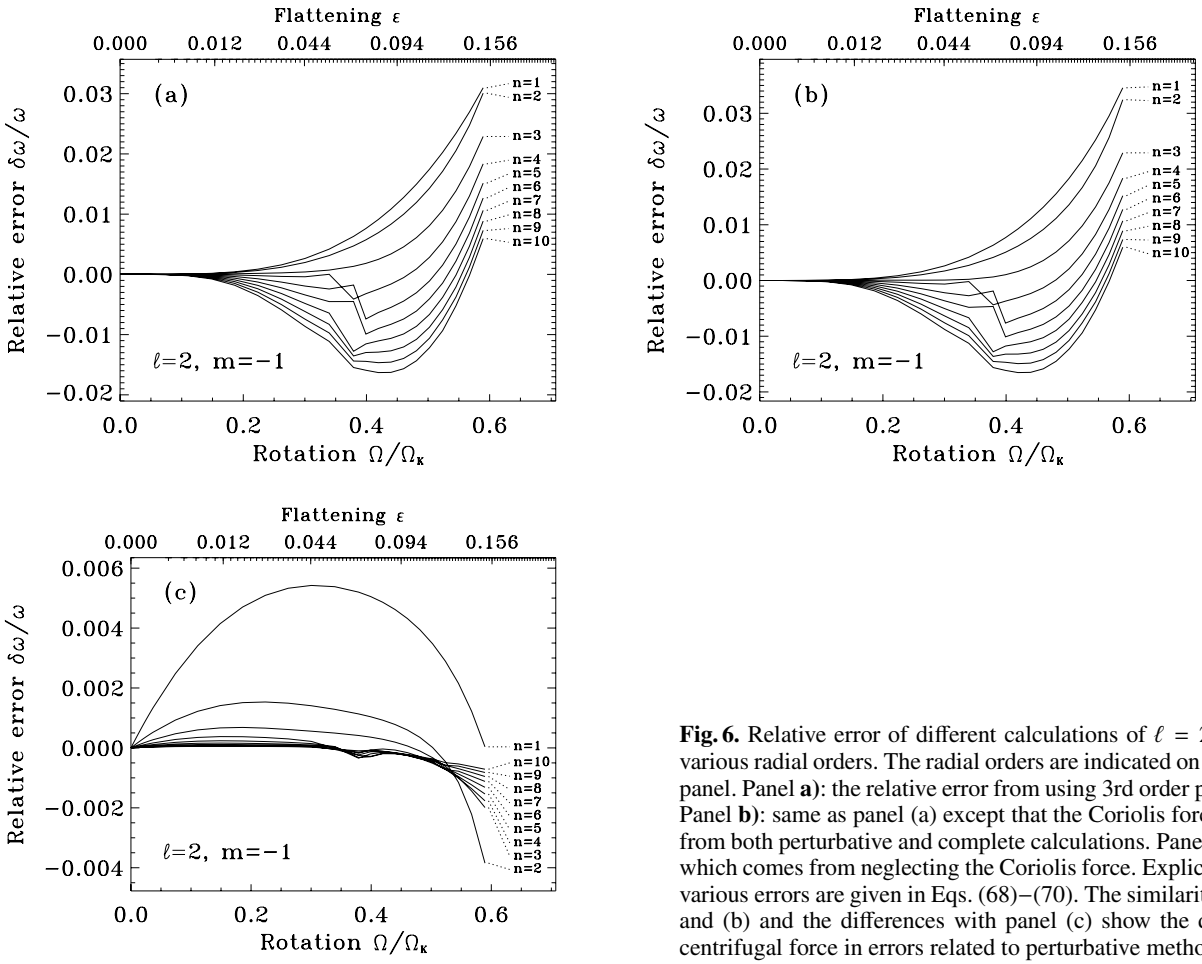

Fig. 6. Relative error of different calculations of $\ell = 2$, $m = -1$ modes of various radial orders. The radial orders are indicated on the right side of each panel. Panel **a)**: the relative error from using 3rd order perturbative methods. Panel **b)**: same as panel (a) except that the Coriolis force has been excluded from both perturbative and complete calculations. Panel **c)**: the relative error which comes from neglecting the Coriolis force. Explicit expressions for the various errors are given in Eqs. (68)−(70). The similarity between panels (a) and (b) and the differences with panel (c) show the dominant role of the centrifugal force in errors related to perturbative methods.

frequencies is the only criteria used for establishing such identifications. Interestingly, establishing a correct mode identification is one of the key difficulties in interpreting δ Scuti stars (e.g. Goupil et al. 2005). Mode misidentification can occur because frequencies are not in the same order in perturbative calculations as in complete ones (in Fig. 5, this can be seen by the dotted lines for the $\ell = 1$, 2 or 3 modes which cross each other, thus indicating an exchange of position between two frequencies) and because one can no longer rely on the usual frequency patterns used in slowly rotating stars (see Paper I). An erroneous mode identification then leads a false interpretation of pulsation frequencies due to an incorrect understanding of the geometry of the pulsation mode and the stellar regions which it probes. This problem is further aggravated by the fact that perturbative methods only give an approximate idea of the structure of a given mode anyway. Fully taking into account the effects of rotation on stellar pulsation increases the likelihood of obtaining a correct identification and gives a better understanding of mode structure, especially when the rotation rate is high. However, in order to obtain such a mode identification, the underlying stellar model needs to be sufficiently close to reality so as enable a successful matching between theoretical predictions and observations. It is possible that even then, mode identification is uncertain due to multiple solutions which fit a set of observed frequencies.

5. Conclusion

In this work we have explored some of the effects of rapid rotation on stellar acoustic pulsations. This was achieved thanks to a numerical method which combines spheroidal geometry and spectral methods, as in Paper I. Through a detailed analysis, we have shown that our results have a 6 to 7 digit accuracy. This analysis included a discussion on the accuracy of the underlying polytropic models, comparisons with Saio (1981), Clement (1984), Christensen-Dalsgaard & Mullan (1994) and Paper I, a test based on the variational principle and some tests on the sensitivity of the results to the parameters of the numerical method.

In the future, the satellite COROT is expected to measure stellar oscillation frequencies with a precision of $0.08\,\mu$Hz (primary targets) or $0.6\,\mu$Hz (secondary targets). In the frequency range considered in this paper, we find that for a $M = 1.9\,M_\odot$, $R = 2.3\,R_\odot$ star, perturbative methods cease to be valid for COROT's primary (secondary) program beyond $v \sin i = 50\,\mathrm{km\,s^{-1}}$ ($v \sin i = 75\,\mathrm{km\,s^{-1}}$, resp.). At a rotation rate of $0.59\,\Omega_K$, the perturbative spectrum is very different from the one based on complete calculations. Therefore, any attempt to interpret stellar pulsations using the perturbative approach at comparable rotation rates is likely to fail. Using complete methods on the other hand increases the likelihood of obtaining a correct mode identification, and gives an accurate description of the structure of pulsation modes. Both of these are crucial when interpreting observed pulsation modes.

Further investigation has shown the dominant role of the centrifugal force in modifying the frequency spectrum and causing perturbative errors. This is because while the effect of the Coriolis force decreases as the frequency increases, the effect of the stellar

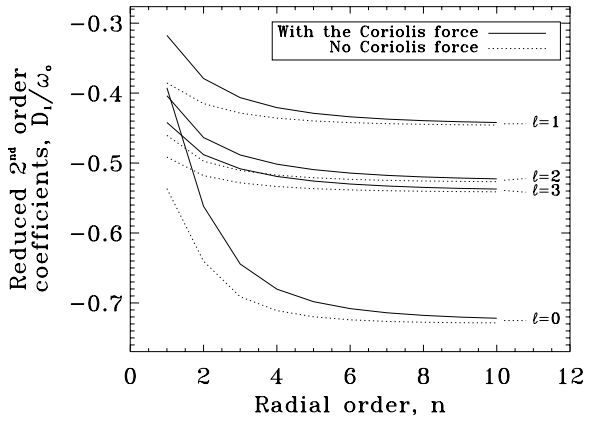

Fig. 7. Ratio of 2nd order perturbative coefficients to corresponding frequencies at $\Omega = 0$, as a function of the radial order n. As n increases, these ratios approach a constant value, which shows the proportional effects of the centrifugal deformation of the star.

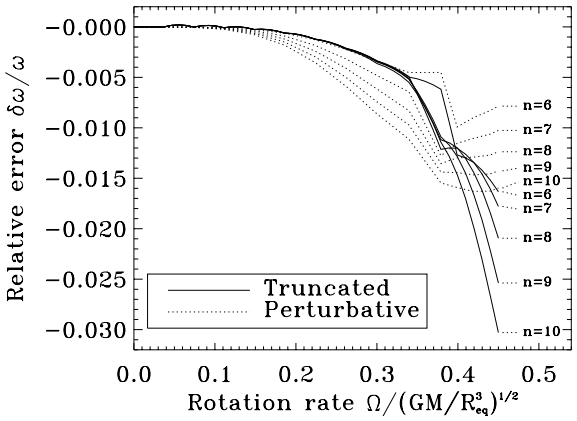

Fig. 8. A comparison between relative errors in perturbative calculations and those in truncated calculations (in which the equilibrium model is reduced to 2 spherical harmonics and the pulsation mode to 2 poloidal + 2 toroidal harmonics). This figure shows that truncated calculations are closer to complete ones than perturbative calculations, which shows the importance of retaining higher powers of Ω in the lower spherical harmonics describing the stellar structure and mode structure. The uneven aspect of the lines corresponding to the truncated calculations are due to interpolation errors.

deformation increases roughly proportionally to the frequencies. Therefore, the errors which arise from perturbative descriptions of the centrifugal distortion are also amplified in higher order modes. As a result, it may be necessary to use complete methods for moderately rotating stars which exhibit high order modes.

Some of the issues which were discussed in Paper I and have yet to be discussed for the present results include: an analysis of the regularities in the oscillation spectrum at high rotation rates and a study of the visibility of the different modes based on their structure. These will be the subject of forthcoming papers. A few preliminary examinations have already confirmed some of the conclusions given in Paper I, such as a strong equatorial concentration of mode structure at high rotation rates, or the transition from one frequency spectrum organisation to another.

Future work includes working with more realistic models, and studying gravity modes in spheroidal geometry. The transition to more realistic models is essential before being able to compare theoretical frequencies with observations. Coming up with realistic models that fully include the effects of rotation and in particular the centrifugal distortion is no easy task, but is the subject of active research (e.g. Roxburgh 2004; Jackson et al. 2005; Rieutord et al. 2005). Calculating the associated pulsation frequencies and comparing them to observations will provide crucial information on stellar structure and enable a better adjustment of these models.

The study of the effects of rapid rotation on g-modes is of interest for the interpretation of γ Doradus stars, which are g-mode pulsators and can be rapid rotators. Previous studies on the non-perturbative effects of the Coriolis force on g-modes (Dintrans et al. 1999; Dintrans & Rieutord 2000) have revealed their important role in altering the geometry and frequencies of these modes. This behaviour is entirely different from that of the high frequency acoustic modes presented here. It is then interesting to understand what the effects of the centrifugal force will be on g-modes and how it will compare with the effects of the Coriolis force.

Acknowledgements. The authors wish to thank Lorenzo Valdettaro for his contribution to the numerical aspects of this work. Many of the numerical calculations were carried out on the Altix 3700 of CALMIP ("CALcul en MIdi-Pyrénées") and on the NEC SX5 of IDRIS ("Institut du Développement et des Ressources en Informatique Scientifique"), both of which are gratefully acknowledged.

References

Baglin, A., Auvergne, M., Barge, P., et al. 2002, in Stellar Structure and Habitable Planet Finding, ed. B. Battrick, F. Favata, I. W. Roxburgh, & D. Galadi, ESA SP-485, 17
Bender, C. M., & Orszag, S. A. 1978, Advanced Mathematical Methods for Scientists and Engineers (McGraw-Hill)
Bonazzola, S., Gourgoulhon, E., & Marck, J.-A. 1998, Phys. Rev. D, 58, 104020
Canuto, C., Hussaini, M. Y., Quarteroni, A., & Zang, T. A. 1988, Spectral Methods in Fluid Dynamics (Springer Verlag)
Chatelin, F. 1988, Valeurs propres de matrices (Paris: Masson)
Christensen-Dalsgaard, J., & Mullan, D. J. 1994, MNRAS, 270, 921
Clement, M. J. 1981, ApJ, 249, 746
Clement, M. J. 1984, ApJ, 276, 724
Clement, M. J. 1986, ApJ, 301, 185
Clement, M. J. 1989, ApJ, 339, 1022
Clement, M. J. 1998, ApJS, 116, 57
Dintrans, B., & Rieutord, M. 2000, A&A, 354, 86
Dintrans, B., Rieutord, M., & Valdettaro, L. 1999, J. Fluid Mechanics, 398, 271
Domiciano de Souza, A., Kervella, P., Jankov, S., et al. 2003, A&A, 407, L47
Domiciano de Souza, A., Kervella, P., Jankov, S., et al. 2005, A&A, 442, 567

Dziembowski, W. A., & Goode, P. R. 1992, ApJ, 394, 670
Espinosa, F., Pérez Hernández, F., & Roca Cortés, T. 2004, in SOHO 14 Helio- and Asteroseismology: Towards a Golden Future, ESA SP-559, 424
Gough, D. O., & Thompson, M. J. 1990, MNRAS, 242, 25
Goupil, M.-J., Dupret, M. A., Samadi, R., et al. 2005, JA&A, 26, 249
Hachisu, I., Eriguchi, Y., & Sugimoto, D. 1982, Progress of Theoretical Physics, 68, 191
Hunter, C. 2001, MNRAS, 328, 839
Hurley, M., Roberts, P. H., & Wright, K. 1966, ApJ, 143, 535
Ipser, J., & Lindblom, L. 1990, ApJ, 355, 226
Jackson, S., MacGregor, K. B., & Skumanich, A. 2005, ApJS, 156, 245
Karami, K., Christensen-Dalsgaard, J., Pijpers, F. P., Goupil, M.-J., & Dziembowski, W. A. 2005 [arXiv:astro-ph/0502194]
Ledoux, P. 1951, ApJ, 114, 373
Lignières, F., Rieutord, M., & Reese, D. 2006a, A&A, in press
Lignières, F., Rieutord, M., & Reese, D. 2006b, Mem. Soc. Astron. It., 77, 425
Lynden-Bell, D., & Ostriker, J. P. 1967, MNRAS, 136, 293
Peterson, D. M., Hummel, C. A., Pauls, T. A., et al. 2006, ApJ, 636, 1087
Rieutord, M. 1987, Geophys. Astrophys. Fluid Dynamics, 39, 163
Rieutord, M. 2006, A&A, 451, 1025
Rieutord, M., & Valdettaro, L. 1997, J. Fluid Mechanics, 341, 77
Rieutord, M., Dintrans, B., Lignières, F., Corbard, T., & Pichon, B. 2005, in SF2A 2005: Semaine de l'Astrophysique Francaise (EDP Sciences), 759
Roxburgh, I. W. 2004, A&A, 428, 171
Saio, H. 1981, ApJ, 244, 299
Seidov, Z. F. 2004 [arXiv:astro-ph/0402130]
Soufi, F., Goupil, M.-J., & Dziembowski, W. A. 1998, A&A, 334, 911
Suárez, J. C., Bruntt, H., & Buzasi, D. 2005, A&A, 438, 633
Tassoul, M. 1980, ApJS, 43, 469
Unno, W., Osaki, Y., Ando, H., Saio, H., & Shibahashi, H. 1989, Nonradial oscillations of stars, 2nd ed. (University of Tokyo Press)
Valdettaro, L., Rieutord, M., Braconnier, T., & Frayssé, V. 2006, Journal of Computational and Applied Mathematics, in press [arXiv:physics/0604219]
Yoshida, S., & Eriguchi, Y. 1995, ApJ, 438, 830
Yoshida, S., & Eriguchi, Y. 2001, MNRAS, 322, 389

Online Material

Appendix A: "Generalised" Frobenius method

A.1. Description

The starting point in this method is the following equation:

$$\frac{\mathrm{d}Y(x,y,z)}{\mathrm{d}x} + \frac{1}{x}A(x,y,z)Y(x,y,z) = 0. \tag{A.1}$$

This equation looks very much like a first order Frobenius equation except that two other variables, y and z, intervene in the different terms (for a description of the more traditional version of the Frobenius method, see Bender & Orszag 1978). The quantity $Y(x,y,z)$ can be a scalar or a vector. The operator $A(x,y,z)$ can include derivatives in the y and z directions and needs to be analytic in the x direction, so that we can write:

$$A(x,y,z) = \sum_{n=0}^{\infty} A_n(y,z)x^n. \tag{A.2}$$

We then look for the behaviour of $Y(x,y,z)$ along the boundary $x = 0$. If we develop $Y(x,y,z)$ in the following manner,

$$Y(x,y,z) = \sum_{n=0}^{\infty} Y_n(y,z)x^{n+\alpha}, \tag{A.3}$$

then we obtain the following zeroth order equation:

$$\alpha Y_0(y,z) + A_0(y,z)Y_0(y,z) = 0, \tag{A.4}$$

where α is the leading power of x in $Y(x,y,z)$. Therefore, to obtain α, one needs to solve an eigenvalue problem in terms of the coordinates y and z, along the entire surface $x = 0$. The remaining Y_n are defined through the following recurrence relation:

$$n \geq 1, \quad [(\alpha+n)Id + A_0]\, Y_n = -\sum_{k=0}^{n-1} A_{n-k}Y_k, \tag{A.5}$$

where $Id(Y) \equiv Y$. This series is defined only if for each $n \geq 1$, the operator $[(\alpha+n)Id + A_0]$ is invertible. The next step is then to search under what mathematical conditions the series defined by Eq. (A.5) converges. However, this step is quite complicated and therefore beyond the scope of this paper.

A.2. Application

In our case, we are only interested in obtaining the leading behaviour of our solutions near the surface. Therefore we will only solve the zeroth order equation (Eq. (A.4)) after having established the expressions for Y_0 and A_0. We start by defining $x = 1 - \zeta$ as the variable that will be used in the Frobenius series. The surface of the star then corresponds to $x = 0$ and its interior to positive values of x.

It is then necessary to choose a vector Y so that Eqs. (33)−(38) can be put in the form given by Eq. (A.1). This implies choosing the variables which are differentiated once with respect to x. Our choice is therefore $Y = [\Pi, u^\zeta, \mathcal{G} = \partial_x\Psi, \Psi]^t$. Having chosen the vector Y, it is then necessary to find the associated system of equations, by eliminating the variables (b, u^θ, u^ϕ), and then to extract the zeroth order equation (see Eq. (A.4)). In fact, it is much simpler to do both steps simultaneously, given the complexity of Eqs. (33)−(38).

Before giving the final result, it is important to point out that when N is not an integer, a mild singularity occurs on the surface of the star, due to the presence of fractional powers in the enthalpy, starting with x^{N+2} (Hunter 2001). This in fact invalidates the use of Frobenius series in its present form from a strictly mathematical point of view, since these only use integer powers of x. This problem can be solved by including fractional powers in the solution, as is done in Christensen-Dalsgaard & Mullan (1994), the lowest one being x^{N+1} (this is not in contradiction with Christensen-Dalsgaard & Mullan (1994), for which the variable y_4 contains x^N, because y_4 includes $\partial_{xx}H$ in its expression whereas our variables do not). As a result, the zeroth order equation remains unaffected and can therefore give the correct behaviour of the solution near the surface:

$$\alpha \begin{bmatrix} \Pi_0 \\ u_0^\zeta \\ \mathcal{G}_0 \\ \Psi_0 \end{bmatrix} + \begin{bmatrix} N\left(1-\frac{\gamma}{\Gamma_1}\right) & \frac{NH_x}{\lambda\Lambda(1-\varepsilon)R_s^2}\left(\frac{\gamma}{\Gamma_1}-1\right) & 0 & 0 \\ -\frac{\lambda\Lambda(1+N)(1-\varepsilon)R_s^2}{H_x\Gamma_1} & \frac{1+N}{\Gamma_1} & 0 & 0 \\ 0 & 0 & 0 & 0 \\ 0 & 0 & 0 & 0 \end{bmatrix} \begin{bmatrix} \Pi_0 \\ u_0^\zeta \\ \mathcal{G}_0 \\ \Psi_0 \end{bmatrix} = 0. \tag{A.6}$$

This equation is based on the following development of the enthalpy near the surface:

$$H(x,\theta) = H_x(\theta)x + \frac{1}{2}H_{xx}(\theta)x^2 + H_N(\theta)x^{N+2} + o(x^2). \tag{A.7}$$

The characteristic equation is $\det(A_0 - X.Id) = X^4 - NX^3 = 0$. The eigenvalues are therefore $\alpha = -N$ and $\alpha = 0$, the second value being triply degenerate. The first value is rejected because it leads to solutions that diverge on the surface of the star. The three remaining eigensolutions are bounded near the surface, which is in complete agreement with the results of Hurley et al. (1966), who applied the Frobenius method to the spherical case. By choosing $\alpha = 0$, we also ensure that $[(\alpha + n)Id + A_0]$ is invertible for $n \geq 1$. These three bounded solutions and any of their linear combinations satisfy the following analytical constraint:

$$\lambda \Pi_0 = \frac{H_x}{\Lambda(1-\varepsilon)R_s^2} u_0^\zeta, \tag{A.8}$$

which is, in fact, equivalent to saying that $\delta p/\rho_0$ goes to zero on the outer boundary (where δp represents the Lagrangian variation of the pressure). We can use the previous results to establish the behaviour of different quantities near the surface:

$$p = O\left(x^N\right), \tag{A.9}$$
$$\rho = O\left(x^{N-1}\right), \tag{A.10}$$
$$u^\zeta = O(1), \tag{A.11}$$
$$u^\theta = O(1), \tag{A.12}$$
$$u^\phi = O(1), \tag{A.13}$$
$$\Psi = O(1). \tag{A.14}$$

Equation (A.8) shows that $\delta p/H^N = o(1)$. The next relevant power in a power series expansion of $\delta p/H^N$ is x^1 (this remains true even when N is not an integer since the first fractional power of $\delta p/H^N$ is $N+1$). By applying the equation $\delta p = c_o^2 \delta\rho$, it can also be shown that $\delta\rho/H^{N-1} = O(x)$. As a result we obtain the following behaviour for both Lagrangian perturbations:

$$\delta p = O\left(x^{N+1}\right), \tag{A.15}$$
$$\delta\rho = O\left(x^N\right). \tag{A.16}$$

The results on ρ, p, $\delta\rho$, δp are interesting when we consider the equilibrium model. Since $\rho_o \propto H^N$ and $P_o \propto H^{N+1}$, we deduce that the leading behaviour of the equilibrium density and pressure are $\rho_o = O\left(x^N\right)$ and $P_o = O\left(x^{N+1}\right)$, respectively. This implies that the ratio of the Eulerian density perturbation to the equilibrium density (ρ/ρ_o) and the corresponding ratio for pressure both become unbounded as one approaches the surface of the star. This is problematic because the sum $\rho_o + A\,\rho\,\cos(\omega t)$ (which corresponds to the total density) will periodically reach negative values close to the surface of the star for any non-zero amplitude A. However, the ratio of the Lagrangian density perturbation to the equilibrium density remains bounded as one approaches the surface, and the same applies to the pressure. This suggests that a Lagrangian description is physically more appropriate.

Appendix B: Projection onto the spherical harmonic base

B.1. Integral operators

In order to project the fluid equations onto the harmonic basis, it is necessary to define a number of integral operators. The prototype to one of these operators is as follows:

$$J^m_{\ell\ell'}(G)(\zeta) = \iint_{4\pi} G(\zeta,\theta)\partial_\theta Y^m_{\ell'}(\theta,\phi)\left\{Y^m_\ell(\theta,\phi)\right\}^* \mathrm{d}\Omega, \tag{B.1}$$

where $\mathrm{d}\Omega = \sin\theta \mathrm{d}\theta\mathrm{d}\phi$, G is an arbitrary function, x^* is the complex conjugate of x and $J^m_{\ell\ell'}(.)$ is the operator. $J^m_{\ell\ell'}(G)$ is a two-dimension array of indexes ℓ and ℓ' (the value of m is fixed) composed of functions depending on ζ only. The remaining operators are given in the following table:

	$\left\{Y^m_\ell\right\}^*$	$\left\{\partial_\theta Y^m_\ell\right\}^*$	$\left\{\mathrm{D}_\phi Y^m_\ell\right\}^*$
$Y^m_{\ell'}$	$I^m_{\ell\ell'}(G)$	$Jc^m_{\ell\ell'}(G)$	$Kc^m_{\ell\ell'}(G)$
$\partial_\theta Y^m_{\ell'}$	$J^m_{\ell\ell'}(G)$	$L^m_{\ell\ell'}(G)$	$Mc^m_{\ell\ell'}(G)$
$\mathrm{D}_\phi Y^m_{\ell'}$	$K^m_{\ell\ell'}(G)$	$M^m_{\ell\ell'}(G)$	$N^m_{\ell\ell'}(G)$

If G is a real function than $I^m_{\ell\ell'}(G)$, $J^m_{\ell\ell'}(G)$, $Jc^m_{\ell\ell'}(G)$, $L^m_{\ell\ell'}(G)$ and $N^m_{\ell\ell'}(G)$ are all real functions whereas $K^m_{\ell\ell'}(G)$, $Kc^m_{\ell\ell'}(G)$, $M^m_{\ell\ell'}(G)$, and $Mc^m_{\ell\ell'}(G)$ are purely imaginary. There are symmetries between some of these operators: for example $J^m_{\ell\ell'}(G^*) = \left\{Jc^m_{\ell'\ell}(G)\right\}^*$. The same applies for $K^m_{\ell\ell'}(G)$ and $Kc^m_{\ell\ell'}(G)$, and for $M^m_{\ell\ell'}(G)$ and $Mc^m_{\ell\ell'}(G)$.

In order to calculate these integrals, we use Gauss' quadrature. This gives accurate integrals when G is a "polynomial" of $\cos\theta$ (the coefficients of the polynomial can depend on ζ), for the operators $I^m_{\ell\ell'}(G)$, $L^m_{\ell\ell'}(G)$, $M^m_{\ell\ell'}(G)$, $Mc^m_{\ell\ell'}(G)$ and $N^m_{\ell\ell'}(G)$. For the operators $J^m_{\ell\ell'}(G)$, $K^m_{\ell\ell'}(G)$, $Jc^m_{\ell\ell'}(G)$ and $Kc^m_{\ell\ell'}(G)$, G needs to be of the form $\sin\theta P(\cos\theta)$ where P is a polynomial. These integrals are calculated with L_{res} collocation points, where L_{res} is generally greater than $L_{\max}$, the harmonic resolution of the pulsations.

Having defined the different integral operators, it is now possible to give explicitly the fluid equations projected onto the spherical harmonic basis. In what follows, we have used the following conventions:

$$I^m_{\ell\ell'}(G)\,u^{\ell'}_m \equiv \sum_{\ell'} I^m_{\ell\ell'}(G)\,u^{\ell'}_m, \qquad \begin{matrix} -L^m_{\ell\ell'} \\ +N^m_{\ell\ell'} \end{matrix}(G) \equiv -L^m_{\ell\ell'}(G) + N^m_{\ell\ell'}(G)\,. \tag{B.2}$$

It is also worth pointing out that in the following matrices, the summation on ℓ' applies to an entire line of the matrix. For example,

$$\begin{bmatrix} +I^m_{\ell\ell'}(A) - J^m_{\ell\ell'}(B) & u^{\ell'}_m \\ -K^m_{\ell\ell'}(C) + N^m_{\ell\ell'}(D) & v^{\ell'}_m \end{bmatrix}, \tag{B.3}$$

is equivalent to:

$$\sum_{\ell'=|m|}^{L} \left\{ I^m_{\ell\ell'}(A) - J^m_{\ell\ell'}(B) \right\} u^{\ell'}_m + \sum_{\ell'=|m|}^{L} \left\{ -K^m_{\ell\ell'}(C) + N^m_{\ell\ell'}(D) \right\} v^{\ell'}_m. \tag{B.4}$$

B.2. Continuity equation

$$\lambda b^\ell_m = \begin{bmatrix} -I^m_{\ell\ell'}\left(\dfrac{\zeta^2 H}{r^2 r_\zeta}\right) & \partial_\zeta u^{\ell'}_m \\ -I^m_{\ell\ell'}\left(\dfrac{2\zeta H}{r^2 r_\zeta} + \dfrac{\zeta^2 N H_\zeta}{r^2 r_\zeta}\right) & u^{\ell'}_m \\ +I^m_{\ell\ell'}\left(\dfrac{\ell'(\ell'+1)\zeta H}{r^2 r_\zeta}\right) - J^m_{\ell\ell'}\left(\dfrac{\zeta N H_\theta}{r^2 r_\zeta}\right) & v^{\ell'}_m \\ -K^m_{\ell\ell'}\left(\dfrac{\zeta N H_\theta}{r^2 r_\zeta}\right) & w^{\ell'}_m \end{bmatrix}, \tag{B.5}$$

where we have made use of the following identities:

$$-\ell(\ell+1)Y^m_\ell = \partial^2_{\theta\theta} Y^m_\ell + \cot\theta \partial_\theta Y^m_\ell + \frac{1}{\sin^2\theta}\partial^2_{\phi\phi} Y^m_\ell, \tag{B.6}$$

$$0 = \partial_\theta \mathrm{D}_\phi Y^m_\ell + \cot\theta \mathrm{D}_\phi Y^m_\ell - \frac{1}{\sin\theta}\partial_\phi \partial_\theta Y^m_\ell. \tag{B.7}$$

B.3. Adiabatic energy equation

$$\lambda\left(\Pi^\ell_m - \frac{\Gamma_1}{(N+1)\Lambda} b^\ell_m\right) = \left(\frac{\Gamma_1}{\gamma} - 1\right) \begin{bmatrix} +I^m_{\ell\ell'}\left(\dfrac{\zeta^2 H_\zeta}{\Lambda r^2 r_\zeta}\right) & u^{\ell'}_m \\ +J^m_{\ell\ell'}\left(\dfrac{\zeta H_\theta}{\Lambda r^2 r_\zeta}\right) & v^{\ell'}_m \\ +K^m_{\ell\ell'}\left(\dfrac{\zeta H_\theta}{\Lambda r^2 r_\zeta}\right) & w^{\ell'}_m \end{bmatrix}. \tag{B.8}$$

B.4. Poisson's equation

$$0 = \begin{bmatrix} +I^m_{\ell\ell'}\left(\dfrac{r^2 + r^2_\theta}{r^2_\zeta}\right) & \partial^2_{\zeta\zeta}\Psi^{\ell'}_m \\ +I^m_{\ell\ell'}\left(r^2 c_\zeta\right) - 2J^m_{\ell\ell'}\left(\dfrac{r_\theta}{r_\zeta}\right) & \partial_\zeta \Psi^{\ell'}_m \\ -\ell(\ell+1) & \Psi^\ell_m \\ -I^m_{\ell\ell'}\left(r^2 H^{N-1}\right) & b^{\ell'}_m \end{bmatrix}, \tag{B.9}$$

where we have made use of the Eq. (B.6).

B.5. Euler's equations

$$\lambda \begin{bmatrix} +I^m_{\ell\ell'}\left(\dfrac{\zeta^2 r_\zeta H}{r^2}\right) & u^{\ell'}_m \\ +J^m_{\ell\ell'}\left(\dfrac{\zeta r_\theta H}{r^2}\right) & v^{\ell'}_m \\ +K^m_{\ell\ell'}\left(\dfrac{\zeta r_\theta H}{r^2}\right) & w^{\ell'}_m \end{bmatrix} = \begin{bmatrix} +K^m_{\ell\ell'}\left(\dfrac{2\Omega H\zeta\sin\theta}{r}\right) & v^{\ell'}_m \\ -J^m_{\ell\ell'}\left(\dfrac{2\Omega H\zeta\sin\theta}{r}\right) & w^{\ell'}_m \\ -I^m_{\ell\ell'}(H) & \partial_\zeta \Pi^{\ell'}_m \\ -I^m_{\ell\ell'}(H) & \partial_\zeta \Psi^{\ell'}_m \\ -I^m_{\ell\ell'}\left(NH_\zeta\right) & \Pi^{\ell'}_m \\ +I^m_{\ell\ell'}\left(\dfrac{H_\zeta}{\Lambda}\right) & b^{\ell'}_m \end{bmatrix}, \tag{B.10}$$

$$\lambda \begin{bmatrix} +Jc^m_{\ell\ell'}\left(\dfrac{\zeta r_\theta}{r^2}\right) & u^{\ell'}_m \\ +L^m_{\ell\ell'}\left(\dfrac{r^2+r_\theta^2}{r^2 r_\zeta}\right)+N^m_{\ell\ell'}\left(\dfrac{1}{r_\zeta}\right) & v^{\ell'}_m \\ +M^m_{\ell\ell'}\left(\dfrac{r^2+r_\theta^2}{r^2 r_\zeta}\right)-Mc^m_{\ell\ell'}\left(\dfrac{1}{r_\zeta}\right) & w^{\ell'}_m \end{bmatrix} = \begin{bmatrix} -Kc^m_{\ell\ell'}\left(\dfrac{2\Omega\zeta\sin\theta}{r}\right) & u^{\ell'}_m \\ +M^m_{\ell\ell'}\left(\dfrac{2\Omega(r_\theta\sin\theta+r\cos\theta)}{rr_\zeta}\right) & v^{\ell'}_m \\ -Mc^m_{\ell\ell'} & \\ -L^m_{\ell\ell'}\left(\dfrac{2\Omega(r_\theta\sin\theta+r\cos\theta)}{rr_\zeta}\right) & w^{\ell'}_m \\ -N^m_{\ell\ell'} & \\ -L^m_{\ell\ell'}\left(\dfrac{1}{\zeta}\right)-Jc^m_{\ell\ell'}\left(\dfrac{NH_\theta}{\zeta H}\right) & \Pi^{\ell'}_m \\ -N^m_{\ell\ell'}\left(\dfrac{1}{\zeta}\right) & \Psi^{\ell'}_m \\ +Jc^m_{\ell\ell'}\left(\dfrac{H_\theta}{\Lambda\zeta H}\right) & b^{\ell'}_m \end{bmatrix}, \tag{B.11}$$

$$\lambda \begin{bmatrix} +Kc^m_{\ell\ell'}\left(\dfrac{\zeta r_\theta}{r^2}\right) & u^{\ell'}_m \\ +Mc^m_{\ell\ell'}\left(\dfrac{r^2+r_\theta^2}{r^2 r_\zeta}\right)-M^m_{\ell\ell'}\left(\dfrac{1}{r_\zeta}\right) & v^{\ell'}_m \\ +N^m_{\ell\ell'}\left(\dfrac{r^2+r_\theta^2}{r^2 r_\zeta}\right)+L^m_{\ell\ell'}\left(\dfrac{1}{r_\zeta}\right) & w^{\ell'}_m \end{bmatrix} = \begin{bmatrix} +Jc^m_{\ell\ell'}\left(\dfrac{2\Omega\zeta\sin\theta}{r}\right) & u^{\ell'}_m \\ +L^m_{\ell\ell'}\left(\dfrac{2\Omega(r_\theta\sin\theta+r\cos\theta)}{rr_\zeta}\right) & v^{\ell'}_m \\ +N^m_{\ell\ell'} & \\ +M^m_{\ell\ell'}\left(\dfrac{2\Omega(r_\theta\sin\theta+r\cos\theta)}{rr_\zeta}\right) & w^{\ell'}_m \\ -Mc^m_{\ell\ell'} & \\ +M^m_{\ell\ell'}\left(\dfrac{1}{\zeta}\right)-Kc^m_{\ell\ell'}\left(\dfrac{NH_\theta}{\zeta H}\right) & \Pi^{\ell'}_m \\ +M^m_{\ell\ell'}\left(\dfrac{1}{\zeta}\right) & \Psi^{\ell'}_m \\ -Mc^m_{\ell\ell'} & \\ +Kc^m_{\ell\ell'}\left(\dfrac{H_\theta}{\Lambda\zeta H}\right) & b^{\ell'}_m \end{bmatrix}. \tag{B.12}$$

Appendix C: The variational test

The present formulation of the variational test is the same as that of Unno et al. (1989), apart from the following differences: we use the velocity rather than the displacement, hence the extra time derivatives; the star's volume is no longer spherical; the integral on the gravity wave energy is based on the effective gravity and uses the local vertical direction rather than $\boldsymbol{e}_r$; the integral on the gravitational potential energy has been extended to infinite space.

The different resultant integrals are given by the following explicit formulas and are calculated numerically using Gauss' quadrature method in the angular direction and a spectral expansion in the radial direction (we use a radial resolution of 101 points and an angular resolution of 200 points):

$$\int_V \rho_\mathrm{o}\|\boldsymbol{v}\|^2 \mathrm{d}V = \int_V H^N \left[|u^\zeta|^2\frac{\zeta^4}{r^4}+|u^\theta|^2\frac{\zeta^2(r^2+r_\theta^2)}{r^4 r_\zeta^2}+|u^\phi|^2\frac{\zeta^2}{r^2 r_\zeta^2}+2\Re\left\{\left(u^\zeta\right)^* u^\theta\right\}\frac{\zeta^3 r_\theta}{r^4 r_\zeta}\right]\mathrm{d}V, \tag{C.1}$$

$$\int_V \rho_\mathrm{o} N_\mathrm{o}^2|\boldsymbol{v}\cdot\boldsymbol{e}_g|^2\mathrm{d}V = \int_V \frac{NH^{N-1}}{\Lambda}\left(1-\frac{\gamma}{\Gamma_1}\right)\frac{\zeta^2}{r^4 r_\zeta^2}\left|\zeta u^\zeta\partial_\zeta H+u^\theta\partial_\theta H\right|^2\mathrm{d}V \tag{C.2}$$

$$\int_V \frac{|p|^2}{\rho_\mathrm{o} c_\mathrm{o}^2}\mathrm{d}V = \int_V \frac{(N+1)\Lambda H^{N-1}}{\Gamma_1}|\Pi|^2\mathrm{d}V, \tag{C.3}$$

$$\int_V \rho_\mathrm{o}\boldsymbol{\Omega}\cdot(\boldsymbol{v}^*\times\boldsymbol{v})\,\mathrm{d}V = 2i\Omega\int_V H^N\left[\left(\frac{\cos\theta}{r_\zeta}+\frac{r_\theta\sin\theta}{rr_\zeta}\right)\frac{\zeta^2\left(u_r^\theta u_i^\phi-u_r^\phi u_i^\theta\right)}{r^2 r_\zeta}+\frac{\zeta^3\sin\theta\left(u_r^\zeta u_i^\phi-u_r^\phi u_i^\zeta\right)}{r^3 r_\zeta}\right]\mathrm{d}V, \tag{C.4}$$

$$\int_{V\text{ or }V_2}\|\boldsymbol{\nabla}\Psi\|^2\mathrm{d}V = \int_{V\text{ or }V_2}\frac{r^2+r_\theta^2}{r^2 r_\zeta^2}\left|\partial_\zeta\Psi\right|^2+\frac{1}{r^2}\left|\partial_\theta\Psi\right|^2+\frac{1}{r^2\sin\theta^2}\left|\partial_\phi\Psi\right|^2-\frac{2r_\theta}{r^2 r_\zeta}\Re\left(\partial_\zeta\Psi^*\partial_\theta\Psi\right)\mathrm{d}V, \tag{C.5}$$

where $\mathrm{d}V = r^2|r_\zeta| \sin\theta \mathrm{d}\theta\mathrm{d}\zeta$, $u_r^\zeta = \Re\left(u^\zeta\right)$, $u_i^\zeta = \Im\left(u^\zeta\right)$ etc. For the integral on the gravitational potential, it is useful to decompose infinite space into three domains: $V \cup V_2 \cup V_3 = V_\infty$. V is the volume of the star, V_2 is the volume comprised between the star and the sphere of radius 2, and V_3 is the space outside the sphere of radius 2 (see Fig. 1). The integral on the first two domains is given by the expression above. For the third domain, it is based on the spherical harmonic decomposition of the gravitational potential. In empty space, a gravitational potential will take on the following form as it obeys the equation $\Delta\Psi = 0$ and vanishes towards infinity:

$$\Psi = \sum_\ell \Psi_m^\ell Y_\ell^m = \sum_\ell \frac{A^\ell}{r^{\ell+1}} Y_\ell^m, \tag{C.6}$$

where the A^ℓ are constants. This form of Ψ then leads to the following expression:

$$\int_{V_3} \|\boldsymbol{\nabla}\Psi\|^2 \mathrm{d}V = \sum_\ell \frac{|A^\ell|^2(\ell+1)}{r_{\mathrm{ext}}^{2\ell+1}} = \sum_\ell r_{\mathrm{ext}}(\ell+1)\left|\Psi_m^\ell(r_{\mathrm{ext}})\right|^2, \tag{C.7}$$

where $r_{\mathrm{ext}} = 2$ is the radius of the inner sphere of V_3. This expression corresponds to the surface integral of Unno et al. (1989).

2.5.3 A3 : Gravity modes in rapidly rotating stars. Limits of perturbative methods

“Gravity modes in rapidly rotating stars. Limits of perturbative methods”

Ballot, J., Lignières, F., Reese, D., Rieutord, M.

sous presse, A&A, 2010 (preprint arXiv :1005.0275)

Astronomy & Astrophysics manuscript no. 14426
May 4, 2010

Gravity modes in rapidly rotating stars

Limits of perturbative methods

J. Ballot[1], F. Lignières[1], D. R. Reese[2], and M. Rieutord[1]

[1] Laboratoire d'Astrophysique de Toulouse-Tarbes, Université de Toulouse, CNRS, 14 avenue E. Belin, 31400 Toulouse, France
e-mail: jballot@ast.obs-mip.fr
[2] LESIA, UMR8109, Université Pierre et Marie Curie, Université Denis Diderot, Observatoire de Paris, 92195 Meudon, France

Received 13 March 2010 / Accepted 3 May 2010

ABSTRACT

Context. CoRoT and Kepler missions are now providing high-quality asteroseismic data for a large number of stars. Among intermediate-mass and massive stars, fast rotators are common objects. Taking into account the rotation effects is needed to correctly understand, identify, and interpret the observed oscillation frequencies of these stars. A classical approach is to consider the rotation as a perturbation.

Aims. In this paper, we focus on gravity modes, such as those occurring in γ Doradus, Slowly Pulsating B (SPB), or Be stars. We aim to define the suitability of perturbative methods.

Methods. With the Two-dimensional Oscillation Program (TOP), we performed complete computations of gravity modes – including the Coriolis force, the centrifugal distortion and compressible effects – in 2-D distorted polytropic models of stars. We started with the modes $\ell = 1$, $n = 1$–14, and $\ell = 2$–3, $n = 1$–5, 16–20 of a non-rotating star, and followed these modes by increasing the rotation rate up to 70% of the break-up rotation rate. We then derived perturbative coefficients and determined the domains of validity of the perturbative methods.

Results. Second-order perturbative methods are suited for computing low-order low-degree mode frequencies up to rotation speeds $\sim$100 km s^{-1} for typical γ Dor stars or $\sim$150 km s^{-1} for B stars. The domains of validity can be extended by a few tens of km s^{-1} thanks to the third-order terms. For higher-order modes, the domains of validity are noticeably reduced. Moreover, for modes with frequencies smaller than the Coriolis frequency 2Ω, perturbative methods are inefficient. We interpret this failure as a consequence of a modification in the shape of the resonant cavity that is not taken into account in the perturbative approach.

Key words. Asteroseismology – Stars: oscillations, rotation – Methods: numerical

1. Introduction

CoRoT (Convection, Rotation and planetary Transits, Baglin et al. 2006) and Kepler (Borucki et al. 2007) are space missions providing uninterrupted high-quality photometry time series over several months or years ideally suited for asteroseismic study. Asteroseismology provides very accurate determinations of the stellar parameters (mass, radius, age...) and probes stellar structure to constrain physical processes occurring in stars. The first step towards this goal requires correctly understanding the structure of the observed oscillation spectra, and especially correctly identifying the observed modes. In the case of main-sequence (e.g. Michel et al. 2008; Benomar et al. 2009; Chaplin et al. 2010) and giant (e.g. Miglio et al. 2009; Hekker et al. 2009; Bedding et al. 2010) FGK stars with solar-like oscillations, the spectrum structure is well understood, which eases the interpretation.

The spectra of classical pulsators is often noticeably more complex. For instance, the high-quality observations of δ Scuti (e.g. García Hernández et al. 2009; Poretti et al. 2009) and γ Doradus (e.g. Mathias et al. 2009) stars have exhibited very rich and complex spectra of acoustic (p) and gravity (g) modes, respectively, containing several hundred –or more– modes. Interpreting their spectra is very challenging today. Indeed, these stars are generally spinning rapidly and the effects of rotation on the mode frequencies must be considered.

Here, we shall be concerned with gravity modes, i.e. low-frequency modes driven by the buoyancy force. They are excited and observed in a large panel of stars, for instance in γ Dor, SPB and some Be stars. The γ Dor stars form a class of main-sequence stars with type around F0V that can sometimes rotate rapidly (e.g. De Cat et al. 2006, and reference therein), while the rotation rate of Be stars is extreme, usually very close to their break-up limit $\Omega \approx \Omega_K \equiv \sqrt{GM/R^3}$ (e.g. Frémat et al. 2006).

The effects of rotation on the oscillation modes can be treated as a perturbation where the rotation rate is the small parameter. A first-order correction has been proposed by Ledoux (1951), second-order by Saio (1981), Dziembowski & Goode (1992) or Suárez et al. (2006), and third-order terms have been developed by Soufi et al. (1998). While perturbative methods are expected to be accurate enough for slowly rotating stars, their true domain of validity cannot be determined in the absence of exact calculations to compare with.

In the last few years, calculations of p modes with both the centrifugal distortion and the Coriolis force have been performed in polytropic models of stars (Lignières et al. 2006; Reese et al. 2006) and realistic 2-D stellar structures (Lovekin & Deupree 2008; Reese et al. 2009). Lignières et al. (2006) and Reese et al. (2006) have shown that, above $\Omega \sim 0.15\Omega_K$, perturbation methods fail to reproduce low degree and low order p-mode frequencies ($\ell \leq 3$ and $n \leq 10$) with the accuracy of CoRoT long runs. The structure of the modes is also drastically modified and this

leads to deep changes in the structure of the p-mode spectrum (Reese et al. 2008; Lignières & Georgeot 2008, 2009).

We have used an oscillation code based on Reese et al. (2006) to perform g-mode calculations with a complete description of the rotational effects on the modes. In this paper, we focus on the limits of validity of perturbative methods. The models and the method are described in Sect. 2. We then derive the perturbative coefficients from the complete computations (Sect. 3), and compare the results obtained with both methods to determine and discuss the domains of validity of perturbative methods (Sect. 4) before concluding in Sect. 5.

2. Models and Methods

We consider for this work fully radiative stars. Since the gravity modes are driven by the buoyancy force, they cannot exist in convective regions. SPB and γ Dor stars have large radiative zones with a convective core, and even a thin convective envelope for the latter. The effects of convective cores are not considered here, since we are mainly interested in the general behavior of g modes under rotation effects.

2.1. 2-D stellar models

As in Lignières et al. (2006) and Reese et al. (2006), we approximate the equilibrium structure of rotating stars with self-gravitating uniformly-rotating polytropes. They are described in the co-rotating frame by the three following equations:

$$p_o = K\rho_o^{1+1/\mu} \quad (1)$$

$$\boldsymbol{\nabla} p_o = \rho_o \boldsymbol{g}_o \quad (2)$$

$$\Delta\psi_o = 4\pi G\rho_o \quad (3)$$

where p_o is the pressure, ρ_o the density, ψ_o the gravitational potential, K the polytropic constant, μ the polytropic index, G the gravitational constant, and $\boldsymbol{g}_o$ the effective gravity defined as

$$\boldsymbol{g}_o = -\boldsymbol{\nabla}(\psi_o - \Omega^2 s^2/2) \quad (4)$$

with s the distance to the rotation axis. Due to the centrifugal distortion, the star is not spherical and a suited surface-fitting spheroidal system of coordinates (ζ, θ, ϕ) based on Bonazzola et al. (1998) has been used. Hereafter, we also classically denote r the distance to the center, and z the coordinate along the rotation axis. This equation system is numerically solved with the ESTER (Evolution STEllaire en Rotation) code as described in Rieutord et al. (2005). This is a spectral code using Chebychev polynomials in the ζ-direction, and spherical harmonics Y_ℓ^m with even ℓ and $m = 0$ in the horizontal one. For this work, we have computed models decomposed on spherical harmonics up to degree $L_{\rm model} = 32$. This resolution is sufficient to accurately model the centrifugal effects for the maximal value of Ω that we have considered. In the pseudo-radial direction, the resolution is the same as the one we use for the frequency computation (see Sect. 2.3, $n_r = 96$ generally).

To approximate a fully radiative star, we have chosen the polytropic index $\mu = 3$. We have considered models spinning with rotation frequency Ω between 0 and $0.7\Omega_K$, where $\Omega_K = \sqrt{GM/R_{eq}}$ is the Keplerian break-up rotation rate for a star of mass M and equatorial radius R_{eq}.

2.2. Linearized equations for the oscillations

In the co-rotating frame, the equations governing the temporal evolution of small adiabatic inviscid perturbations of the equilibrium structure read, in the co-rotating frame,

$$\partial_t \rho = -\boldsymbol{\nabla}\cdot(\rho_o \boldsymbol{v}) \quad (5)$$

$$\rho_o \partial_t \boldsymbol{v} = -\boldsymbol{\nabla} p + \rho \boldsymbol{g}_o - \rho_o \boldsymbol{\nabla}\psi - 2\rho_o \boldsymbol{\Omega}\times\boldsymbol{v} \quad (6)$$

$$\partial_t p - c_o^2 \partial_t \rho = \frac{\rho_o N_o^2 c_o^2}{\|\boldsymbol{g}_o\|^2} \boldsymbol{v}\cdot\boldsymbol{g}_o \quad (7)$$

$$\Delta\psi = 4\pi G\rho \quad (8)$$

where ρ, p, $\boldsymbol{v}$, and ψ are the Eulerian perturbations of density, pressure, velocity, and gravitational potential $c_o^2 = \Gamma_1 p_o/\rho_o$ the adiabatic sound speed and N_o the Brunt-Väisälä frequency, defined as

$$N_o^2 = \boldsymbol{g}_o \cdot \left(\frac{\boldsymbol{\nabla}\rho_o}{\rho_o} - \frac{1}{\Gamma_1}\frac{\boldsymbol{\nabla} p_o}{p_o} \right). \quad (9)$$

$\Gamma_1 = (\partial \ln p/\partial \ln\rho)_{\rm ad}$ denotes the first adiabatic exponent. In Eq. (7) we have used the structure barotropicity, ensured by the uniform rotation.

The 2-D distribution of the Brunt-Väisälä frequency is shown in Fig. 1 for the most rapidly rotating model we have considered, together with the profiles of N_o along the polar and equatorial radii which are compared to the N_o profile of the non-rotating star. It is worth noting that within about the inner half of the star, the deviations from sphericity induced by the centrifugal force remain limited. We also see that N_o diverges at the surface of the polytrope because ρ_o and p_o vanish there.

Looking for time-harmonic solutions $\propto \exp(i\omega t)$ of the system (5)–(8), we obtain an eigenvalue problem which we then solve using the Two-dimensional Oscillation Program (TOP). The details of this oscillation code closely follow Reese et al. (2006). The equations are projected on the spherical harmonic basis Y_ℓ^m. Due to the axisymmetry of the system, the projected equations are decoupled relatively to the azimuthal order m, but contrary to the spherical non-rotating case, they are coupled for all degrees ℓ of the same parity.

2.3. Resolutions and method accuracy

The different sources of error of our numerical method have been discussed in Valdettaro et al. (2007) and tested in a context similar to the present one in Lignières et al. (2006) and Reese et al. (2006).

The numerical resolution has been chosen to ensure a sufficient accuracy for the computed frequencies. In the horizontal direction, the resolution is given by the truncation of the spherical harmonics expansion. The highest degree of the expansion is $L = 2n_\theta + |m|$ and, for most of the calculations presented here we have used $L = 40 + |m|$, i.e. $n_\theta = 20$ coupled spherical harmonics. In the pseudo-radial direction ζ, the solution has been expanded onto $n_r = 96$ Chebychev polynomials.

Using higher resolutions ($n_r = 96$, $L = 80$ and $n_r = 144$, $L = 80$), we find that the relative agreement of the frequencies always remains better than 5×10^{-8}. It also does not affect the mode significantly as illustrated in Fig. 2 where the spectral expansion of the radial velocity component of the $(\ell, m, n) = (1, 0, 14)$ mode at $\Omega = 0.7\Omega_K$ is displayed for the three different resolutions. Figure 2 also shows that a unique –or even a few– spherical harmonics would not properly describe such an eigenmode.

2.4. Following modes with rotation

We have computed the frequencies of $\ell = 1$ to 3 modes in a non-rotating polytrope. We recall that without rotation the system to solve becomes decoupled with respect to ℓ, hence the modes

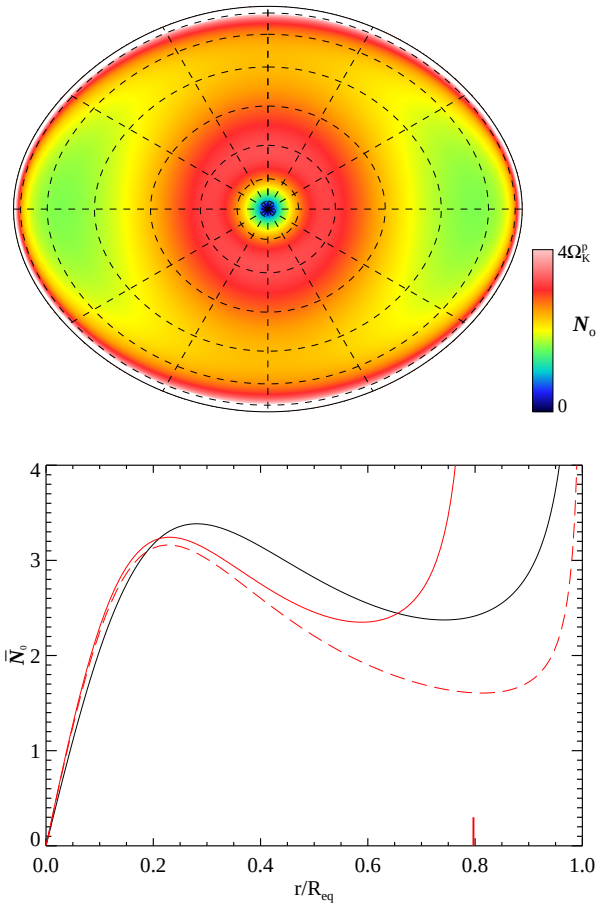

Fig. 1. *(top)* Map in the meridional plane of the Brunt-Väisälä frequency N_o for the model with $\Omega = 0.7\Omega_K$. N_o has been normalized by $\Omega_k^p = \sqrt{GM/R_p}$ where R_p is the polar radius. Dashed lines show the shape of the spheroidal grid we have used. *(bottom)* Solid black lines show the profile of N_o normalized by Ω_K^p for the non-rotating star. Red lines show N_o for the model $\Omega = 0.7\Omega_K$ along the polar (solid line) and equatorial radius (dashes). A thick red tick on the x-axis indicates the polar radius R_p.

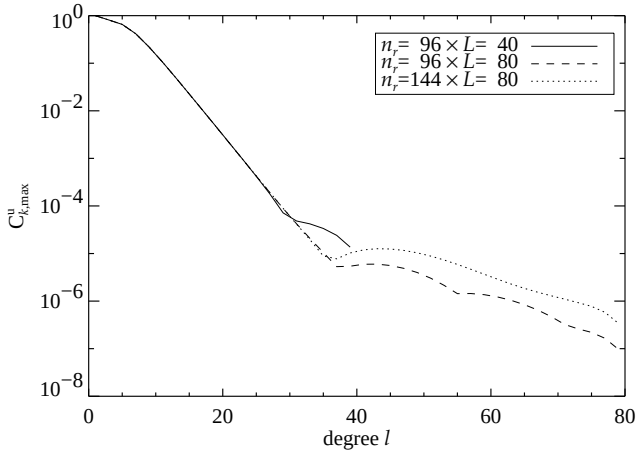

Fig. 2. Spectrum $C^u_{k,max}$ as a function of the degree ℓ of the radial velocity of the mode $(\ell, m, n) = (1, 0, 14)$ at $\Omega = 0.7\Omega_K$. $C^u_{k,max}(\ell)$ is the absolute value of the highest Chebychev coefficient in the decomposition on the spherical harmonics of degree ℓ of the radial component of $\boldsymbol{v}$. The spectrum is normalized to its maximum value. The different lines correspond to different spatial resolutions.

are represented with only one spherical harmonic. A reference frequency set, $\omega^{(0)}_{\ell,n}$, has been computed from a 1-D polytropic model with a radial resolution $n_r = 512$.

We then follow the variation of the frequency of each mode of degree ℓ_0, azimuthal order m_0 and radial order n_0 by slowly increasing, step by step, the rotation rate. The Arnoldi-Chebychev method requires an initial guess for the frequency, and returns the solutions which are the closest to this guess. The guess we provide is extrapolated from the results at lower rotation rates: we compute from the three last computed points a quadratic extrapolation at the desired rotation rate. For the first point ($\Omega = 0$), we use as guess the frequency obtained in 1-D. For the second point, we extrapolate a guess with the asymptotic relation $\omega_{\ell_0,m_0,n_0} \approx \omega^{(0)}_{\ell_0,m_0} + m_0\Omega/[\ell_0(\ell_0+1)]$ (Ledoux 1951).

Among the solutions found around the initial guess, we select the correct one by following this strategy:

1. For each calculated mode, we determine, from its spatial spectrum (like the ones shown Fig. 2), the two dominant degrees, ℓ_1 and ℓ_2.
2. We compare ℓ_1 and ℓ_2 with the degree ℓ_0 of the mode we are following.
3. We select the solutions such that $\ell_1 = \ell_0$; if none of the solutions verifies this criterion, we select the solutions such that $\ell_2 = \ell_0$.
4. If more than one solution has been selected at this point, we consider the projection of the modes on the spherical harmonic $Y^{m_0}_{\ell_0}$ and we compare it to the projection of the mode at a lower rotation rate. The solution which gives the highest correlation is finally selected.

This method allows us to have a semi-automatic procedure that limits the need to manually tag the modes. Nevertheless, there are two limitations. The first one is inherent to the density of the g-mode spectrum. Indeed, according to the asymptotic relation from Tassoul (1980), on a given frequency interval, the number of modes of degree ℓ goes roughly as $\sqrt{\ell(\ell+1)}$. If our resolutions, both in latitude and radius, were infinite, it would be almost impossible to find the desired solution: there would always be an infinite number of other solutions closer to the initial guess than the searched mode. In practice the spatial resolution is finite and we noticed that, in most cases, the number of solutions in a small interval is limited enough to allow us to find the desired solution. Another way of avoiding this difficulty is to add thermal dissipation which disperses the different solutions in the complex plane. This also proved successful in finding a specific solution.

The second difficulty comes from the so-called avoided crossings. Two modes with the same m and the same parity cannot have the same frequency. This implies that the two curves associated to their evolution with Ω cannot cross each other. Figure 3 illustrates this phenomenon with modes $\ell = 1$ and $\ell = 3$: the frequencies become closer and closer, but since the curves cannot cross, the modes exchange their properties. During an avoided crossing, the two modes have the mixed properties of the two initial modes. With our mode following method, when the coupling is strong and the avoided crossing takes long, the method can follow the wrong branch. For instance, in the

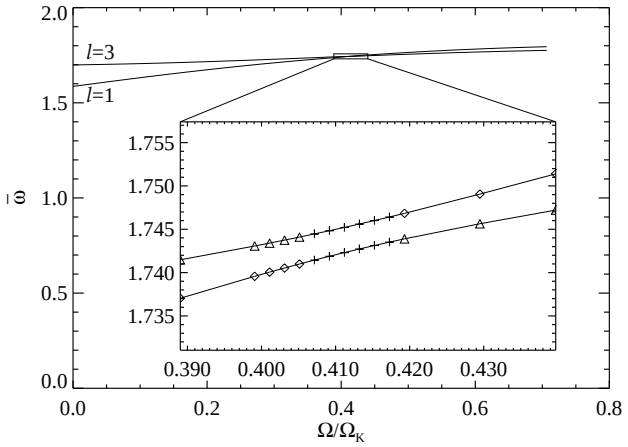

Fig. 3. Evolution with the rotation rate of the frequency of the modes ($\ell = 1, m = 1, n = 1$) and ($\ell = 3, m = 1, n = 3$), with a zoom on a region where an avoided crossing between these two modes occurs. At a given rotation rate, a diamond (respectively, a triangle) indicates the mode is dominated by the component $\ell = 1$ (respectively, $\ell = 3$). Crosses indicate that the modes are hardly discernible: they are both dominated by $\ell = 1$ and their structures are very similar.

case illustrated in Fig. 3, if the program follows the $\ell = 1$ mode, it continues sometimes on the $\ell = 3$ branch instead of jumping to the other branch.

3. Perturbative coefficients

The approach we have used to determine the perturbative coefficients in the paper is very close to the one of Reese et al. (2006).

3.1. Determining perturbative coefficients

In the perturbative approach, frequencies are developed as a function of the rotation rate, Ω. For instance, to the third order, it reads

$$\bar{\omega}^{pert}_{\ell,m,n} = \bar{\omega}^{(0)}_{\ell,n} + C^1_{\ell,m,n}\bar{\Omega} + C^2_{\ell,m,n}\bar{\Omega}^2 + C^3_{\ell,m,n}\bar{\Omega}^3 + O(\bar{\Omega}^4), \quad (10)$$

where $\omega^{(0)}_{\ell,n}$ is the frequency for the non-rotating case, and $C^j_{\ell,m,n}$ the perturbative coefficients. The bar denotes the normalization $\bar{\omega} = \omega/\Omega^p_K$ and $\bar{\Omega} = \Omega/\Omega^p_K$. We have normalized the frequencies by Ω^p_K since the polar radius is expected to be a slowly varying function of Ω in real stars, as opposed to R_{eq}.

The coefficients $C^j_{\ell,m}$ can be numerically calculated from the complete computations since they are directly linked to the j-th derivative of the function $\bar{\omega}_{\ell,m,n}(\Omega)$ at $\Omega = 0$. However, to improve the accuracy, we have used symmetry properties of the problem: changing Ω in $-\Omega$, one easily shows that

$$C^j_{\ell,-m,n} = (-1)^j C^j_{\ell,m,n} \qquad \forall m. \quad (11)$$

We denote

$$x = \bar{\Omega}^2, \quad (12)$$

$$y^D_{\ell,m,n} = \frac{\bar{\omega}_{\ell,m,n} - \bar{\omega}_{\ell,-m,n}}{2\bar{\Omega}} \qquad m > 0, \quad (13)$$

$$y^S_{\ell,m,n} = \frac{1}{x}\left[\frac{\bar{\omega}_{\ell,m,n} + \bar{\omega}_{\ell,-m,n}}{2} - \bar{\omega}^{(0)}_{\ell,n}\right] \qquad m \geq 0, \quad (14)$$

and we get

$$y^D_{\ell,m,n} = C^1_{\ell,m,n} + C^3_{\ell,m,n}x + \cdots + C^{2k+1}_{\ell,m,n}x^k + O(x^{k+1}) \quad (15)$$

$$y^S_{\ell,m,n} = C^2_{\ell,m,n} + C^4_{\ell,m,n}x + \cdots + C^{2k+2}_{\ell,m,n}x^k + O(x^{k+1}). \quad (16)$$

We note that $C^j_{\ell,m=0,n}$ vanish for odd j.

We compute $y^D_{\ell,m,n}$ and $y^S_{\ell,m,n}$ on a grid of k points from $\Omega = \delta\bar{\Omega}$ to $k\delta\bar{\Omega}$. We use the Eqs (15) and (16) to calculate the terms $C^j_{\ell,m,n}$ with the $(k-1)$-th-order interpolating polynomials. The determination of the coefficients $C^j_{\ell,m,n}$ is then accurate to the $(2k-1)$-th-order in $\bar{\Omega}$. In practice we use a typical step $\delta\bar{\Omega} = 2 \times 10^{-3}$ and $k = 4$. In Eq. (14), we use $\bar{\omega}^{(0)}_{\ell,n} = [\bar{\omega}_{\ell,m,n}(\Omega = 0) + \bar{\omega}_{\ell,-m,n}(\Omega = 0)]/2$, thus we are totally independent of the 1-D solutions.

By expressing explicitly the dependence on m of the perturbative coefficients, Eq. (10) becomes:

$$\bar{\omega}^{pert}_{\ell,m,n} = \bar{\omega}^{(0)}_{\ell,n} + mC_{\ell,n}\bar{\Omega} + (S^1_{\ell,n} + m^2S^2_{\ell,n})\bar{\Omega}^2 + m(T^1_{\ell,n} + m^2T^2_{\ell,n})\bar{\Omega}^3 + O(\bar{\Omega}^4) \quad (17)$$

The form of the first order comes from Ledoux (1951), the second order from Saio (1981) and the third is derived from Soufi et al. (1998). We have verified that the derived coefficients fit these relations with a very good accuracy (see below). We have listed these coefficients in Table 1.

To know the coefficients for another normalization, for instance for $\tilde{\omega} = \omega/\Omega_K$, one can use the following development:

$$\tilde{\Omega} = \frac{\Omega}{\Omega_K} = \bar{\Omega} + A\bar{\Omega}^3 + O(\bar{\Omega}^5). \quad (18)$$

The perturbed frequencies in this new normalization express then

$$\tilde{\omega}^{pert}_{\ell,m,n} = \bar{\omega}^{(0)}_{\ell,n} + mC_{\ell,n}\tilde{\Omega} + (S^1_{\ell,n} + A\bar{\omega}^{(0)}_{\ell,n} + m^2S^2_{\ell,n})\tilde{\Omega}^2 + m(T^1_{\ell,n} + m^2T^2_{\ell,n})\tilde{\Omega}^3 + O(\tilde{\Omega}^4) \quad (19)$$

From our models we have computed $A \approx 0.77164$.

3.2. Coefficient accuracy and comparisons with previous works

The zeroth-order coefficients $\bar{\omega}^{(0)}_{\ell,n}$ have been compared to the 1-D computations and we have found agreement within 10^{-9}. We have also compared our results to previous frequency computations of in a non-rotating polytropic model performed by Christensen-Dalsgaard & Mullan (1994) with a totally different method. We have renormalized their results for g modes (Table 4 of their paper) to thier dynamical frequency $\nu_g = 99.8557\,\mu$Hz (Eq. 3.2 of their paper). The relative differences with our results do not exceed 5×10^{-8}.

The choice done for the step $\delta\bar{\Omega}$ is important for the accuracy of the terms $C^j_{\ell,m,n}$. Ideally, we should choose $\delta\bar{\Omega}$ as small as possible, but when it is too small, the numerical noise, produced by the uncertainties on the computed $\omega_{\ell,m,n}$ (Sect. 2.3), drastically increases. We have then chosen the value of $\delta\bar{\Omega}$ to have the best trade-off. These uncertainties on $C^j_{\ell,m,n}$ determinations have been taken into account for the estimated accuracy of the coefficients $C_{\ell,n}$, $S^i_{\ell,n}$ and $T^i_{\ell,n}$.

The first-order perturbative coefficients $C_{\ell,n}$ are expressed with integrals of the eigenmodes in the non-rotating model

Table 1. Perturbative coefficients (see development Eq. 17) for g modes with frequency $\bar{\omega} > 0.255$, radial order $n \leq 25$, and $\ell \leq 3$ in a polytropic stellar model with an index $\mu = 3$.

n	$\bar{\omega}^{(0)}_{\ell,n}$	$C_{\ell,n}$	$S^1_{\ell,n}$	$S^2_{\ell,n}$	$T^1_{\ell,n}$	$T^2_{\ell,n}$
	$\ell = 1$					
1	1.5861677	0.47187464	0.0027	-0.1215	0.0742	–
2	1.1338905	0.46515116	0.1946	-0.0991	0.1255	–
3	0.8807569	0.46565368	0.3473	-0.0779	0.1769	–
4	0.7195665	0.46890412	0.4801	-0.0604	0.2383	–
5	0.6082150	0.47259900	0.6021	-0.0458	0.3131	–
6	0.5267854	0.47600569	0.7176	-0.0330	0.4016	–
7	0.4646791	0.47895730	0.8289	-0.0215	0.5037	–
8	0.4157567	0.48146486	0.9374	-0.0108	0.6188	–
9	0.3762235	0.48358671	1.0440	-0.0007	0.7469	–
10	0.3436109	0.48538634	1.1490	0.0089	0.8877	–
11	0.3162449	0.48692017	1.2530	0.0182	1.0411	–
12	0.2929509	0.48823507	1.3562	0.0272	1.2069	–
13	0.2728805	0.48936906	1.4586	0.0360	1.3852	–
14	0.2554057	0.49035278	1.5606	0.0445	1.5758	–
	$\ell = 2$					
1	2.2168837	0.16413695	-0.0603	-0.1283	0.1162	0.0019
2	1.6817109	0.13416727	0.2040	-0.1171	0.1492	-0.0186
3	1.3499152	0.13379919	0.3992	-0.1267	0.2263	-0.0409
4	1.1271730	0.13720207	0.5686	-0.1417	0.3295	-0.0666
5	0.9676634	0.14084985	0.7244	-0.1587	0.4555	-0.0964
6	0.8478758	0.14409412	0.8717	-0.1767	0.6031	-0.1307
7	0.7546269	0.14685697	1.0136	-0.1952	0.7716	-0.1695
8	0.6799744	0.14918725	1.1517	-0.2140	0.9608	-0.2128
9	0.6188542	0.15115489	1.2870	-0.2330	1.1704	-0.2607
10	0.5678867	0.15282450	1.4201	-0.2521	1.4006	-0.3132
11	0.5247312	0.15424993	1.5517	-0.2713	1.6500	-0.3700
12	0.4877153	0.15547464	1.6819	-0.2905	1.9198	-0.4315
13	0.4556123	0.15653342	1.8111	-0.3098	2.2095	-0.4975
14	0.4275023	0.15745412	1.9395	-0.3291	2.5190	-0.5679
15	0.4026818	0.15825915	2.0672	-0.3484	2.8482	-0.6429
16	0.3806035	0.15896664	2.1943	-0.3678	3.1970	-0.7223
17	0.3608352	0.15959137	2.3209	-0.3872	3.5655	-0.8062
18	0.3430314	0.16014547	2.4470	-0.4066	3.9536	-0.8945
19	0.3269120	0.16063895	2.5728	-0.4259	4.3613	-0.9873
20	0.3122481	0.16108017	2.6983	-0.4453	4.7884	-1.0846
21	0.2988504	0.16147607	2.8234	-0.4648	5.2351	-1.1863
22	0.2865611	0.16183254	2.9484	-0.4842	5.7013	-1.2924
23	0.2752477	0.16215452	3.0731	-0.5036	6.1869	-1.4030
24	0.2647981	0.16244623	3.1976	-0.5230	6.6920	-1.5180
25	0.2551166	0.16271128	3.3220	-0.5424	7.2164	-1.6374
	$\ell = 3$					
1	2.6013404	0.06527813	-0.1840	-0.0702	0.0898	0.0117
2	2.0582624	0.04834015	0.0662	-0.0551	0.0478	0.0014
3	1.6990205	0.05125011	0.2366	-0.0576	0.0593	-0.0023
4	1.4466219	0.05532661	0.3818	-0.0631	0.0803	-0.0054
5	1.2597371	0.05898678	0.5132	-0.0695	0.1071	-0.0085
6	1.1157943	0.06207639	0.6359	-0.0764	0.1389	-0.0120
7	1.0015072	0.06465872	0.7527	-0.0836	0.1753	-0.0158
8	0.9085566	0.06682318	0.8653	-0.0909	0.2162	-0.0200
9	0.8314693	0.06864897	0.9747	-0.0983	0.2616	-0.0246
10	0.7664974	0.07020016	1.0817	-0.1058	0.3113	-0.0296
11	0.7109883	0.07152736	1.1869	-0.1133	0.3652	-0.0350
12	0.6630115	0.07267052	1.2906	-0.1208	0.4235	-0.0409
13	0.6211284	0.07366127	1.3931	-0.1284	0.4859	-0.0471
14	0.5842454	0.07452488	1.4946	-0.1360	0.5526	-0.0537
15	0.5515158	0.07528169	1.5953	-0.1437	0.6234	-0.0608
16	0.5222741	0.07594820	1.6953	-0.1513	0.6985	-0.0683
17	0.4959899	0.07653788	1.7947	-0.1590	0.7776	-0.0761
18	0.4722351	0.07706183	1.8936	-0.1666	0.8609	-0.0844
19	0.4506608	0.07752926	1.9920	-0.1743	0.9483	-0.0931
20	0.4309792	0.07794783	2.0901	-0.1820	1.0399	-0.1022
21	0.4129512	0.07832398	2.1878	-0.1897	1.1356	-0.1117
22	0.3963764	0.07866313	2.2853	-0.1974	1.2353	-0.1216
23	0.3810855	0.07896988	2.3825	-0.2051	1.3392	-0.1320
24	0.3669346	0.07924815	2.4794	-0.2128	1.4472	-0.1427
25	0.3538006	0.07950128	2.5762	-0.2205	1.5592	-0.1538

(Ledoux 1951). We have then computed these terms with our 1-D eigensolutions and compared them to $C^1_{\ell,m,n}/m$. The results are consistent within 10^{-8}.

An explicit computation of 2nd- and 3rd-order coefficients requires calculating the 1st- and 2nd-order corrections of the eigenfunctions, which is not so straightforward. It is the reason why we have performed a direct numerical computation of these coefficients. The numerical errors we have estimated for $S^i_{\ell,n}$ and $T^i_{\ell,n}$ are generally around 10^{-5} and always smaller than 10^{-4}. We have then checked the consistency of our computations with the 2nd-order calculations of Saio (1981) for g modes with $n = 1$ to 3. In this work, all frequencies were normalized by the dynamical frequency $\Omega_K^{(0)}$ of the non-rotating polytrope. By noticing that $\Omega/\Omega_K^{(0)} = \bar{\Omega} + A\bar{\Omega}^3 + O(\bar{\Omega}^5)$ with $A = 0.18391$, and using the relation (19), we have been able to compare these results with ours. We get a good qualitative agreement, with absolute differences better than 10^{-2}, which is reasonable relative to the lower accuracy of Saio's computations. It gives an interesting consistency check for our calculations. Overall, the perturbative coefficients listed in Table 1 have been determined with high accuracy.

4. Domains of validity of perturbative approaches

From the previously computed coefficients, we calculate mode frequencies with the 1st to 3rd-order perturbative approximations for rotation rates ranging from $\Omega = 0$ to $0.7\Omega_K$ and compare them to complete computations. Figure 4 illustrates such a comparison by showing the evolution of the frequencies of the seven m components of an $\ell = 3$ mode together with their 2nd-order perturbative approximation. We clearly observe that the agreement between both approaches at low rotation progressively disappears as the rotation increases.

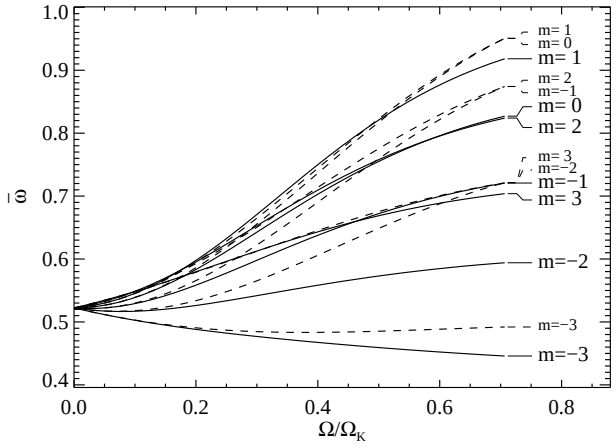

Fig. 4. Evolution with the rotation rate of the frequencies of the components of the ($\ell = 3$, $n = 16$) multiplet obtained with a complete computation (solid line) and with the 2nd-order perturbative approximation (dashed lines).

To define the domains of validity of perturbative approaches, we fix the maximal departure $\delta\bar{\omega}$ allowed between the perturbed frequencies $\bar{\omega}^{pert}_{\ell,m,n}$ and the "exact" ones $\bar{\omega}_{\ell,m,n}$. For each mode and each approximation order, we define the domain of validity $[0, \Omega_v]$ such that $|\bar{\omega}^{pert}_{\ell,m,n}(\Omega) - \bar{\omega}_{\ell,m,n}(\Omega)| < \delta\bar{\omega}\ \forall\Omega < \Omega_v$. The precision of the observed frequencies $\delta\nu$ can be related to the normalized error $\delta\bar{\omega}$ through

$$\delta\bar{\omega} = 2\pi\,\delta\nu\,\sqrt{\frac{R^3}{GM}}. \tag{20}$$

From this expression, we see that for a fixed precision $\delta\nu$, the normalized error $\delta\bar{\omega}$ depends on the dynamical frequency $\nu_g = (GM/R^3)^{\frac{1}{2}}/(2\pi)$ of the star considered. We shall thus display the domains of validity of the perturbative approximations for two types of stars with different dynamical frequencies, a typical γ Dor star and a typical B star. The γ Dor star is such that $M = 1.55M_\odot$, $R = 1.6R_\odot$, i.e. $\nu_g = 61\ \mu$Hz while the B star has $M = 4M_\odot$, $R = 7R_\odot$, i.e. $\nu_g = 11\ \mu$Hz. For the frequency precision, we have chosen $\delta\nu = 0.1\ \mu$Hz which corresponds to the resolution of an oscillation spectrum after a hundred days. This is a typical accuracy for a CoRoT long run. Accordingly, the normalized error $\delta\bar{\omega}$ is equal to 1.6×10^{-3} for the γ Dor star and 9.3×10^{-3} for the B star. It must be noted that the domains of validity will not be affected by the numerical errors of $\bar{\omega}^{pert}_{\ell,m,n}$ (cf. Sect. 3.2) and $\bar{\omega}_{\ell,m,n}$ (cf. Sect. 2.3) as the values of $\delta\bar{\omega}$ remain at least an order of magnitude larger.

We have determined the domains of validity of 1st-, 2nd- and 3rd-order methods for low-degree $\ell \leq 3$ modes. Specifically, we have considered $\ell = 1$ modes with $n = 1$ to 14, and $\ell = 2$ and 3 low-order ($n = 1$ to 5) and high-order ($n = 16$ to 20) modes. The domains of validity are shown in Fig. 5 for both types of stars. Globally, the domains of validity extend to higher rotation rates for B stars than for γ Dor stars. This is simply due to the increase in the normalized tolerance $\delta\bar{\omega}$. Besides, we observe distinct behaviors in the high and low-frequency ranges.

In the high-frequency range, 2nd-order perturbative methods give satisfactory results up to $\sim$100 km s^{-1} for γ Dor stars and up to $\sim$150 km s^{-1} for B stars. The 3rd-order terms improve the results and increase the domains of validity by a few tens of km s^{-1}. These results are to be contrasted with those found for p modes where the domains of validity are restricted to smaller rotation rates. For δ Scuti stars, which have similar stellar parameters as γ Dor, Reese et al. (2006) found $\sim$50–70km s^{-1} as a limit for perturbative methods. In addition, the 3rd-order terms do not improve the perturbative approximation in this case, as p modes are weakly sensitive to the Coriolis force. The rather good performance of perturbative methods at describing high-frequency g modes indicates in particular that the 2nd-order term gives a reasonable description of the centrifugal distortion. This might be surprising considering the significant distortion of the stellar surface ($R_{eq}/R_p = 1.08$ at $\Omega = 0.4\Omega_K$). Actually, the energy of g modes is concentrated in the inner part of the star where the deviations from sphericity remain small (as shown in Fig. 1-*top*), thus feeling a much smaller distortion that is amenable to a perturbative description. A particular feature that induces a strong deviation from the perturbative method concerns mixed pressure-gravity modes that arise as a consequence of the centrifugal modification of the stellar structure. For example, we found that, above a certain rotation rate, the $\ell = 3, n = 1$ mode becomes a mixed mode with a p-mode character in the outer low-latitude region associated with a drop in the Brunt-Väisälä frequency N_o (see Fig. 1).

The domains of validity of perturbative methods are strongly reduced in the low-frequency range. For γDor stars, 2nd-order perturbative methods are only valid below $\sim$50 km s^{-1}. Indeed, a striking feature of Fig. 5 is that perturbative methods fail to recover the correct frequencies in the inertial regime $\omega < 2\Omega$ (delimited by a magenta curve). In particular, we observe that although increasing the tolerance $\delta\bar{\omega}$ between the left (γ Dor)

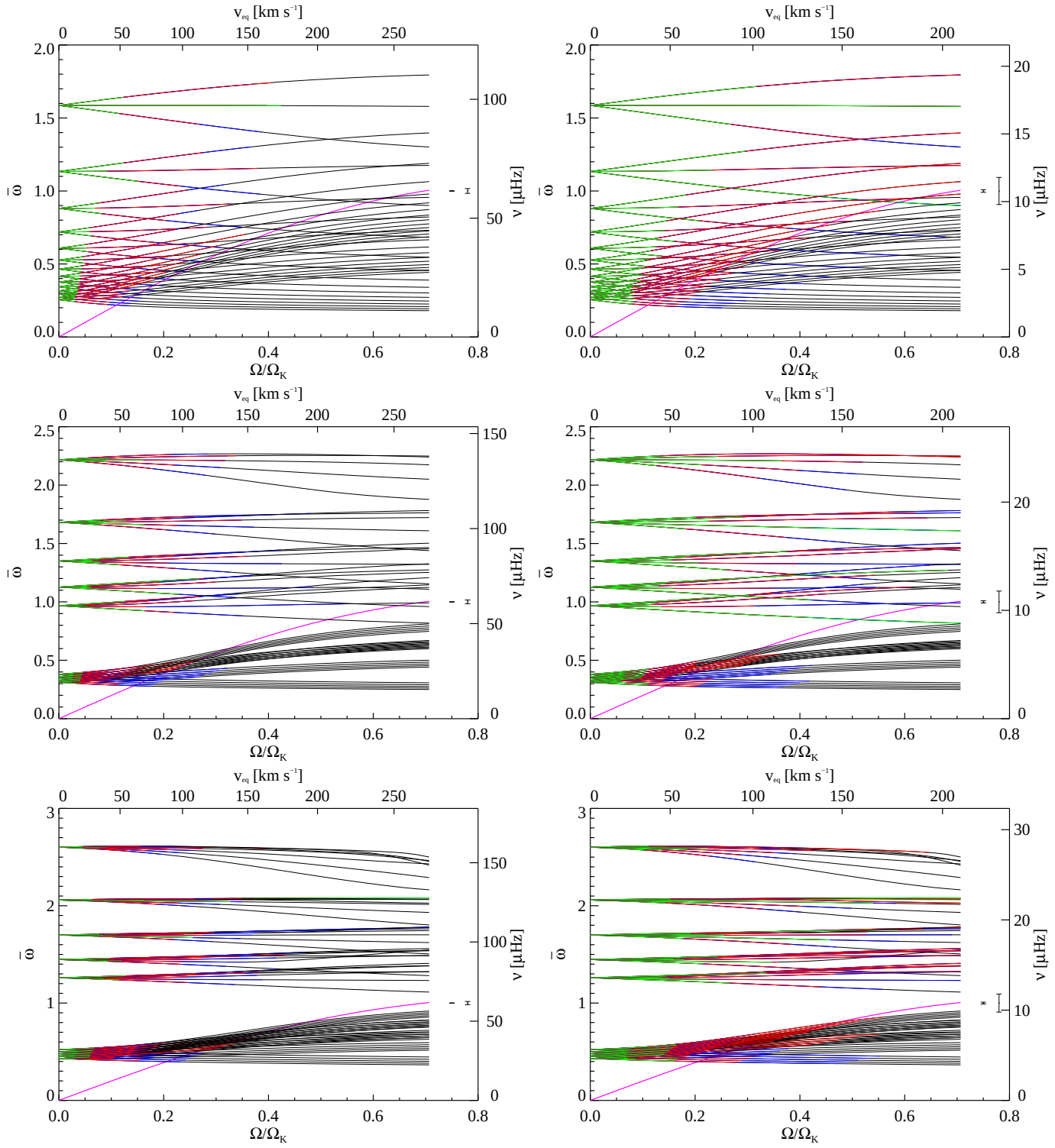

Fig. 5. Evolution of the frequencies of $\ell = 1, 2, 3$ modes *(top to bottom)*. Frequencies are computed in the co-rotating frame. Perturbative approximations have been tested for a typical γ Dor *(left panels)* and for a B star *(right panels)*. Green/red/blue parts of curves indicate that 1st/2nd/3rd order is sufficient to reproduce complete calculations within an error $\delta\nu = 0.1\,\mu$Hz. Error bars on the right-hand side of each panel show $\delta\nu$ and $10 \times \delta\nu$. Magenta lines indicate $\omega = 2\Omega$. For each plot, bottom x-axis and left y-axis show dimensionless units whereas top x-axis and right y-axis show physical units.

and right (B star) panels subtantially extends the domains of validity in the $\omega > 2\Omega$ regime very little improvement is observed in the $\omega < 2\Omega$ regime.

In the following, we argue that the failure of the perturbative method in the sub-inertial regime $[0, 2\Omega]$ is related to changes in the mode cavity that are not taken into account by the perturbative method. Indeed, we observed that modes in the inertial regime do not explore the polar region and that the angular size of this forbidden region increases with $2\Omega/\omega$. This is illustrated in Fig. 6 for a particular mode. Such a drastic change in

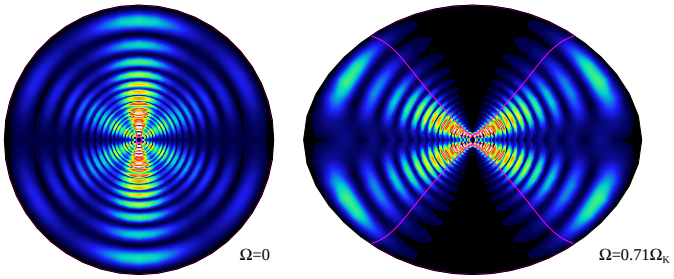

Fig. 6. *(Left)* Meridional distribution of kinetic energy $\frac{1}{2}\rho_o \boldsymbol{v}^2$ of the g mode ($\ell = 3, m = -1, n = 16$) in a non-rotating star. To enhance the contrast, it is scaled by r^2. *(Right)* The same for $\Omega = 0.7\Omega_K$. Magenta lines indicate the critical surface $\Gamma = 0$.

the shape of the resonant cavity has a direct impact on the associated mode frequency. As perturbative methods totally ignore this effect, they can not provide an accurate approximation of the frequencies in this regime.

This interpretation is supported by the analytical expression of the forbidden region determined by Dintrans & Rieutord (2000) for gravito-inertial modes. Indeed for frequencies $\omega < 2\Omega$, modes are mixed gravity-inertial modes, since the Coriolis force becomes a restoring force. In the context of their spherical model, and within the anelastic approximation and the Cowling approximation, they have shown that gravito-inertial waves with a frequency ω only propagate in the region where

$$\Gamma = r^2\omega^2[N_o^2 + (2\Omega)^2 - \omega^2] - (2\Omega N_o z)^2 > 0 \qquad (21)$$

It implies that, when $\omega < 2\Omega$, a critical latitude $\theta_c = \arcsin[\omega/(2\Omega)]$ appears above which waves cannot propagate. Even though this expression does not strictly apply to our non-spherical geometry, we have overplotted the critical surfaces $\Gamma = 0$ with the energy distributions of our eigenmodes (see Fig. 6 for an illustration). For the non-rotating case, there is only a small circle close to the center, corresponding to the classical turning point $\omega = N_o$. For the mode with $\omega < 2\Omega$, the polar forbidden region delineated by $\Gamma = 0$ agrees pretty well with the energy distribution of our complete computation.

5. Conclusion

In the present work, we have computed accurate frequencies for g modes in polytropic models of uniformly spinning stars. We started from high- and low-frequency low-degree ($\ell \leq 3$) g modes of a non-rotating star and followed them up to $\Omega = 0.7\Omega_K$. This allowed us to provide a table of numerically-computed perturbative coefficients up to the 3rd order for a polytropic stellar structure (with index $\mu = 3$). This table can serve as a reference to test the implementation of perturbative methods. We have then determined the domains of validity of perturbative approximations. For the high-frequency (low-order) modes, 2nd-order perturbative methods correctly describe modes up to $\sim 100\,\mathrm{km\,s^{-1}}$ for γ Dor stars and up to $\sim 150\,\mathrm{km\,s^{-1}}$ for B stars. The domains of validity can be extended by a few tens of $\mathrm{km\,s^{-1}}$ with 3rd-order terms. However, the domains of validity shrink at low frequency. Especially, perturbative methods fail in the inertial domain $\omega < 2\Omega$ because of a modification in the shape of the resonant cavity.

In a next step we plan to compare our complete computations with the so-called traditional approximation, which is also extensively used to determine g-mode frequencies (e.g Berthomieu et al. 1978; Lee & Saio 1997). We will also analyze how rotation affects the regularities of the spectrum – such as the period spacing – and compare it to the predictions of the perturbative and traditional methods. In the present study, we have focused on low degree modes, but a more complete exploration clearly needs to be performed. In particular we might look for the singular modes predicted by Dintrans & Rieutord (2000). It requires to take care of dissipative processes which play an important role in this case.

Acknowledgements. The authors acknowledges support through the ANR project Siroco. Many of the numerical calculations were carried out on the supercomputing facilities of CALMIP ("CALcul en MIdi-Pyrénées") which is gratefully acknowledged. The authors also warmly thank Boris Dintrans for discussions and useful comments on this work. DRR gratefully acknowledges support from the CNES ("Centre National d'Études Spatiales") through a postdoctoral fellowship.

References

Baglin, A., Michel, E., Auvergne, M., & The COROT Team. 2006, in ESA Special Publication, Vol. 624, Proceedings of SOHO 18/GONG 2006/HELAS I, Beyond the spherical Sun
Bedding, T. R., Huber, D., Stello, D., et al. 2010, ApJ, in press
Benomar, O., Baudin, F., Campante, T. L., et al. 2009, A&A, 507, L13
Berthomieu, G., Gonczi, G., Graff, P., Provost, J., & Rocca, A. 1978, A&A, 70, 597
Bonazzola, S., Gourgoulhon, E., & Marck, J. 1998, Phys. Rev. D, 58, 104020
Borucki, W. J., Koch, D. G., Lissauer, J., et al. 2007, in Astronomical Society of the Pacific Conference Series, Vol. 366, Transiting Extrapolar Planets Workshop, ed. C. Afonso, D. Weldrake, & T. Henning, 309
Chaplin, W. J., Appourchaux, T., Elsworth, Y., et al. 2010, ApJ, in press
Christensen-Dalsgaard, J. & Mullan, D. J. 1994, MNRAS, 270, 921
De Cat, P., Eyer, L., Cuypers, J., et al. 2006, A&A, 449, 281
Dintrans, B. & Rieutord, M. 2000, A&A, 354, 86
Dziembowski, W. A. & Goode, P. R. 1992, ApJ, 394, 670
Frémat, Y., Neiner, C., Hubert, A., et al. 2006, A&A, 451, 1053
García Hernández, A., Moya, A., Michel, E., et al. 2009, A&A, 506, 79
Hekker, S., Kallinger, T., Baudin, F., et al. 2009, A&A, 506, 465
Ledoux, P. 1951, ApJ, 114, 373
Lee, U. & Saio, H. 1997, ApJ, 491, 839
Lignières, F. & Georgeot, B. 2008, Phys. Rev. E, 78, 016215
Lignières, F. & Georgeot, B. 2009, A&A, 500, 1173
Lignières, F., Rieutord, M., & Reese, D. 2006, A&A, 455, 607
Lovekin, C. C. & Deupree, R. G. 2008, ApJ, 679, 1499
Mathias, P., Chapellier, E., Bouabid, M., et al. 2009, in American Institute of Physics Conference Series, Vol. 1170, American Institute of Physics Conference Series, ed. J. A. Guzik & P. A. Bradley, 486–488
Michel, E., Baglin, A., Auvergne, M., et al. 2008, Science, 322, 558
Miglio, A., Montalbán, J., Baudin, F., et al. 2009, A&A, 503, L21
Poretti, E., Michel, E., Garrido, R., et al. 2009, A&A, 506, 85
Reese, D., Lignières, F., & Rieutord, M. 2006, A&A, 455, 621
Reese, D., Lignières, F., & Rieutord, M. 2008, A&A, 481, 449
Reese, D. R., MacGregor, K. B., Jackson, S., Skumanich, A., & Metcalfe, T. S. 2009, A&A, 509, 183
Rieutord, M., Corbard, T., Pichon, B., Dintrans, B., & Lignières, F. 2005, in SF2A-2005: Semaine de l'Astrophysique Francaise, ed. F. Casoli, T. Contini, J. M. Hameury, & L. Pagani, 759
Saio, H. 1981, ApJ, 244, 299
Soufi, F., Goupil, M. J., & Dziembowski, W. A. 1998, A&A, 334, 911
Suárez, J. C., Goupil, M. J., & Morel, P. 2006, A&A, 449, 673
Tassoul, M. 1980, ApJS, 43, 469
Valdettaro, L., Rieutord, M., Braconnier, T., & Fraysse, V. 2007, Journal of Computational and Applied Mathematics, 205, 382

2.5.4 A4 : Regular patterns in the acoustic spectrum of rapidly rotating stars

"Regular patterns in the acoustic spectrum of rapidly rotating stars"

Reese D., Lignières F. and Rieutord M.

A&A 481, 449-452, 2008

A&A 481, 449–452 (2008)
DOI: 10.1051/0004-6361:20078075

Astronomy & Astrophysics

Regular patterns in the acoustic spectrum of rapidly rotating stars

D. Reese[1,2], F. Lignières[2], and M. Rieutord[2]

[1] Department of Applied Mathematics, University of Sheffield, Hicks Building, Hounsfield Road, Sheffield S3 7RH, UK
e-mail: D.Reese@sheffield.ac.uk
[2] Laboratoire d'Astrophysique de Toulouse-Tarbes, Université de Toulouse, CNRS, 14 Av. Édouard Belin, 31400 Toulouse, France

Received 13 June 2007 / Accepted 14 January 2008

ABSTRACT

Context. Rapid rotation modifies the structure of the frequency spectrum of pulsating stars, thus making mode identification difficult.
Aims. We look for new forms of organisation for the frequency spectrum that can provide a basis for mode identification at high rotation rates.
Methods. Acoustic modes in uniformly rotating polytropic models of stars are computed using a numerical code that fully takes the effects of rotation (centrifugal distortion and Coriolis acceleration) into account. All low-degree modes, $\ell = 0$ to 3, with radial orders $n = 1{-}10$ and $21{-}25$ for $N = 3$ polytropic models and $n = 1{-}10$ for $N = 1.5$ polytropic models are followed from a zero rotation rate up to 59% of the break-up velocity.
Results. We find an empirical formula that gives a good description of the high-frequency range of the computed acoustic spectrum for high rotation rates. Differences between this formula and complete eigenmode calculations are shown to be substantially smaller than those obtained with a 3rd order perturbative method valid at low rotation rates.

Key words. stars: oscillations – stars: rotation

1. Introduction

Asteroseismology has provided a way of probing stellar interiors based on the interpretation of observable stellar pulsations. In order for such interpretations to be successful, it is necessary to identify pulsation frequencies by correctly associating them with theoretically calculated pulsation modes. This is important because the geometry of a pulsation mode determines which regions of the star it probes. One way of doing this is by using regular patterns which occur in stellar frequency spectra. While being quite successful in the case of the Sun and a number of slowly rotating stars (Michel 2006), mode identification based on pattern recognition has proved to be very difficult in rapidly rotating stars (e.g. Goupil et al. 2005). One of the basic reasons for this is that a proper understanding of the structure of the frequency spectrum has not yet been achieved in the case of such stars. Up to now, mainly perturbative methods, valid at low rotation rates, have been used to evaluate the effects of rotation on pulsation modes and their frequencies. While providing a useful context in which to interpret pulsations of slowly rotating stars, they are unable to correctly predict the structure of the frequency spectrum in rapidly rotating stars. This is particularly clear in Fig. 5 of Reese et al. (2006), in which perturbative calculations of frequencies are compared with complete eigenmode calculations for a polytropic stellar model rotating at 59% of the critical angular velocity. As a result, many stars remain out of reach for asteroseismology. This mainly concerns early-type stars such as δ Scuti, which can reach projected equatorial velocities ($v \sin i$) of 200 km s^{-1} (Rodríguez et al. 2000), β Cephei stars ($v \sin i \lesssim 300$ km s^{-1}, Stankov & Handler 2005), and ζ Oph stars ($v \sin i \lesssim 400$ km s^{-1}, Balona & Dziembowski 1999). Interestingly, the star ζ Oph ($v \sin i = 380$ km s^{-1}) has been observed by MOST and WIRE, thus revealing the presence of 19 different pulsation modes (Walker et al. 2005; Bruntt, private communication).

Recently, Lignières et al. (2006a) and Reese et al. (2006) came up with a numerical code which overcomes the limitations of perturbative methods and enables one to accurately evaluate the effects of rapid rotation on stellar pulsations. By analysing their results, it is possible to gain a better understanding of the structure of the frequency spectrum at rapid rotation rates. In the case of spherically symmetric stars, the origin of the regular frequency patterns can be attributed to the integrability of the ray dynamics which asymptotically describes the acoustic wave propagation (Gough 1993). However, in the case of rapidly rotating stars, acoustic ray dynamics is no longer integrable (Lignières et al. 2006b), and it is an open question whether or not patterns will appear in the spectrum of frequencies. Nonetheless, Lignières et al. (2006a) have shown that for axisymmetric modes calculated without the Coriolis force, it is possible to obtain asymptotic patterns in the spectrum of frequencies.

In this paper, using again stellar polytropic models and a complete non-perturbative computation of their axisymmetric and non-axisymmetric acoustic modes, we show that regular frequency patterns are present in the acoustic spectrum and that they can be used to identify modes.

2. An empirical formula

In order to obtain frequency patterns for rapidly rotating stars, we start off with the set of pulsation frequencies computed in Reese et al. (2006) plus some additional frequencies. The $n = 1{-}10,\ 21{-}25$, $\ell = 0{-}3$, $m = -\ell$ to ℓ modes for $N = 3$ polytropic models, and the $n = 1{-}10$, $\ell = 0{-}3$, $m = -\ell$ to ℓ modes for $N = 1.5$ polytropic models were followed from a zero rotation rate up to 59% of the break-up velocity. This enabled us

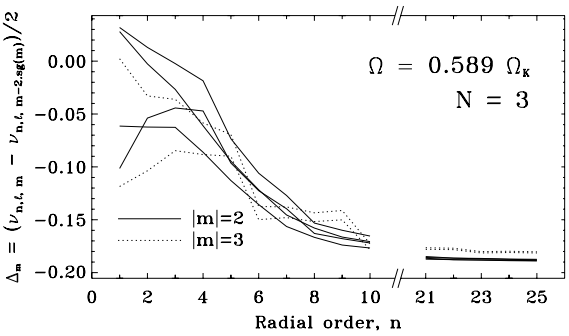

Fig. 1. Frequency differences $\Delta_m = \frac{\omega_{n,\ell,m}-\omega_{n,\ell,m-2\cdot\mathrm{sg}(m)}}{2}$ as a function of the radial order n for the $N = 3$ polytropic models. The frequencies have been scaled by $\Omega_\star$. For high radial orders, these differences converge to a limit which does not depend on ℓ or m.

to label the modes in rapidly rotating stars based on their correspondence with modes in non-rotating stars. We looked for patterns in this frequency spectrum and found that the frequencies approximately obey the following empirical formula in a corotating frame:

$$\omega_{n,\ell,m} = \Delta_n n + \Delta_\ell \ell + \Delta_m |m| + \alpha^{\pm}. \quad (1)$$

In order to obtain frequencies in an inertial frame, one needs to add the geometrical term $-m\Omega$.

This formula is a generalisation of Eq. (42) of Lignières et al. (2006a) by including the Coriolis effect and the case of non-axisymmetric modes. The terms Δ_n, Δ_ℓ, Δ_m and $\alpha^{\pm}$, which depend on the stellar structure, have been computed here for different rotation rates. The parameter α^+ (resp. α^-) is an additive constant for symmetric, $\ell + m$ even (resp. antisymmetric, $\ell + m$ odd), modes with respect to the equator. We note that the term for non-axisymmetric modes depends on $|m|$ rather than m. Indeed, at rapid rotation rates or high radial orders, the effects of the Coriolis force become negligible in comparison with the effects of the centrifugal force, as can be seen in Fig. 6 of Reese et al. (2006). The centrifugal force leads to frequency shifts which do not depend on the sign of m. In order to know how these shifts scale with $|m|$, we plot in Fig. 1 the differences $\left(\omega_{n,\ell,m} - \omega_{n,\ell,m-2.\mathrm{sg}(m)}\right)/2$ as a function of the radial order. We increment the azimuthal order by 2 rather than 1 to insure that the two modes have the same parity. As shown in Fig. 1, these differences converge towards a limit which slightly depends on $|m|$ as the radial order increases. This justifies using a linear dependence on $|m|$ as a first approximation. The fact that these increments only converge at high radial orders shows that Eq. (1) describes an asymptotic behaviour of the computed acoustic modes.

In Table 1, we give the values of Δ_n, Δ_ℓ, Δ_m, α^+ and α^-, scaled by $\Omega_\star$, for $N = 3$ polytropic models. These are given for different rotation rates scaled either by $\Omega_\star = \sqrt{GM/R_{\mathrm{pol}}^3}$ or by $\Omega_K = \sqrt{GM/R_{\mathrm{eq}}^3}$, the Keplerian break-up velocity, where R_{eq} (resp. R_{pol}) is the equatorial (resp. polar) radius. These values were obtained by calculating various frequency separations and averaging them for radial orders $21 \le n \le 25$. At zero rotation, they agree pretty well with the theoretical values, $\Delta_n/\Omega_\star = 1.238$ and $\Delta_\ell/\Omega_\star = 0.619$ corresponding to the asymptotic description of low degree and high order acoustic modes in non-rotating stars (Mullan & Ulrich 1988). The last line contains the same parameters but calculated for frequencies in which the Coriolis force has been neglected. The fact that it is essentially the same as the line before shows that the Coriolis force plays almost no role in Eq. (1) nor ultimately in the frequency spectrum for sufficiently high radial orders.

Table 1. Coefficients for Eq. (1), for $N = 3$ polytropes.

$\frac{\Omega}{\Omega_K}$	$\frac{\Omega}{\Omega_\star}$	$\frac{\Delta_n}{\Omega_\star}$	$\frac{\Delta_\ell}{\Omega_\star}$	$\frac{\Delta_m}{\Omega_\star}$	$\frac{\alpha^+}{\Omega_\star}$	$\frac{\alpha^-}{\Omega_\star}$
0.000	0.000	1.248	0.543	0.000	1.758	1.761
0.037	0.037	1.246	0.545	–0.007	1.757	1.764
0.111	0.110	1.239	0.515	–0.031	1.770	1.843
0.186	0.181	1.234	0.395	–0.031	1.727	1.942
0.262	0.249	1.229	0.279	–0.036	1.680	2.006
0.339	0.311	1.220	0.191	–0.064	1.614	2.020
0.419	0.368	1.194	0.189	–0.142	1.666	2.068
0.502	0.419	1.154	0.201	–0.182	1.661	2.036
0.589	0.461	1.102	0.194	–0.185	1.598	1.953
0.589	0.461	1.102	0.194	–0.185	1.587	1.943

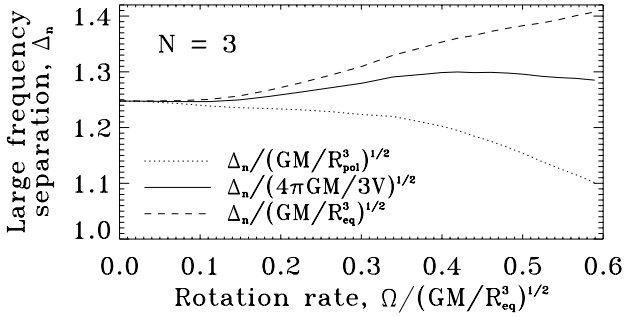

Fig. 2. The large frequency separation Δ_n as a function of the rotation rate Ω. Δ_n has been scaled with different quantities so as to show which other stellar quantity best matches this frequency separation. As can be seen, Δ_n is roughly proportional to the square root of the mean density of the star.

An important consequence of the values given in Table 1 concerns the small frequency separation. In non-rotating stars, the so-called small frequency separation $\omega_{n+1,\ell,m} - \omega_{n,\ell+2,m}$ goes to zero in the high frequency limit because the ratio Δ_n/Δ_ℓ is 2. For rapidly rotating stars, Table 1 clearly shows that this ratio departs from 2 by taking on larger values. This, of course, invalidates the use of the small frequency separation as a mode identification scheme.

In Fig. 2, we plot Δ_n scaled with different quantities as a function of Ω. As can be seen from the figure, Δ_n is roughly proportional to $\sqrt{GM/V}$ where M is the mass and V the volume of the star. This suggests that Δ_n may be related in a simple way to the mean density of the star.

3. Accuracy of the formula

We now turn our attention to evaluating the accuracy of formula (1). In Fig. 3, we plot the correspondence between a spectrum based on Eq. (1) and the frequencies given by the eigenmode calculations for $\Omega = 0.59\,\Omega_K$. As can be seen, the two sets of frequencies match pretty well, especially for high radial orders. This represents a drastic improvement over 3rd order perturbative calculations (see Fig. 5 of Reese et al. 2006).

Table 2 contains the mean quadratic error $\langle \mathcal{E} \rangle^{1/2}$ both for 3rd order perturbative calculations and empirical ones. These errors as well as the probability p of mode inversion (explained below) have been calculated for modes with $21 \le n \le 25$ except for the last line where $1 \le n \le 10$. Physically, an error of $0.0036\,\Delta_n$ at $\Omega = 0.59\,\Omega_K$ corresponds to 0.16 μHz for an $M = 1.9\,M_\odot$,

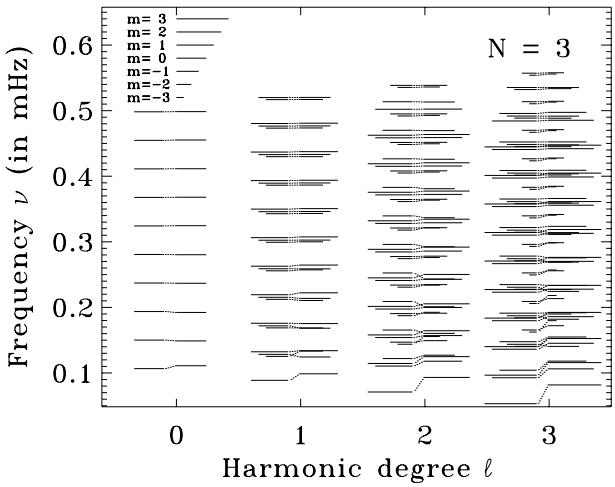

Fig. 3. Comparison between frequencies based on Eq. (1) and complete eigenmode calculations, both of which are given in an inertial frame. ℓ and m are indicated on the figure, and the radial orders are $n = 1$ to 10. This figure contains four columns subdivided into two, the left part corresponding to Eq. (1) and the right part to complete calculations. The oblique dotted lines in between show the correspondence between the two sets of frequencies. The units are the same as in Fig. 5 of Reese et al. (2006), which allows direct comparison. As can be seen from comparing these figures, Eq. (1) gives a much better description of the frequency spectrum than a 3rd order perturbative formula.

Table 2. Different measurements of the errors for the perturbative and empirical methods (for $N = 3$).

	Perturbative		Asymptotic	
$\frac{\Omega}{\Omega_K}$	$\frac{\langle\varepsilon^2\rangle^{1/2}}{\Delta_n}$	p	$\frac{\langle\varepsilon^2\rangle^{1/2}}{\Delta_n}$	p
0.037	0.0005	0.0000	0.0114	0.0000
0.111	0.0370	0.0054	0.0141	0.0044
0.186	0.1793	0.0294	0.0124	0.0022
0.262	0.4325	0.0595	0.0135	0.0047
0.339	0.7436	0.0826	0.0174	0.0041
0.419	0.9924	0.1073	0.0109	0.0013
0.502	1.0674	0.1237	0.0085	0.0025
0.589	0.9885	0.1497	0.0036	0.0035
0.589	0.3506	0.0319	0.1235	0.0059

$R_{\rm pol} = 2.3\,R_\odot$, $N = 3$ polytropic star. The errors on the last line can be made smaller by calculating the increments Δ_n, Δ_ℓ etc. using radial orders $1 \le n \le 10$, which in practise observers are likely to do.

Another useful quantity to appreciate the reliability of an approximate formula at mode identification is the probability p of inverting the identification of two randomly selected frequencies when using such a formula. This probability is defined as:

$$p = \frac{\text{Number of inversions}}{\text{Number of pairs of modes}} \tag{2}$$

where an inversion occurs for modes A and B when $\left(\omega_A^{\rm approx.} - \omega_B^{\rm approx.}\right)(\omega_A - \omega_B) < 0$. When $p = 1$, the spectrum is in reverse order, whereas $p = 0$ means the order is identical. In Table 2, p is calculated for both methods, based on frequencies in the inertial frame so as to be closer to observations. For example, $p = 0.0035$ means that out of 3160 frequency pairs, 11 were inverted. As shown, the empirical formula gives a far better idea of the order in which modes appear in the frequency spectrum at $\Omega = 0.59\,\Omega_K$ than a 3rd order perturbative approach.

As expected, the perturbative method gives best results for low rotation rates, whereas Eq. (1) is more efficient above $\Omega = 0.11\,\Omega_K$, for high radial orders. This is because, by construction, Eq. (1) preserves the regularity of the frequency spectrum whereas perturbative methods do not. Also, comparing the last two lines of Table 2 again shows that Eq. (1) works better for high frequencies, whereas the perturbative approach works better for low frequencies, where the centrifugal force has a smaller effect.

4. Discussion

The preceding sections show that at rapid rotation rates, it is possible to describe the computed frequency spectrum using a formula similar to the asymptotic one found by Tassoul (1980). Quite significantly, Table 2 shows that the accuracy of this formula increases at high rotations, thus suggesting that eigenmodes reach an asymptotic régime at lower radial orders for these rapid rotations.

In the rapid rotation régime, a forthcoming study based on ray dynamics (Lignières & Georgeot 2008) shows that Eq. (1) holds for low-degree, high order modes which concentrate at middle latitudes as rotation increases. This modification of mode geometry leads to a reorganisation of node placement as can be seen in Fig. 3 of Reese (2008), characterised by a different set of quantum numbers, $(\tilde{n} = 2n + \varepsilon, \tilde{\ell} = \frac{\ell - |m| - \varepsilon}{2}, \tilde{m} = m)$ where $\varepsilon = (l + m) \bmod 2$. Based on these quantum numbers, Eq. (1) then takes on the following form:

$$\omega_{n,\ell,m} = \tilde{\Delta}_n \tilde{n} + \tilde{\Delta}_\ell \tilde{\ell} + \tilde{\Delta}_m |m| + \tilde{\alpha}^{\pm} \tag{3}$$

where $\tilde{\Delta}_n = \Delta_n/2$, $\tilde{\Delta}_\ell = 2\Delta_\ell$, $\tilde{\Delta}_m = \Delta_\ell + \Delta_m$, $\tilde{\alpha}^+ = \alpha^+$ and $\tilde{\alpha}^- = \alpha^- + \Delta_\ell - \Delta_n/2$. With the numerical values from Table 1, we find that $\tilde{\alpha}^+ \simeq \tilde{\alpha}^-$. The same also applies for the $N = 1.5$ polytropic model. This suggests that the true asymptotic formula is closer to Eq. (3) in which $\tilde{\alpha}^+ = \tilde{\alpha}^- = \tilde{\alpha}$. Applying this new formula leads to errors which are only slightly larger in spite of the fact there is now one less free parameter.

Equation (3) also accentuates the $|m|$ dependence of the azimuthal term since $\tilde{\Delta}_m$ is of the same order of magnitude as the variation on Δ_m. This suggests that the azimuthal term $\tilde{\Delta}_m$ expressed in these new quantum numbers should take on a different form, and calls for further investigation. But as can be seen from Table 2, Eqs. (1) and (3) remain effective at identifying low-degree (observable) pulsation modes.

For higher degree modes, Lignières et al. (2006b) pointed out the existence of other types of modes, namely chaotic and whispering gallery modes, which correspond, respectively, to intermediate and high values of ℓ at zero rotation. As shown in Lignières & Georgeot (2008), the frequency spectra of these modes have different organisations.

Finally, it must be underlined that the results presented here are based on polytropic stellar models. Naturally, the question arises whether or not these patterns still exist in the case of more realistic models. In the non-rotating case, sharp chemical gradients lead to the break-down of the assumptions behind asymptotic analysis. Nonetheless, rather than removing the equidistant frequency pattern, these lead to a periodic component which is added to the asymptotic formula (e.g. Gough 1990). If the rapidly rotating case behaves similarly, then it may be expected that these sharp chemical gradients also merely perturb the asymptotic frequency pattern without removing it altogether.

5. Conclusion

The formulae (1) and (3) that we presented are the signature of an asymptotic régime of high order acoustic oscillations in rapidly rotating polytropic stars. As opposed to perturbative methods, which are valid at low rotation rates, they give an accurate description of the frequency spectrum by preserving its basic structure and consequently provide a basis for mode identification schemes. This is a timely result as seismology space missions are collecting large data sets of unprecedented quality on rapidly rotating stars.

A key issue for future theoretical studies will be to relate the seismic observables $\tilde{\Delta}_n$, $\tilde{\Delta}_\ell$ and $\tilde{\Delta}_m$ to the physical properties of the star. Acoustic ray dynamics combined with semi-classical quantization methods is expected to play a crucial role in this context.

Acknowledgements. Many of the numerical calculations were carried out on the Altix 3700 of CALMIP ("CALcul en MIdi-Pyrénées") and on Iceberg (University of Sheffield), both of which are gratefully acknowledged. D.R.'s work was supported in part by the European Helio- and Asteroseismology Network (HELAS), a major international collaboration funded by the European Commission's Sixth Framework Programme. This work was also supported in part by the Programme National de Physique Stellaire (PNPS of CNRS/INSU) and the Agence Nationale de la Recherche (ANR), project SIROCO.

References

Balona, L. A., & Dziembowski, W. A. 1999, MNRAS, 309, 221
Gough, D. O. 1990, in Progress of Seismology of the Sun and Stars, ed. Y. Osaki, & H. Shibahashi, Lecture Notes in Physics (Berlin: Springer Verlag), 367, 283
Gough, D. O. 1993, in Les Houches Summer School Proceedings (1987), ed. J.-P. Zahn, & J. Zinn-Justin, 399
Goupil, M.-J., Dupret, M. A., Samadi, R., et al. 2005, JApA, 26, 249
Lignières, F., & Georgeot, B. 2008, submitted
Lignières, F., Rieutord, M., & Reese, D. 2006a, A&A, 455, 607
Lignières, F., Vidal, S., Georgeot, B., & Reese, D. 2006b, in SF2A-2006: Semaine de l'Astrophysique Française, ed. D. Barret, F. Casoli, G. Lagache, A. Lecavelier, & L. Pagani, 479
Michel, E. 2006, Commun. Asteroseismol., 147, 40
Mullan, D. J., & Ulrich, R. K. 1988, ApJ, 331, 1013
Reese, D. 2008, in HELAS II: Helioseismology, Asteroseismology and MHD Connections, in press
Reese, D., Lignières, F., & Rieutord, M. 2006, A&A, 455, 621
Rodríguez, E., López-González, M. J., & López de Coca, P. 2000, A&AS, 144, 469
Stankov, A., & Handler, G. 2005, ApJS, 158, 193
Tassoul, M. 1980, ApJS, 43, 469
Walker, G. A. H., Kuschnig, R., Matthews, J. M., et al. 2005, ApJ, 623, L145

2.5.5 A5 : Asymptotic theory of stellar oscillations based on ray dynamics

“Asymptotic theory of stellar oscillations based on ray dynamics”

Lignières F.

Lectures Notes in Physics, Berlin : Spinger, sous presse, 2010

Asymptotic theory of stellar oscillations based on ray dynamics

F. Lignières

[1] Université de Toulouse; UPS; Laboratoire d'Astrophysique de Toulouse-Tarbes (LATT); F-31400 Toulouse, France
[2] CNRS; Laboratoire d'Astrophysique de Toulouse-Tarbes (LATT); F-31400 Toulouse, France E-mail: francois.lignieres@ast.obs-mip.fr

Abstract. This lecture is concerned with the extension of the asymptotic theory of stellar oscillations beyond the case of a non-rotating, non-magnetic spherically symmetric star. It is shown that ray models that describe propagating waves in the short-wavelength limit provide a natural framework for this extension. The basic tools to construct an asymptotic theory from a ray model and some general results obtained in the context of quantum physics are first described. Then, a recent application to the high-frequency acoustic modes of rapidly rotating stars is presented.

1 Introduction

The asymptotic theory of stellar oscillations has played a major role in the development of helio and asteroseismology. By providing analytical formulas for the modes and the frequencies [1–5], the theory allows a deep understanding of the oscillation properties that, in turn, enables to construct identification and inversion tools for seismology [4,6]. Although the theory is asymptotic (that is formally valid in the limit of modes of vanishing wavelength) and assumes linear adiabatic oscillations, it proved sufficiently accurate to describe observed modes like the high frequency p-modes of the Sun and the low frequency g-modes in white dwarfs.

The asymptotic theory of stellar oscillations has been however restricted to situations where the eigenvalue problem is fully separable. For a non-magnetic non-rotating spherically symmetric star, the modes are indeed separable in the three spherical coordinates. Spherical harmonics form the angular part of the mode while its radial part verifies a 1D boundary value problem. The asymptotic theory then consists in applying a short-wavelength approximation to the radial eigenvalue problem to obtain an analytical solution for the radial part of the mode and the eigenfrequencies (see the references above for the details). Such a simplification is however not possible in many cases of practical interest for stellar seismology. The rapid rotation of most upper-main-sequence pulsating stars (δ Scuti stars, γ Doradus stars, Be stars, pulsating B stars) destroys the mode separability due both to the centrifugal flattening of the star [7] and to the angular coupling induced by the Coriolis force [8]. Strong magnetic fields also prevent mode separability like in roAp stars [9]. An asymptotic theory for these stars would be of great importance to interpret their frequency spectra,

notably as high quality data are acquired by spatial missions (MOST, COROT, KEPLER).

In this lecture, I shall be concerned by the extension of the asymptotic theory of stellar oscillations to non-separable situations. Such a theory has been recently proposed for acoustic modes in rapidly rotating stars and has been successfully confronted with numerical computed high frequency p-modes of uniformly rotating polytropic stars [10]. I will thus mainly consider acoustic stellar waves in the following although many aspects of the construction of the asymptotic theory are general and should be also relevant for other stellar waves. In particular I will show that ray models of stellar waves provide a natural framework to extend the asymptotic theory of stellar oscillations to non-separable problems. Much as optical rays describe short-wavelength traveling electromagnetic waves in the geometrical optics limit, it is indeed possible to construct a ray model that describes traveling stellar waves in a short-wavelength asymptotic limit. But as we are interested in modes, that is in standing waves, the central issue for an asymptotic theory based on a ray model is to construct modes from positively interfering traveling waves. This is not an easy task in the general case. Fortunately, as commented in the next paragraph, this ray model route has already been taken in quantum physics to describe short-wavelength quantum waves and we can benefit from the results obtained in this field. Another objective of this lecture is to present cases where the asymptotic organization of the oscillation frequency spectrum is significantly more complex than in non-rotating, non magnetic, spherically symmetric stars. For example, the frequency spectrum of high-frequency acoustic modes in rapidly rotating stars can be described as a superposition of independent frequency subsets that are either regular (with different type of frequency patterns) or irregular but with generic statistical properties.

In quantum physics, the ray model of the quantum waves corresponds to the classical limit of the quantum system. Since Bohr's model of the Hydrogen atom, numerous efforts have been made to relate the classical and the quantum properties of quantum systems and in particular to compute the eigenstates and the energy levels from the classical trajectories. This is exactly the same issue as constructing stellar oscillation modes from the ray model of stellar waves. Early works in quantum physics have concentrated on the case where the Hamiltonian that describes the classical dynamics is integrable. In this case, a general procedure has been found that enables to construct the eigenstates and the energy levels from the classical dynamics. This procedure is known as the EBK semiclassical quantization after the name of its main contributors Einstein, Brillouin and Keller [11–13]. More recently, in the last thirty years, the issue of relating the properties of the quantum system to those of its classical limit has been considered in the wider context of non-integrable Hamiltonian dynamics. In particular, a basic issue has been to determine how the chaotic dynamics of a classical system manifests itself in the properties of the eigenstates and energy levels of the associated quantum system. This field of research has been called quantum chaos and it produced a number of important results which have since been applied

to other wave phenomena, such as those observed in e.g. microwave resonators [24], lasing cavities [25], quartz blocks [26], and underwater waves [27].

Is it possible to use quantum chaos theory to construct an asymptotic theory of stellar oscillations from a ray model ? Since quantum chaos results are based on the Hamiltonian character of the classical dynamics, they are in principle applicable to any wave problem whose ray model is governed by Hamiltonian dynamics. As we shall see in the following, this is indeed the case for many type of waves as long as the dissipative effects can be neglected and the boundary conditions do not destroy the Hamiltonian character of their ray dynamics.

The document is organized as follows. In section 2, wave equations occurring in quantum physics, optics and acoustic stellar oscillations are written down to emphasize their similarities. The ray models of these three types of waves together with their Hamiltonian formulations are derived in a unified way. Some results of quantum chaos studies are presented in section 3. In particular, features of the energy level spectra that are sensitive to the integrable or chaotic nature of the classical dynamics are described. In section 4, a recent asymptotic analysis of acoustic modes in rapidly rotating stars based on acoustic ray dynamics is briefly presented.

2 Wave equations and ray models

In this section, I first emphasize the similarities between three wave equations respectively governing the quantum eigenstates of a single particle in a potential, the monochromatic electromagnetic waves in a linear, isotropic, transparent medium and the adiabatic high-frequency acoustic waves in stars. This allows to describe in a unified way the short-wavelength approximation of these wave equations which then leads to the eikonal equation and the ray model. The Hamiltonian formulation of the equations governing the rays is then explicited.

In quantum physics, the eigenstates of a single non-relativistic particle in a potential V are solutions of the time-independent Schrödinger equation:

$$\Delta\Psi + \frac{2m}{\hbar^2}[E - V(\boldsymbol{x})]\Psi = 0 \tag{1}$$

where the wavefunction associated with the particle is $\psi(\boldsymbol{x}, t) = \Psi(\boldsymbol{x})e^{(-iEt/\hbar)}$, $\Psi(\boldsymbol{x})$ is the eigenstate, E is the energy, m is the mass and $\hbar$ is the reduced Planck constant.

In optics, monochromatic electromagnetic waves in a linear, isotropic, transparent medium of refractive index n verify:

$$\Delta\hat{\mathbf{E}} + \left[\frac{\omega}{c}n(\boldsymbol{x})\right]^2 \hat{\mathbf{E}} = 0 \tag{2}$$

where $\hat{\mathbf{E}}(\boldsymbol{x})$ is the complex amplitude of the electric field $\mathbf{E} = \Re\{\hat{\mathbf{E}}e^{(-i\omega t)}\}$, ω is the wave pulsation and c is the speed of light.

The wave equation that governs monochromatic high-frequency adiabatic linear acoustic waves in uniformly rotating stars can be written in the following form:

$$\Delta\hat{\Psi} + \frac{\omega^2 - \omega_c^2}{c_s^2}\hat{\Psi} = 0 \tag{3}$$

where $\hat{\Psi}$ is complex amplitude of the full wave solution $\Psi = \Re\{\hat{\Psi}e^{(-i\omega t)}\}$, ω is the pulsation, c_s is the sound speed and $\omega_c(\boldsymbol{x}, \omega)$ is the cut-off frequency which provokes the wave reflection at the star surface. The high-frequency hypothesis enables to neglect the gravity waves, the effect of the Coriolis force and the perturbation of the gravitational potential. Furthermore, while non-adiabatic effects are known to be important near the surface of stars, the adiabaticity hypothesis is generally good enough to compute accurate oscillation frequencies.

Note that different forms of Eq (3) have been proposed in the literature, the expression of ω_c and the relation between Ψ and physical quantities such as the pressure perturbation or the Lagrangian displacement ξ depend on the choice of the dependent variable and on the assumptions made. For example, if the variation of the background gravity is neglected in the perturbation equation (see [14] p. 493), Eq. (3) is obtained with $\Psi = \rho_0^{1/2} c_s^2 \boldsymbol{\nabla}\cdot\xi$ and $\omega_c = \frac{c_s}{2H_\rho}(1 - 2\mathbf{n_0}\cdot\boldsymbol{\nabla}H_\rho)^{1/2}$ where ρ_0 is the background density, ξ is the Lagrangian displacement, H_ρ is the background density scaleheight and $\mathbf{n_0}$ a unit vector opposite to the gravity direction. If this approximation is not made, the expressions of ω_c and Ψ are more complex and ω_c generally depends on ω ([14], p. 439). It can also be shown that in centrifugally distorted stars high-frequency adiabatic acoustic waves are also governed by an equation of the form (3), the expressions of ω_c and Ψ being given in [10].

The three wave equations (1), (2), (3), have a similar form :

$$\Delta\Psi + K^2(\boldsymbol{x})\Psi = 0 \tag{4}$$

$K(\boldsymbol{x})$ being equal to $\sqrt{2m(E-V)}/\hbar$ in the quantum case, $\omega n/c$ in the optical case and $\sqrt{\omega^2 - \omega_c^2}/c_s$ in the acoustic case. The solutions of the eigenvalue problem will thus only depend on the specific form of $K^2(\boldsymbol{x})$ and on the boundary conditions.

There is a particular situation where these three problems are identical. It occurs when K is constant and the domain of propagation is bounded by a closed curve where a given boundary condition is applied on Ψ. The two-dimensional version of this problem is called a quantum billiard because in the short wavelength limit the rays are straight lines and the reflections on the boundary are specular. Quantum billiards play an important role in quantum chaos theory (an example is shown in the next section). In quantum physics, this corresponds to the idealized situation where the potential V vanishes inside the domain and goes to infinity outside the domain, K being equal to $\sqrt{2mE}/\hbar$. In optics, a quantum billiard is obtained with linearly polarized electromagnetic waves propagating in an homogeneous two-dimensional cavity bounded by a perfectly conducting medium, K is then equal to $\omega n/c$. For acoustic waves, the sound speed has to

be uniform inside the domain ($K = \omega/c_s$) and the surface has to behave as a reflecting wall. This is not, however, a realistic model for the stellar acoustic waves since we know that c_s is strongly inhomogeneous in stars.

The short-wavelength approximation (also known as WKB, WKBJ, or JWKB approximation) of the wave equation (4) consists in looking for wave-like solutions of the form $\Psi = A(\boldsymbol{x}) \exp[i\Phi(\boldsymbol{x})]$ under the assumption that their wavelength is much shorter than the typical lengthscale of variation of the background medium. The amplitude term $A(\boldsymbol{x})$ is assumed to vary on the background lengthscale L while the oscillating term $\exp[i\Phi(\boldsymbol{x})]$ varies much more rapidly. This suggests to expand the solution as

$$\Phi = \Lambda(\Phi_0 + \tfrac{1}{\Lambda}\Phi_1..) \quad \text{and} \quad A = A_0 + \tfrac{1}{\Lambda}A_1.. \tag{5}$$

where $1/\Lambda$ is the ratio between the wavelength of the solution and the background lengthscale. When this expansion is introduced into Eq. (4), the dominant $O(\Lambda^2)$ term yields the so-called eikonal equation:

$$K(\boldsymbol{x})^2 = \Lambda^2(\boldsymbol{\nabla}\Phi_0)^2. \tag{6}$$

This implies that $K(\boldsymbol{x})$ must be of the order of Λ which, according to the expressions of K, indicates that the small wavelength limit corresponds to high-energy levels for the quantum system and to high frequencies for the optical and acoustic systems. In the eikonal equation describing stellar acoustic waves, the ω_c term must be retained since its increase near the star surface is responsible for the back-reflection of the waves and thus eventually for the formation of the modes through constructive interferences. The next order of the expansion (5) enables to relate A_0 to Φ_0.

The eikonal equation can be viewed as a local dispersion relation. Indeed, a local wavevector $\boldsymbol{k}$ can be defined from the spatial phase term $\Phi(\boldsymbol{x})$ by the relation $\boldsymbol{k} = \boldsymbol{\nabla}\Phi$ (recall that, in an homogeneous medium, the spatial phase would be $\Phi(\boldsymbol{x}) = \boldsymbol{k}_0 \cdot \boldsymbol{x}$ with $\boldsymbol{k}_0$ a uniform wavevector) so that the eikonal equation reads :

$$D(\boldsymbol{k}, \omega, \boldsymbol{x}) = K^2 - \boldsymbol{k}^2 = 0. \tag{7}$$

Instead of trying to solve directly the eikonal equation as a PDE (Partial Differential Equation) verified by the function $\Phi(\boldsymbol{x})$, the ray model consists in searching solutions for the phase along a given path $\boldsymbol{x}(s)$. To find these solutions, one has to solve the coupled differential equations that determine the ray path and the evolution of $\boldsymbol{k}(s)$ along it (and then integrate $\boldsymbol{k} = \boldsymbol{\nabla}\Phi$ along the ray).

We now demonstrate that, for a general eikonal equation $D(\boldsymbol{k}, \omega, \boldsymbol{x}) = 0$, these coupled equations can be written in a Hamiltonian form. Let's consider a general coordinate system $[x_1, x_2, x_3]$ and compute the partial derivative of D with respect to each coordinate x_i:

$$\frac{\partial D}{\partial x_i} + \sum_{j=1}^{N=3} \frac{\partial D}{\partial k_j}\frac{\partial k_j}{\partial x_i} = 0 \qquad i = 1, .., 3 \tag{8}$$

where k_j is defined as $k_j = \frac{\partial \Phi}{\partial x_j}$. From the definition of k_j, we have that $\frac{\partial k_j}{\partial x_i} = \frac{\partial^2 \Phi}{\partial x_i \partial x_j} = \frac{\partial^2 \Phi}{\partial x_j \partial x_i} = \frac{\partial k_i}{\partial x_j}$. Thus, Eq. (8) can be written as:

$$\frac{\partial D}{\partial x_i} + \sum_{j=1}^{N=3} \frac{\partial D}{\partial k_j} \frac{\partial k_i}{\partial x_j} = 0 \qquad i = 1, .., 3 \tag{9}$$

If we consider a path $\boldsymbol{x}(s)$ defined by $\frac{dx_i}{ds} = \frac{\partial D}{\partial k_i}$, the derivative of k_i following this path is given by :

$$\frac{dk_i}{ds} = \sum_{j=1}^{N=3} \frac{\partial k_i}{\partial x_j} \frac{dx_j}{ds} = \sum_{j=1}^{N=3} \frac{\partial k_i}{\partial x_j} \frac{\partial D}{\partial k_j} \qquad i = 1, .., 3 \tag{10}$$

As $\frac{dk_i}{ds}$ corresponds to the second term on the left hand side of Eq. (9), the equations defining the ray model are

$$\frac{dx_i}{ds} = \frac{\partial D}{\partial k_i} \qquad i = 1, .., 3 \tag{11}$$

$$\frac{dk_i}{ds} = -\frac{\partial D}{\partial x_i} \qquad i = 1, .., 3 \tag{12}$$

These are Hamilton's equations where D is the Hamiltonian and x_i and k_i are the conjugate variables, x_i the position variables and k_i the momentum variables (see [15] p. 317 for a similar demonstration). The above derivation is valid for any coordinate system $[x_i]$. The momentum variables k_i are the covariant component of the wave vector $\boldsymbol{k}$ in the natural basis associated with $[x_i]$, the definition of the natural basis being $\boldsymbol{e_i} = \partial \boldsymbol{x} / \partial x^i$.

This Hamiltonian formulation can be simplified in two special cases that are relevant for the there wave equations considered in this section. First, when D can be written as $D(\boldsymbol{k}, \omega, \boldsymbol{x}) = H(\boldsymbol{k}, \boldsymbol{x}) - \omega$, the above equations become :

$$\frac{dx_i}{ds} = \frac{\partial H}{\partial k_i} \qquad i = 1, .., 3 \tag{13}$$

$$\frac{dk_i}{ds} = -\frac{\partial H}{\partial x_i} \qquad i = 1, .., 3 \tag{14}$$

where the ray path now moves at the group velocity $\frac{\partial H}{\partial k_i}$. According to the expression of $K(x)$ for the three wave equations considered, this formulation holds with $H = ck/n$ for the optical rays and $H = \sqrt{c_s^2 \boldsymbol{k}^2 + \omega_c^2}$ for stellar acoustic rays. It is also the case for the quantum system with $D = H(\boldsymbol{p}, \boldsymbol{x}) - E$ where $H = \boldsymbol{p}^2/2m + V(\boldsymbol{x})$ is the Hamiltonian and $\boldsymbol{p} = \hbar \boldsymbol{k}$ is the momentum vector.

Second, when the Hamiltonian can take the form $D = \boldsymbol{p}^2/2m + V(\boldsymbol{x})$, Hamilton's equations reduce to the classical vectorial form:

$$\frac{d\boldsymbol{x}}{dt} = \frac{\boldsymbol{p}}{m} \tag{15}$$

$$\frac{d\boldsymbol{p}}{dt} = -\boldsymbol{\nabla} V \tag{16}$$

where the second equation is simply the Newton's second law for the conservative force associated with the potential V. The classical limit of the quantum system can obviously be written in this form. It is also possible in the other cases since the eikonal equations of the electromagnetic and acoustic waves can be written $0 = \boldsymbol{p}^2/2m + V(\boldsymbol{x})$ where $m = 1$, $\boldsymbol{p} = \boldsymbol{k}$ and the potential V is respectively $V = -\frac{1}{2}\left[\frac{\omega n}{c}\right]^2$ in the optical case and $V = -\frac{1}{2}\frac{\omega^2-\omega_c^2}{c_s^2}$ in the acoustic case. The total energy D is thus fixed to zero but the frequency ω acts as a parameter that modifies the potential.

In this section, we have derived the ray models of three similar wave equations and have shown that they can be described by Hamiltonian dynamics. A direct consequence is that the bulk of knowledge accumulated on Hamiltonian dynamics is available to characterize the ray properties. For example, as shown in section 4, acoustic rays become more and more chaotic as the rotation of the star increases [10]. The deep understanding of the transitions from integrability to chaos in Hamiltonian dynamics is extremely useful to characterize such an evolution. But what is still more important in the context of this lecture is that the special properties of the Hamiltonian systems can be used to construct an asymptotic theory of stellar oscillation based on the ray model. This will be considered in the next section.

Before concluding this section, it must be reminded that some effects which have not been considered in the present analysis would modify the Hamiltonian character of the ray equations. Dissipative effects produce a concentration of phase space volume that can not be described by Hamiltonian dynamics. Thus the acoustic ray model does not take into account non-adiabatic effects in stars. Another non-Hamiltonian effect can be induced by the presence of a sharp boundary between two media (like the strong gradients at the upper limit of a core convective zone) since an incident ray divides into a reflected ray and a transmitted ray. There have been however attempts to extend the ray dynamics approach to account for the splitting of rays at such discontinuities [16]. Finally, in some circumstances, the reflection of waves at a wall can lead to a focusing or defocusing effect that destroys the Hamiltonian character of the ray dynamics. This is for example the case for the reflection of gravity waves if the wall is inclined with respect to the direction of the gravity [17].

3 Regular versus irregular energy level spectra in quantum systems

As acoustic stellar waves of short-wavelength can be described by rays and as the ray dynamics is Hamiltonian, one wonders whether the oscillation modes formed by these waves are sensitive to the nature, chaotic or integrable, of the Hamiltonian ray dynamics. This question has been considered in the context of quantum physics an overview of the results being available in classical textbooks [18–20]. Here, I shall focus on the results that concerns the organization of the energy level spectra for quantum systems that are either classically integrable or completely chaotic. The situation where the dynamics is mixed in the sense

that regular and chaotic motions coexist in phase space is mentioned in the next section, in the context of acoustic rays in rapidly rotating stars. We also restrict ourselves to bounded systems where the energy spectrum is known to be discrete.

3.1 Regular spectrum

Energy level spectra of quantum system whose classical limit is integrable are said to be regular in the sense that they can be described by a smooth function of N integers $(n_1, n_2, n_3..., n_N)$, where N is the number of degree of freedom of the Hamiltonian:

$$E_i = f(n_1, n_2, n_3, ...) \tag{17}$$

This remarkable property results from the fact that the phase space of integrable systems is entirely structured by N-dimensional invariant surfaces (also called invariant tori because these surfaces have the topology of a N-torus). These surfaces are said to be invariant because any trajectories starting on the surface remains on the surface as time goes on.

Let us first come back to the construction of a solution $\Psi = A(\boldsymbol{x}) \exp[i\Phi(\boldsymbol{x})]$ from a ray solution $[\boldsymbol{x}(s), \boldsymbol{k}(s)]$. To obtain the spatial phase $\Phi(\boldsymbol{x})$, the expression $\boldsymbol{k} = \boldsymbol{\nabla}\Phi$ is integrated along the ray :

$$\Phi(\boldsymbol{x}) = \Phi(\boldsymbol{x}_0) + \int_{\boldsymbol{x}_0}^{\boldsymbol{x}} \boldsymbol{k}(s) \cdot \boldsymbol{dx}(s) \tag{18}$$

If a phase space trajectory crosses its starting position $\boldsymbol{x}_0$ at a later time, the phase function $\Phi(\boldsymbol{x})$ will be multivalued on that position. Thus, the necessary condition that the function $\Psi(\boldsymbol{x}) = A(\boldsymbol{x}) \exp[i\Phi(\boldsymbol{x})]$ is single-valued on the position space requires that the variation of Φ between these two phase space points $[\boldsymbol{x}_0, \boldsymbol{k}_0]$ and $[\boldsymbol{x}_0, \boldsymbol{k}_1]$ is a multiple of 2π (provided the phase of A does not change which is true outside the caustic). More generally, trajectories that crosses a surface $\Phi = const.$ must also verify such a condition.

To implement this condition of positive interference is not easy in the general case, notably when the trajectories are chaotic. But, in integrable systems, trajectories stay on a well-defined structure of phase space and the condition of positive interferences can be shown to apply to any closed contour C on the torus (and not necessarily to a contour that follows a phase space trajectory). Furthermore, the fact that the action integral $\int_C \boldsymbol{k} \cdot \boldsymbol{dx}$ is identical for any contours C' obtained by continuously deforming C on the torus (known as the Poincaré-Cartan theorem) reduces the condition to N independent conditions:

$$\int_{C_i} \boldsymbol{k} \cdot \boldsymbol{dx} = 2\pi(n_i + \frac{\beta_i}{4}) \tag{19}$$

where C_i are N topologically independent closed paths on the N-dimensional torus. The integer β_i called the Maslov index is introduced to account for a $\pi/2$ phase lag that must be added each time the contour crosses a caustic. Indeed,

the caustic corresponds to the boundary of the torus projection onto position space; the amplitude A taken in the position space is discontinuous there, leading to the $\pi/2$ phase loss (see [13] for details). Eq. (19) is the EBK semiclassical quantization condition mentioned before. In practice, the usual way to apply it is to choose contours C_i for which the formulas (19) are simple to compute. Gough [14] applied the EBK quantization to acoustic rays in a non-rotating spherically symmetric star and found that the result is practically identical to the usual asymptotic theory that uses of the separability of the wave equations.

The existence of the function (17) defining the energy level spectrum then follows from the expression of the Hamiltonian in the action-angle coordinates $[\boldsymbol{I}, \boldsymbol{\theta}]$. This a particular coordinate system of integrable systems such that the momentum coordinates $I_1, I_2, I_3..$ are defined by the action integrals (19) (divided by 2π) and are constant of motions. The Hamiltonian is thus a function of the N actions only (since $dI_i/dt = \partial H/\partial\theta_i = 0$), $H(I_1, I_2, I_3..)$. Consequently, the EBK formulas (19) appears as quantization formulas for the actions, $I_i = n_i + \frac{\beta_i}{4}$, and the energy level spectrum is simply determined by $E_i = H(I_1, I_2, I_3..) = f(n_1, n_2, n_3, ...)$.

An important remark about the EBK quantization is that it essentially requires the presence of an invariant torus in phase space. Thus, as we shall see in the next section, it can be also applied to non-integrable systems if invariant tori are present in phase space.

3.2 Irregular spectrum

When the classical dynamics is chaotic, a smooth function like (17) can not be found and the energy spectrum is said to be irregular. Instead, the spectrum of a classically chaotic quantum system is best characterized by its statistical properties.

To show this, it is first necessary to define the fluctuations of the density of energy level, $d^{fluct}(E)$. The total density $d(E)$ is such that the number of energy level comprised between E_a and E_b is equal to $\int_{E_a}^{E_b} d(E)\mathrm{d}E$. This quantity can then be split into a mean density of level $d^{av}(E)$ and the deviation from the mean $d^{fluct}(E)$:

$$d(E) = d^{av}(E) + d^{fluct}(E) \quad \text{where} \quad d^{av}(E) = \tfrac{1}{2\Delta}\int_{E-\Delta}^{E+\Delta} d(E)\mathrm{d}E \qquad (20)$$

and Δ is the averaging scale. The interest of this expression is that the mean density $d^{av}(E)$ does not depend on the chaotic or integrable nature of the dynamics, while the fluctuations about this mean $d^{fluct}(E)$ do.

The mean density $d^{av}(E)$ depends on the global properties of the system considered. This has been shown by Weyl [21] who provided an analytical estimate of $d^{av}(E)$ in the high-energy limit. Accordingly, the mean number of modes whose energy level is below E, $N(E) = \int_{-\infty}^{E} d^{av}(E')\mathrm{d}E'$, is approximatively equal to the volume of phase space available (that is the volume of the $H < E$ region) divided by the mean phase space volume occupied by an individual mode, that is $(2\pi\hbar)^N$. The mean density $d^{av}(E)$ is then obtained by derivating this quantity

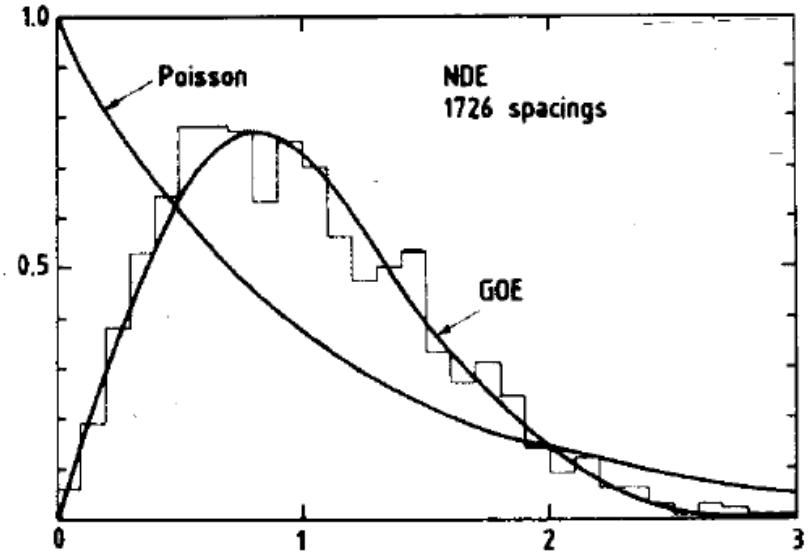

Fig. 1. Statistical distribution of the spacings between consecutive nuclear energy levels, the GOE distribution and the Poisson distribution. From Bohigas et al., 1983 [22].

with respect to E. As an example, for a two-dimensional quantum billiard, the phase space volume such that $H < E$ is simply $\int_{H(\boldsymbol{p},\boldsymbol{x})<E} d^2\boldsymbol{p}d^2\boldsymbol{x} = 2\pi mEA$ where A is the area of the billiard, thus $d^{av}(E) = mA/(2\pi\hbar^2)$. As expected, the mean level density does not depend on the nature of dynamics inside the billiard but only on its area (see [10] for an application of the Weyl's formula to acoustic stellar oscillations).

A simple way to characterize the fluctuations of the level density $d^{fluct}(E)$ is to consider the statistical distribution of the spacing between consecutive energy levels $S_i = E_{i+1} - Ei$ (the energy levels E_i are labeled in ascending order). The mean level difference ΔE (computed over the averaging scale Δ) is the inverse of the mean level density $d^{av}(E)$. Thus, to characterize the deviations from the mean, the energy differences are scaled by ΔE. Statistical distributions of $s_i = (E_{i+1} - Ei)/\Delta E$ have been determined for different systems, either experimentally or through the numerical computations of theoretical problem.

The first experimental evidence of a universal distribution for classically chaotic systems has been obtained from nuclear energy levels. Figure 1 shows an histogram of s_i for 1726 consecutive energy level spacings which has been determined from the analysis of 27 different nuclei [22]. Also shown on this figure is a distribution $P(s) = \pi s/2 \exp(-\pi s^2/4)$ called the Wigner's surmise that

fits closely the data. This distribution corresponds to an heuristic model that was proposed long before by Wigner. Confronted to the difficulty of defining an Hamiltonian for the nucleus, Wigner assumed that the statistical properties of nuclear spectra are similar to that of Hamiltonians taken at random. As the Hamiltonian operator projected on a basis of eigenstates is represented by infinite matrices, this idea can be pursued by looking at the eigenvalue spectra of random matrices. Basic requirements on the matrices, namely that the results should not depend on the choice of the eigenstate basis and that the matrix elements are independent random variables, enables to specify the matrix ensemble. For time-reversible problems, this ensemble called GOE for Gaussian Orthogonal Ensemble corresponds to real, symmetric matrices where each matrix element follows a Gaussian distribution, the width of the distribution of off-diagonal elements being twice that of diagonal elements. The Wigner distribution $P(s) = \pi s/2 \exp(-\pi s^2/4)$ provides a good approximation to the statistical distribution of their eigenvalue consecutive spacings. Thus, the experimental evidence shown in Fig. 1 provided the first striking agreement between real data and the prediction of the random matrix theory.

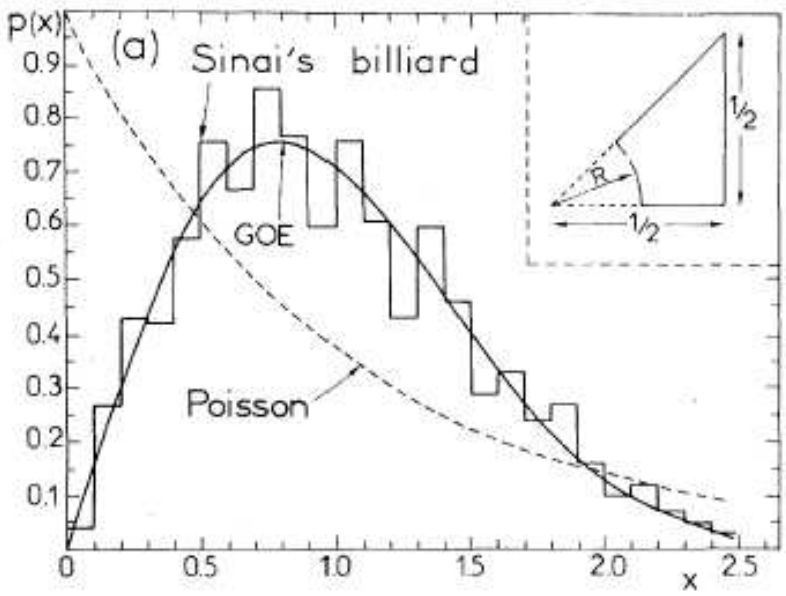

Fig. 2. Statistical distribution of the spacings between consecutive energy levels of the Sinaï billiard, the GOE distribution and the Poisson distribution. The Sinaï billiard is shown in the insert. From Bohigas et al., 1984 [23].

The level spacing distribution has been also determined for numerically computed spectra of quantum billiards. Figure 2 presents the result obtained by Bohigas et al. [23] for a chaotic billiard, namely the Sinai billiard, showing again a good agreement with the Wigner's surmise. Since then, similar evidences have been obtained in quantum systems (from the atomic level of rare-earth atoms) and in other wave systems whose ray dynamics is chaotic (with dedicated experiments using microwave resonators [24], or quartz blocks [26]). This led to the conjecture that the distribution of consecutive level spacing is indeed universal in classically completely chaotic systems and corresponds to the prediction of the random matrix theory.

Conversely, the spectra of integrable systems are predicted to be uncorrelated, and in general this leads to fluctuations given by the Poisson distribution $P(s) = \exp(-s)$ if $N > 1$ [28]. As shown in Figs. 1 and 2, the prediction is strikingly different from the chaotic case. In particular, a distinctive property of classical chaotic system is that $P(s) = 0$ at $s \to 0$. This level repulsion effect can be interpreted as the consequence of avoiding crossing effects between coupled modes in non-integrable systems.

Other statistical properties of the energy level spectrum, the level clustering and the spectral rigidity, have been shown to be sensitive to the nature of the dynamics (see for example [18] for a brief description of these properties).

4 Application to the asymptotic theory of acoustic modes in rapidly rotating stars

The basic tools to construct an asymptotic theory from a ray model and some general results obtained in the context of quantum physics have been presented in the previous sections. They have been used recently to propose an asymptotic theory of the high-frequency acoustic modes in rapidly rotating stars [10]. In this section, we give a brief description of this theory with emphasis on the type of predictions that can be made and on the confrontation of these predictions with the numerically computed modes.

The acoustic ray dynamics has been studied in polytropic models of star whose rotation has been progressively increased. For each rotation rate, the Hamiltonian equations governing the ray dynamics are integrated numerically for many different initial conditions. Then, to visualize the structure of the phase space, the standard method of the Poincaré Surface of Section (PSS) is used. As the system is symmetric with respect to the rotation axis of the star, the projection of the angular momentum on this axis $L_z = r \sin\theta k_\phi$ is a constant of motion, where $k_\phi = \boldsymbol{k} \cdot \boldsymbol{e}_\phi$ and $\boldsymbol{e}_\phi$ is a unit vector in the azimuthal direction. The number of degree of freedom is then reduced to $N = 2$ and the PSS is a 2-dimensional surface. The chosen PSS has been constructed by computing the intersection of the phase space trajectories with the curve defined by $r_p(\theta) = r_s(\theta) - d$, situated at a small fixed radial distance d from the stellar surface $r_s(\theta)$.

The acoustic ray dynamics becomes non-integrable as soon as the rotation is not zero and undergoes a smooth transition towards chaos as the rotation

increases. Dynamical systems in such a transition are said to be mixed as chaotic trajectories coexist with stable phase space structures (like island chains formed around stable periodic orbits or invariant tori). The main features of the phase space at a relatively high rotation rate are shown in Fig. 3 where the PSS for $L_z = 0$ trajectories is displayed together with four acoustic rays shown on the position space and on the PSS.

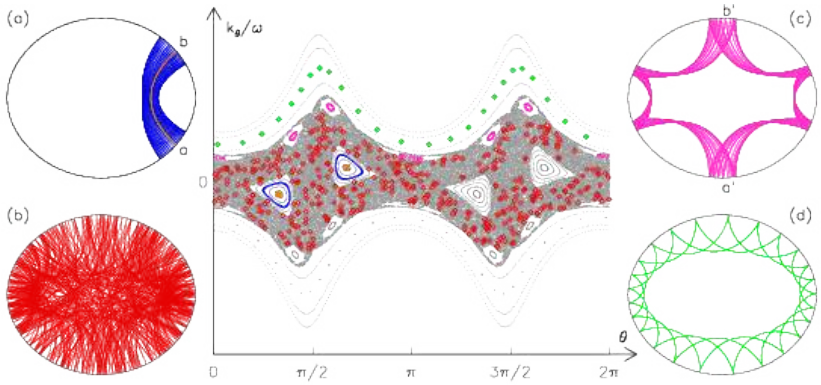

Fig. 3. (Color online) PSS at $\Omega = 0.59(GM/R_e^3)^{1/2}$ and typical acoustic rays associated with the four main phase space structures : (a) a 2-period island ray (blue/dark grey) and the associated periodic orbit with endpoints a and b (orange/light grey), (b) a chaotic ray (red/grey), (c) a 6-period island ray (magenta/light grey) and (d) a whispering gallery ray (green/light grey). On the PSS, (colored/grey) symbols (diamonds for the chaotic and whispering gallery rays, crosses for the 2-period and 6-period island rays) specify the points where these trajectories cross the PSS. M denotes the mass of the star and R_e its equatorial radius.

For such mixed systems, quantum chaos studies [29,30] predict that the different phase space regions shown in Fig. 3 (the two island chains, the chaotic regions, and the whispering gallery region) are quantized independently. The frequency spectrum is then described as a superposition of independent frequency subsets associated with these phase space regions. In addition, the large number of invariant structures in the island chains regions and in the whispering gallery region enables to apply the EBK quantization method leading to regular frequency subsets. By contrast, the frequency subset associated with the chaotic region is expected to be irregular but with generic statistical properties such as described in the previous section. The island chains shown in Fig. 3 have been quantized in [31] to obtain:

$$\omega_{n\ell} = n\delta_n + \ell\delta_\ell + \alpha \quad \text{where} \quad \delta_n = \frac{\pi}{\int_{\rm a}^{\rm b} d\sigma/c_s} \tag{21}$$

where σ is the curvilinear coordinate along the periodic orbit and the integral is computed between the end points of the orbit (these points are shown in Fig. 3

for the 2-period and the 6-period periodic orbits and are denoted (a,b) and (a',b'), respectively). The regular spacing δ_n depends on the sound speed along the periodic orbit while δ_ℓ (whose expression is given in [31]) depends on the sound speed and on its transverse derivative along the same orbit. The integers n and ℓ are the number of nodes of the corresponding modes in the directions parallel and transverse to the orbit.

The above predictions on high-frequency p-modes have been confronted with numerically computed axisymmetric modes (using the same star model). The first prediction is that modes can be classified as chaotic modes, island modes or whispering gallery modes. This can indeed be achieved with the help of a phase-space representation of the modes. With this classification, the frequency spectrum computed in the range $[9\omega_1, 12\omega_1]$ (where ω_1 is the lowest acoustic frequency) has been split into the four subspectra shown in Fig. 4.

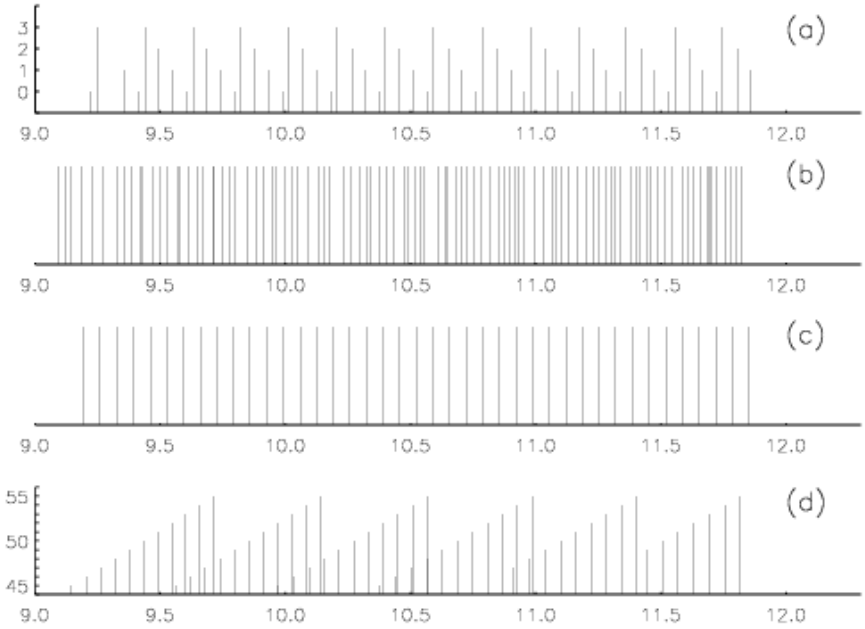

Fig. 4. Frequency subspectra of four classes of axisymmetric p-modes of a $\Omega = 0.59(GM/R_e^3)^{1/2}$ polytropic model of star: (a) the 2-period island modes, (b) the chaotic modes antisymmetric with respect to the equator, (c) the 6-period island modes, and (d) some whispering gallery modes. For the subspectra (a) and (d), the height of the vertical bar specifies one of the two quantum numbers characterizing the mode.

From these data, we could verified that, in accordance with the asymptotic theory, (i) the subspectra associated with the structured phase space region are regular, (ii) the theoretical expression of δ_n agrees with the empirical values within a few percent, (iii) the distribution of the consecutive frequency spacings

taken from the chaotic sub-spectrum agrees reasonably well with the Wigner's distribution.

The asymptotic theory based on the acoustic ray model can thus reproduce quantitative and qualitative features of the actual high-frequency spectrum. However, there are also some limitations to the asymptotic theory that does not exist in the case of a non-rotating spherically symmetric star. Maybe the most important one is that the prediction of the chaotic subspectra concerns its statistical properties but not the individual frequencies. There exist a Fourier-like formula (called the Gutzwiller trace formula [20]) that relates all the periodic orbits of the chaotic phase space to the whole spectrum, but this formula is very delicate to use in practice. Another limitation concerns the coupling between two modes of similar frequencies associated with two dynamically independent regions of phase space. The avoided crossing effect between such modes is not taken into account by the ray dynamics and is thus expected to induce deviations from the asymptotic behavior.

Despite these limitations, the a priori information that the asymptotic theory provides on the structure of the frequency spectrum should be important to interpret the observed frequency spectra of rapidly rotating stars. For example, synthetic spectra given by the asymptotic theory (complemented by informations on the visibility and the excitation of the modes) might be used to construct and test identification schemes. In this context, a first step would be to disentangle the regular part from the irregular part of the spectrum.

5 Conclusions

We have seen that ray models can be used to construct asymptotic theory of modes even when the eigenvalue problem is not separable. The methods and concepts, developed in the context of quantum physics, rely on the Hamiltonian character of the ray dynamics. For example, the structure of the frequency (or energy level) spectrum has been shown to depend on the nature of the Hamiltonian dynamics (integrable, fully chaotic, mixed). It is regular for an integrable system, irregular for a fully chaotic system, and a superposition of regular and irregular spectra for a mixed system. These methods and concept have been used to construct an asymptotic theory based on the Hamiltonian acoustic ray dynamics that has been successfully confronted to numerically computed adiabatic p-modes. In principle, the same procedure could be applied to model other types of stellar oscillation modes.

References

1. Yu. V. Vandakurov: Astron. Zh. **44**, 786 (1967).
2. M. Tassoul: Astrophys. J. Suppl. Ser. **43**, 469 (1980).
3. M. Tassoul: Astrophys. J. **358**, 313 (1990).
4. F.-L. Deubner, D. O. Gough: Annu. Rev. Astron. Astrophys. **22**, 593 (1984).
5. I. W. Roxburgh, S. V. Vorontsov: Mon. Not. R. Astron. Soc. **317**, 141 (2000).

6. J. Christensen-Dalsgaard: Rev. Mod. Phys. **74**, 1073 (2002).
7. F. Lignières, M. Rieutord, D. Reese: Astron. Astrophys. **455**, 607 (2006).
8. B. Dintrans, M. Rieutord: Astron. Astrophys. **354**, 86 (2000).
9. H. Saio: Mon. Not. R. Astron. Soc. **360**, 1022 (2005).
10. F. Lignières, B. Georgeot: Astron. Astrophys. **500**, 1173 (2009).
11. Einstein, A.: Deutsche Phys. Ges. **19**, 82 (1917).
12. Brillouin, L.: J. Phys. Radium **7** , 353 (1926).
13. J. B. Keller, S. I. Rubinow: Annals of Physics **9**, 24 (1960).
14. D. O. Gough, in *Les Houches Lectures Session XLVIII*, J.-P. Zahn, J. Zinn-Justin, Eds. (North-Holland, Amsterdam, 1993), pp. 399-559.
15. J. Lighthill: *Waves in fluids* (Cambridge University Press, Cambridge 1978).
16. R. Blümel, T. M. Antonsen, B. Georgeot, E. Ott, R. E. Prange: Phys. Rev. Lett. **76**, 2476 (1996); R. Blümel, T. M. Antonsen, B. Georgeot, E. Ott, R. E. Prange: Phys. Rev. E **53**, 3284 (1996).
17. O. M. Phillips: *Dynamics of the upper ocean* (Cambridge University Press, Cambridge 1967).
18. E. Ott: *Chaos in dynamical systems* (Cambridge University Press, Cambridge 1993).
19. M.-J. Giannoni, A. Voros, J. Zinn-Justin, Eds., *Les Houches Lectures Session LII* (North-Holland, Amsterdam, 1991).
20. M.C. Gutzwiller *Chaos in classical and quantum mechanics* (Springer, Berlin 1990).
21. H. Weyl: Math. Ann. **71**, 441 (1912).
22. O. Bohigas, R. Haq, A. Pandey, in *Nuclear data in Science and Technology* (Reidel, Dordrecht), pp. 809 (1983).
23. O. Bohigas, M.-J. Giannoni, C. Schmit: Phys. Rev. Lett. **52**, 1 (1984).
24. H.-J. Stöckmann, J. Stein: Phys. Rev. Lett. **64**, 2215 (1990).
25. J. U. Nöckel, A. D. Stone: Nature **385**, 45 (1997).
26. C. Ellegaard *et al.*: Phys. Rev. Lett. **77**, 4918 (1996).
27. M. G. Brown *et al.*: J. Acoust. Soc. Am. **113**, 2533 (2003).
28. M. V. Berry, M. Tabor: R. Soc. Lond. Proc. Ser. A **356**, 375 (1977).
29. I. C. Percival: J. Phys. B **6**, L229 (1973).
30. M. V. Berry, M. Robnik: J. Phys. A **17**, 2413. (1984).
31. F. Lignières, B. Georgeot: Phys. Rev. E **78**, 016215 (2008).

2.5.6 A6 : Wave chaos in rapidly rotating stars

“Wave chaos in rapidly rotating stars”

Lignières F. and Georgeot, B.

Phys. Rev. E. 78, 016215-016219, 2008

Wave chaos in rapidly rotating stars

François Lignières[1,*] and Bertrand Georgeot[2]
[1]*Laboratoire d'Astrophysique de Toulouse-Tarbes, Université de Toulouse, CNRS, 31400 Toulouse, France*
[2]*Laboratoire de Physique Théorique, Université de Toulouse, UPS, CNRS, 31062 Toulouse, France*
(Received 3 October 2007; published 31 July 2008)

The effects of rapid stellar rotation on acoustic oscillation modes are poorly understood. We study the dynamics of acoustic rays in rotating polytropic stars and show using quantum chaos concepts that the eigenfrequency spectrum is a superposition of regular frequency patterns and an irregular frequency subset respectively associated with near-integrable and chaotic phase space regions. This opens fresh perspectives for rapidly rotating star seismology and also provides a potentially observable manifestation of wave chaos in a large-scale natural system.

DOI: 10.1103/PhysRevE.78.016215 PACS number(s): 05.45.Mt, 97.10.Sj, 97.10.Kc

Since helioseismology revolutionized our knowledge of the Sun's interior, many efforts, including space missions (MOST, COROT, and KEPLER), have been undertaken to detect oscillation frequencies in a large variety of stars [1,2]. But to access the information contained in these data, the observed frequencies must be first associated with the right stellar oscillation modes. This crucial identification process requires a full understanding of the properties of the oscillation spectrum and, for slowly rotating stars like the Sun, the asymptotic theory of high-frequency acoustic modes provided such an understanding [1]. Both the approximate treatment of the centrifugal distortion [3] and the lack of asymptotic theory have so far hindered reliable identification in rapidly rotating pulsators. This long-standing problem mainly concerns massive and intermediate-mass stars [4] like the δ Scuti star Altaïr, whose surface oblateness has been measured by interferometry [5]. Accurate computations of acoustic modes fully taking into account the effect of rotation on the oscillations have only recently been performed for polytropic models of rotating stars [6]. Here we construct the dynamics of acoustic rays to understand the properties of the frequency spectrum.

The acoustic ray model is analogous to the geometrical optics limit of electromagnetic waves or the classical limit of quantum mechanics. The construction of eigenmodes from stellar acoustic rays has already been considered in the integrable case of a nonrotating spherically symmetric star [7]. However, when the ray dynamics is no longer integrable, the problem is known to become of a deeply different nature. This issue has been mostly investigated by the quantum chaos community in the context of the classical limit of quantum systems [8] and the developed concepts have been applied to other wave phenomena such as those observed in, e.g., microwave resonators [9], lasing cavities [10], quartz blocks [11], and underwater waves [12]. The potential interest for stellar seismology has been suggested [13] but not yet demonstrated.

Our star model is a self-gravitating uniformly rotating monatomic perfect gas ($\Gamma=5/3$) where pressure and density follow a polytropic relation $P_e \propto \rho_e^{1+1/N}$ with $N=3$. Neglecting the Coriolis force and the gravitational potential perturbations, small-amplitude adiabatic perturbations around this equilibrium verify

$$\partial_t \rho + \boldsymbol{\nabla}\cdot(\rho_e \mathbf{v}) = 0, \quad \partial_t \mathbf{v} = -\frac{\boldsymbol{\nabla} P}{\rho_e} + \frac{\rho}{\rho_e}\mathbf{g}_e, \quad dP = c_s^2 d\rho, \tag{1}$$

where the density ρ, pressure P, and velocity $\mathbf{v}$ describe the perturbation, while c_s is the sound velocity and $\mathbf{g}_e$ is the effective gravity resulting from the gravitational and centrifugal potentials. As other quantities characterizing the star model, c_s and $\mathbf{g}_e$ vary in the meridian plane of the rotating star. Neglecting gravity waves, these equations can be reduced to the form $(\omega_c^2-\omega^2)\Phi - c_s^2\Delta\Phi = 0$ where $\Phi = \hat{P}/c_s^3$ is related to the time-harmonic pressure perturbation $P = \mathrm{Re}[\hat{P}\exp(-i\omega t)]$ and $\omega_c = \sqrt{(15/64)(\mathbf{g}_e/c_s)^2 + (3/8)\boldsymbol{\nabla}\cdot\mathbf{g}_e}$ is the cutoff frequency whose sharp increase in the outermost layers of the star provokes the back reflection of acoustic waves. The WKB approximation then leads to the eikonal equation $\omega^2 = c_s^2\mathbf{k}^2 + \omega_c^2$. The acoustic ray is the trajectory tangent to the wave vector $\mathbf{k}$ at the point $\mathbf{x}$ and its evolution can be described by Hamilton's equations, $H = \sqrt{c_s^2\mathbf{k}^2 + \omega_c^2}$ being the Hamiltonian [7]. Rays heading toward the star center tend to be refracted by increasing sound velocity while close to the surface nonspecular reflection takes place at $\omega_c = \omega$. As rotation increases, the isocontours of c_s and ω_c are distorted together with the star surface. In the following, we restrict ourselves to axisymmetric modes $L_z = 0$, thus reducing the phase space to four dimensions.

The acoustic ray dynamics has been investigated by integrating numerically the Hamilton's equations and the resulting dynamics is visualized using the standard tool of the Poincaré surface of section (PSS). As rays do not reach the star boundary, the PSS is defined by $r_p(\theta) = r_s(\theta) - d$, where the distance $d = 0.08 r_s(\pi/2)$ from the star surface $r_s(\theta)$ has been chosen such that all but a few whispering gallery rays cross the PSS (only outgoing rays are taken). The two coordinates of the PSS are θ, the colatitude, and k_θ/ω, k_θ being the angular component of $\mathbf{k}$ in the natural basis associated with the coordinate system $[\zeta = r_s(\theta) - r, \theta]$. We use the scaled variable k_θ/ω as, in the limit $\omega \gg \omega_c$, the ray dynamics be-

*ligniere@ast.obs-mip.fr

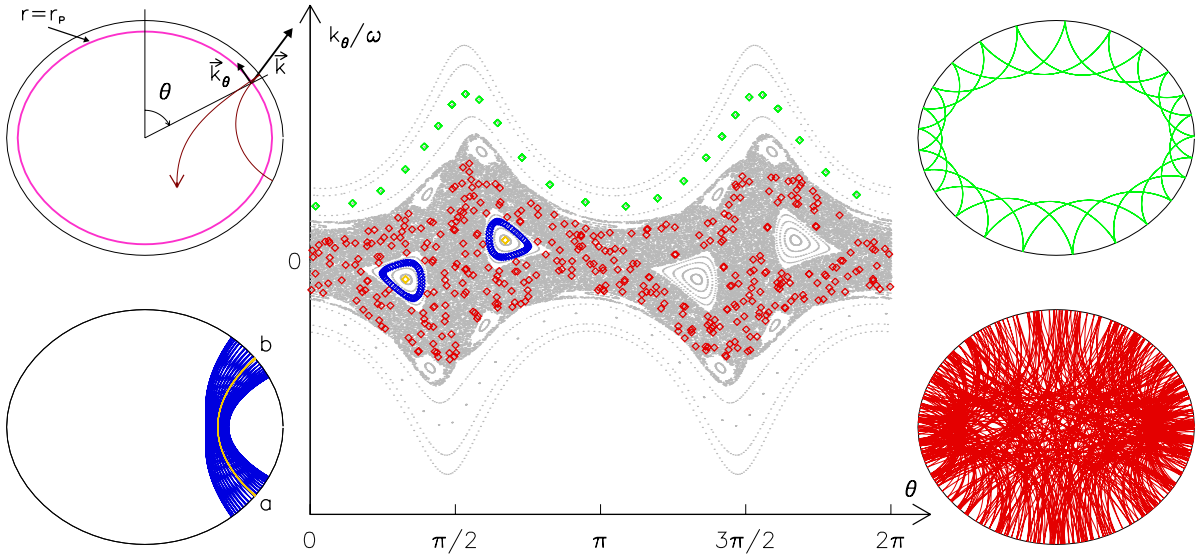

FIG. 1. (Color online) PSS and typical acoustic rays at a rotation equal to 59% of the Keplerian limit. A whispering gallery ray [green (light gray)], an island ray [blue (dark gray)], and a chaotic ray [red (gray)] are shown on the physical space and on the PSS (diamonds in the center figure). The central orbit of the island is also shown (yellow between points a and b). k_θ/ω is in units of $\sqrt{r_s^3(0)/GM}$ with M the stellar mass and G the gravitational constant.

comes independent of the frequency away from the reflection points. We found that increasing the stellar rotation leads to a soft transition from integrability to chaos analogous to the one described by the Kolmogorov-Arnold-Moser (KAM) theorem. As illustrated in Fig. 1 for a given rotation rate, the phase space shows a mixed structure where chaotic regions coexist with a whispering gallery region close to the boundary and regular islands around stable periodic orbits. As the rotation increases, both the chaotic region and the central island chain get larger. A crucial feature of the dynamics is that each region is dynamically isolated from the other by invariant tori which prevent communication between them. Such a situation has been found several times in the domain of quantum chaos, and generally it was surmised [14] that the stationary waves localized on one of these regions form an independent subset with specific dynamical properties. The frequency spectrum thus appears as the superposition of independent frequency subsets reflecting the phase space structure. This surmise has been found to be a good approximation for many systems, although some correlations may remain between the frequency subsets due to modes localized at the border between zones or the presence of partial barriers in phase space [15].

It is therefore important to know if this spectrum organization is valid in the high-frequency limit where it is supposed to hold, and even more important to assess if it is still relevant to the observable acoustic modes. We have thus numerically computed exact axisymmetric modes of Eq. (1), using the method described in [6], in the frequency range $[\omega_1, 12\omega_1]$, ω_1 being the lowest acoustic frequency. To establish a link with the asymptotic ray dynamics, we use a phase-space representation of the modes known as the Husimi distribution [16]. In order to compare a three-dimensional mode with the acoustic rays on a two-dimensional plane, the mode amplitude is first scaled by the square root of the distance to the rotation axis [7]. The Husimi distribution is then constructed from a cut taken along the PSS: $H(s_0,k_0) = |\int \Phi'(s)\exp[-(s-s_0)^2/(2\Delta^2)]\exp(ik_0 s)ds|^2$. Here Φ' is the scaled version of Φ, the integral is taken along the curve $r = r_p$, and k is the moment in the direction tangent to this curve; Δ is the width of the Gaussian wave packet on which Φ' is projected. In Fig. 2, (s_0,k_0) is replaced by (θ,k_θ) for comparison with data from Fig. 1. Except for some of the largest-length-scale modes close to the frequency ω_1, we find that the Husimi distribution enables us to unambiguously associate the modes with the main structures of phase space. As illustrated in Fig. 2, we distinguished the island modes trapped in the main stable islands, the chaotic modes localized in the central chaotic region, and the whispering gallery modes associated with the whispering gallery region. We note that, due to the relatively low frequency considered, the chaotic modes do not spread over all parts of the chaotic region.

Having defined subsets of modes, we can now analyze the properties of the corresponding frequency subsets. As shown in Fig. 3, the frequency spacings of the island modes display striking regularities which lead to the simple empirical formula

$$\omega_{n\ell} = n\delta_n + \ell\,\delta_\ell + \alpha, \tag{2}$$

where n and ℓ are natural integers, and δ_n and δ_ℓ are uniform frequency spacings. The α constant being fixed by a given island mode frequency, the formula proves sufficiently accurate to identify the other island modes among the whole set of computed frequencies. The phase space representation of these modes reveals that these regular patterns can be attributed to the existence of the stable island region in phase space. Although a zoom on this region would show a complex structure involving chaotic trajectories and chains of small islands nested between deformed surviving tori, these

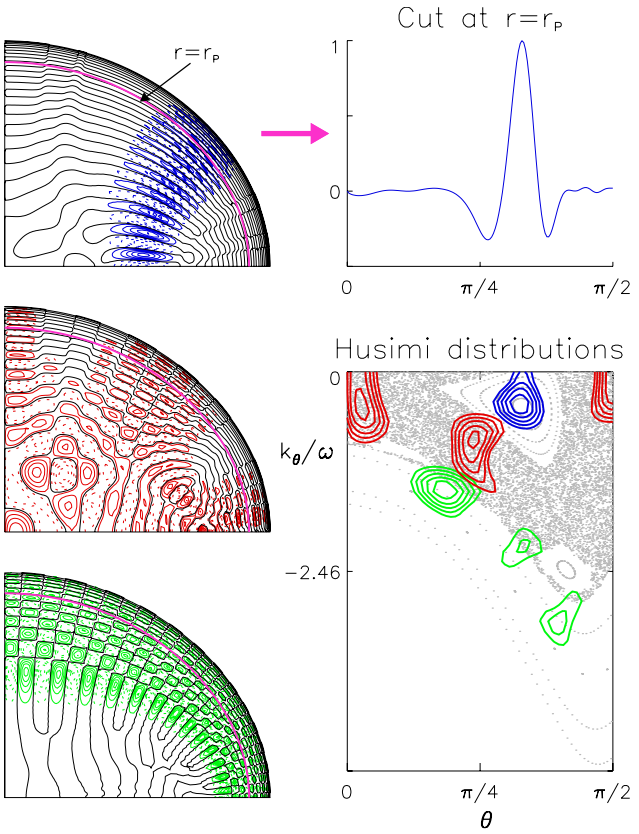

FIG. 2. (Color online) Comparison of numerically computed acoustic modes from (1) with phase space ray dynamics on the PSS. Three typical modes have been selected: island mode [blue (dark gray)], chaotic mode [red (gray)], and whispering gallery mode [green (light gray)]. Left: Spatial distribution of Φ' on one-quarter of a meridian plane. Black lines are the nodal lines, full (dashed) colored (gray) lines are the level curves for positive (negative) values. Magenta line at $r=r_p$ is the chosen PSS. Right top: Cut of the island mode along the PSS, from the pole to the equator. Right bottom: Level curves of the Husimi distributions of the three modes [for the same of value of $\Delta=0.12r_s(\pi/2)$], showing that they are mainly concentrated inside the main stable island (for the island mode), in the chaotic region (for the chaotic mode), or in the whispering gallery region (for the whispering gallery mode).

small-scale details can be overlooked for the relatively large wavelengths considered here. To retrieve formula (2) and to find out how δ_n and δ_ℓ relate to the properties of the star, we follow an approach inspired by the quantization of laser modes in cavities [17]. Indeed, far from the boundary, our problem can be translated into the propagation of light in an inhomogeneous medium, $1/c_s$ playing the role of the medium index. Close to the stable orbit, we can apply the paraxial approximation. In this case, it is known that the wave beam solution is [18] $\Phi(\sigma,\xi)\propto H_\ell[\sqrt{2}\xi/w(\sigma)]\exp[-\xi^2/w(\sigma)^2]\exp[-i\phi(\sigma,\xi)]$, where σ,ξ are coordinates parallel and transverse to the central periodic orbit (the yellow curve in Fig. 1); H_ℓ is the Hermite polynomial of degree ℓ. The spreading of the beam in the transverse direction is described by $w(\sigma)$, which verifies $(1/c_s)d/d\sigma[(1/c_s)(dw/d\sigma)]+\alpha(\sigma)w=4/w^3$, where $\alpha(\sigma)=(1/c_s^3)\partial^2 c_s/\partial\xi^2$. The wave phase is $\phi(\sigma,\xi)=\omega\int_0^\sigma d\sigma'/c_s-2(\ell+1)\int_0^\sigma c_s d\sigma'/w^2+\xi^2/(2c_sR)$ where $R=w/(dw/d\sigma)$ is the radius of curvature of the beam wave front. Numerically computed island modes have a transverse variation confirming this approximation. We then obtain a stationary solution by imposing the requirement that the wave interferes constructively with itself. This requires that the phase accumulated following the periodic orbit ($\xi=0$) from one side of the boundary to the other side is $\omega\int_a^b d\sigma/c_s-2(\ell+1)\int_a^b c_s d\sigma/w^2=n\pi$. This leads to the formula (2) with $\delta_n=\pi/(\int_a^b d\sigma/c_s)$ and $\delta_\ell=2(\int_a^b c_s d\sigma/w^2)/(\int_a^b d\sigma/c_s)$. The numerical value of δ_n obtained from the island mode frequencies shown in Fig. 3 [equal to 0.5514 in units of $\sqrt{GM/r_s^3(0)}$ where M is the stellar mass and G the gravitational constant] is well approximated, within 2.2%, by the theoretical one (equal to 0.5635 in the same units). While δ_n probes the sound velocity along the path of the periodic orbit, δ_ℓ is obtained by solving the second-order equation verified by w together with the two boundary conditions given by the necessity to match R with the radius of curvature of the two bounding surfaces. Thus, δ_ℓ probes the second-order transverse derivative of the sound velocity along the same path as well as the radius of curvature of the bounding surfaces. We note that similar modes around stable periodic orbit have been constructed in other systems, usually with the more systematic procedure of finding the normal forms and using Einstein-Brillouin-Keller quantization [15,19].

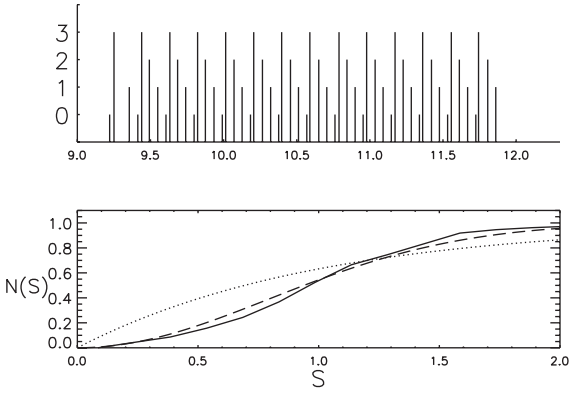

FIG. 3. Top: Island mode frequencies in the interval $[9\omega_1,12\omega_1]$ showing the regular spacings corresponding to formula (2); height reflects the value of the quantum number ℓ. Bottom: Integrated spacing distribution for the chaotic modes in the same interval (full line). Data correspond to around 200 modes from two symmetry classes. The dashed line is the result for the Gaussian orthogonal ensemble of random matrix theory while the dotted line corresponds to the Poisson distribution characteristic of integrable systems.

Having shown that modes whose Husimi distribution is localized in the near-integrable region display integrablelike quantization conditions, we now turn to the modes localized in the chaotic region. The subset of chaotic mode frequencies shows typical signatures of wave chaos such as frequency repulsion. Indeed, in Fig. 3, the integrated distribution of consecutive frequency spacings $S_i=\omega_{i+1}-\omega_i$ (normalized by the mean frequency spacing of those modes) is much closer to the random matrix theory result typical of chaotic systems [20] than to the Poisson distribution result characteristic of

integrable systems. This frequency statistics together with the fact that the corresponding modes are all localized in the chaotic region of the ray dynamics give a strong evidence that wave chaos occurs in rapidly rotating stars. The difficulty of solving Eq. (1) even with state-of-the-art computational techniques prevents us reaching a larger-frequency sample and making detailed comparison with random matrix theory as in, e.g., [20].

The whispering gallery modes and the modes trapped in smaller island chains being associated with near-integrable regions of phase space, their frequencies are therefore expected to display regular patterns. The detail study of these regularities shall be considered elsewhere as it requires more mode calculations with a higher numerical resolution. It is also important to point out that these modes will be the most difficult to detect. Indeed, due to their small latitudinal wavelength (see Fig. 2), the positive and negative light intensity fluctuations strongly cancel out when integrated over the visible disk.

Our results demonstrate that ray dynamics and quantum chaos concepts provide a qualitative and quantitative insight into the frequency spectrum of rapidly rotating stars. In particular, we are able to separate the spectrum of a reasonably realistic star model into integrable and chaotic subsets. Being much less demanding than a direct eigenmode computation as well as easily adaptable to nonaxisymmetric modes (for which regular frequency patterns have also been found numerically [21]) and to more realistic stellar models, ray dynamics will be essential to investigate the asymptotic properties of the oscillation spectrum.

The present analysis opens further perspectives in the seismology of rapidly rotating stars. The observed spectra differ from theoretical ones, as poorly understood mechanisms governing the intrinsic mode amplitude determine the frequencies that are actually detected. In this context, *a priori* information on the structure of the spectrum is crucial in order to identify the observed frequencies with specific stellar oscillation modes. Our results strongly suggest first looking for regular patterns to identify the island modes and to determine seismic observables such as δ_n and δ_ℓ containing information on the star's interior. The remaining chaotic modes are also of special interest for seismology purposes: they are highly sensitive to small changes of the stellar model [22] and, in contrast to nonradial acoustic modes of slowly rotating stars which avoid the star's center, they probe this region, which is crucial for stellar evolution theory. If enough chaotic modes are seen, their mean frequency spacing, which is known to depend on the volume of the chaotic region, will constrain the stellar rotation.

We thank S. Vidal, D. Reese, M. Rieutord, and L. Valdettaro for their help at various stages of this work. We also thank CALMIP ("Calcul en Midi-Pyrénées") for the use of their supercomputer. This work was supported by the Programme National de Physique Stellaire of INSU/CNRS and the SIROCO project of the Agence National de la Recherche.

[1] J. Christensen-Dalsgaard, Rev. Mod. Phys. **74**, 1073 (2002).
[2] A. Gautschy and H. Saio, Annu. Rev. Astron. Astrophys. **33**, 75 (1995); A. Baglin *et al.*, in *Stellar Structure and Habitable Planet Finding*, edited by F. Favata, I. W. Roxburgh, and D. Galadi, ESA Special Publciation 485 (ESA Publications Division, Noordwijk, 2002), pp. 17–24.
[3] M.-J. Goupil *et al.*, in *Delta Scuti and Related Stars*, edited by M. Breger and M. Montgomery, ASP Conf. Ser. No. 210 (Astronomical Society of the Pacific, San Francisco, 2000), pp. 267–284.
[4] D. W. Kurtz, Astrophys. Space Sci. **284**, 29 (2003).
[5] J. D. Monnier *et al.*, Science **317**, 342 (2007); D. L. Buzasi *et al.*, Astrophys. J. **619**, 1072 (2005).
[6] F. Lignières, M. Rieutord, and D. Reese, Astron. Astrophys. **455**, 607 (2006); D. Reese, F. Lignières, and M. Rieutord, *ibid.* **455**, 621 (2006).
[7] D. O. Gough, in *Astrophysical Fluid Dynamics*, edited by J.-P. Zahn and J. Zinn-Justin, Proceedings of the Les Houches Summer School of Theoretical Physics, XLVII (North-Holland, Amsterdam, 1993), pp. 399–559.
[8] *Chaos and Quantum Physics*, edited by M.-J. Giannoni, A. Voros, and J. Zinn-Justin, Proceedings of the Les Houches Summer School of Theoretical Physics, LII (North-Holland, Amsterdam, 1991).
[9] H.-J. Stöckmann and J. Stein, Phys. Rev. Lett. **64**, 2215 (1990).
[10] J. U. Nöckel and A. D. Stone, Nature (London) **385**, 45 (1997).
[11] C. Ellegaard, T. Guhr, K. Lindemann, J. Nygard, and M. Oxborrow, Phys. Rev. Lett. **77**, 4918 (1996).
[12] M. G. Brown *et al.*, J. Acoust. Soc. Am. **113**, 2533 (2003).
[13] J. Perdang, *Seismology of the Sun and the Distant Stars* (Reidel, Dordrecht, 1986), pp. 141–171.
[14] I. C. Percival, J. Phys. B **6**, L229 (1973); M. V. Berry and M. Robnik, J. Phys. A **17**, 2413 (1984).
[15] O. Bohigas, S. Tomsovic, and D. Ullmo, Phys. Rep. **223**, 43 (1993).
[16] S.-J. Chang and K.-J. Shi, Phys. Rev. A **34**, 7 (1986).
[17] H. Kogelnik and T. Li, Appl. Opt. **5**, 1550 (1966).
[18] G. V. Permitin and A. I. Smirnov, Sov. Phys. JETP **82**, 395 (1996); M. Bornatici and O. Maj, Plasma Phys. Controlled Fusion **45**, 707 (2003).
[19] V. F. Lazutkin, *KAM Theory and Semiclassical Approximations to Eigenfunctions* (Springer, Berlin, 1993).
[20] O. Bohigas, M.-J. Giannoni, and C. Schmit, Phys. Rev. Lett. **52**, 1 (1984).
[21] D. Reese, F. Lignières, and M. Rieutord, Astron. Astrophys. **481**, 449 (2008).
[22] R. Schack and C. M. Caves, Phys. Rev. Lett. **71**, 525 (1993); G. Benenti *et al.*, Eur. Phys. J. D **20**, 293 (2002).

2.5.7 A7 : Asymptotic analysis of high-frequency acoustic modes in rapidly rotating stars

"Asymptotic analysis of high-frequency acoustic modes in rapidly rotating stars"

Lignières F. and Georgeot B.

A&A 500, 1173-1192, 2009

A&A 500, 1173–1192 (2009)
DOI: 10.1051/0004-6361/200811165

Astronomy & Astrophysics

Asymptotic analysis of high-frequency acoustic modes in rapidly rotating stars

F. Lignières[1,2] and B. Georgeot[3,4]

[1] Université de Toulouse, UPS, Laboratoire d'Astrophysique de Toulouse-Tarbes (LATT), 31400 Toulouse, France
e-mail: francois.lignieres@ast.obs-mip.fr
[2] CNRS, Laboratoire d'Astrophysique de Toulouse-Tarbes (LATT), 31400 Toulouse, France
[3] Université de Toulouse, UPS, Laboratoire de Physique Théorique (IRSAMC), 31062 Toulouse, France
[4] CNRS, LPT (IRSAMC), 31062 Toulouse, France

Received 16 October 2008 / Accepted 10 March 2009

ABSTRACT

Context. The asteroseismology of rapidly rotating pulsating stars is hindered by our poor knowledge of the effect of the rotation on the oscillation properties.
Aims. Here we present an asymptotic analysis of high-frequency acoustic modes in rapidly rotating stars.
Methods. We study the Hamiltonian dynamics of acoustic rays in uniformly rotating polytropic stars and show that the phase space structure has a mixed character, with regions of chaotic trajectories coexisting with stable structures like island chains or invariant tori. To interpret the ray dynamics in terms of acoustic mode properties, we then use tools and concepts developed in the context of quantum physics.
Results. Accordingly, the high-frequency acoustic spectrum is a superposition of frequency subsets associated with dynamically independent phase space regions. The subspectra associated with stable structures are regular and can be modelled through EBK quantization methods, while those associated with chaotic regions are irregular but with generic statistical properties. The results of this asymptotic analysis are successfully compared with the properties of numerically computed high-frequency acoustic modes. The implications for the asteroseismology of rapidly rotating stars are discussed.

Key words. hydrodynamics – waves – chaos – stars: oscillations – stars: rotation

1. Introduction

Interpreting the oscillation spectra of rapidly rotating stars is a long standing unsolved problem of asteroseismology. It has so far prevented any direct probe of the interior of stars in large fractions of the HR diagram, mostly in the range of intermediate and massive stars. Progress is nevertheless expected from the current spatial seismology missions (in particular COROT and KEPLER), as well as from recent modelling efforts on the effect of rotation on stellar oscillations. New numerical codes have been able to accurately compute oscillation frequencies in centrifugally distorted polytropic models of stars (Lignières et al. 2006; Reese et al. 2006) and are now extended to more realistic models (Reese et al. 2009). In particular the previous calculations based on perturbative methods have been shown to be inadequate for these stars (Reese et al. 2006; Lovekin & Deupree 2008). Nevertheless, interpreting the data requires an understanding of the mode properties that goes far beyond an accurate computation of frequencies. Indeed, the necessary identification of the observed frequencies with theoretical frequencies is a largely underconstrained problem that requires a priori information on the spectrum to be successful. Knowledge of the structure of the frequency spectrum is crucial in this context. For slowly rotating pulsating stars, this structure is characterised by regular frequency patterns that can be analytically derived from an asymptotic theory of the high-frequency acoustic modes.

Until recently, the asymptotic structure of the frequency spectrum of rapidly rotating stars was completely unknown. Our first calculations of low-degree ($\ell = 0$–7) and low-order ($n = 1$–10) acoustic axisymmetric modes in centrifugally distorted polytropic stars (Lignières et al. 2006) have revealed regular frequency patterns both similar to and different from those of spherically symmetric stars. This was confirmed with more realistic calculations including the Coriolis force and has also been extended to non-axisymmetric and higher frequency modes (Reese et al. 2008). The analogy with the non-rotating case suggests an asymptotic analysis could model these empirical regular patterns.

The asymptotic analysis presented in this paper is based on acoustic ray dynamics. This approach can be viewed as a natural extension of the asymptotic analysis developed for non-rotating stars (Vandakurov 1967; Tassoul 1980, 1990; Deubner & Gough 1984; Roxburgh & Vorontsov 2000). In this case, spherical symmetry enables the initial 3D boundary value problem to be reduced to a 1D boundary value problem in the radial direction. Asymptotic solutions of this 1D boundary value problem can then be obtained using a short-wavelength approximation that consists in looking for wave-like solutions under the assumption that their wavelength is much shorter than the typical length-scale of the background medium. As rotation breaks the spherical symmetry, the eigenmodes are no longer separable in the latitudinal and radial directions and the 3D boundary value problem of acoustic modes in rapidly rotating stars cannot be reduced to a 1D boundary value problem. Thus, the short-wavelength approximation is directly applied to the 3D equations governing linear adiabatic stellar perturbations. This leads to an acoustic

ray model that describes the propagation of locally plane waves. Since we are concerned by oscillation modes, the main issue of an asymptotic analysis based on ray dynamics is to construct standing-wave solutions from the short-wavelength propagating waves described by the acoustic rays.

The short-wavelength approximation of wave equations is standard in physics, best known examples being the geometric optics limit of electromagnetic waves or the classical limit of quantum mechanics. We shall see that, similar to these cases, the acoustic rays in stars can be described as trajectories of a particle in the framework of classical Hamiltonian mechanics. As is well known in quantum physics (Gutzwiller 1990; Ott 1993), the issue of constructing modes from ray dynamics depends crucially on the nature of this Hamiltonian motion.

Indeed, Hamiltonian systems can have one of two very different behaviours. If there are enough constants of motion, the dynamics is integrable, and trajectories organise themselves in families associated with well-defined phase space structures. In contrast, chaotic systems display exponential divergence of nearby trajectories, and a typical orbit is ergodic in phase space. The modes constructed from these different dynamics are markedly different. For integrable systems, the eigenfrequency spectrum can be described by a function of N integers, N being the number of degrees of freedom of the system. In contrast, the spectrum of chaotic systems shows no such regularities. However, the spectrum possesses generic statistical properties that can be predicted. In the past thirty years, the field called quantum chaos has developed concepts and methods to relate non-integrable ray dynamics to properties of the associated quantum systems (and more generally of wave systems).

We shall see that the acoustic ray dynamics in rotating stars undergoes a transition from an integrable system at zero rotation to a mixed system, which is a system with a phase space containing integrable and chaotic regions. Because the acoustic ray dynamics of rotating stars is non-integrable, we are led to use quantum chaos theory to predict the asymptotic properties of acoustic modes.

In the following, we describe in detail the ray dynamics, the predictions on the modes properties, and their validation through a comparison with numerically computed acoustic modes. But, before going into the technical details of this analysis, we would like to summarise our results, emphasizing those that are practical for mode identification. These results were obtained for a sequence of uniformly rotating polytropic models, but we expect them to be qualitatively correct for a wider range of models. At high rotation rates, the frequency spectrum can be generically described as the superposition of an irregular frequency subset and of various regular frequency subsets, each showing specific patterns. This spectrum structure is significantly more complex than in the spherical case where all acoustic frequencies follow the same organisation as given by Tassoul's formula (Tassoul 1980). However, in the observed spectrum, only two frequency subsets are expected to dominate. One subset (the subset of island modes) shows regular patterns that are both similar to and different from those found in non-rotating stars. (It corresponds to the modes subset studied by Lignières et al. 2006; and Reese et al. 2008.) These modes are associated with rays whose dynamics is near-integrable and consequently asymptotic formulas describing their regular patterns can be derived. The second frequency subset (the subset of chaotic modes) is associated with chaotic rays. Although it does not follow a regular pattern, specific statistical properties of this frequency subset can be predicted. Besides, the asymptotic analysis provides an estimate of the proportion of mode in each subset. The transition from the non-rotating case occurs as follows. At moderate rotation, the regular subset of island modes is superposed on another regular subset (the subset of whispering gallery modes), which is a direct continuation of the non-rotating spectrum. At this stage, chaotic modes are rare and difficult to observe. As rotation increases, the number of chaotic modes increase, while whispering gallery modes become less and less visible. Obviously, such a priori information on the frequency spectrum should be useful for the mode identification. One should, however, keep in mind that the asymptotic analysis is not supposed to be accurate for the lowest frequency p-modes. Although a detailed study of the asymptotic analysis limit of validity has not been performed yet, numerical results indicate that the regular patterns are quite accurate down to 5th radial order (see Lignières et al. 2006; Reese 2007). At lower radial orders, the asymptotic mode classification in different subsets could still be applicable.

The paper is organised as follows. The equations governing the star model, the small perturbations about this model, the short-wavelength approximation of these perturbations, and the ray model for progressive acoustic waves are all presented in Sect. 2. A detailed numerical study of the acoustic ray dynamics was conducted for uniformly rotating polytropic models of stars.

The results are analysed in Sect. 3 using Poincaré surface of section, a standard tool for visualizing the phase space structure. It shows that, as rotation increases, the dynamics undergoes a transition from integrability (at zero rotation) to a mixed state where parts of the phase space display integrable behaviour and while other parts are chaotic.

We then relate the acoustic ray dynamics to the asymptotic properties of the acoustic modes (Sect. 4). We first summarize the results obtained in the context of quantum physics, distinguishing the cases where the Hamiltonian system is integrable, fully chaotic, or of mixed nature. In accordance with this theory, we show that the asymptotic acoustic spectrum of the uniformly rotating polytropic models of stars is a superposition of regular frequency patterns and irregular frequency subsets, respectively associated with near-integrable and chaotic phase space regions. The average number of modes associated with each phase space region depends directly on its volume (in phase space). These predictions are then successfully compared with the actual properties of high-frequency acoustic modes computed for a particular fast-rotating stellar model.

In Sect. 5, after a critical discussion of the assumptions of the asymptotic analysis, we show how our results can be used for the mode identification and for the seismic studies of rapidly rotating stars. The conclusion is given in Sect. 6.

The present work complements and extends a short recent paper (Lignières & Georgeot 2008) by giving all the details needed for the analysis and by presenting new results concerning (i) the ray dynamics at different rotation rates and for non-vanishing values of the angular momentum projection onto the rotation axis L_z; (ii) the analysis of extra regular patterns visible for some specific values of rotation; (iii) the number of modes in each frequency subset predicted by the asymptotic analysis; and (iv) the visibility of the chaotic modes.

2. Formalism and numerical methods

In this section we present the equations governing the star model (Sect. 2.1), the small perturbations about this model (Sect. 2.2), the short-wavelength approximation of these perturbations (Sect. 2.3) and the ray model for progressive acoustic waves (Sect. 2.4). The numerical method used to compute the ray trajectories is described in Sect. 2.5. The oscillation modes

were computed with the code described in Lignières et al. (2006) and Reese et al. (2006).

2.1. Polytropic model of rotating star

The model is a self-gravitating uniformly rotating monatomic gas ($\Gamma = 5/3$) that verifies a polytropic relation assumed to give a reasonably good approximation of the relation between the pressure and the density in the star (Hansen 1994):

$$P_0 = K\rho_0^{1+1/\mu} \quad (1)$$

$$0 = -\nabla P_0 - \rho_0 \nabla \left(\psi_0 - \Omega^2 w^2/2\right) \quad (2)$$

$$\Delta\psi_0 = 4\pi G\rho_0 \quad (3)$$

where P_0 is the pressure, ρ_0 the density, K the polytropic constant, μ the polytropic index, ψ_0 the gravitational potential, Ω the rotation rate, w the distance to the rotation axis, and G the gravitational constant.

The uniform rotation ensures that the fluid is barotropic. A pseudo-enthalpy can then be introduced $h_0 = \int \mathrm{d}P_0/\rho_0 = (1+\mu)P_0/\rho_0$ and the integration of the hydrostatic equation reads:

$$h_0 = h_\mathrm{c} - (\psi_0 - \psi_\mathrm{c}) + \frac{1}{2}\Omega^2 w^2 \quad (4)$$

where the subscript "c" denotes the value in the centre of the polytropic model. Equation (4) is then inserted into Poisson's equation to yield

$$\Delta\psi_0 = 4\pi G\rho_\mathrm{c}\left(1 - \frac{\psi_0 - \psi_\mathrm{c}}{h_\mathrm{c}} + \frac{\Omega^2 d^2}{2h_\mathrm{c}}\right)^\mu. \quad (5)$$

Equation (5) is solved numerically with an iterative scheme, as described in Rieutord et al. (2005).

Specifying the mass and the rotation rate of the star is not sufficient to determine the polytropic model in physical units. This requires fixing an additional parameter, for example, the stellar radius (see Hansen 1994; for the non-rotating case and see Christensen-Dalsgaard & Thompson 1999, for a brief discussion of a suitable parameter choice for rotating stars). In the following, however, we only present dimensionless quantities that do not depend on the choice of this additional parameter. The rotation rate Ω is compared to $\Omega_K = \left(GM/R_\mathrm{e}^3\right)^{1/2}$ the limiting rotation rate for which the centrifugal acceleration equals the gravity at the equator, M being the stellar mass and R_e the equatorial radius. The star flatness is $\epsilon = 1 - R_\mathrm{p}/R_\mathrm{e}$ where R_p is the polar radius. The acoustic frequencies shall be expressed in terms of $\omega_0 = \left(GM/R_\mathrm{p}^3\right)^{1/2}$, the inverse of a dynamical timescale, or ω_1 the lowest acoustic mode frequency of the stellar model considered.

2.2. Perturbation equations and boundary conditions

Time-harmonic small amplitude perturbations of the star model are studied under two basic assumptions. The first is to neglect the Coriolis force. This a natural assumption to study high-frequency acoustic modes since the oscillation timescale is asymptotically much shorter than the Coriolis force timescale $1/(2\Omega)$. Moreover, complete calculations by Reese et al. (2006, see Fig. 6 of this paper) have shown that Coriolis force effects on the frequency are already very weak for a relatively low radial order (say $n \approx 5$). The second basic assumption is to neglect the viscosity and the non-adiabatic effects. This is a standard approximation in the asymptotic analysis since these effects have little influence on the value of the frequency. Both assumptions have important consequences on the acoustic ray dynamics described below. Neglecting the Coriolis force ensures that the dynamics is symmetric with respect to the time reversal while the absence of diffusion processes makes the dynamics conservative. Finally, the Cowling approximation that is valid for high frequencies enables neglecting the perturbation of the gravitational potential. Under these assumptions, the linear equations governing the evolution of small amplitude perturbations read:

$$\partial_t\rho + \nabla\cdot(\rho_0\boldsymbol{u}) = 0, \quad (6)$$

$$\rho_0\partial_t\boldsymbol{u} = -\nabla P + \rho\boldsymbol{g}_0, \quad (7)$$

$$\partial_t P + \boldsymbol{u}\cdot\nabla P_0 = c_\mathrm{s}^2\ (\partial_t\rho + \boldsymbol{u}\cdot\nabla\rho_0), \quad (8)$$

where $\boldsymbol{u}$, ρ, and P, are respectively the Eulerian perturbations of velocity, density and pressure. The sound speed is $c_\mathrm{s} = \sqrt{\Gamma P_0/\rho_0}$, with Γ the first adiabatic exponent of the gas, and $\boldsymbol{g}_0 = -\nabla\left(\psi_0 - \Omega^2 w^2/2\right)$ the effective gravity.

As in Pekeris (1938), because the pressure and the temperature of the stellar model is zero at the surface, the only condition to impose on the perturbations is to be regular everywhere.

2.3. The short-wavelength approximation of the perturbation equations

The acoustic ray model results from a short-wavelength approximation of the perturbation Eqs. (6)–(8), called the Wentzel-Kramers-Brillouin (WKB) approximation. Time-harmonic wave-like solutions of the form

$$\Psi = \Re\{A(\boldsymbol{x})\exp[\mathrm{i}\Phi(\boldsymbol{x}) - \mathrm{i}\omega t]\} = \Re\{\hat{\Psi}(\boldsymbol{x})\exp(-\mathrm{i}\omega t)\} \quad (9)$$

are sought under the assumption that their wavelength is much shorter than the typical lengthscale of the background medium. As discussed by Gough (1993), one expects a better approximation if the starting Eqs. (6)–(8) are first reduced to a so-called normal form that avoids first-order derivatives. This is done in Sect. A.1 leading to

$$\frac{\omega_\mathrm{c}^2 - \omega^2}{c_\mathrm{s}^2}\hat{\Psi} + \frac{N_0^2}{\omega^2}\left[\Delta - \frac{1}{g_0^2}(\boldsymbol{g}_0\cdot\nabla)(\boldsymbol{g}_0\cdot\nabla)\right]\hat{\Psi} = \Delta\hat{\Psi} \quad (10)$$

where $\hat{\Psi} = \hat{P}/\alpha$, $\hat{P}$ is the complex amplitude associated with the pressure perturbation $P = \Re\{\hat{P}\exp(-\mathrm{i}\omega t)\}$ and α is a function of the background star model given by Eq. (A.8). The expressions of the cut-off frequency ω_c and the Brunt-Väisälä frequency N_0 are given respectively by (A.5) and (A.3). The two left hand-side terms of Eq. (10) account for acoustic and gravity waves, respectively.

As explained in Sect. A.2, the WKB approximation is then applied to (10). The dominant term of the expansion in powers of the ratio between the wavelength solution and the background typical lengthscale yields an equation governing the phase $\Phi(\boldsymbol{x})$, the so-called eikonal equation. The amplitude $A(\boldsymbol{x})$ is determined at the next order as a function of $\Phi(\boldsymbol{x})$. By neglecting the gravity waves by taking the high-frequency limit, the eikonal equation reads:

$$\omega^2 = \omega_\mathrm{c}^2 + c_\mathrm{s}^2 k^2 \quad (11)$$

where $\boldsymbol{k} = \nabla\Phi$ is the wavevector. Moreover, for a polytropic model of star and using the approximation $\omega \gg N_0$ valid for

high-frequency acoustic modes, the function α is proportional to $\rho_0^{1/2}$ and the cut-off frequency ω_c is simplified to

$$\omega_c^2 = \left[\frac{\Gamma\mu(\mu+2)}{2(\mu+1)} - 2\right]\frac{g_0^2}{2h_0} + \frac{1}{2}\left(2 - \frac{\Gamma\mu}{\mu+1}\right)\boldsymbol{\nabla}\cdot\boldsymbol{g}_0. \quad (12)$$

In the range of high-frequency acoustic modes, the ω_c term is expected to be much smaller than ω in most parts of the star except near the surface where ω_c diverges. Note also that, despite the chosen notation, ω_c^2 can be negative near the centre.

2.4. The acoustic ray model as a Hamiltonian system

The acoustic ray model consists in finding solutions to the eikonal Eq. (11) along some path called the ray path. This problem can be written in a Hamiltonian form where the solutions $(\boldsymbol{x}(t), \boldsymbol{k}(t))$ are conjugate variables of the Hamiltonian and t, the parameter along the path, is a time-like variable. To derive the Hamiltonian equations from the eikonal equation, one can apply a procedure valid for a general eikonal equation $D(\boldsymbol{k}, \omega, \boldsymbol{x}) = 0$ (e.g. Ott 1993). This leads to the Hamiltonian $H' = \omega = \sqrt{c_s^2\boldsymbol{k}^2 + \omega_c^2}$ (e.g. Lighthill 1978). Another useful Hamiltonian formulation can be readily obtained by considering a path normal to the wavefront $\Phi(\boldsymbol{x}) = \text{const}$. This method is also used to determine optical rays in isotropic media of variable index (Born 1999), the quantity $(\sqrt{1-\omega_c^2/\omega^2})/c_s$ playing the role of the medium index $n(\boldsymbol{x})$. The ray path is thus defined by

$$\frac{\mathrm{d}\boldsymbol{x}}{\mathrm{d}s} = \frac{\boldsymbol{k}}{\|\boldsymbol{k}\|} = \frac{\boldsymbol{\nabla}\Phi}{\|\boldsymbol{\nabla}\Phi\|} \quad (13)$$

where s is the curvilinear coordinate along the ray. Differentiating (13) and using (11) then leads to the following system of ODEs:

$$\frac{\mathrm{d}\boldsymbol{x}}{\mathrm{d}t} = \tilde{\boldsymbol{k}} \quad (14)$$

$$\frac{\mathrm{d}\tilde{\boldsymbol{k}}}{\mathrm{d}t} = -\boldsymbol{\nabla}W \quad (15)$$

$$W = -\frac{1}{2c_s^2}\left(1 - \frac{\omega_c^2}{\omega^2}\right) \quad (16)$$

where we use the frequency-scaled wavevector $\tilde{\boldsymbol{k}} = \boldsymbol{k}/\omega$ and the time-like variable t such that $\mathrm{d}t = c_s\mathrm{d}s/(1-\omega_c^2/\omega^2)^{1/2}$.

As W only depends on the spatial variable $\boldsymbol{x}$, the second equation has the classical form of Newton's second law for the conservative force associated with the potential W (for a unit mass and a time variable t). This system can thus be written in a Hamiltonian form where

$$H = \frac{\tilde{\boldsymbol{k}}^2}{2} + W(\boldsymbol{x}) \quad (17)$$

is the Hamiltonian. According to the eikonal Eq. (11), H is equal to zero and the dynamics is therefore fully determined by the potential well W, where frequency ω appears as a parameter. As $\omega \gg \omega_c$ away from the near surface layers, the potential increase towards the star centre is given by the sound speed increase. Close to the surface, the potential barrier is due to the sharp increase in ω_c and provokes the wave back-reflection. While the location of the reflection surface depends on the frequency ω, we found that the dynamics is not strongly dependent on ω in the range of high-frequency acoustic modes considered here. This can be expected since, as ω_c diverges towards the surface of the polytropic model of star, the location of $\omega = \omega_c$ does not vary rapidly with ω.

Because the potential is symmetric with respect to the rotation axis of the star, the angular momentum projection on this axis $\tilde{L}_z = r\sin\theta\tilde{k}_\phi$ is a constant of motion, where $\tilde{k}_\phi = \tilde{\boldsymbol{k}}\cdot\boldsymbol{e}_\phi$ and $\boldsymbol{e}_\phi$ is a unit vector in the azimuthal direction and $[r, \theta, \phi]$ are the spherical coordinates. Consequently, the projection of the ray trajectory on the meridional plane rotating with the ray at an angular velocity $\mathrm{d}\phi/\mathrm{d}t = \tilde{L}_z/(r\sin\theta)^2$ is governed by the two-degree-of-freedom Hamiltonian:

$$H_r = \frac{\tilde{\boldsymbol{k}}_p^2}{2} + W_r(\boldsymbol{x}) \quad (18)$$

where $\tilde{\boldsymbol{k}}_p = \tilde{\boldsymbol{k}} - \tilde{k}_\phi\boldsymbol{e}_\phi$ is the wavevector projected onto the rotating meridional plane and W_r the effective potential of the reduced Hamiltonian H_r which now also depends on $\tilde{L}_z$ as a parameter

$$W_r(\boldsymbol{x}) = \frac{\tilde{L}_z^2}{2(r\sin\theta)^2} - \frac{1}{2c_s^2}\left(1 - \frac{\omega_c^2}{\omega^2}\right). \quad (19)$$

2.5. Numerical method for the ray dynamics

The acoustic ray dynamics has been investigated by integrating numerically Eqs. (14) and (15) using a 5th-order Runge-Kutta method. The step size of the integration is chosen automatically to keep the local error estimate smaller than a given tolerance. To what extent this control of the local error ensures that the numerical solution is close to the true solution depends on the stability of the problem. For chaotic trajectories, the numerical error tends to grow rapidly, while for stable trajectories this error remains of the same order as the relative error. The rapid growth of numerical errors is one of the characteristics of chaotic dynamics; however, this does not prevent simulating such systems since for hyperbolic systems the shadowing theorem (Anosov 1967; Sauer et al. 1997) ensures that an exact trajectory will remain close to the dynamics of each computed point for arbitrary times. Thus while a numerical trajectory diverges from the exact one, it nevertheless remains close to another exact trajectory, and therefore numerical errors do not prevent obtaining accurate phase space plots. We checked that the Poincaré surfaces of section shown in the next section are not significantly modified by decreasing the maximum allowed local error. We also checked the influence of the resolution of the background polytropic stellar model. Increasing this resolution from 62 to 92 Gauss-Lobatto points in the pseudo-radial direction has no significant effect on the Poincaré surface of section. Finally, the Hamiltonian conservation is used as an independent accuracy test of the computation.

3. Acoustic ray dynamics in rotating stars

In this section, we show that rotation strongly modifies the acoustic ray dynamics. Indeed, we find that, as rotation increases, the dynamics undergoes a transition from integrability (at zero rotation) to a mixed state where parts of the phase space display integrable behaviour while other parts are chaotic.

The nature of a dynamical system is best investigated by considering the structure of its phase space which contains both position and momentum coordinates. We thus first introduce the Poincaré surface of section (hereafter the PSS) which is a standard tool to visualize the phase space (Sect. 3.1). Then we describe the phase space structure at zero rotation (Sect. 3.2) and the main features of the generic phase space structure at high

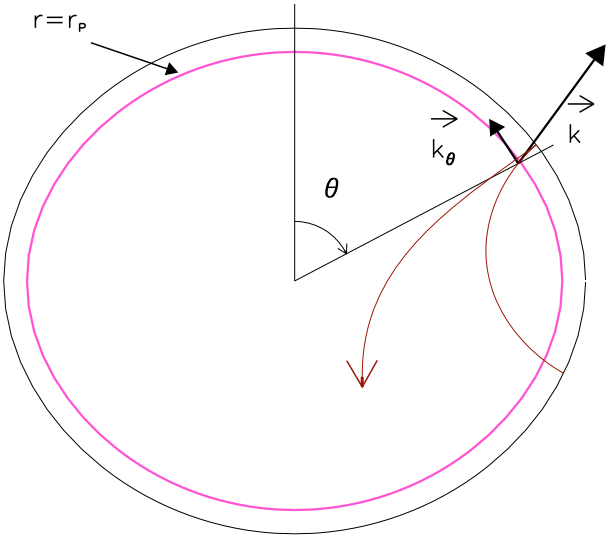

Fig. 1. (Colour online) Intersection of an outgoing acoustic ray (red/arrow headed) with the $r = r_{\rm p}(\theta)$ curve (magenta/thick). The point on the associated PSS is specified by the colatitude θ and the scaled latitudinal wavenumber component k_θ/ω at the intersection.

rotation rates (Sect. 3.3). The detail of the transition to chaos as rotation increases is analysed in Sect. 3.4. As this last section makes use of several specific tools and theorems of dynamical system theory, it might be skipped at first reading.

3.1. Phase space visualization: the Poincaré surface of section

As shown in Sect. 2.4, acoustic rays with a given L_z are governed by a Hamiltonian with two degrees of freedom $H_{\rm r}$. The associated phase space is therefore four-dimensional and difficult to visualize. A PSS is constructed by computing the intersection of the phase space trajectories with a chosen $(2N-1)$-dimensional surface, where N is the number of degrees of freedom of the system. If H is time-independent, then energy conservation implies that phase space trajectories stay on a $(2N-1)$-dimensional surface. The PSS is thus a $(2N-2)$-dimensional surface in general and a 2-dimensional surface in the present case.

Different choices are possible for the PSS, although some conditions are required to obtain a good description of the dynamics (see for example Ott 1993). First, to provide a complete view of phase space, the PSS must be intersected by all phase space trajectories. Here we chose the curve $r_{\rm p}(\theta) = r_{\rm s}(\theta) - d$ situated at a fixed radial distance d from the stellar surface $r_{\rm s}(\theta)$ displayed in Fig. 1. As shown in Sect. B.1 for the non-rotating case, the distance d can be chosen such that all relevant trajectories intersect this curve. The second condition is that, given a point on the PSS, the next point on the PSS has to be uniquely determined. This is ensured by counting the intersection with $r_{\rm p}(\theta) = r_{\rm s}(\theta) - d$ only when the trajectory comes from one side of the $r = r_{\rm p}(\theta)$ curve. (Here we consider the trajectories coming from the inner side.) Finally, the coordinate system used to display the PSS is chosen so that any surface of the PSS is conserved by the dynamics in the same way as four-dimensional volumes are preserved in phase space. The coordinates $[\theta, \tilde{k}_\theta]$ where $\tilde{k}_\theta$ is the latitudinal component of $\tilde{\boldsymbol{k}}$ in the natural basis $(\boldsymbol{E}^\zeta, \boldsymbol{E}^\theta, \boldsymbol{E}^\phi)$ associated with the coordinate system $[\zeta = r_{\rm s}(\theta) - r, \theta, \phi]$ fulfil this condition (as shown in Sect. B.2).

The PSS have been obtained by following many trajectories of different initial conditions. The number of trajectories, together with the time during which they are computed, determine the resolution by which the phase space is investigated. In principle, we should display PSS computed for different values of frequency ω. However, as ω is varied in the range of frequency considered here, we found that the PSS remained practically unchanged. As discussed in Sect. 2.4, this stems from the dynamics of the frequency-scaled wavevector $\boldsymbol{k}/\omega$ being weakly dependent on ω in this frequency range.

3.2. The non-rotating case $\Omega = 0$

The PSS at $\Omega = 0$ is described in this section. It will serve as a reference to investigate the evolution of the dynamics with rotation. Due to spherical symmetry, the norm of the angular momentum with respect to the star centre

$$\tilde{L} = \sqrt{\tilde{k}_\theta^2 + \left(\frac{\tilde{L}_z}{\sin\theta}\right)^2} \tag{20}$$

is a conserved quantity. It follows that the intersection of any trajectory with the PSS belongs to a curve of the form

$$\tilde{k}_\theta^2 = \tilde{L}^2 - \left(\frac{\tilde{L}_z}{\sin\theta}\right)^2 . \tag{21}$$

For $\tilde{L}_z = 0$, these are the two straight lines $\tilde{k}_\theta = \pm\tilde{L}$ (see Fig. 3), while Eq. (21) yields a closed curve for $\tilde{L}_z \neq 0$, the trajectories being constrained to latitudes less than $\arcsin(|\tilde{L}_z|/\tilde{L})$ (see Fig. 5). This curve varies from a near rectangle to an ellipse as $\tilde{L}_z$ grows from 0^+ to $\tilde{L}$.

The simplicity of the PSS reflects that the system is integrable ((20) indeed provides the second invariant (in addition to $H_{\rm r}$) of the reduced two-degree-of-freedom dynamical system). Every integrable system is structured in N-dimensional surfaces that are associated with specific values of the N constants of motion. This means that any trajectory is constrained to stay on one of these surfaces forever. They are called invariant tori because they are invariant through the dynamics and have a torus-like topology. As we verify in the following, they play a crucial role in the transition to chaos, as well as in the mode construction. The PSS at $\Omega = 0$ actually visualize the intersection of these tori with the $r = r_{\rm p}$ surface.

Important is that the invariant tori can have two different types that determine their fate once the rotation is increased. Rational (or resonant) tori are such that all trajectories on the torus are periodic orbits (i.e. trajectories that close on themselves in phase space). In contrast, irrational tori are such that any trajectory densely covers the whole torus.

3.3. Phase space structure at high rotation rates

The main features of the phase space at high rotation rates are shown in Fig. 2 where the PSS at $\Omega = 0.59\Omega_K$ is displayed with four acoustic rays shown on the position space, as well as on the PSS. These rays belong to the three different types of phase space structures always present at high rotation rates. First, a large chaotic region appears (the grey region in Fig. 2). Chaotic rays, e.g. the red ray, are not constrained to stay on tori (that is on one-dimensional curves on the PSS) and thus fill up a phase space volume densely and ergodically (i.e. a surface on the PSS). Second, the island chain embedded in the large chaotic region is a common structure of phase space at high rotation rate.

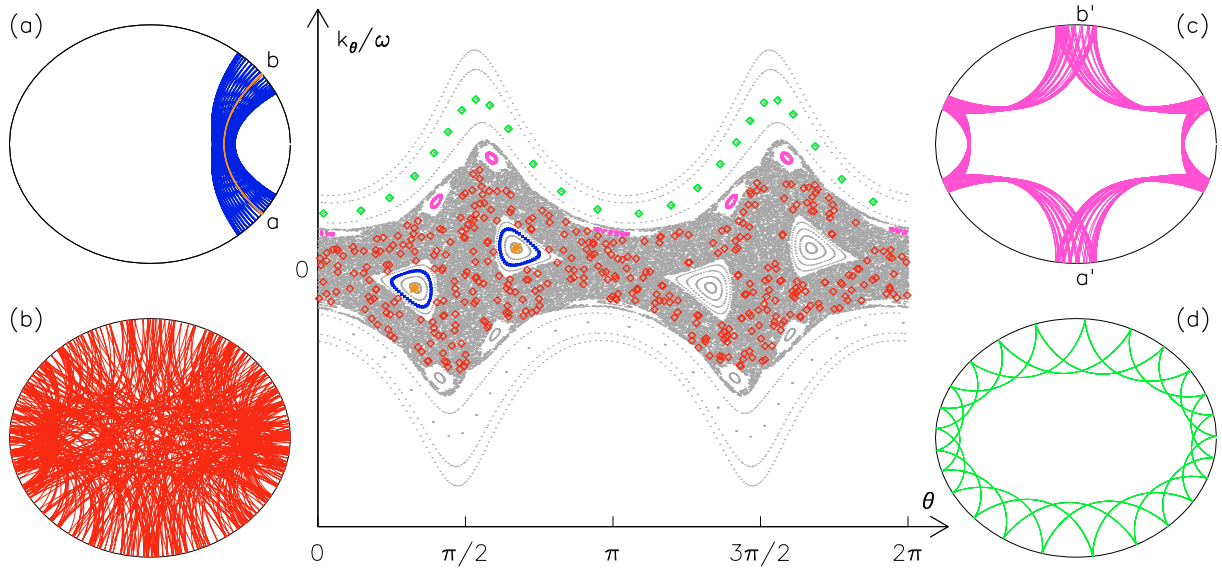

Fig. 2. (Colour online) PSS at $\Omega = 0.59\Omega_K$ and typical acoustic rays associated with the four main phase space structures: **a)** a 2-period island ray (blue/dark grey) and the associated periodic orbit with endpoints a and b (orange/light grey), **b)** a chaotic ray (red/grey), **c)** a 6-period island ray (magenta/light grey) and **d)** a whispering gallery ray (green/light grey). On the PSS, (coloured/grey) symbols (diamonds for the chaotic and whispering gallery rays, crosses for the 2-period and 6-period island rays) specify the points where these trajectories cross the PSS.

An important property of the island chain is to be structured by invariant tori centred on the periodic orbit of period 2 (the orange ray). The PSS also shows smaller island chains like the one formed around a 6-period periodic orbit (see the magenta ray). However, contrary to the 2-period island chain, such structures survive only up to a certain rotation rate. Third, the undulated curves present in the high $\tilde{k}_\theta$ region are formed by whispering gallery type trajectories (like the green ray), that is trajectories following the outer boundary. The associated tori correspond to the deformation of non-rotating tori that have not been destroyed yet at this rotation rate. Overall this type of phase space organisation is typical of mixed systems with coexistence of chaotic regions and invariant tori (the structures encountered in integrable systems).

The main phase space structures are dynamically independent since no trajectory can cross from one region to the next. We show in Sect. 4 that the very existence of these structures enables the spectrum to be organised into independent frequency subsets. In the next section, the generic character of these structures is checked by computing the PSS at different rotations.

3.4. Transition to chaos $\Omega \neq 0$

The evolution of the dynamics with increased rotation is first described for $\tilde{L}_z = 0$ and then for $\tilde{L}_z \neq 0$.

3.4.1. The $\tilde{L}_z = 0$ case

The PSS computed at the three rotation rates $\Omega/\Omega_K = [0, 0.15, 0.32]$ corresponding to the three flatness $\epsilon = [0, 0.01, 0.05]$ are displayed in Fig. 3 to illustrate the effect of a small centrifugal deformation on the ray dynamics. This perturbation of the integrable $\Omega = 0$ system is very similar to one described by the KAM-theorem (Chirikov 1979; Giannoni et al. 1991; Ott 1993; Gutzwiller 1990; Lichtenberg & Lieberman 1992; Lazutkin 1993). Indeed, for a smooth, small perturbation of an integrable Hamiltonian, this theorem states that the tori of the integrable system that survived the perturbation occupy most of the phase space volume. More specifically, while being continuously perturbed, most of the irrational tori can still be associated with N invariants, thus keeping their torus structure. This is the case for the undulated lines observed in the high $\tilde{k}_\theta$ domain of Fig. 3. In contrast, all rational tori are immediately destroyed for a non-vanishing perturbation. The KAM theorem implies that, despite the destroyed rational tori forming a dense set in the phase space, the volume they occupy vanishes as the perturbation goes to zero.

The theory of KAM-type transition to chaos also describes how resonant tori disappear. In our case, they correspond to one-dimensional curves on the PSS, formed by families of periodic orbits. All orbits of the same torus will have the same period q. The so-called Poincaré-Birkhoff theorem predicts that a (smooth) small perturbation will transform this one-dimensional curve into a chain of q stable points belonging to the same periodic orbit and surrounded by stable islands, intertwined with q unstable periodic points. A small chaotic zone appears in the vicinity of the unstable fixed points and grows with the perturbation. The stable islands have themselves an intricate self-similar structure of small island chains surrounded by invariant structure (tori). This phenomenon is illustrated at $\Omega/\Omega_K = 0.15$ in Fig. 3 where, near the $\tilde{k}_\theta = 0$ curve, we can observe the 2-period island chain around the $q = 2$ stable periodic points and the small chaotic region around the corresponding unstable points. This results from the destabilization of the resonant torus associated with the periodic orbits along the diameters of the spherical star. The widths of the island chains (resonance width) are expected to be approximately proportional to the square root of the perturbation, and they decrease with q.

What occurs for large perturbations following the KAM-type transition of integrable Hamiltonians has been studied in many systems. The general phenomenology that emerges also corresponds to what we observe in our system for increased rotation (see the PSS of Fig. 4 computed for $\Omega/\Omega_K = [0.32, 0.59, 0.81]$ corresponding to the flatness $\epsilon = [0.05, 0.15, 0.25]$). The surviving irrational tori, as well as the island chains, are progressively destroyed. This leads to the enlargement of the chaotic regions that were originally confined by these tori. This is illustrated in

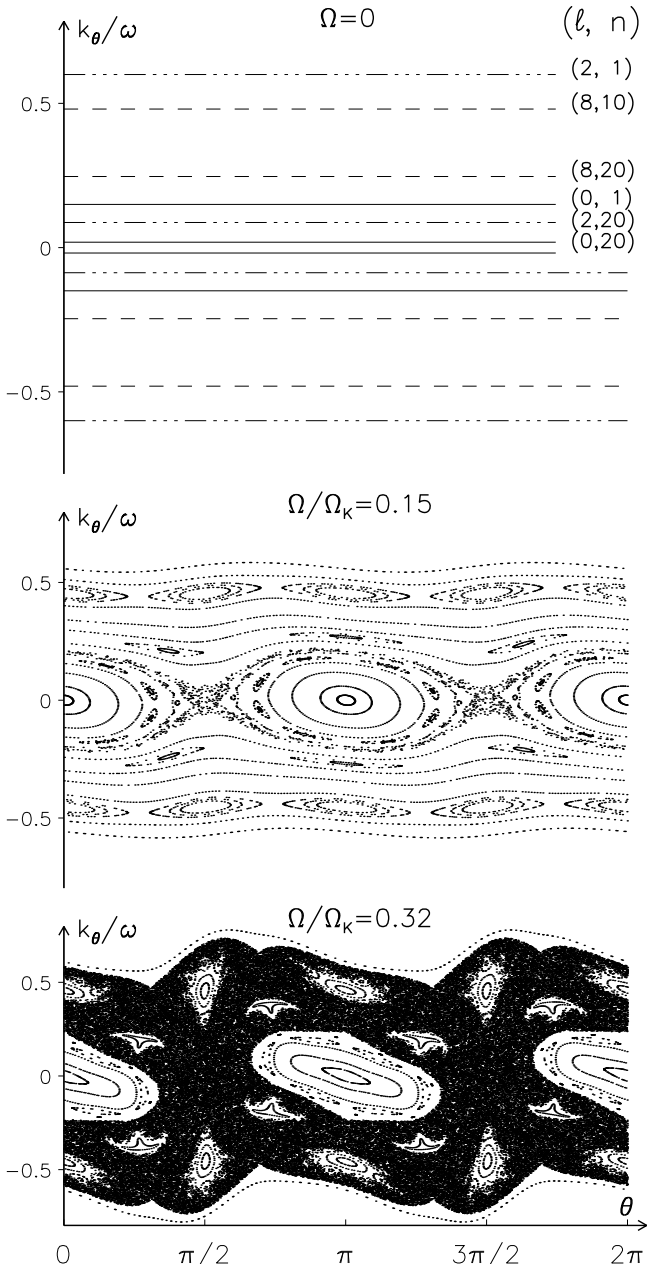

Fig. 3. Three $\tilde{L}_z = 0$ PSS at low rotation rates showing the transition to chaos. The unit of k_θ/ω is ω_0^{-1}. Island chains and chaotic regions respectively appear around stable and unstable periodic orbits. On the $\Omega = 0$ PSS, the straight lines correspond to intersections with mode-carrying-tori specified by the degree and radial order of the mode.

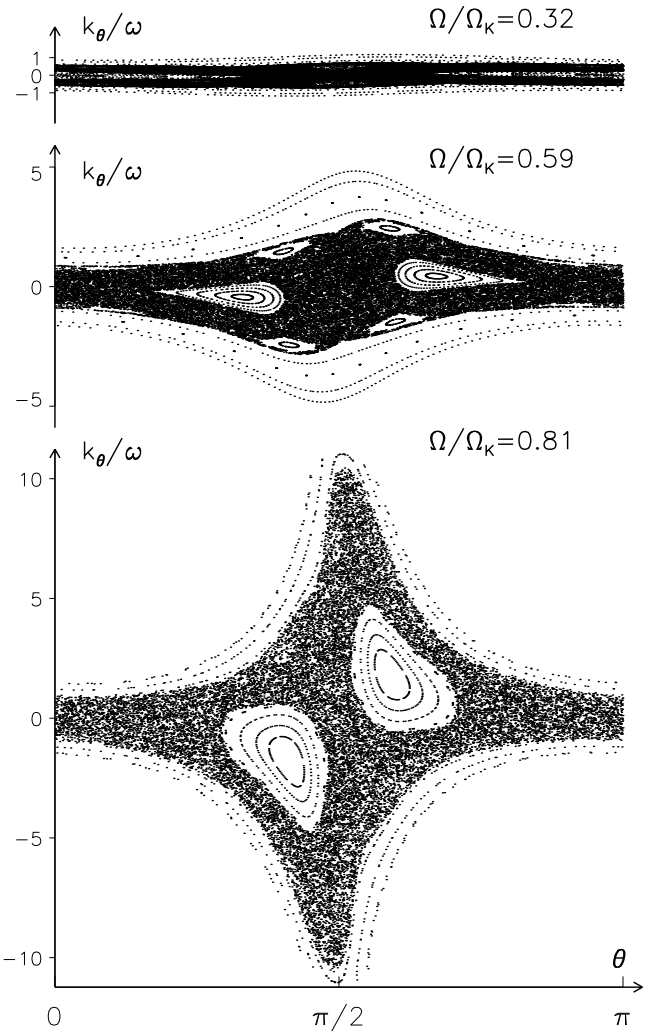

Fig. 4. Three $\tilde{L}_z = 0$ PSS visualizing the evolution of phase space as a function of rotation. All these PSS show the 2-period periodic orbit island chain embedded in a central chaotic region. As rotation increases, the 2-period island chain moves towards the equator while the central chaotic region enlarges. Note that the first $\Omega = 0.32\Omega_K$ PSS is displayed with a different scale in Fig. 3. The units are the same as in Fig. 3.

Figs. 3 and 4 where the surface of the central chaotic region becomes progressively larger with rotation. The island chains typically undergo a series of bifurcations for increasing perturbation. The most common bifurcation is the period-doubling one, where a stable periodic orbit of period q is changed to an unstable orbit plus a stable orbit of period $2q$. As the sequence of bifurcations goes on, stable orbits have longer and longer periods until they eventually disappear. The destruction of stable regions is visible between $\Omega = 0.59\Omega_K$ and $\Omega = 0.81\Omega_K$ (Fig. 4), as the 6-period island chain embedded in the chaotic central region at $\Omega = 0.59\Omega_K$ has disappeared at higher rotation. As mentioned above, that the largest stable island originates from a short periodic orbit (here a 2-period periodic orbit) is also a common feature of the KAM-type transitions to chaos.

While not visible in this figure, a zoom on other regions of the PSS would show the same process going on at small scales. It is however clear that the irrational tori associated with high values of $\tilde{L}$ survive longer. This property is also encountered in classical billiards (Lazutkin 1993), where tori close to the billiard boundary are the most robust.

3.4.2. The $\tilde{L}_z \neq 0$ case

Qualitatively, the transition to chaos is very similar to the $\tilde{L}_z = 0$ case. This is shown in Fig. 5 where PSS computed for $\tilde{L}_z = 0.4/\omega_0$ are shown for increased rotation. The main effect of increasing $\tilde{L}_z$ is to delay the transition towards chaos to higher rotation rates. Indeed by comparing PSS computed at the same rotation rate (see Figs. 4 and 5), one observes that the central chaotic region is more constrained by surviving tori for higher $\tilde{L}_z$ values. For example at $\Omega = 0.32\Omega_K$ the central chaotic region is much more developed for $\tilde{L}_z = 0$ than for $\tilde{L}_z = 0.4/\omega_0$. The $\Omega = 0.59\Omega_K$ PSS provides another example since for $\tilde{L}_z = 0.4/\omega_0$ the island chain associated with the 6-period orbit is separated by a surviving KAM tori from the central chaotic

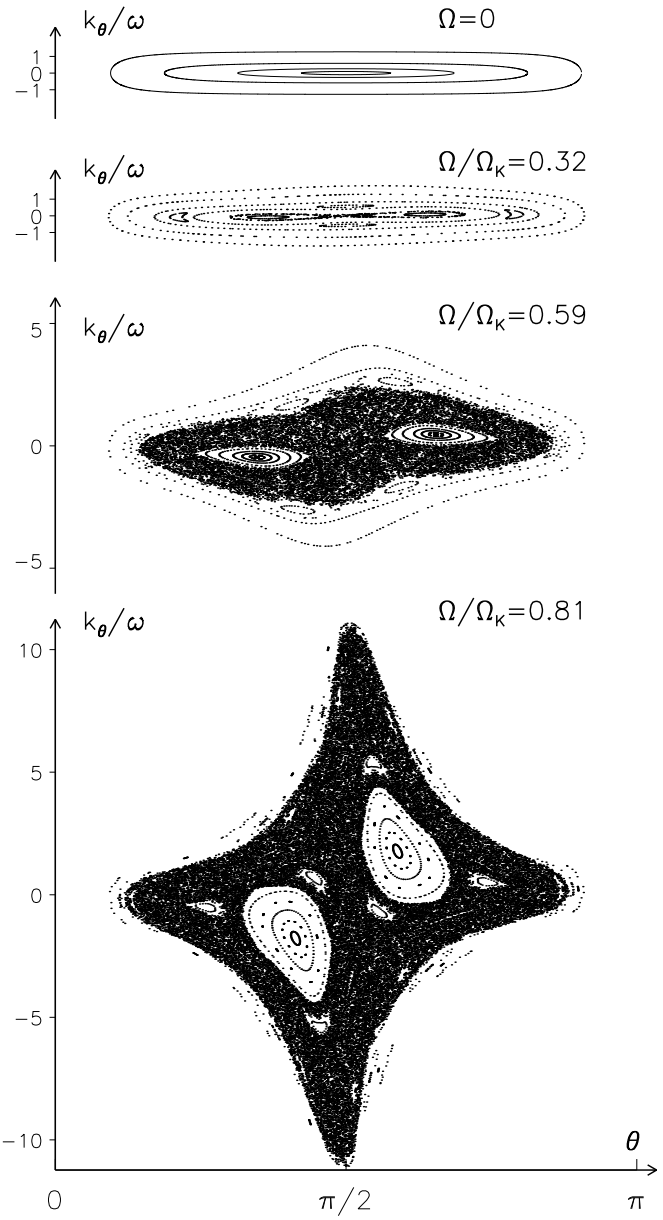

Fig. 5. Three $\tilde{L}_z = 0.4/\omega_0$ PSS visualizing the evolution of phase space as a function of rotation. The evolution is qualitatively similar to the $\tilde{L}_z = 0$ case, although the enlargement of the central chaotic region occurs at higher rotation rates. Same units as in Fig. 3.

region, while such a stable structure has already been destroyed for $\tilde{L}_z = 0$. Finally, at $\Omega = 0.81\Omega_K$, we can observe that the central chaotic region for $\tilde{L}_z = 0.4/\omega_0$ contains visible surviving structures, while this is not the case for $\tilde{L}_z = 0$.

The slower transition to chaos can be interpreted as caused by the angular constraint $-\arcsin(|\tilde{L}_z|/\tilde{L}) < \theta < \arcsin(|\tilde{L}_z|/\tilde{L})$ imposed on the dynamics. This is compatible with the trajectories for infinite $\tilde{L}_z$ being confined to the equatorial plane, and the dynamics becoming integrable because of the circular symmetry of this asymptotic limit.

4. The asymptotic properties of the acoustic modes

In this section, we show that ray dynamics provides a qualitative and quantitative understanding of the high-frequency acoustic modes. The question to be addressed is how to construct modes, i.e. standing waves, from the short-wavelength propagating waves described by ray dynamics. Such mode construction is expected to be approximately valid in the asymptotic regime of high frequencies. (This asymptotic regime is called the semi-classical regime in a quantum physics context.) As mentioned in the introduction, the answer depends on the nature of the Hamiltonian system. For integrable systems, each phase space trajectory remains on an invariant torus and this enables the construction of modes from a positively interfering superposition of these travelling waves on the torus. This is no longer the case for chaotic systems, where the ray dynamics provides no invariant structures on which to build modes.

Thus for integrable systems, the modes and the frequencies can in principle be explicitly determined from the acoustic rays through well-known formulas called Einstein-Brillouin-Keller (EBK) quantization after the name of its main contributors. We recall the results obtained by Gough (1993) when applying the EBK method to spherical stars (Sect. 4.1). While this procedure is not applicable to chaotic systems, other concepts and methods have been developed and tested in quantum physics to interpret the non-integrable dynamics. These concepts have also been applied to other wave phenomena, such as those observed in e.g. microwave resonators (Stöckmann & Stein 1990), lasing cavities (Nöckel & Stone 1997), quartz blocks (Ellegaard et al. 1996), and underwater waves (Brown et al. 2003). Their potential interest for helioseismology has been suggested, although not demonstrated, by Perdang (1988) and Kosovichev & Perdang (1988). Here, we apply them to the non-integrable ray dynamics of rapidly rotating stars. More specifically, we have seen in Sect. 3 that the ray dynamics of such stars corresponds to a mixed system where parts of phase space display integrable behaviour and other parts chaotic dynamics. In this case, the organisation/classification of modes in the semi-classical regime is expected to closely follow the structure of phase space. Near-integrable regions of phase space like the island chains are amenable to EBK quantization, leading to a regular frequency spectrum, while the modes originating in chaotic regions have an irregular frequency spectrum with generic statistical properties. Another important information provided by ray dynamics is the averaged number of modes that can be constructed from a given phase space region. This number is proportional to the volume of the region considered.

In the following, we explain these concepts and methods in the context of stellar acoustics (Sects. 4.1–4.3). Then, their relevance in describing the asymptotic properties of the acoustic modes is tested by comparing their predictions to the actual properties of high-frequency acoustic modes (Sects. 4.4–4.7). These modes are axisymmetric modes in the frequency range $[9\omega_1, 12\omega_1]$, ω_1 being the lowest acoustic mode frequency of the stellar model considered. They were computed for a $\Omega = 0.59\Omega_K$ uniformly rotating $\mu = 3$ polytropic model of star and under the same assumptions as for ray dynamics (adiabatic perturbations, no Coriolis acceleration, Cowling approximation).

4.1. The integrable case $\Omega = 0$

To build modes from the ray dynamics, the wave-like solution $\hat{\Psi} = A(\boldsymbol{x}) \exp[\mathrm{i}\Phi(\boldsymbol{x})]$ is regarded as a function of the phase space variables $\boldsymbol{x}, \boldsymbol{k} = \boldsymbol{\nabla}\Phi$ that is subsequently projected onto the position space. The condition that $\exp[\mathrm{i}\Phi(\boldsymbol{x})]$ be single-valued on the position space requires that, for any phase space trajectory that closes on itself in the position space, the variation in Φ along this closed contour is a multiple of 2π. As trajectories of an

integrable system stay on invariant tori, this condition leads to the EBK formula

$$\int_{C_j} \boldsymbol{k} \cdot \mathrm{d}\boldsymbol{x} = 2\pi\left(n_j + \frac{\beta_j}{4}\right) \tag{22}$$

where C_j is any closed contour on a given torus and n_j and β_j are non-negative integers. The integer β_i called the Maslov index is introduced to account for a $\pi/2$ phase lag that must be added each time the contour crosses a caustic. Indeed, the caustic corresponds to the boundary of the torus projection onto position space; the amplitude A taken in the position space is discontinuous there, leading to the $\pi/2$ phase loss (see Keller & Rubinow 1960, for details).

While this expression is valid for any closed contour on the torus, it can be shown that it gives the same condition for all contours that can be continuously deformed to the same one. Thus in fact the EBK quantization yields N independent conditions, as only N topologically independent closed paths exist on an N-dimensional torus. As these closed paths do not need to be actual trajectories of the dynamical system, the usual way to construct EBK solutions is to choose contours for which the formulas are simple to compute. The quantization conditions thus select a particular torus on which a mode can be built, irrespective of whether the torus is resonant or non-resonant. For spherical stars, three independent contours on a torus specified by L, L_z and ω can be obtained by varying one of the spherical coordinates and fixing the other two. Using similar contours, Gough (1993) obtained the three conditions:

$$\int_{r_\mathrm{i}}^{r_\mathrm{e}} \left(\frac{\omega^2 - \omega_\mathrm{c}^2}{c_\mathrm{s}^2} - \frac{L^2}{r^2}\right)^{1/2} \mathrm{d}r = \left(n - \frac{1}{2}\right)\pi, \quad L = \ell + \tfrac{1}{2}, \quad L_z = m \tag{23}$$

where n, ℓ, m are non negative integer, and r_i and r_e are the internal and external caustic respectively. Note that $L = \omega\tilde{L}$ and $L_z = \omega\tilde{L}_z$. The associated eigenmodes have also been explicitly constructed from the trajectories on the selected torus. As shown by Gough (1993), the result of this EBK quantization is practically identical to the usual asymptotic theory of acoustic modes in spherical stars, which uses the separability of the three-dimensional eigenvalue problem and a WKB approximation of the resulting 1-D boundary value problem in the radial direction (in the usual analysis, $L = \sqrt{\ell(\ell+1)}$, differs from the EBK result, especially at low ℓ values). This shows that the integers n, ℓ, m derived from the EBK quantization conditions do correspond to the order, degree, and the azimuthal number of the acoustic modes in spherical stars.

The tori on which the eigenmodes are constructed can be visualized on the PSS. For example, the $(\ell, n, m) = (8, 10, 0)$ mode is associated with the torus $\tilde{L} = \pm(\ell + 1/2)/\omega_{n,\ell,m}$, $\tilde{L}_z = 0$ and its imprint on the PSS are the straight lines $\tilde{k}_\theta = \pm\tilde{L}$. The intersection of various mode-carrying tori with the $\tilde{L}_z = 0$ PSS are shown in Fig. 3. High radial order modes approach the central $\tilde{k}_\theta = 0$ line, while high-degree modes occupy the high $\tilde{k}_\theta$ region.

4.2. Chaotic systems

It has been widely recognised in the past few decades that most dynamical systems are not integrable and therefore display various degrees of chaos. The quantum chaos field has studied quantum systems whose short-wavelength classical limit displays such chaotic behaviour. As recognised early by Einstein (1917), the EBK quantization explained in the above paragraph cannot be applied to these systems. Indeed, no N-dimensional invariant structure exists on which to apply conditions of constructive interference like the EBK condition. Rather, the semi-classical limit of these chaotic systems yields a Fourier-like formula that connects the set of all classical periodic orbits to the whole spectrum. This formula, called the Gutzwiller trace formula (Gutzwiller 1990) is much more delicate to use than EBK formulas, since it represents a divergent sum from which information can only be extracted through refined mathematical and numerical methods.

On the other hand, the very complexity of chaotic systems leads to statistical universalities. Indeed, in a similar way as statistical physics emerges from the random behaviour of individual particles, in chaotic systems the randomness induced by chaos leads to robust statistical properties of eigenmodes. In contrary to modes of integrable systems, which are localized on individual tori selected by the EBK conditions, in chaotic systems modes are generally not associated to a specific structure in phase space and are ergodic on the energy surface. It has been found that one can model such systems by replacing the Hamiltonian by a matrix whose entries are random variables with Gaussian distributions. Such ensembles of *random matrices*, which contain no free parameter but take the symmetries of the system into account, can give precise predictions, which have been found to accurately describe many statistical properties of the modes of systems with a chaotic classical limit. This has been conjectured and checked numerically for many systems (Bohigas et al. 1984; Giannoni et al. 1991).

The comparison with the predictions of the Random Matrix Theory (hereafter the RMT) is often done through the statistical analysis of the frequency spectrum. In general the density of modes as a function of the frequency

$$d(\omega) = \sum_n \delta(\omega - \omega_n) \tag{24}$$

where δ is the delta function, can be written as the sum of two functions

$$d(\omega) = d^{\mathrm{av}}(\omega) + d^{\mathrm{fluct}}(\omega). \tag{25}$$

The quantity $d^{\mathrm{av}}(\omega)$ (hereafter called the Weyl term) is a smooth function that describes the average density of modes at a given frequency. It has been known from the beginning of the twentieth century that this term can be calculated from general geometric features of the system such as phase space volume and therefore is independent of the chaotic or integrable nature of the dynamics ($d^{\mathrm{av}}(\omega)$ is estimated for stellar acoustic modes in Sect. 4.7). In contrast, the function d^{fluct} that describes the fluctuations around the mean position of eigenfrequencies strongly depends on the nature of the dynamics. (Most textbooks on this subject use the quantum physics terminology, that is "energy level" instead of frequency and "density of states" instead of density of modes.)

The spectra of integrable systems are predicted to be uncorrelated, and in general this leads to fluctuations given by the Poisson distribution (Berry & Tabor 1977). In contrast, for chaotic systems these fluctuations should be given by the RMT. The RMT has therefore been developed to analytically compute the predictions for specific quantities, which in turn could be compared to numerical data for real systems. A popular quantity to describe fluctuations in spectra is the *spacing distribution* $P(\delta)$, which is the distribution of spacings in frequency between consecutive eigenfrequencies, once the frequency differences have been rescaled by the Weyl term such that the average spacing is one. The function $P(\delta)$ measures the correlations at short distances in frequency in the spectrum. It does not

give information about all statistical properties, but it is nevertheless very useful since the predictions are strikingly different for the Poisson distribution and for the RMT. While the Poisson distribution corresponds to $P(\delta) = \exp(-\delta)$, the prediction of the RMT is the Wigner distribution $P(\delta) = \pi\delta/2\exp(-\pi\delta^2/4)$, which displays frequency repulsion (level repulsion in the quantum terminology) at short distances (small δ) and falls off faster than Poisson at large δ.

4.3. Mixed systems

We have seen in Sect. 3 that the acoustic ray dynamics in rotating stars has a mixed character as chaotic regions coexist with stables structures like island chains or invariant tori. Such mixed systems are actually the most common in nature, completely integrable and chaotic systems being limiting cases.

In the context of quantum chaos, seminal studies of these systems by Percival (1973) and Berry & Robnik (1984) led to conjecture that a good description of their spectrum at high energy is obtained by quantizing the structured and chaotic parts independently. While a zoom on island regions would reveal a complex structure involving chaotic trajectories and chains of smaller islands, these small scale details can be neglected for the island quantization if the mode wavelength remains larger than these scales. Instead, the presence of a large number of invariant structures constrains enough the dynamics to make the system similar to a purely integrable structure to which EBK quantization applies. These region are then called near-integrable.

Subsets of modes can be associated to the different near-integrable island chains, while other subsets correspond to the chaotic zones. In each subset, the modes behave as if they were constructed from an isolated system; thus, in mixed systems the frequency spectrum can be described as a superposition of independent frequency subsets associated with the different phase space regions. Subsequent works have shown this picture to be a good approximation of actual spectra, although in some cases certain correlations are present between the frequency subsets due to the presence of partial barriers in phase space or to the existence of modes localized at the border between zones (Bohigas et al. 1993).

Because the acoustic ray dynamics of rapidly rotating stars is of this mixed type, one can expect such an organisation of the spectrum to be valid, even though the modes have quite long wavelength compared to previous studies in quantum chaos. To test this hypothesis, it is convenient to compute a phase-space representation of the modes. Indeed, the chaotic or near-integrable zones are well-defined in phase space, while their projections in position space, where modes are usually pictured, are generally much more difficult to separate.

4.4. Associating modes to rays

Constructing phase space representations for modes has been envisioned since the beginning of quantum mechanics, since it enables testing the quantum-classical correspondence accurately. In contrast to states of a classical system, which are defined by a point in phase space, modes have always a finite extension in phase space since they have a finite wavelength and their localization in wavenumber space is, according to Fourier analysis, inversely proportional to their localization in physical space. Any mode occupies a finite volume of the order of $(2\pi)^N$ in the physical/wavenumber phase space (a $(2\pi/\omega)^N$ volume in the physical/scaled-wavenumber $(\boldsymbol{x}, \tilde{\boldsymbol{k}})$ phase space or a $(2\pi\hbar)^N$ volume in the position/momentum phase space of quantum physics). Wigner (1932) was the first to construct a phase space function representing a mode, but this so-called Wigner function has the disadvantage of being positive or negative, and so cannot be interpreted as a probability distribution of the mode. To circumvent this problem, one way is to smooth the Wigner function by a Gaussian convolution. The resulting function, called the Husimi distribution function (Chang & Shi 1986), is always real and nonnegative and can be equally understood as the projection of the mode onto a Gaussian wave packet centred on $\boldsymbol{x}$ and $\tilde{\boldsymbol{k}}$:

$$\mathcal{H}(\boldsymbol{x}, \tilde{\boldsymbol{k}}) = \left| \int \Psi(\boldsymbol{x}') \exp\left(-\|\boldsymbol{x}' - \boldsymbol{x}\|^2 / \left(2\Delta_x^2\right)\right) \exp(\mathrm{i}\omega\tilde{\boldsymbol{k}} \cdot \boldsymbol{x}') \mathrm{d}\boldsymbol{x}' \right|^2 \quad (26)$$

where $\Psi(\boldsymbol{x}')$ is the mode and $\exp(-\|\boldsymbol{x}' - \boldsymbol{x}\|^2/(2\Delta_x^2))\exp(\mathrm{i}\omega\tilde{\boldsymbol{k}})$ the Gaussian wavepacket. In this expression, the width of the wavepacket Δ_x determines the resolution of the Husimi function in the spatial direction, the resolution in the scaled-wavenumber $\Delta_{\tilde{k}}$ being such that $\Delta_x\Delta_{\tilde{k}} \approx 1/\omega$. These quantities determine the minimal extent of the mode representation in both directions.

The computed modes are 3D modes and they shall be compared with the reduced ray dynamics computed on a 2D meridional plane. As shown in the spherical case by Gough (1993), the amplitude of a 3D axisymmetric mode constructed from acoustic rays obtained on neighbouring meridional planes decreases as $(r\sin\theta)^{(-1/2)}$ because the distance between the planes and thus the density of rays increases away from the rotation axis. Thus, the computed 3D modes were scaled by $(r\sin\theta)^{(1/2)}$ to better represent the mode amplitude on a meridional plane. Moreover, to obtain a phase-space representation limited to the PSS, we actually computed the Husimi's distribution function of the 1D cut of the mode taken along the PSS:

$$\mathcal{H}(s, \tilde{k}) = \left| \int \Psi'(s') \exp\left(-(s' - s)^2 / \left(2\Delta_s^2\right)\right) \exp(\mathrm{i}\omega\tilde{k}s') \mathrm{d}s' \right|^2 \quad (27)$$

where Ψ' is the scaled version of the mode $\hat{\Psi} = \hat{P}/\alpha$ solution of Eqs. (6)–(8), s is a curvilinear coordinate along the curve $r = r_\mathrm{p}$, and $\tilde{k} = \tilde{\boldsymbol{k}} \cdot \boldsymbol{e}_\mathrm{p}$ is the scaled wavenumber in the direction tangent to this curve, $\boldsymbol{e}_\mathrm{p}$ being a unit vector tangent to the curve. Then, $\mathcal{H}$ is expressed in terms of the PSS coordinates using the following relations between $[\theta, \tilde{k}_\theta]$ and $[s, \tilde{k}]$:

$$s = \int_{\theta_0}^{\theta} \left(r_\mathrm{p}^2 + \left(\frac{\mathrm{d}r_\mathrm{p}}{\mathrm{d}\theta}\right)^2\right)^{1/2} \mathrm{d}\theta' \quad \tilde{k} = \tilde{k}_\theta \boldsymbol{E}^\theta \cdot \boldsymbol{e}_\mathrm{p}. \quad (28)$$

The vector $\boldsymbol{E}^\theta$ is defined in Sect. B.2. Integral (27) is performed in the interval $[\theta - \pi, \theta + \pi]$, the mode being prolonged by symmetry outside the $[0, \pi]$ interval.

The Husimi function has been computed for the axisymmetric modes of the $\Omega = 0.59\Omega_K$ star, and its contour plot is compared with the PSS of the ray dynamics computed for the same star model. Figure 6 illustrates this process by showing the position space, as well as the phase space representation of four typical modes. As can be observed, the modes can be clearly associated with one of the main structures of the phase space, namely, the 2-period island chain, the large central chaotic region, the 6-period island chain or the whispering gallery region. On the PSS, we note, however, that the Husimi function is symmetric with respect to $\tilde{k}_\theta$ while the dynamics is not. This difference stems from the PSS being only constructed with $\tilde{k}_\mathrm{r} > 0$ intersecting trajectories, while the Husimi function computed from

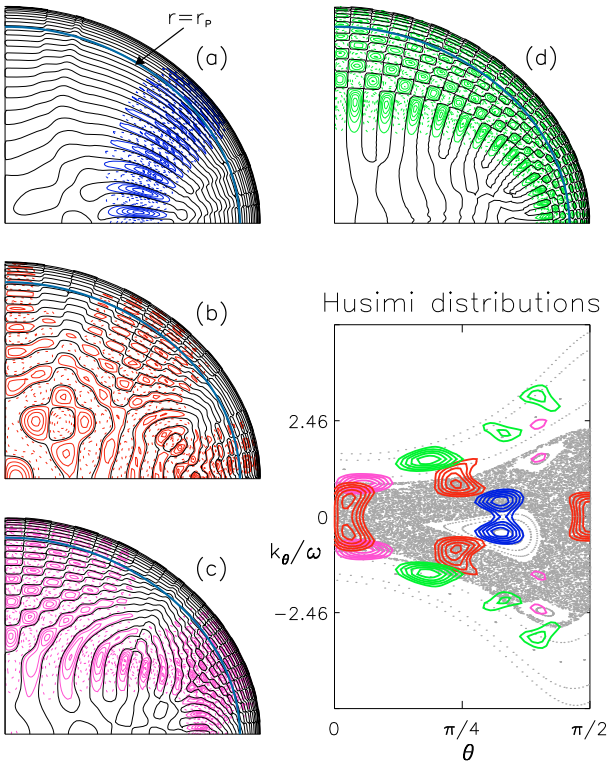

Fig. 6. (Colour online) Four axisymmetric modes and their phase space representation: **a)** a 2-period island mode (blue/dark grey), **b)** a chaotic mode (red/grey), **c)** a 6-period island mode (magenta/light grey), and **d)** a whispering gallery mode (green/light grey). The amplitude distribution of the scaled mode Ψ' is represented by its nodal lines (black) and its positive (full coloured/grey lines) and negative (dashed coloured/grey lines) level curves. The Husimi distributions of the four modes computed for the same $\Delta_s = 0.12R_e$ are represented by their level curves.

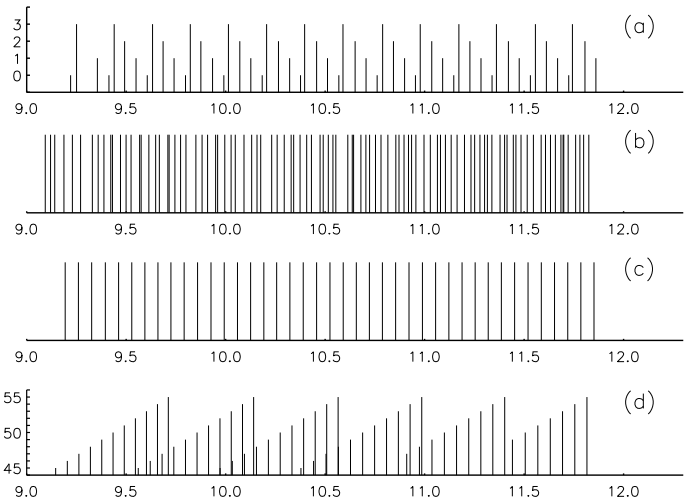

Fig. 7. Frequency subspectra of four classes of axisymmetric modes: **a)** the 2-period island modes, **b)** the chaotic modes antisymmetric with respect to the equator, **c)** the 6-period island modes, and **d)** some whispering gallery modes. For the subspectra **a)** and **d)**, the height of the vertical bar specifies one of the two quantum numbers characterising the mode.

the mode cut on the $r = r_p$ contains no information about the sign of $\tilde{k}_r$. Nevertheless, in the high-frequency interval $[9\omega_1, 12\omega_1]$ that we studied in detail, any ambiguity on the phase space location can always be resolved using the additional information on the mode distribution in the position space. In this frequency interval, we thus classified the modes according to their localization in phase space distinguishing the 2-period island modes, the chaotic modes, the 6-period island modes and the whispering gallery modes associated with the corresponding phase space regions. As a result, the full frequency spectrum can be decomposed into subspectra associated with phase space structures. Figure 7 displays the four subspectra.

In the following, we analyse these subspectra and test whether the Percival and Berry-Robnik conjecture described in Sect. 4.3 applies to acoustic modes in rapidly rotating stars. We first study the regular character of the subspectra issued from near-integrable phase space regions (Sect. 4.5) and then consider the spectrum of chaotic modes (Sect. 4.6).

4.5. The regular spectra

A spectrum is said to be regular if it can be described by a function of N integers, N being the degree of freedom of the system. In accordance with previous studies by Lignières et al. (2006), Lignières & Georgeot (2008), and Reese et al. (2008), the spectrum of the 2-period island modes is well-fitted by the empirical formula

$$\omega_{n\ell} = n\delta_n + \ell\delta_\ell + \alpha, \tag{29}$$

confirming the regular nature of this spectrum that is also clearly apparent in Fig. 7a.

The 6-period island mode spectrum shown in Fig. 7c is also regular, since it is closely fitted by the even simpler formula

$$\omega_{n'} = n'\delta'_n + \alpha'. \tag{30}$$

Indeed, the root mean square error between this empirical fit and the actual spectrum is equal to 1.9 percent of δ'_n, where δ'_n has been determined as the mean of the spacing between consecutive frequencies and α' is fixed such that the model is exact at a reference frequency.

While a simple linear law, such as Eqs. (29) or (30), does not apply to the whispering gallery modes, there is strong evidence that this subspectrum is also regular. Thanks to the regularity of the nodal lines pattern (as apparent in Fig. 6d), two integers corresponding to the number of nodes along the polar axis and to the number of nodes following the internal caustic can be easily attributed to each mode. When plotted against the number of caustic nodes (as in Fig. 7d), the spectrum clearly shows a regular behaviour. That the function of these two integers describing the spectrum is not as simple as Eqs. (29) or (30) is expected from what we know about the regular spectrum of high-degree modes in spherical stars (see for example Christensen-Dalsgaard 1980).

The regularity of the three subspectra issued from near-integrable phase space regions is fully in accordance with the Percival's conjecture. An important consequence is that the theoretical model of these spectra can in principle be obtained from the EBK quantization of the invariant structures of the corresponding near-integrable regions. As a result we should be able to relate the potentially observable quantities δ_n, δ_ℓ, or δ'_n to the star properties. In practice, the standard method is first to construct the normal forms around the central periodic orbit in order to describe the dynamics in the island, and then use the EBK quantization scheme to find the asymptotic formula for the

modes (Bohigas et al. 1993; Lazutkin 1993). While such a programme is outside the scope of the present paper, we mention below the result obtained in Lignières & Georgeot (2008) for the 2-period island modes using an equivalent procedure, which may be more physically transparent, and extend it to the 6-period island modes.

As already noted, the propagation of acoustic waves in our system is similar to the propagation of light in an inhomogeneous medium, where the role of the medium index is played by $1/c_s$. The construction of standing-wave solutions between two bounding surfaces has been investigated intensively in the context of the study of laser modes in cavities (Kogelnik & Li 1966) and consists in applying the paraxial approximation in the vicinity of the optical axis. While generally applied to homogeneous media, this approximation can be extended to the inhomogeneous case as in Permitin & Smirnov (1996); Bornatici & Maj (2003). Applying this formalism to the acoustic modes associated with periodic orbits, Lignières & Georgeot (2008) found a model spectrum equivalent to Eq. (29) with

$$\delta_n = \frac{\pi}{\int_a^b \mathrm{d}\sigma/c_s} \quad \text{and} \quad \delta_\ell = 2\frac{\int_a^b c_s \mathrm{d}\sigma/w^2}{\int_a^b \mathrm{d}\sigma/c_s} \tag{31}$$

where σ is the curvilinear coordinate along the periodic orbit and the integral is computed between the end points of the orbit (these points are shown in Fig. 2 for the 2-period and the 6-period periodic orbits being denoted (a, b) and (a′, b′), respectively). The quantity $w(\sigma)$ in the expression of δ_ℓ describes the spreading of the wave beam in the direction transverse to the periodic orbit and verifies a differential equation that depends on the sound speed and its transverse derivative taken along the periodic orbit. Moreover, the integers n and ℓ correspond respectively to the number of nodes in the directions parallel and transverse to the orbit (see Lignières & Georgeot 2008, for details). When applied to the 2-period periodic orbit, this theoretical expression of δ_n yields a value $0.5635\omega_0$ that differs from its empirical value by only 2.2 percent.

The 6-period island mode spectrum can be modelled in the same way. In the frequency interval considered, these modes have a similar structure in the direction transverse to the central orbit and should therefore be associated with the same ℓ value. The model spectrum has thus the same form as Eq. (30) where

$$\delta'_n = \frac{\pi}{\int_{a'}^{b'} \mathrm{d}\sigma/c_s}. \tag{32}$$

As for the 2-period modes, we find that this theoretical value of δ'_n differs by only a few percent from the empirical determination of $\delta'_n = 0.186\omega_0$.

These two examples show that ray dynamics can provide a quite accurate model of the near-integrable spectra in the relatively low-frequency regime considered here. Moreover, model (29) of the 2-period island mode spectrum remains reasonably accurate at lower frequencies (Lignières et al. 2006) and can be extended to non-axisymmetric modes (Reese et al. 2008).

4.6. The chaotic modes

A large subset of the frequencies correspond to modes localized in the chaotic zone of phase space (the chaotic modes). As we have seen in Sect. 4.2, one should not expect regular patterns for this part of the spectrum. Rather, the chaotic character of the phase space should be reflected in specific statistical properties of the subspectrum, which should follow predictions from Random Matrix Theory. To test this predictions, we have studied the distribution of the consecutive frequency spacings $\delta_i = \omega_{i+1} - \omega_i$ of the chaotic modes. Figure 8 shows the integrated distribution $N(\Delta) = \int_0^\Delta P(\delta)\mathrm{d}\delta$ (with spacings normalized by the mean level spacing within the chaotic subset, as should be done). The distribution is constructed from the two independent distributions obtained for the equatorially symmetric and antisymmetric modes, corresponding to around 187 modes in total. Although the difficulty of solving Eqs. (6)–(8) prevents us from reaching such large frequency samples as can be obtained for other systems (Bohigas et al. 1984), the numerically computed $N(\Delta)$ agrees well with the RMT predictions, and is clearly different from the Poisson distribution typical of integrable systems. This result indicates that these modes, selected by the comparison between their localization in phase space and the ray dynamics, indeed have the frequency statistics expected for chaotic modes. We therefore think that this validates the ray model, and gives strong evidence that wave chaos actually occurs in rapidly rotating stars.

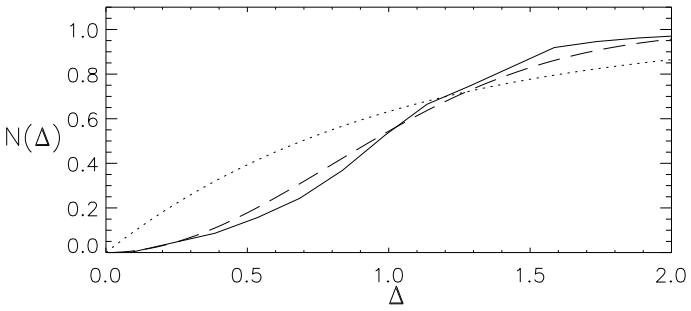

Fig. 8. Integrated spacing distribution $N(\Delta)$ of the chaotic modes (full line). The dashed line shows $N(\Delta)$ for the Gaussian Orthogonal Ensemble of the RMT, while the dotted line shows the integrated Poisson distribution typical of integrable systems.

The modes we identify as chaotic are located in the chaotic zone but cover only part of it, as for the example of Fig. 6. We think this is partly due to the relatively low frequency considered, which prevents the ergodicity of the modes from being clearly visible. In addition, it is known that certain low-energy eigenfunctions of chaotic systems called scars are concentrated along short periodic orbits of the system (Heller 1984). In this case, rather than being ergodic, some individual modes are effectively localized in the vicinity of such orbits. This effect can create some subsequences of low-energy modes with regular frequency patterns, even if the distribution of frequency spacings follows the predictions of the RMT. Precise investigation of this phenomenon in the context of stellar acoustic modes may be important.

4.7. Predicting the number of modes in each subspectrum: the Weyl formula

In this section, we show that ray dynamics enables an estimate of the number of chaotic and island modes present within a given frequency interval. This information is complementary to the regular/irregular properties of the associated subspectra shown in the previous section and it is crucial to building an asymptotic model of the frequency spectrum.

We have seen in Sect. 4.2 that the density of modes as a function of the frequency $d(\omega)$ can be written as the sum of a smooth part $d^{\mathrm{av}}(\omega)$ and an oscillatory part $d^{\mathrm{fluct}}(\omega)$ (see Eq. (25)). At the beginning of the twentieth century, Weyl analytically derived an

asymptotic expansion of $d^{\rm av}(\omega)$ (Weyl 1912). The leading term of the Weyl formula can be obtained from general principles. We have seen (Sect. 4.4) that in average a mode occupies a $(2\pi)^N$ volume in the physical/wavenumber phase space. The averaged number of modes in a given phase space volume can thus be estimated as the volume of phase space available divided by $(2\pi)^N$, the volume occupied by one mode. In the following, we first verify that the leading term of the Weyl formula yields a reasonable estimate of the number of modes in the case of spherically symmetric stars. Then, we calculate the phase space volume of the chaotic and island regions and confront the result with those obtained from the numerical computation of modes at $\Omega = 0.59\Omega_K$.

The Hamiltonian formulation $H' = \omega = \sqrt{c_{\rm s}^2 \boldsymbol{k}^2 + \omega_{\rm c}^2}$ is best suited to this calculation. The averaged number of modes below a given frequency ω reads as

$$\bar{N}(\omega) = \frac{1}{(2\pi)^N} \mathcal{V}(\omega) \tag{33}$$

where $\mathcal{V}(\omega)$ is the phase space volume corresponding to energies lower than ω defined as

$$\mathcal{V}(\omega) = \int_{\mathcal{A}(\omega)} {\rm d}\boldsymbol{k}^N {\rm d}\boldsymbol{x}^N \tag{34}$$

where $\mathcal{A}(\omega)$ is the phase space region defined as $H'(\boldsymbol{x}, \boldsymbol{k}) \leq \omega$.

For spherical stars, the dynamics can be reduced to the one-degree-of-freedom dynamics characterised by the reduced Hamiltonian $H^{\rm sph} = \sqrt{c_{\rm s}(r)^2 (k_{\rm r}^2 + L^2/r^2) + \omega_{\rm c}^2}$. Applying the above formula to $H^{\rm sph}$, the double integral $\mathcal{V}(\omega)$ can be integrated over $k_{\rm r}$ to give

$$\bar{N}^{\rm sph}(\omega) = \frac{1}{\pi} \int_{r_{\rm i}}^{r_{\rm e}} \sqrt{\frac{\omega^2 - \omega_{\rm c}^2}{c_{\rm s}^2} - \frac{L^2}{r^2}} {\rm d}r, \tag{35}$$

which is thus the estimated number of modes of given L and L_z with a frequency lower than ω. This estimation can be compared to the results of the usual asymptotic theory (see Eq. (23)). Accordingly, $\bar{N}^{\rm sph}(\omega) = n - 1/2$, where n is the radial order associated to the frequency ω but is also the number of modes below the frequency ω for fixed values of L and L_z. We therefore conclude that, in the 1D-spherical case, the first term of Weyl's formula yields a reasonable approximation of the averaged mode density.

In rotating stars, to estimate $\bar{N}(\omega)$ the number of modes below ω for a given L_z, we use the two-degree-of-freedom Hamiltonian $H'_{\rm r} = \omega = \sqrt{c_{\rm s}^2 (\boldsymbol{k}_{\rm p}^2 + L_z^2/(r\sin\theta)^2) + \omega_{\rm c}^2}$, and integrate the 4-dimensional volume integral in the wavenumber directions to obtain

$$\bar{N}(\omega) = \frac{1}{4\pi} \iint_{S_{\rm m}} \frac{\omega^2 - \omega_{\rm c}^2}{c_{\rm s}^2} - \frac{L_z^2}{(r\sin\theta)^2} {\rm d}S_{\rm m} \tag{36}$$

where $S_{\rm m}$ is the portion of the meridional plane surface where the integrand is positive. While providing the total number of modes, this expression does not give the fraction of chaotic, island, or whispering gallery modes that are important quantities for modelling the spectrum. These quantities can nevertheless be obtained by computing the corresponding phase space volumes and by applying Eq. (33). This has been done for $\Omega/\Omega_K = 0.59$, since at this rotation rate we can compare the results of Weyl's formula to the numbers of chaotic and island modes obtained from the direct mode computation and the classification through the Husimi distribution.

The 4-dimensional phase space volumes were evaluated using a Monte-Carlo quadrature method: points are randomly chosen in a known volume $V_{\rm M}$ that includes the volume V to be computed. The proportion of points inside V approximates the ratio $V/V_{\rm M}$, thus providing an approximate value of V. To decide whether a given point is inside or outside V, we used space-filling trajectories on the torus delimiting the volume V. Two phase space volumes were computed at $\Omega/\Omega_K = 0.59$. The first one includes the large chaotic region, as well as the island chains around the 2-period and 6-period orbits. The second volume corresponds to the 2-period island chain. The details of the calculation and an estimation of the error on the volume determination are given in Sect. C.

As a result, the leading term of the Weyl formula yields 34 ± 2 modes in the 2-period island chain and 270 ± 8 modes outside the whispering gallery region in the frequency interval $[9.42\omega_1, 11.85\omega_1]$. This value has to be compared with the 50 island modes and the 276 modes outside the whispering gallery region obtained using the Husimi phase space representation of the modes computed in the same frequency interval.

The difference between the estimation given by (33) and the actual number of modes in each subset of the frequency spectrum most likely corresponds to the next order in the asymptotic expansion of the density of modes. Indeed, Eq. (33) is only the first term in an asymptotic expansion, the next term usually being proportional to the length of the boundary between phase space zones. At relatively low frequency, this term can be significant. Another source of imprecision can stem from how, at such relatively low frequency, some partial barriers in phase space can trap island-like modes in the vicinity of the island, enlarging the effective size of the regular zone. Indeed, for some of the modes classified as island modes, the Husimi distribution is not entirely inside the island, the outer part remaining close to the island. Nevertheless, our study shows that Eq. (33) gives a reliable estimate of the relative sizes of the frequency subsets that can be obtained without any knowledge of the spectrum itself.

5. Discussion and applications to asteroseismology

In this section we discuss the validity of the assumptions of our asymptotic analysis and the implications of our results for the asteroseismology of rapidly rotating stars.

5.1. Assumptions of the asymptotic analysis

The WKB assumption underlying the asymptotic analysis is not justified for the lowest frequency acoustic modes. While determining the limit of validity of the different results presented here is outside the scope of the paper, we know that the regularities of the 2-period island mode subspectrum are relevant down to about the 5th radial order acoustic pulsations (see Lignières et al. 2006; and Reese et al. 2008, for details).

Another important precaution when applying the present analysis stems from the interpretation of the ray dynamics depending on the frequency range considered. Indeed, if extremely high-frequency modes were to exist, their properties would closely follow the phase space structure up to its smallest details. This means, for example, that such modes could be associated with the very small chaotic regions that exist inside the island chains or in between the surviving KAM tori of the whispering gallery regions. On the other hand, finite-wavelength effects have to be taken into account when interpreting the ray dynamics at finite frequencies. For example, the regularities of

the island mode spectra in the $[9\omega_1, 12\omega_1]$ interval show that the small chaotic zones within the island chain can be overlooked in this frequency range. The same reasoning holds if one wants to interpret the ray dynamics at small rotation rates (see Fig. 3). The tiny chaotic regions predicted by the KAM theorem could be interpreted as a proof for the existence of a chaotic mode frequency subset at vanishingly small rotation. However, these modes should have such a short wavelength to "fit in" the chaotic region that they may simply not exist (because they are strongly dissipated by diffusive effects or their frequency is so high that they are not reflected at the surface).

Ray dynamics cannot directly account directly for the coupling effects between two modes associated with two dynamically isolated regions of phase space (as occurs for example in the well known tunneling effect). Indeed, while trajectories cannot cross the dynamical barrier between the chaotic and the island chain regions, an island mode can be present on either side of the barrier if its frequency is very close to the one of a chaotic mode (and vice versa). As usual for mode avoided crossings, the mode distribution can thus be significantly perturbed by the coupling, but the frequency is only slightly affected especially in the high-frequency regime. Quantifying the effects of such avoided crossings would require a specific study.

The WKB assumption that the wavelength is much shorter than the typical background lengthscale breaks down for low-frequency acoustic mode but also when the typical lengthscale of the stellar model becomes very small. This can occur in real stars, especially at the upper limit of the core convective zone where strong composition gradients build in during evolution. The effect of such a discontinuity has been studied for spherical stars (Vorontsov 1988; Gough 1990; Ballot et al. 2004) and has been found to add an oscillatory component to Tassoul's asymptotic formula, but not to remove the asymptotic structure altogether. To treat the discontinuities properly in non-spherical stars, the ray dynamics approach has to be extended by taking into account the splitting of rays at the discontinuity, corresponding to the reflected and transmitted waves. Once this is incorporated in the formalism, quantum chaos techniques can be applied as done for billiards in Bluemel et al. (1996a,b), and the Weyl formula can also be computed (Prange et al. 1996).

Apart from the treatment of eventual sound-speed discontinuities, the asymptotic analysis presented in this paper for uniformly rotating polytropic stellar models can be readily applied to realistic stellar models. The details of the dynamics will change because they depend on the sound speed distribution of the model considered. However, we do not expect that the mixed character of the dynamics and thus the irregular/regular nature of the spectrum will change. This has to be confirmed by specific ray dynamics studies. In particular, the effects of the advection by a differentially rotating flow should be investigated.

Lifting the two assumptions concerning the adiabaticity of the perturbations and the Coriolis force omission should not significantly modify the results of the asymptotic analysis. Non-adiabatic calculations are known to have a small effect on the frequency values, while the legitimate omission of the Coriolis force for high-frequency motions is already relevant for quite low frequency as shown in Reese et al. (2006).

5.2. Implications for mode identification

The asymptotic analysis provides qualitative and quantitative information that can be used to identify high-frequency acoustic modes in an observed spectrum. First the basic structure of the spectrum can be readily deduced from the ray dynamics phase space structure visualized by the PSS. Indeed, we have seen that the $\Omega = 0.59\Omega_K$ PSS correctly predicts that the spectrum of axi-symmetric modes is a superposition of four frequency subsets, three regular and one irregular. If we now look at the $\Omega = 0.81\Omega_K$ PSS, we see that the spectrum structure should be similar except that the regular subspectrum associated with the 6-period island chain is no longer present since this island chain has disappeared at this rotation rate. In the same way, at $\Omega = 0.15\Omega_K$, we expect a simple superposition of a whispering gallery subspectrum and a 2-period island mode subspectrum since the chaotic regions are not developed enough at this rotation rate. Such information, while only qualitative, is crucial for guiding the identification process. Moreover this information is obtained at relatively low computing cost since the PSS calculation is much less demanding than the numerical computation of modes and frequencies.

Then, the EBK quantization of the near-integrable regions provides the values of the uniform frequency spacings (as given by Eq. (29)) that should be present in the observed spectrum. When analysing an observed spectrum, the star model is not known, so that only estimates of these uniform spacings can be obtained. However, these estimates enable to focus the search for regularities on a narrower range of values.

Finally as we also know the frequency statistics of chaotic modes and the number of modes in each subspectrum (through Weyl's formula), the asymptotic analysis enables construction of asymptotic spectra. The chaotic mode frequencies can be obtained as a realization of the Wigner distribution, although in this case, their frequencies could not be individually identified with observed ones. Nevertheless, such a synthetic spectrum should be very useful when testing identification methods, especially the search for the regularities hidden in the complete spectrum (see below).

Among the additional information that can help constraint the mode identification are the mode visibility and the mode excitation. The excitation mechanism has been studied so far in the spherically symmetric case and needs to be reconsidered for rapidly rotating stars. The mode visibility also deserves specific study, notably the calculation of the intensity variations induced by the oscillation in a gravity darkened atmosphere. However, the visibility strongly depends on the cancellation effects on the disk-integrated light. Here, we can estimate this effect by integrating the surface Lagrangian temperature perturbation of the axisymmetric modes computed for the $\Omega = 0.59\Omega_K$ rotating polytropic star. The disk-averaging factor is defined as

$$D(i) = \frac{1}{\pi R_e^2 \delta T_0} \iint_{S_v} \delta T(\theta, \phi) \mathrm{d}\boldsymbol{S} \cdot \boldsymbol{e}_i \tag{37}$$

where i is the inclination angle between the line-of-sight and the rotation axis, $\boldsymbol{e}_i$ is a unit vector in the observer's direction, δT is the spatial part of the Lagrangian temperature perturbation at the stellar surface and S_v the visible part of the stellar surface. The mode amplitude is normalized by δT_0 the root mean square of the perturbation over the whole stellar surface

$$\delta T_0 = \left(\frac{\iint_S \delta T^2(\theta, \phi) \mathrm{d}S}{S} \right)^{1/2}, \tag{38}$$

and the projected visible surface is normalized by πR_e^2, the visible disk surface for a star seen pole-on. With these normalizations the disk-averaging factor of an hypothetical mode uniformly distributed on the surface and seen pole-on is unity. The method of the calculation is explained in Appendix D and

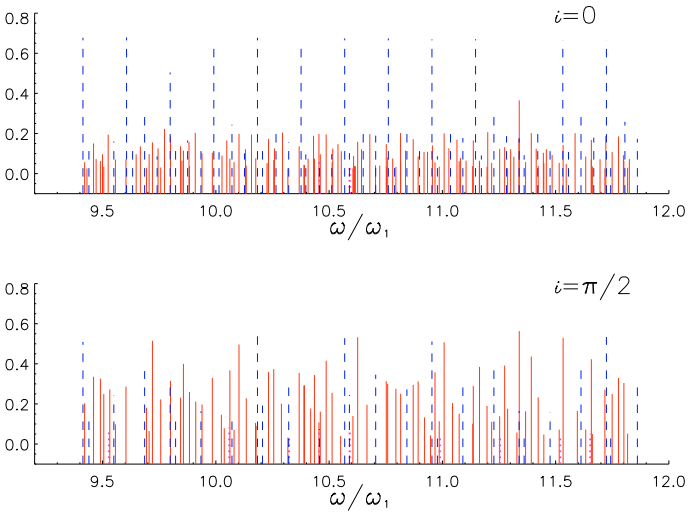

Fig. 9. (Colour online) Frequency spectra of axisymmetric modes where the amplitude is given by the normalized disk-averaging factor $D(i)$ for a star seen pole-on $i = 0$ and equator-on $i = \pi/2$. Only frequencies such that $D(i) \geq 2.5\%$ are displayed, and antisymmetric modes fully cancel out equator-on. The 2-period island modes (blue/dashed lines) and the chaotic modes (red/continuous lines) are the most visible, while only a few 6-period island modes (magenta/dotted lines) and no whispering gallery mode exceed the 2.5% level.

corrects the calculation described in Appendix C of Lignières et al. (2006), which actually only provides an approximate value of $D(i)$.

Figure 9 shows the spectrum of axisymmetric modes whose disk-averaging factor exceeds 2.5 percent. It appears that the disk-averaging effect does not allow to discard as many modes as for spherical stars. Indeed, in a given frequency interval and for the same visibility threshold, we find that the number of visible modes is more than three time higher in the $\Omega = 0.59\Omega_K$ star than in a spherical star. Among the four classes of modes, the 2-period island modes and the chaotic modes have similar visibilities and are significantly more visible than the 6-period island modes and whispering gallery modes. In Fig. 9, a few 6-period island modes are visible while no whispering gallery modes exceed the chosen threshold.

The relatively high visibility of the chaotic modes with respect to the 2-period island modes was not expected as the typical horizontal wavelength of the chaotic modes is generally significantly shorter than the one of the 2-period island modes (see Fig. 6). We think that this stems from the irregular nature of the node pattern of the chaotic modes, which makes the cancellation effect less effective than for regularly spaced nodes (like the whispering gallery modes). A practical consequence of this property is that, at such a rotation rate, methods to disentangle the regular spectrum from the irregular one should be developed.

5.3. Seismic constraints

Constraints on the star can be obtained once the island and chaotic modes subspectra are separated. Through the quantization formulas of the regular modes, the asymptotic analysis provides the relation between regular frequency spacings and the physical properties of the star. For example, according to Eq. (31), the seismic observable δ_n depends on the value of the sound velocity along the path of the 2-period periodic orbit. The quantity δ_ℓ depends in addition on the second order transverse derivative of the sound velocity along the same path and the radius of curvature of the bounding surfaces. The 2-period periodic orbit remains along the polar axis up to relatively high rotation rates (see Fig. 3 at $\Omega/\Omega_K = [0.15, 0.32]$). This implies that all the modes trapped within the corresponding island chain probe the centre of the star, which is known to be crucial for stellar evolution theory. It would be worth investigating whether high-order and low-degree modes of rapidly rotating solar-type pulsators are in this case. Other informations on the star can be deduced from the numbers of island modes or chaotic modes. Indeed the number of mode in each class is related to the volume of the corresponding phase space regions (see Sect. 4.7) which in turns depends on the stellar model.

Further constraints on the star are expected from the identification of the chaotic modes. In contrast to the regular modes built on invariant torus, the modes built on chaotic region are not localized in phase space and are expected be ergodic within their region of propagation. This property turns out to be of particular interest for asteroseismology. The chaotic modes of the main chaotic region are indeed distributed all over the position space and do not avoid the stellar core as do all the non-radial modes in non-rotating stars. Thus, in rapidly rotating stars, the chaotic p-modes have the potential of probing the physics of the core. While the sensitivity of the chaotic modes to this physics needs to be tested, quantum chaos studies indicate that the spatial distribution of chaotic modes is highly sensitive to changes in the models (Schack & Caves 1993; Benenti et al. 2002).

6. Conclusion

We constructed the ray dynamics in uniformly rotating polytropic stars and presented the tools and concepts that enable to interpret it in terms of modes properties. Accordingly, the acoustic frequency spectrum of rapidly rotating polytropic stars is a superposition of frequency subsets associated with dynamically independent phase space regions. The spectra associated with near-integrable regions are regular, while those associated with chaotic regions are irregular but with specific statistical properties. Besides this global qualitative understanding of the spectrum organisation, the ray dynamics also provides quantitative information. The EBK quantization of the near-integrable regions enables explicit construction of the modes and the spectrum from the ray dynamics. For the chaotic modes, the analysis of Sect. 4.6 shows that a parameter-free model for their frequency statistics exists. Moreover, we have seen in Sect. 4.7 that we can estimate the number of modes in each frequency subset from the ray dynamics. These results have been compared with the properties of acoustic modes computed in the frequency interval $[9\omega_1, 12\omega_1]$ showing that the present asymptotic analysis does provide a quite accurate qualitative and quantitative understanding of the actual spectrum in this frequency range.

The analysis of Sect. 5 argues for the importance of this asymptotic analysis for the mode identification and for the asteroseismology of rapidly rotating stars. Indeed, the asymptotic results and the estimation of the mode visibilities tells us that the separation of the frequencies between chaotic and regular modes is a necessary prerequisite for analysing the spectrum. When this is done, the observed regular spacings like δ_n and δ_ℓ can be related to the internal property of the star thanks to the asymptotic analysis.

Further work on this theory could help the analysis of the observed spectra. First, it is important to establish more precise formulas such as Eq. (31) for the regular modes corresponding to the different stability islands. The structure of chaotic modes at low frequency should be studied in more detail, in frequency

ranges lower than the ones used in the present work. This will allow the asymptotic analysis to be tested in frequency ranges where it is not supposed to hold, but which are part of the observed spectra. Encouragingly, the regularity of the 2-period island modes has already been demonstrated in a relatively low radial order range $5 \leq n \leq 10$ (Lignières et al. 2006; Reese et al. 2008), and more generally, in quantum mechanics the semi-classical analysis has been found to apply in much lower energy ranges than expected. Such a study would also allow testing for the presence of scars (see Sect. 4.6), which should be seen only at low frequencies and can organise part of the chaotic subspectrum. These studies will in particular enable productions of theoretical synthetic spectra that embody all the semi-classical information and can be used to test methods of analysis before dealing with actual spectra.

Outside the scope of the asymptotic analysis per se, the mode identification would greatly benefit from accurate visibility computations, modes excitation studies, and obviously more realistic models of centrifugally distorted rapidly rotating stars (Roxburgh 2006; MacGregor et al. 2007; Espinosa Lara & Rieutord 2007).

In conclusion, we believe that the asymptotic analysis we present is a promising way to interpret the spectrum of rapidly rotating stars. We have demonstrated that it can describe numerical spectra, and think that with suitable refinements it should provide an important tool for analysis of observed spectra such as those obtained by the instruments COROT and KEPLER.

Acknowledgements. We thank D. Reese, M. Chapuy, S. Vidal, M. Rieutord and L. Valdettaro for their help at various stages of this work. We also thank CALMIP ("CALcul en MIdi-Pyrénées") for the use of their supercomputer. This work was supported by the Programme National de Physique Stellaire of INSU/CNRS and the SIROCO project of the Agence National de la Recherche.

Appendix A: The WKB approximation of the stellar oscillation Eqs. (6)–(8)

The equations are first written in a normal form, then the eikonal equation is obtained using the WKB approximation.

A.1. Normal form

We first eliminate the perturbation velocity $\boldsymbol{u}$ from Eqs. (6)–(8) governing the evolution of the perturbations. Using Eq. (7), the time derivative of Eqs. (6) and (8) read:

$$\partial_{\rm tt}^2\rho + \boldsymbol{\nabla}\cdot(\rho\boldsymbol{g}_0) = \Delta P, \tag{A.1}$$

$$c_{\rm s}^2(\partial_{\rm tt}^2 + N_0^2)\rho = \partial_{\rm tt}^2 P + \frac{c_{\rm s}^2 N_0^2}{g_0^2}\boldsymbol{g}_0\cdot\boldsymbol{\nabla}P \tag{A.2}$$

where N_0 is the Brunt-Väisälä frequency defined as

$$N_0^2 = \boldsymbol{g}_0\cdot\left(\frac{\boldsymbol{\nabla}\rho_0}{\rho_0} - \frac{1}{\Gamma}\frac{\boldsymbol{\nabla}P_0}{P_0}\right). \tag{A.3}$$

Seeking harmonic solutions in time, the variable are written $F = \hat{F}\exp(\mathrm{i}\omega t)$. Then, using Eq. (A.2), $\hat{\rho}$ is expressed in terms of $\hat{P}$ and replaced in Eq. (A.1) to yield

$$\begin{aligned}&\left[-\omega^4 + \omega^2 c_{\rm s}^2 f\boldsymbol{\nabla}\cdot\left(\frac{\boldsymbol{g}_0}{c_{\rm s}^2 f}\right)\right]\hat{P}\\ &+\left[\omega^2\left(1+\frac{c_{\rm s}^2N_0^2}{g_0^2}\right) - c_{\rm s}^2 f\boldsymbol{\nabla}\cdot\left(\frac{N_0^2\boldsymbol{g}_0}{g_0^2 f}\right)\right]\boldsymbol{g}_0\cdot\boldsymbol{\nabla}\hat{P}\\ &-\frac{c_{\rm s}^2N_0^2}{g_0^2}\boldsymbol{g}_0\cdot\boldsymbol{\nabla}(\boldsymbol{g}_0\cdot\boldsymbol{\nabla}\hat{P}) - \omega^2 c_{\rm s}^2 f\Delta\hat{P} = 0.\end{aligned} \tag{A.4}$$

We then look for a function α such that the substitution $\hat{P} = \alpha\hat{\Psi}$ eliminates the first derivative term. The result is given by Eq. (10) where

$$\begin{aligned}\omega_{\rm c}^2 = {}&\frac{g_0^2B^2}{4c_{\rm s}^2} + c_{\rm s}^2 f\boldsymbol{\nabla}\cdot\left(\frac{\boldsymbol{g}_0}{c_{\rm s}^2 f}\right)\\ &-\frac{c_{\rm s}^2}{2}\boldsymbol{\nabla}\cdot\left(\frac{B\boldsymbol{g}_0}{c_{\rm s}^2}\right) + \frac{(1-f)}{2}Bg_0^2\boldsymbol{\nabla}\cdot\left(\frac{\boldsymbol{g}_0}{g_0^2}\right),\end{aligned} \tag{A.5}$$

where

$$B = 1 + \frac{c_{\rm s}^2N_0^2}{g_0^2} - c_{\rm s}^2\boldsymbol{\nabla}\cdot\left(\frac{(1-f)\boldsymbol{g}_0}{fg_0^2}\right) \tag{A.6}$$

$$f = 1 - \frac{N_0^2}{\omega^2}\cdot \tag{A.7}$$

The α function is given by

$$\boldsymbol{\nabla}\alpha = \frac{B}{2c_{\rm s}^2}\alpha\boldsymbol{g}_0. \tag{A.8}$$

The expression of $\omega_{\rm c}$ can be simplified in the limit $\omega \gg N_0$ to give

$$\omega_{\rm c}^2 = \frac{g_0^2}{4c_{\rm s}^2}\left(1+\frac{c_{\rm s}^2N_0^2}{g_0^2}\right)^2 + \frac{c_{\rm s}^2}{2}\boldsymbol{\nabla}\cdot\left(\left(1-\frac{c_{\rm s}^2N_0^2}{g_0^2}\right)\frac{\boldsymbol{g}_0}{c_{\rm s}^2}\right)\cdot \tag{A.9}$$

For polytropes $P_0 = K\varrho_0^{1+1/\mu}$, the quantities describing the equilibrium model can be expressed in terms of the enthalpy h_0 as follows

$$\begin{aligned}&\boldsymbol{g}_0 = \boldsymbol{\nabla}h_0 \qquad\qquad c_{\rm s}^2 = \tfrac{\Gamma}{\mu+1}h_0\\ &N_0^2 = \left(\tfrac{\mu\Gamma}{\mu+1}-1\right)\frac{g_0^2}{c_{\rm s}^2}\cdot\end{aligned} \tag{A.10}$$

Equation (A.9) can then be simplified to give Eq. (12). We note that while the $\omega \gg N_0$ is expected to be valid for acoustic modes in real stars, that the Brunt-Väisälä frequency becomes infinite at the surface of a polytropic model implies that this approximation is not valid close to the surface of such models.

A.2. Eikonal equation

We look for wave-like solutions (9) of the normal form of the perturbation Eq. (10) under the assumption that $1/\Lambda$ the ratio between the wavelength of the solution and the background typical lengthscale is very small. Accordingly, the solution is expanded as

$$\Phi = \Lambda(\Phi_0 + \tfrac{1}{\Lambda}\Phi_1\ldots) \quad A = A_0 + \tfrac{1}{\Lambda}A_1\ldots \tag{A.11}$$

and the eikonal equation corresponds to the leading order of the expanded solution.

The highest $O(\Lambda^2)$ terms verify

$$\frac{\omega^2-\omega_{\rm c}^2}{c_{\rm s}^2} + \frac{N_0^2}{\omega^2}\Lambda^2(\boldsymbol{\nabla}\Phi_0)_\perp^2 = \Lambda^2(\boldsymbol{\nabla}\Phi_0)^2 \tag{A.12}$$

where the $(\boldsymbol{\nabla}\Phi_0)_\perp = \boldsymbol{\nabla}\Phi_0 - (\boldsymbol{\nabla}\Phi_0\cdot\boldsymbol{n}_0)\boldsymbol{n}_0$, $\boldsymbol{n}_0$ being the outward unit vector in the direction opposite to the effective gravity. The effective eikonal equation then depends on the ordering of ω/ω_0 with respect to Λ. If $\omega/\omega_0 = O(\Lambda)$, then the above equation simplifies to

$$\frac{\omega^2-\omega_{\rm c}^2}{c_{\rm s}^2} = (\boldsymbol{\nabla}\Phi_0)^2, \tag{A.13}$$

which corresponds to the dispersion relation of acoustic waves. The ω_c term is retained because its sharp increase near the surface provokes the back reflection of the acoustic wave.

On the other hand, if $\omega/\omega_0 = O(1)$, then we obtain

$$-\frac{\omega_c^2}{c_s^2} + \frac{N_0^2}{\omega^2}(\boldsymbol{\nabla}\Phi_0)_\perp^2 = (\boldsymbol{\nabla}\Phi_0)^2, \tag{A.14}$$

which corresponds to gravity waves. This relation has been obtained under the assumption that the Coriolis force is negligible. While justified for high-frequency acoustic waves, this assumption is not necessarily true for gravity waves where the frequency is limited by N_O.

Finally, the next order of the expansion (A.11) yields the amplitude A_0 in terms of Φ_0 (see for example Lighthill 1978).

Appendix B: Properties of the PSS

Two specific properties of the $r_p(\theta) = r_s(\theta) - d$ PSS are considered below. First, we check in the non-rotating case that the distance d can be chosen so that all relevant trajectories intersect the $r_p(\theta) = r_s(\theta) - d$ curve. Second, we define a coordinate system of the PSS that ensures that any surface of the PSS is conserved by the dynamics.

B.1. Choice of the distance to the stellar surface

In the non-rotating case, Eq. (21) enables to characterise the trajectories that do not cross the PSS for a given value of d, the distance to the stellar surface. The radius of the internal caustic of these trajectories r_i must be such that $r_i > r_p$. Using the definition of r_i and assuming that $\omega \gg \omega_c(r_i)$ implies that $\tilde{L} > r_p/c_s(r_p)$. According to the relation between $\tilde{L}$ and ℓ, the degree of the corresponding mode $\tilde{L} = (\ell + 1/2)/\omega$ (see Eq. (23) in Sect. 4.1), we find that these trajectories are associated with high-degree modes ($\ell > 136$) for the chosen value of $d = 0.08R_e$ and for $\omega = 8.4\omega_1$, where ω_1 is the lowest acoustic mode frequency of the stellar model under consideration. These modes are thus irrelevant for asteroseismology since their amplitude strongly cancels out when integrated over the visible disk.

B.2. Area-preserving coordinates of the PSS

For a PSS defined by $r_p(\theta) = r_s(\theta) - d$, we show here that θ, the colatitude, and $\tilde{k}_\theta = k_\theta/\omega$, k_θ the angular component of $\boldsymbol{k}$ in the natural basis associated with the coordinate system $[\zeta = r_s(\theta) - r, \theta, \phi]$ are area-preserving coordinates of the PSS.

First we show that, for a general coordinate system x_i, the spatial coordinates x_i and the covariant component $\tilde{k}_i$ of the vector $\tilde{\boldsymbol{k}}$ in the natural basis are conjugate variables of the Hamiltonian H given by Eq. (17). The natural basis associated to a coordinate system x_i is defined by $(\boldsymbol{E}_1, \boldsymbol{E}_2, \boldsymbol{E}_3)$ where $\boldsymbol{E}_i = \partial\boldsymbol{x}/\partial x^i$. The contravariant component $\tilde{k}^i$ of the velocity $\tilde{\boldsymbol{k}} = \dot{\boldsymbol{x}}$ thus verifies $\dot{x}_i = \tilde{k}^i$. (The notation $\dot{x}_i$ denotes a derivative with respect to the time-like coordinate t). If $L(\dot{\boldsymbol{x}}, \boldsymbol{x}, t)$ is the Lagrangian of a system expressed in a coordinate system x_i, it is well known that a Legendre transformation leads to a Hamiltonian $H = \sum \dot{x}_i \partial L/\partial \dot{x}_i - L$ where $p_i = \partial L/\partial \dot{x}_i$ is conjugate to x_i. The Lagrangian $L = \frac{\tilde{k}^2}{2} - W(\boldsymbol{x})$ being associated with the Hamiltonian H given by Eq. (17), the momentum variable p_i can be simply computed

$$p_i = \frac{\partial L}{\partial \dot{x}_i} = \frac{1}{2}\frac{\partial \tilde{\boldsymbol{k}}\cdot\tilde{\boldsymbol{k}}}{\partial \tilde{k}^i} = \tilde{\boldsymbol{k}}\cdot\frac{\partial \tilde{\boldsymbol{k}}}{\partial \tilde{k}^i} = \tilde{\boldsymbol{k}}\cdot\boldsymbol{E}_i = \tilde{k}_i \tag{B.1}$$

thus showing that $[x_i, \tilde{k}_i]$ are conjugate variables of H.

Moreover, for a given conjugate coordinate system $[x_i, p_i]$, the coordinates $[x_2, x_3, p_2, p_3]$ of the PSS defined by $x_1 = \text{const.}$ are known to be area-preserving (Ott 1993). Thus, in our case, $[\zeta, \theta, \tilde{k}_\zeta, \tilde{k}_\theta]$ is a conjugate coordinate system for the reduced Hamiltonian H_r and the system $[\theta, \tilde{k}_\theta]$ is area-preserving for the PSS $\zeta = \text{const.}$ The natural basis and its conjugate reads $\boldsymbol{E}_\zeta = -\boldsymbol{e}_r$, $\boldsymbol{E}_\theta = (\mathrm{d}r_s/\mathrm{d}\theta)\,\boldsymbol{e}_r + r_p\boldsymbol{e}_\theta$ and $\boldsymbol{E}^\zeta = -\boldsymbol{e}_r + [(\mathrm{d}r_s/\mathrm{d}\theta)/r_p]\boldsymbol{e}_\theta$, $\boldsymbol{E}^\theta = (1/r_p)\boldsymbol{e}_\theta$ in terms of the unit vector associated with the spherical coordinates $(\boldsymbol{e}_r, \boldsymbol{e}_\theta)$. Thus, with respect to the wavevector components in spherical coordinates $\tilde{k}_r^{\mathrm{sph}}, \tilde{k}_\theta^{\mathrm{sph}}$, the $\tilde{k}_\theta$ component reads $\tilde{k}_\theta = (\mathrm{d}r_s/\mathrm{d}\theta)\,\tilde{k}_r^{\mathrm{sph}} + r_p\tilde{k}_\theta^{\mathrm{sph}}$.

Appendix C: Calculation of phase space volumes

Following the Monte-Carlo quadrature method (Press et al. 1992), N_S points are randomly chosen in a known volume V_S that includes the volume V to be computed. The proportion of points inside V approximates the ratio V/V_S, thus providing an estimated value of V. The standard deviation error yields an estimate of the relative error, $\sqrt{(V_M/V - 1)/N_S}$, showing that the sampling volume V_S has to be as close as possible to the volume V and that the number of sampling points must be large.

In our case, the main practical issue is thus to determine if a given point in phase space is inside or outside the 4-dimensional volume to be computed. The two volumes that we computed are specified by two limiting frequencies $9.42\omega_1 \le H_r'(\boldsymbol{x}, \boldsymbol{k}) \le 11.85\omega_1$ and for each value of H_r' by the 3D volume inside a given 2D torus. The first torus considered separates the whispering gallery region from the chaotic region, its imprint on the $r = r_p$ PSS being shown in Fig. C.1. The volume inside this torus includes the large chaotic region, as well as the island chains around the 2-period and 6-period orbits. The second volume corresponds to the 2-period island chain and is delimited by a torus also shown in Fig. C.1.

To determine whether a given point $\boldsymbol{x}_0, \boldsymbol{k}_0$ is inside or outside these volumes, one could construct the $r = r_p$ PSS associated to the value of the Hamiltonian $H_r'(\boldsymbol{x}_0, \boldsymbol{k}_0)$, advance the dynamics from $\boldsymbol{x}_0, \boldsymbol{k}_0$ until the trajectory cross the $r = r_p$ PSS, and find out whether the crossing point is inside or outside the torus. Here, to simplify the procedure, we used the fact that the $r = r_p$ PSS plotted against the scaled wavenumber $\tilde{\boldsymbol{k}}$ appeared to be insensitive to values of the frequency ω in the domain considered. We thus consider the point $\boldsymbol{x}_0, \boldsymbol{k}_0/H_r'(\boldsymbol{x}_0, \boldsymbol{k}_0)$ and determine its location in the scaled phase space computed for a given frequency. To control this supposedly weak frequency effect the computation has been performed for the two extreme frequencies $\omega = 9.42\omega_1$ and $\omega = 11.85\omega_1$. Moreover, instead of advancing the dynamics up to the $r = r_p$ PSS, we construct a local PSS (either from a $\zeta = \text{const.}$ surface or a $\tilde{k}_\zeta = \text{const.}$ surface) to compare the location of the $\boldsymbol{x}_0, \boldsymbol{k}_0$ point with the local imprint of the delimiting torus. In practice, the imprint of the delimiting torus is not a continuous curve as the torus is actually obtained from a space filling trajectory on the torus. We therefore follow such a trajectory over a sufficiently large number of time step to increase the number of point of the torus imprint on the different PSS. This procedure has been tested using trajectories which are known to

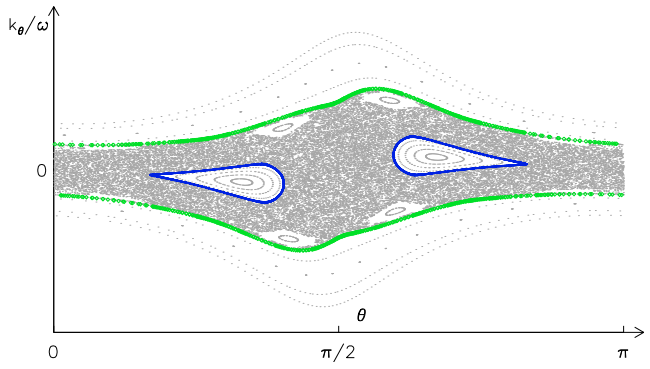

Fig. C.1. (Colour online) Intersection of two trajectories with the PSS at $\Omega = 0.59\Omega_K$. The crosses (blue) correspond to a trajectory on a torus containing most of the 2-period island chain. The diamonds (green) correspond to a trajectory on a torus bounding the central chaotic region.

be either inside or outside the torus (like for example trajectories on nested tori inside the 2-period island chain). The number of points wrongly located by this procedure can be made small enough to have a negligible effect when compared to the statistical error on the volume determination. Furthermore, the integration domain has been divided into three subdomains following the pseudo-radial direction ζ. This enables to limit the ratio V/V_S as the sampling volumes can be more easily reduced in each subdomain.

Accordingly, the number of modes within the 2-period island chain is 33 ± 1 if we use the bounding torus computed for $\omega = 9.42\omega_1$ and 34 ± 1 for $\omega = 11.85\omega_1$. The effect of changing the frequency is small in this case and the number of modes can be estimated to 34 ± 2. Likewise, the number of modes outside the whispering gallery region is 263 ± 1 for $\omega = 9.42\omega_1$ bounding torus and 276 ± 2 for $\omega = 11.85\omega_1$. The frequency effect is stronger but still reasonable for the present purpose. We took the mean value of 270 modes with an error of ± 8 mode.

Appendix D: Calculation of the disk-integration factor

According to the definition of the disk-integration factor, Eq. (37), we are led to calculate integrals of the form

$$I = \iint_{S_v} F(\theta,\phi)\mathrm{d}\boldsymbol{S}\cdot\boldsymbol{e}_i \tag{D.1}$$

$$= \iint_{S_v} G(\theta,\phi,i)\mathrm{d}\mu\mathrm{d}\phi \tag{D.2}$$

where $\mu = \cos\theta$ and $F(\theta,\phi) = W(\theta)\mathrm{e}^{\mathrm{i}m\phi}$ is the surface distribution of the eigenfunction. The spherical coordinate system $[r,\theta,\phi]$ is such that the polar axis is the rotation axis, and the meridional plane $\phi = 0$ is chosen parallel to $\boldsymbol{e}_i$. The condition $\mathrm{d}\boldsymbol{S}\cdot\boldsymbol{e}_i = 0$ on the stellar surface defines a curve that separates the visible part of the surface S_v from the invisible one (the surface is supposed to be convex). We call this the visibility curve.

We used two methods to compute the integral I. The first one is approximate because it assumes that the visibility curve is contained in a plane, but it is easy to compute accurately. The second method does not make this assumption but requires more computing time to complete accurate calculations.

The vector $\mathrm{d}\boldsymbol{S}$ at the star's surface reads as

$$\mathrm{d}\boldsymbol{S} = \sin\theta r_\mathrm{s}\left(r_\mathrm{s}^2 + \left(\frac{\mathrm{d}r_\mathrm{s}}{\mathrm{d}\theta}\right)^2\right)^{1/2}\boldsymbol{e}^\mathrm{s}\mathrm{d}\theta\mathrm{d}\phi \tag{D.3}$$

where $\boldsymbol{e}^\mathrm{s}$ denotes the unit vector perpendicular to the surface and $r_\mathrm{s}(\theta)$ is the stellar surface. Thus, the function to integrate can be written as

$$F(\theta,\phi)\mathrm{d}\boldsymbol{S}\cdot\boldsymbol{e}_i = A(\theta)\sin\theta\cos i\mathrm{e}^{\mathrm{i}m\phi} - B(\theta)\sin\theta\sin i\cos\phi\mathrm{e}^{\mathrm{i}m\phi} \tag{D.4}$$

where

$$A = r_\mathrm{s}\frac{\mathrm{d}}{\mathrm{d}\theta}\left(r_\mathrm{s}\sin\theta\right)W(\theta) \tag{D.5}$$

$$B = r_\mathrm{s}\frac{\mathrm{d}}{\mathrm{d}\theta}\left(r_\mathrm{s}\cos\theta\right)W(\theta). \tag{D.6}$$

D.1. First method

The colatitude verifying $\mathrm{d}\boldsymbol{S}\cdot\boldsymbol{e}_i = 0$ for $\phi = 0$ is denoted $\theta_\mathrm{L}(i)$. As the inclination angle i can be restricted to $[0,\pi/2]$, we have $\pi/2 < \theta_\mathrm{L}(i) < \pi$, and the angle α defined as $\alpha(i) = \theta_\mathrm{L}(i) - \pi/2$ verifies $0 < \alpha(i) < \pi/2$. We assume that the visibility curve is the intersection of the stellar surface with the plane $\sin\alpha x + \cos\alpha z = 0$, where the vector $\boldsymbol{e}_\alpha$ of Cartesian coordinates $(\sin\alpha, 0, \cos\alpha)$ is normal to this plane. Then, the integral is most simply calculated in the coordinate system in which the polar axis is aligned with the direction of the vector $\boldsymbol{e}_\alpha$. This coordinate system results from a rotation of angle α around the y axis of the original coordinate system, the new angular variables being denoted θ' and ϕ'.

To express the integrand in these coordinates, we use the formula relating the spherical harmonics in both systems:

$$Y_\ell^m(\theta,\phi) = \sum_{m'=-\ell}^{+\ell} d^\ell_{mm'}(\alpha)Y_\ell^{m'}(\theta',\phi') \tag{D.7}$$

where $d^\ell_{mm'}(\alpha)$ do not generally have a simple form (Edmonds 1960). Then, using the spherical harmonic expansion of G, we obtain

$$G = \sum_{\ell=0}^{+\infty}\sum_{m=-\ell}^{+\ell} G_m^\ell(i)Y_\ell^m(\theta,\phi) \tag{D.8}$$

$$= \sum_{\ell=0}^{+\infty}\sum_{m=-\ell}^{+\ell}\sum_{m'=-\ell}^{+\ell} G_m^\ell(i)d^\ell_{mm'}(\alpha)Y_\ell^{m'}(\theta',\phi'). \tag{D.9}$$

Integrating over the longitude ϕ', from 0 to 2π, the terms involving $Y_\ell^{m'}(\theta',\phi')$ vanish if $m' \neq 0$. It follows that

$$I = 2\pi\sum_{\ell=0}^{+\infty}\sum_{m=-\ell}^{+\ell} J_\ell G_m^\ell(i)\hat{Y}_\ell^m(\alpha) \tag{D.10}$$

where we use the relations

$$d^\ell_{m0}(\alpha) = \sqrt{\frac{4\pi}{2\ell+1}}\hat{Y}_\ell^m(\alpha) \tag{D.11}$$

$$\mathrm{d}\mu\mathrm{d}\phi = \mathrm{d}\mu'\mathrm{d}\phi' \quad \text{where } \mu' = \cos\theta', \tag{D.12}$$

and defined J_ℓ as

$$J_\ell = \sqrt{\frac{4\pi}{2\ell+1}}\int_0^1 \hat{Y}_\ell^0(\mu')\mathrm{d}\mu' \tag{D.13}$$

$$= \begin{cases} 0 & \text{if } \ell \text{ is even and } \ell \neq 0, \\ 1 & \text{if } \ell = 0, \\ (-1)^{\frac{\ell-1}{2}}\frac{1.3\ldots(\ell-2)}{2.4\ldots(\ell+1)} & \text{if } \ell \text{ is odd and } \ell \neq 1, \\ \frac{1}{2} & \text{if } \ell = 1. \end{cases} \tag{D.14}$$

To determine the coefficients $G_m^\ell(i)$, we use the expression of G derived from Eq. (D.4):

$$G = A(\theta)\cos i e^{im\phi} - B(\theta)\sin i\cos\phi e^{im\phi}. \quad \text{(D.15)}$$

It follows that

$$G_k^\ell = 0 \text{ if } k \neq m-1, m, m+1 \quad \text{(D.16)}$$

so that the integral now reads

$$I/2\pi = I_{m-1} + I_m + I_{m+1} \text{ where} \quad \text{(D.17)}$$
$$I_m = \cos i \hat{A}_m(\alpha) \quad \text{(D.18)}$$
$$I_{m-1} = -\frac{\sin i}{2}\hat{B}_{m-1}(\alpha) \quad \text{(D.19)}$$
$$I_{m+1} = -\frac{\sin i}{2}\hat{B}_{m+1}(\alpha) \quad \text{(D.20)}$$

where $\hat{A}_m$ denotes

$$\hat{A}_m(\alpha) = \sum_{\ell=|m|}^{+\infty} J_\ell A_m^\ell \hat{Y}_\ell^m(\alpha) \quad \text{(D.21)}$$
$$A_m^\ell = 2\pi\int_0^\pi A(\theta)\hat{Y}_\ell^m(\theta)\sin\theta d\theta \quad \text{(D.22)}$$

the $\hat{B}_m$ terms being defined accordingly. For modes that are equatorially anti-symmetric and axisymmetric ($m = 0$), $\hat{A}_0(\alpha) = J_0 A_0^0 \hat{Y}_0^0(\alpha)$ and $\hat{B}_1(\alpha) = \hat{B}_{-1}(\alpha) = 0$, thus the integral I reduces to

$$I = 4\pi\sqrt{\pi}A_0^0\cos(i). \quad \text{(D.23)}$$

D.2. Second method

The visibility curve is no longer assumed to be planar. The integration over the visible surface is first performed in the azimuthal direction and then in latitude. If $0 \leq \theta \leq \pi/2 - \alpha$, the integration is between 0 and 2π, while in the interval $\pi/2 - \alpha \leq \theta \leq \pi/2 + \alpha$ one has to integrate between the two limiting azimuths $-\phi_L(\theta, i)$ and $\phi_L(\theta, i)$ verifying $d\boldsymbol{S}\cdot\boldsymbol{e}_i = 0$. The integration domain is thus divided in two sub-domains, such that

$$S_v = \left[0, \frac{\pi}{2} - \alpha\right] \times [0, 2\pi] \cup \left[\frac{\pi}{2} - \alpha, \frac{\pi}{2} + \alpha\right] \times [-\phi_L, \phi_L]. \quad \text{(D.24)}$$

According to Eq. (D.4), the integration over ϕ can be made analytically as it involves quadratures of $e^{im\phi}$ and $\cos\phi e^{im\phi}$ over $[0, 2\pi]$ and $[-\phi_L, \phi_L]$. Then, depending on the value of m, the integral I reads as

$$I = \begin{cases} 2\pi\int_0^{\frac{\pi}{2}-\alpha} a d\theta + 2\int_{\frac{\pi}{2}-\alpha}^{\frac{\pi}{2}+\alpha} a\phi_L - b\sin(\phi_L)d\theta & \text{if } m = 0 \\ -\pi\int_0^{\frac{\pi}{2}-\alpha} b d\theta + \int_{\frac{\pi}{2}-\alpha}^{\frac{\pi}{2}+\alpha} 2a\sin(\phi_L) & \\ -b\left(\phi_L + \frac{1}{2}\sin(2\phi_L)\right)d\theta & \text{if } m = \pm 1 \\ \int_{\frac{\pi}{2}-\alpha}^{\frac{\pi}{2}+\alpha} \frac{2a}{m}\sin(m\phi_L) - b\left(\frac{\sin[(m+1)\phi_L]}{m+1} + \frac{\sin[(m-1)\phi_L]}{m-1}\right)d\theta & \\ \text{if } m \neq 0, \pm 1. & \end{cases} \quad \text{(D.25)}$$

where $a(\theta, i) = A(\theta)\sin\theta\cos i$ and $b(\theta, i) = B(\theta)\sin\theta\sin i$.

D.3. Tests

The methods have been tested in the case of an uniformly distributed function on the surface of an ellipsoïd where they should both give the same result. Then, the error introduced by the approximation of method 1 is estimated in the case of a Roche model surface.

D.3.1. Ellipsoïd

The surface being a quadric, the visibility curve is planar. Method 1 is therefore exact and should give the same result as method 2. In addition, the visible surface (obtained by taking $F = 1$) can be obtained analytically. Indeed, the dimensionless equation of the ellipsoïd is

$$x^2 + y^2 + \frac{z^2}{\tilde{R}_p} = 1, \quad \text{(D.26)}$$

and in spherical coordinates

$$r = \frac{1}{\sqrt{1 + \frac{1-\tilde{R}_p^2}{\tilde{R}_p^2}\cos^2\theta}} \quad \text{(D.27)}$$

where the distance have been normalized by the equatorial radius R_e and $\tilde{R}_p = R_p/R_e$. As $d\boldsymbol{S}$ is parallel to $(2x, 2y, 2z/\tilde{R}_p^2)$ and $\boldsymbol{e}_i = (\sin i, 0, \cos i)$, surface points verifying $d\boldsymbol{S}\cdot\boldsymbol{e}_i = 0$ belong to the plane:

$$x\sin i + \frac{z\cos i}{\tilde{R}_p^2} = 0. \quad \text{(D.28)}$$

By definition of the angle α, we have

$$\tan\alpha = \tilde{R}_p^2\tan i. \quad \text{(D.29)}$$

In addition, using Eq. (D.28) and the relation between the Cartesian and spherical coordinates, the equation of the intersection between the plane $x\sin i + (z\cos i)/\tilde{R}_p^2 = 0$ and the ellispsoïd is given by Eq. (D.27) and

$$\cos\phi_L = -\frac{\cot\theta\cot i}{\tilde{R}_p^2} = -\cot\theta\cot\alpha. \quad \text{(D.30)}$$

Thus,

$$\phi_L(\theta, i) = \arccos(-\cot\theta\cot\alpha) \quad \text{(D.31)}$$

is defined if $\pi/2 - \alpha \leq \theta \leq \pi/2 + \alpha$ and verifies $0 \leq \phi_L \leq \pi$.

The visible surface can be calculated analytically as the visible curve is an ellipse. This can be seen using the Cartesian coordinates obtained by the rotation of angle α about the Oy axis:

$$x' = \cos\alpha x - \sin\alpha z \quad \text{(D.32)}$$
$$y' = y \quad \text{(D.33)}$$
$$z' = \sin\alpha x + \cos\alpha z. \quad \text{(D.34)}$$

The curve is then contained in the plane $z' = 0$ and verifies

$$\left(\cos^2\alpha + \frac{\sin^2\alpha}{\tilde{R}_p^2}\right)x'^2 + y'^2 = 1. \quad \text{(D.35)}$$

The surface of this ellipse can be calculated as well as its projection in the direction $\boldsymbol{e}_i$, denoted S_v^p:

$$S_v^p/R_e^2 = \pi\cos(\alpha - i)\sqrt{\frac{1 + \tan^2 i\tilde{R}_p^4}{1 + \tan^2 i\tilde{R}_p^2}} \quad \text{(D.36)}$$
$$= \pi\cos i\sqrt{1 + \tan^2 i\tilde{R}_p^2}. \quad \text{(D.37)}$$

Both methods were successfully tested against this analytical expression. Method 1 is simpler because it does not require a numerical integration. It is also very accurate, although it is necessary to use the analytical value of θ_L, if one wants to reach machine precision.

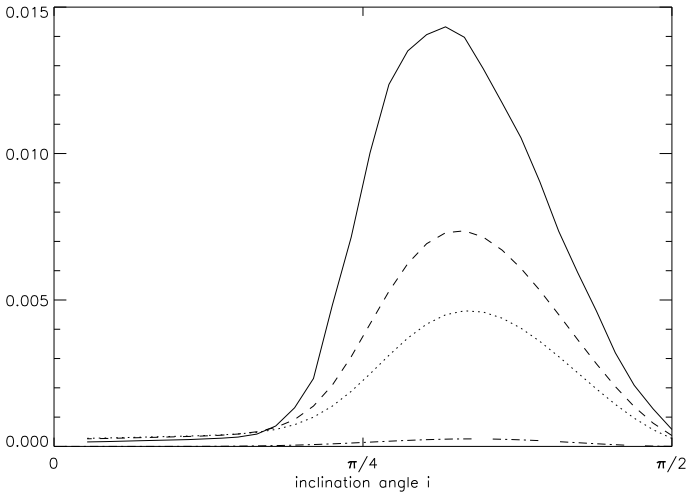

Fig. D.1. Relative error of the projected visible surface computed with method 1 for Roche models of different flatnesses: 0.1526 (dot-dashed), 0.2594 (dotted) 0.2804 (dashed), 0.3092 (continuous line).

D.3.2. Method 1 versus Method 2

Method 1 is approximate because it assumes that the curve on the surface verifying $\mathrm{d}\boldsymbol{S}\cdot\boldsymbol{e}_i = 0$ is planar and contained in the plane $\sin\alpha x + \cos\alpha z = 0$. Nevertheless, the associated error is not expected to be large since it concerns a small part of the whole visible surface. To test this, we simply computed the integral for $F = 1$ with both methods for a surface given by a Roche model of the rotating star. Method 2 computes the projected visible surface, while the quantity calculated by method 1 is smaller because the integration includes a region where $\mathrm{d}\boldsymbol{S}\cdot\boldsymbol{e}_i < 0$ and excludes a visible region of equivalent surface that is symmetrical with respect to the star centre. The difference between the two quantities can also be calculated by directly computing the integral:

$$2\int_{\frac{\pi}{2}}^{\frac{\pi}{2}+\alpha} a\phi_{\mathrm{L}} - b\sin(\phi_{\mathrm{L}})\mathrm{d}\theta, \tag{D.38}$$

using either the correct value of ϕ_{L} or the one corresponding to the assumption of method 1, that is,

$$\cos\phi'_{\mathrm{L}} = -\cot\theta\cot\alpha. \tag{D.39}$$

In Fig. D.1, the relative error on the projected visible surface due to method 1 is plotted for Roche model surfaces of different flatness.

It appears that, except for the near critical values of the flatness, the visible surface that is not considered by method 1 is a very small fraction of the total visible surface. Using method 1 is therefore a good approximation in these cases. For near critical flatness, the difference remains small, although it can be useful to test the results of method 1 with method 2.

References

Anosov, D. V. 1967, Proc. Steklov. Inst. Math., 90, 1
Ballot, J., Turck-Chièze, S., & García, R. A. 2004, A&A, 423, 1051
Benenti, G., Casati, G., Montangero, S., & Shepelyansky, D. L. 2002, Eur. Phys. J. D, 20, 293
Berry, M. V., & Tabor, M. 1977, Proc. R. Soc. A, 356, 375
Berry, M. V., & Robnik, M. 1984, J. Phys. A, 17, 2413
Bluemel, R., Antonsen, T. Jr., Georgeot, B., Ott, E., & Prange, R. E. 1996a, Phys. Rev. Lett., 76, 2476
Bluemel, R., Antonsen, T. Jr., Georgeot, B., Ott, E., & Prange, R. E. 1996b, Phys. Rev. E, 53, 3284
Bohigas, O., Giannoni, M.-J., & Schmit, C. 1984, Phys. Rev. Lett., 52, 1
Bohigas, O., Tomsovic, S., & Ullmo, D. 1993, Phys. Rep., 223, 43
Born, M., & Wolf, E. 1999, Principles of optics, 7th edn. (Cambridge Univ. Press)
Bornatici, M., & Maj, O. 2003, Plasma Phys. Control. Fusion, 45, 707
Brown, M. G., Colosi, J. A., Tomsovic, S., et al. 2003, J. Acoust. Soc. Am., 113, 2533
Chang, S.-J., & Shi, K.-J. 1986, Phys. Rev. A, 34, 7
Chirikov, B. V. 1979, Phys. Rep., 52, 263
Christensen-Dalsgaard, J. 1980, MNRAS, 190, 765
Christensen-Dalsgaard, J., & Thompson, M. J. 1999, A&A, 350, 852
Deubner, F.-L., & Gough, D. 1984, ARA&A, 22, 593
Einstein, A. 1917, Deutsche Phys. Ges., 19, 82
Ellegaard, C., Guhr, T., Lindemann, K., Nygaard, J., & Oxborrow, M. 1996, Phys. Rev. Lett., 77, 4918
Espinosa Lara, F., & Rieutord, M. 2007, A&A, 470, 1013
Giannoni, M.-J., Voros, A., & Zinn-Justin, J. (ed.) 1991, Les Houches Lectures Session LII (North-Holland)
Gough, D. O. 1990, in Progress of Seismology of the Sun and Stars, ed. Y. Osaki, & H. Shibahashi, Lecture Notes in Physics (Springer-Verlag), 367, 283
Gough, D. O. 1993, in Les Houches Lectures Session XLVIII, ed. J.-P. Zahn, & J. Zinn-Justin (North-Holland), 399
Gutzwiller, M. 1990, Chaos in Classical and Quantum Mechanics (Springer)
Hansen, C. J., & Kawaler, S.D. 1994, Stellar interiors (Springer)
Heller, E. J. 1984, Phys. Rev. Lett., 53, 1515
Keller, J. B., & Rubinow, S. I. 1960, Ann. Phys., 9, 24
Kogelnik, H., & Li, T. 1966, Appl. Opt., 5, 1550
Kosovichev, A. G., & Perdang, J. 1988, in Seismology of the Sun and Sun-Like Stars, ESA SP-286, 539
Lazutkin, V. F. 1993, KAM Theory and Semiclassical Approximations to Eigenfunctions (Springer)
Lichtenberg, A., & Lieberman, M. 1992, Regular and Chaotic Dynamics (Springer)
Lighthill, J. 1978, Waves in Fluids (Cambridge University Press)
Lignières, F., & Georgeot, B. 2008, Phys. Rev. E, 78, 016215
Lignières, F., Rieutord, M., & Reese, D. 2006, A&A, 455, 607
Lovekin, C. C., & Deupree, R. G. 2008, ApJ, 679, 1499
MacGregor, K. B., Jackson, S., Skumanich, A., & Metcalfe, T. S. 2007, ApJ, 663, 560
Nöckel, J. U., & Stone, A. D. 1997, Nature, 385, 45
Ott, E. 1993, Chaos in Dynamical Systems (Cambridge Univ. Press)
Pekeris, C. L. 1938, ApJ, 88, 189
Percival, I. C. 1973, J. Phys. B, 6, L229
Perdang, J. 1988, in Multimode Stellar Pulsations, ed. G. Kovacs, L. Szabados, & B. Szeidl (Budapest: Kultura), 209
Permitin, G. V., & Smirnov, A. I. 1996, JETP, 82, 395
Prange, R. E., Ott, E., Antonsen, T. Jr, Georgeot, B., & Bluemel, R. 1996, Phys. Rev. E, 53, 207
Press, W. H., Teukolsky, S. A., Vetterling, W. T., & Flannery, B. P. 1992, Numerical Recipes, 2th edn. (Cambridge Univ. Press)
Rieutord, M., Dintrans, B., Lignières, F., Corbard, T., & Pichon, B. 2005, in Semaine de l'Astrophysique Française, ed. F. Combes et al., Conf. Ser., 759 (EDP Sciences)
Reese, D. 2007, Ph.D. Thesis
Reese, D., Lignières, F., & Rieutord, M. 2006, A&A, 455, 621
Reese, D., Lignières, F., & Rieutord, M. 2008, A&A, 481, 449
Reese, D. R., MacGregor, K. B., Jackson, S., Skumanich, A., & Metcalfe, T. S. 2009, A&A, in press [arXiv:0903.4854]
Roxburgh, I. W. 2006, A&A, 454, 883
Roxburgh, I. W., & Vorontsov, S. V. 2000, MNRAS, 317, 141
Sauer, T., Grebogi, C., & Yorke, J. A. 1997, Phys. Rev. Lett., 79, 59
Schack, R., & Caves, C. M. 1993, Phys. Rev. Lett., 71, 525
Stöckmann, H.-J., & Stein, J. 1990, Phys. Rev. Lett., 64, 2215
Tassoul, M. 1980, ApJS, 43, 469
Tassoul, M. 1990, ApJ, 358, 313
Vandakurov, Y. V. 1967, AZh, 44, 786
Vorontsov, S. V. 1988, in Advances in Helio- and Asteroseismology, ed. J. Christensen-Dalsgaard, & S. Frandsen (Reidel), IAU Symp., 123, 151
Weyl, H. 1912, Math. Ann., 71, 441
Wigner, E. P. 1932, Phys. Rev., 40, 749

Chapitre 3

Magnétisme des étoiles de masse intermédiaire

Pour décrire le magnétisme des étoiles non dégénérées, il convient de distinguer deux catégories d'étoile, les étoiles qui comme le Soleil possèdent une zone convective d'épaisseur significative sous leur surface et celles qui n'en possèdent pas. Cette deuxième catégorie d'étoile comprend les étoiles massives et de masse intermédiaire dans la phase pré-séquence-principale et sur la séquence principale. Pour la première catégorie d'étoile, on s'attend à ce que, comme pour le Soleil, un champ magnétique soit engendré par un effet dynamo dans leur enveloppe convective. Les observations semblent confirmer cette idée simple puisque des champs magnétiques ont été détectés dans les différents type d'étoile de cette catégorie : T Tauri, jumeaux solaires, étoiles de type solaire en rotation rapide, naines M complètement convectives, géantes rouges (Donati & Landstreet 2009) et tout récemment la supergéante rouge Bételgeuse (Aurière et al. 2010). Donc, même si la dynamo dans une enveloppe convective d'étoile restent un sujet mal compris car très complexe à modéliser, la question de l'origine du champ de ces étoiles ne fait pas débat. On dispose d'ailleurs aujourd'hui de nombreuses contraintes observationnelles sur la topologie du champ à la surface de ces étoiles, l'activité associée et la durée des cycles dans des conditions physiques variées de masse et de rotation et on peut penser que, dans les prochaines années, ces contraintes feront progresser notre compréhension de la dynamo de type solaire.

La situation est très différente pour les étoiles massives et de masse intermédiaire. Tout d'abord, on ne dispose pas d'un prototype à proximité comme le Soleil. Ensuite, les observations actuelles indiquent que

seulement 5 à 10 % de ces étoiles possèdent un champ magnétique. Certes, les propriétés de ces champs, qui furent les premiers champs détectés après celui du Soleil (Babcock 1947), sont bien caractérisées. Mais on ne comprend pas pourquoi le champ n'est détecté que dans une faible proportion de ces étoiles. En particulier, l'hypothèse du champ fossile selon laquelle le champ a été engendré au cours de la formation de ces étoiles n'explique pas cette propriété. Une explication possible serait tout simplement que ce chiffre de 5 à 10 % ne reflète en réalité que la limite de sensibilité des observations. Une autre question en suspend concerne les phénomènes d'activité observés dans l'atmosphère d'étoiles massives et d'étoiles jeunes de masse intermédiaire (les étoiles Ae/Be de Herbig). Ces phénomènes semblent être d'origine magnétique ; cependant, les tentatives de détection directe du champ n'ont pas permis de confirmer cette hypothèse. On voit donc que, contrairement au cas du magnétisme de type solaire, ce sont ici les questions de base concernant l'existence et l'origine du magnétisme qui ne sont pas résolues (on trouvera une revue de ces questions dans Lignières (2004)).

Au cours de ma thèse, j'ai étudié un scénario pour expliquer l'origine de l'activité des étoiles de Herbig. L'idée est que la perte de moment cinétique provoquée par le vent stellaire des étoiles de Herbig force une enveloppe turbulente en rotation différentielle dans laquelle un champ magnétique serait engendré (Lignières et al. 1996, 2000). Je me suis de nouveau intéressé au magnétisme des étoiles de masse intermédiaire dans le cadre d'observations spectropolarimétriques effectuées d'abord avec Musicos puis avec Narval. Le premier résultat que je vais présenter concerne la mise en évidence d'une limite inférieure de 100 Gauss (en champ longitudinal) à la valeur du champ magnétique des étoiles Ap/Bp et d'un désert magnétique parmi les étoiles A pour des valeurs de champ longitudinal comprises entre environ 1 Gauss et 100 Gauss. J'ai participé à ces observations mais ma principale contribution a été de proposer un scénario pour expliquer l'existence du champ critique et du désert magnétique (Aurière et al. 2007, **A8**), (Aurière et al. 2010, **A9**). L'autre résultat que je vais présenter concerne la détection d'un champ magnétique de très faible amplitude à la surface de l'étoile de masse intermédiaire Véga. Il suggère qu'une nouvelle classe d'étoiles magnétiques jusqu'alors invisible existe parmi les étoiles de masse intermédiaire et éventuellement aussi parmi les étoiles massives (Lignières et al. 2009, **A10**). Nous verrons aussi les premiers résultats de la tentative de détection d'un champ sur l'autre étoile A très brillante : Sirius.

3.1 Désert magnétique dans les étoiles A et champ critique des étoiles Ap/Bp

À l'exception de Véga (voir Sect. 3.2), toutes les étoiles de masse intermédiaire de la séquence principale où un champ magnétique a été détecté appartiennent à la classe des Ap/Bp, un groupe d'étoiles chimiquement particulière. Le champ de ces étoiles est caractérisé par une forte composante dipolaire et une stabilité temporelle à long terme. Bien que l'amplitude de ces champs puisse atteindre des valeurs très élevées (jusqu'à $\sim$ 30 kG), l'étude d'échantillons non biaisés montre plutôt des valeurs moyennes du champ longitudinale de l'ordre de 300 Gauss (Bohlender & Landstreet 1990). La question de la présence de champs faibles parmi les Ap/Bp ou d'autres étoiles de masse intermédiaire restait cependant en suspend.

Un relevé spectropolarimétrique de 28 étoiles réalisé avec Musicos a alors permis de caractériser les étoiles Ap/Bp à champ faible. Sur un échantillon de 28 étoiles, 27 ont montré une signature Zeeman et le champ de la 28ème a pu être détecté dès les premières observations avec le nouveau spectropolarimètre Narval. Ce résultat confirme l'hypothèse selon laquelle toutes les étoiles qui présentent des anomalies d'abondance de type Ap/Bp possèdent un champ magnétique. De plus, les modèles de dipôles obliques de ces champs (obtenus à partir de la modulation rotationnelle de la signature Zeeman) indiquent que le champ dipolaire est presque toujours supérieur à 300 Gauss. Si l'étoile est vue par le pôle magnétique, cela correspond à un champ longitudinal de 100 Gauss.

Une interprétation possible de cette limite inférieure était que le phénomène Ap/Bp, c'est-à-dire l'existence des anomalies d'abondance caractéristique de cette classe d'étoile, n'apparaissait que au delà d'une certain valeur du champ magnétique. C'est une explication plausible car les anomalies d'abondances dans les Ap/Bp sont extrêmes par rapport aux autres étoiles A chimiquement particulière comme les Am. Or, un fort champ magnétique a la capacité de limiter fortement les mouvements du plasma et donc le mélange induit par ces mouvements. L'atmosphère devient alors suffisamment stable pour que les phénomènes de diffusion radiative agissent sans les limitations dues aux mouvements tels que ceux des petites zones de convection des étoiles A ou ceux induits par la rotation différentielle.

Mais, si cette interprétation était correcte, une population d'étoile A magnétique à champ inférieur à 100 Gauss prolongeant la distribution du champ magnétique des Ap/Bp devrait exister. Or, un relevé spectropolarimétrique de 63 étoiles de masse intermédiaire non Ap/Bp de différents types (dont 22 étoiles

B, A, F normales, 25 étoiles Am, 10 étoiles HgMn, 2 λ Bootis) réalisé avec Musicos n'avait pas permis de détecter de champ magnétique alors que le seuil de détection en champ longitudinal était de quelques dizaines de Gauss (un autre relevé de 138 étoiles non Ap/Bp réalisé avec le mode polarimétrique de l'instrument Fors1 sur le VLT n'avait rien donné non plus, mais avec un seuil de détection plus élevé) (Shorlin et al. 2002). Donc plutôt qu'un prolongement dans la distribution des intensités du champ longitudinal, ces observations indiquent l'existence d'un décrochage dans cette distribution. C'est que j'ai appelé le désert magnétique des étoiles de masse intermédiaire. Réduit initialement à quelques dizaines de Gauss, l'écart entre la limite inférieure du champ des Ap/Bp et le seuil de détection des mesures spectropolarimétriques a significativement augmenté avec la mise en service des nouveaux spectropolarimètres Narval et Espadons. Un nouvel échantillon d'étoiles non Ap/Bp (12 étoiles Am, 3 étoiles HgMn et une étoile A) observé avec Narval a confirmé l'existence d'un "désert magnétique" entre 100 Gauss, le champ longitudinal critique des Ap/Bp, et un seuil de détection de l'ordre du Gauss (Aurière et al. 2010, **A9**).

Pour l'interpréter, j'ai essayé d'imaginer ce que seraient les conséquences observationnelles de l'évolution d'un ensemble d'étoile possédant des champs magnétiques structurés à grande échelle avec une distribution des intensités allant de champs forts aux champs faibles. Je me suis basé sur ce que l'on sait de la stabilité des champs magnétiques dans les enveloppes radiatives d'étoiles en rotation différentielle et en particulier sur l'excellent article de revue de Spruit (1999). La stabilité dépend de l'intensité du champ magnétique. Si le champ est suffisamment fort, il impose la rotation solide dans l'étoile, si le champ est faible, la rotation différentielle modifie la configuration magnétique et la rend instable. L'existence de configurations magnétiques stables à champ fort est principalement supportée par l'observation des champs d'étoiles Ap et des naines blanches qui ont des champs stables et structurés à grandes échelles. Des configurations de champ stables sont également étudiées par simulation numérique et tendent à confirmer les travaux théoriques précédents selon lesquels le champ doit posséder à la fois des composantes poloïdales et toroïdales pour être stable (Braithwaite 2009). Si, en revanche, le champ est faible, on sait qu'une rotation différentielle induira en quelques périodes de rotation un fort champ azimutal par advection de la composante poloïdale du champ. Or un champ qui devient principalement azimutal est sujet à l'instabilité de Tayler qui est une instabilité de type pinch. Dans ce cas, la configuration de champ à grande échelle sera détruite par le développement de l'instabilité qui se fait à grandes échelles azimutales $m = 1$ mais à petites échelles dans les directions latitudinales et radiales (Brun &

Zahn 2006).

J'ai donc proposé le scénario suivant pour interpréter l'existence du désert magnétique en champ longitudinal entre $\sim$ 1 Gauss et $\sim$ 100 Gauss (publié en même temps que les observations de Musicos dans Aurière et al. (2007, **A8**)) : Supposons qu'il existe un champ magnétique critique au delà duquel les configurations magnétiques sont stables et en deçà duquel toute configuration magnétique à grande échelle est instable vis à vis d'une instabilité. Le champ résultant de l'instabilité sera structuré à petite échelle ce qui diminuerait très significativement le champ longitudinal observé par effet d'annulation entre les polarités de signe opposé réparties sur la surface visible de l'étoile. Donc, en partant d'un échantillon d'étoiles comprenant à la fois des configurations de champs stables et instables, ce scénario induit un saut important dans la valeur du champ longitudinal. Si de plus, la valeur du champ longitudinal résultant du développement de l'instabilité est inférieure au seuil de détection des instruments, un tel scénario aboutit bien à un désert magnétique entre le seuil de détection et la valeur minimale des champs stables.

Pour déterminer le champ critique qui apparaît dans le scénario et le comparer au champ minimal des Ap/Bp, il faut établir à partir de quelle intensité du champ, la force de Lorentz empêche, en supprimant la rotation différentielle, l'évolution vers une configuration instable. On peut estimer le temps nécessaire pour engendrer, par advection de la composante poloïdale axisymétrique $\vec{B}_p^{\rm sym}$, une configuration de champ dominée par le champ toroïdal, à partir de l'équation d'induction de la composante toroïdale du champ B_ϕ :

$$\partial_t B_\phi = r \sin\theta \vec{B}_p^{\rm sym} \cdot \vec{\nabla}\Omega \tag{3.1}$$

L'amplitude du champ toroïdal devient du même ordre de grandeur que le champ poloïdal initial au bout d'un temps :

$$t_w = \frac{\ell}{r\Omega} \tag{3.2}$$

où $\ell = \Omega/|\vec{\nabla}\Omega|$ est l'échelle qui caractérise le gradient de la vitesse angulaire.

Le temps minimal de rétroaction du champ magnétique sur la rotation différentielle est le temps mis par une onde d'Alfvén pour se propager sur l'échelle de distance du gradient de vitesse angulaire :

$$t_A = \frac{\ell(4\pi\rho)^{1/2}}{B} \tag{3.3}$$

En disant que les deux processus agissent sur un même temps caractéristique, on obtient une esti-

mation locale du champ critique au delà duquel la rotation différentielle est supprimée avant d'avoir pu engendrer une configuration dominée par un champ toroïdal[1] :

$$B_c = (4\pi\rho)^{1/2} r\Omega \tag{3.4}$$

Donc, si $B < B_c$, la rotation différentielle induira une configuration dominée par le champ toroïdal qui est susceptible d'être instable vis-à-vis de l'instabilité de Tayler. Le seuil de cette instabilité donné par Spruit est le suivant :

$$B_\phi > (4\pi r\rho)^{1/2} \Omega^{1/2} N^{1/4} \frac{\eta^{1/2}}{\kappa^{1/4}} \tag{3.5}$$

Si on l'applique à la surface d'une étoile A typique on s'aperçoit que le champ poloïdal initial devrait être très faible ($B_p \sim 10^{-3}$ Gauss) pour que le champ toroïdal induit par advection soit stable vis-à-vis de l'instabilité de Tayler. Considérant des valeurs de champ magnétique observables, on conclut donc que le champ critique détermine si la configuration magnétique évolue vers une configuration stable (si $B > B_c$) ou instable (si $B < B_c$).

Le critère local Eq. (3.4) devra être testé dans un modèle global (au moins bidimensionnel) de l'advection du champ magnétique (voir Sect. 5.2.2). Néanmoins, il est encourageant de constater que la valeur du champ critique ainsi obtenue est quantitativement tout à fait compatible avec les champs observés dans les Ap à champ faible. De plus, même si les relevés spectropolarimétriques les plus complets ont été réalisés dans la gamme des étoiles de masse intermédiaire, le champ critique ainsi calculé est également compatible avec les champ magnétiques des étoiles B et O (Aurière et al. 2007, **A8**). Ce scénario pourrait donc expliquer comment à partir d'une distribution initiale (fossile) du champ magnétique des étoiles chaudes, on aboutit à une situation ou seulement la fraction des étoiles ayant un champ initial suffisamment fort conserve un champ structuré à grande échelle détectable par les moyens actuels. Par ailleurs, il prédit une dépendance du champ critique avec la rotation ($B_c \propto \Omega$) qui semble en accord avec les données existantes mais que l'on doit pouvoir tester plus précisément par un relevé spectropolarimétrique des étoiles Ap en rotation rapide (voir Sect. 5.2.1). Actuellement, ce scénario ne prédit pas le devenir des configurations magnétiques instables par instabilité de Tayler. Sont-ils dissipés par diffusion ohmique ? Sont-ils régénérées par un mécanisme dynamo tel que celui proposé dans ma thèse (Lignières

[1] dans la situation théorique où le champ initial est purement axisymétrique vis-à-vis de l'axe de rotation, un certain niveau de rotation différentielle peut persister entre les surfaces magnétiques alors que l'effet d'advection du champ est supprimé - Loi de Ferraro

et al. 1996) ou plus récemment par Spruit (2002) ?

3.2 Découverte du champ magnétique de Véga

Malgré de très nombreuses tentatives, la recherche de champ magnétique dans les étoiles de masse intermédiaire ne faisant pas partie de la classe des étoiles Ap/Bp est longtemps restée infructueuse. La dernière tentative en date, un relevé spectropolarimétrique d'étoiles A à raies étroites mené par M. Aurière sur Narval, avait permis d'abaisser la limite supérieure du champ de ces étoiles à quelques Gauss (Aurière et al. 2010, **A9**). Le programme de recherche de pulsations sur Véga par spectroscopie (voir Sect. 2.4) était l'occasion d'abaisser encore ce seuil (puisque le temps de pose était 10 fois supérieur à celui de la précédente tentative) et il a donc été réalisé pour l'essentiel dans le mode polarimétrique de Narval. Comme le montre la Figure 3.1, les 4 nuits d'observations spectropolarimétriques dédiées à Véga ont finalement permis de détecter avec assurance un signal polarisé circulairement. Il s'agit du signal polarimétrique de plus faible amplitude détecté à ce jour par Narval ou Espadons, même si des niveaux de polarisation du même ordre de grandeur (entre 2 et 3 fois supérieurs) ont été récemment détectés dans des étoiles à enveloppe convective (Aurière et al. 2009; Aurière et al. 2010). Les nombreux tests effectués à ce jour pour écarter la possibilité d'un signal spurieux (voir notamment la Figure 3.3 ci-dessous) sont tous compatibles avec une origine stellaire du signal et donc avec la présence d'un champ magnétique longitudinal de -0.6 ± 0.3 Gauss à la surface de Véga. C'est la première détection d'un champ magnétique dans une étoile de masse intermédiaire qui n'est pas chimiquement particulière du type Ap et de plus l'intensité du champ longitudinal est inférieure de deux ordres de grandeur au champ des Ap. Véga doit donc être considérée comme le premier membre d'une nouvelle classe d'étoile magnétique, distincte des étoiles Ap et dont on ne connaît pas à ce jour l'étendue (Lignières et al. 2009, **A10**).

Du point de vue théorique, le champ de Véga pourrait être engendré par une dynamo qui agirait soit dans une enveloppe radiative en rotation différentielle (Lignières et al. 1996; Spruit 2002) soit dans le coeur convectif de l'étoile (MacDonald & Mullan 2004). Il pourrait aussi être le résultat de la déstabilisation d'un champ à grande échelle de type Ap (voir Sect. 3.1). Même si ces modèles doivent être précisés dans le futur, ils sont déjà très utiles pour guider les observations notamment parce qu'ils suggèrent (i) que le champ de Véga est intrinsèquement variable (alors qu'aucune variabilité n'a été détectée dans les champs connus des étoiles massives et de masse intermédiaire), (ii) que la rotation joue

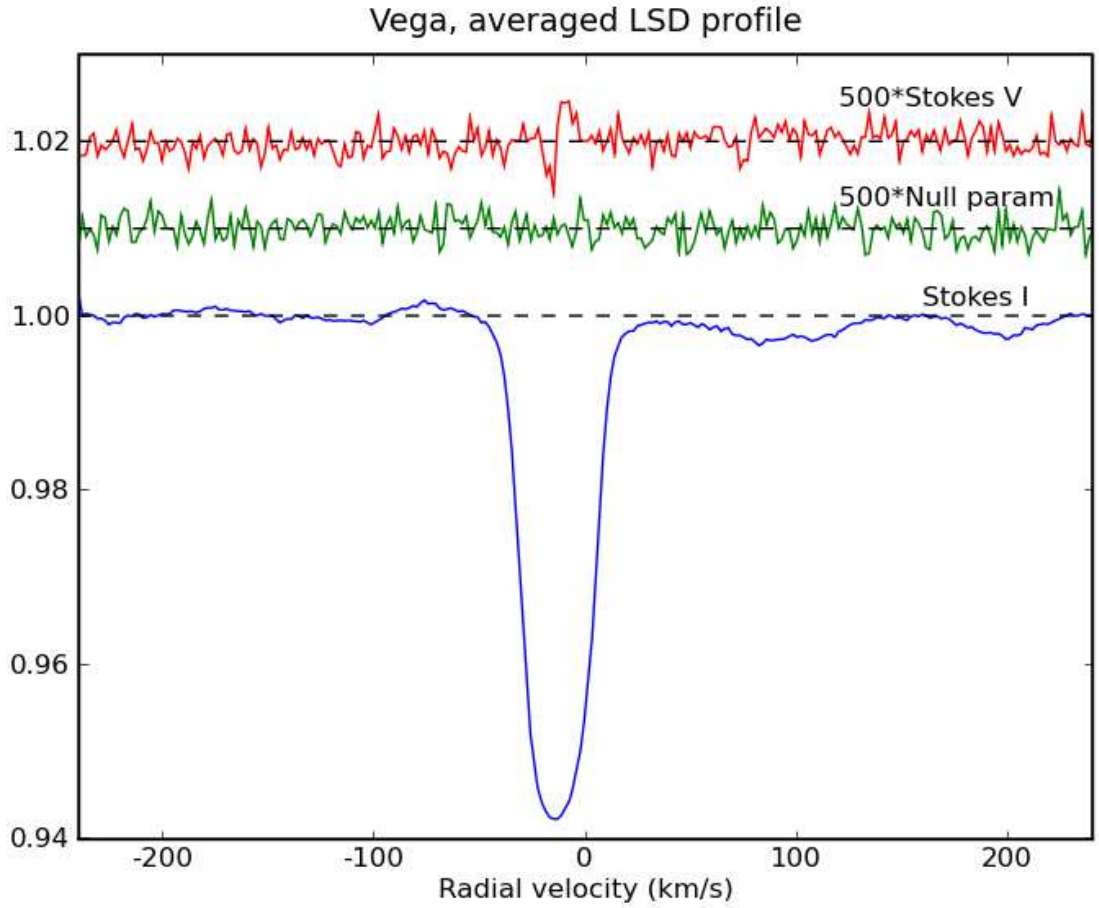

FIG. 3.1 – Détection d'un champ magnétique sur Véga avec NARVAL au TBL : Moyenne des 257 profils moyens obtenus par la méthode de déconvolution du spectre (Least Square Deconvolution) en Stokes I (bleu/bas) et en Stokes V (rouge/haut) en fonction de la vitesse radiale. La courbe verte/milieu est une combinaison des paramètres de Stokes qui doit être nulle en l'absence de bruit. Cette courbe et celle en Stokes V sont décalées verticalement et agrandies d'un facteur 500. Un signal polarisé de très faible amplitude ($V/I \sim 10^{-5}$) est détecté sans ambiguïté. Le niveau de bruit, correspondant à l'écart-type des fluctuations du signal en dehors de la raie, est en effet $\sigma = 2 \times 10^{-6} I_c$ où I_c est l'intensité du continu.

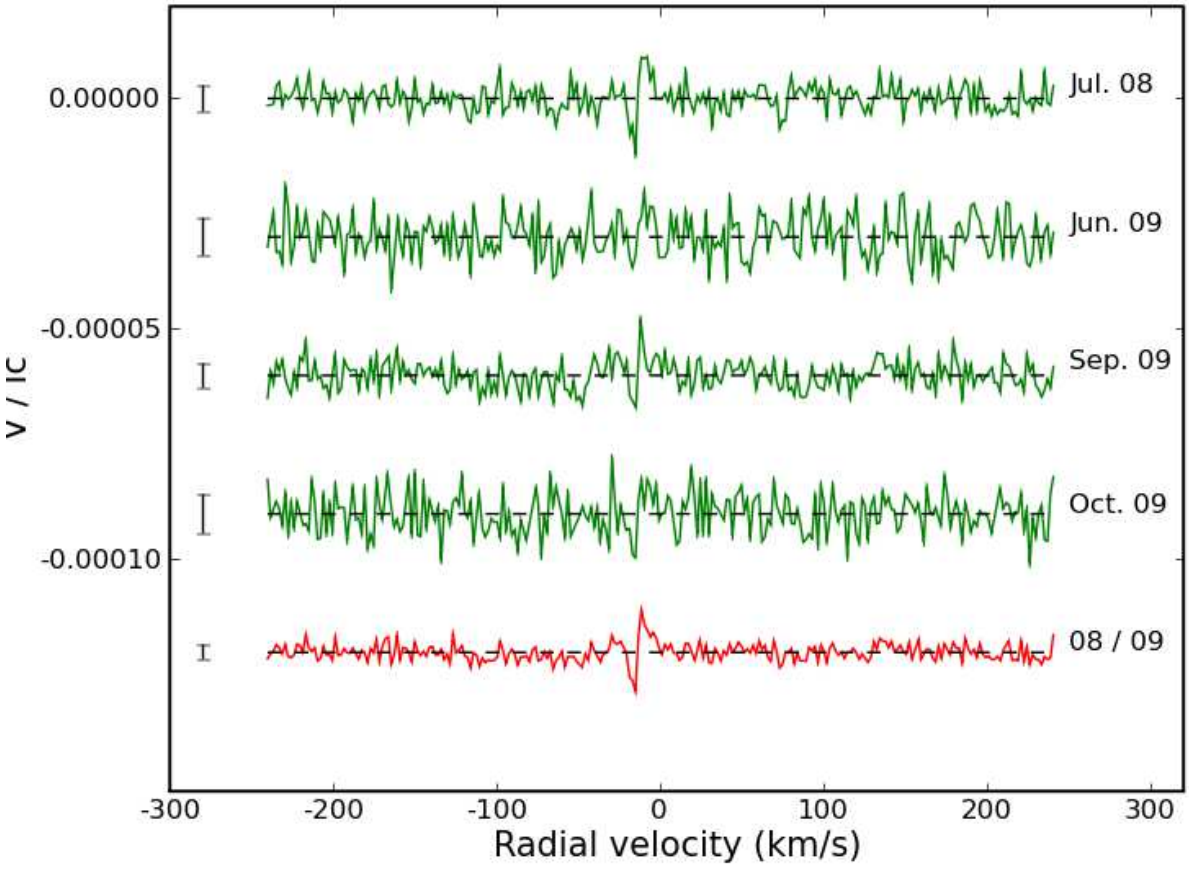

FIG. 3.2 – Moyennes des profils LSD en Stokes V obtenus durant quatre récentes campagnes d'observation de Véga (en vert). Moyenne de l'ensemble des 799 profils LSD en Stokes V des quatre campagnes (en rouge). Les niveaux de bruit pour chaque campagne sont donnés par des barres d'erreur sur la gauche des profils.

un rôle central sur l'intensité du champ généré et (iii) que la plupart des étoiles A non Ap (c'est-à-dire 90 à 95 % des étoiles cette classe de masse) ont un champ magnétique similaire à celui de Véga.

De nouvelles observations sont donc nécessaires pour d'une part confirmer et caractériser autant que possible le champ de Véga et d'autre part rechercher de nouveaux membres à cette classe d'étoile magnétique. En tant que PI des demandes de temps à Narval et Espadons, j'ai été amené à définir une stratégie observationnelle pour cette nouvelle exploration qui ne fait que commencer (voir Sect. 5.2.1). Je décris ici les premiers résultats des observations réalisées sur Véga et Sirius, et qui ont été analysées par P. Petit (un article Petit et al. sera soumis très prochainement).

Concernant Véga, trois campagnes d'observations ont été menées depuis la campagne de juillet 2008,

deux avec Narval en juin 2009 et octobre 2009 et une avec Espadons en septembre 2009 (le PI de cette dernière demande a été G. Wade). La Figure 3.2 montre les moyennes des profils de Stokes V obtenus pour chacune des 4 campagnes ainsi que la moyenne sur l'ensemble des spectres obtenus aux cours des 4 campagnes. Le signal polarimétrique est présent systématiquement et il ne montre pas de variation évidente entre les différentes campagnes. La moyenne sur l'ensemble des spectres permet néanmoins d'augmenter de façon significative le rapport signal-sur-bruit. Une autre confirmation de la présence d'un champ magnétique sur Véga peut être obtenu en tirant parti de la sensibilité de l'effet Zeeman au facteur de Landé associé aux raies d'absorption. Comme on s'y attend pour un signal polarisé par effet Zeeman, le signal polarisé de Véga est de plus faible amplitude si on se restreint aux raies à faible facteur de Landé alors qu'il est de plus forte amplitude pour les raies à fort facteur de Landé. Cet effet est montré à la Figure 3.3.

Une recherche de modulation rotationnelle des profils Stokes V a été effectuée sur les deux campagnes d'observations les plus longues (juillet 2008 et septembre 2009). Même si la faiblesse du signal et la durée limitée des observations rendent difficile la détection d'une modulation rotationnelle, une période de rotation $P \sim 18$h est trouvée avec le même degré de confidence dans ces deux jeux de données indépendants. Cette période est tout à fait compatible avec celle trouvée par Takeda et al. (2008) à partir des signatures spectrales de l'assombrissement gravitationnel induit par la force centrifuge. Elle est en revanche en clair désaccord avec la période de ~ 12h déduite de l'analyse interférométrique de ce même effet d'assombrissement gravitationnel (Peterson et al. 2006). Notre résultat suggère que le magnétisme de type Véga n'est pas limité aux étoiles dont la rotation est extrême. En effet, une période de 18h correspond à une vitesse équatoriale de 175 km/s, proche de la vitesse de rotation typique des étoiles A normales (150 km/s), alors qu'une période de 12h indiquerait une rotation proche de la vitesse critique $\Omega \sim 0.9\Omega_K$.

Avec la période de rotation, l'imagerie Zeeman-Doppler permet de reconstruire des cartes de champ magnétique compatibles avec les données. La Figure 3.4 montre la distribution du champ obtenu pour la campagne de juillet 2008. On observe une concentration de champ au pôle et des structures de relativement petites échelles aux plus basses latitudes. Il s'agit de la première image Zeeman-Doppler de la surface d'une étoile A non chimiquement particulière. Le degré de corrélation des cartes obtenues en juillet 2008 et septembre 2009 est relativement important et n'indique pas pour l'instant de variabilité intrinsèque du champ entre ces deux observations. Une campagne d'observations est prrogrammée en

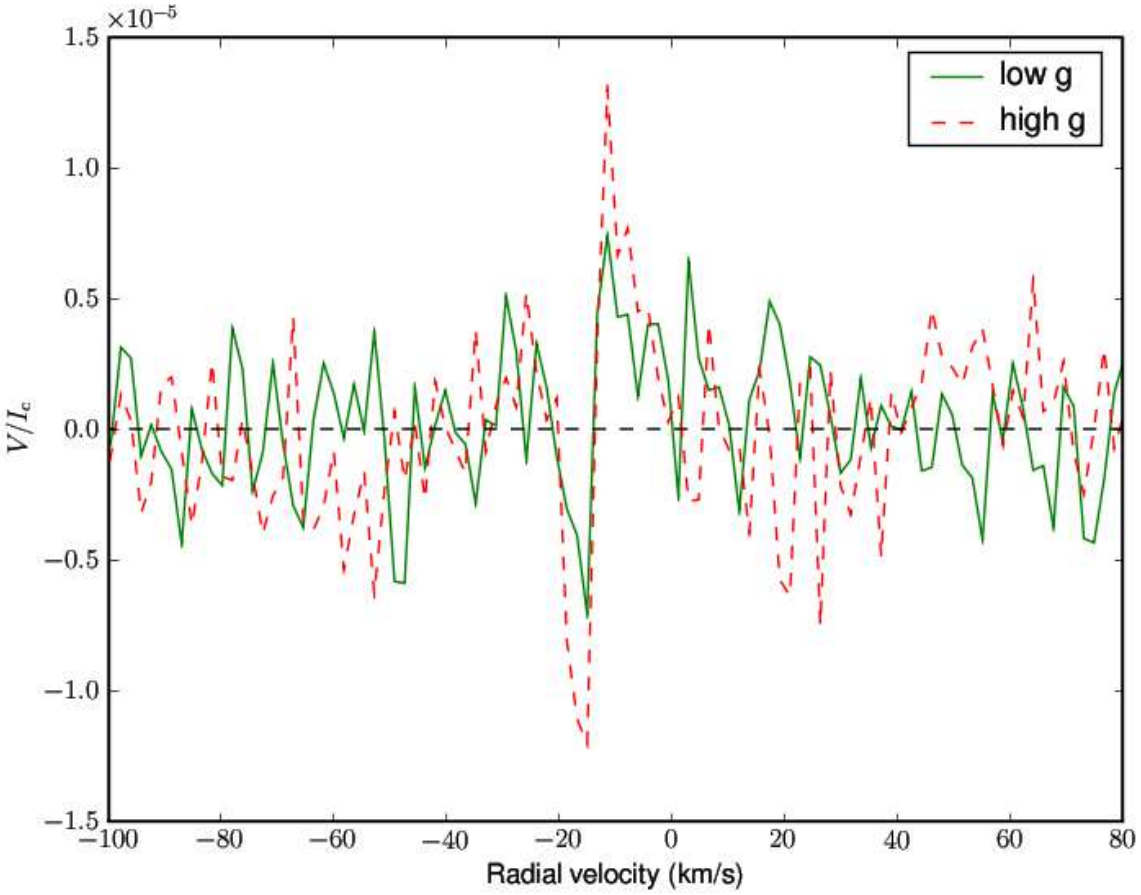

FIG. 3.3 – Moyenne des profils LSD en Stokes V calculés avec des listes de raie à faibles facteurs de Landé (en vert) et à forts facteurs de Landé (en rouge).

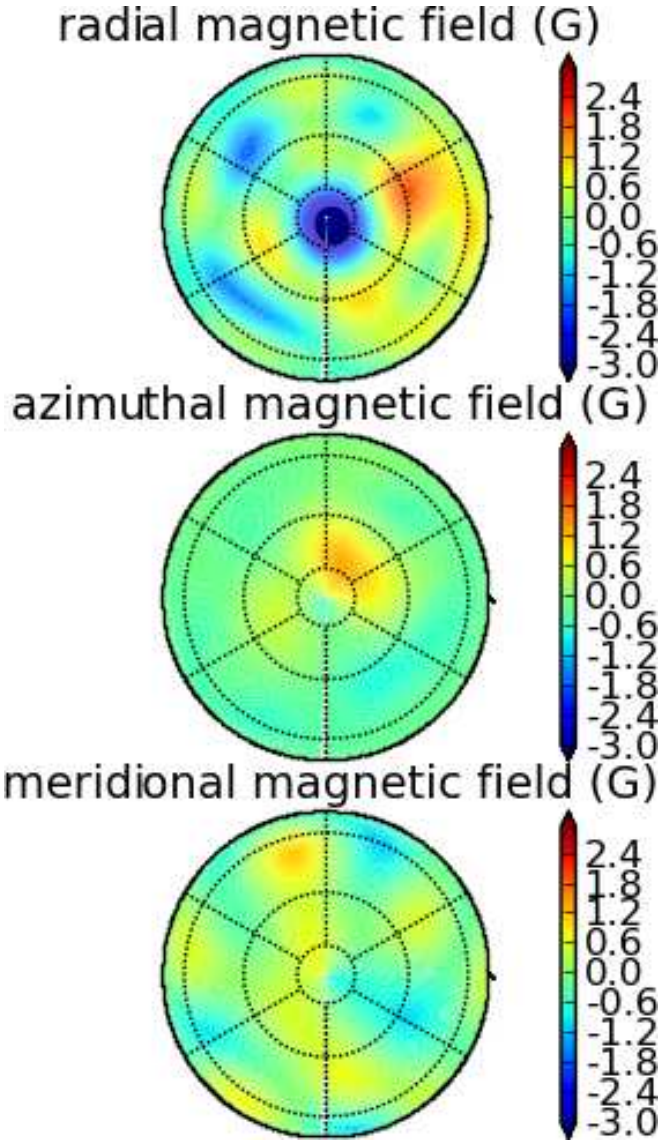

FIG. 3.4 – Carte du vecteur champ magnétique de Véga en projection polaire (observations de juillet 2008). Les trois composantes du champ magnétique sont représentées séparément et l'intensité du champ est exprimée en Gauss.

juillet 2010 sur Narval, elle devrait permettre de confirmer la période de rotation et de continuer l'étude de la variabilité du champ.

Après Véga, l'objet le mieux adapté pour rechercher un champ magnétique de faible amplitude dans une étoile de masse intermédiaire est Sirius (car elle est très brillante et a un faible v sini). De plus, Sirius étant une étoile sous métallique de type Am, on sait que sa vitesse de rotation doit être inférieure à ~ 100 km/s. La présence ou l'absence de champ sur Sirius sera donc très importante puisque cela donnera une nouvelle indication sur la rôle de la rotation et nous dira si l'on a intérêt à se concentrer sur les étoiles qui ne sont pas Am pour explorer la nouvelle classe d'étoile magnétique. Cela rendrait l'exploration plus difficile car, les étoiles Am ayant une vitesse de rotation limitée, elles constituent la majorité des étoiles brillantes à raies étroites qui sont les cibles les plus faciles pour la recherche de champs magnétiques. Une première campagne d'observations spectropolarimétriques dédiée à Sirius a été réalisée au CFHT en 2010. Bien que seulement la moitié des observations prévues ait pu être exploitée, la moyenne des profils LSD en Stokes V représentée à la Figure 3.2 montre une détection marginale d'un signal polarisé. À noter qu'il existe aussi une observation de Sirius réalisée par Aurière et al. (2010) où l'on retrouve, certes avec un moins bon rapport signal-sur-bruit, une forme similaire du signal polarisé, décalée en vitesse radiale. Nous essayons bien évidemment de confirmer cette détection par de nouvelles observations de Sirius. Une telle confirmation laisserait penser que toutes les étoiles non Ap/Bp de masse intermédiaire possèdent un champ magnétique.

3.3 Autres programmes d'observation des champs magnétiques stellaires

J'ai participé à différents programmes d'observation spectropolarimétrique menés par des chercheurs du LATT, sur les étoiles Ap, les étoiles A et les géantes rouges avec M. Aurière, sur les étoiles très froides (les naines M) avec J. F. Donati et J. Morin et sur les étoiles de type solaire avec P. Petit. J'ai contribué à ces recherches en tant qu'observateur (et réalisé en moyenne une mission d'une semaine au TBL tous les ans entre 2001 et 2007) mais aussi, en tant que modélisateur, en participant à la rédaction des demandes (dans certains cas) et à l'interprétation des résultats. Je participe également à Mimes, un Large Programme du CFHT consacré aux champs magnétiques des étoiles massives et des étoiles Ap (P.I. G. Wade). Un des résultats de ce premier relevé spectropolarimétrique d'envergure dans le domaine

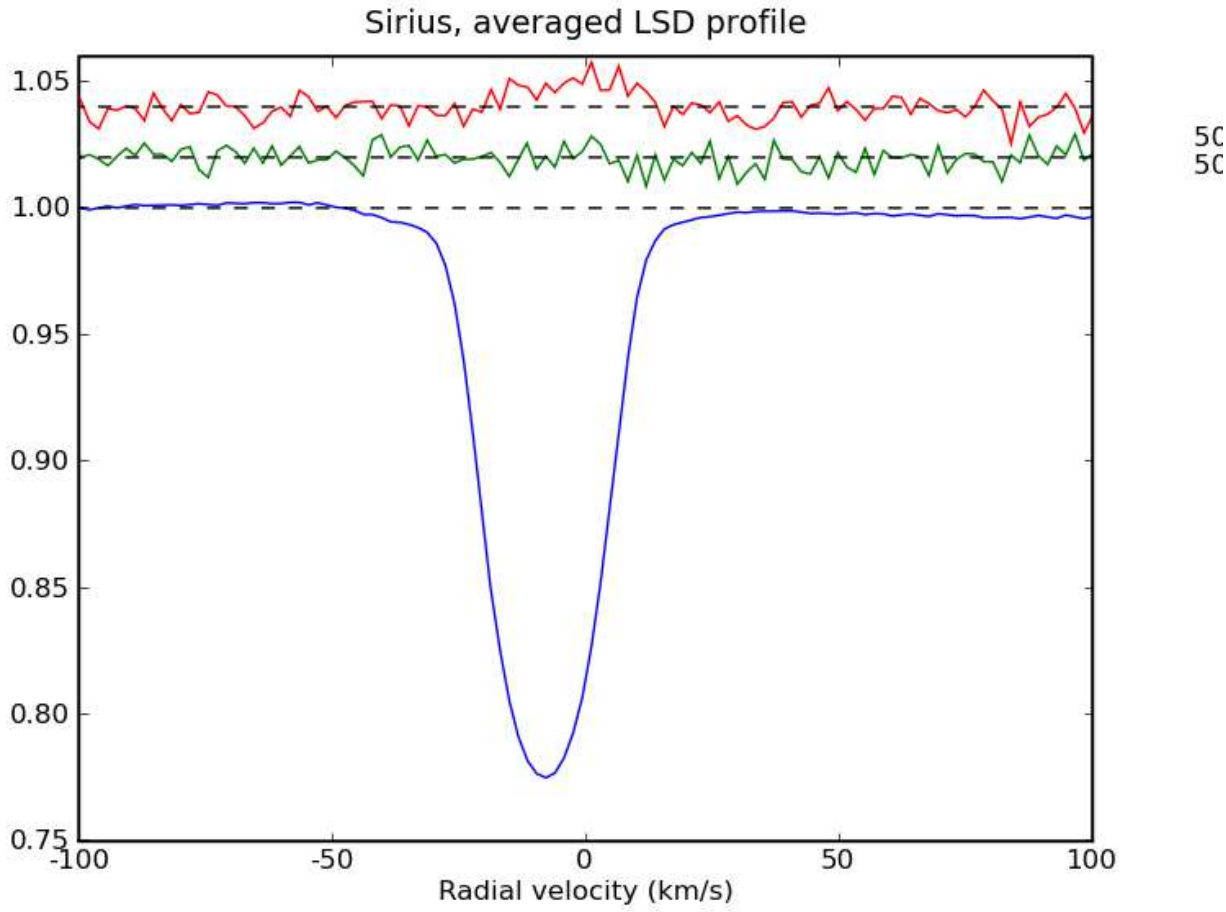

FIG. 3.5 – Moyenne de 86 profils LSD en Stokes I (bleu) et Stokes V (rouge), en fonction de la vitesse radiale. La courbe verte/milieu est une combinaison des paramètres de Stokes qui doit être nulle en l'absence de bruit. Cette courbe et celle en Stokes V sont décalées verticalement et agrandies d'un facteur 500. Un signal polarisé circulairement est observé à un niveau de $2 \times 10^{-5} I_c$ alors que le niveau de bruit est de $9 \times 10^{-6} I_c$ où I_c est l'intensité du continu. La forme du signal diffère de celle de Véga puisqu'on observe un lobe positif au centre de la raie et possiblement deux lobes négatifs dans les ailes. Le champ longitudinal associé à cette détection marginal est 0.5 ± 0.3 G, une valeur similaire au champ de Véga.

des étoiles massives qui m'intéresse particulièrement est la possibilité de tester, dans cette gamme de masse, l'existence d'un champ magnétique critique et sa relation avec la rotation des étoiles.

3.4 Articles A8-A10

3.4.1 A8 : Weak magnetic fields in Ap/Bp stars. Evidence for a dipole field lower limit and a tentative interpretation of the magnetic dichotomy

"Weak magnetic fields in Ap/Bp stars. Evidence for a dipole field lower limit and a tentative interpretation of the magnetic dichotomy"

Aurière M., Wade G. A., Silvester J., Lignières F. et al.

A&A 475, 1053-1065, 2007

A&A 475, 1053–1065 (2007)
DOI: 10.1051/0004-6361:20078189

Astronomy & Astrophysics

Weak magnetic fields in Ap/Bp stars⋆,⋆⋆,⋆⋆⋆

Evidence for a dipole field lower limit and a tentative interpretation of the magnetic dichotomy

M. Aurière[1], G. A. Wade[2], J. Silvester[2,3], F. Lignières[1], S. Bagnulo[4], K. Bale[2], B. Dintrans[1], J. F. Donati[1], C. P. Folsom[2], M. Gruberbauer[5], A. Hui Bon Hoa[1], S. Jeffers[6], N. Johnson[2], J. D. Landstreet[7], A. Lèbre[8], T. Lueftinger[5], S. Marsden[9], D. Mouillet[1], S. Naseri[1], F. Paletou[1], P. Petit[1], J. Power[2], F. Rincon[1], S. Strasser[10], and N. Toqué[11]

[1] Laboratoire d'Astrophysique de Toulouse-Tarbes, Université Paul Sabatier, CNRS, Observatoire Midi-Pyrénées, 57 avenue d'Azereix, 65008 Tarbes, France
e-mail: michel.auriere@ast.obs-mip.fr
[2] Department of Physics, Royal Military College of Canada, PO Box 17000, Station "Forces", Kingston, Ontario, Canada K7K 4B4
[3] Department of Physics, Queen's University, Kingston, Ontario, Canada
[4] Armagh Observatory, College Hill, Armagh BT61 9DG, Northern Ireland
[5] Institut für Astronomy, University of Vienna, Türkenschanzstrasse 17, 1180 Wien, Austria
[6] Sterrekundig Instituut Utrecht, Universiteit Utrecht, PO Box 80000, 3508 TA Utrecht, The Netherlands
[7] Department of Physics & Astronomy, The University of Western Ontario, London, Ontario, Canada, N6A 3K7
[8] GRAAL, Université Montpellier II, CNRS, 62 place Eugène Bataillon, 34095 Montpellier, France
[9] Anglo-Australian Observatory, PO Box 296, Epping, NSW 1710, Australia
[10] Department of Astronomy, University of Minnesota, 116 Church Street, S.E., Minneapolis 55455, USA
[11] Department of Physics and Astronomy, Saint Mary's University, 923 Robie Street, Halifax, Nova Scotia, B3H3C3, Canada

Received 29 June 2007 / Accepted 17 September 2007

ABSTRACT

Aims. We investigated a sample of 28 well-known spectroscopically-identified magnetic Ap/Bp stars, with weak, poorly-determined or previously undetected magnetic fields. The aim of this study is to explore the weak part of the magnetic field distribution of Ap/Bp stars.

Methods. Using the MuSiCoS and NARVAL spectropolarimeters at Télescope Bernard Lyot (Observatoire du Pic du Midi, France) and the cross-correlation technique Least Squares Deconvolution (LSD), we obtained 282 LSD Stokes V signatures of our 28 sample stars, in order to detect the magnetic field and to infer its longitudinal component with high precision (median $\sigma = 40$ G).

Results. For the 28 studied stars, we obtained 27 detections of Stokes V Zeeman signatures from the MuSiCoS observations. Detection of the Stokes V signature of the 28th star (HD 32650) was obtained during science demonstration time of the new NARVAL spectropolarimeter at Pic du Midi. This result clearly shows that when observed with sufficient precision, all firmly classified Ap/Bp stars show detectable surface magnetic fields. Furthermore, all detected magnetic fields correspond to longitudinal fields which are significantly greater than some tens of G. To better characterise the surface magnetic field intensities and geometries of the sample, we phased the longitudinal field measurements of each star using new and previously-published rotational periods, and modeled them to infer the dipolar field intensity ($B_{\rm d}$, measured at the magnetic pole) and the magnetic obliquity (β). The distribution of derived dipole strengths for these stars exhibits a plateau at about 1 kG, falling off to larger and smaller field strengths. Remarkably, in this sample of stars selected for their presumably weak magnetic fields, we find only 2 stars for which the derived dipole strength is weaker than 300 G. We interpret this "magnetic threshold" as a critical value necessary for the stability of large-scale magnetic fields, and develop a simple quantitative model that is able to approximately reproduce the observed threshold characteristics. This scenario leads to a natural explanation of the small fraction of intermediate-mass magnetic stars. It may also explain the near-absence of magnetic fields in more massive B and O-type stars.

Key words. stars: chemically peculiar – stars: magnetic fields

1. Introduction

The magnetic chemically peculiar Ap/Bp stars are the non-degenerate stars for which the strongest magnetic fields have been measured (Landstreet 1992). Although the fields are thought to be fossil remnants of flux swept up during star formation or produced via dynamo action on the pre-main sequence, their origin is not understood in any real detail (e.g. Moss 2001).

⋆ Based on data obtained using the Télescope Bernard Lyot at Observatoire du Pic du Midi, CNRS and Université Paul Sabatier, France.

⋆⋆ Figures 7 to 32 are only available in electronic form at http://www.aanda.org

⋆⋆⋆ Table 3 is only available in electronic form at the CDS via anonymous ftp to cdsarc.u-strasbg.fr (130.79.128.5) or via http://cdsweb.u-strasbg.fr/cgi-bin/qcat?J/A+A/475/1053

Furthermore, the role of the magnetic field in the diffusion processes which are responsible for their chemical peculiarity has been studied in only a schematic fashion.

Although more than one thousand main sequence A-type stars have been catalogued as magnetic Ap/Bp stars (Renson et al. 1991) following the scheme of Preston (1974), direct measurements of the magnetic field have been obtained for only a few hundred of them (Romanyuk 2000; Bychkov et al. 2003). Examination of the published measurements shows that the majority of the reported values are rather large. For example, 55% of the 210 stars of the catalogue of Romanyuk (2000) with published magnetic field measurements have a maximum unsigned line-of-sight (longitudinal) magnetic field B_ℓ larger than 1 kG. On the other hand, according to Bohlender & Landstreet (1990), the median root-mean-square (rms) longitudinal magnetic field of Ap stars (based on a small magnitude-limited sample observed by Borra & Landstreet 1980) is only about 300 G (the largest rms field they report is only 710 G). This implies that most Ap stars have relatively weak ($\lesssim$1 kG) magnetic fields, and that the available observations are strongly biased toward stars with the strongest and most easily-measured fields. One consequence of this bias is that the weak-field part of the magnetic field distribution of Ap stars is poorly studied. It is not known if it increases monotonically toward arbitrarily small field strength, or if it is truncated at a minimum magnetic field strength (as proposed by Glagolevskij & Chountonov 2002).

In order to improve our knowledge of the weak-field part of the magnetic field distribution of Ap stars, we have undertaken a study of a sample of 28 well-known spectroscopically-identified Ap/Bp stars, with very weak, poorly-determined or previously-undetected magnetic fields. We describe our survey in Sect. 2 and report our observational and modeling results in Sects. 3 and 4. We discuss the implications of our results, suggesting one possible interpretation involving the stability of large scale magnetic fields, in Sect. 5 and give our conclusions in Sect. 6.

2. The weak-field Ap stars survey

2.1. The selected sample

Our sample is composed of spectroscopically-identified Ap/Bp stars belonging to the HD catalogue. Twelve stars were selected based on the observations of Borra & Landstreet (1980) and Bohlender et al. (1993), identifying stars for which no significant detection of the magnetic field was obtained. Thirteen additional targets are stars for which only old photographic measurements of the magnetic field were available, typically by Babcock (1958), and for which measurements have poor precision and do not provide a significant detection of the magnetic field; these stars were generally selected using the catalogues of Romanyuk (2000) or Bychkov et al. (2003). Finally, 3 stars of our sample were selected which had not been observed for magnetic field before this work. The observational properties of the 28 stars are presented in Table 1. Section 3.2 gives more details on each star and on the obtained results.

Because all of these stars are relatively bright, most have been known for decades and have been well studied. All appear in the Hipparcos catalogue (Perryman et al. 1997), and all but 6 have $\sigma_\pi/\pi < 0.2$. The majority have photometrically-determined rotational periods and published values of $v \sin i$. Many have been studied using high-resolution spectroscopy and Doppler Imaging. Therefore the classification of this sample as *bona fide* Ap/Bp stars is generally quite firm. As a consequence of this careful selection (and as will be described later in the paper), *no* non-Ap/Bp star has been mistakenly included in the sample.

2.2. Observations and reduction

Stokes V and Stokes I spectra of the 28 sample stars were obtained during 10 observing runs, from July 2001 to June 2006. We used the MuSiCoS spectropolarimeter attached the Bernard Lyot telescope (TBL) at Observatoire du Pic du Midi. The MuSiCoS spectropolarimeter is composed of a cross-dispersed echelle spectrograph (Baudrand & Böhm 1992) and a dedicated polarimeter module (Donati et al. 1999). The spectrograph is a table-top instrument, fed by a double optical fibre directly from the Cassegrain-mounted polarimeter. In one single exposure, this apparatus allows the acquisition of a stellar spectrum in a given polarisation (Stokes V in this case) throughout the spectral range 450 to 660 nm with a resolving power of about 35 000. Spectra in both orthogonal polarisations are recorded simultaneously by the CCD detector. A complete Stokes V exposure consists of a sequence of four subexposures, between which the quarter-wave plate is rotated by 90°. This has the effect of exchanging the beams in the whole instrument, and in particular switching the positions of the two orthogonally polarised spectra on the CCD, thereby reducing spurious polarisation signatures.

The echelle polarisation spectra were reduced using the ESpRIT package (Donati et al. 1997). The observation and reduction procedures are more thoroughly described by Shorlin et al. (2002).

The correct operation of the MuSiCoS instrument, and in particular the absence of spurious magnetic field detections, is supported by other data obtained during these same observing runs, including studies of non-magnetic A-type stars (e.g. Shorlin et al. 2002), magnetic A, B and O-type stars (e.g., Ryabchikova et al. 2005a; Donati et al. 2001; Wade et al. 2006a) and magnetic late-type stars (e.g. Petit et al. 2005).

MuSiCoS has recently been decomissioned, and has been replaced with NARVAL (Aurière 2003), the new-generation spectropolarimeter which is a copy of the ESPaDOnS instrument in operation at the Canada-France-Hawaii Telescope (Donati 2004, 2007: in preparation). The main improvements of NARVAL in polarisation mode with respect to MuSiCoS are a spectral resolution of about 65 000, spectral response between 370 nm and 1000 nm, and an overall sensitivity increased by a factor of about 30.

2.3. Physical properties of the sample

For each of the sample stars, we have determined effective temperature $T_{\rm eff}$, luminosity L and radius R, to allow us to identify the appropriate line mask for Least-Squares Deconvolution (Sect. 2.5) and for determination of the rotational axis inclination for the dipole magnetic field model (Sect. 2.7).

Effective temperatures of stars of our sample were derived using Geneva and Strömgren photometry (obtained from the General Catalogue of Photometric Data (GCPD); Mermilliod et al. 1997) using the calibrations of Hauck & North (1982) and Moon & Dworetsky (1985). Effective temperatures reported in Table 1 are the average of the two estimates when both were available, or the single one which could be derived when only one photometric set was available. We have assumed for $T_{\rm eff}$ an uncertainty of the order of 3% for propagation of uncertainties in all calculations using the effective temperature.

Table 1. Observational properties of the weak-field Ap star sample. Columns give ID and HD number, visual magnitude, spectral classification, effective temperature, luminosity and radius (with associated 1σ error bars), adopted LSD mask temperature, number of observations obtained and detection level (d = definite detection; m = marginal detection), maximum observed unsigned longitudinal field in G, 1σ error in G, and peak longitudinal field detection significance $z = |B_l^{\max}|/\sigma$. $B_{\rm d}^{\min,3.3}$ is the minimum dipole field (at 2σ) inferred from the maximum measured longitudinal field and Eq. (7).

ID	HD	m_V	Spec Type	$T_{\rm eff}^{\pm}$ (K)	$\log L$ ($L_\odot$)	R ($R_\odot$)	Mask (kK)	#	Det. level	$\lvert B_\ell\rvert^{\max} \pm \sigma$ (G)	z	$B_{\rm d}^{\min,3.3}$ (G)
HN And	8441	6.7	A2p	9060 ± 300	1.90 ± 0.16	3.6 ± 0.9	9	8	8d	157 ± 18	8.7	399
43 Cas	10221	5.5	A0sp	10660 ± 350	2.11 ± 0.09	3.3 ± 0.7	11	10	8d	148 ± 34	4.3	264
ι Cas	15089	4.5	A5p	8360 ± 275	1.38 ± 0.05	2.3 ± 0.4	9	12	12d	486 ± 23	20.8	1452
	15144	5.8	A6Vsp	8480 ± 280	1.21 ± 0.07	1.9 ± 0.3	9	6	6d	631 ± 15	42.0	1983
21 Per	18296	5.0	B9p	9360 ± 310	2.08 ± 0.11	4.2 ± 1.0	10	2	2d	213 ± 20	10.6	571
9 Tau	22374	6.7	A2p	8390 ± 275	1.48 ± 0.13	2.6 ± 0.7	9	2	2d	523 ± 24	21.7	1568
56 Tau	27309	5.3	A0sp	12730 ± 420	2.06 ± 0.08	2.2 ± 0.4	12	12	12d	804 ± 50	16.1	2323
11 Ori	32549	4.7	A0sp	10220 ± 335	2.35 ± 0.12	4.7 ± 1.2	11	11	1d3m	186 ± 39	4.7	356
	32650	5.4	B9sp	11920 ± 390	2.11 ± 0.07	2.7 ± 0.5	12	18	2m3d	91 ± 18	5.0	237
	37687	7.0	B8	9450 ± 310	2.18 ± 0.25	4.6 ± 1.9	10	2	2d	766 ± 119	6.4	1742
137 Tau	39317	5.5	B9spe	10130 ± 330	2.19 ± 0.14	4.0 ± 1.1	11	8	3d1m	216 ± 59	3.6	323
	40711	8.5	A0	8070 ± 265	1.94 ± 0.61	4.8 ± 5.3	9	3	1d1m	528 ± 38	13.8	1492
	43819	6.2	B9IIIsp	10880 ± 355	2.15 ± 0.20	3.3 ± 1.2	11	8	8d	628 ± 25	25.1	1907
15 Cnc	68351	5.6	B9sp	10290 ± 340	2.65 ± 0.21	6.6 ± 2.4	10	16	1d4m	325 ± 47	6.9	762
3 Hya	72968	5.7	A1spe	9840 ± 320	1.55 ± 0.08	2.0 ± 0.4	10	13	13d	427 ± 16	27.4	1304
45 Leo	90569	6.0	A0sp	10250 ± 335	1.78 ± 0.10	2.5 ± 0.5	11	10	10d	541 ± 23	23.5	1634
	94427	7.3	A5	7250 ± 240	1.05 ± 0.11	2.1 ± 0.5	8	8	8d	356 ± 41	8.6	904
EP Uma	96707	6.0	F0sp	7780 ± 255	1.54 ± 0.08	3.2 ± 0.6	8	21	7d7m	69 ± 33	2.3	128
65 Uma	103498	6.9	A1spe	9220 ± 300	2.06 ± 0.20	4.2 ± 1.5	9	14	12d1m	169 ± 19	8.9	432
21 Com	108945	5.4	A2pvar	8870 ± 290	1.72 ± 0.09	3.1 ± 0.6	9	13	12d1m	234 ± 54	4.3	416
ω Her	148112	4.6	B9p	9330 ± 305	1.86 ± 0.08	3.2 ± 0.6	10	12	11d	204 ± 21	9.7	535
45 Her	151525	5.2	B9p	9380 ± 310	2.18 ± 0.13	4.7 ± 1.2	11	14	2d3m	146 ± 38	3.8	231
	171586	6.4	A2pvar	8760 ± 290	1.37 ± 0.10	2.1 ± 0.5	10	5	5d	375 ± 56	6.6	868
	171782	7.8	A0p	9660 ± 315	1.76 ± 0.30	2.7 ± 1.3	10	6	2d1m	333 ± 78	4.2	584
19 Lyr	179527	5.9	B9sp	10370 ± 340	2.63 ± 0.16	6.4 ± 1.9	11	11	8d2m	156 ± 46	3.4	211
4 Cyg	183056	5.1	B9sp	11710 ± 385	2.69 ± 0.11	5.3 ± 1.2	12	13	13d	290 ± 42	6.9	680
	204411	5.3	A6pe	8750 ± 290	1.97 ± 0.07	4.2 ± 0.8	9	12	12d	88 ± 14	6.0	198
κ Psc	220825	4.9	A0p	9450 ± 310	1.40 ± 0.05	1.9 ± 0.3	10	12	12d	312 ± 25	12.8	865

Luminosity was inferred using the GCPD-reported visual magnitude, the Hipparcos parallax and the bolometric correction relations of Balona (1994). Radius was then inferred directly from the luminosity and temperature via the Stefan-Boltzmann equation for a uniform spherical star.

The inferred values of $T_{\rm eff}$, $\log L/L_\odot$ and $R/R_\odot$ are reported in Table 1. For the 20 stars which we have in common with the study of Kochukhov & Bagnulo (2006), these values are all in good agreement. As pointed out by Landstreet et al. (2007), the assumed uncertainties of Kochukhov & Bagnulo (2006), which are comparable to our own, are probably somewhat underestimated. However, as our fundamental parameters are not to be used for detailed evolutionary studies, we consider them to be sufficient for this study.

2.4. Least-Squares Deconvolution and magnetic field detection

The primary aim of our study is to detect line circular polarisation (a "Stokes V Zeeman signature") which is characteristic of the longitudinal Zeeman effect produced by the presence of a magnetic field in the stellar photosphere. For this we used the Least-Squares Deconvolution (LSD) procedure, first used by Donati et al. (1997) to study the magnetic fields of active late-type stars and by Wade et al. (2000a,b) for Ap stars. This method enables the "averaging" of several hundred (and possibly several thousand in some stars) lines and thus to obtain Stokes I and Stokes V profiles with greatly improved S/N.

LSD provides a single quantitative criterion for the detection of Stokes V Zeeman signatures: we perform a statistical test in which the reduced χ^2 statistic is computed for the Stokes V profile, both inside and outside the spectral line (Donati et al. 1997). The statistics are then converted into detection probabilities, which are assessed to determine if we have a definite detection (dd, false alarm probability smaller than 10^{-5}), a marginal detection (md, false alarm probability greater than 10^{-5} and smaller than 10^{-3}), or no detection at all (nd). A diagnostic null spectrum (called N in the following) is also obtained using the same subexposures obtained for Stokes V, but by pair processing those corresponding to identical azimuths of the quarter-wave plate. By checking that a signal is detected only in V and not in N, and that any detected signature is located within the line profile velocity interval, we can distinguish between real magnetic signatures and (infrequent) spurious signatures. In addition, using the full resolved Stokes V profile enables the detection of the magnetic field, even if the integrated line-of-sight component is very weak, or even null.

2.5. LSD masks

LSD is a cross-correlation method which requires comparison of our observed spectra with synthetic line masks (Donati et al. 1997; Shorlin et al. 2002). To obtain the most realistic masks, we used spectral line lists from the Vienna Atomic Line Database (VALD; Piskunov et al. 1995; Ryabchikova et al. 1997; Kupka et al. 1999). To take into account the chemical peculiarities of

Ap/Bp stars, we employed an abundance table in which the abundance of metals (Al, Si, S, Ti, V, Mn, Fe, Co, Ni, Zn, Sr, Y, Zr, Ba, La, Ce, Pr, Nd, Eu, Gd, Dy) is 10x solar, except for Cr which was increased to 100x solar (e.g. Shorlin et al. 2002). Masks were then compiled for effective temperature ranging from 7000–13 000 K, with $\log g = 4.0$, a microturbulence of 2 km s^{-1}, and including all metal lines with a central depth greater than 10% of the continuum. We also compiled a series of masks assuming solar abundances. We have found in other studies that the magnetic field measurements are not very sensitive to the mask temperature within a couple of thousand K (Wade et al., in preparation). We therefore computed masks spaced every 1000 K.

LSD was performed for several temperatures and in some cases the most significant magnetic field detection was obtained for a temperature somewhat hotter than that given by the photometric data. This occurred several times for the hottest sample stars – this can be seen in Table 1. In the case of the cool Ap star EP UMa, a solar abundance mask gave a better result (better detection of magnetic field and smaller error bars on B_ℓ) than Ap abundances as described above. These discrepancies probably result from differences between the true chemical peculiarities of individual stars and those assumed in the line masks. For the discrepant hot stars, we computed the longitudinal magnetic field for a mask temperature between that corresponding to the best detection and the derived effective temperature. For EP UMa, we used solar abundance masks in our analysis. The number of lines used in the LSD ranged from 1500 to 3000, and is anticorrelated with the temperature.

2.6. Longitudinal magnetic field

The longitudinal magnetic field was inferred from each of the Stokes I and V profile sets, using the first-order moment method. According to this method, the longitudinal field B_ℓ (in G) is calculated from the Stokes I and V profiles in velocity units as:

$$B_\ell = -2.14 \times 10^{11} \frac{\int v V(v) \mathrm{d}v}{\lambda g c \int [I_\mathrm{c} - I(v)] \mathrm{d}v}, \quad (1)$$

(Rees & Semel 1979; Donati et al. 1997; Wade et al. 2000b) where λ, in nm, is the mean wavelength of the LSD profile, c is the velocity of light (in the same units as v), and g is the mean value of the Landé factors of all lines used to construct the LSD profile. Integration ranges used for evaluation of Eq. (1) were computed automatically, beginning and ending 15 km s^{-1} before/after the location in the line wings at which the residual flux was equal to 85% of the continuum flux. The accuracy of this technique for determining high-precision longitudinal field measurements has been clearly demonstrated by Wade et al. (2000b), Donati et al. (2001) and Shorlin et al. (2002).

The resultant longitudinal magnetic field measurements, which are reported in Table 3, are remarkably precise (this table is only available on line). The 282 measurements, with a median 1σ uncertainty of 40 G, represent the largest compilation of high-precision stellar magnetic field measurements ever published.

2.7. Modeling the longitudinal field variation

To characterise the dipole components of the magnetic fields of our sample stars, we use the oblique rotator model (ORM, Stibbs 1950) as formulated by Preston (1967). This model provides a good first approximation of the large scale magnetic field of Ap stars (e.g. Landstreet 1988). Because of the weakness of the longitudinal magnetic field observed for the stars of our sample, we do not expect to be able to detect departures from a global dipolar configuration.

To begin, we added to our high-precision data set additional good-quality published magnetic field measurements collected by Bychkov et al. (2003). Details of these collected measurements were kindly provided by Dr. Victor Bychkov. Then, we searched the literature for rotational periods for each of our sample stars. For many stars, published rotational periods were available which provided an acceptable folded phase variation $B_\ell(\phi)$ of the magnetic measurements. However, for some stars, the published rotational period or periods did not provide an acceptable folded magnetic field variation, and for others, no published period was available. For these latter stars, we used a modified Lomb-Scargle technique to attempt to infer the rotational period, both directly from the longitudinal field measurements, as well as from the variations of the LSD Stokes I and V profiles. The period searches of LSD profiles were performed by treating each pixel in the Stokes I and V profiles as an independent timeseries (similar to the technique described by Adelman et al. 2002). Individual periodograms were subsequently weighted according to their amplitude of variation and averaged to characterise variability of the whole LSD profile. Acceptable periods were identified by establishing the 99% confidence threshold, and candidate periods were evaluated by phasing the LSD profiles and longitudinal field measurements.

Results of the period searches for individual stars are provided in their appropriate subsections in Sect. 3. Ultimately, acceptable rotational periods were obtained for 24 stars, and these periods are reported in Table 2.

We also searched the literature for published values of the projected rotational velocity ($v \sin i$) of each star, which we compared to the value measured from the LSD Stokes I profile by fitting rotationally-broadened synthetic profiles. Sometimes significant discrepancies were found between our values of $v \sin i$ and those reported in the literature. These discrepacies are discussed in Sect. 3, and the adopted rotational velocities (generally those obtained from the LSD profiles) are shown in Table 2.

Each phased longitudinal field variation $B_\ell(\phi)$ was then fit using a 1st order sine function:

$$B_\ell(\phi) = B_0 + B_1 \sin 2\pi(\phi + \phi_0). \quad (2)$$

The phased and fit longitudinal field variations are shown in Fig. 1. The reduced χ^2 of this fit (χ^2_2), along with those of linear fits through $B_\ell = 0$ (the "null field" model, χ^2_0) and through the weighted mean of the measurements (the "constant field" model, χ^2_1), of each star, are reported in Table 2. χ^2_lim, the 2σ upper limit for admissible models, computed according to Press et al. (1992), is reported in Table 2 as well. A comparison of these reduced χ^2 values with each other allows us to evaluate the significance of the detection of the longitudinal magnetic field and its variability. Although variability of the longitudinal field cannot be established for a few stars ($\chi^2_1 < \chi^2_\mathrm{lim}$), the only star for which the longitudinal field is not detected with more than 2σ confidence is HD 96707 (for which $\chi^2_0 < \chi^2_\mathrm{lim}$).

For a tilted, centred magnetic dipole, the surface polar field strength B_d is derived from the variation of the longitudinal magnetic field B_ℓ with rotational phase ϕ using Preston's (1967) well-known relation:

$$B_\mathrm{d} = B_\ell^\mathrm{max} \left(\frac{15+u}{20(3-u)} (\cos\beta \cos i + \sin\beta \sin i) \right)^{-1}, \quad (3)$$

Table 2. Results of the magnetic field modeling. The contents of the columns are described in Sect. 2.7. The uncertainties associated with the derived dipole parameters i, β and $B_{\rm d}$ correspond to 2σ.

star	Period	$v \sin i$	χ^2_0	χ^2_1	χ^2_2	$\chi^2_{\rm lim}$		i	β	$B_{\rm d}$	$B_{\rm d}^{\rm min}$	$B_{\rm d}^{\rm max}$
	(d)	(km s^{-1})						(°)	(°)	(10^3 G)	(10^3 G)	(10^3 G)
8441	69.2	2	13.71	6.69	1.75	3.35	49	$33 \pm 73^{+17}_{-61}$		0.683	0.415	2.931
10221	3.15459	24	5.90	1.81	1.56	2.71	27	$11 \pm 42^{+38}_{-41}$		0.375	0.195	1.202
15089	1.74033	48	57.83	56.37	1.83	2.14	45	$11 \pm 80^{+7}_{-12}$		2.031	1.560	2.999
15144	2.99787	13	1305.83	4.57	0.04	2.71	24	$8 \pm 9^{+6}_{-3}$		2.100	2.007	2.281
27309	1.568884	57	157.42	2.43	1.74	2.63	53	$17 \pm 5^{+11}_{-5}$		3.673	2.325	8.022
32549	4.6393	47	7.19	8.56	1.75	2.75	65	$27 \pm 77^{+11}_{-74}$		0.546	0.312	28.176
32650	2.7347	30	4.48	1.92	1.19	1.72	37	$12 \pm 45^{+31}_{-30}$		0.229	0.153	0.477
39317	2.6541	45	4.97	1.84	2.24	3.18	36	$12 \pm 20^{+69}_{-20}$		0.560	0.113	2.252
43819	15.02	10	135.66	59.32	3.45	4.18	63	$66 \pm 42^{+47}_{-42}$		2.626	2.488	78.367
68351	4.16	33	7.85	2.17	1.38	2.00	28	$37 \pm 46^{+36}_{-41}$		0.649	0.437	71.486
72968	5.6525	16	360.16	4.51	1.22	2.03	61	$18 \pm 5^{+7}_{-4}$		2.388	1.451	6.702
90569	1.04404	13	170.38	36.08	1.93	3.07	9	$4 \pm 81^{+5}_{-7}$		5.157	2.946	11.284
94427	1.9625	8	37.58	46.61	2.12	3.72	8	$4 \pm 89^{+1}_{-4}$		8.957	3.806	25.519
96707	3.515	37	0.82	0.91	0.77	1.21	53	$16 \pm 90^{+0}_{-90}$		0.100	0.0	0.492
103498	15.830	13	25.43	29.71	6.55	7.44	75	$68 \pm 80^{+10}_{-11}$		0.600	0.572	6.751
108945	2.01011	65	5.31	6.00	2.10	2.83	57	$18 \pm 85^{+3}_{-61}$		0.735	0.333	1.509
148112	3.04296	44.5	40.67	0.93	0.95	1.73	56	$16 \pm 3^{+11}_{-3}$		1.042	0.579	2.370
151525	4.1164	35	2.74	2.86	0.97	1.70	37	$19 \pm 78^{+11}_{-43}$		0.545	0.208	1.927
171586	2.1308	37	10.86	8.27	2.59	6.60	48	$19 \pm 46^{+40}_{-40}$		1.422	0.716	4.413
171782	4.4674	24	6.88	1.12	1.79	3.79	51	$51 \pm 5^{+85}_{-5}$		1.651	0.213	22257.276
179527	7.098	33	6.57	7.70	0.30	1.30	74	$32 \pm 81^{+8}_{-34}$		0.522	0.409	1.233
183056	2.9919	26	25.02	28.74	1.59	2.32	74	$8 \pm 49^{+37}_{-32}$		1.558	1.172	3.938
204411	4.8456	5.4	20.75	5.43	0.57	1.46	7	$5 \pm 81^{+7}_{-12}$		0.968	0.416	4.509
220825	1.42539	38	78.54	90.05	2.29	3.18	35	$54 \pm 83^{+7}_{-80}$		1.957	1.141	21.045

where $B_\ell^{\rm max} = |B_0| + B_1$ and u denotes the limb darkening parameter (equal to approximately $u = 0.5$ for our sample). The rotational axis inclination and obliquity angles i and β are related by

$$\tan\beta = \frac{1-r}{1+r}\cot i, \tag{4}$$

where $r = (|B_0| - B_1)/(|B_0| + B_1)$.

We have determined the inclination i for each of our stars assuming rigid rotation, and computing:

$$\sin i = \frac{P_{\rm rot} v \sin i}{50.6R}, \tag{5}$$

where $P_{\rm rot}$ is the adopted stellar rotational period in days, $v \sin i$ is the adopted projected rotational velocity in km s^{-1}, and R is the computed stellar radius in solar units. The magnetic obliquity β was then inferred from Eq. (4) and the polar strength of the dipole $B_{\rm d}$ from Eq. (3). Uncertainties associated with all parameters (at 2σ, including a max(2 km s^{-1}, 10%) uncertainty on $v \sin i$) were propagated through the calculations of i, β and $B_{\rm d}$. The resultant dipole magnetic field models are reported in Table 2.

An important and interesting consequence of Eq. (3), independent of all parameters except limb-darkening, is:

$$B_{\rm d} \geq \frac{20(3-u)}{15+u} B_\ell^{\rm max}, \tag{6}$$

which, for typical limb-darkening u, yields:

$$B_{\rm d} \gtrsim 3.3 B_\ell^{\rm max}. \tag{7}$$

Therefore, exclusive of the model geometry, a lower limit on the surface dipole component of the magnetic field is obtained directly from the maximum measured value of the longitudinal field. The maximum measured longitudinal field is reported in Col. 11 of Table 1, and the inferred lower limit (2σ) of $B_{\rm d}$, $B_{\rm d}^{\rm min,3.3}$ is reported in Col. 13 of Table 1. It is clear from these data that $B_{\rm d}$ for most of our sample is larger than a few hundred G at 2σ.

3. Observational results

3.1. Global results as compared to previous work

All of the 28 Ap stars studied were found to exhibit significant circular polarisation in their spectral lines. Table 1 gives our global result. For a majority of the sample, the detection of the magnetic field was obtained during the first observation. For some objects, obtaining a positive detection of the magnetic field required several observations, sometimes spanning several observing seasons. This was due to observations at phases in which the polarisation was especially weak, and due to low S/N ratio resulting from poor meteorological conditions. The number of observations and of Zeeman detections of each star is also indicated in Table 1.

No significant or recent detection of the magnetic field has been reported in the past for essentially all stars of our sample. Shorlin et al. (2002), using MuSiCoS and the same procedure as in this paper, did not detect the magnetic field of 3 Ap stars they observed. For two of these stars, they suggested a misclassification. We re-observed the third star, HD 148112 (ω Her), and easily detected its field. Glagolevskij & Chountonov (2002) observed 11 weakly-magnetic Ap stars and detected no magnetic fields in any of them. More recently, Glagolevskij et al. (2005) presented 9 stars in which they detected no longitudinal fields, with B_ℓ weaker than 100 G. Five of these stars were observed during this work and the magnetic field was detected for all of

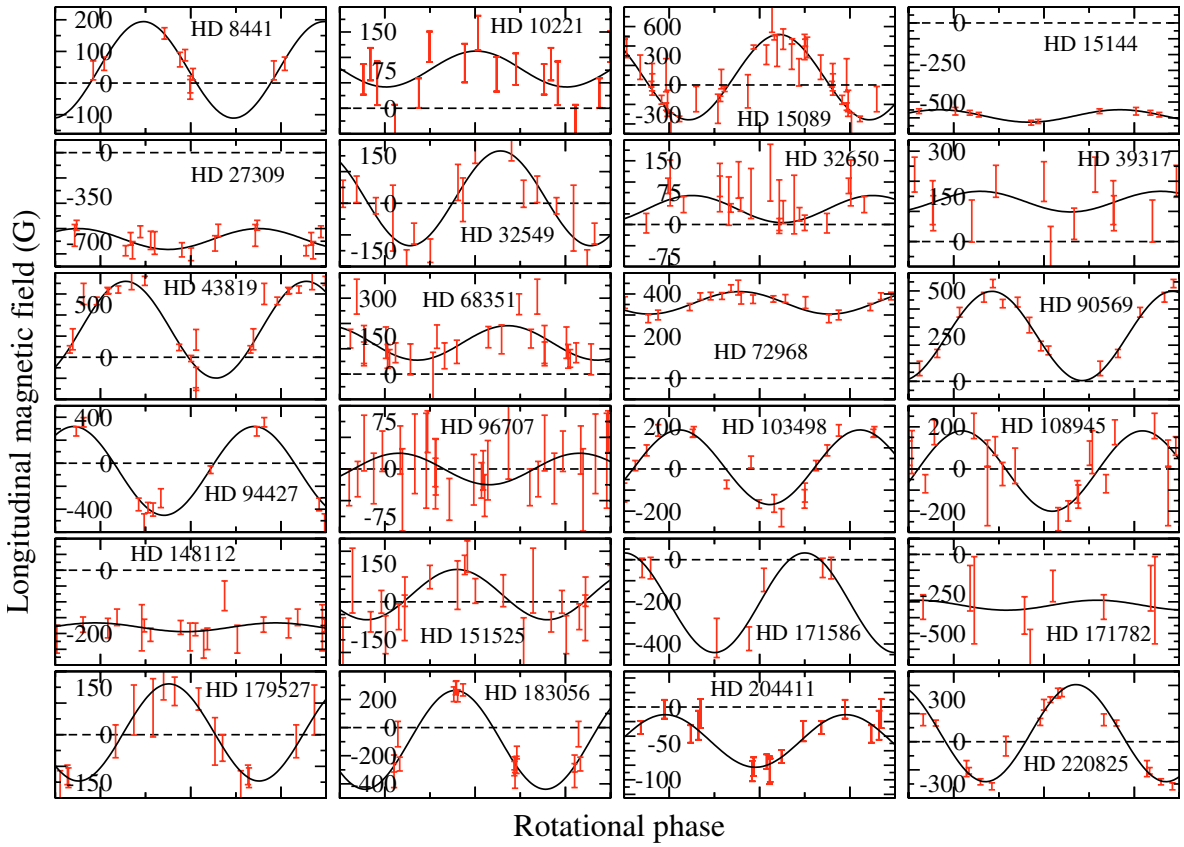

Fig. 1. Phased longitudinal field measurements of sample stars. The vertical (longitudinal field) scale differs in each frame, and is indicated in each frame in units of G. The horizontal (phase) axis in each frame runs from –0.25 to 1.25 cycles.

them. Hubrig et al. (2006) and Kochukhov & Bagnulo (2006) reduced FORS1 observations of about 100 Ap stars, among which were about 50 stars for which they detected the magnetic field for the first time. Four stars of their sample are in common with ours: 9 Tau, 21 Com, ω Her and 45 Her. In this study, the magnetic field is detected and measured for each of them, we give details in Sect. 3.2. on the results of the FORS1 investigations.

Our higher detection rate of magnetic field with respect to other techniques is certainly due to in part to the S/N improvement associated with the LSD method. In addition, our magnetic field detection criterion is based on measurement of significant circular polarisation within the velocity-resolved line profile (the Stokes V signature). This signature amplitude is only weakly sensitive to the global magnetic field geometry, and generally varies by only a factor of a few during the stellar rotational cycle, unlike the longitudinal field (which frequently varies by orders of magnitude, and which can vanish completely at some phases). Finally, the fact that we insist on performing multiple observations of each star is also an important factor in our superior magnetic field detection rate.

One set of LSD profiles will be shown for each of the studied stars in the online version of the paper. However, Figs. 2 and 3 illustrate the case of 21 Per (HD 18296) when the field was respectively 213 ± 20 G (10σ longitudinal field detection) and −39 ± 24 G (insignificant longitudinal field detection). However, both of these observations correspond to highly significant detections of the Stokes V Zeeman signatures. Figure 4 illustrates the non-detection of magnetic field in HD 32650 with MuSiCoS, and Fig. 5 shows the Zeeman detection of this same star obtained with NARVAL on 12 March 2007.

We now present our Zeeman detection and modeling results for each star of our sample.

3.2. Results obtained for each star

3.2.1. HN And (HD 8441)

HN And is a well-studied SB1 A2p star (e.g. North et al. 1998; Adelman et al. 1995) for which no clear magnetic field detection has been reported. Babcock (1958) presented measurements of a relatively weak (some hundreds of G) field, and Bychkov et al. (2003) did not present any new significant Zeeman detection. Preston (1971) and Mathys & Lanz (1992) did not succeed in measuring its field. We observed this star 8 times and obtained 8 definite Zeeman detections. Figure 7 shows the LSD Stokes V and Stokes I profiles when the longitudinal magnetic field was B_ℓ = 155 ± 18 G.

In the literature we find periods for HN And of 2.9632 days (Steinitz 1965) based on magnetic data from Babcock (1958), 106.27 days from radial velocity measurements (Renson 1965) later shown to be the rotation period of the binary (North et al. 1998), 69.5 days based on Stromgren (Wolff & Morrison 1973) and Johnson (Rakosch & Fiedler 1978) photometry, and 1.80889 days (Bychkov et al. 2005) based mostly on the same magnetic data as Steinitz (1965). Examining our periodogram near these periods, we only find a strong χ^2 minimum near 69.5 days in both Stokes V and I. The LSD profiles phase in a sensible fashion at this minimum, thus we can be confident that it is the correct period. Based on our analysis we adopt $P_{\rm rot} = 69.2^{+0.6}_{-0.5}$ d, where the uncertainties correspond to 99% confidence.

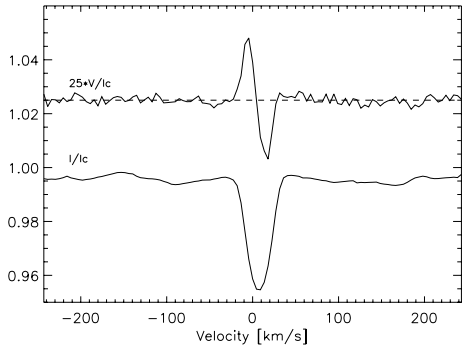

Fig. 2. LSD profiles of 21 Per (HD 18296) on 01 Sep. 05. From bottom to top, Stokes I and Stokes V are presented. For display purposes, the profiles are shifted vertically, and Stokes V profile is expanded by a factor of 25. The dashed line illustrates the zero level for the Stokes V profile.

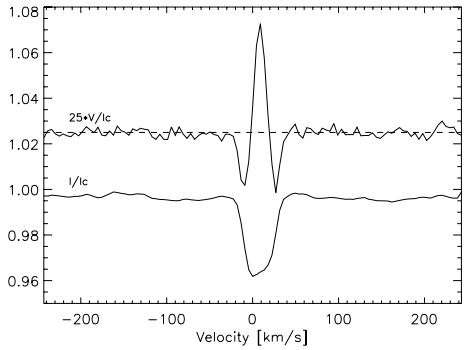

Fig. 3. LSD profiles of 21 Per on 02 Sep. 05 (same as Fig. 2).

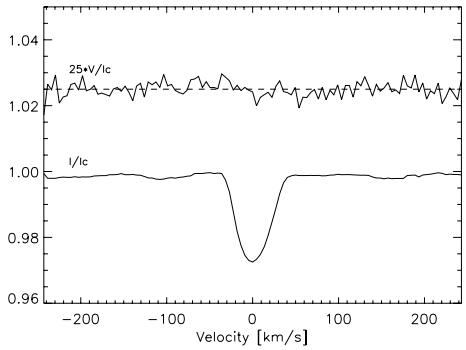

Fig. 4. LSD profiles (ND) of HD 32650 on 12 Feb. 04 observed with MuSiCoS (same as Fig. 2, no Zeeman detection).

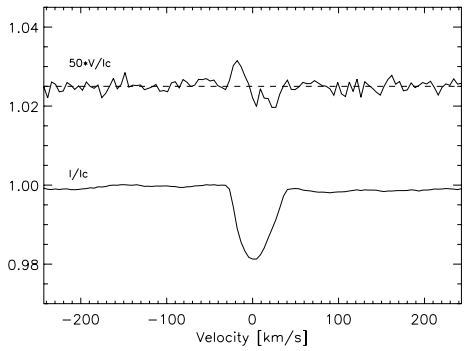

Fig. 5. LSD profiles (DD) of HD 32650 on 12 Mar. 07 as observed with NARVAL (same as Fig. 2 but Stokes V profile is expanded by a factor of 50, definite Zeeman detection).

The projected rotational velocity of HN And is very low, and is also not well known. North et al. (1998) report $v \sin i < 2.35$ km s^{-1}. Our $R = 35\,000$ spectra do not allow us to improve upon this estimate. Using a high-resolution ($R = 110\,000$) CFHT-Gecko spectrum of this star in our possession, we have attempted to estimate $v \sin i$ by modeling the 6150 Å region. The best fit is obtained for $v \sin i \simeq 3$ km s^{-1} and very weak magnetic field (0–500 G). However, acceptable fits are also obtained for moderate fields (1–1.5 kG) and intermediate rotation (1.5–2 km s^{-1}). For calculation of the dipole field, we adopt $v \sin i = 2$ km s^{-1} which results (at 2σ confidence) in $i = 49 \pm 33$, $\beta = 73^{+17}_{-61}$ and $415 \leq B_{\rm d} \leq 2931$ G (with $B_{\rm d}^{\rm min,3,3} = 399$ G). Larger values of $v \sin i$ result in an increased value of the inferred $B_{\rm d}$, and assuming $v \sin i = 1$ km s^{-1} (which we believe is the smallest value admissible by the line profiles), the weakest admissible field remains essentially unchanged.

3.2.2. 43 Cas, HD 10221

43 Cas is a classical Ap star in which magnetic field has been sought for around 50 years, but neither Babcock (1958), Borra & Landstreet (1980) nor Glagolevskij & Chountonov (2002) could detect it. Glagolevskij et al. (2005) reported a 4σ detection. In this paper, the Stokes V Zeeman signal is clearly detected on 8 occasions. Figure 8 shows the LSD Stokes V and Stokes I profiles when the longitudinal magnetic field was measured to be $B_\ell = 148 \pm 34$ G. Hildebrandt (1975) found a photometric period of 3.1848 d. for 43 Cas, which was refined to 3.15459 d from Hipparcos data (van Leeuwen et al. 1997). The projected rotational velocity, measured from modeling of the strongly-variable LSD Stokes I profiles, is 24 km s^{-1}. We derive $i = 27 \pm 11°$, $\beta = 42^{+38}_{-41}°$ and $195 \leq B_{\rm d} \leq 1202$ G (with $B_{\rm d}^{\rm min,3,3} = 264$ G).

3.2.3. ι Cas, HD 15089

The magnetic field of ι Cas was not detected by Borra & Landstreet (1980), but was by Kuschnig et al. (1998). As shown in Fig. 9 and Table 3, the field is easily detected (12 definite detections), and a rather large longitudinal field is measured ($B_\ell = -348 \pm 28$ G). The rotational period of this star has been recently confirmed by Hipparcos (1.74033 d), and Kuschnig et al. (1998) give $v \sin i = 48$ km s^{-1} (consistent with Royer et al. 2002, and somewhat lower than the LSD profiles which give 52 km s^{-1}). We adopt $v \sin i = 48$ km s^{-1}. We have included 18 additional measurements from Kuschnig et al. (1998), and obtain $i = 45 \pm 11°$, $\beta = 80^{+7}_{-12}°$ and $1560 \leq B_{\rm d} \leq 2999$ (with $B_{\rm d}^{\rm min,3,3} = 1452$ G).

3.2.4. HD 15144

Only rather old investigations concerning the magnetic field are published for this star. Our observations confirm the existence of a rather strong negative magnetic field at the surface of HD 15144 as already inferred by Babcock (1958) and Bonsack (1981). Figure 10 shows the LSD Stokes profiles when the longitudinal magnetic field was measured as $B_\ell = -631 \pm 15$ G.

We have employed the 2.99787 d photometric period of van Genderen (1971), and we adopt $v \sin i = 13$ km s^{-1} from the LSD profiles. We obtain $i = 24 \pm 8°$, $\beta = 9^{+6}_{-3}°$ and $2007 \leq B_{\rm d} \leq 2281$ (with $B_{\rm d}^{\rm min,3,3} = 1983$ G).

3.2.5. 21 Per, HD 18296

21 Per was not detected significantly by Borra & Landstreet (1980). Its rather weak longitudinal field was measured by Glagolevskij et al. (1995). We detect it easily on two occasions, and our error bars on B_ℓ are about 10 times smaller than those of previous measurements. Figure 2 shows the LSD spectrum when the field was 213 ± 20 G, while Fig. 3 corresponds to a cross-over phase when the longitudinal field is as small as -39 ± 24 G.

Although some photographic longitudinal field measurements are reported in the catalogue of Bychkov et al. (2003), their uncertainties appear to be seriously underestimated. Given the small number of precise magnetic field measurements of this star, we are unable to derive a dipole field model. However, from the peak value of the longitudinal field obtained here, we can infer that $B_\mathrm{d} > 571$ G with 2σ confidence.

3.2.6. 9 Tau, HD 22374

9 Tau appears to have been only observed for magnetic field by Babcock (1958). Our two observations provide an easy Zeeman detection. Figure 11 shows the LSD Stokes profiles when the longitudinal magnetic field was measured to be $B_\ell = 523 \pm 24$ G. Although we are unable to model the dipole field, we infer that $B_\mathrm{d} > 1568$ G with 2σ confidence.

3.2.7. 56 Tau, HD 27309

Neither Borra & Landstreet (1980) nor Glagolevskij (as reported in the catalogue of Bychkov et al. 2003) could detect the field of this star. 56 Tau is generously detected in each of our 12 observations and the longitudinal field reaches $B_\ell = -775 \pm 40$ G (Fig. 12).

The rotational period $P = 1.5688840 \pm 0.00000470$ d is from North & Adelman (1995). Although Royer et al. (2002) report $v \sin i = 44$ km s^{-1}, we find that this value seriously underestimates the width of the LSD profiles, and adopt $v \sin i = 57$ km s^{-1}. Using these values, we derive $i = 53 \pm 17°$, $\beta = 5^{+11\,\circ}_{-5}$ and $2325 \leq B_\mathrm{d} \leq 8022$ G (with $B_\mathrm{d}^{\mathrm{min},3,3} = 2323$ G).

3.2.8. 11 Ori, HD 32549

Borra & Landstreet (1980) could not detect the magnetic field of 11 Ori. We detect significant Stokes V signatures in 4 of our 11 observations. Our best circular polarisation detection is obtained at a crossover phase, when the longitudinal field is as weak as -8 ± 26 G (Fig. 13). Using the photometric period of 4.6394 d (van Leeuwen et al. 1997) and the LSD-measured $v \sin i$ of 47 km s^{-1}, we obtained $i = 65 \pm 27°$, $\beta = 77^{+11\,\circ}_{-74}$ and $312 \leq B_\mathrm{d} \leq 28176$ G (with $B_\mathrm{d}^{\mathrm{min},3,3} = 356$ G).

3.2.9. HD 32650

This star is classified as B9pSi by Cowley & Cowley (1969) and spectrophotometry was obtained by Adelman (1997, 1980). It was found to be a large amplitude variable (up to 0.1 mag in U-band). We did not detect its field with MuSiCoS, although we observed it several times. However the magnetic field of HD 32650 was detected (marginally) during science demonstration observations with NARVAL, and has since been detected definitively and repeatedly with this instrument. Figure 4 shows our MuSiCoS observation on 12 February 2004. Figure 5 shows one definite Zeeman detection with NARVAL on 12 March 07 when $B_\ell = 91 \pm 18$ G.

Using the rotational period of HD 32650 from Adelman (1997) and $v \sin i = 30$ km s^{-1} (from the LSD profiles) we modeled the combined MuSiCoS + NARVAL longitudinal field variation, obtaining $i = 37 \pm 12°$, $\beta = 45^{+31\,\circ}_{-30}$ and $153 \leq B_\mathrm{d} \leq 477$ (with $B_\mathrm{d}^{\mathrm{min},3,3} = 237$ G). This is one of the weakest dipole intensities inferred in this study.

3.2.10. HD 37687

This star is located in the direction of the Ori OB1 association. Morrel & Levato (1991) did not find it to be a member. However the Hipparcos parallax and proper motions do not appear conclusive alone, and radial velocity measurements will be necessary to conclude definitively on the membership. Magnetic splitting of the very sharp spectral lines of HD 37687 was not resolved in the investigation of Mathys & Lanz (1992). We detected easily the magnetic field of this star for the very first time (Fig. 14) from only 2 LSD profiles. We find that the longitudinal magnetic field reaches $B_\ell = 766 \pm 119$ G (on 17 Feb. 05). From the maximum longitudinal field measured, we infer a lower limit of $B_\mathrm{d} > 1742$ G with 2σ confidence.

3.2.11. 137 Tau, HD 39317

The magnetic field of this star was not detected by Borra & Landstreet (1980). In this study 137 Tau was observed 8 times and its magnetic field detected 3 times, reaching a peak value $B_\ell = 222 \pm 58$ G on 10 Feb. 05 (Fig. 15). Using $P = 2.6541$ d (Renson & Manfroid 1981) and the LSD-measured $v \sin i$ of 45 km s^{-1}, we obtain $i = 36 \pm 12°$, $\beta = 20^{+69\,\circ}_{-20}$ and $113 \leq B_\mathrm{d} \leq 2252$ G (with $B_\mathrm{d}^{\mathrm{min},3,3} = 323$ G).

3.2.12. HD 40711

El'kin et al. (2003) observed this star and obtained a lower limit for the longitudinal magnetic field of more than several hundred G. We obtain three observations of this star, Fig. 16 shows our Stokes V and Stokes I LSD profiles on 13 Feb. 04 when the longitudinal magnetic field was $B_\ell = -528 \pm 38$ G. We obtain a 2σ lower limit on the dipole intensity of $B_\mathrm{d} > 1492$ G.

3.2.13. HD 43819

This star is well studied for photometric and abundance properties (Lopez-Garcia & Adelman 1994; Adelman & Young 2005). Adelman & Young (2005) found a period of 15.0313 days, stable over a 30 year time span, which is compatible with the Hipparcos period (van Leeuwen et al. 1997). Gollnow (1971) reported one insignificant longitudinal field measurement, and Bychkov et al. (2003) reported additional observations. Figure 17 corresponds to a crossover phase when B_ℓ was as weak as -12 ± 29 G.

Using the period of Adelman & Young (2005) and $v \sin i = 10$ km s^{-1} from the LSD profiles, and including the better-quality magnetic field measurements reported by Bychkov et al. (2003), we obtain $i = 63 \pm 66$, $\beta = 42^{+47\,\circ}_{-42}$ and $2626 \leq B_\mathrm{d} \leq 78367$ G (with $B_\mathrm{d}^{\mathrm{min},3,3} = 1907$ G).

3.2.14. 15 Cnc, HD 68351

This star was previously observed by Babcock (1958) and Bohlender et al. (1993), who did not obtain any significant magnetic field detection. We observed it 16 times and detected the magnetic field 5 times. Figure 18 presents our Stokes profiles obtained on 07 Feb. 03 when the longitudinal magnetic field was $B_\ell = 325 \pm 45$ G.

The period is not very well known, and we adopt that of Stepień (1968; $P = 4.116$ d). With $v \sin i = 33$ km s^{-1} from the LSD profiles, we obtain $i = 28 \pm 37°$, $\beta = 46^{+36°}_{-41}$ and $437 \leq B_\mathrm{d} \leq 71486$ G (with $B_\mathrm{d}^{\mathrm{min},3,3} = 762$ G).

3.2.15. 3 Hya, HD 72968

This star has been observed by Babcock (1958) and van den Heuvel (1971) who did not obtain a significant detection of its magnetic field. We detected it easily 13 times. Figure 19 presents our Stokes profiles when the longitudinal magnetic field was $B_\ell = 390 \pm 16$ G.

Adelman (1998) reports a photometric period of 11.305 days, which according to our data appears to be twice the magnetic period. With a period of 5.6525 d and $v \sin i = 16$ km s^{-1}, we obtain $i = 61 \pm 18°$, $\beta = 5^{+7°}_{-4}$ and $1451 \leq B_\mathrm{d} \leq 6702$ G (with $B_\mathrm{d}^{\mathrm{min},3,3} = 1304$ G).

3.2.16. 45 Leo, HD 90569

This star was observed by Babcock (1958) and Bonsack (1976) who detected the magnetic field. However, their measurements have poor precision. Leroy (1993) measured linear polarisation in the direction of this star, but it is likely at least partly due to interstellar polarisation. We detected the magnetic field of 45 Leo easily 10 times. Figure 20 presents our Stokes profiles when the longitudinal magnetic field was $B_\ell = 541 \pm 23$ G.

Adopting the period $P = 1.04404$ d of Adelman (2006) and measuring $v \sin i = 13$ km s^{-1}, we find $i = 9 \pm 4°$, $\beta = 81^{+5°}_{-7}$ and $2946 \leq B_\mathrm{d} \leq 11284$ G (with $B_\mathrm{d}^{\mathrm{min},3,3} = 1634$ G).

3.2.17. HD 94427

This star is poorly studied, but we detected its magnetic field clearly on 8 occasions. Figure 21 presents our Stokes profiles when the longitudinal magnetic field was $B_\ell = 356 \pm 41$ G.

We have determined the rotational period of 1.9625 d from the LSD profile variations. With $v \sin i = 8$ km s^{-1}, we obtain $i = 8 \pm 4°$, $\beta = 89^{+1°}_{-4}$ and $3806 \leq B_\mathrm{d} \leq 25519$ G (with $B_\mathrm{d}^{\mathrm{min},3,3} = 904$ G).

3.2.18. EP UMa, HD 96707

Several studies of EP UMa measured a rather large magnetic field: van den Heuvel (1971), Bychkov et al. (1997), Leone & Catanzaro (2001). This star was observed previously with MuSiCoS by Johnson (2004), who obtained 5 detections of Stokes V signatures from 7 observations, but with a longitudinal field never larger than 119 ± 58 G. From the total of 21 LSD Stokes V profiles of EP UMa (the 7 observations of Johnson (1994) plus an additional 14 observations), we have obtained 7 definite Zeeman detections, 7 marginal detections and 7 non-detections, as defined in Sect. 2.2. We confirm the result of Johnson (2004) – the magnetic field of EP UMa is very weak, and the longitudinal component is never larger than about 100 G.

Figure 22 presents our LSD profiles of EP UMa when the longitudinal magnetic field was $B_\ell = 59 \pm 33$ G. The period of rotation of EP UMa has been subject of debate, with the main uncertainty being whether to choose the 3.516 d photometric period of Adelman et al. (1999), or the magnetic period of twice this value (7.0286 d) reported by Leone & Catanzaro (2001). Using our Stokes profiles, we find independently a magnetic period of $P = 3.515^{+0.009}_{-0.026}$, consistent with the photometric period. Adopting therefore the photometric period and $v \sin i = 37$ km s^{-1}, we obtain $i = 53 \pm 16°$, $\beta = 90^{+0}_{-90}{}°$, and $0 \leq B_\mathrm{d} \leq 492$ G (with $B_\mathrm{d}^{\mathrm{min},3,3} = 128$ G). EP UMa exhibits one of the weakest dipole fields of any star in the sample, and it is the only star in our sample for which the longitudinal field is not significantly detected (although the presence of a field is confirmed via the Stokes V profiles).

3.2.19. 65 UMa, HD 103498

This star is part of a double system. Its magnetic field has been reported by Bychkov et al. (2003), who indicate that it reaches an extreme value of about –800 G. We observed this star 14 times and detected its magnetic field 13 times. We find that the maximum unsigned longitudinal field is never larger than about 200 G. Figure 23 presents our LSD profiles when the longitudinal magnetic field was $B_\ell = -166 \pm 20$ G. Using the LSD Stokes I and V profiles, we have determined a rotational period of 15.830 d and $v \sin i = 13$ km s^{-1}. The magnetic field geometry is described by $i = 75 \pm 68°$, $\beta = 80^{+10°}_{-11}$ and $572 \leq B_\mathrm{d} \leq 6751$ G (with $B_\mathrm{d}^{\mathrm{min},3,3} = 432$ G).

3.2.20. 21 Com, HD 108945

21 Com is a member of the Mel 111 cluster in Coma Ber (Bounatiro 1993). This star was observed by Borra & Landstreet (1980) who obtained no detection of its magnetic field. Shorlin et al. (2002) detected it with MuSiCoS. Using FORS1 at VLT, Hubrig et al. (2006) presented one measurement of the longitudinal magnetic field as a new detection, $B_\ell = -347 \pm 51$ G, whereas Kochukhov & Bagnulo (2006), using the same observational data, could not detect the magnetic field, with $B_\ell = 65 \pm 116$ G. We observed 21 Com 13 times with MuSiCoS and detected its magnetic field each time. Figure 24 presents our LSD profiles when the longitudinal magnetic field was $B_\ell = -238 \pm 55$ G.

We adopt the best magnetic period near that of Kreidl et al. (1990): $P = 2.01011$ d, and $v \sin i = 65$ km s^{-1} from Shorlin et al. (2002). Our derived magnetic field geometry is $i = 57 \pm 18°$, $\beta = 85^{+3}_{-61}{}°$ and $333 \leq B_\mathrm{d} \leq 1509$ G (with $B_\mathrm{d}^{\mathrm{min},3,3} = 416$ G).

3.2.21. ω Her, HD 148112

Borra & Landstreet (1980) detected the magnetic field in ω Her and report 9 measurements, but with rather large uncertainties (σ between 115 and 285 G). Shorlin et al. (2002) and Bychkov et al. (2005) add one measurement each, the values of which suggest a small amplitude of variation. Kochukhov & Bagnulo (2006) and Hubrig et al. (2006) did not detect the magnetic field. From our 12 observations of ω Her we obtained 11 definite detections. Figure 25 presents our LSD profiles when the longitudinal magnetic field was $B_\ell = -204 \pm 21$ G.

We have adopted the rotational period $P = 3.04296$ d and $v \sin i = 44.5$ km s^{-1} of Hatzes (1991) (we obtained 46 km s^{-1}

from the LSD profiles). The derived field geometry is $i = 56 \pm 16°$, $\beta = 3^{+11}_{-3}°$ and $579 \leq B_d \leq 2370$ G (with $B_d^{min,3,3} = 535$ G).

3.2.22. 45 Her, HD 151525

This star is the one for which detection of the magnetic field required the longest time. Babcock (1958) observed it, and Kochukhov & Bagnulo (2006) and Hubrig et al. (2006) did not detect the magnetic field. We observed it 14 times and obtained 2 definite Zeeman detections and 3 marginal detections. Figure 26 presents our LSD profiles when the longitudinal magnetic field was $B_\ell = 146 \pm 38$ G.

We used the period $P = 4.1164$ d and $v \sin i = 35$ km s^{-1} of Hatzes (1991) (we obtained 36 km s^{-1} from the LSD profiles) to model the magnetic field geometry, obtaining $i = 37 \pm 19°$, $\beta = 78^{+11}_{-43}°$ and $208 \leq B_d \leq 1927$ G (with $B_d^{min,3,3} = 231$ G).

3.2.23. HD 171586

HD 171586 is a classical Ap star (Babcock 1958), which is located in the direction of the open cluster IC 4756. However, Gray & Corbally (2002) found that HD 171586 is not a cluster member. Only one magnetic observation by Babcock (1958) has been reported (Bychkov et al. 2003). We observed and detected this star 5 times. Figure 27 shows the LSD profiles when the longitudinal magnetic field was measured as $B_\ell = -375 \pm 56$ G.

We have adopted the period of Winzer (1974) of $P = 2.1308$ d which produces a reasonable phasing of the data, along with $v \sin i = 37$ km s^{-1} from the LSD profiles. We obtain $i = 48 \pm 19°$, $\beta = 46^{+40}_{-40}°$ and $716 \leq B_d \leq 4413$ G (with $B_d^{min,3,3} = 868$ G).

3.2.24. HD 171782

This star is located in the direction of IC 4756, but Herzog & Sanders (1975) discarded it as a member because of relative proper motion measurements. No magnetic field measurements has been reported for HD 171782. We observed this star 6 times and detected it 3 times. Figure 28 shows the LSD profiles when the longitudinal magnetic field was measured to be $B_\ell = -133 \pm 78$ G.

Adopting the 4.4674 d period of Adelman & Meadows (2002) and $v \sin i = 24$ km s^{-1} measured from the LSD profiles, we obtain $i = 51 \pm 51°$, $\beta = 5^{+85}_{-5}°$ and $B_d \geq 213$ G (with $B_d^{min,3,3} = 584$ G). Note, due to the large uncertainties associated with i and β, that the derived B_d upper limit for this star is unrealistically large.

3.2.25. 19 Lyr, HD 179527

The magnetic field of 19 Lyr was not detected by Borra & Landstreet (1980). We observed this star 11 times with MuSiCoS and obtained 10 Zeeman detections. Figure 29 shows the LSD profiles at a cross-over phase, when the longitudinal magnetic field was as weak as $B_\ell = -42 \pm 42$ G.

Using the photometric period $P = 7.098$ d of Adelman & Rice (1999) and LSD-derived $v \sin i = 33$ km s^{-1}, we obtain $i = 74 \pm 32$, $\beta = 81^{+8}_{-44}°$ and $409 \leq B_d \leq 1233$ (with $B_d^{min,3,3} = 211$ G).

3.2.26. 4 Cyg, HD 183056

The magnetic field of 4 Cyg was not detected by Borra & Landstreet (1980). We observed the star 13 times with MuSiCoS and obtained a Zeeman detection each time. Figure 30 shows the LSD profiles when the longitudinal magnetic field was $B_\ell = 330 \pm 83$ G.

Using the LSD profile variations of this star, we obtain a rotational period of 2.9919 d and $v \sin i = 26$ km s^{-1}. The derived magnetic geometry is $i = 74 \pm 8°$, $\beta = 49^{+37}_{-32}°$ and $1172 \leq B_d \leq 3938$ G (with $B_d^{min,3,3} = 680$ G).

3.2.27. HD 204411

The surface magnetic field of HD 204411 was estimated by Preston (1971) to be about 500 G. Johnson (2004) detected the magnetic field with MuSiCoS. Here we have obtained 12 observations of this star with 12 definite Zeeman detections, although the longitudinal field is always smaller than 100 G. Figure 31 shows the LSD profiles when the longitudinal magnetic field was $B_\ell = -88 \pm 14$ G.

We have derived a rotational period of 4.8456 d from LSD profiles. Figure 1 shows that B_ℓ presents a clear variation, although HD 204411 has been for a long time considered as a very long-period photometric and/or spectroscopic variable (Preston 1970; Adelman 2003). The spectral lines of this star are sufficiently sharp that $v \sin i$ cannot be accurate determined from our spectra, and we adopt $v \sin i = 5.4$ km s^{-1} (Ryabchikova et al. 2005b). The derived magnetic geometry is $i = 7 \pm 5°$, $\beta = 81^{+7}_{-12}°$ and $416 \leq B_d \leq 4509$ G (with $B_d^{min,3,3} = 198$ G). This range of field intensities is consistent with the estimate of the surface field reported by Ryabchikova et al. (2005b).

3.2.28. κ Psc, HD 220825

The magnetic field of κ Psc was not detected by Borra & Landstreet (1980). We observed the star 12 times, detecting it each time. Figure 32 shows the LSD profiles when the longitudinal magnetic field was $B_\ell = 350 \pm 24$ G.

We adopt the 1.420 d period of Kreidl & Schneider (1989; the only published period that fits out measurements) and $v \sin i = 38$ km s^{-1} from the LSD profiles. We derive $i = 35 \pm 54°$, $\beta = 83^{+7}_{-80}°$ and $1141 \leq B_d \leq 21045$ G (with $B_d^{min,3,3} = 865$ G).

4. Modeling results

4.1. Qualitative summary of the survey

Tables 1 and 3, Figs. 2 to 5 and Figs. 7 to 32 show that for all of the 28 weak-field Ap/Bp sample stars, the magnetic field of every sample star could be detected when sufficient tenacity and precision were employed. Thus our first conclusion is that all magnetic Ap/Bp stars, when confidently identified through spectroscopic and photometric observations, can be shown to host a measurable surface magnetic field. In every case, it was found that the longitudinal field measurements could be modeled assuming an oblique, centred dipole without any significant inconsistencies.

4.2. Distribution of dipole intensities B_d of the weakest-field Ap stars

For 24 of our sample stars, a sufficient number of longitudinal field measurements were obtained to allow modeling of the

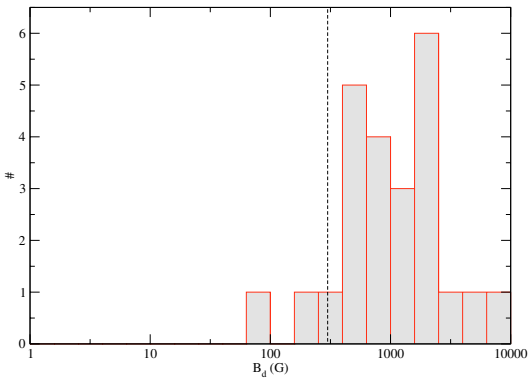

Fig. 6. Histogram of best-fit derived dipole field strengths of the stars in our sample.

dipolar magnetic field geometry in the manner described in Sect. 2.7. The results of this modeling are summarised in Table 2.

Figure 6 shows the histogram of the derived best-fit dipole strengths $B_{\rm d}$. The remarkable characteristic of this diagram is the near-absence of Ap stars in our sample with $B_{\rm d}$ below 300 G. Only 2 stars (HD 32650 and HD 96707) are found to have best-fit model dipole field intensities below 300 G. This number increases to only 4 stars if we consider the lower limit of the dipole strength (either $B_{\rm d}^{\rm min}$ or $B_{\rm d}^{\rm min,3.3}$, whichever is larger). Moreover, no star is constrained to have $B_{\rm d}$ below 300 G (i.e. the maximum-field model for every star has $B_{\rm d}$ larger than 300 G).

This result cannot be due to a detection threshold effect, because the magnetic field has been detected for every star in the sample. Nor is it likely that it is due to a selection effect, as our sample was constructed specifically to include the Ap/Bp stars with the weakest magnetic fields.

What is clearly demonstrated is that the number of Ap/Bp stars does not continue to increase monotonically to arbitrarily small field strengths. Instead, it appears to plateau around 1 kG, and to decline rapidly below about 300 G.

That this result is not an artifact of the modeling technique that we have employed is supported by the distribution of peak longitudinal fields measured for the sample, and the minimum dipole strengths derived directly from those measurements (Cols. 11 and 13 of Table 1). Because these minimum strengths are dependent on essentially no i, β or period (dipole field strength and known limb-darkening are the only model assumptions), they provide firm 2σ lower limits on the surface field intensity of each star. In addition, those stars for which the data quality is sufficiently good show excellent agreement between the 2σ minimum field intensities $B_{\rm d}^{\rm min}$ and $B_{\rm d}^{\rm min,3.3}$.

The derived surface field intensities $B_{\rm d}$ are probably themselves only lower limits on the true surface field. When sufficient data are available, detailed models of magnetic Ap stars nearly always show evidence of higher-order multipolar contributions to the magnetic field (e.g. Landstreet 1988; Landstreet & Mathys 2000). These higher-order field components contribute only weakly to the longitudinal field variation, although they can have surface intensities comparable to that of the dipole component. Therefore the magnetic field models derived here probably systematically underestimate the true surface field intensity.

A straightforward interpretation of the behaviour observed in Fig. 6 is that there exists a minimum magnetic field strength necessary for the generation of the chemical peculiarities of Ap/Bp stars. One possible implication of this hypothesis is that there may exist a potentially large population of A-type stars which host magnetic fields which are not sufficiently strong to generate Ap-type peculiarities (Vauclair & Vauclair 1982). However, large, high precision investigations of non-Ap tepid stars (e.g. Shorlin et al. 2002; Wade et al. 2006b; Bagnulo et al. 2006), which are able to rule out the presence of dipole fields with intensities below 300 G in many stars, suggest that no such population exists, and that the Ap/Bp stars are the only A-type stars with detectable magnetic fields.

5. Interpretation

The 100% Zeeman detection rate obtained in our survey strongly suggests that all Ap/Bp stars host detectable magnetic fields. Moreover, it appears that a threshold magnetic field of about 300 G exists below which fields are very rare, and perhaps altogether absent.

A possible interpretation of this result is that there exists a critical field strength above which stable magnetic configurations exist and below which any large scale field configuration is destroyed by some instability. The instability is expected to result in the presence of opposite polarities at small length scales, thus strongly reducing the magnitude of the integrated longitudinal field through cancellation effects. For a sample of stars containing both stable and unstable field configurations, this scenario would imply a strong jump in the measured values of the longitudinal fields or a lower bound of the magnetic field, depending on the detection limit.

The existence of stable large scale magnetic fields in stars is primarily supported by the observations of the magnetic fields of Ap stars and white dwarfs. Theoretically, although no stable field configuration is known in an analytical form, it has been proposed that the combination of azimuthal and poloidal field might be stable as a recent numerical simulation tends to confirm (Braithwaite & Spruit 2004). However, when the magnetic field is sufficiently weak to be wound up by differential rotation, the resulting field, predominantly azimuthal with respect to the rotation axis, can be subject to various instabilities. As recently reviewed by Spruit (1999) (see also Spruit 2004), the most vigorous of these instabilities is a pinch-type instability first considered in a stellar context by Tayler (1973). Here, we estimate the critical magnetic field below which the winding-up process induces an instability and above which the action of magnetic torques on the differential rotation limits the winding-up before the instability sets in. The winding-up time scale is $t_w = 1/(q\Omega)$ where $q = r\|\nabla\Omega\|/\Omega = r/\ell$ is a dimensionless measure of the differential rotation. The winding-up of the axisymmetric part of the original poloidal field $\boldsymbol{B}_{\rm p}^{\rm sym}$ by the differential rotation being governed by $\partial_t B_\phi = r\sin\theta \boldsymbol{B}_{\rm p}^{\rm sym}\cdot\boldsymbol{\nabla}\Omega$, the time scale t_w corresponds more specifically to the time necessary to produce an azimuthal field component B_ϕ of the same amplitude as $\boldsymbol{B}_{\rm p}^{\rm sym}$. On the other hand, Lorentz forces will affect the differential rotation after a Alfvén travel time calculated on the shear length scale ℓ, that is $t_A = \ell(4\pi\varrho)^{1/2}/B$. Equating both time scales gives a local order of magnitude estimate of the critical magnetic field, $B_{\rm c} \simeq (4\pi\varrho)^{1/2} r\Omega$. Its value can be expressed in terms of the equipartition field of a typical Ap star as follows:

$$\frac{B_{\rm c}}{B_{\rm eq}} \simeq 2\left(\frac{P_{\rm rot}}{5_{\rm day}}\right)^{-1}\left(\frac{r}{3\,R_\odot}\right)\left(\frac{T}{10^4\ {\rm K}}\right)^{-1/2}. \quad (8)$$

As $B_{\rm eq} = 170$ G at the surface ($\tau_{5000} = 2/3$) of a typical Ap star ($\log g = 4, T_{\rm eff} = 10^4$ K) the derived critical field is close to the 300 G observational threshold ($B_{\rm eq}^2 = 8\pi P$, P is the pressure). Calculation of the critical field $B_{\rm c}$ for each star in the sample

also shows that most stars satisfy $B_d > B_c$, and all stars satisfy $B_d^{max} > B_c$. Moreover, the magnetic field of the 5 stars with rotational period under 2d (HD 10589, HD 27309, HD 90569, HD 94427, HD 220825) is compatible with the dependence of B_c on P_{rot} ($B_c \propto P_{rot}^{-1}$) since their dipolar fields $B_d = 2-9$ kG are substantially greater than the sample median $B_d \approx 1.4$ kG. It is however important to stress that although the local order of magnitude estimate of B_c is coherent with the present observational data, a detailed and non-local modeling is required to specify the critical field strength below which differential rotation destabilizes large scale field configurations. Note that the threshold value of the magnetic field is also higher than the magnetic field threshold necessary to trigger the Tayler instability, according to the criterion given by Spruit (1999). The large scale field is then destroyed by the development of the instability. An example of the non-linear evolution of such unstable configurations has been recently considered in a solar context (Brun & Zahn 2006) confirming that the resulting field is structured on small latitudinal length scales.

The above scenario can thus qualitatively explain the existence of an apparent lower bound in the strength of magnetic fields of Ap stars. By extension, such a model could provide a basis to explain why magnetic fields are observed in only a small fraction of intermediate-mass stars. If the initial magnetic field strength probability distribution of intermediate-mass stars increases (say) exponentially toward weak fields, the large majority of A-type stars, after formation, would have fields weaker than the critical field described by Eq. (8). The fields of such stars would be unstable and decay; they would therefore appear at the main sequence showing no evidence of a magnetic field.

Another advantage of the scenario described above is that it may also naturally explain the even greater rarity of magnetic fields detected in massive stars. For a typical main sequence A0p star (with $P = 5$ d, $R = 3\ R_\odot$ and $T_{eff} = 10\,000$ K), Eq. (8) yields $B_c \simeq 2\,B_{eq} \sim 300$ G. However, for a main sequence B0p star (with $T_{eff} = 31\,000$ K, $R = 7.2\ R_\odot$ and $P = 2$ d), $B_c \simeq 7B_{eq} \sim 2$ kG. With a substantially larger critical field strength, massive stars are substantially less likely to retain their magnetic fields (assuming an initial field probability distribution similar to that of Ap stars, decreasing toward strong fields). Massive stars in which relatively weak magnetic fields have been detected are all quantitatively in agreement with Eq. (8): β Cep (Donati et al. 2001; B0, $B_c \simeq 361$ G, observed $B_d = 360$ G), τ Sco (Donati et al. 2006b; B0, $B_c \simeq 70$ G, observed $B \sim 500$ G), θ^1 Ori C (Donati et al. 2002; O7, $B_c \simeq 300$ G, observed $B_d \simeq 1.1$ kG), HD 191612 (Donati et al. 2006a, $B_c \simeq 20$ G, estimated minimum $B_d \sim 1.5$ kG).

6. Conclusion

We have investigated a sample of 28 well-known spectroscopically-identified magnetic Ap/Bp stars, obtaining 282 new Stokes V Zeeman signatures and longitudinal magnetic field measurements using the MuSiCoS and NARVAL spectropolarimeters. Magnetic field is detected in all sample stars, and the inferred longitudinal fields are significantly greater than some tens of G. To characterise the surface magnetic field intensities of the sample, we modeled the longitudinal field data to infer the intensity of the dipolar field component. The distribution of derived dipole strengths for these stars exhibits a plateau at about 1 kG, falling off to larger and smaller field strengths. Remarkably, in this sample of stars selected for their presumably weak magnetic fields, we find only 2 stars for which the derived dipole strength is weaker than 300 G. Interpreting this "magnetic threshold" as a critical value necessary for the stability of large-scale magnetic fields leads to a natural explanation of the small fraction of intermediate-mass magnetic stars. It may also explain the near-absence of magnetic fields in more massive B and O-type stars.

Acknowledgements. This research has made use of databases operated by CDS, Strasbourg, France, Vienna Atomic Line Database (VALD), Austria, and Observatoire de Genève, Switzerland. GAW and JDL acknowledge Discovery Grant support from the Natural Sciences and Engineering Research Council of Canada (NSERC). We are very grateful to Dr. Victor Bychkov for providing his collected magnetic field measurements and to Dr. Thierry Roudier for providing IDL routines and making the final LSD figures.

References

Adelman, S. J. 1980, A&A, 86, 149
Adelman, S. J. 1997, PASP, 109, 9
Adelman, S. J. 1998, A&AS, 128, 245
Adelman, S. J. 2003, A&A, 401, 357
Adelman, S. J. 2006, PASP, 118, 77
Adelman, S. J., & Rice, R. H. 1999, A&AS, 136, 111
Adelman, S. J., & Meadows, S. A. 2002, A&A, 390, 1023
Adelman, S. J., & Young, K. J. 2005, A&A, 429, 317
Adelman, S. J., Pyper, D. M., Lopez-Garcia, Z., & Caliskan, H. 1995, A&A, 296, 467
Adelman, S. J., Rayle, K. E., & Pi, C.-L. M. 1999, A&AS, 136, 379
Adelman, S. J., Gulliver, A.F., Kochukhov, O., & Ryabchikova, T. A. 2002, ApJ, 575, 449
Aurière, M. 2003, in Magnetism and Activity of the Sun and Stars, ed. J. Arnaud, & N. Meunier, EAS Publ. Ser., 9, 105
Babcock, H. W. 1958, ApJS, 3, 141
Bagnulo, S., Landstreet, J. D., Mason, E., et al. 2006, A&A, 450, 777
Balona, L. A. 1994, MNRAS, 268, 119
Baudrand, J., & Böhm, T. 1992, A&A, 259, 711
Bohlender, D. A., & Landstreet, J. D. 1990, MNRAS, 247, 606
Bohlender, D. A., Landstreet, J. D., & Thompson, I. B. 1993, A&A, 269, 355
Bonsack, W. K. 1976, PASP, 88, 19
Bonsack, W. K. 1981, PASP, 93, 756
Borra, E. F., & Landstreet, J. D. 1980, ApJS, 42, 421
Bounatiro, L. 1993, A&AS, 100, 531
Braithwaite, J., & Spruit, H. C. 2004, Nature, 431, 14
Brun, A. S., & Zahn, J.-P. 2006, A&A, 457, 665
Bychkov, V. D., Kostynchuk, L. Y., & Shtol', V. G. 1997, in Stellar Magnetic fields, proceedings, 110
Bychkov, V. D., Bychkova, L. V., & Madej, J. 2003, A&A, 407, 631
Bychkov, V. D., Bychkova, L. V., & Madej, J. 2005, A&A, 430, 1143
Cowley, A., & Cowley, C. 1969, AJ, 74, 375
Donati, J.-F. 2004, in Scientific highlights 2004 (EDP Sciences) ed. F. Combes, et al., 217
Donati, J.-F., Semel, M., Carter, B. D., Rees, D. E., & Cameron, A. C. 1997, MNRAS 291, 658
Donati, J.-F., Catala, C., Wade, G. W., et al. 1999, A&AS, 134, 149
Donati, J.-F., Wade, G. A., Babel, J., Henrichs, H. F., et al. 2001, MNRAS 326, 1265
Donati, J.-F., Babel, J., Harries, T. J., et al. 2002, MNRAS, 333, 55
Donati, J.-F., Howarth, I. D., Bouret, J.-C., et al. 2006a, MNRAS, 365, L6
Donati, J.-F., Howarth, I. D., Jardine, M. M., et al. 2006b, MNRAS, 370, 629
El'kin, V. G., Kudryavtsev, D. O., & Romanyuk, I. I. 2003, AstL, 29, 400
van Genderen, A. M. 1971, A&A, 14, 48
Glagolevskij, Y. V., & Chountonov, G. A. 2002, Astrophysics, 45, 408
Glagolevskij, Y. V., El'kin, V. G., Romanyuk, I. I., & Shtol, V. G. 1995, AstL, 21, 168
Glagolevskij, Y. V., Ryabchikova, T. A., & Chountonov, G. A. 2005, AstL, 31, 327
Gollnow, H. 1971, Observatory, 91, 37
Gray, R. O., & Corbally, C. J. 2002, AJ, 124, 989
Hatzes, A. P. 1991, MNRAS, 253, 89
Hauck, B., & North, P. 1982, A&A, 114, 23
Herzog, A. D., & Sanders, W. L. 1975, A&AS, 19, 211
van den Heuvel, E. P. J. 1971, A&A, 11, 461
Hildebrandt, G. 1975, AN, 296, 277
Hubrig, S., North, P., Schöller, M., & Mathys, G. 2006, AN, 327, 289
Johnson, N. M. 2004, Thesis, Master of Science in Physics, Royal Military College of Canada
Kochukhov, O., & Bagnulo, S. 2006, A&A, 450, 763

Kreidl, T. J., & Schneider, H. 1989, IBVS, 3282
Kreidl, T. J., Garrido, R., Huang, L., et al. 1990, MNRAS, 245, 642
Kupka, F. G., Piskunov, N. E., Ryabchikova, T. A., et al. 1999, A&AS, 138, 119
Kuschnig, R., Wade, G. A., Hill, G. M., & Piskunov, N. 1998, CoSka, 27, 470
Landstreet, J. D. 1988, ApJ, 326, 967
Landstreet, J. D. 1992, A&ARv, 4, 35
Landstreet, J. D., & Mathys, G. 2000, A&A, 359, 213
Landstreet, J. D., Bagnulo, S., Andretta, V., et al. 2007, A&A, 470, 685
van Leeuwen, F., Evans, D. W., Grenon, M., et al. 1997, A&A, 323, L61
Leone, F., & Catanzaro, G. 2001, A&A, 365, 118
Leroy, J. L. 1995, A&AS, 114, 79
Lopez-Garcia, Z., & Adelman, S. J. 1994, A&AS, 107, 353
Mathys, G., & Lanz, T. 1992, A&A, 256, 169
Mermilliod, J.-C., Mermilliod, M., & Hauck, B. 1997, A&AS, 124, 349
Moon, T. T., & Dworetsky, M. M. 1985, MNRAS, 217, 305
Morrell, N., & Levato, H. 1991, ApJS, 75, 965
Moss, D. 2001, in Magnetic fields across the Hertzprung-Russell Diagram, ed. G. Mathys, S. K. Solanki, & D. T. Wickramasinghe, 305
North, P., & Adelman, S. J. 1995, A&AS, 111, 41
North, P., Carquillat, J.-M., Ginestet, N., et al. 1998, A&AS, 130, 223
Perryman, M. A. C., Lindegren, L., Kovalesky, J., et al. 1997, A&A, 323, L49
Petit, P., Donati, J.-F., & Aurière, M. 2005, A&A, 361, 837
Piskunov, N. E., Kupka, F., Ryabchikova, T. A., et al. 1995, A&A, 112, 525
Press, W. H., Teukolsky, S. A., Vetterling, W. T., & Flannery, B. P. 1992, Numerical Recipes in C (Cambridge University Press), 693
Preston, G. W. 1967, ApJ, 150, 547
Preston, G. W. 1970, PASP, 82, 878
Preston, G. W. 1971, ApJ, 164, 309
Preston, G. W. 1974, ARA&A, 12, 257
Rakosch, K. D., & Fiedler, W. 1978, A&AS, 31, 83
Rees, D. E., & Semel, M. D. 1979, A&A, 74, 1
Renson, P. 1965, Information Bulletin on Variable Stars, 108
Renson, P., & Manfroid, J. 1981, A&AS, 44, 23
Renson, P., Gerbaldi, M., & Catalano, F. A. 1991, A&AS, 89, 429
Romanyuk, I. I. 2000, in Magnetic fields of chemically peculiar and related stars, ed. Y. VGlagolevskij, & I. IRomanyuk (Moscow), 18
Royer, F., Grenier, S., Baylac, M.-O., et al. 2002, A&A, 393, 897
Ryabchikova, T. A., Piskunov, N. E., Kupka, F., & Weiss, W. W. 1997, Baltic Astron., 6, 244
Ryabchikova, T. A., Wade, G. A., Aurière, M., et al. 2005a, A&A, 429, L55
Ryabchikova, T. A., Leone, F., & Kochukhov, O. 2005b, A&A, 438, 973
Shorlin, S. L. S., Wade, G. A., Donati, J.-F., et al. 2002, A&A, 392, 637
Spruit, H. C. 1999, A&A, 349, 189
Spruit, H. C. 2004, in Stellar rotation, ed. A. Maeder & P. Eenens, IAU Symp., 215, 356
Steinitz, R. 1965, BAIN, 18, 125
Stepień, K. 1968, ApJ, 154, 945
Stibbs, D. W. N. 1950, MNRAS, 110, 395
Tayler, R. J. 1973, MNRAS, 161, 365
Vauclair, S., & Vauclair, G. 1982, ARA&A, 20, 37
Wade, G. A., Donati, J. F., Landstreet, J. D., & Shorlin, S. L. S. 2000a, MNRAS, 313, 823
Wade, G. A., Donati, J. F., Landstreet, J. D., & Shorlin, S. L. S. 2000b, MNRAS, 313, 851
Wade, G. A., Fullerton, A. W., Donati, J.-F., et al. 2006a, A&A, 451, 195
Wade, G. A., Aurière, M., Bagnulo, S., et al. 2006b, A&A, 451, 293
Winzer, J. E. 1974, AJ, 79, 124
Wolff, S. C., & Morrison, N. D.1973, PASP, 85, 141

Online Material

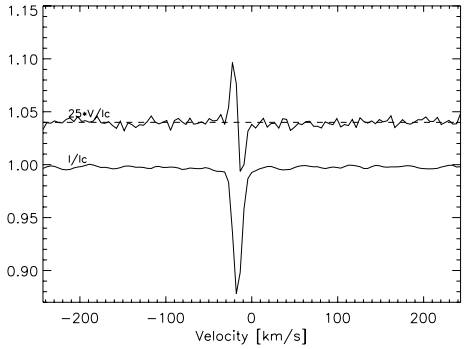

Fig. 7. LSD profiles of HN And (HD 8441) on 25 Jan. 06. From bottom to top, Stokes *I* and Stokes *V* are presented. For display purposes, the profiles are shifted vertically, and the Stokes *V* profile is expanded by a factor of 25. The dashed line illustrates the zero level for the Stokes *V* profile.

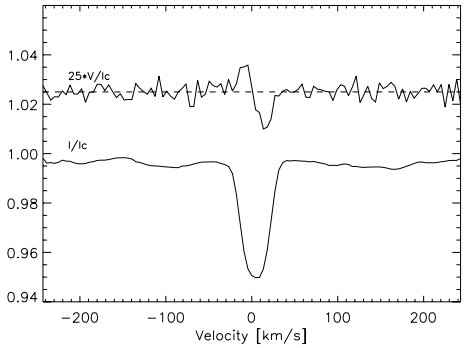

Fig. 8. LSD profiles of 43 Cas (HD 10221) on 14 Jan. 06 (same as Fig. 7).

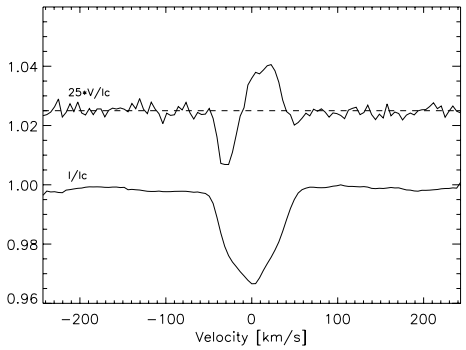

Fig. 9. LSD profiles of ι Cas (HD 15089) on 24 Aug. 04 (same as Fig. 7).

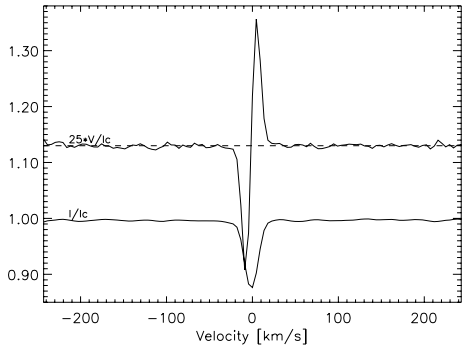

Fig. 10. LSD profiles of HD 15144 on 10 Dec. 01 (same as Fig. 7).

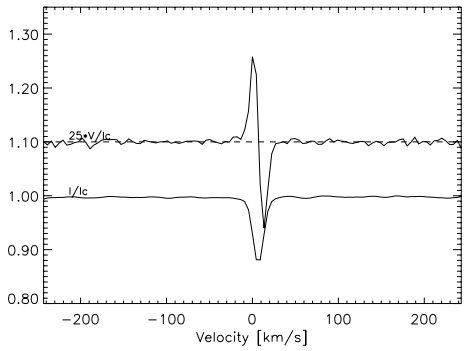

Fig. 11. LSD profiles of 9 Tau (HD 22374) on 02 Feb. 04 (same as Fig. 7).

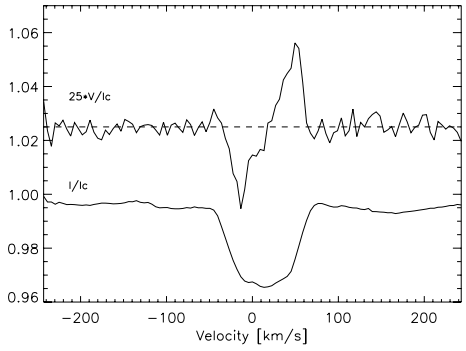

Fig. 12. LSD profiles of 56 Tau (HD 27309) on 11 Dec. 01 (same as Fig. 7).

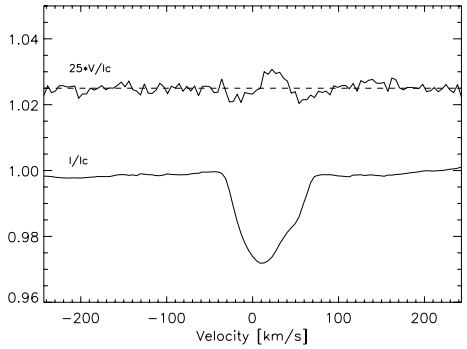

Fig. 13. LSD profiles of 11 Ori (HD 32549) on 20 Jan. 06 (same as Fig. 7).

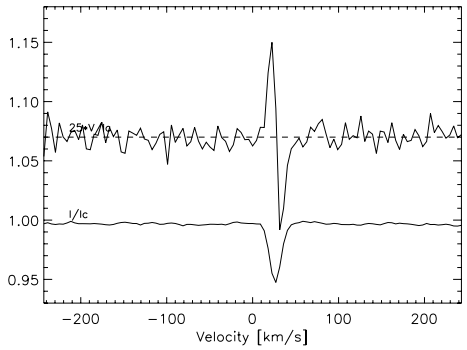

Fig. 14. LSD profiles of HD 37687 on 17 Feb. 04 (same as Fig. 7).

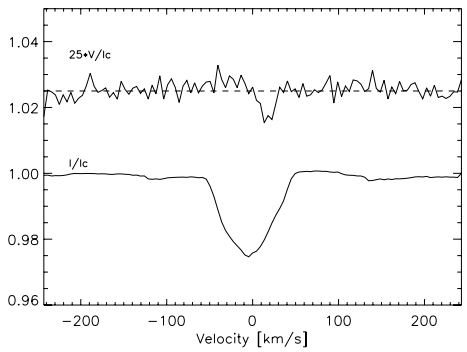

Fig. 15. LSD profiles of 137 Tau (HD 39317) on 10 Feb. 05 (same as Fig. 7).

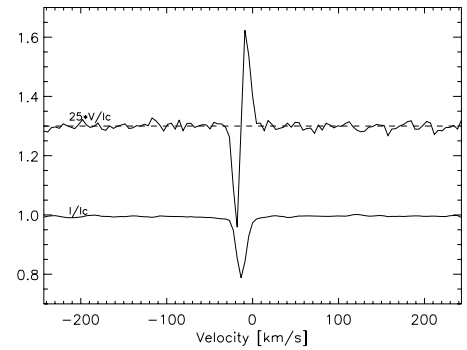

Fig. 16. LSD profiles of HD 40711 on 13 Feb. 04 (same as Fig. 7).

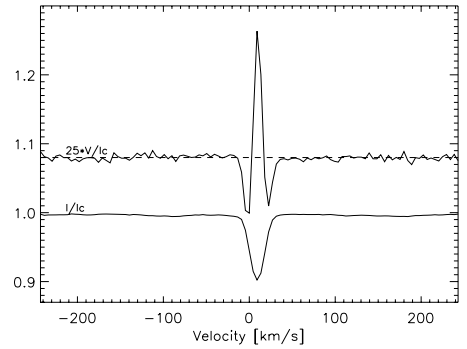

Fig. 17. LSD profiles of HD 43819 on 17 Dec. 01 (same as Fig. 7).

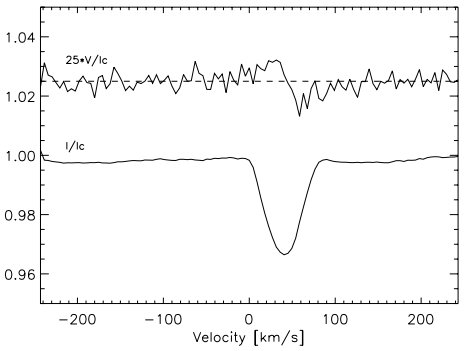

Fig. 18. LSD profiles of 15 Cnc (HD 68351) on 07 Feb. 03 (same as Fig. 7).

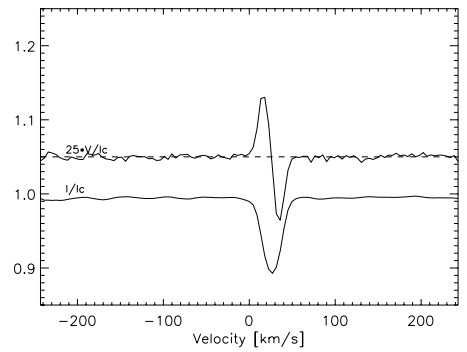

Fig. 19. LSD profiles of 3 Hya (HD 72968) on 18 Dec. 01 (same as Fig. 7).

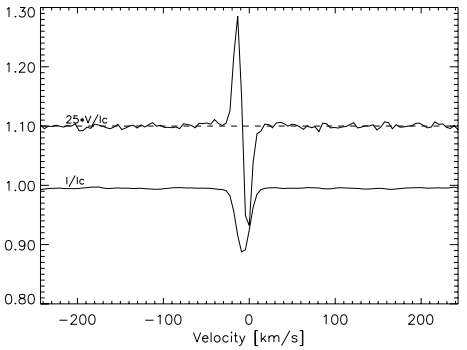

Fig. 20. LSD spectrum of 45 Leo (HD 90569) on 17 Dec. 01 (same as Fig. 7).

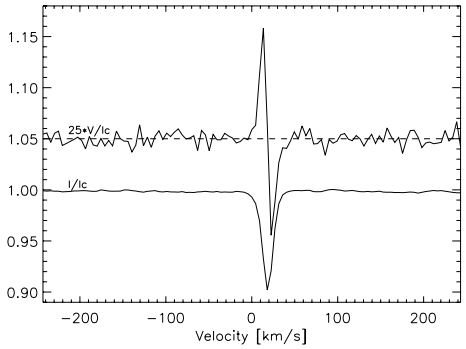

Fig. 21. LSD profiles of HD 94427 on 11 Feb. 04 (same as Fig. 7).

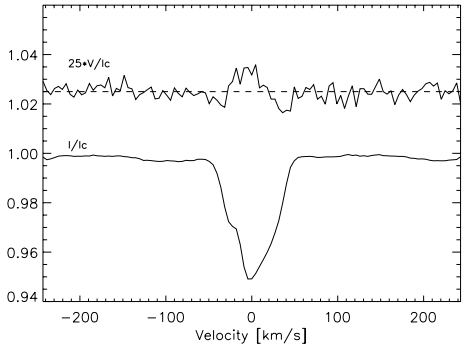

Fig. 22. LSD profiles of EP Uma (HD 96707) on 06 Feb. 06 (same as Fig. 7).

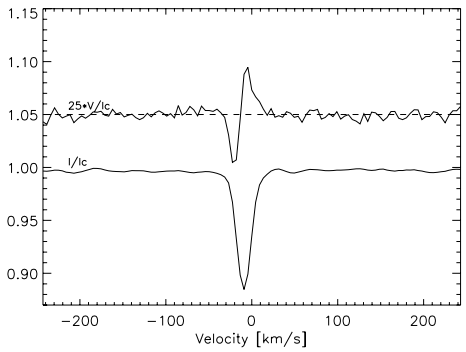

Fig. 23. LSD profiles of 65 Uma (HD 103498) on 11 Dec. 01 (same as Fig. 7).

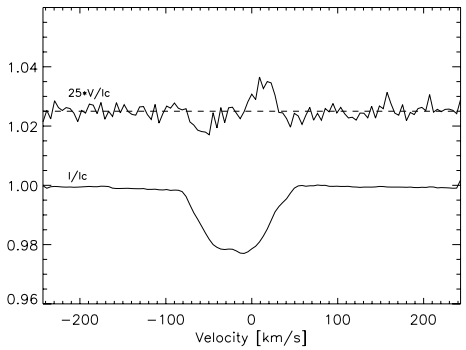

Fig. 24. LSD profiles of 21 Com (HD 108945) on 07 Feb. 03 (same as Fig. 7).

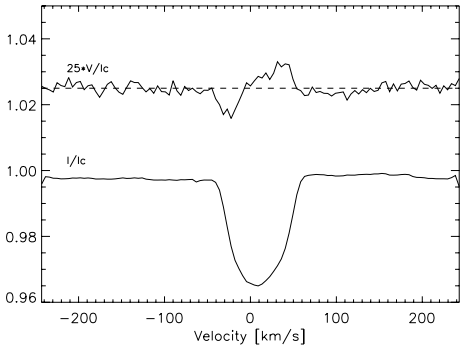

Fig. 25. LSD profiles of ω Her (HD 148112) on 03 Jul. 01 (same as Fig. 7).

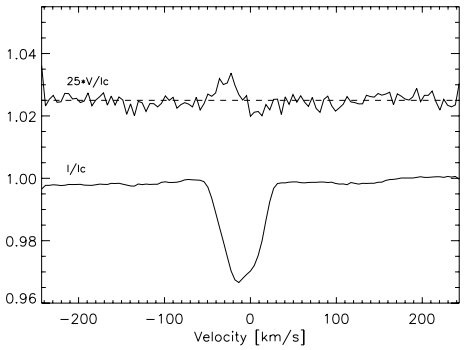

Fig. 26. LSD profiles of 45 Her (HD 151525) on 29 Jul. 03 (same as Fig. 7).

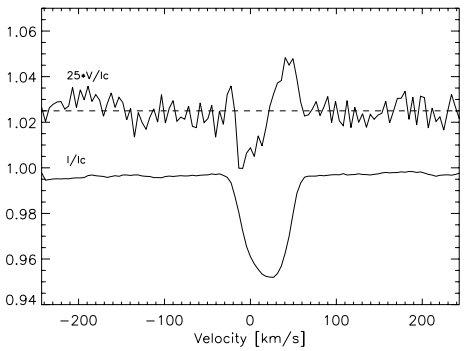

Fig. 27. LSD profiles of HD 171586 on 31 Jul. 04 (same as Fig. 7).

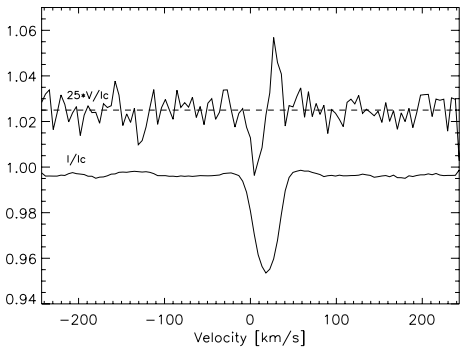

Fig. 28. LSD profiles of HD 171782 on 30 Aug. 05 (same as Fig. 7).

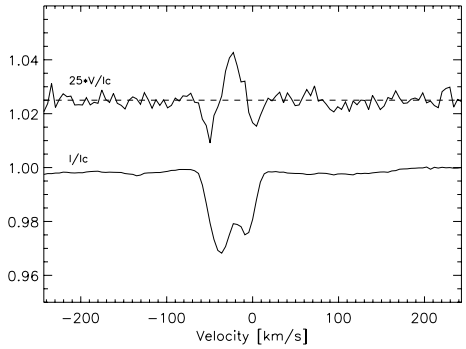

Fig. 29. LSD profiles of 19 Lyr (HD 179527) on 13 Aug. 05 (same as Fig. 7).

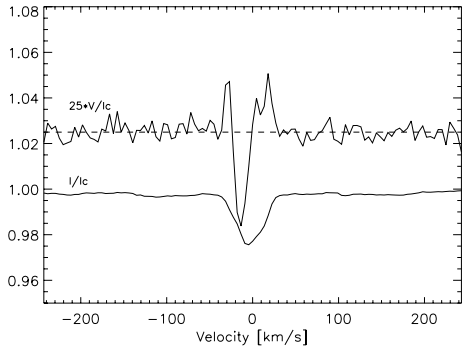

Fig. 30. LSD profiles of 4 Cyg (HD 183056) on 24 Jun. 03 (same as Fig. 7).

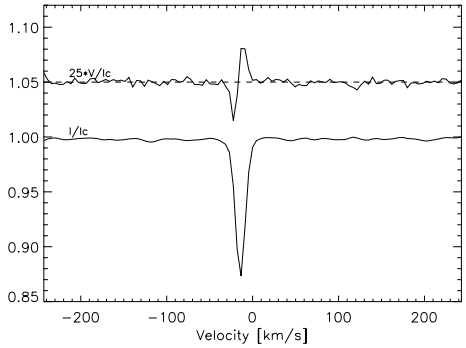

Fig. 31. LSD profiles of HD 204411 on 27 May 06 (same as Fig. 7).

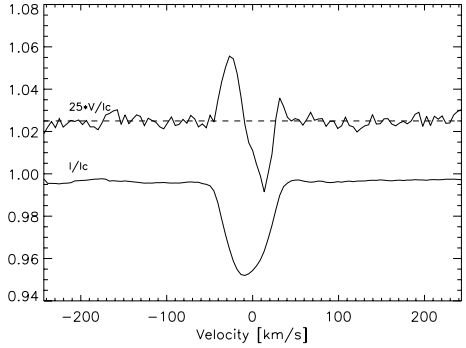

Fig. 32. LSD profiles of κ Psc (HD 220825)on 14 Jul. 04 (same as Fig. 7).

3.4.2 A9 : No detection of large-scale magnetic fields at the surfaces of Am and HgMn stars

“No detection of large-scale magnetic fields at the surfaces of Am and HgMn stars”

Aurière M., Wade G. A., Lignières F. et al.

soumis à A&A

Astronomy & Astrophysics manuscript no. wfam08
May 29, 2010

No detection of large-scale magnetic fields at the surfaces of Am and HgMn stars⋆

M. Aurière[1], G.A. Wade[2], F. Lignières[1], A. Hui-Bon-Hoa[1], J.D. Landstreet[3,4], I. Iliev[5], J.-F. Donati[1], P. Petit[1], T. Roudier[1], S. Théado[1]

[1] Laboratoire d'Astrophysique de Toulouse-Tarbes, CNRS, Université de Toulouse, 57 Avenue d'Azereix, 65008 Tarbes, France
e-mail: michel.auriere@ast.obs-mip.fr e-mail: ligniere@ast.obs-mip.fr e-mail: alain.hui@ast.obs-mip.fr e-mail: donati@ast.obs-mip.fr e-mail: petit@ast.obs-mip.fr e-mail: roudier@ast.obs-mip.fr e-mail: stheado@ast.obs-mip.fr
[2] Department of Physics, Royal Military College of Canada, PO Box 17000, Station 'Forces', Kingston, Ontario, Canada K7K 4B4
e-mail: gregg.wade@rmc.ca
[3] Department of Physics & Astronomy, The University of Western Ontario, London, Ontario, Canada, N6A 3K7
e-mail: jlandstr@uwo.ca
[4] Armagh Observatory, College Hill, Armagh, Northern Ireland BT61 9DG
e-mail: jls@arm.ac.uk
[5] Institute of Astronomy, Bulgarian Academy of Sciences, 72 Tsarigradsko shose, 1784 Sofia, Bulgaria
e-mail: iliani@astro.bas.bg

Received ??; accepted ??

ABSTRACT

Aims. We investigate the magnetic dichotomy between Ap/Bp and other A-type stars by performing a deep spectropolarimetric study of Am and HgMn stars.
Methods. Using the NARVAL spectropolarimeter at the Télescope Bernard Lyot (Observatoire du Pic du Midi, France), we obtained high-resolution circular polarisation spectroscopy of 12 Am stars and 3 HgMn stars.
Results. Using Least Squares Deconvolution (LSD), no magnetic field is detected in any of the 15 observed stars. Uncertaintiies as low as 0.3 G (respectively 1 G) have been reached for surface-averaged longitudinal magnetic field measurements for Am (respectively HgMn) stars.
Conclusions. Associated with the results obtained previously for Ap/Bp stars, our study confirms the existence of a magnetic dichotomy among A-type stars. Our data demonstrate that there is at least one order of magnitude difference in field strength between Zeeman detected stars (Ap/Bp stars) and non Zeeman detected stars (Am and HgMn stars). This result confirms that the spectroscopically-defined Ap/Bp stars are the only A-type stars harbouring detectable large-scale surface magnetic fields.

Key words. stars: chemically peculiar – stars: magnetic field

1. Introduction

The spectroscopically-selected **"magnetic Ap/Bp stars" (hereafter Ap/Bp stars),** corresponding to about 5% of main sequence (MS) A and B stars (Wolff 1968), are known to host relatively strong, ordered magnetic fields. On the other hand, the remaining 95% of MS stars at these spectral types appear to have no detectable magnetic field (with the exception of the very small magnetic field recently detected on Vega by Lignières et al. 2009). This is the so-called magnetic dichotomy. Using the MuSiCoS and NARVAL spectropolarimeters, Aurière et al. (2007) studied the weak part of the magnetic field distribution of Ap/Bp stars. They found, as had previously been assumed, that all confidently spectroscopically-classified Ap/Bp stars, when observed with sufficient precision and tenacity, show evidence for organised magnetic fields with model dipole polar strength stronger than about 300 G. However, demonstrating the existence of a magnetic field dichotomy relies not only on establishing the universal presence of large scale fields in Ap/Bp stars , but also showing confidently that no such fields are detectable in the non-Ap/Bp

Send offprint requests to: M. Aurière, michel.auriere@ast.obs-mip.fr

⋆ Based on data obtained using the Télescope Bernard Lyot at Observatoire du Pic du Midi, CNRS/INSU and Université de Toulouse, France.

stars. The most recent sensitive surveys of apparently non magnetic A and B stars have led to non-detection of magnetic fields at the level of a few tens of G (Shorlin et al. 2002, Bagnulo et al. 2006). Shorlin et al. (2002) used the high-resolution MuSiCoS spectropolarimeter to search for Stokes V Zeeman signatures in spectra of 63 non-Ap/Bp intermediate-mass stars, finding no evidence of magnetic fields, with a median longitudinal field (B_ℓ) formal error of just 22 G. Bagnulo et al. (2006) used the low-resolution FORS1 spectropolarimeter to measure magnetic fields of a large sample of intermediate-mass stars in open clusters. In their sample of 138 non-Ap/Bp stars, no magnetic field was detected, with a median longitudinal field error bar of 136 G. To refine our understanding of the dichotomy, using the possibilities of new instruments (Donati and Landstreet, 2009), in this study we employ NARVAL to observe bright slow rotators among the Am and HgMn stars previously studied by Shorlin et al (2002). In the following, we will describe our observations (Sect. 2) and our results for each category of stars (Sect. 3)**, then give our discussion on magnetic dichotomy and conclusion.**

2. Observations and reduction

2.1. Observations with NARVAL

The observations took place in March and September 2007, at the 2-m Télescope Bernard Lyot (TBL) of Pic du Midi Observatory with the NARVAL high-resolution spectropolarimeter (Aurière 2003). In operation since December 2006, NARVAL is a copy of ESPaDOnS installed at CFHT at the end of 2004 (Donati et al., 2006). NARVAL is a fiber–fed echelle spectropolarimeter with which the whole spectrum from 370 nm to 1000 nm is recorded in each exposure. The 40 grating orders are aligned on the CCD frame using two cross-disperser prisms. NARVAL was used in polarimetric mode with a spectral resolution of about 65000. Stokes I (unpolarised) and Stokes V (circular polarisation) parameters were obtained by means of 4 sub-exposures between which the retarders (Fresnel rhombs) were rotated in order to exchange the beams in the whole instrument and to reduce spurious polarization signatures. We aimed to get long exposures, up to 6400s, on our bright targets in order to be able to detect ultra-weak or complex magnetic fields. In order to avoid saturation of the CCD we made short sub exposures (e.g. 4, 8 second subexposures for each Stokes V series in the case of Sirius).

2.2. Reduction and magnetic field detection

During the technical tests and science demonstration time, magnetic and non magnetic stars were observed which showed that NARVAL works properly and is 30 times more efficient than the previous instrument, MuSiCoS (Baudrand & Böhm 1992, Donati et al. 1999), which was used by Shorlin et al. (2002). Since then, a great number of new results have been obtained that confirm the high scientific efficiency of ESPaDOnS and NARVAL (e.g. in Donati and Landstreet 2009). The extraction of the spectra was done using Libre-ESpRIT (Donati et al. 1997), a fully automatic reduction package installed at the TBL. In order to carry out the Zeeman analysis, Least-Squares Deconvolution analysis (LSD, Donati et al. 1997) was applied to all observations. **We used line masks with solar abundances, $\log g$ = 4, temperatures close to the values given by Shorlin et al. (2002; see our Table 1), and with a central depth greater than 10% of the continuum.** For our sample, this method enabled us to average **from about 500 (highest temperature HgMn star) to about 5000 (coolest Am star) lines** and to obtain Stokes V profiles with signal-to-noise ratio (S/N) increased by a factor of about **10 to 40.** LSD provides a single quantitative criterion for the detection of Stokes V Zeeman signatures: we perform a statistical test in which the reduced χ^2 statistic is computed for the Stokes V profile, both inside and outside the spectral line (Donati et al. 1997). The statistics are then converted into detection probabilities, which are assessed to determine if we have a definite detection (DD, false alarm probability smaller than 10^{-5}), a marginal detection (MD, false alarm probability greater than 10^{-5} and smaller than 10^{-3}), or no detection at all (nd). **Also included in the output are "diagnostic null" spectra N, which are in principle featureless, and therefore serve to diagnose the presence of spurious contributions to the Stokes V spectra**. We then computed the longitudinal magnetic field B_l in G, using the first-order moment method adapted to LSD profiles (Rees and Semel 1979, Donati et al. 1997, Wade et al. 2000). For a few selected stars we constructed line masks that matched the stellar spectrum in detail, by modifying individual line depths in the mask. While these custom masks naturally provided a better representation of the Stokes I and V spectra, they did not result in any change in the detection diagnosis, or any significant improvement in the longitudinal field upper limit. As a consequence, all results presented here correspond to solar abundance line masks.

Finally, we measured for each star (generally the primary) the radial velocity RV from the averaged LSD Stokes I profile, using a gaussian fit. The long term stability of NARVAL is about 30 m/s (e.g. Aurière et al. 2009a) but the absolute uncertainty of individual measurements relative to the local standard of rest is about 1 km s^{-1}.

Table 1 gives for each star its V magnitude, spectral class, **used mask temperature**, $v \sin i$, and, for each observation, the date, HJD (corresponding to the RV measurement), number of exposures and total exposure time, RV, the detection level, and the inferred longitudinal magnetic field with its standard error in G.

Table 1. Summary of observations.

ID	HD	V mag.	Spec.	Mask K	$v \sin i$ km s^{-1}	Date	HJD 2450000 +	#	Exp. s	RV km s^{-1}	Detect. Level	B_ℓ G	σ G
Am Stars													
Sirius	48915	-1.47	A1m	10000	16.5 (2)	12Mar07	4172.33	32	1024	-7.3	nd	-0.10	0.32
α Gem B	60178	2.9	A2m	9000	20 (1)	13Mar07	4173.41	4	2800	-16.3	nd	-0.40	0.79
15 UMa	78209	4.5	F3m	7500	38 (1)	14Mar07	4174.43	1	3200	+0.7	nd	-1.74	2.17
τ UMa	78362	4.6	F3m	7250	11.3 (1)	11Mar07	4171.39	1	3200	-8.7	nd	-0.6	0.54
λ UMa	89021	3.4	A2m	9000	53 (3)	11Mar07	4171.51	3	3600	+19.9	nd	2.77	2.91
β UMa	95418	2.3	A1V	9500	48 (3)	14Mar07	4174.50	6	2880	-12.0	nd	-3.03	2.93
θ Leo	97633	3.3	A2V	9250	23.5 (1)	12Mar07	4172.53	3	3600	+7.4	nd	1.60	1.39
32 Vir	110951	5.2	F0IVm	7250	19.3 (1)	12Mar07	4172.58	1	3600	-39.3	(md)	2.15	1.62
						13Mar07	4173.58	1	3600	-45.0	(md)	-1.27	1.53
						02Apr08	4559.49	1	3600	-57.5	nd	-2.53	1.98
λ Vir	125337	4.5	A2m	9500		13Mar07	4173.63	2	3200		nd	-4.47	2.88
Comp. A					36 (4)	13Mar07	4173.63	2	3200	+11.5	nd	-1.20	2.69
Comp. B					10 (4)	13Mar07	4173.63	2	3200	-27.9	nd	-3.12	1.41
22 Boo	126661	5.4	F0m	8000	36 (1)	13Mar07	4173.68	1	3200	-27.6	nd	-1.44	2.18
	141675	5.8	A3m	8000	33 (1)	14Mar07	4174.66	1	3600	-0.8	nd	-4.91	3.11
ϵ Ser	141795	3.7	A2m	8500	33.5 (1)	12Mar07	4172.65	2	3200	-10.0	nd	-0.79	1.40
HgMn													
κ Cnc	78316	5.2	B8	13000	6.8 (2)	13Mar07	4173.46	1	3200	+76.2	nd	-1.05	3.12
ι CrB	143807	4.9	A0	10500	1.0 (5)	11Mar07	4171.67	2	6400	-19.6	nd	0.07	1.34
ϕ Her	145389	4.2	B9	11000	8.0 (6)	12Mar07	4172.70	3	4800	-15.4	nd	-1.76	1.99

Note: Individual columns show target ID, HD number, spectral class, **mask temperature,** $v \sin i$ (number of reference given at the end of the note), date observed, associated HJD, number of exposures acquired, total exposure time, RV, Detection diagnosis, longitudinal field B_ℓ and its uncertainty σ. References for $v \sin i$: (1) Shorlin et al. 2002; (2) Landstreet et al. 2009; (3) Fekel 2003; (4) Zaho et al. 2007; (5) Dubaj et al. 2005; (6) Zavala et al. 2007.

3. Results of the present survey

3.1. The sample

Our aim is to search for magnetic fields on non Ap/Bp A-type stars in order to establish definitively the gap of the magnetic dichotomy. Shorlin et al. (2002) showed the great influence of the value of $v \sin i$ on the sensitivity of a magnetic survey using high-resolution spectropolarimetry. In order to reduce the errors in our survey, we choose here to observe the most promising objects already observed by Shorlin et al. (2002).

Am stars are frequently found in close binaries (Abt & Levy 1985), likely because tidal interactions in such systems slow stellar rotation and thereby reduce rotational mixing. This is also the case for HgMn stars (Ryabchikova 1998). This property does not hamper our study, but the interesting cases of the SB2 stars 32 Vir and λ Vir are discussed in detail in Sect.3.2. Table 1 presents the observed RV values for our sample stars. Table 1 shows that no Zeeman detection was obtained for any of our sample stars (the case of 32 Vir is discussed in Sect. 3.3). The results are discussed further for Am and HgMn stars in Sect. 3.2 and 3.3 respectively.

3.2. Am stars

Am stars are cool A-type stars that can be considered as "ordinary" slowly rotating A-stars (Takeda et al. 2008). A large number of Am stars deserve a sensitive magnetic survey with NARVAL; we observed 12 of them, among them the bright star Sirius. Our main selection criterion for the stars observed was low $v \sin i$, which we required to be smaller than 50 km s^{-1}, and is often much smaller. Our sample stars are generally on the main sequence, but two of them, 32 Vir and 22 Boo, have already left it. The main result of our study (no Zeeman detection and very low upper limits for a possible surface-averaged longitudinal magnetic field) is visible on Table 1, but we give comments about some stars below.

Sirius: Besides being the brightest star in the sky after the Sun, Sirius is a hot Am star. Observing it enabled us to reach the highest precision obtained in our survey, namely 0.32 G for our B_ℓ determination. With 32 Stokes V series, we got a total exposure of 1024 s. Fig.1 shows the composite LSD profiles. The huge enlargement of Stokes V and Stokes N show that the amplitude of the noise is currently smaller than $10^{-5} I_c$. A kind of flat feature appears on Stokes V profile at the position of the absorption line in the intensity profile. It is not significant with respect to the LSD detection statistical test. Splitting our spectra into two equal subsets show that this feature is more visible on our second subset, and is probably due to noise. No magnetic field is therefore detected on Sirius and the corresponding B_l value is 0.10 ± 0.32 G (1σ). Equally small or even smaller errors in Stokes V profiles and B_l measurements were obtained with NARVAL in the case of

the normal A-star Vega (Lignières et al. 2009) and the red giant Pollux (Aurière et al. 2009a), and sub-G magnetic fields could be detected at a significant level in these stars.

α Gem B (Castor B): Castor is a multiple system composed of three visual stars, each of which is by itself a spectroscopic binary. Castor A and Castor C were out of the slit during the NARVAL observations. Castor A and B have been now resolved in X-rays and this observation shows that the late-type secondaries within each spectroscopic binary are the sites of the X-ray production (Stelzer & Burwitz 2003). Our non-detection of a magnetic field confirms the absence of magnetic activity at the surface of the A-type star Castor B.

λ UMa: Our observations confirm that the 3 σ detection (66 ± 22 G) of a magnetic field by Shorlin et al. (2002) is spurious, as suspected by those authors. We have improved the precision of field measurement by a factor greater than 7 with respect to the MuSiCoS result, though the corresponding error on B_ℓ is one of the worst in this paper, 2.91 G, due to the relatively large $v \sin i$ of 50 km s^{-1}.

θ Leo: This star is considered to a hot Am star (Smith 1974, Adelman 2004) and as a standard of radial velocity (Morse et al. 1991). Because of its moderate $v \sin i$ = 23.5 km s^{-1}, the field measurement is one of the most accurate in the survey (σ = 1.39 G) for early A-type stars.

32 Vir: 32 Vir is a well known SB2 whose primary appears to be of ρ Puppis-type δ Scuti star, i.e. an evolved pulsating Am star (Mitton and Stickland 1979). Fig.2 shows the LSD Stokes profiles derived from a total integration of 3600s obtained on 12 March 2007. The Stokes I LSD profile easily resolves the two components, the Am star corresponding to the sharp line. In both the Stokes V and null polarization N profiles, a small signal is visible at the RV of the Am star, and the LSD statistics announce a Marginal Detection. Since this detection is obtained also, even more strongly, on the null polarization N profile, it is suspected to be spurious. However weak magnetic fields in subgiant stars have been detected in the course of another magnetic survey with NARVAL (Aurière et al. 2009b). We therefore observed 32 Vir again in the same conditions on 13 March 2007 and on 02 April 2008, and got the same result: a weak signal was again visible on Stokes V and N profiles, MD again in 2007 but nd in 2008. Now 32 Vir is both a binary star and a pulsating star (Lampens and Boffin 2000). Bertiau (1957) derived an orbit with a period of 38.3 days and a semi amplitude of 48 km s^{-1}. When observed in 2007 the RV of the primary star's line in the Stokes I LSD profile of 32 Vir was respectively 39.3 km s^{-1} and -45.0 km s^{-1} (Table 1). As a δ Scuti star, 32 Vir has a period of about 0.07 day (Bartolini et al. 1983, Kurtz et al. 1976). The RV variation due to pulsations is unknown, but could be similar to that observed for ρ Puppis itself, i.e. 8.6 km s^{-1} (Mathias et al. 1997). These rapid RV variations due to the binary and pulsating status of the star induce shifts in RV between the LSD profiles of the four sub-exposures, which lead to detection of spurious polarization signals **(Donati et al. 1997)**. Because of the different time-lags between combinations of sub-exposures used for getting N and Stokes V profiles, the spurious signal is expected to be stronger on the former than on the latter profiles. This process is probably the reason for the signal detections obtained on both 2007 dates, and the weak presence of a signal in the 2008 observation.

λ Vir: This star is a well-known double lined spectroscopic Am binary: both stars are very similar in chemical abundances but the primary component is broad-lined and the secondary is sharp-lined (Zhao et al. 2007). Our NARVAL observations enabled us to resolve the two components on our LSD Stokes V profiles, as already presented by Shorlin et al. (2002). In Table 1 we show that neither of the two components indicates a Zeeman detection and we have included individual B_ℓ measurements for each of the two components.

22 Boo: 22 Boo is considered to be an Am star which has already left the main sequence (Burkart et al. 1980, Bertet 1990). This is a particularly interesting object for a magnetic survey since a dynamo driven magnetic field may appear during the subgiant phase (Aurière et al. 2009b). However no Zeeman detection occur at a level of σ = 2.18 G for B_ℓ.

3.3. HgMn stars

The HgMn stars are generally considered as having the most stable atmospheres among intermediate mass stars (Vauclair and Vauclair, 1982). **However, some binary HgMn stars have been shown to display spectroscopic variations (Adelman et al. 2002, Kochukhov et al. 2005, Hubrig et al. 2006a, Briquet et al. 2010).** The non-uniform surface abundances invoked to explain these variations appear to evolve with time (Kochukhov et al. 2007). It has been proposed that they could host strong magnetic fields of peculiar topology (Hubrig et al. 2006b, 2008), and that such fields could be responsible for the surface structures. Wade et al. (2006) performed a sensitive magnetic study of the brightest HgMn star, α And, and placed a 3σ upper limit of about 100 G on the possible presence of any undetected pure dipolar, quadripolar or octupolar surface magnetic fields. Because of the rather large $v \sin i$ (52 km s^{-1}), the 1σ error bars reached 6 G at the smallest, even with ESPaDOnS. We have observed here with NARVAL 3 of the brightest of the HgMn stars having $v \sin i$ 5 times smaller than α And. The resulting uncertainties of B_ℓ are finally 2 to 4 times smaller than those obtained for α And.

κ Cnc: **For this classical HgMn star (Zöchling & Muthsam, 1987), our non detection with a 1 σ error of 3 G for the longitudinal magnetic field confirms the result of Shorlin et al. 2002, that there is not a strong surface magnetic field**, as suggested by older observations.

ι CrB: Observations of this star with the Gecko spectrograph attached to the Canada-France-Hawaii Telescope have resolved the two components of the spectroscopic bi-

nary (Dubaj et al. 2005). The $v \sin i$ of the HgMn component was measured to be only about 1 km s^{-1}; Shorlin et al. (2002) were only able to find an upper limit of $v \sin i <$ 10 km s^{-1}. Our measurement of this star has the best precision obtained for the HgMn stars of our sample, about 1 G. Figure 3 shows the Stokes V and Stokes I LSD profiles for ι CrB.

ϕ Her: This star is a spectroscopic binary which has recently been resolved (Zavala et al. 2007) and for which the mass of the CP star has been refined (Torres, 2007). No field is detected, with an longitudinal field uncertainty of about 2 G.

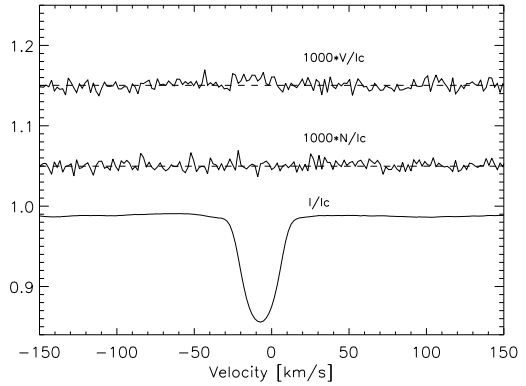

Fig. 1. LSD profiles of the Am star Sirius as observed on 12 March 2007 with NARVAL. From bottom to top: Stokes I, zero polarization N and Stokes V profiles. For display purposes, the profiles are shifted vertically and the Stokes V and diagnostic N profiles are expanded by a factor of 1000. The dashed line illustrates the zero level for the Stokes V and null N profiles.

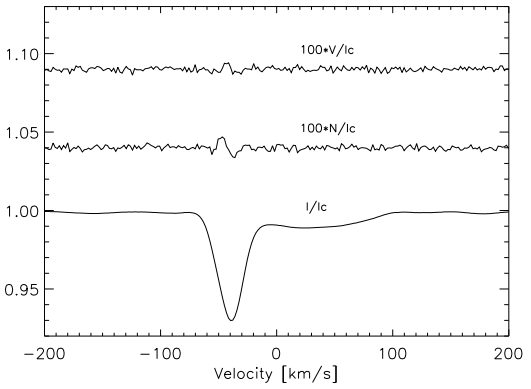

Fig. 2. LSD profiles of the Am star 32 Vir. as observed on 12 March 2007 with NARVAL. From bottom to top: Stokes I, zero polarization N and Stokes V profiles. For display purposes, the profiles are shifted vertically and the Stokes V and diagnostic N profiles are expanded by a factor of 100.

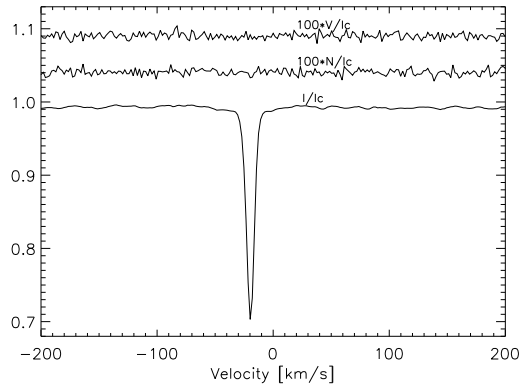

Fig. 3. LSD profiles of the HgMn star ι CrB on 11 Mar 07 as observed with NARVAL From bottom to top, Stokes I, zero polarization, and Stokes V are presented. For display purposes, the profiles are shifted vertically, and Stokes V and diagnostic N profiles are expanded by a factor of 100.

4. The magnetic dichotomy

No Zeeman detection was obtained for any of the 15 stars of our sample, although we have achieved an precision improvement of more than one order of magnitude with respect to the work of Shorlin et al. (2002). **Although we have obtained only one observation for the majority of the stars of our sample, the non-detection of significant Stokes V signatures is a strong negative result because magnetic configurations can produce detectable V signatures through the line profile even for zero longitudinal magnetic field.** Error bars in the range of 0.3 to 3 G have been obtained for our measurements of the surface-average longitudinal magnetic fields and can therefore be used to set upper limits of this component of the magnetic field **of about 10 G (3 σ). Table 1 of Aurière et al. (2007) shows that for the weak magnetic Ap/Bp stars, $|B_\ell|^{max}$ is generally above 100 G, i.e. about 10 times stronger than the present upper limit. Therefore, a very significant gap of at least one order of magnitude is now established between upper limits of fields that might be present in non-detected Am/HgMn stars and the fields consistently detected in Ap/Bp stars.**

To interpret this result in term of magnetic intensity, some assumption has to be done for the magnetic topology. Taking into account the results of Aurière et al. (2007) who deduced the existence of a threshold magnetic field of about 300 G at the surface of Ap/Bp stars, for geometrical configurations similar to those observed in weakly Ap/Bp stars, large scale magnetic fields with dipole field strength greater than about 30 G are not present at the surface of Am and HgMn stars. Moreover, the high-resolution spectropolarimetric techniques used in this study have been shown to be sensitive to both the large-scale (e.g. Aurière et al. 2009a) and smaller-scale

(e.g. Petit et al. 2004) magnetic fields of active late-type stars. While there is certainly a limit to this sensitivity, the very high precision obtained in our survey does not support previous reports of strong, complex fields in Am (Lanz & Mathys 1993) and HgMn stars (Hubrig et al. 2006b, 2008).

The report of a weak magnetic field (of about one G) in Vega (Lignières et al., 2009) is consistent with the existence of a magnetic dichotomy in the A-type stars. The instability scenario of Aurière et al. (2007) gives a possible explanation of this gap. The Ap/Bp stars are those for which the surface magnetic field is strong enough to resist to differential rotation and instabilities such as the Tayler instability (Spruit, 1999). Conversely, stars with a large scale magnetic field of lower strength are subjected to instabilities that will strongly reduce their surface-averaged longitudinal field through cancellation effects. This dichotomy between stable and unstable large scale field configurations naturally leads to a gap in the values of the longitudinal fields.

5. Conclusion

Our limited survey of 15 A-type star of peculiarity types other than Ap/Bp shows that none of them appear to host a large scale magnetic field having a surface-averaged longitudinal magnetic field of more than 3 G. Taken together with the result of Aurière et al. (2007), who showed the existence of a magnetic threshold of about 300 G for dipole strength in Ap/Bp stars, this result confirms the existence of a magnetic dichotomy, and shows that it corresponds to a gap of more than one order of magnitude in field strength. In fact, up to now a magnetic field has been detected by spectropolarimetry for a non Ap/Bp star only in Vega, and the surface averaged-longitudinal magnetic field appears to be smaller than one G (Lignières et al., 2009). Our result can be simply explained by the instability scenario described in Aurière et al. (2007).

Acknowledgements. This research has made use of databases operated by CDS, Strasbourg, France. GAW and JDL acknowledge Discovery Grant support from the Natural Sciences and Engineering Research Council of Canada (NSERC). II acknowledges support from Bulgarian NSF grants D002-85 and D002-362.

References

Abt H.A., Levy S.G. 1985, ApJS, 59, 229
Adelman S.J., Gulliver A.F., Kochukhov O., Ryabchikova T.A. 2002, ApJ, 575, 449
Adelman, S.J. 2004, in "The A-Star Puzzle", J Zverko, J. Ziznovsky, S.J. Adelman & W.W.Weis, eds, 1
Aurière M., 2003 in "Magnetism and Activity of the Sun and Stars", Eds J. Arnaud and N. Meunier, EAS Publ. Series 9,105
Aurière M, Wade G.A. , Silvester J., Lignières et al. 2007, A&A, 475, 1053
Aurière M, Wade G.A. , Konstantinova-Antova R. et al. 2009a, A&A, 504, 231
Aurière M, Konstantinova-Antova R., Petit P. et al. 2009b, in Cosmic Magnetic fields: From Planets, to Stars and Galaxies, K.G. Strassmeier, A.G. Kosovichev & J.E. Beckman, eds, 431
Bagnulo S., Landstreet J.D., Mason E., Andretta V., et al. 2006, A&A, 450, 777
Bartolini C., Grilli F., Parmeggiani G., Piccioni A., Silveri P. 1983, A&ASS, 53, 139
Baudrand J., Böhm T. 1992, A&A, 259, 711
Berthet S. 1990, A&A, 227, 156
Bertiau F.C. 1957, ApJ, 125, 696
Burkhart C., Van't Veer C., Coupry M.F. 1980, A&A, 92, 132
Briquet M., Korhonen H., González J.F., Hubrig S., Hackman T. T. 2010, A&A, 511, in press
Donati J.-F., Semel M., Carter B.D., Rees D.E., Cameron A.C. 1997, MNRAS, 291, 658
Donati J.-F., Catala C., Wade G.W., et al. 1999, A&AS, 134, 149
Donati J.-F., Landstreet J.D. 2009, ARA&A, 47, 333
Donati J.-F., Catala C., Landstreet J., Petit P. 2006, in Casini R., Lites B., eds, Solar Polarization Workshop n4 Vol.358 of ASPC series, 362
Dubaj D., Monier R., Alecian G., LeBlanc F. 2005, in Scientific Highlights 2005 of SF2A, EDP SCiences, F. Casoli, T. Contini, J.M. Hameury and L. Pagani, eds, 335
Fekel F.C. 2003, PASP, 115, 807
Hubrig S., North P., Savanov I. et al. 2006a, MNRAS, 371, 1953
Hubrig S., North P., Schöller M., Mathys G. 2006b, AN, 327, 289
Hubrig S., González J.F., Arlt R. 2008, CoSka, 38, 415
Kochukhov O., Piskunov N., Sachkov M., Kudryavtsev D. 2005, A&A, 439, 1093
Kochukhov O., Adelman S.J., Gulliver A.F., Piskunov N. 2007, NatPh, 3, 526
Kurtz D.W., Breger M., Evans S.W. 1976, ApJ, 207, 181
Lampens P., BoffinH.M.J. 2000, in "Delta Scuti and Related Stars", ASPCS, 210, 309, M. Breger & M.H. Montgomery, eds.
Landstreet J.D., Kupka F., Ford H.A. et al. 2009, A&A, 503, 973
Lanz, T., Mathys G. 1993, A&A, 280, 486
Lignières F., Petit P., Böhm T., Aurière M. 2009, A&A, 5000, L41
Mathias P., Gillet D., Aerts C., Breitfellner M.G. 1997, A&A, 327, 1077
Mitton J., Stickland D.J. 1979, MNRAS, 186, 189
Morse J.A., Mathieu R.D., Levine S.E. 1991, AJ, 101, 1495
Petit P., Donati J.-F., Oliveira J., Aurière M. et al. 2004, MNRAS, 351, 826
Rees D.E., Semel M.D. 1979, A&A, 74, 1
Ryabchikova T.A. 1998, CoSka, 27, 319
Shorlin S.L.S., Wade G.A., Donati J.-F. et al. 2002, A&A 392, 637
Smith M.A. 1974, ApJ, 189, 101
Spruit H.C. 1999, A&A 349, 189
Stelzer B., Burwitz V. 2003, A&A, 402, 719
Takeda Y., Han I., Kang D-I et al. 2008, JTKAS, 41, 83
Torres G. 2007, AJ, 133, 2684
Vauclair S., Vauclair G. 1982, ARA&A 20, 37
Wade G.A., Donati J.F., Landstreet J.D& Shorlin S.L.S. 2000, MNRAS, 313, 851
Wade G.A., Aurière M., Bagnulo S. et al. 2006, A&A, 451, 293

Wolff S.C. 1968, PASP 80, 281
Zhao M., Monnier J.D., Torres G. et al. 2007, ApJ, 659, 626
Zavala R.T., Adelman S.J., Hummel C.A. et al. 2007, APJ, 655, 1046
Zöchling J., Muthsam H. 1987, A&A, 176, 75

3.4.3 A10 : First evidence of a magnetic field on Vega. Towards a new class of magnetic A-type stars

"First evidence of a magnetic field on Vega. Towards a new class of magnetic A-type stars"

Lignières F., Petit P., Bohm T., Aurière M.

A&A 500, L41-L44, 2009

A&A 500, L41–L44 (2009)
DOI: 10.1051/0004-6361/200911996

Astronomy & Astrophysics

Letter to the Editor

First evidence of a magnetic field on Vega

Towards a new class of magnetic A-type stars⋆

F. Lignières[1,2], P. Petit[1,2], T. Böhm[1,2], and M. Aurière[1,2]

[1] Université de Toulouse, UPS, Laboratoire d'Astrophysique de Toulouse-Tarbes (LATT), 31400 Toulouse, France
e-mail: ligniere@ast.obs-mip.fr
[2] CNRS, Laboratoire d'Astrophysique de Toulouse-Tarbes (LATT), 31400 Toulouse, France

Received 6 March 2009 / Accepted 27 April 2009

ABSTRACT

We report the detection of a magnetic field on Vega through spectropolarimetric observations. We acquired 257 Stokes V, high signal-to-noise and high-resolution echelle spectra during four consecutive nights with the NARVAL spectropolarimeter at the 2-m Telescope Bernard Lyot of Observatoire du Pic du Midi (France). A circularly polarized signal in line profiles is unambiguously detected after combining the contribution of about 1200 spectral lines for each spectrum and summing the signal over the 257 spectra. Due to the low amplitude of the polarized signal, various tests have been performed to discard the possibility of a spurious polarized signal. They all point towards a stellar origin of the polarized signal. Interpreting this polarization as a Zeeman signature leads to a value of -0.6 ± 0.3 G for the disk-averaged line-of-sight component of the surface magnetic field. This is the first strong evidence of a magnetic field in an A-type star which is not an Ap chemically peculiar star. Moreover, this longitudinal magnetic field is smaller by about two orders of magnitude than the longitudinal magnetic field (taken at its maximum phase) of the most weakly magnetic Ap stars. Magnetic fields similar to the Vega magnetic field could be present but still undetected in many other A-type stars.

Key words. stars: magnetic fields – stars: early-type – stars: individual: Vega

1. Introduction

Despite recent progress in stellar magnetic field measurements, spectropolarimetric surveys of early-type stars indicate that photospheric magnetic fields can only be detected in a small fraction of these stars. Without direct constraints on the magnetic field of the vast majority of early-type stars, our understanding of the role of magnetic fields on the structure and evolution of intermediate mass and massive stars is necessarily limited. In this Letter, we report the detection of a magnetic field on Vega and argue that Vega is probably the first member of a new class of yet undetected magnetic A-type stars.

The proportion of stars hosting a detectable magnetic field is more firmly established for main sequence stars of intermediate mass (late-B and A-type stars) than for massive stars (early B and O-type stars) or intermediate mass pre-main-sequence stars (Herbig Ae/Be stars). Magnetic A-type stars are indeed identified with the group of Ap-Bp chemically peculiar stars (excluding the subgroup of HgMn stars) since all known magnetic A-type stars belong to this group and, when observed with sufficient precision, Ap/Bp stars always show photospheric magnetic fields (Landstreet 1992; Aurière et al. 2007). The incidence of the Ap/Bp chemical peculiarity among A-type stars then leads to a 5−10% estimate of magnetic stars (Wolff 1968). Note that magnetic field detections have been reported for a few Am and HgMn stars (Lanz & Mathys 1993; Mathys & Hubrig 1995) but remain debated because they could not be confirmed by further investigations (see the discussion in Shorlin et al. 2002). Thanks to new high-resolution spectropolarimeters, magnetic fields are now also detected in pre-main-sequence stars and in massive stars. According to recent surveys, the fraction of magnetic stars among Herbig Ae/Be stars is 7% (Wade et al. 2009), while the rate of detection for early B and O-type stars is also small (Bouret et al. 2008; Schnerr et al. 2008).

The magnetic fields of Ap/Bp stars are characterized by a strong dipolar component, a long-term stability and dipolar strengths ranging from a lower limit of about 300 Gauss to tens of kilo-Gauss (Landstreet 1992; Aurière et al. 2007). Thus, if a population of weak dipolar-like fields corresponding to a weak field continuation of Ap/Bp stars exists, a longitudinal component of the magnetic field in the range of 10 to 100 Gauss should have been detected by recent spectropolarimetric surveys of non Ap/Bp stars (Shorlin et al. 2002; Wade et al. 2006; Bagnulo et al. 2006; Aurière et al. 2008). Instead, these surveys suggest there is a dichotomy between the population of strong, stable and dipolar-like magnetic fields corresponding to the Ap/Bp stars and the rest of A-type stars, whose magnetic properties remain unknown, except that their surface longitudinal magnetic field should be very small.

Vega is well suited for the search of magnetic fields among A-type non Ap/Bp stars. Its brightness and its low equatorial projected velocity ensure high signal-to-noise V spectra, while the number of spectral lines of an A0-type star is important enough to allow a very large multiplex gain by gathering the polarimetric signal of all the lines using a cross-correlation technique (Least-Squares Deconvolution, Donati et al. 1997, LSD hereafter). Another advantage of Vega's brightness is that its fundamental parameters are well known relative to other more anonymous stars (Gray 2007). In particular, spectral

⋆ Based on observations at Telescope Bernard Lyot of Observatoire du Pic du Midi, CNRS/INSU and Université de Toulouse, France.

analysis and interferometric observations have shown that Vega is a rapidly rotating star seen nearly pole-on (Aufdenberg et al. 2006; Peterson et al. 2006; Takeda et al. 2008).

Vega was already included in a previous spectropolarimetric survey of A-type non Ap/Bp stars using NARVAL at the Telescope Bernard Lyot of Pic du Midi, but the analysis of its 11 Stokes V spectra was not conclusive. Here we present the results of a four night observing run fully dedicated to Vega, during which more than 300 Stokes V spectra were obtained. Summing the information over a large number of these spectra leads to an unambiguous detection of a polarized signal.

The observations are described and interpreted in the next section. In Sect. 3, the origin of a ∼1 G longitudinal magnetic field in an A-type non Ap/Bp star is discussed and some of the perspectives opened by this field detection are considered. Our conclusions are given in Sect. 4.

2. Instrumental setup, data reduction and multi-line extraction of Zeeman signatures

The observing material was gathered at the Telescope Bernard Lyot (Observatoire du Pic du Midi, France) using the NARVAL spectropolarimeter. As a strict copy of ESPaDOnS (Petit et al. 2003), NARVAL spectra provide a simultaneous coverage of the whole optical domain (from 370 nm to 1000 nm) at high spectral resolution (R = 65 000). The instrument consists of a bench-mounted spectrograph and a Cassegrain-mounted polarimeter, with an optical fiber carrying the light between the two units. A series of 3 Fresnel rhombs (two half-wave rhombs that can rotate about the optical axis and one fixed quarter-wave rhomb) are used in the polarimeter, followed by a Wollaston prism which splits the incident light into two beams, respectively containing light linearly polarized perpendicular/parallel to the axis of the prism. Each Stokes V spectrum is obtained from a combination of four sub-exposures taken with the half-wave rhombs oriented at different azimuths (Semel et al. 1993). The data reduction is performed by Libre-Esprit, a dedicated, fully automated software described by Donati et al. (1997).

The data were collected during 4 consecutive nights in the summer of 2008, from July 25 to July 28, using 6 s integration times for each sub-exposure of the Stokes V sequences (except the first two sequences of the run, for which exposure times of 15 and 10 s were adopted). We retained the 257 Stokes V spectra with a typical peak signal-to-noise ratio (S/N hereafter) of 1500 per 1.8 km s^{-1}, around λ = 600 nm.

For each spectrum, both Stokes I and V parameters were processed using the LSD cross-correlation method (Donati et al. 1997). Using a line mask computed from a stellar atmospheric model with $T_{\rm eff}$ = 10 000 K and $\log g$ = 4.0 (Kurucz 1993), we calculated LSD line profiles from a total of 1200 photospheric lines. The multiplex gain in the S/N from the raw spectra to the LSD mean profiles is about 30, reducing the noise level of the cross-correlation profiles to between $\sigma = 3$ and $7 \times 10^{-5} I_{\rm c}$, where σ is the standard deviation of the noise and $I_{\rm c}$ stands for the intensity of continuum. Since no signature was observed above noise level in individual Stokes V LSD profiles, we then calculated an average of the 257 profiles, where each profile is weighted by its S/N. In this global profile, the noise in the Stokes V parameter is further decreased to $\sigma = 2 \times 10^{-6} I_{\rm c}$ (Fig. 1) and a signature is now observed in circular polarization with an amplitude of $10^{-5} I_{\rm c}$ (that is 5 times the noise level). Running a χ^2 test on the signature (Donati et al. 1992), we found a reduced χ^2 of 3.5, which corresponds to a false-alarm probability of 3×10^{-11}.

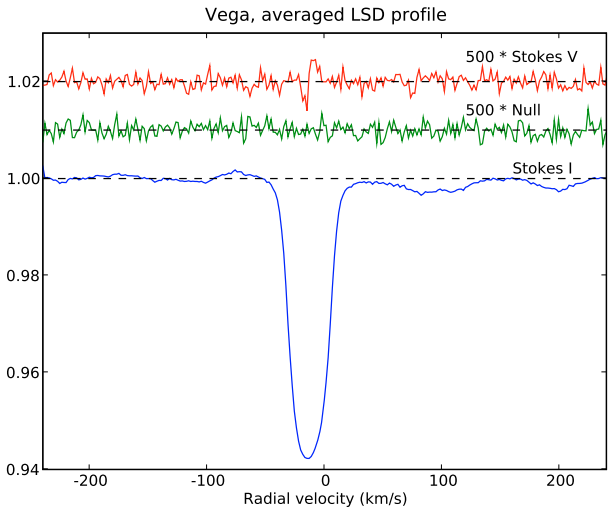

Fig. 1. Average of the 257 normalized Stokes I (blue/bottom) and Stokes V (red/upper) LSD profiles of Vega, as a function of the radial velocity. The green/middle curve is the "null" profile. The Stokes V and null curves are shifted vertically and expanded by a factor of 500. Dashed lines indicate the continuum level for Stokes I, and the zero level for the circular and null polarization.

Various tests have been performed to make sure that the polarization is of stellar origin and not due to an artefact of the instrument or the reduction process. This is particularly important in the present case, as the amplitude of the polarized signal is the lowest detected by NARVAL to date. A strong test to discard the possibility of a spurious signal is the "null" profile calculated from a different combination of the four sub-exposures constituting the polarimetric sequence (Donati et al. 1997). As shown in Fig. 1, no detectable counterpart of the Stokes V signal is seen in the "null" profile (note that a similar conclusion is reached by calculating another null profile (not shown here) from another possible combination of the sub-exposures). We then checked that the signal possesses the expected properties of a stellar polarized signal. First, we split the whole time-series into two independent subsets, containing respectively the first and second half of the observing run, both subsets having equivalent signal-to-noise ratios. As can be seen in Fig. 2a, the polarized signal is present in both sets, the false-alarm probabilities based on the χ^2 test being 5×10^{-6} and 6×10^{-3}, respectively. Second, we built two line-lists from the atmospheric model, containing all spectral lines with Landé factors respectively higher and lower than $g_{\rm c}$ = 1.2. The Stokes V profiles computed from the two line-lists are plotted in Fig. 2b. As expected, the amplitude of the polarized signal appears higher for the high Landé factor lines than for the low Landé factor lines. The peak-to-peak amplitudes of the polarized signals taken inside the line profile are respectively $2.8 \times 10^{-5} I_{\rm c}$ and $2.0 \times 10^{-5} I_{\rm c}$. Their difference slightly exceeds the noise level ($\sigma = 6 \times 10^{-6} I_{\rm c}$ and $5 \times 10^{-6} I_{\rm c}$, respectively) and their ratio is roughly consistent with the ratio of the average Landé factors of the line-lists (g_m = 1.51 and g_m = 0.94 respectively), taking into account that the corresponding Stokes I LSD profiles have a similar depth, within 10%. Third, we checked that the signal was still consistently recovered when other ways of splitting our line-list were considered (low versus high excitation potential or low versus high wavelengths). Finally, we tested the effect of changing the line mask. Indeed, spectroscopic and interferometric studies of Vega have shown that its surface temperature is inhomogeneous, due to the gravity darkening effect induced by its rapid rotation. According

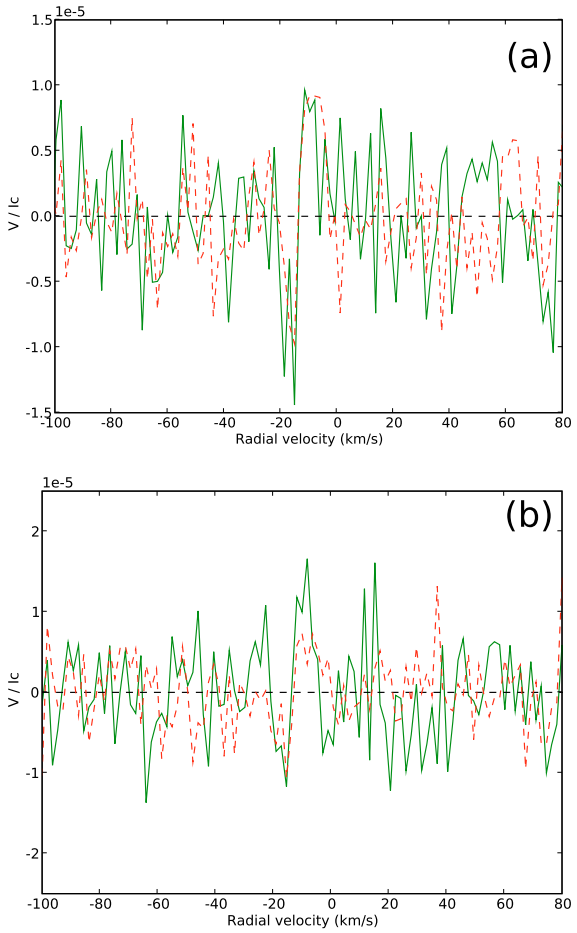

Fig. 2. **a)** Averaged LSD Stokes V line profiles obtained from two independent subsets of the whole observing material, containing respectively the first (green/continuous) and second (red/dashed) half of the observing run. **b)** Stokes V profiles obtained from spectral lines with Landé factors higher (resp. *lower*) than 1.2 (green/full and red/dashed lines, respectively).

to the latest model based on interferometric results (Yoon et al. 2008), the equatorial velocity of Vega is 274 km s^{-1} and the effective temperature and the gravity decrease from 9988 K and $\log g = 4.07$ at the pole to 7600 K and $\log g = 3.5$ at the equator. There is a significant discrepancy with the spectroscopic analysis of Takeda et al. (2008), who find that the polar to equator temperature difference is only ~900 K while the equatorial velocity is reduced to 175 km s^{-1}. Taking the extreme case of a $T_{\rm eff}$ = 7500 K and $\log g = 3.5$ stellar atmosphere, we computed the LSD line profiles (not shown here) for the associated line mask and this time obtained a false-alarm probability of 10^{-1}. The polarized signal is consistent with the one derived from our previous (hotter) atmospheric model but the low significance of the detection is due to the inadequacy of the line mask that results in a much higher noise level.

These tests strongly support that the signal is of stellar origin and therefore that Vega possesses a magnetic field.

The circularly polarized signal has the typical anti-symmetric shape of a Zeeman signature (Fig. 1). However, as compared to the width of the Stokes I line profile, it only shows up within a limited range of radial velocities about the line-center. This suggests that the magnetic field distribution is axisymmetric and confined in the polar region. However, a more detailed analysis will be needed to specify the surface field distribution of Vega. First, as the 257 spectra at our disposal cover a range of rotation phases, Zeeman signatures from non-axisymmetric magnetic features, if any, are mostly averaged out from the time-averaged line profile. Second, due to Vega's temperature inhomogeneities, the weak line profiles range from flat-bottomed to "V" shapes (Yoon et al. 2008; Takeda et al. 2008). As the LSD profile is obtained by assuming that all lines have a common profile, its interpretation in terms of the surface field distribution is not straightforward in the present context.

We use the center-of-gravity method (Rees & Semel 1979) to estimate the longitudinal magnetic field B_ℓ:

$$B_\ell = -2.14 \times 10^{11} \frac{\int v V(v) {\rm d}v}{\lambda_0 g_m c \int (I_{\rm c} - I(v)) {\rm d}v} \quad (1)$$

where v (km s^{-1}) is the radial velocity, λ_0 (nm) the mean wavelength of the line-list used to compute the LSD profiles, g_m the mean Landé factor and c (km s^{-1}) the light velocity. The integration limits cover a ±30 km s^{-1} velocity range around the line centroid. Using this equation, we obtain $B_\ell = -0.6 \pm 0.3$ G.

3. Discussion

Three basic features distinguish the present detection from previous measurements of magnetic fields in main-sequence stars of intermediate mass: (i) it is the first time a magnetic field is detected in an A-type star which is not an Ap/Bp chemically peculiar star (if we exclude the debated field detections in a few Am and HgMn stars, Lanz & Mathys 1993; Mathys & Hubrig 1995; discussed in Shorlin et al. 2002). (ii) The longitudinal magnetic field of Vega is smaller by about two orders of magnitude than the field of the most weakly magnetic Ap/Bp stars. Indeed, the longitudinal field of a 300 G dipolar field aligned with the stellar rotation axis and viewed pole-on is close to 100 G, that is about two orders of magnitude larger than the 0.6 G field of Vega. The longitudinal component of a dipolar field actually depends on its angle with respect to the rotation axis. But, whatever this angle, the amplitude of the circular polarization in the LSD Stokes V profile of a 300 G dipolar field will be more than one order of magnitude larger than that of Vega. (iii) The LSD Stokes V profile of Vega is also qualitatively distinct from LSD Stokes V profiles of Ap/Bp stars since the polarized signal of Vega is concentrated in the weakly Doppler shifted regions of the projected stellar disk.

These marked observational differences between Vega and the Ap/Bp magnetic stars suggest that we should consider Vega as a new type of magnetic A-type star. As there is no reason to believe Vega is unique among A-type stars, Vega should be considered as the first member of a new class of magnetic A-type stars.

The existence of such a new class might help understand some otherwise puzzling observations of the pre-main-sequence and post-main-sequence intermediate mass stars. The Herbig Ae/Be stars show a strong activity (e.g. Böhm & Catala 1995) which has led investigators to suspect a widespread presence of magnetic fields in these stars (Catala et al. 1989). Nevertheless, these magnetic fields have not been found, since only a small fraction of Herbig Ae/Be stars appears to host one (Wade et al. 2009). Note that a similar discrepancy between widespread activity and a small fraction of detected fields exists in OB stars (Henrichs et al. 2005; Schnerr et al. 2008). A new class of magnetic A-type stars would shed new light on this issue. Indeed, the progenitors of these magnetic A-type stars could be the Herbig Ae/Be stars where magnetic fields have not been

detected yet, this non-detections being compatible with the fact that magnetic fields of the same intensity are much more difficult to detect in the faint Herbig Ae/Be stars than in a bright A-type star like Vega. On the post-main-sequence side, the study of the white dwarf magnetic fields suggests that Ap/Bp stars are not sufficient to be the progenitors of magnetic white dwarfs (Wickramasinghe & Ferrario 2005). A new class of magnetic A-type stars might also help to resolve this issue.

The consequences for Vega itself should also be considered. Its magnetic field could indeed trigger active phenomena in its atmosphere. Signs of spectroscopic variability have been reported, but have not been confirmed since (Charlton & Meyer 1985). On the other hand, despite its status as a photometric standard, a photometric variability of 1−2% with occasional excursions to 4% has been reported (Gray 2007). This might be produced by photospheric temperature inhomogeneities induced by its magnetic field. However, because of the near pole-on configuration of Vega, the variability would rather be due to intrinsic changes of the magnetic field than to rotational modulation.

The origin of Vega's magnetic field could be attributed to one of the three mechanisms generally invoked for early-type stars, namely (i) the fossil field hypothesis; (ii) the envelope dynamo; (iii) the convective core dynamo. Let us first consider the fossil field hypothesis, whereby the ISM magnetic field is confined and amplified during stellar formation. It is regarded as the most consistent explanation of the magnetic fields observed in Ap/Bp stars (Moss 2001), but, as proposed by Aurière et al. (2007), it could also account for another population of stars hosting weak longitudinal magnetic fields. Their argument is based on the fact that large-scale, organized magnetic field configurations are subjected to a pinch-type instability driven by differential rotation (Tayler 1973; Spruit 1999) when the magnetic field drops below a critical value. Consequently, for a distribution of large scale organized fields of different strengths issued from the star formation process, the instability would produce a magnetic dichotomy between a population of strong and stable large scale fields like in Ap/Bp stars and another population where the destabilized configuration is now structured at small length scales, thus resulting in a weak longitudinal field. A simple estimate of the critical field has been found to be consistent with the reported lower limit of Ap/Bp stars. Here, both the detection of a very small longitudinal field in Vega and the gap between this field and the lowest magnetic fields of Ap/Bp stars reinforce this scenario. Nevertheless, this scenario is not complete as it does not say what happens to the destabilized field configuration, which could either decay or be regenerated by a dynamo.

The magnetic field of Vega could indeed be generated by an envelope dynamo where the energy source is the rotation of the star. Following Spruit (2002), the dynamo loop initiated by the differential rotation could be closed by the pinch-type instability mentioned above. This interesting possibility has been investigated by numerical simulations in a simplified cylindrical configuration (Braithwaite 2006) and in a solar context (Zahn et al. 2007), leading to opposite outcomes. Simulations in more realistic conditions for A-type stars are clearly needed to test this envelope dynamo. An important issue concerns the origin of the envelope differential rotation, which is a basic ingredient of this dynamo but which is not forced by a strong stellar wind in A-type stars, contrary to what is expected to occur in OB and Herbig Ae/Be stars (Lignières et al. 1996). The third possibility is a dynamo in the convection core. While magnetic fields are likely to be generated there, an efficient mechanism to transport it throughout the radiative envelope to the star surface has not yet clearly been identified (MacDonald & Mullan 2004).

We note that in the three cases considered, the magnetic field is expected to be structured at small scales and also probably variable in time. This calls for a spectropolarimetric monitoring of Vega that will investigate the surface distribution and the temporal variation of its magnetic field.

4. Conclusion

A circularly polarized signal has been detected by accumulating a large number of high-quality echelle spectra of Vega with the NARVAL spectropolarimeter. The data analysis strongly supports a stellar origin of the polarization and thus the presence of a magnetic field on Vega. Due to the unprecedented low level of the detected polarization, new independent measurements will still be important to confirm this result. A magnetic field on Vega suggests that other A-type stars which are not Ap/Bp stars host weak magnetic fields and that their study can shed a new light on early-type star magnetism. While a spectropolarimetric survey of bright A-type stars will be necessary to find these stars, a detailed investigation of Vega's magnetic field should also provide clues to the origin of this magnetism.

Acknowledgements. We thank the team of the Telescope Bernard Lyot for providing service observing and the referee, Prof. J. Landstreet, for useful comments which helped to improve the manuscript.

References

Aufdenberg, J. P., Mérand, A., Coudé du Foresto, V., et al. 2006, ApJ, 645, 664
Aurière, M., Wade, G. A., Silvester, J., et al. 2007, A&A, 475, 1053
Aurière, M., Wade, G. A., Lignières, F., et al. 2008, Cont. Ast. Obs. Skalnate Pleso, 38, 211
Bagnulo, S., Landstreet, J. D., Mason, E., et al. 2006, A&A, 450, 777
Böhm, T., & Catala, C. 1995, A&A, 301, 155
Bouret, J.-C., Donati, J.-F., Martins, F., et al. 2008, MNRAS, 389, 75
Braithwaite, J. 2006, A&A, 449, 451
Catala, C., Simon, T., Praderie, F., et al. 1989, A&A, 221, 273
Charlton, J. C., & Meyer, B. S. 1985, PASP, 97, 60
Donati, J.-F., Semel, M., Carter, B. D., Rees, D. E., & Collier Cameron, A. 1997, MNRAS, 291, 658
Donati, J.-F., Semel, M., & Rees, D. E. 1992, A&A, 265, 669
Gray, R. O. 2007, in The Future of Photometric, Spectrophotometric and Polarimetric Standardization, ASP Conf. Ser., 364, 305
Henrichs, H. F., Schnerr, R. S., & Ten Kulve, E. 2005, in The Nature and Evolution of Disks Around Hot Stars, ASP Conf. Ser., 337, 114
Kurucz, R. 1993, CDROM # 13 (ATLAS9 atmospheric models) and # 18 (ATLAS9 and SYNTHE routines, spectral line data base), Smithsonian Astrophysical Observatory, Washington, DC
Landstreet, J. D. 1992, A&ARv., 4, 35
Lanz, T., & Mathys, G. 1993, A&A, 280, 486
Lignières, F., Catala, C., & Mangeney, A. 1996, A&A, 314, 465
MacDonald, J., & Mullan, D. J. 2004, MNRAS, 348, 702
Mathys, G., & Hubrig, S. 1995, A&A, 293, 810
Moss, D. 2001, in Magnetic Fields Across the Hertzsprung-Russell Diagram, ASP Conf. Ser., 248, 305
Peterson, D. M., Hummel, C. A., Pauls, T. A., et al. 2006, Nature, 440, 896
Petit, P., Donati, J.-F., & The ESPaDOnS Project Team 2003, EAS Publ. Ser., 9, 97
Rees, D. E., & Semel, M. 1979, A&A, 74, 1
Schnerr, R. S., Henrichs, H. F., Neiner, C., et al. 2008, A&A, 483, 857
Semel, M., Donati, J.-F., & Rees, D. E. 1993, A&A, 278, 231
Shorlin, S. L. S., Wade, G. A., Donati, J.-F., et al. 2002, A&A, 392, 637
Spruit, H. C. 1999, A&A, 349, 189
Spruit, H. C. 2002, A&A, 381, 923
Takeda, Y., Kawanomoto, S., & Ohishi, N. 2008, ApJ, 678, 446
Tayler, R. J. 1973, MNRAS, 161, 365
Wade, G. A., Aurière, M., Bagnulo, S., et al. 2006, A&A, 451, 293
Wade, G. A., Alecian, E., Grunhut, J., et al. 2009 [arXiv:0901.0347]
Wickramasinghe, D. T., & Ferrario, L. 2005, MNRAS, 356, 1576
Wolff, S. C. 1968, PASP, 80, 281
Yoon, J., Peterson, D. M., Zagarello, R. J., Armstrong, J. T., & Pauls, T. 2008, ApJ, 681, 570
Zahn, J.-P., Brun, A. S., & Mathis, S. 2007, A&A, 474, 145

Chapitre 4

Mouvements turbulents dans les intérieurs stellaires

J'ai abordé la question centrale de la modélisation des mouvements turbulents dans différents contextes : d'une part dans les zones radiatives où ces mouvements sont entièrement négligés par le modèle standard et d'autre part dans les zones convectives où ils sont modélisés de façon trop simplifiées par le modèle de longueur de mélange. Pour cela, j'ai contribué au développement d'un code numérique cartésien (le code Balaïtous) dont les principales caractéristiques sont décrites à la fin de ce chapitre.

4.1 Transport turbulent dans les intérieurs radiatifs

La rotation engendre des mouvements macroscopiques dans les zones radiatives qui ont un impact direct sur l'évolution stellaire car ils redistribuent les éléments chimiques. On distingue généralement les mouvements de circulation méridienne axisymétriques des mouvements à plus petites échelles dit "turbulents". Dans ce cadre je me suis intéressé à la modélisation du transport turbulent notamment celui induit par la rotation différentielle. La plupart des travaux de références sur le sujet ayant été réalisés dans un contexte géophysique, un certain nombre de mes travaux se sont également placés dans ce contexte (Lignières et al. 1998, 2000; Toqué et al. 2006, **A11**). Mais j'ai aussi engagé une étude approfondie d'un effet dynamique spécifique des zones radiatives stellaires : l'effet de la diffusivité thermique (Lignières 1999; Lignières et al. 1999, 2005). Pour l'essentiel, je mentionnerai ici les travaux réalisés après 2000.

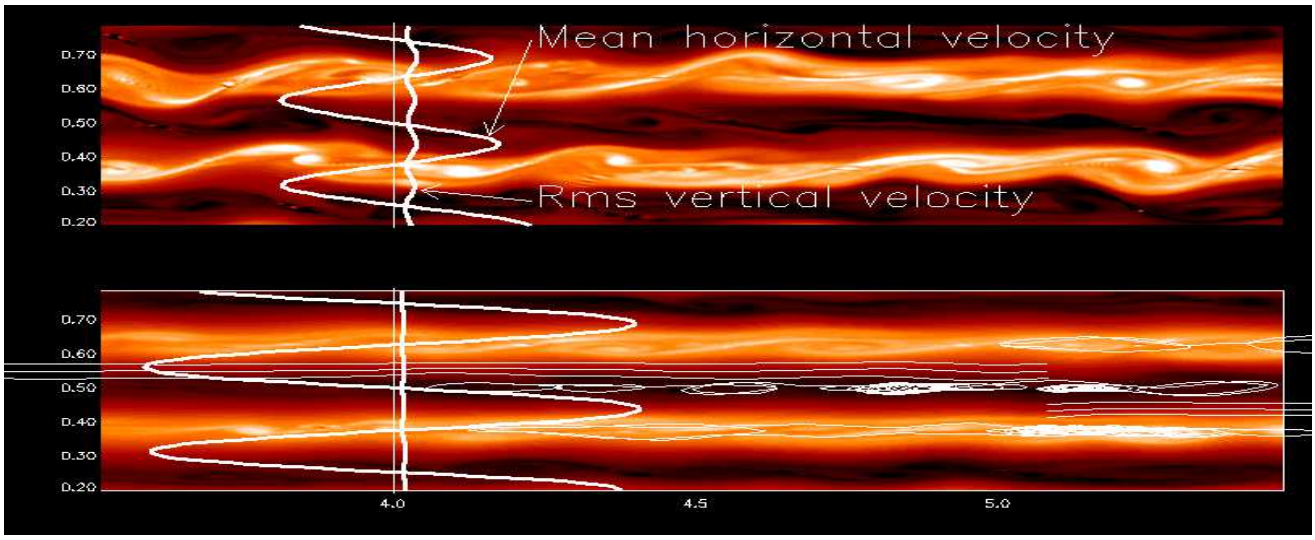

FIG. 4.1 – Zoom sur la distribution de la vorticité pour deux anisotropies différentes. Les profils verticaux de la vitesse horizontale moyenne et des fluctuations moyennes de vitesse verticale sont également représentés avec quelques trajectoires typiques de particules.

Dans les zones radiatives stellaires, les coefficients de transport dérivés des observations (par héliosismologie ou détermination spectroscopique des abondances de surface) sont supérieurs par plusieurs ordres de grandeur à des estimations simples de type longueur de mélange basées sur la rotation différentielle et une longueur caractéristique comme par exemple l'épaisseur de la tachocline dans le cas solaire. Dans le cadre de la thèse de N. Toqué (en co-tutelle avec l'Université de Montréal - A. Vincent), nous avons montré par des simulations numériques d'écoulements cisaillés qu'une forte anisotropie de la turbulence entre mouvements verticaux et mouvements horizontaux pouvait aider à comprendre ce phénomène (Toqué et al. 2006, **A11**). Nous observons en effet que le rapport entre le coefficient de transport effectif et l'estimation de type longueur de mélange décroît lorsque l'anisotropie augmente. Notre interprétation est que dans les couches faiblement cisaillées les fortes vitesses horizontales diminuent le temps de présence des particules dans les structures où les vitesses verticales sont suffisamment cohérentes pour assurer un transport verticale efficace. Ces structures ne sont en effet pas advectées par l'écoulement horizontal moyen car elles sont liées aux régions de fortes concentration de la vorticité situées au coeur des couches fortement cisaillées où la vitesse moyenne est naturellement très différente. La Figure 4.1 représente un zoom de la distribution de vorticité pour deux anisotropies différentes de l'écoulement. Les profils verticaux de la vitesse horizontale moyenne et des fluctuations moyennes de vitesse verticale sont aussi montrés ainsi que quelques trajectoires typiques de particules.

Dans les codes d'évolution stellaire actuels, la contribution des mouvements turbulents au transport des éléments chimiques est décrite par des coefficients de transport dont les expressions ont été obtenues sur la base d'arguments phénoménologiques (Zahn 1992). Ces expressions doivent donc être testées par différents moyens et notamment par la modélisation directe. J'ai abordé ce problème par une étude de stabilité linéaire, la simulation numérique et la modélisation phénoménologique.

L'étude que j'ai faite de la stabilité d'une couche de cisaillement de type Kelvin-Helmholtz dans une atmosphère stratifiée de façon stable en présence d'une forte diffusivité thermique (Lignières et al. 1999) a permis en particulier de confirmer la forme du critère de stabilité proposé par J.P. Zahn (ce critère est très utilisé dans la littérature). Mais, il faudrait en principe poursuivre cette étude dans le régime non-linéaire par des simulations numériques. Néanmoins, il existe, du fait de la forte diffusivité thermique, un très grand écart entre les échelles de temps dynamique et les échelles de temps diffusif qui pénalise très fortement les simulations numériques. Pour résoudre ce problème majeur, j'ai établi une forme asymptotique des équations de Boussinesq valable dans la limite des très fortes diffusivités et pour laquelle le problème numérique disparaît. Cette forme nouvelle des équations permet également d'élucider en partie le rôle dynamique subtil joué par la diffusivité thermique puisque celle-ci peut soit favoriser soit limiter les mouvements verticaux dans une zone radiative en diminuant l'amplitude de la force de rappel d'Archimède ou en augmentant la dissipation de l'énergie cinétique convertie en énergie interne par le travail de la force d'Archimède (Lignières 1999).

J'ai depuis commencé des simulations numériques d'un écoulement cisaillé plan-parallèle dans une atmosphère stratifiée de façon stable dans lequel la diffusivité thermique est progressivement augmentée. Pour explorer le régime des très grandes diffusivités thermiques, nous utiliserons la forme asymptotique des équations de Boussinesq. La configuration de l'écoulement est de type "shearing-box" dans le sens où le gradient vertical de vitesse horizontal est maintenu constant mais à la différence du cas "shearing-box" nous imposons une vitesse verticale nulle aux bords inférieurs et supérieurs du domaine et une condition de glissement sans frottement pour la vitesse transverse. Le cisaillement moyen est maintenu constant par l'introduction d'une force en volume et par une condition aux bords qui fixe le gradient de vitesse horizontale à la valeur voulue. Cette configuration a été utilisée par Schumacher (2001) car elle permet d'atteindre un état statistiquement stationnaire plus facilement que dans la configuration "shearing-box". Un gradient vertical de température constant est imposé de la même façon pour assurer une fréquence de Brunt-Väisälä N_0 uniforme. Nous savons que la diffusivité thermique n'a un effet

sur la dynamique que si celle-ci est affectée par la force d'Archimède. Or, pour notre configuration d'écoulement, il existe un nombre de Richardson, $Ri = N_0^2/(dU/dz)^2$, en deçà duquel l'énergie turbulente croît au cours du temps et au delà duquel la stratification stable "tue" la turbulence. En nous plaçant au nombre de Richardson critique, nous pouvons donc obtenir un écoulement turbulent, statistiquement stationnaire, et significativement affecté par la force d'Archimède. Au cours du stage de M1 de F. Soubiran, nous avons obtenu un écoulement de ce type pour différentes valeurs du nombre de Reynolds (ces simulations à $128 \times 128 \times 128$ points ont été réalisées avec le code Balaïtous). Nous avons ensuite augmenter la diffusivité thermique dans ces simulations, passant d'un nombre de Péclet $Pe = UL/\kappa$ de 1000 à 1 (les simulations à Pe=1 sont très longues à effectuer car le pas de temps numérique doit être très petit). L'effet le plus évident sur l'écoulement concerne les corrélations entre les fluctuations de vitesses verticales et les fluctuations de température, car le coefficent de corrélation augmente d'un facteur deux entre Pe=1000 et Pe=10 (il passe de 0.4 à 0.8). En effet, à forte diffusivité thermique, les fluctuations de température sont fortement amorties ; les termes d'advection de température qui dépendent de l'amplitude de ces fluctuations sont donc faibles alors que, en présence du gradient vertical moyen de température, les déplacements verticaux provoquent toujours des fluctuations de température. Ceci explique la forte corrélation entre vitesses verticales et fluctuations de température. Pour explorer les régimes à très petit nombre de Péclet, nous allons maintenant coder puis simuler les équations asymptotiques. Nous disposerons ainsi d'une série d'écoulements turbulents, stratifiés de façon stable, dans lesquels la diffusivité thermique joue un rôle croissant. Nous pourrons alors étudier le transport d'un scalaire passif dans ces écoulements pour quantifier le rôle de la diffusivité thermique sur le transport et tester les prescriptions proposées notamment par Zahn (1992).

Par ailleurs, j'ai aussi proposé, sur la base d'arguments phénoménologiques, une estimation des échelles caractéristiques de la turbulence dans les zones radiatives d'étoile (Lignières et al. 2005). La Figure 4.2 présente les échelles verticales et les critères de suppression de la turbulence en fonction du régime de diffusivité thermique et de la vitesse turbulente verticale typique u_z. On peut également déduire de ce type de raisonnement que le coefficient de transport turbulent vertical doit être supérieur à la diffusivité thermique si celle-ci ne joue pas de rôle important sur la dynamique alors que ce coefficient doit être inférieur à la diffusivité thermique dans le régime où elle contrôle l'effet de la force d'Archimède. Comme l'ont montré Michaud & Zahn (1998), les coefficients de transport effectif $D_{\rm eff}$ des éléments chimiques que l'on peut estimer à partir des observations sont très faibles (dans le Soleil $D_{\rm eff}/\kappa \sim$

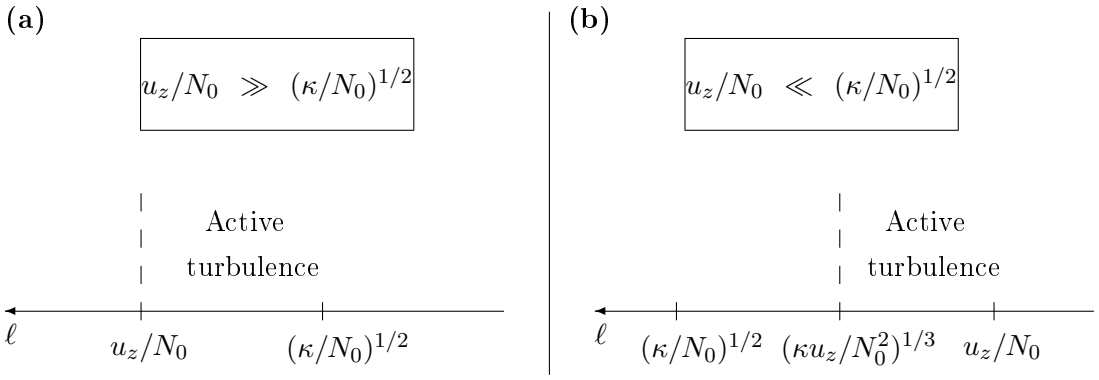

FIG. 4.2 – Échelles verticales de la turbulence **(a)** lorsque la diffusivité thermique ne modifie pas l'effet de la force d'Archimède sur les plus grandes échelles de la turbulence, $l_z = u_z/N_0$ **(b)** lorsque la diffusivité thermique contrôle l'effet de la force d'Archimède sur les plus grandes échelles de la turbulence, $l_z = (\kappa u_z/N_0^2)^{1/3}$.

2×10^{-4}). En supposant que le transport observé soit effectivement du à des mouvements turbulents, on en déduit que la diffusivité thermique devrait jouer un rôle prépondérant sur la dynamique de ces mouvements. Si de plus, on fait une hypothèse de type longueur de mélange, c'est-à-dire $D_{\rm eff} = l_z u_z$, on peut déduire des relations précédentes sur les échelles caractéristiques, une estimation de l'échelle de longueur verticale typique des mouvements turbulents :

$$l_z = [(\kappa D_{\rm eff})/N_0^2]^{1/4} \tag{4.1}$$

et de la vitesse verticale typique de ces mouvements :

$$u_z = [(D_{\rm eff}^3 N_0^2)/\kappa^2]^{1/4} \tag{4.2}$$

Cette approche nous servira également pour analyser les résultats des simulations numériques mentionnés ci-dessus.

4.2 Convection thermique à la surface du Soleil

L'origine des différentes échelles du mouvement observées à la surface du Soleil reste mal comprise. Ma contribution s'inscrit dans le cadre d'un projet combinant l'observation à haute résolution spatiale et temporelle de la surface du Soleil avec des simulations numériques de convection compressible.

Le travail d'interprétation des observations que j'ai effectué avec Th. Roudier (Roudier et al. 2003,

A12) a permis de proposer un regroupement des granules par familles (les TFG pour" Trees of Fragmenting Granules") qui semblent être associées à des échelles mésogranulaires du mouvements. Un autre intérêt de ce type d'analyse est que les propriétés statistiques de la dynamique des granules ainsi déterminées peuvent être utilisées pour tester le réalisme des simulations numériques de la surface solaire. Les premières comparaisons que nous avons effectuées (Roudier 2004) indiquent que la durée de vie des TFG et le transport advectif d'un scalaire passif ne sont pas reproduits de façon réaliste dans les simulations réalisées par Rieutord et al. (2002) avec le code de Stein & Nordlund.

Dans le cadre de la thèse de F. Rincon, des simulations de convection compressible ($1024 \times 1024 \times 82$ points) à très grand rapport d'aspect (le rapport de la longueur de la boîte sur sa hauteur est de 40 ce qui n'avait jamais été tenté auparavant) ont été réalisées avec le code Balaïtous pour étudier l'origine des différentes échelles horizontales de la convection. Alors que l'existence même de la mésogranulation a pu apparaître douteuse, ces simulations mettent en évidence une échelle similaire à la mésogranulation, d'origine convective et qui pourrait être l'échelle dominante de la convection solaire juste sous la surface, l'échelle granulaire étant formée dans une couche limite thermique de surface. De plus, ces simulations ont montré que l'échelle horizontal de ces mouvements tend à augmenter au cours du temps sans que l'on sache très bien ce qui va limiter ce phénomène. Ces deux principaux résultats sont décrits dans Rincon et al. (2005, **A13**).

4.3 Code Balaïtous

Le code Balaïtous est un code MHD 3D cartésien modulaire pour la résolution des équations de la magnétohydrodynamique dans les intérieurs stellaires (dynamo cinématique, MHD dans l'approximation de Boussinesq, MHD compressible). La discrétisation spatiale est pseudo spectrale dans deux directions et aux différences finies compactes dans la troisième direction. Il a été développé initialement comme un code Boussinesq par F. Califano et A. Mangeney. J'ai ensuite fait évolué ce code (parallélisation, équations MHD, nouvelles méthodes aux différences finies compactes, écriture modulaire du programme) puis j'ai encadré F. Rincon qui y a introduit les effets de la compressibilité au cours de sa thèse.

Des évolutions du code permettant de diminuer le temps de calcul (parallélisation dans une direction d'espace actuellement non parallélisée, avancement en temps implicite pour le terme de diffusion de la chaleur) ou de considérer d'autres configurations (géométrie sphérique, conditions aux limites de type

"shearing box") sont envisagées à moyen terme.

4.4 Articles A11-A13

4.4.1 A11 : Reduction of the vertical transport in two-dimensional stably stratified forced shear flows

“Reduction of the vertical transport in two-dimensional stably stratified forced shear flows”

Toqué N., Lignières F., Vincent A.

Geophys. and Astrophys. Fluid Dynamics 100, 85-105, 2006

Geophysical and Astrophysical Fluid Dynamics,
Vol. 100, No. 2, April 2006, 85–105

Taylor & Francis
Taylor & Francis Group

Reduction of vertical transport in two-dimensional stably stratified forced shear flows

NATHALIE TOQUÉ*†, FRANÇOIS LIGNIÈRES‡ and ALAIN VINCENT§

†ICA, Department of Astronomy and Physics, Saint Mary's University,
Halifax, NS, Canada, B3H 3C3
‡Laboratoire d'Astrophysique de Toulouse et Tarbes – Université Paul Sabatier Toulouse 3,
UMR 5572, 14, Avenue Edouard Belin, 31400 Toulouse, France
§Département de Physique, Université de Montréal, C.P. 6128,
Succ. Centre-Ville, Montréal, QC, Canada, H3C 3J7

(*Received 22 August 2005; in final form 20 December 2005*)

The effect of stable stratification on the vertical transport of passive contaminants in forced, stationary, two-dimensional (2D) and inhomogeneous shear turbulence is investigated numerically. The mean flow consists of several superimposed parallel sheared layers in a stably stratified medium. We find that, as stratification increases, the vertical transport decreases much faster than predicted by mixing length estimates. For the highest stratification, particles vertical dispersion nearly vanishes. The proposed interpretation emphasizes the role of weakly sheared layers where the relative increase of the mean horizontal velocity with respect to the root-mean-square (rms) vertical velocity causes the decrease of the Lagrangian correlation timescale.

Keywords: Shear flows; Stable stratification; Turbulent diffusion

1. Introduction

Turbulent diffusion of contaminants in stably stratified flows is ubiquitous in nature, taking place in the oceans and planetary atmospheres (Csanady 1973, Turner 1973). It also plays an important role in stellar interiors where spectroscopic and helioseismic data have revealed that mixing of chemical elements does occur in the stably stratified layers (also called the radiative zone) of the sun and other stars (Charbonneau and Michaud 1991, Chaboyer and Zahn 1992, Pinsonneault 1997). The constraints that the observations put on the effective vertical transport of contaminants in radiative zones are very severe. Effective diffusivities are smaller by various order of magnitude than estimates of the eddy diffusivity

*Corresponding author. Email: n_toque@yahoo.ca

Geophysical and Astrophysical Fluid Dynamics
ISSN 0309-1929 print/ISSN 1029-0419 online © 2006 Taylor & Francis
http://www.tandf.co.uk/journals
DOI: 10.1080/03091920600642048

(Michaud and Zahn 1998). For example, in the solar radiative zone, the effective diffusivity derived from helioseismology is ten order of magnitude smaller than the eddy diffusivity based on the differential rotation and the thickness of the tachocline – a layer where the rotation rate changes from differential rotation in the convection zone to nearly solid-body rotation in the interior.

Previous studies of turbulent diffusion in stably stratified medium have shown that diffusion of contaminants is reduced in the direction of stratification (in the following the vertical direction). This is not surprising considering the effect of the restoring buoyancy force on vertical motions. However, a mixing length estimate of the eddy diffusivity coefficient, $\ell_z u_z$, which takes into account the decrease of the root-mean-square (rms) vertical velocity u_z, is not sufficient to account for the reduction of the vertical transport observed in laboratory experiments (Britter *et al.* 1983) or numerical simulations (Kimura and Herring 1996, Kaneda and Ishida 2000). Here, ℓ_z, is the vertical correlation length of the vertical velocity fluctuations (Tennekes and Lumley 1972).

Vincent *et al.* (1996) have shown that for a given rms vertical velocity, vertical eddy diffusivity decreases as the rms horizontal velocity increases. The decrease of the ratio of the vertical eddy diffusivity to the mixing length estimate is inversely proportional to the flow anisotropy defined as the ratio of horizontal to vertical rms velocities. They attributed this effect to the stronger horizontal turbulence which smoothes contaminant fluctuations. The proposed mechanism could help understand the low effective diffusivity within stellar radiative zones. However, these results have been obtained solving the advection-diffusion equation of the contaminant concentration for stochastic velocity fields. The main objective of the present article is to test their results and interpretation for physical flows which are solutions of the Navier–Stokes equations.

We shall consider the vertical transport of contaminants in approximatively stationary two-dimensional (2D) stably stratified sheared turbulence driven by Kelvin–Helmholtz instabilities. The chosen forcing creates and maintains superimposed sheared layers in an initially linearly stratified atmosphere. After a transition through Kelvin–Helmholtz instability, a statistically stationary turbulent flow sets in. Lagrangian particles are then released and followed over a large number of eddy turnover times. We also consider the diffusion of a horizontal layer of contaminant by solving the advection-diffusion equation. We investigate a very low Prandtl number regime, $Pr = 1.9 \times 10^{-4}$, in order to approach physical conditions encountered in stellar interiors where thermal diffusion of radiative origin is very high. For example, in the solar radiative zone, the Prandtl number is of the order of 10^{-5}.

This particular flow configuration has been chosen because it allows to study the contaminant transport in statistically stationary conditions for a wide range of anisotropy. In laboratory experiments and numerical simulations, stably stratified turbulence has often been studied in homogeneous conditions where the mean shear and the stratification are uniform (Rohr *et al.* 1988, Gerz *et al.* 1989, Holt *et al.* 1992). These spatially homogeneous turbulent flows are unsteady while one would require at least approximate stationarity during the time necessary to establish the statistical property of the contaminant vertical transport. Stationarity can be obtained through nonuniform forcing and, in this work, we consider forced Kelvin–Helmholtz sheared layers which are superimposed to avoid boundary effects on the contaminant vertical transport. The restriction to two dimensions is motivated by the fact that it

has proved very useful to investigate the Kelvin–Helmholtz sheared layers (Ho and Huerre 1984, Comte *et al.* 1989) and, by its relatively lower computing cost which allows the exploration of a broader range of parameters.

The plan of the article is as follows: The basic equations are given in section 2. In section 3, the parameter range of the simulations and the main characteristics of the flow are presented. In section 4, results on the vertical transport of contaminants are presented and analyzed. Section 5 is devoted to the discussion and conclusions.

2. Basic equations and numerical model

We consider the Navier–Stokes equations in the Boussinesq approximation (Chandrasekhar 1961). The motion of the passive contaminant is studied solving the advection-diffusion equation governing its concentration as well as following Lagrangian particles. At the top and the bottom of the flow, the boundaries conditions are of free-slip type for the velocity, the temperature remaining unchanged. In the horizontal direction, the boundary conditions are periodic. The momentum injection is driven by a horizontal force, $\rho_o f(z)\mathbf{e}_x$, where $f(z)$ is alternatively positive and negative

$$f(z) = (-1)^i f_o, \quad \frac{iL}{(n+1)} \leq z < \frac{(i+1)L}{(n+1)}, \quad i \in [0, n], \tag{1}$$

where L is the vertical extent of the computational domain and f_o is a constant acceleration. The forcing generates n sheared layers in the flow, n being fixed to 7 in the following. This value has been chosen in order to avoid that the contaminant mixing layer reaches the top and bottom boundaries during the numerical simulation. The definition of the half-width of the sheared layers is $l_s = 1/2 \times L/7$. The initial profile of the temperature is a linear function of the vertical coordinate z. The uniform temperature gradient is given by $\Delta T/L$, where ΔT is the temperature difference across the computational domain. It is positive as we consider a stably stratified medium. When released in the flow, the initial distribution of the passive contaminant has a Gaussian vertical profile characterized by a half-width equal to $0.1L$. Figure 1 displays a sketch of the forcing term and of the initial distributions of temperature and passive contaminant. Dimensionless equations are obtained using L, f_o, ΔT, defined earlier as well as C_m, which is the spatial average of the initial contaminant concentration. The governing equations with the inertial term written in the rotational form read

$$\frac{\partial \mathbf{v}}{\partial t} = \mathbf{v} \times \boldsymbol{\omega} - \nabla P + \frac{1}{R_e}\nabla^2 \mathbf{v} + f\mathbf{e_x} + Ri\theta \mathbf{e_x}, \quad \nabla \cdot \mathbf{v} = 0, \tag{2a, b}$$

$$\frac{\partial \theta}{\partial t} + \mathbf{v} \cdot \nabla \theta = -v_z \frac{\mathrm{d}T_0}{\mathrm{d}z} + \frac{1}{P_e}\nabla^2 \theta, \tag{2c}$$

$$\frac{\partial C}{\partial t} + \mathbf{v} \cdot \nabla C = \frac{1}{Pe_C}\nabla^2 C, \tag{2d}$$

where $(\mathbf{e_x}, \mathbf{e_z})$ are respectively the horizontal and vertical unit vectors, $P = p + (v_x^2 + v_z^2)/2$, with $p(x, z, t)$ the pressure and $(v_x(x, z, t), v_z(x, z, t))$ the horizontal

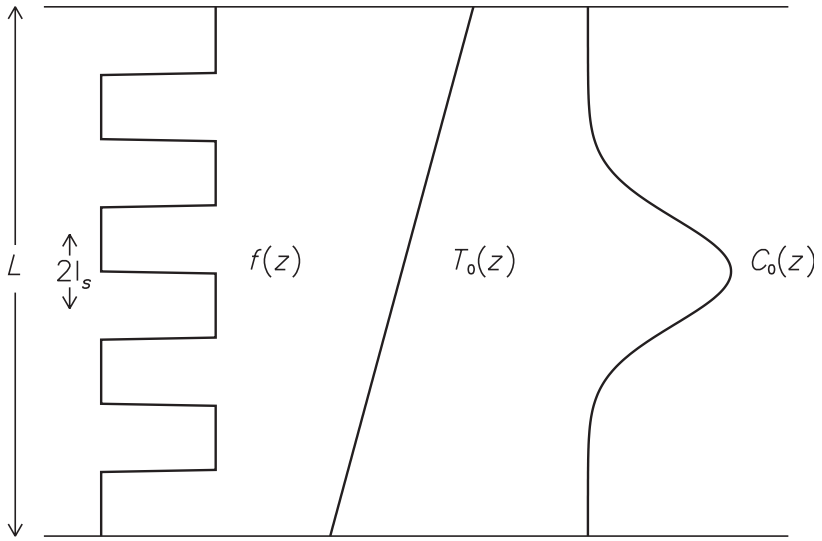

Figure 1. Sketch showing the vertical profiles of the forcing term $f(z)$, the initial temperature $T_0(z)$, and the initial passive contaminant concentration $C_0(z)$. The vertical extent of the domain L and the shear layer half-width l_s are also indicated.

and vertical components of the flow velocity, $\boldsymbol{\omega} = \boldsymbol{\nabla} \times \mathbf{v}$ is the vorticity, $C(x, z, t)$ is the passive contaminant concentration, and $\theta(x, z, t)$ is the temperature perturbation with respect to the initial temperature profile $T_0(z)$. Note that according to the chosen dimensions, $\mathrm{d}T_0/\mathrm{d}z = 1$. The PDE system (2) depends on four dimensionless numbers, the Richardson number, $Ri = N^2 L/f_o$, where $N = \sqrt{g\alpha\Delta T/L}$ is the Brünt–Väisälä frequency, α being the volume expansion coefficient and g the gravity, the Reynolds number, $Re = \sqrt{L^3 f_o}/\nu$, the thermal Péclet number, $Pe = \sqrt{L^3 f_o}/\kappa$, and the Péclet number of the contaminant, $Pe_C = \sqrt{L^3 f_o}/D$, where ν is the kinematic viscosity of the fluid, κ is the thermal diffusivity, and D is the contaminant molecular diffusivity.

We use a code based on the pseudospectral method which has been initially developed by (Deane 1997). The nonlinear terms are calculated in real space with the collocation method. Aliasing is removed by the "2/3" truncation rule. The transformations from real to wavenumber space and vice-versa are done by Fast Fourier Transform. In the vertical direction, the vertical velocity component, the temperature perturbation and the contaminant concentration are expanded into sine series to satisfy the boundary conditions. Accordingly, the horizontal velocity component is expanded into cosine series. Equations (2) are advanced in time using a second-order Leapfrog scheme except for the viscous and diffusive terms which are treated implicitly with the Cranck–Nicholson scheme. The velocity is first advanced without taking into account the pressure term. The pressure contribution is then added in order to ensure a divergent free velocity field. Lagrangian particles tracking is based on an explicit second-order Heun scheme for time advancement and on a fourth-order Hermite polynomial interpolation method used to determine the particle velocity at an instantaneous position from the velocity on grid points (Balachandar and Maxey 1989).

3. Parameter range and flow description

Our purpose is to study the vertical transport of contaminants in a forced stably stratified shear turbulence with increasing strength of the stratification. As in

(Vincent *et al.* 1996) we shall consider in particular the relation between the vertical transport and the flow anisotropy defined as

$$A = \sqrt{\frac{\langle v_x^2 \rangle}{\langle v_z^2 \rangle}}, \tag{3}$$

the ratio between the horizontal and the vertical components of the velocity. The brackets $\langle\ \rangle$ denote an average over the two spatial directions, the vertical average being limited to the extent of the contaminant mixing layer. Each simulation proceeds in two steps. First, a statistically stationary flow with a given anisotropy is established. Then the contaminant is released and its vertical transport is analyzed.

Initially, the forcing generates accelerated horizontal strips of alternatively positive and negative velocity. At their interface, the shear grows while the local Richardson number decreases. When the local Richardson number reaches 1/4, velocity perturbations are introduced and a Kelvin–Helmholtz type instability develops in each sheared layer (although the Mile's criterion is not strictly adequate for our nonsteady flow). Nonlinear effects soon become important and the vertical motions induced by the instability drive a vertical flux of horizontal momentum which tends to limit the shear between the strips.

In neutral conditions ($N=0$), the vertical transport of horizontal momentum is very efficient. The initial seven sheared layers mix together and, after a nondimensional time $t=8$, there are only two sheared layers left. Thus, despite the vertically inhomogeneous forcing, turbulence manages to homogenize the flow in that direction. By contrast, momentum transport between sheared layers decreases in sufficiently stratified conditions and the sheared layers do not mix. The local Richardson number stays lower than 0.1 inside sheared layers. This leads to a statistically stationary state as shown in figure 2 where the anisotropy evolution is displayed for different strengths of the initial stable stratification. Table 1 summarizes the parameters of the different simulations numbered from 1 to 10 as the Richardson number, $Ri = N^2 L/f_o$, increases from 100 to 2000. The Reynolds number keeps similar values around 5000. The thermal Péclet number and the Péclet number of the tracer are respectively chosen equal to 1 and 5000. Table 1 shows that we obtained a wide range of values for the flow anisotropy, A, ranging from 1 to 35, as well as Froude numbers ranging from 1.43 to 0.47. The Froude number characterizes the effect of the stratification on turbulent motions and is defined by $Fr = v/l\sqrt{Ri}$ where $l = \pi/2 \times \int (E(k)/k)\mathrm{d}k / \int E(k)\mathrm{d}k$ is the integral scale and $v = \sqrt{\langle v_x'^2 + v_z'^2 \rangle}$ a typical velocity fluctuation. $v_x' = v_x - \langle v_x \rangle_x$ is the horizontal velocity fluctuations with respect to the mean horizontal velocity $\langle v_x \rangle_x$, and $v_z' = v_z - \langle v_z \rangle_x$ is the vertical velocity fluctuations with respect to the mean vertical velocity $\langle v_z \rangle_x$ which is very close to zero. The symbol $\langle\ \rangle_x$ denotes the horizontal average. Note that, for each run, the Reynolds number has been chosen in order to ensure that the effective turbulent Reynolds number, $Re_t = lv \times Re$, keeps similar values. Such as the turbulent Reynolds number, the turbulent Péclet number of the contaminant, $Pe_{Ct} = lv \times Pe_C$, remains between 125 and 230. Table 1 displays for each Richardson number, time averaged values of the anisotropy, the Froude number, the turbulent Reynolds number, the turbulent thermal Péclet number and the turbulent Péclet number of the contaminant. This temporal mean, $\langle\ \rangle_t$ is taken over the period during which the contaminant transport

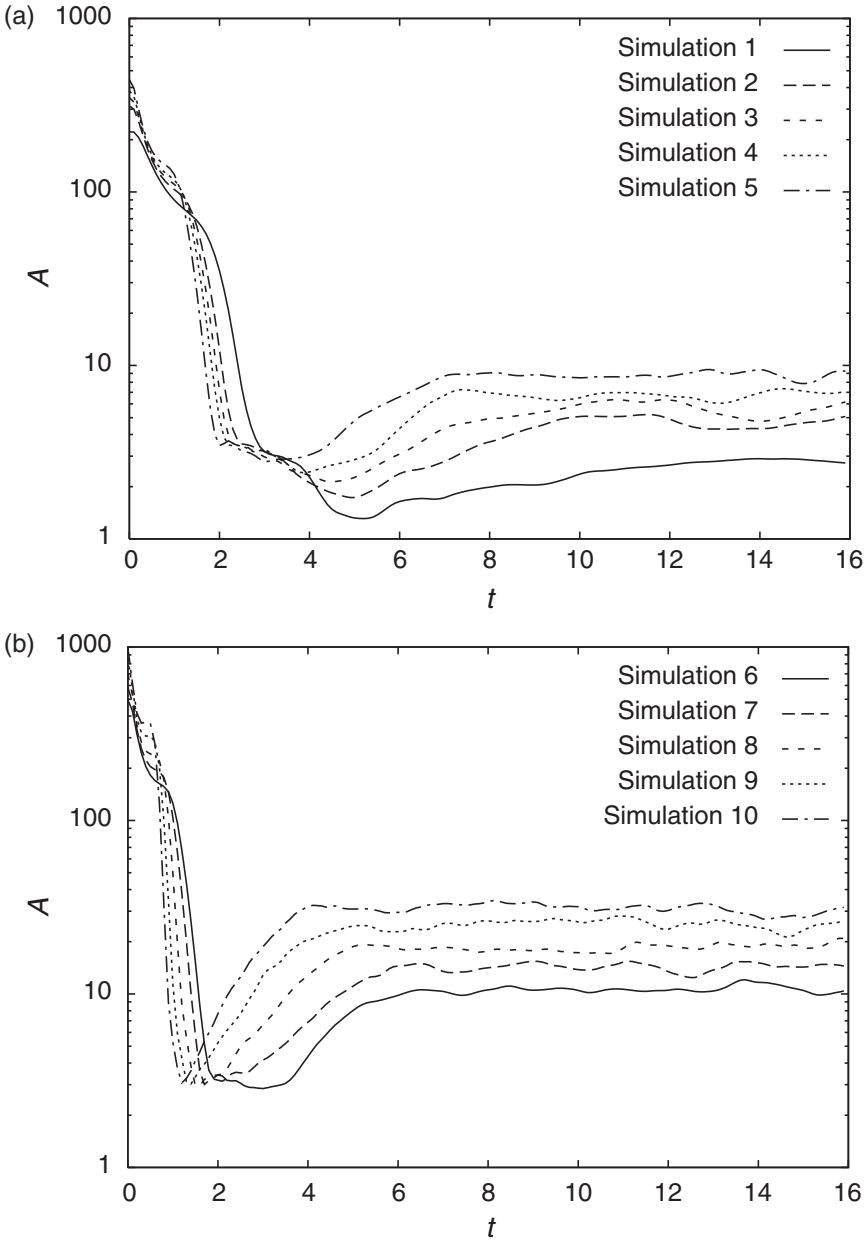

Figure 2. Evolution of the flow anisotropy A towards a statistically steady state for all simulations listed in table 1. The final value of the anisotropy increases with the strength of the stratification.

Table 1. Simulation parameters: in addition to the two dimensionless numbers Ri and Re of the runs, the table lists effective parameters characterizing the flow. The symbol $\langle\ \rangle_t$ denotes the temporal mean calculated over ~ 100 turnover times after the anisotropy has reached a statistically stationary state.

Number of simul.	Sim1	Sim2	Sim3	Sim4	Sim5	Sim6	Sim7	Sim8	Sim9	Sim10
Ri	100	200	250	300	400	500	700	1000	1500	2000
Re	4950	5000	5000	5050	5050	5100	5150	5200	5400	5555
$\langle Re_t \rangle_t$	153.45	145	130	126.25	141.4	122.4	154.5	114.4	167.4	200
$\langle Fr \rangle_t$	1.43	1.06	0.9	0.8	0.79	0.67	0.65	0.47	0.5	0.5
$\langle Pe_t \rangle_t$	0.031	0.029	0.026	0.025	0.028	0.024	0.03	0.022	0.031	0.036
$\langle Pe_{Ct} \rangle_t$	155	145	130	125	140	120	150	110	155	180
$\langle A \rangle_t$	2.79	5.12	5.79	7.15	8.33	10.54	14.07	18.76	25.14	31.14

has been studied. This period starts after a statistically steady state has been reached and lasts approximatively 100 eddy turnover times, $\tau = l/v$. The temporal averages are not sensitive to the exact number of eddy turnover times.

The Schmidt number, $Sc = \nu/D = 1$, and the Prandtl number, $Pr = 1.9 \times 10^{-4}$, are kept constant for all simulations. A direct consequence of such a low Prandtl number is the irrelevance of gravity modes in our simulations as they are very strongly damped by thermal diffusion. Indeed, as shown for example in (Ligniéres 1999), harmonic perturbations in an inviscid linearly stably stratified atmosphere can only oscillate under the condition: $2k_x/\left(k_x^2 + k_z^2\right)^{3/2} > 1/Pe\sqrt{Ri}$, where k_x and k_z denote respectively the dimensionless horizontal and vertical wave numbers of the perturbation. Because of the limited size of the computational domain, only some large scale modes verify this condition. Moreover these modes play no dynamic role as their thermal damping time scale is very short.

The aspect ratio of the computational domain is equal to 6 in order to allow the presence of numerous large scale structures ($\sim$20 vortices) in the horizontal direction. The number of grid points is 1536 in the horizontal direction and 256 in the vertical one.

The 2D structure of the flow is shown in figure 3(a) and (c), where isovorticity outlines are respectively plotted for simulation 2 ($Ri = 200$) and simulation 6 ($Ri = 500$). In figure 4, we also have plotted the vertical variations of the mean horizontal velocity $\langle v_x \rangle_x$ and of the vertical velocity fluctuations $\sqrt{\langle v_z'^2 \rangle_x}$ for two different initial stratifications ($Ri = 200$ and $Ri = 1000$). Vorticity is initially distributed in layers and after the instability develops, it concentrates into vortices centered on the sheared layer centerline. Then, its evolution depends on the strength of stratification. While the vertical advection of vortices tends to homogenize the vorticity distribution in the neutral case (not shown here), vortices stay within the strongly sheared layers in the stratified cases. The vertical extent of these vortices also tends to reduce for higher Richardson number. In the strongly stratified cases, between sheared layers where vorticity concentrates, an interface layer is obvious. This layer is depleted of vorticity, weakly sheared, and highly anisotropic [see figure 4(a)]. In figure 4(b) we note that, contrary to the mean horizontal velocity and the anisotropy, the vertical velocity fluctuations does not present very important variations across the strongly and weakly sheared layers. Note also that the mean horizontal velocity dominates the contribution of the horizontal velocities to the anisotropy except in the near vicinity of the sheared layer centerline where it is null.

Due to the high thermal diffusivity, temperature fluctuations and consequently the turbulent heat flux are very small. The horizontally averaged temperature is not modified by this turbulent heat flux and remains a linear function of the vertical coordinate.

The contaminant is released once the flow has reached a statistically stationary state. The initially homogeneous layer of contaminant mixes and a mixing layer slowly grows with time. Since velocity boundary layers develop at the top and the bottom of the computational domain, the runs are stopped before the mixing layer reaches these boundaries (at $t = 19.9$ for the least stratified simulation). This already corresponds to a large number ($\sim$100) of eddy turnover times, $\tau = l/v$. Figure 5 illustrates this behavior by showing the vertical profile of the mean concentration $\langle C \rangle_x$ at three different times for the least stratified simulation ($Ri = 100$). At the last time ($t = 19.9$), the tracer reaches the vertical limits of the domain and the run is stopped.

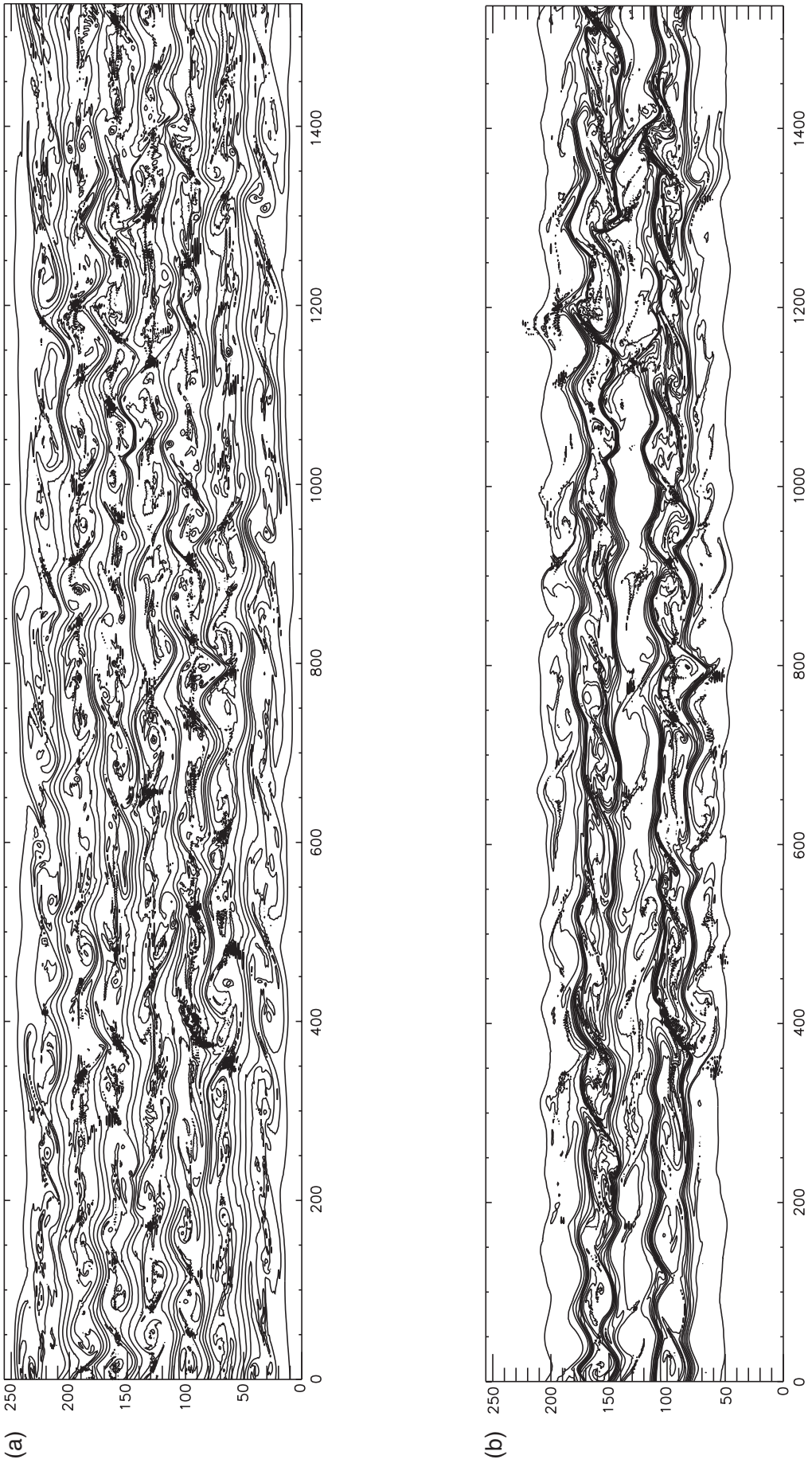
(a)
250
200
150
100
50
0
0
200
400
600
800
1000
1200
1400
(b)
250
200
150
100
50
0
0
200
400
600
800
1000
1200
1400

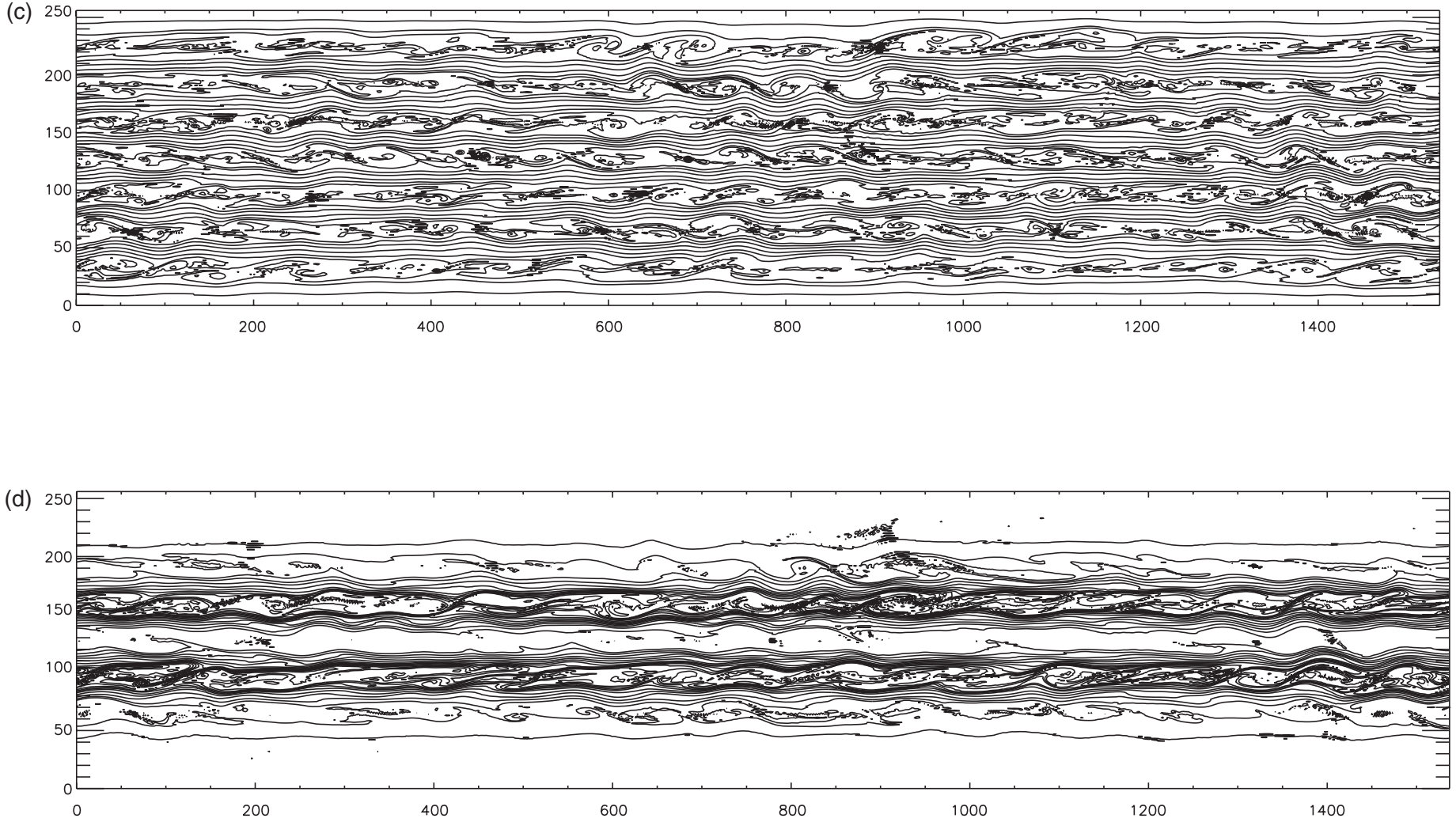

Figure 3. From the top to the bottom: Isovorticity (a) outlines above isotracer (b) outlines for the simulation 2 ($Ri = 200$) at the time $t = 21.4$. Then, isovorticity (c) outlines above isotracer (d) outlines for the simulation 6 ($Ri = 500$) at the time $t = 21.4$.

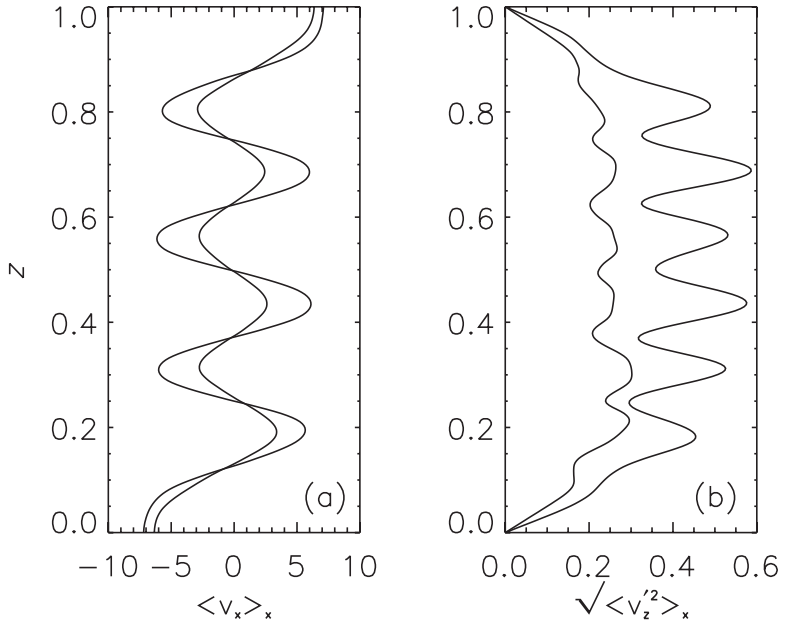

Figure 4. Vertical profiles of the mean horizontal velocity $\langle V_x \rangle_x$ (a) and of the vertical velocity fluctuations $\sqrt{\langle v_z^2 \rangle_x}$ (b) for two values of the initial stratification. Simulation 2 ($Ri = 200$) is represented by a continuous line, simulation 8 ($Ri = 1000$) by a dotted-dashed line.

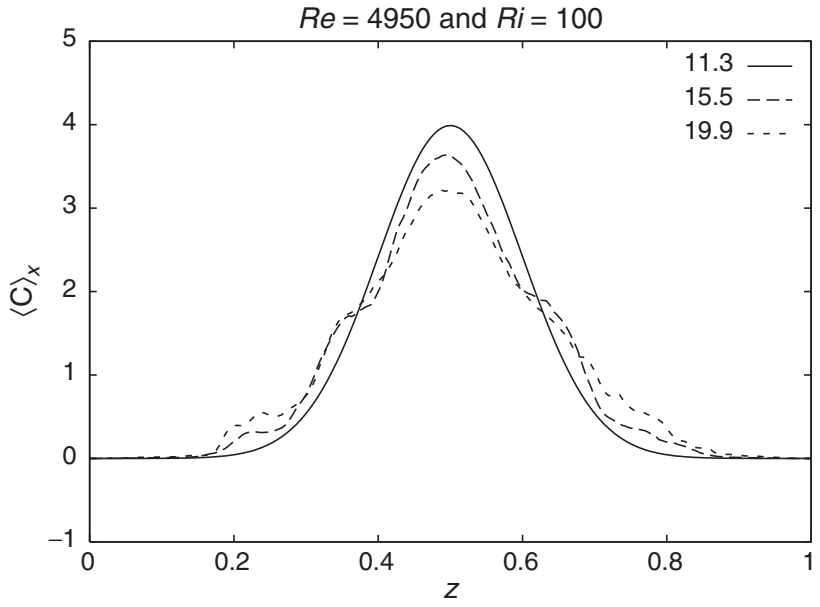

Figure 5. Vertical profiles of the mean contaminants concentration $\langle C \rangle_x$ at three different times for the simulation 1 ($Ri = 100$). At the last time ($t = 19.9$), the contaminant reaches the vertical limits of the domain and the run is stopped.

For higher stratifications, the run duration can be longer as the mixing layer grows slower. Note that the mean concentration profiles are used to define the mixing layer extent as the layer which contains 99% of the contaminant mass. Figure 3(b) and (d) show isotracer outlines for the simulation 2 ($Ri = 200$) and the simulation 6 ($Ri = 500$). Comparing with isovorticity outlines, advection of contaminant by vortices in shearing zones is obvious. The vertical extent of the mixed zone is reduced for the largest Richardson number.

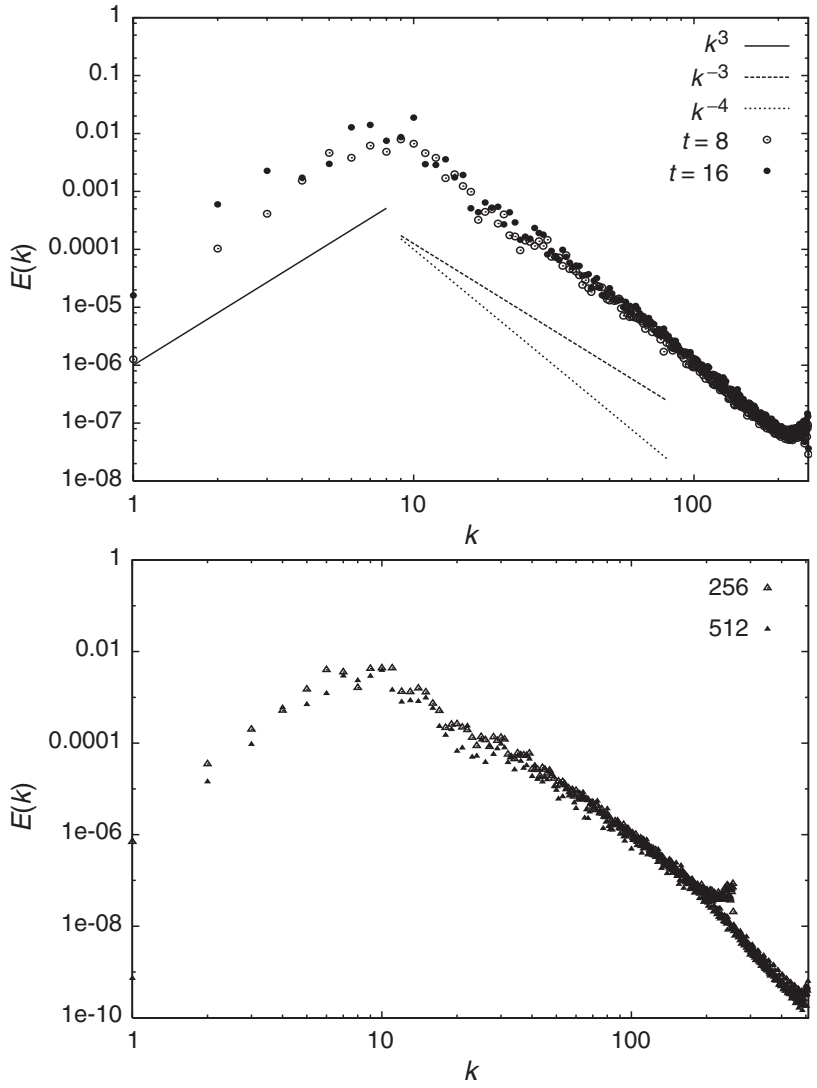

Figure 6. At the top, kinetic energy spectra at 2 times, $t = 8$ and $t = 16$, for the simulation 8 ($Ri = 1000$). At the bottom, kinetic energy spectra at $t = 8$ for two vertical resolutions, 256 and 512, for the simulation 8 ($Ri = 1000$).

At the top of figure 6, we plotted kinetic energy power spectra at two different times for the $Ri = 1000$ simulation and at the bottom, kinetic energy power spectra at the earliest time for two resolutions. When the vertical resolution equal to 256 is doubled, spectra agree very well in the inertial range which shows that our simulations are enough resolved. From $k = 10$ and over one decade of the inertial range, kinetic energy power spectra are well fitted by a straight line with a rate equal to -4 in agreement with previous simulations of unstratified 2D mixing layer (Lesieur 1987). For $k \leq 10$, the exponent is close to 3. Because of the small Prandtl number value, $Pr = 1.9 \times 10^{-4}$, temperature spectra are expected to be of inertial–diffusive type. The -8 exponent that we find (see figure 7) can be interpreted as a direct consequence of the simplified thermal balance, $v_z \, \mathrm{d}T_0/\mathrm{d}z = \nabla^2\theta/Pe$, which corresponds to an asymptotic form of the Boussinesq equation in the limit of small Péclet numbers (Ligniéres 1999). In figure 8 contaminant spectra are plotted for $Ri = 100$ and $Ri = 1000$ runs. From $k = 10$ and over half a decade, the spectrum exponent is closed to -2 for the lowest Richardson number and to -1 for the largest one.

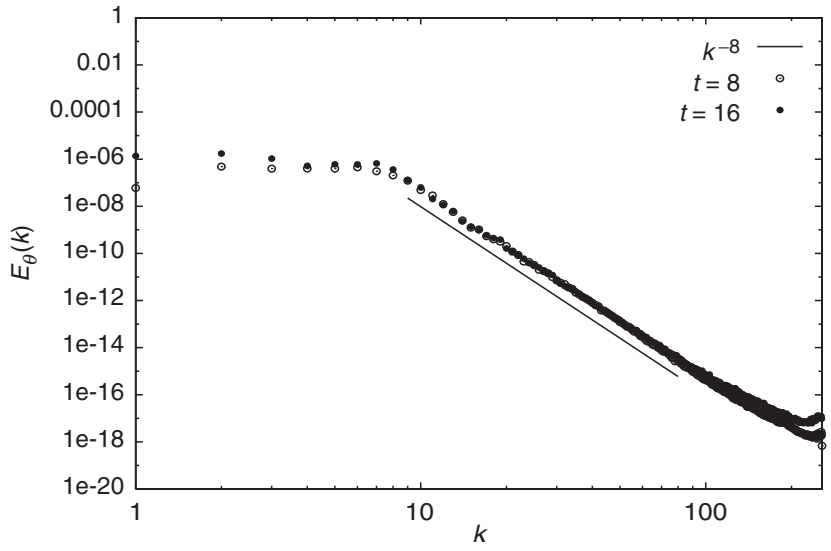

Figure 7. Temperature spectra at 2 times, $t = 8$ and $t = 16$, for the simulation 8 ($Ri = 1000$).

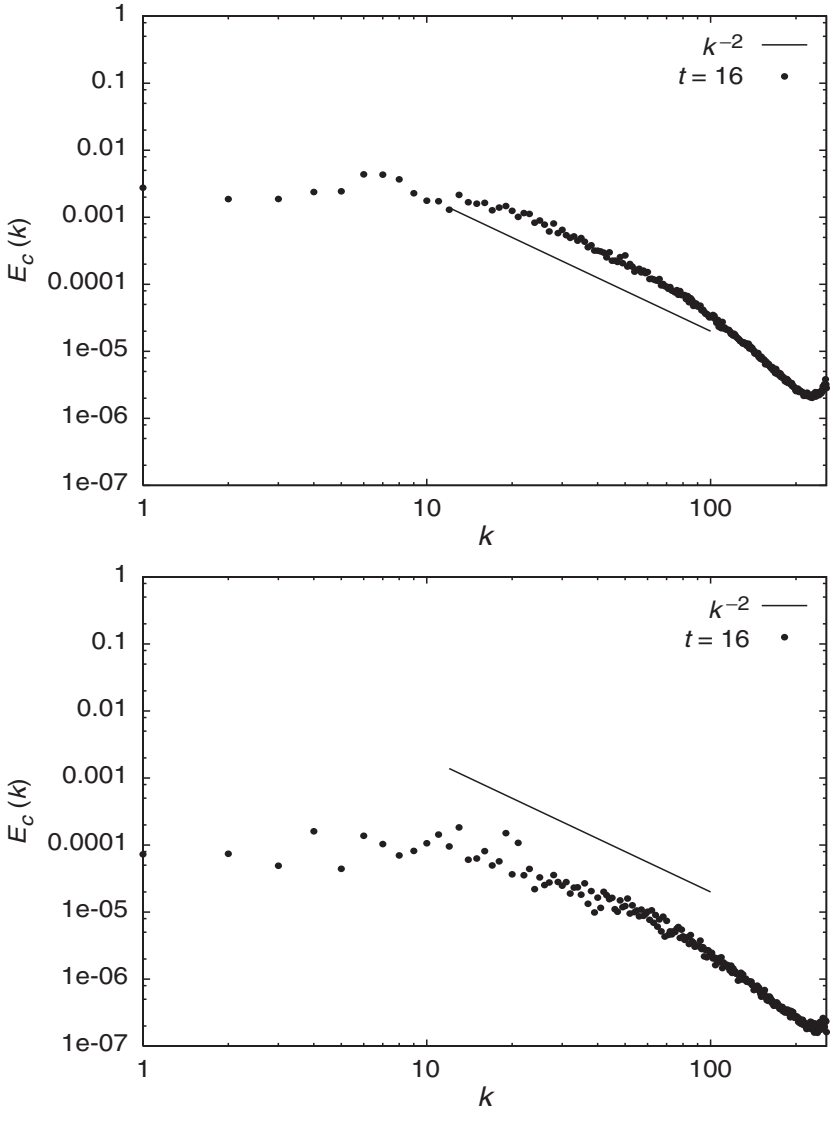

Figure 8. Contaminant spectra at the time $t = 16$ for the simulation 1 ($Ri = 100$) at the top and the simulation 8 ($Ri = 1000$) at the bottom.

4. Results

4.1. *Turbulent transport and particles dispersion*

We first analyze the vertical flux of contaminant $F(t,z) = -\langle v_z C \rangle_x$ and investigate its relation with the concentration gradient $\mathrm{d}\langle C \rangle_x/\mathrm{d}z$. At any vertical level within the mixing layer and at any time after a statistically stationary state has been reached, we can associate a flux value to a corresponding concentration gradient. The large dispersion of the flux values for a given concentration gradient is reduced by averaging the flux values on concentration gradients intervals. The resulting relation between flux and gradient is plotted in figure 9 for all the simulations. The number of concentration gradient values per interval is fixed at 1500. We observe that the shape of the curves is similar for all initial Richardson numbers. The flux decreases with stratification

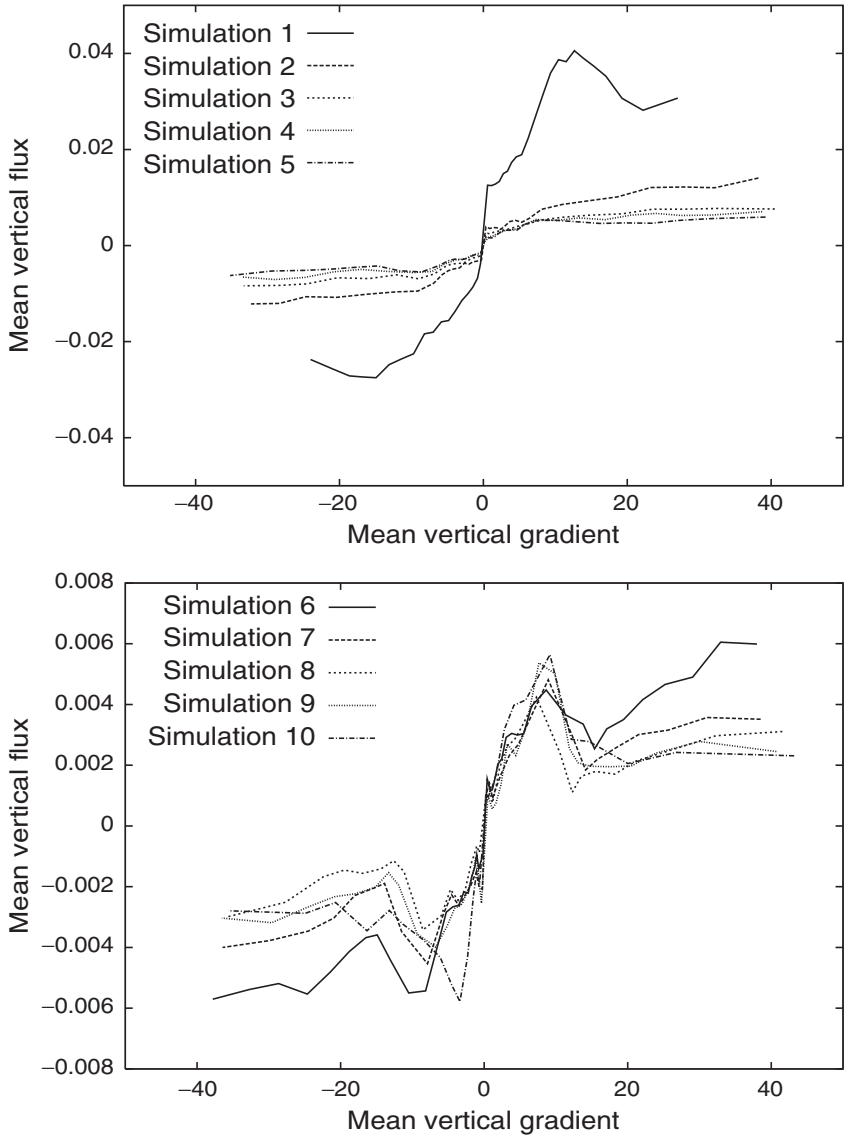

Figure 9. Mean vertical flux of the contaminant as a function of the mean vertical gradient of the contaminant for the first five simulations of the table 1 at the top and for the last five at the bottom. The mean flux is defined as an average over 1500 values of $F = -\langle v_z C \rangle_x$ associated to 1500 consecutive values of $\mathrm{d}\langle C \rangle_x/\mathrm{d}z$. The mean vertical gradient of the contaminant corresponds to the average of these 1500 consecutive values of $\mathrm{d}\langle C \rangle_x/\mathrm{d}z$. Above $Ri = 1000$, the mean flux no longer decreases with stratification.

and keeps similar values from $Ri = 1000$. We also notice that the curve is not linear as it should be for a Fourier/Fick law between flux and gradient.

A simple way of determining the eddy diffusivity is to calculate the mean of the ratio $\langle v_z C \rangle_x / (\mathrm{d}\langle C \rangle_x / \mathrm{d}z)$ over time and vertical levels. However, this definition requires to exclude vanishing values of $\mathrm{d}\langle C \rangle_x / \mathrm{d}z$ from the mean. Although this is possible in general, we found that the result depends on the extent of the interval of excluded values. This property can be attributed to the near discontinuity at the origin clearly visible in figure 9. Instead, we define the eddy diffusivity D_t as the ratio between a mean flux and a mean concentration gradient:

$$D_t = \frac{\langle |F| \rangle_{zt}}{\langle |\mathrm{d}\langle C \rangle_x / \mathrm{d}t| \rangle_{zt}} \tag{4}$$

where the symbol $\langle || \rangle_{zt}$ denotes an average of absolute values over a vertical and a temporal domain. As before, the vertical domain is the mixing layer extent and the temporal domain corresponds to approximatively 100 eddy turnover times after a statistically stationary state has been reached.

The variation of the vertical transport with stratification is illustrated in figure 10 where the ratio, $D_t / l_z u_z$, is plotted against the anisotropy A on logarithmic scale. The mixing length estimate of the eddy diffusion, $l_z u_z$, uses the rms vertical velocity u_z, defined as $u_z = \langle \langle v_z'^2 \rangle_x^{1/2} \rangle_{zt}$, and the mean vertical integral scale l_z which is also a spatio-temporal average of the vertical integral scales, $\mathcal{L}_z(z,t) = \int_0^{1-z} \langle v_z'(z) v_z'(z+z') \rangle_x \mathrm{d}z' / \langle v_z'^2 \rangle_x$, calculated at each time and at each level z within the upper half of the mixing layer. Note that, l_z, is close to the shearlayer half-width $l_s = 1/2 \times L/7$, up to the $Ri = 700$ simulation. Above $Ri = 700$, l_z decreases to approximatively half this value. First of all, figure 10 shows that the mixing length eddy diffusivity, $l_z u_z$, always severely overestimates the actual vertical transport. Second, it shows that the ratio $D_t / l_z u_z$ decreases when stratification increases up to the $Ri = 500$ run. For stronger stratification, we have seen that the turbulent flux of

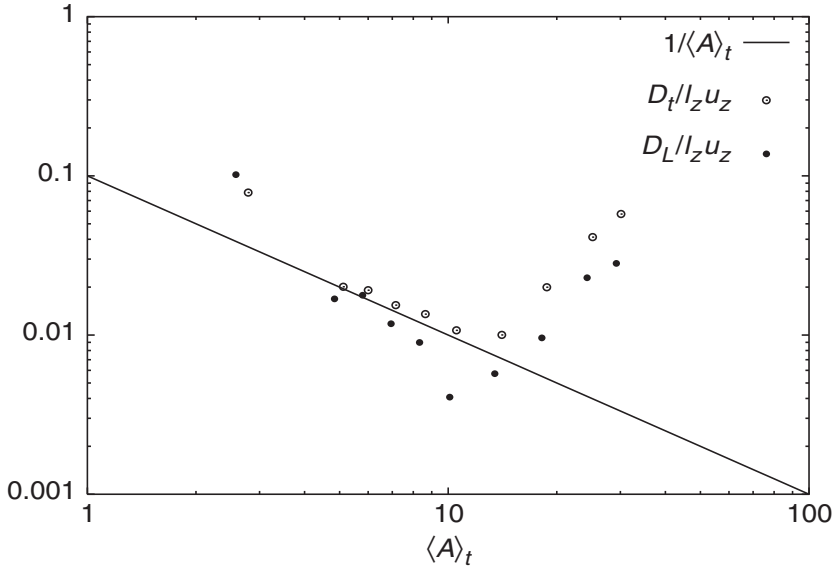

Figure 10. Turbulent and Lagrangian diffusion coefficients as a function of the mean anisotropy. A straight line corresponding to a $1/\langle A \rangle_t$ law is also displayed.

contaminant keeps similar values (see figure 9). However, $D_t/l_z u_z$ increases above $Ri = 700$ because u_z decreases.

We now consider the vertical dispersion of Lagrangian particles in order to investigate how the stratification acts to reduce the transport. Particles initially located at the grid points have been tracked during a large number (~ 100) of eddy turnover times. To avoid boundary effects, we only analyzed the displacement of the 280869 particles initially covering five of the seven sheared layers. Figure 11 displays the rms vertical displacement $\langle (z - z_0)^2 \rangle_p^{1/2}$ of these particles *versus* time for all the simulations. The symbol $\langle\ \rangle_p$ denotes an average over all the Lagrangian particles. A straight line with rate equal to 1/2 is displayed in figure 11 and it clearly shows that the dispersion rate is slower than classical diffusion. Another striking property is that from $Ri = 500$ the mean vertical displacement nearly levels off.

The Lagrangian dispersion coefficient taken from the classical diffusion theory, $D_L(t) = 1/2 \times \mathrm{d}\langle (z - z_0)^2 \rangle / \mathrm{d}t$ (Batchelor 1949), is used to determine the ratio $D_L/l_z u_z$. The ratio is displayed in figure 10 as a function of anisotropy. Note that the

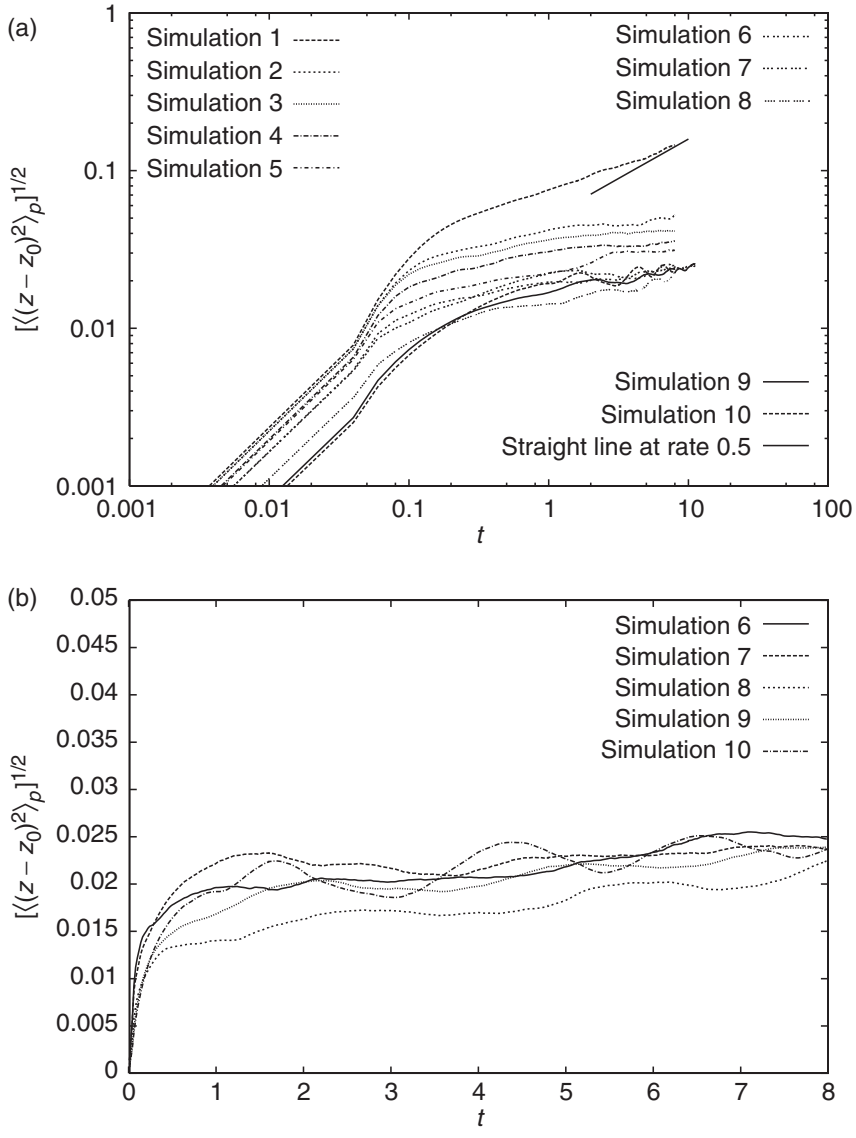

Figure 11. Rms vertical displacement of Lagrangian particles as a function of time for all simulations at the top and for the five highest stratified flows at the bottom.

definitions of the rms vertical velocity and integral scale are different here since the vertical average is taken over the five sheared layer initially containing the particles and not over the mixing layer. But the resulting values of the rms vertical velocity and integral scale are very similar to the ones calculated before. Figure 10 shows that the variations of D_L tend to confirm the behavior observed for the eddy diffusivity D_t.

4.2. *The role of anisotropy*

In this subsection, we shall interpret the two main results obtained previously, namely (i) the reduction of the vertical transport is much stronger than predicted by the mixing length coefficient and (ii) the dispersion rate is sub-diffusive and nearly vanishes for the strongest stratification.

We first noticed that vertical dispersion is very sensitive to the starting level of the particles. Indeed, whereas the dispersion of particles located in the strongly sheared part of the sheared layer is not much affected by stratification, the dispersion of particles initially situated in the weakly sheared interface layer between two sheared layers undergoes a very strong reduction with stratification. It follows that the global decrease of the vertical transport with stratification is mainly controlled by the behavior of the particles starting in the weakly sheared layer. Moreover, as we have seen that the vertical velocity fluctuations do not present important variations across the layers [see figure 4b], the reduced dispersion in the weakly sheared layer is not due to a local decrease of the vertical velocity. It should therefore be an effect of the Lagrangian correlation timescale. The Lagrangian autocorrelation function of the vertical velocity is related to the mean-square vertical displacement by Monin and Yaglom (1987):

$$\left\langle (z - z_0)^2 \right\rangle_l (t, z_0) = \int_{t_0}^{t} \int_{t_0}^{t} \left\langle V_z(t_1, z_0) V_z(t_2, z_0) \right\rangle_l \mathrm{d}t_1 \, \mathrm{d}t_2, \tag{5}$$

where $\langle\ \rangle_l$ denotes an average over the 1536 particles of that particular level z_0 and $V_z(t_1, z_0)$ is the Lagrangian vertical velocity at time t_1 of a particle that started at level z_0 and time t_0. We can thus define a Lagrangian correlation time as

$$\tau_L(t, z_0) = \left(\frac{\left\langle (z - z_0)^2 \right\rangle_l}{\langle V_z^2 \rangle_l} \right)^{1/2} = \frac{1}{\langle V_z^2 \rangle_l} \int_{t_0}^{t} \int_{t_0}^{t} \left\langle V_z(t_1) V_z(t_2) \right\rangle_l \mathrm{d}t_1 \, \mathrm{d}t_2. \tag{6}$$

Note that we do not use the classical Lagrangian integral scale $\tau_L^c = \int_0^\infty \langle V_z(t_1) V_z(t_1 + t') \rangle \mathrm{d}t'$ because it is only useful under the assumption that the Lagrangian autocorrelation function is stationary and we show later that this assumption is not verified here. Figure 12 shows, at a given time, the vertical profile of the Lagrangian correlation time $\tau_L(t, z_0)$ respectively for weakly ($Ri = 200$) and strongly ($Ri = 1000$) stratified cases. We observe that for particles starting within the sheared layer the Lagrangian correlation time has similar values for the two stratifications considered. There is, however, a striking difference for particles starting in the weakly sheared layers as the Lagrangian correlation time nearly vanishes for the strongest stratification. In this case, the vertical dispersion is so small that particles tend to stay in the weakly sheared layers. As stratification increases a larger proportion of particles does not disperse out of the weakly sheared layer. This effect explains the

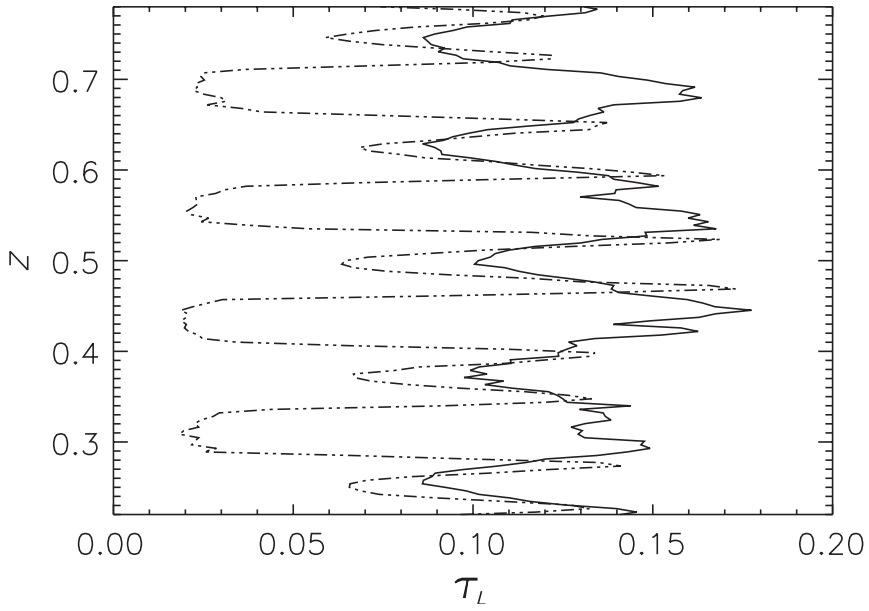

Figure 12. Lagrangian correlation time as a function of the starting level for two values of the initial stratification. Simulation 2 ($Ri = 200$) is represented by a continuous line, simulation 8 ($Ri = 1000$) by a dotted-dashed line. The Lagrangian correlation time is displayed at a given time.

decrease of $D_t/l_z u_z$ between $Ri = 100$ and $Ri = 500$. Above $Ri = 500$, most particles starting in the weakly sheared layers stay there and the dispersion is limited to the strongly sheared layer thickness which has little variations between $Ri = 500$ and $Ri = 2000$. This explains why the vertical dispersion shown in figure 11 keeps similar values above $Ri = 500$.

As noted before the anisotropy of the flow steadily increases with stratification in the weakly sheared layers and, as we show now, the reduction of the Lagrangian timescale in these layers can be attributed to the increase in flow anisotropy. As shown in figure 3(c), vortices in the stably stratified cases remain concentrated in the strongly sheared layers, close to the null mean horizontal velocity of the sheared layer centerline. The spatial structures of the vertical velocity field induced by these vortices are therefore nearly static. The consequence is that particles present in the weakly sheared layers are swept across the static spatially correlated structure of the vertical velocity field by the strong local horizontal motions. If L_x denotes the horizontal correlation length of the vertical velocity, the travel time through a structure of correlated vertical velocity is L_x/U_m where U_m is the local mean horizontal flow. This provides a crude estimate of the Lagrangian timescale for particles remaining in the weakly sheared layer. The corresponding eddy diffusivity coefficient $(L_x/U_m)w^2 = L_x w/A$ depends on the flow anisotropy. Note that this phenomenon has been considered by various authors (Horntrop and Majda 1994) in very simple flow configurations. This estimate concerns only particles remaining in the weakly sheared layer, but the number of particles concerned increases with A. Furthermore, we have seen that the stratification primarily affects the dispersion of the particles starting in the weakly sheared layer. Then, as $L_x/l_z \approx cste$ until $Ri = 500$, this estimate predicts that the ratio $D_t/l_z u_z$ is proportional to $1/A$. In figure 10, a straight line corresponding to a $1/A$ law has been drawn. It appears to approximatively describe the decrease of $D_t/l_z u_z$ in the range from $Ri = 200$ up to $Ri = 500$.

This relation between anisotropy and turbulent transport can be translated into a relation between stratification and turbulent transport. The anisotropy can be related to the shear as $A \sim U_x^{\max}/u_z = (\Delta U_x)^{\max}/u_z$ where $U_x^{\max}$ is the maximum mean horizontal velocity in the sheared layer and $(\Delta U_x)^{\max}$ is the maximum velocity difference with respect to the null velocity of sheared layer centerline. Moreover, the shear increases with stratification and we noticed that the dimensionless number $RiPe = N^2 l_s^3/\kappa(\Delta U_x)^{\max}$ keeps an approximatively constant value of $(RiPe)_c = 0.09$ for the simulations below $Ri = 500$. Note that we chose $RiPe$ instead of Ri since $RiPe$ controls the linear stability of the Kelvin–Helmholtz type sheared layer when the Péclet number becomes smaller than unity (Ligniéres *et al.* 1999). As $D_t/l_z u_z$ is approximatively proportional to $1/A$ between $Ri = 200$ and $Ri = 500$, it follows that D_t should be proportional to $(l_z u_z^2/N^2) \times (\kappa(RiPe)_c/l_s^3)$ in this domain. Figure 13 which displays the ratio $(D_t N^2/l_z u_z^2) \times (l_s^3/\kappa(RiPe)_c)$ shows that such a relation is compatible with our data.

Following Taylor (1921), in the idealized case of stationary homogeneous turbulence, the mean-square vertical displacement $\langle (z - z_0)^2 \rangle$ grows linearly with time in the limit $t \gg \tau_L^c$ and if $\tau_L^c \neq 0$. Although the conditions $t \gg \tau_L^c$ and $\tau_L^c \neq 0$ are verified in the present flow, the homogeneity assumption is not fulfilled as shown by the strong vertical variation of the Lagrangian correlation time (see figure 12). As a consequence, the Lagrangian autocorrelation function $\langle V_z(t_1) V_z(t_1 + t') \rangle$ is not independent of t_1 and the vertical dispersion is not expected to be diffusive (Monin and Yaglom 1987).

The quasi-suppression of the vertical dispersion in the most stratified cases is directly related to the very strong reduction of the dispersion in the weakly sheared layers. These layers act as a barrier which limits the vertical displacements inside the strongly sheared layer. This interpretation is confirmed by a simple estimate of the resulting dispersion: If we assume that particles starting in the weakly sheared layers have no vertical displacement whereas particles starting in the strongly sheared layers have a mean displacement equal to the half-width of these layers, we find a vertical dispersion of 0.0175 which is a value close to the final vertical displacement of the most strongly

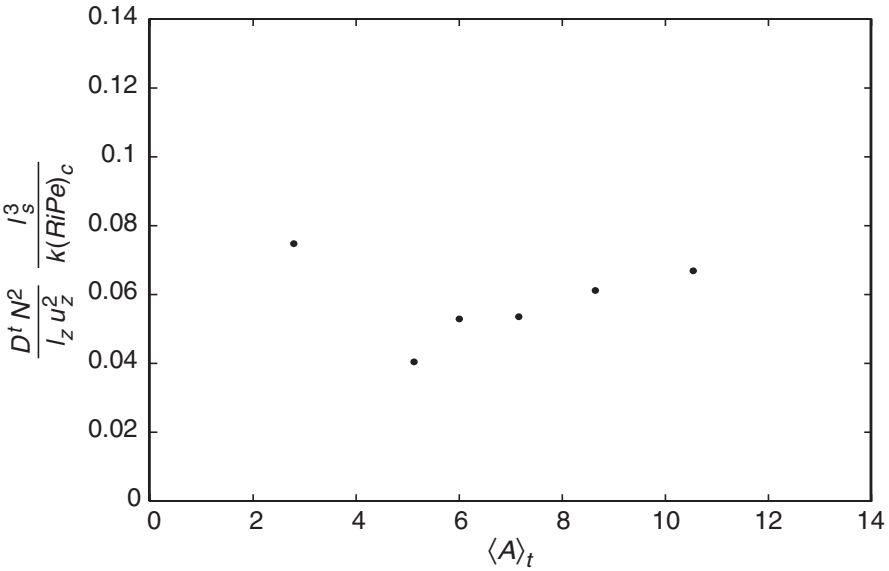

Figure 13. The ratio $(D_t N^2/l_z u_z^2) \times (l_s^3/\kappa(RiPe)_c)$ as a function of the mean anisotropy for the first five simulations (from $Ri = 100$ up to $Ri = 500$).

stratified cases shown in figure 11. (We also assumed, according to figure 12, that the width of the strongly and weakly sheared layers are equal.)

5. Discussion and conclusion

We introduced a forcing that creates and maintains several superimposed parallel sheared layers. As initial stratification increases, the shear which is necessary to maintain a stationary turbulence also increases together with the flow anisotropy. We observed that weakly sheared layers between strongly sheared layers become depleted of strong vortices for increased stratification. There, contaminants are advected by strong mean horizontal flows across nearly static flow structure and the associated Lagrangian correlation time decreases as the local mean horizontal flow increases. This phenomenon explains the reduction of vertical transport with stratification. For the strongest stratification, the Lagrangian correlation time nearly vanishes and the weakly sheared layers act as a barrier that particles can no longer cross.

At first sight, we may wonder whether this barrier effect is a direct consequence of the forcing. Indeed, the forcing tends to maintain superimposed sheared layers and the reduction of the vertical transport is explained by a strong inhomogeneous shear. However, the forcing, only by itself, cannot impose the layered structure of the flow vorticity shown in figure 3(c) and cannot generate the associated high anisotropy values. The simulation in the neutral case ($N = 0$) shows that indeed, despite the forcing, the vertical transport of horizontal momentum reduces the number of shear layers while the distribution of vorticity tends to be homogenized vertically, and the anisotropy remains very close to one. This is in fact the stratification which enables to maintain the seven sheared layers by inhibiting vertical transport of horizontal momentum.

We found that the relation between the anisotropy and the vertical transport of contaminants obtained by Vincent *et al.* (1996) $D_t/l_z u_z \propto 1/A$, is quantitatively compatible with our results in a limited range of anisotropy $5 < A < 10$.

It must be stressed that, contrary to Vincent *et al.* (1996), the anisotropy of the present flow is mainly due to the mean horizontal flow whereas the ratio between the rms fluctuating horizontal and vertical velocity remains close to one. Moreover, the physical interpretation of the anisotropy role is different. While Vincent *et al.* (1996) propose that stronger horizontal turbulence induces a more efficient contaminant mixing by molecular diffusion, we find here that the rapid horizontal sweeping of particles across correlated structures of the vertical velocity diminishes the vertical displacements and thus decreases the associated generation of fluctuations of contaminant concentration. The small contribution of molecular mixing processes in the transport reduction is highlighted by the small difference between the Lagrangian dispersion coefficient and the eddy diffusivity (see figure 10). Indeed, this difference is due to molecular mixing and, according to Vincent *et al.* (1996), it would be expected to grow significantly as anisotropy increases. Above $A = 10$, there is also a strong discrepancy with Vincent *et al.*'s (1996) results (see figure 10). But it is simply due to the fact that, in our flow, the anisotropy varies vertically. Indeed, while the weakly sheared layers where the anisotropy is large act as a barrier above $A = 10$, the vertical transport is dominated by transport in layers of small anisotropy. It can therefore no longer decrease because of anisotropy. This is not the case in Vincent *et al.* (1996) where the flow and the anisotropy are statistically homogeneous in the vertical direction.

However, it should be reminded that the restriction to two dimensions does not allow definite conclusions. The 2D Kelvin–Helmholtz billows are known to undergo a secondary transition leading to 3D turbulence. Experiments and numerical simulations of free sheared layers also show that coherent structures consisting of quasi-2D spanwise rollers are still present after the transition and coexist with fine scale motions (Balaras *et al*. 2001). We expect that the structure of weakly sheared layers relatively depleted of vorticity alternating with strong sheared layers persists in 3D. The mechanism of transport inhibition should then also play a role in 3D even if other mechanisms associated with the 3D flows could significantly modify the property of the vertical transport.

The quasi-suppression of vertical dispersion observed in our simulations provides another example of this phenomenon in stably stratified turbulence. However, the mechanism responsible for it is different from previous cases. The interpretation of Kaneda and Ishida (2000) involves gravity waves which play no dynamic role in our simulations because of the low Prandtl number. Also, the model of Pearson *et al*. (1983) predicts that the suppression of vertical dispersion is limited to the thermal diffusion time scale of the fluid elements. Again because of the low Prandtl number, this time is very small in our simulation and consequently Pearson *et al*.'s (1983) model cannot be applied to our results. Contrary to both models, the mechanism proposed here is directly related to the strong inhomogeneity of turbulence which involves layers with strong vortices superimposed on layers which are depleted of vorticity.

Strong vertical inhomogeneities in the velocity and density field known as horizontal 'layers' are a common feature of stably stratified turbulence in geophysical, experimental and numerical flows (Metais and Herring 1989, Park *et al*. 1994, Galmiche and Hunt 2002, Mack and Schoeberlein 2003). While the coherent forcing considered in the present work does not reproduce the random distribution of these horizontal layers, the mechanism of vertical transport inhibition that we outlined could also play a role in this type of flows.

References

Balachandar, S. and Maxey, M.R., Methods for evaluating fluid velocities in spectral simulations of turbulence. *Comput. Phys*., 1989, **83**, 96–125.

Balaras, E., Piomelli, U. and Wallace, J.M., Self-similar states in turbulent mixing layers. *J. Fluid Mech*., 2001, **446**, 1–24.

Batchelor, G.K., Diffusion in a field of homogeneous turbulence. *Australian J. Sci. Res*., 1949, **A2**, 437–450.

Britter, R.E., Hunt, J.C.R., Marsh, G.L. and Snyder, W.H., The effects of stable stratification on turbulent diffusion and the decay of grid turbulence. *J. Fluid Mech*., 1983, **127**, 27–44.

Chaboyer, B. and Zahn, J.-P., Effect of horizontal turbulent diffusion on transport by meridional circulation. *Astron. Astrophys*., 1992, **253**, 173–177.

Chandrasekhar, S., *Hydrodynamic and Hydromagnetic Stability*, 1961 (Dover Publications: USA).

Charbonneau, P. and Michaud, G., Meridional circulation and diffusion in A and early F stars. *Astrophys. J*., 1991, **370**, 693–708.

Comte, P., Lesieur, M., Laroche, H. and Normand, X., Numerical simulations of turbulent plane shear layers. *Turbulent Shear Flows*, 1989, **6**, 360.

Csanady, G., Turbulent diffusion in the environment. In: *Geophysics and Astrophysics Monographs*, edited by B.M. McCormac, 1973 (Dordrecht Reidel Publishing Company: Dordrecht, Holland).

Deane, A.E., Spectral and spectral-element methods. In *Lectures Notes in High Performance Computational Physics*, 1997 (NASA Goddard Space Flight Center: Greenbelt, MD, USA).

Galmiche, M. and Hunt, J.C.R., The formation of shear and density layers in stably stratified turbulent flows: linear processes. *J. Fluid Mech*., 2002, **455**, 243–262.

Gerz, T., Schumann, U. and Elghobashi, S.E., Direct numerical simulation of stratified homogeneous turbulent shear flows. *J. Fluid Mech.*, 1989, **200**, 563–594.
Herring, J.R. and Metais, O., Numerical experiments in forced stably stratified turbulence. *J. Fluid Mech.*, 1989, **202**, 97–116.
Ho, C. and Huerre, P., Perturbated free shear layers. *Annu. Rev. Fluid Mech.*, 1984, **16**, 365–424.
Holt, S.E., Koseff, J.R. and Ferziger, J.H., A numerical study of the evolution and structure of homogeneous stably stratified sheared turbulence. *J. Fluid Mech.*, 1992, **237**, 499–539.
Horntrop, D.J. and Majda, A.J., Subtle statistical behaviour in simple models for random advection-diffusion, *Math. Sci. Univ. Tokyo*, 1994, **1**, 23–70.
Kaneda, Y. and Ishida, T., Suppression of vertical diffusion in strongly stratified turbulence. *J. Fluid Mech.*, 2000, **402**, 311–327.
Kimura, Y. and Herring, J.R., Diffusion in stably stratified turbulence. *J. Fluid Mech.*, 1996, **328**, 253–269.
Lesieur, M., *Turbulence in Fluids, Mechanics of Fluids and Transport Processes*, 1987 (Kluwer Academic Publishers Group: Amsterdam).
Ligniéres, F., The small Péclet-number approximation in stellar radiative zone. *Astron. Astrophys.*, 1999, **348**, 933–939.
Ligniéres, F., Califano, F. and Mangeney, A., Shear layer instability in highly diffusive stably stratified atmosphere, *Astron. Astrophys.*, 1999, **349**, 1027–1036.
Mack, S.A. and Schoeberlein, H.C., Richardson number and ocean mixing: towed chain observations. *J. Phys. Oceanogr.*, 2003, **34**, 736–754.
Metais, O. and Herring, J.R., Numerical simulations of freely evolving turbulence in stably stratified fluids. *J. Fluid Mech.*, 1989, **202**, 117–148.
Michaud, G. and Zahn, J.-P., Turbulent transport in stellar interiors. *Theoret. and Comput. Fluid Dynamics*, 1998, **11**, 183–193.
Monin, A.S. and Yaglom, A.M., *Statistical Fluid Mechanics*, 1987 (The MIT Press: USA).
Park, Y.-G., Whitehead, J.A. and Gnanadeskian, A., Turbulent mixing in stratified fluids: layer formation and energetics. *J. Fluid Mech.*, 1994, **279**, 279–311.
Pearson, H.J., Puttock J.S. and Hunt, J.C.R., A statistical model of fluid-element motions and vertical diffusion in a homogeneous stratified turbulent flow. *J. Fluid Mech.*, 1983, **129**, 219–249.
Pinsonneault, M., Mixing in stars. *Annu. Rev. Astron. Astrophys.*, 1997, **35**, 557–605.
Rohr, J.J., Itsweire, E.C., Helland, K.N. and Van Atta, C.W., Growth and decay of turbulence in stably stratified shear flow. *J. Fluid Mech.*, 1988, **195**, 77–111.
Taylor, G.I., Diffusion by continuous movements. *Proceedings of the Mathematical Society of London*, 1921, **20**, 196–212.
Tennekes, H. and Lumley, J.L., A *First Course in Turbulence*, 1972 (The MIT Press: USA).
Turner, J.S., *Buoyancy Effects in Fluids*, 1973 (Cambridge University Press: Cambridge).
Vincent, A., Michaud, G. and Meneguzzi, M., On the turbulent transport of a passive scalar by anisotropic turbulence. *Phys. Fluid*, 1996, **8**, 1312–1320.

4.4.2 A12 : Families of fragmenting granules and their relation to meso and supergranular flow fields

"Families of fragmenting granules and their relation to meso and supergranular flow fields"

Roudier Th., Lignières F., Rieutord M.,
Brandt P.N., Malherbe J.M.

A&A 409, 299-308, 2003

A&A 409, 299–308 (2003)
DOI: 10.1051/0004-6361:20030988

Astronomy & Astrophysics

Families of fragmenting granules and their relation to meso– and supergranular flow fields

Th. Roudier[1], F. Lignières[2], M. Rieutord[2,3], P. N. Brandt[4], and J. M. Malherbe[5]

[1] Laboratoire d'Astrophysique, Observatoire Midi-Pyrénées, 57 avenue d'Azereix, BP 826, 65008 Tarbes, France
[2] Laboratoire d'Astrophysique, Observatoire Midi-Pyrénées, 14 avenue E. Belin, 31400 Toulouse, France
[3] Institut Universitaire de France, France
[4] Kiepenheuer–Institut für Sonnenphysik, Schöneckstrasse 6, 79104 Freiburg, Germany
[5] LESIA, Observatoire de Paris, Section de Meudon, 92195 Meudon, France

Received 17 February 2003 / Accepted 10 June 2003

Abstract. 3D analysis (x, y, t) of the granular intensity field (11–hour time sequence from the Swedish Vacuum Solar Telescope on La Palma, Canary Islands), demonstrates that a significant fraction of the granules in the photosphere are organized in the form of "Trees of Fragmenting Granules" (TFGs). A TFG consists of a family of repeatedly splitting granules, originating from a single granule at its beginning. A striking result is that TFGs can live much longer (up to 8 h) than individual granules (10 min). We find that 62% of the area covered by granules belongs to TFGs of a lifetime >1.5 h. When averaged in time, such long–lived TFGs correspond to coherent diverging flows which may be identified as mesogranules. We also find a correlation between the network and the spatial distribution of TFGs.

Key words. Sun: photosphere – Sun: granulation

1. Introduction

A knowledge of the physical nature of the different flow scales on the Sun is necessary to envisage a realistic model of the generation (production) and diffusion of the magnetic flux on the surface of the quiet Sun, in particular to build the network in the quiet regions, or to understand the action of the different flow scales in the destruction of sunspots. More precisely, the processes which create, and then fragment and disperse Ephemeral Regions populating the quiet network, is not well known today and remains quite speculative (Hagenaar et al. 2003). The generation of these bipolar regions by the local action of the turbulent convection (small–scale local dynamo) is also invoked to explain the low sensitivity of these small dipoles to the sunspot cycle (Hagenaar et al. 2003). The mechanisms produced by the turbulent convective motions at the different scales have to be elucidated to determine in more detail the role of the turbulent dynamo in forming these dipoles.

The links between the various scale motions on the Sun's surface are still poorly understood today. Recently the physical nature of the largest flow scales, i.e. the meso– and supergranulation, has been found to vary depending on the spatial and temporal windows used to compute the flow fields (see Rieutord et al. 2000).

Send offprint requests to: Th. Roudier,
e-mail: roudier@bagn.obs-mip.fr

On the one hand, low resolution measurements of the properties of solar photospheric flows support the existence of different convective scales. In particular, the work of Muller et al. (1992) and Shine et al. (2000) shows the persistence of the supergranulation, and the motion of the mesogranules toward the supergranular boundaries in accordance with the model of Simon et al. (1991). On the other hand, Rieutord et al. (2000) found that computing the flow fields with high spatial (0.7″) and temporal resolution (5 min) reveals the important role of the strong positive divergences (SPDs) in forming the larger scales (meso– and supergranulation).

To link the measurements at low and high spatial resolution, one needs a time sequence of the solar granulation observed over several hours with a field of view at least $1' \times 1'$, to get reliable results up to the largest scale, i.e. the supergranulation. Here we make use of an exceptional 11 h time sequence obtained at the SVST at La Palma.

Using this time sequence we try to understand the different results from low and high resolution analyses, as well as to determine the links between the three scales: granulation, mesogranulation, and supergranulation. Granule evolution was investigated by many authors (e.g. Spruit et al. 1990) in order to characterize the dynamics of the Sun's surface.

One of these approaches has been developed by Kawaguchi (1980) using a 46–min time sequence; he showed the existence of long–lived structures called "families of active granules". From his 2D numerical model Ploner (1994) concluded that

fragmenting granules can split repeatedly for several generations and discussed the link between these long–lived structures and the mesogranulation. Using time-slice of the Sun surface, Müller et al. (2001), found that fragmenting granules can survive by means of their descendants for more than 3 h. Their works suggest that mesogranular flow fields may be generated by actives granules.

In this paper we first present and discuss a new 3D automatic time labeling method of the solar granules. The application of this method to the 11 h time sequence obtained at the SVST confirms the existence of families of active granules and allows a detailed analysis of their statistical properties. We discuss the link between these long–lived families and the mesogranules. Finally, we show some properties of these long–lived structures with relation to the network.

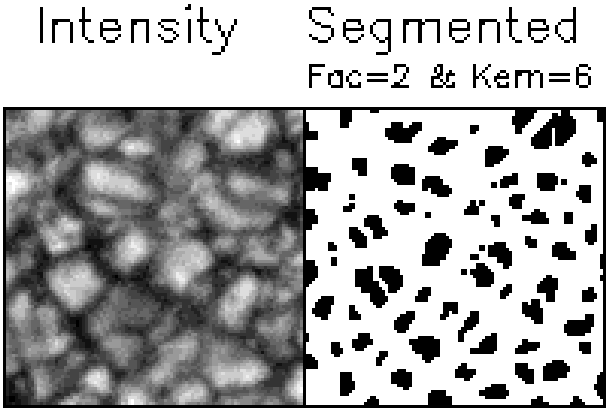

Fig. 1. Example of intensity and binary map using a Gaussian window of kern = 6 pixels size (0.75″) and fac = 2 pixels size (0.25″) for the structuring element of the "Opening" operator.

2. Data

Our analysis is based on a series of 1500 CCD images of size 512×512 pixels ($64'' \times 64''$) of the solar granulation obtained under excellent seeing conditions with the 50 cm Swedish Vacuum Solar Telescope on La Palma (Canary Islands) on June 5, 1993.

A quiet Sun section of that series is extracted from a longer set of observations obtained from 08:07 UT to 19:07 UT close to a pore in spot group NOAA 7519 at position N05, E15. The duration of the analyzed sequence is 8.75 h with a mean time step of 21 s. The images were corrected for dark current and gain, rigidly aligned, and destretched. They have been filtered to remove five-minute oscillations. Most details of the image reduction procedure are given in Simon et al. (1994).

3. Analysis method

In this section we present the method used to detect families of splitting granules.

The transformation of the intensity map into a binary map has been performed following the criterion defined by Strous (1994), i.e. the local curvature of the intensity field $a = I_1 - 2I_2 + I_3$ (I_1, I_2, I_3 being the intensity of three adjacent pixels) computed in four directions. When the second spatial derivatives have the same sign in the four directions, for example negative, the pixel belongs to a bright object (granule), in the opposite case it belongs to a dark intergranule. Before this segmentation, we convolve each frame with a Gaussian window, the size of which is adjusted such as to avoid over– or under–segmentation. In order to avoid false identifications of granules and keep the granule core whatever their size, we used a Gaussian window of 6 pixels size (0.75″).

The segmented granules shown in Fig. 1 have relatively large distances from each other. The granule radial expansion velocity being of order of 2 $\mathrm{km\,s^{-1}}$ and their velocity smaller than 1.0 $\mathrm{km\,s^{-1}}$, such a segmentation prevents spurious granule mixing as granules move less than one pixel between consecutive frames at a lag of 21 s.

Once the segmentation is performed, objects are labeled in each frame. Then, we follow the evolution of the granules by identifying the temporal links in the 3D data box (2D in space and 1D in time). This step is complicated because granules change shape during their lifetime and it is well known that it is quite difficult to define the life history of a typical granule (Spruit et al. 1990). Hence, splitting into multiple objects, merging of objects, and disappearances or appearances between two successive images have all to be taken into account. As our segmentation keeps the core of all the granules, we avoid erroneous detections of temporal links between adjacent granules due to the different sources of noise or the segmentation technique. Two criteria were used to perform the temporal labeling of the granules:

1. From a frame at time t to the next at time $t+1$, we detect for each granule identified at the time t if there exists a granule at the time $t+1$ at the same location with a minimal common area. As our segmentation was very restrictive, we chose the minimal common area to be one pixel;
2. When two or more granules merge, we kept only the label of the larger one in the area.

When these criteria are met, objects are labeled from one frame to the next with the same number, otherwise the number is changed to a new one. We constructed in this way 97 053 objects contained within the 3D (x, y, t) box. Of these 54 135 had a lifetime greater than one frame. And of those 54 135 objects, 5549 had at least one splitting and formed the set of what we shall call "Trees of Fragmenting Granules" (TFGs). The remaining 48586 objects are called individual granules. TFGs are families of repeatedly splitting granules, originating from a single granule at its beginning. Exploding granules represent the most vigorous case of fragmenting granules. Figure 2 shows a 3D view and a time slice of the longest lived TFG. Horizontal arrows indicate the splittings visible in the time slice. This shows that, with 2D time slices, the temporal continuity is only visible during a fraction of the TFG lifetime. Because granules split in any directions, the temporal connection of the repeatedly splitting granules is completely described only in the 3D view.

The method to detect the TFGs depends on the segmentation and on the criterion chosen to control granule merging. The sensitivity of the method to changes of the segmentation

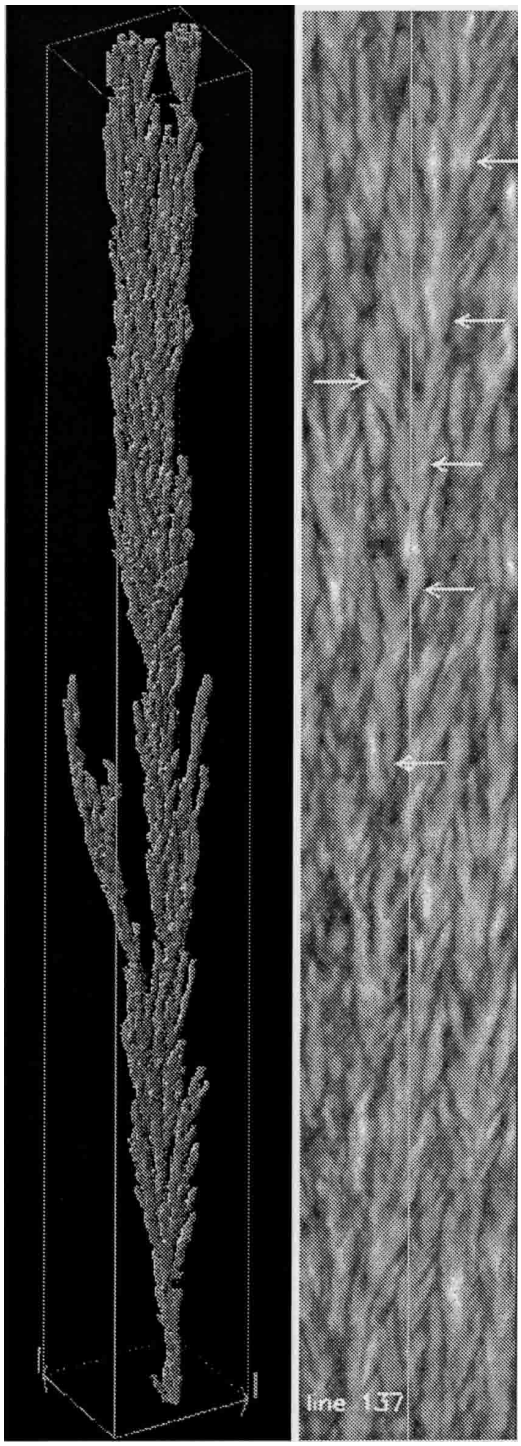

Fig. 2. Left: 3D (x, y, t) representation of the longest-lived TFG (8 h 10 min) of our time sequence which influenced a total area of $15'' \times 17''$ during its life. Right: 2D time slice of one part of the TFG where the repeatedly connected splitting granules, indicated by horizontal arrows, are clearly visible.

parameters, i.e. the Gaussian window or the size of the structuring element, has been tested. We found the method to be quite robust with respect to the temporal labeling of granules in the range of window sizes of 5−8 pixels and of structuring elements of 2−3 pixels. Outside this range the granules are over– or under–segmented leading to a non–conform labeling when compared with direct labeling by eye from the intensity field.

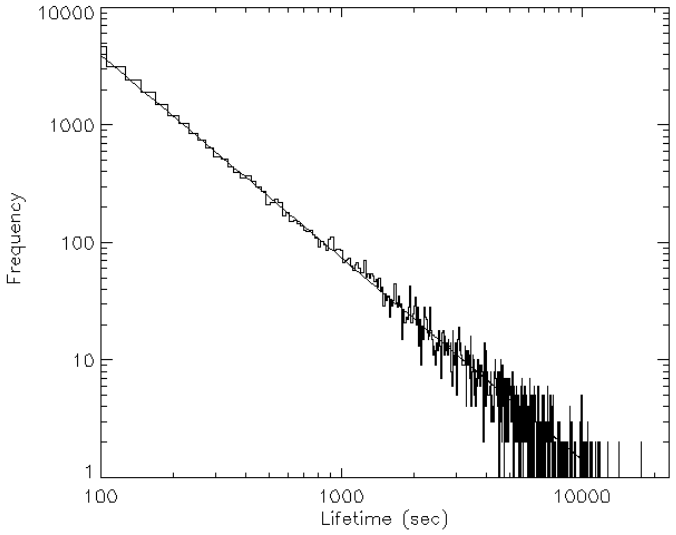

Fig. 3. Lifetime histogram of individual granules and TFGs. It is well fitted by a power law with an exponent equal to −1.72.

The increase of the minimal common area does not modify the results described here because only small granules are affected and these correspond in general to the end of the life of the granules. Finally, the segmentation parameters were also successful in reproducing the statistical properties of the granule lifetimes published by Title et al. (1989) (see Fig. 4 described in the next section).

We tested also the sensitivity of the TFG detection to the granule merging criterion by considering another criterion. We kept the number of the *older* of the two granules which merge at time $t - 1$ as the label of the granule at time t. We verified that this change did not affect the statistical results (like the lifetime histograms, e.g. Fig. 3) found previously when keeping the label of the *larger* granule. This can be explained in the following way.

The number of merging granules relatively to the total number of granules is very low, i.e. 6.6×10^{-3}; this is due to our very strict segmentation method which reduces very strongly the merging. Moreover, the number of families that undergo a change of the family number is very low, i.e. 9×10^{-5} yielding around 30 families, with respect to the total number of families (or granules labeled in time). When looking into more detail, most of the merging cases (97%) were found not to affect the family number because the larger granules correspond to the older ones, or the merging granules belong to the same family at time $t - 1$. Half of the remaining 3% of merging granules are found to be produced by granules whose lifetimes, at time t, are smaller than 5 min.

Hence, the time labeling of the longest–lived families is only affected at their beginning which modifies their origins but not very much their lifetimes.

Regarding the remaining 1.5%, the merging affects the temporal labeling of individual granules and TFGs but their number is very small compared to the total number of families detected in the data cube. We note for these families some trends to collect smaller granules because of the choice of the criterion "number of older granule when merging" is not a local

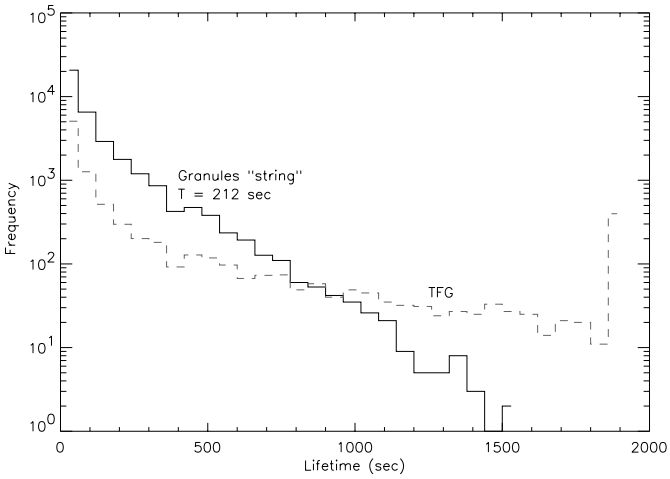

Fig. 4. Lifetime histograms (solid line) of granules for a set of 30 min of our time sequence (i.e. the same duration as the SOUP sequence) measured by the "string" method (like Title et al. 1989) and by our method (dashed line).

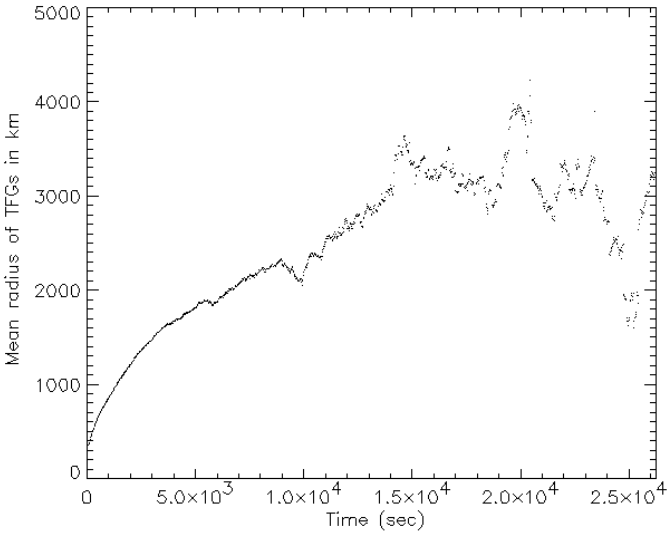

Fig. 5. Average radius of the TFGs as a function of time.

criterion. This is why, in our opinion, "the number of the larger when merging" for time labeling is more suitable because it is a local criterion. It avoids the artificial growth of families developing in this way. However, our analysis shows the very small effects of this choice on the statistical analysis.

4. Families of long–lived, repeatedly fragmenting granules: The TFGs

In this section, we present the statistical properties of the 5549 TFGs found in our sample. We characterize their lifetimes, their expansion radius and velocity, the area covered by TFGs as well as the number of splittings undergone during their lifetime.

As mentioned previously, TFGs are related to the families described by Kawaguchi (1980) in his 46–min time sequence. By comparison, the most striking result of our analysis is the existence of long–lived families, with the longest one lasting 8 h 10 min (shown in Fig. 2). This clearly appears in Fig. 3 which shows the histogram of the lifetimes of individual granules and TFGs. Individual granules have been added to complete the statistics at small lifetimes.

This lifetime histogram is well fitted by a power law $N \propto t^{\gamma}$, with $\gamma = -1.72$. Such a self-similar behavior indicates that we cannot define a characteristic lifetime of the TFGs. By contrast, previous works on the lifetime of solar granulation defined a characteristic life time as the decay rate of an exponential law which fitted well the histogram of individual granule lifetime. The difference between these results and the power law found here is clearly due to the definition of the time labeling. In our case, we detect structures which can merge or split while conserving their temporal continuity. In contrast to this, in the SOUP lifetime measurements for instance, the granules were only considered between their birth and a splitting or a merging event; this was called the "string" method.

Figure 4 exhibits the comparison, for a set of 30 min of our time sequence (i.e. the same duration as the SOUP sequence), between the histogram of granule lifetimes measured by the string method (we find an exponential law with $T = 212$ s in accordance with the SOUP results presented in Title et al. 1989) and the histogram of the granules and TFGs measured by our method.

We now consider the spatial expansion of TFGs which results from the collective effects of granule splittings. The radius of TFGs, defined as the distance of the most distant granule from the centre of gravity of the TFG at that time, has been computed at each time step during the lifetime of all 5549 TFGs. A mean radius, averaged over all TFGs, is then calculated and Fig. 5 exhibits its time evolution. The figure shows that the mean radius increases up to 3000 km (4.1″) in 15 000 s (4.16 h); after this the mean radius stays more or less constant up to 23 500 s (6.5 h). The maximum mean radius of 3200 km corresponds to the typical radius of a mesogranule.

The expansion velocity derived from the mean radius evolution shows a maximum of 0.85 km s^{-1} after 200 s, cf. Fig. 6. This initial step is mainly due to the proper granule expansion. Then the velocity decreases continuously during one hour until it becomes statistically stationary around 0.15 km s^{-1}. Beyond 10 000 s, the expansion velocity shows very large fluctuations (not shown here) associated to the mean radius fluctuations shown in Fig. 5. They are due to the relatively small number of TFGs in this range of lifetime.

The quasi monotonous expansion of TFGs is reflected in the area they cover at the end of their lifetime. Figure 7 shows that the final area covered by TFGs increases as a function of their lifetimes, the plot being well fitted by a power law Area $\propto t^{\alpha}$, with $\alpha = 5/4$. The figure also shows that most of the TFGs cover an area smaller than a disk of radius 4″ which is the mean radius of a mesogranule.

Related to the expansion and the lifetime of TFGs is the total number of splittings that occur in each TFG. As shown in Fig. 9, this number increases with the lifetime of TFGs the relation being fitted by a power law $N \propto t^{\beta}$, with $\beta = 1.8$.

Although the number of TFGs decreases with lifetime, long-lived TFGs still cover a very significant proportion of the

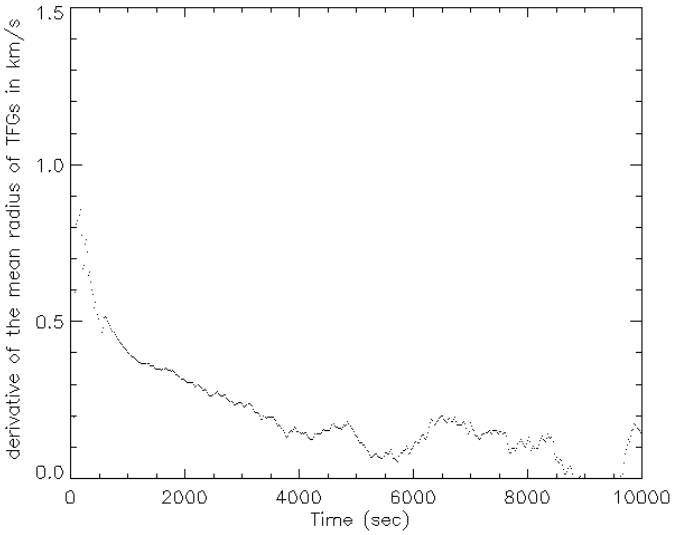

Fig. 6. Expansion velocity of the TFGs as a function of time.

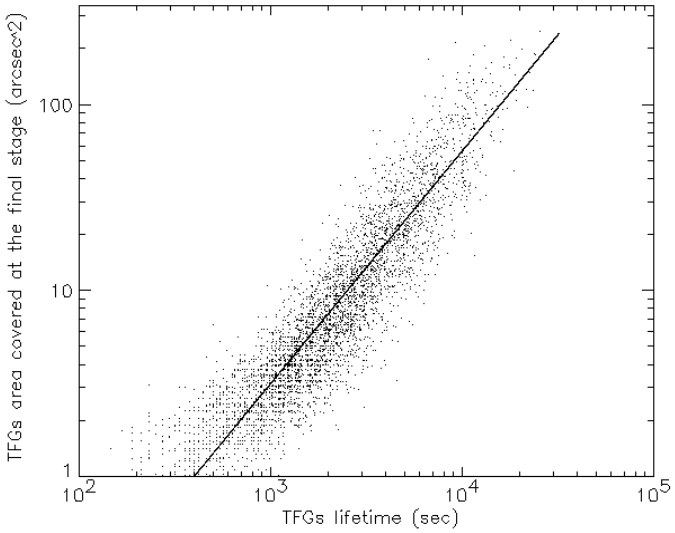

Fig. 7. Area covered by TFGs as a function of their lifetimes.

solar surface. This is shown in Fig. 8 where the proportion of the total area covered by granules belonging to TFGs living more than 1.5 h is displayed during the whole sequence. We see that the area contribution steeply increases in the first hour of the sequence; it then stabilizes to a platform slightly above 15% up to one hour before the end. The lack of contribution at the beginning and the end of the sequence is due to the loss of the TFGs lasting more than 1.5 h which are cut by the begin and end of that period. Such a platform shows that long-lived families are permanently present on the Sun's surface. Moreover, from the total area covered by all granules, i.e. 24%, with our segmentation, we found that 62% of the granule area belongs to TFGs of a lifetime greater than 1.5 h.

The large area covered as well as the temporal coherence of long-lived TFGs suggest that they can play a major role in the dynamics of the solar convection. In the next section, we shall investigate the contribution of these coherent structures to the flow field and relate it to mesogranulation.

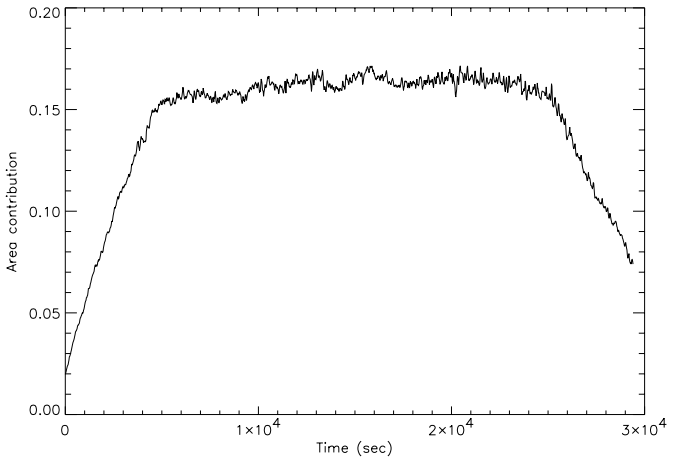

Fig. 8. Time evolution of the area of granules belonging to TFGs living >1.5 h normalized to the total granule area.

5. Relation between TFGs and mesogranules

In the previous section, we showed that long-lived TFGs share some properties with the classical mesogranules, namely the size and the lifetime. In this section, we shall specify this relation by computing the time averaged velocity field at the location of long-lived TFGs.

Flow fields of various TFGs have been obtained using different temporal windows but the same spatial window of 1.5″, a value which is commonly used in the literature. The first temporal window used for each family is its full lifetime. The mean flow fields of the three TFGs shown in Fig. 2 and the one shown in Fig. 10 are plotted in Fig. 11. The mean flow fields of Fig. 11 were computed at the locations where TFGs are present. Only granules belonging to each family were used to derive the velocities in order to delimit the region of the TFG properly. Similar flow fields are obtained if all the granules located in the same field are used.

As can be seen in Fig. 11, the flow fields show a more or less symmetric diverging aspect at the scale of mesogranules. In other words, one can say that the mean flow of these long-lived TFGs is equivalent to a diverging flow at the mesoscale, that is to mesogranules according to the definition given by various authors in the literature (e.g. Simon et al. 1991).

Further evidence of the influence of long-lived TFGs on the large-scale dynamics and its links with mesogranules is given by Figs. 12 and 13. Both figures show the flow field averaged over the whole time sequence (8 h 45 min) but Fig. 13 also displays the projection of the longest-lived TFG shown in Fig. 10. We observe that the granules belonging to that TFG are concentrated at the location where the mean flow field shows a diverging flow at the mesoscale.

In order to investigate the evolution of the TFG flow fields during their lifetime, different temporal windows were used in the computation, i.e. 15 min, 30 min, and 60 min, with a constant spatial window of 1.5″. An example of the resulting flow fields is shown in Fig. 14. The main conclusion: is by increasing the temporal and spatial window the flow fields of a TFG appear as a nearly symmetric divergent velocity field at

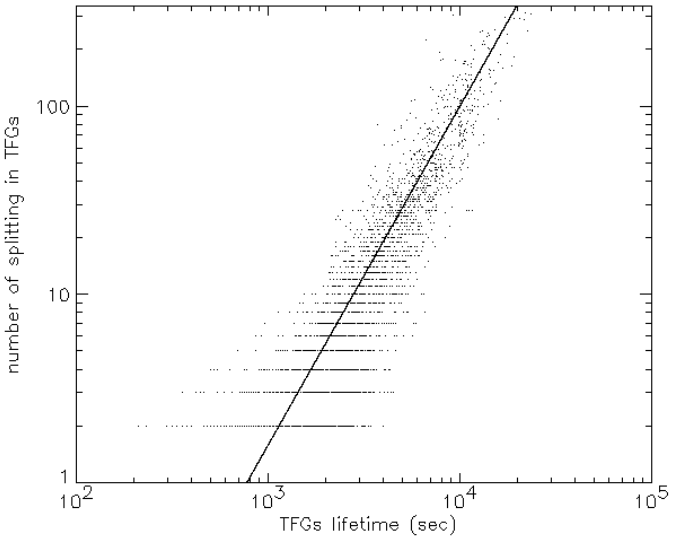

Fig. 9. Number of granule splittings in TFGs as a function of the TFG lifetimes.

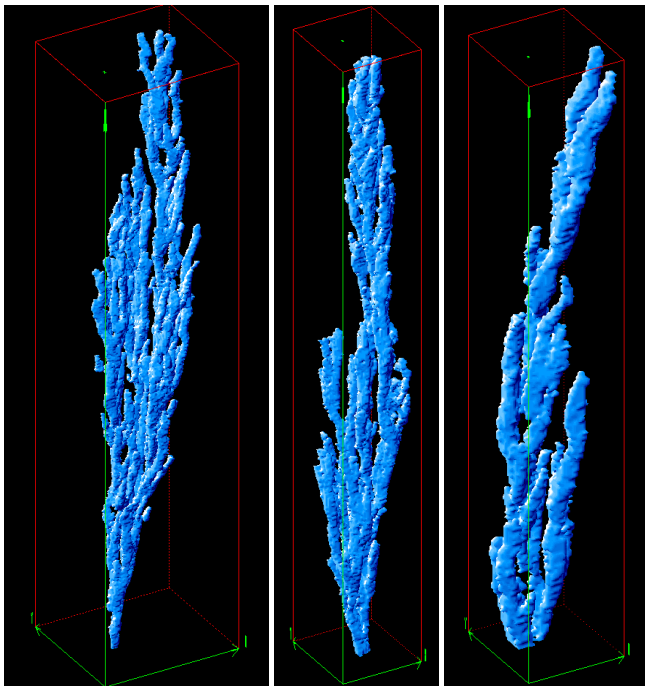

Fig. 10. Three examples of TFGs. From left to right: TFG 15786 lasting 3 h 1 min and extending over 14.6″×13.1″, TFG 1299 (2 h 37 min, 6.9″ × 7.6″) and TFG 1151 (1 h 28 min, 6.8″ × 7.6″).

the scale of the mesogranulation. But for the lower temporal and spatial windows like in Fig. 14 we observe a different behavior like different diverging sources due to close expanding granules of the same TFG. We can say that the repeating fragmenting events of a TFG are equivalent to a positive divergence feature or "a mesogranule", if the temporal window is greater than 30 min.

6. Relation of granular dynamics to the network

Following passive scalars, like corks, over long time scales enables the formation of a network at supergranular scale. This has been done using all the granules to compute the flow field and the location of the corks at the end of the time sequence is shown in Fig. 15. Note that the diffusion coefficient of corks we computed (270 $km^2\ s^{-1}$) is in agreement with previous results (Cadavid et al. 1999). Magnetic fields measured on KPNO magnetograms have been superimposed on the figure, showing a rather good correlation between the cork location and the magnetic network.

In order to correlate the granular dynamics with the network, we plotted in Fig. 16 the density of granule splitting during the whole time sequence along with the final location of the corks. It is striking that corks concentrate at those places and lanes where the density of granule splitting is low; this underlines a close relation between the spatial distribution of the splitting density and the network. We also note that the highest density of splitting is not necessarily located at the centers of the supergranules, some of them being very close to the limit of the network.

Figure 16 also demonstrates clearly that on a long time scale (9 h) the granule splitting does not occur uniformly over the solar surface – which is a new result. This is related to the existence of long-lived TFGs which concentrate the splitting to a small area. This property is again evident in Fig. 17 where the sum of all large granules (diameter >1.4″), generally associated with the long–lived TFGs, is displayed. The correlation between the splitting density and the large granule density is high, i.e. 0.75.

7. Discussion and conclusion

The visual inspection of a white light granulation movie reveals the extreme complexity of the turbulent convection on the Sun's surface. The difficulties in following visually the complete evolution of solar granules is partly due to the large number of explosions which catch our eyes. We seem to concentrate fully on following them, forgetting the evolution of the granules in the vicinity. To follow automatically the granule evolution step by step, one must identify their temporal links in a 3D space-time box.

The quantitative measure of these links is complicated because granules change shape during their life and it is well known that it is quite difficult to define the life history of a typical granule (Spruit et al. 1990). We described in this paper a method of determining the 3D granule links which takes care of the granule splitting into multiple objects, merging of objects and disappearances or appearances between two successive images. Various tests, performed by varying the parameters of our processing algorithm, showed that our method is quite robust with respect to the temporal labeling of the granules.

The application of this processing to the high spatial resolution sequence (duration 8.75 h) observed at the SVST on La Palma in June 1993 (Simon et al. 1994) allowed us to reveal new facets of the properties of the turbulent convection sitting at the top of the convection zone of the Sun. The 3D analysis (x, y, t) of the granulation intensity field demonstrated that a significant fraction of the granules in the photosphere are organized in "Trees of Fragmenting Granules" (TFGs). A TFG consists of a family of repeatedly splitting granules originating

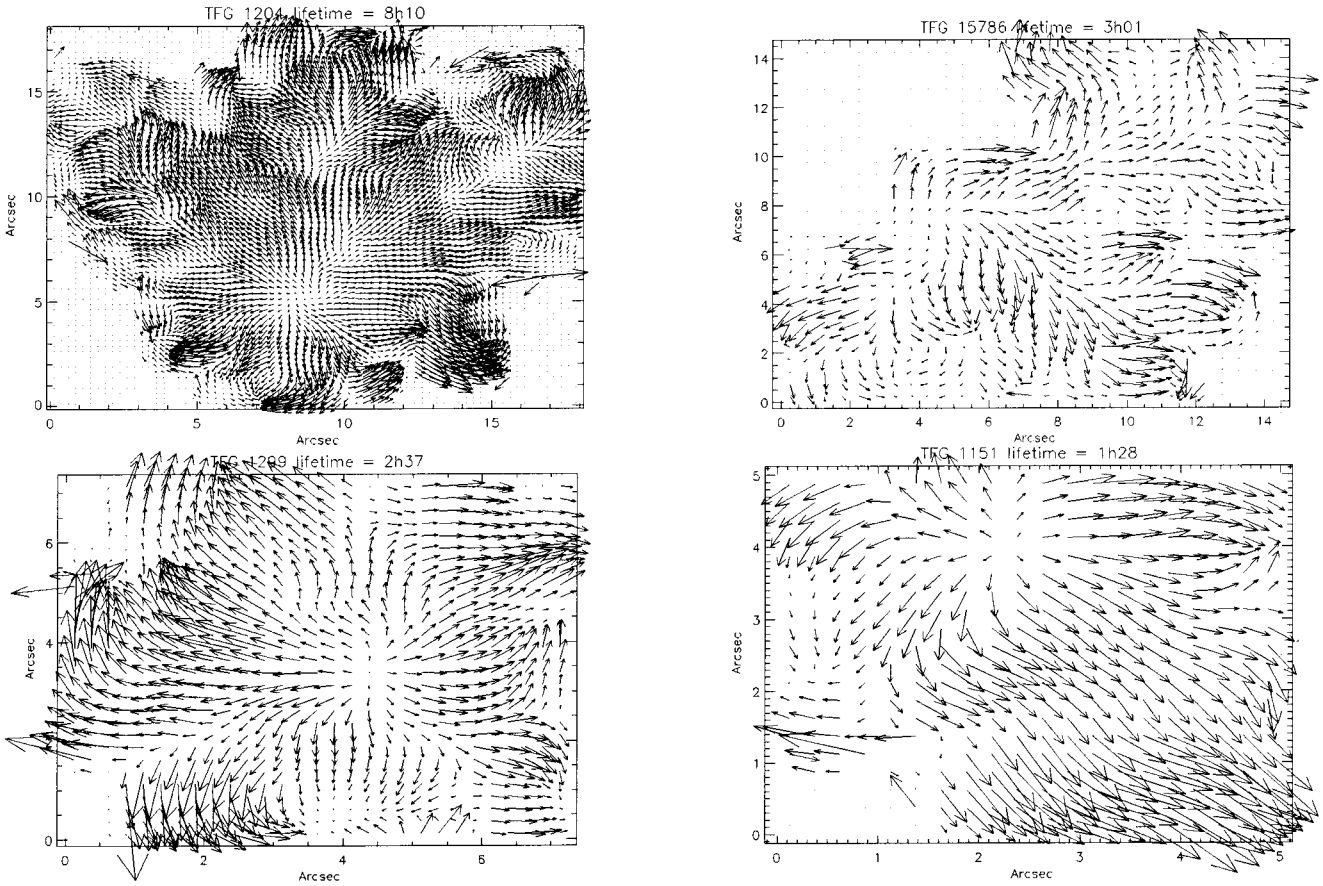

Fig. 11. Four examples of flow fields averaged over the lifetimes of 4 TFGs (8 h 10 min, 3 h 1 min, 2 h 37 min, 1 h 28 min) of our time sequence; they correspond to the longest–lived one shown in Fig. 2 and to the 3 examples of Fig. 10.

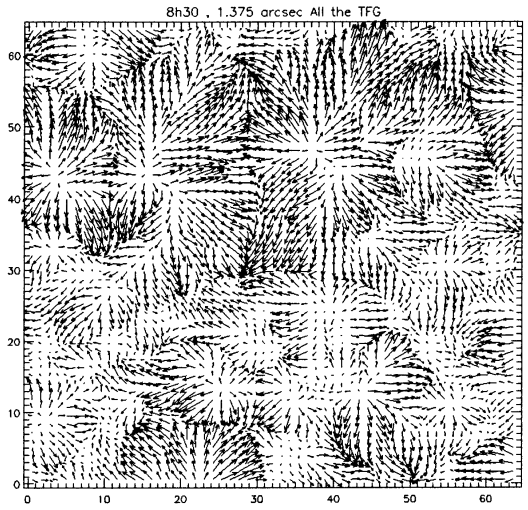

Fig. 12. Flow field averaged over 8 h 45 min.

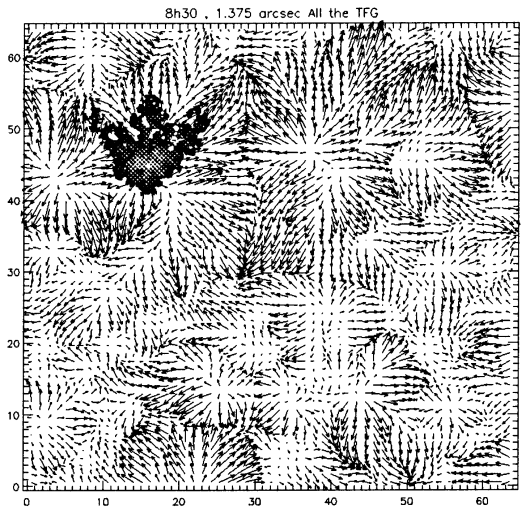

Fig. 13. Flow field averaged over 8 h 45 min with TFG 1204 overplotted.

from a single granule at its beginning. A striking result is that TFGs can live much longer (up to 8h 10min) than individual granules (10 min).

Our study suggests that these longest–lived families are fundamental in structuring the velocity field that we observe on the Sun's surface. First, the longest–lived families (≥1.5 h) cover a large fraction (62%) of the total granule area (defined as per the discussion in Sect. 4). Second, as TFGs lifetimes are much longer than the typical timescale associated with individual granules, the flow induced by such coherent structure should have a strong influence on the dynamics.

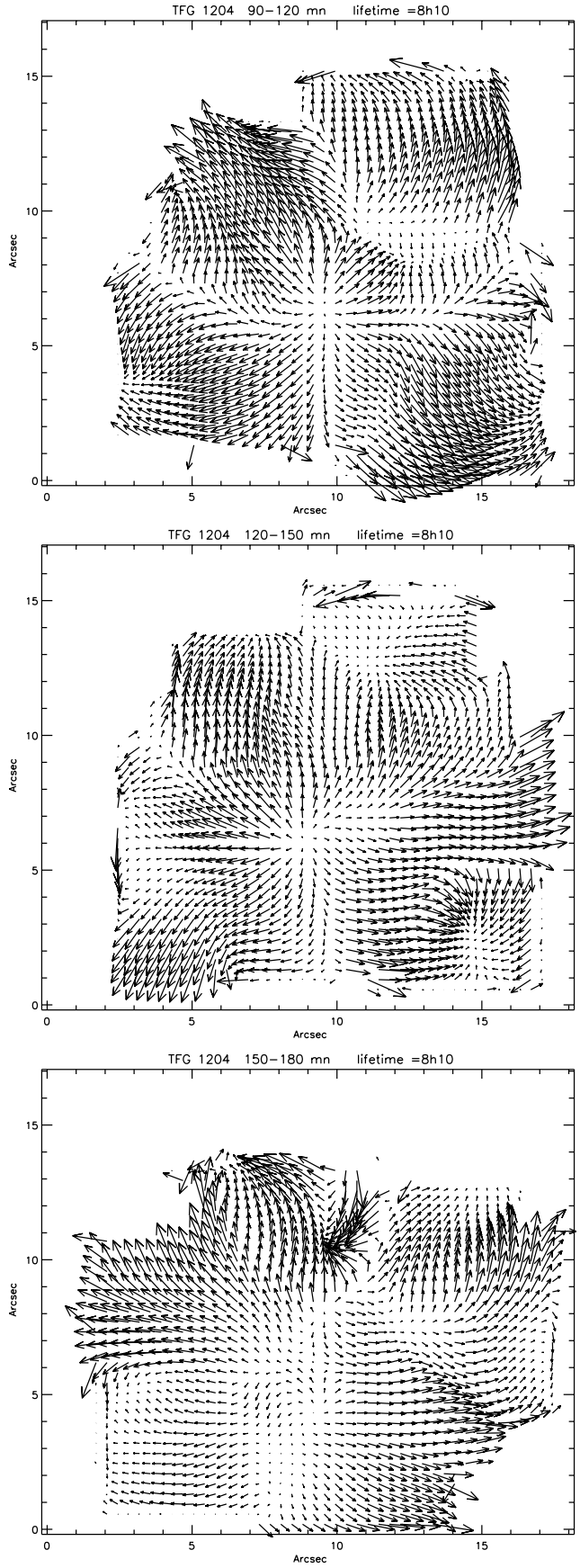

Fig. 14. Example of the horizontal velocity flow field of the longest–lived TFG (cf. Fig. 2) computed with a temporal window of 30 min and a spatial window of 1.5″.

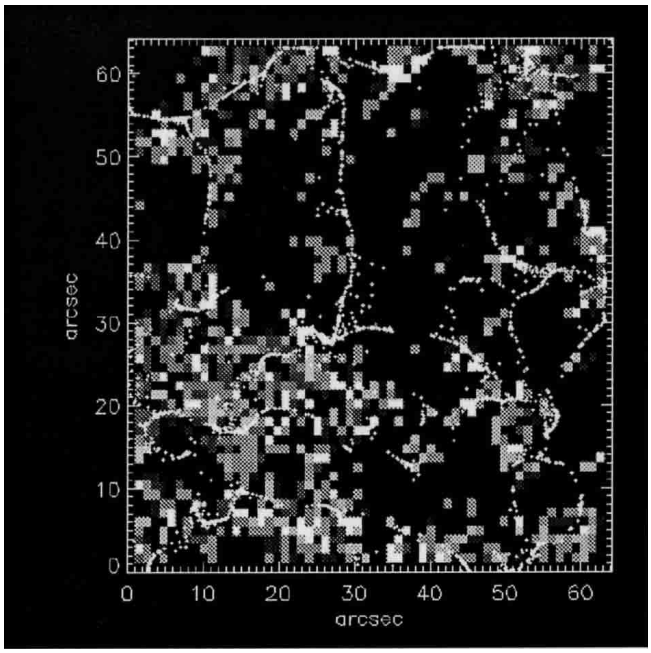

Fig. 15. Magnetic field (grey squares) and final position of the corks (small crosses) due to the motion of all granules.

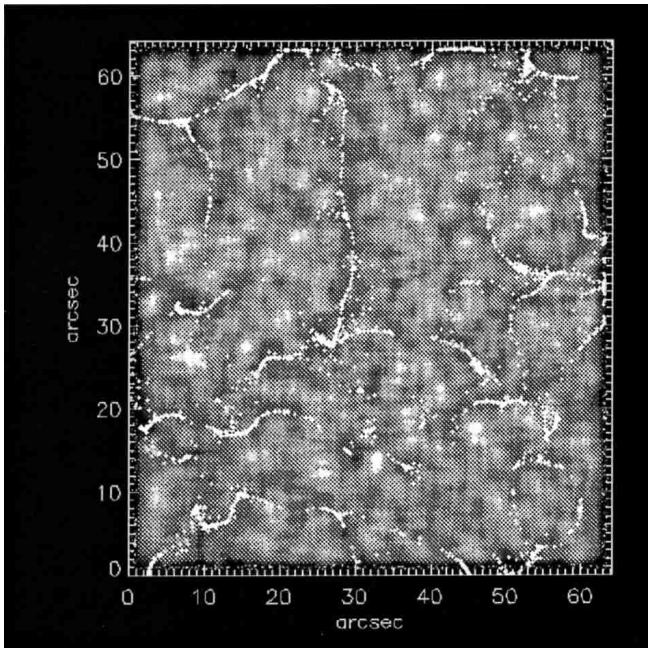

Fig. 16. Density of granule splitting displayed in gray scale (high density = bright, low density = dark) with cork positions superimposed.

We showed also that long-lived TFGs have all the properties of mesogranules, namely the size, the lifetime and the mean diverging flow.

The foregoing results enlighten our view of mesogranulation. They tend to confirm the suggestion made by Strauss & Bonaccini (1997) and by Rieutord et al. (2000) that mesogranulation is not a specific scale of convection driven by the first ionization of helium, but just the large-scale extension of granulation. TFGs show indeed how a coherent meso-scale structure, a diverging flow, actually builds up from motions at

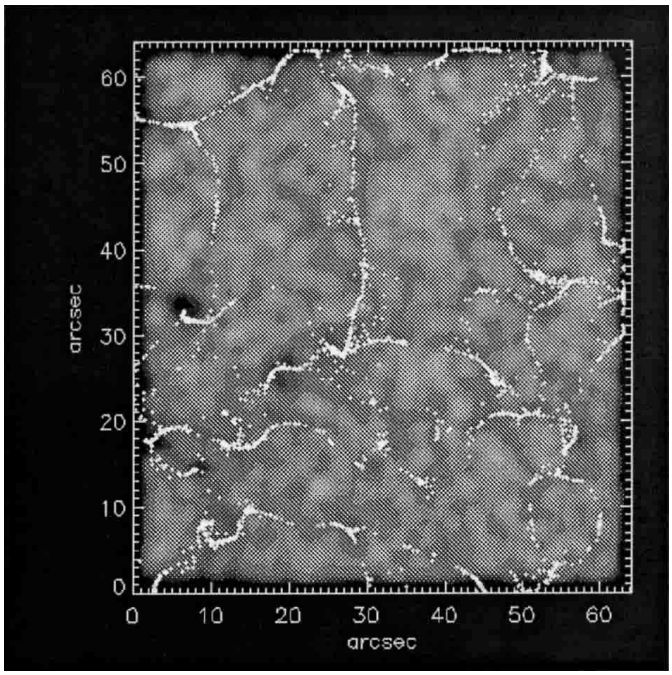

Fig. 17. Positions of corks superimposed on locations of large granules (diameter >1.4″) throughout the whole series, displayed in gray scale (high density = bright, low density = dark).

the granular scale. In this framework, TFGs can be viewed as large scale coherent structures of the solar turbulent convection. Nevertheless the mechanism by which they actually form remains to be understood, as well as the power laws describing their statistical properties. We already note that TFGs are not driven directly by buoyancy since they cover only a fraction of the radiating surface of the Sun.

Note also that these structures, whose maximun radius is around 5″, are in fact the real-space side of the spectral feature noticed in Rieutord et al. (2000) when computing the power spectra of horizontal velocities (see their Fig. 1). This spectral feature was associated with "Strong Positive Divergences" by them, but we show here that the true structure is actually a TFG which may contain many "Strong Positive Divergences".

Concerning the relation between TFGs and supergranules, our work shows that the density of splitting granules is very low on the supergranule boundaries. We also found that, on a long time scale (9 h), the granule splitting does not occur uniformly on the solar surface. This is related to the existence of long-lived TFGs which concentrate the splitting within small areas.

In order to investigate in more detail the possible link between TFGs and supergranulation, one should analyze a longer time sequence like the one used by Shine et al. (2000), but with higher spatial and temporal resolution than they used.

The new insight in the organization of the granulation brought by the concept of TFGs could also help to understand other solar surface phenomena. In the following we discuss some of them.

The persistent structures in the averaged continuum images described by Baudin et al. (1997) and Getling & Brandt (2002) can be interpreted as a consequence of the TFGs which concentrate granules in certain areas in the space-time box.

Hoekzema & Brandt (2000) pointed out the importance of meso-scale flows for solar surface waves. We think that TFGs may play a role in the excitation of these oscillations. Indeed, in the TFGs the splitting granules (or exploders) originating from the same parent evolve nearly parallel in time and at close locations. They split more or less in phase and this introduces an instantaneous large coherent scale. This scale is larger than that of the granulation for the strong downflow where the excitation of the oscillations occurs preferentially (Rimmele et al. 1995). This is in agreement with previous results (Roudier et al. 1997) where holes form along the dark lane (downflow) continuously visible for more than 45 min and systematically distributed at the periphery of mesogranular cells (i.e. the TFGs).

According to November (1989) the mesogranulation is the principal component of the vertical velocity for the supergranular flow. If we identify TFGs with mesogranules, this indicates the important contribution of the TFGs in the supergranular flows. The cork evolution shows that all families contribute to form the network but the effect of the long-lived ones alone (>1.5 h) could be sufficient to produce the network. However, the motions could be influenced by an existing large–scale flow which we cannot exclude. More investigations by numerical simulations are needed to find out if the action of the cumulative effects of the TFGs alone are sufficient to create the network.

The treatment of the anomalous transport in disordered media of magnetic elements (Cadavid et al. 1999) invokes, to interpret their diffusion measurements, "a memory"of the underlying convection. Such a behaviour of the magnetic field diffusion could be ascribed now to the action of TFGs. Indeed, TFGs last up to 8 hours which could represent the sought-after aspect of "memory" required for the granular pattern.

Our findings concerning TFGs and in particular the power laws characterizing their statistical properties should serve as a reference for numerical simulations of the solar surface convection. The existence and properties of TFGs in the large scale numerical simulation described in Rieutord et al. (2001) are currently being investigated.

Acknowledgements. This work was supported by the Centre National de la Recherche Scientifique (CNRS, UMR 5572) and the Programme National Soleil Terre (P.N.S.T.). The authors thank Kitt Peak Observatory (USA) for providing the magnetograms. The support by G. Hosinsky, R. Kever, G. Scharmer, G. W. Simon, and W. Wang in taking the observations as well as by W. Pötzi in the pre-reduction of the data is gratefully acknowledged. The SVST is operated on the island of La Palma by the Royal Swedish Academy of Sciences at the Spanish Observatorio del Roque de los Muchachos of the IAC.

References

Baudin, F., Molowny-Horas, R., & Koutchmy, S. 1997, A&A, 326, 842

Cadavid, A. C., Lawrence, J. K., & Ruzmaikin, A. 1999, ApJ, 521, 844

Getling, A. V., & Brandt, P. N. 2002, A&A, 382, L5

Hagenaar, H. J., Schrijver, C. J., & Title, A. M. 2003, ApJ, 584, 1107

Harvey, J. W. 1965, PASP, 77, 129

Hoekzema, N. M., & Brandt, P. N. 2000, A&A, 353, 389
Kawaguchi, I. 1980, Solar Phys., 65, 207
Muller, R., Auffret, H., Roudier, Th., et al. 1992, Nature, 356, 322
Müller, D. A. N., Steiner, O., Schlichenmaier, R., & Brandt, P. N. 2001, Sol. Phys., 203, 211
November, L. J. 1989, ApJ, 344, 494
Ploner, S. R. O. 1998, Ph.D. Thesis (Zürich)
Rieutord, M., Roudier, T., Malherbe, J. M., & Rincon, F. 2000, A&A, 357, 1063
Rieutord, M., Roudier, T., Ludwig, H. G., Nordlund, Å., & Stein, R. 2001, A&A, 377, 14
Rimmele, T .R., Goode, P. R., Harold, E., & Stebbins, R. T. 1995, ApJ, 444, 119
Roudier, T., Malherbe, J. M., November, L., et al. 1997, A&A, 320, 605
Shine, R. A., Simon, G. W., & Hurlburt, N. E. 2000, Solar Phys., 193, 313
Simon, G. W., Title, A. M., & Weiss, N. O. 1991, ApJ, 375, 775
Simon, G. W., Brandt, P. N., November, L. J., et al. 1994, Large-scale photospheric motions: first results from an extraordinary eleven-hour granulation observation, in Solar Surface Magnetism, ed. R. J. Rutten, & C. J. Schrijver (Dordrecht: Kluwer), 261
Spruit, H. C., Nordlund, Å., & Title, A. M. 1990, ARA&A, 28, 263
Straus, T., & Bonaccini, D. 1997, A&A, 324, 704
Strous, L. H. 1994, Ph.D. Thesis, Utrecht
Title, A. M., Tarbell, T. D., Topka, K. P., et al. 1989, ApJ, 336, 475

4.4.3 A13 : Mesoscale flows in large aspect ratio simulations of turbulent compressible convection

"Mesoscale flows in large aspect ratio simulations of turbulent compressible convection"

Rincon F., Lignières F., Rieutord M.

A&A 430, L57-L60, 2005

A&A 430, L57–L60 (2005)
DOI: 10.1051/0004-6361:200400130

Astronomy & Astrophysics

Letter to the Editor

Mesoscale flows in large aspect ratio simulations of turbulent compressible convection

F. Rincon, F. Lignières, and M. Rieutord

Laboratoire d'Astrophysique de Toulouse-Tarbes, UMR CNRS 5572, Observatoire Midi-Pyrénées, 14 avenue É. Belin, 31400 Toulouse, France
e-mail: rincon@ast.obs-mip.fr

Received 23 August 2004 / Accepted 19 December 2004

Abstract. We present the results of a very large aspect ratio ($A = 42.6$) numerical simulation of fully compressible turbulent convection in a polytropic atmosphere, and focus on the properties of large-scale flows. Mesoscale patterns dominate the turbulent energy spectrum. We show that these structures, which had already been observed in Boussinesq simulations by Cattaneo et al. (2001), have a genuine convective origin and do not result directly from collective interactions of the smaller scales of the flow, even though their growth is strongly affected by nonlinear transfers. If this result is relevant to the solar photosphere, it suggests that the dominant convective mode below the Sun's surface may be at mesoscales.

Key words. Sun: granulation – convection – turbulence

1. Introduction

The origin of solar photospheric flows on horizontal scales larger than granulation ($\ell \sim 1000$ km) has been a puzzling problem for more than forty years, when supergranulation ($\ell \sim 30\,000$ km) was discovered by Hart (1954) and later on confirmed by Simon & Leighton (1964). Even though recent breakthroughs in the field of supergranulation imaging have been made thanks to the emergence of local helioseismology techniques (Duvall & Gizon 2000) and the results of the MDI instrument (Hathaway et al. 2000), its origin is still unclear. The existence of an intermediate scale, mesogranulation ($\ell \sim 8000$ km), is also a matter of debate (Hathaway et al. 2000; Shine et al. 2000; Rieutord et al. 2000; Lawrence et al. 2001).

Meso and supergranulation have long been believed to be due to Helium deep recombinations driving cell-like convection. This view now appears to be out of date (Rast 2003). Several numerical experiments of convection (Cattaneo et al. 1991; Stein & Nordlund 2000) at moderate aspect ratio (A is the ratio of the box width to its depth) have shown a tendency of long-lived large-scale flows to form in depth. Using large aspect ratio ($A = 20$) simulations of Boussinesq convection, Cattaneo et al. (2001) have suggested that mesogranulation may result from nonlinear interactions of granules (see also Rast 2003). A large scale instability (Gama et al. 1994) of granules has also been proposed by Rieutord et al. (2000) to explain supergranulation. Local numerical simulations at $A = 10$ (Rieutord et al. 2002) did not confirm it. DeRosa et al. (2002), using spherical simulations, have computed flows down to supergranular scales. Actually, the emergence of the three distinct scales of granulation, mesogranulation, and supergranulation in the surface layers, among the observed *continuum* of scales, remains a fully open problem that still deserves much work.

In this Letter, we report new results on three-dimensional numerical simulations of fully compressible turbulent convection in a rectangular box with very large aspect ratio $A = 42.6$. This configuration allows us to study accurately the turbulent dynamics at horizontal scales between granulation and supergranulation, which have not been covered by previous numerical simulations. A compressible fluid is used to provide a more realistic model of photospheric convection than a Boussinesq fluid. Also, density stratification should attenuate the effect of an artificial bottom boundary (Nordlund et al. 1994).

In Sect. 2 we present our numerical setup and physical model. Section 3 is devoted to the analysis of the flow. The main consequences of the results are discussed in Sect. 4, which is followed by a short conclusion.

2. Numerical model and run parameters

For the purpose of our investigations we use a code designed to solve the fully compressible hydrodynamic equations for a perfect gas (e.g. Cattaneo et al. 1991) in cartesian geometry. Constant dynamical viscosity and thermal conductivity are assumed. A constant thermal flux is imposed at the bottom, while temperature is held fixed at the surface. The velocity field satisfies stress-free impenetrable boundary conditions. The initial state is a $m = 1$ polytropic atmosphere ($\gamma = 5/3$) with small random velocity $\boldsymbol{v}$, temperature θ, and density ρ perturbations. The initial density contrast between the bottom and top plates is 3, a value for which most of the features of stratification

are already present in the linear convective instability problem (Gough et al. 1976). The Prandtl number is Pr = 0.3 and the Rayleigh number evaluated in the middle of the layer is $R = 3 \times 10^5$ (650 times supercritical). We do not paste several smaller boxes initially, as was the case in the paper by Cattaneo et al. (2001), thus there is no artificial spatial symmetry at $t = 0$.

A sixth-order compact finite difference scheme (Lele 1992) is used in the vertical (gravity $\boldsymbol{g}$) direction and a spectral scheme in the horizontal (periodic) directions. FFTs are implemented via the MPI version of FFTW (Frigo & Johnson 1998). Dealiasing by removal is performed using the 2/3 rule (Canuto et al. 1988). Time-stepping is done with a third-order, low-storage, fully explicit Runge-Kutta scheme. Energy dissipation is handled by Laplacian terms, without any subgrid-scale modelling or hyperviscosity. A very large aspect ratio $A = 42.6$ was achieved using $82 \times 1024 \times 1024$ grid points. The simulation ran on 64 processors and a total of 400 GB of raw data was collected throughout the numerical experiment.

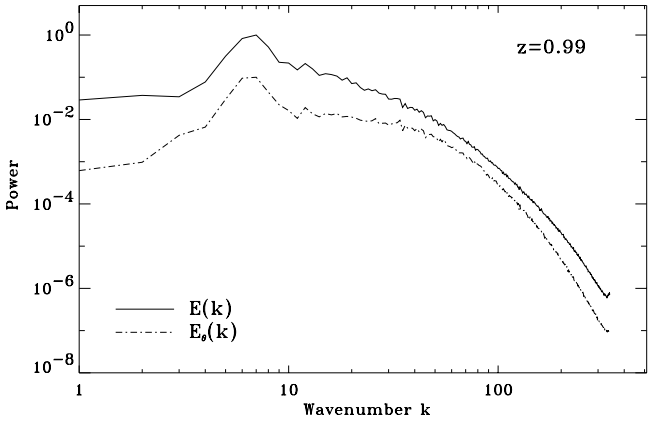

Fig. 1. Normalized momentum $E(k, z)$ and temperature $E_\theta(k, z)$ power spectra at $t = 0.7$ and $z = 0.99$ (the temperature spectrum has been shifted). The maximum around $k \sim 7$ corresponds to mesoscales. Also, a significant power excess in $E_\theta(k, z)$ is observed around $k \sim 40$ close to the surface, in comparison to the deeper layers. This feature is associated with granulation in this simulation.

3. Results

In the following, the depth of the layer d is used as unit of length and the vertical thermal diffusion time $d^2/\kappa_{\rm bot}$ as unit of time ($\kappa_{\rm bot}$ is the thermal diffusivity at the bottom of the layer).

3.1. Flow structure and evolution

We first describe the flow evolution during 0.7 thermal diffusion time, corresponding to twelve turnover times (twice the vertical crossing time based on the rms velocity). Initially, linear growth is observed for a normalized horizontal wavenumber $k \sim 45$ (length $\ell \sim 1$) predicted by linear theory. The maximum of the depth-dependent momentum spectrum (hats denote two-dimensional horizontal Fourier transforms)

$$E(k, z) = \int_{\Omega_k} \left| \widehat{(\rho \boldsymbol{v})}_k(z) \right|^2 k \, \mathrm{d}\Omega_k \tag{1}$$

then progressively shifts from $k \sim 45$ to $k \sim 5$–8 ($\ell \sim 5$–8) at the end of the simulation (Fig. 1). As can be seen in Fig. 2, the integral scale reaches $L_{\rm int} \sim 7$. Horizontal temperature maps at different times (Fig. 3) clearly show that the dominant scale of the flow increases during the simulation. This coherent pattern is best seen in the middle of the layer, but most of the in-depth dynamics are still clearly visible in the surface layers. In the upper layers, a second distinct smaller scale appears (bottom-right picture of Fig. 3). Its vertical extent ($0.2\,d$) corresponds to the surface region of superadiabatic stratification, while the interior is almost isentropic. Referring to the Sun, we shall identify this thermal boundary layer scale with granulation, thus the larger internal scale is a mesoscale.

Next we shall try to explain the growth and saturation of the integral scale as well as the origin of the observed mesoscales.

3.2. Convective origin of mesoscales

After the linear growth, saturation of the velocity amplitude at $k \sim 45$ occurs. At that time, this mode is the scale of

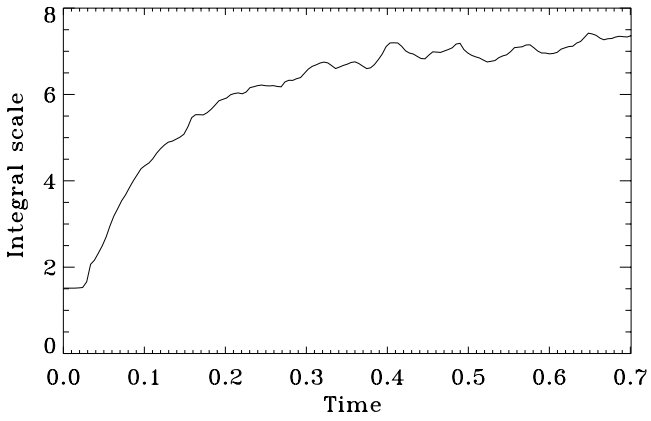

Fig. 2. Integral scale $L_{\rm int}(z) = \frac{\pi}{2} \int k^{-1} E(k, z)\, \mathrm{d}k \Big/ \int E(k, z)\, \mathrm{d}k$ evolution at $z = 0.87$. This scale represents the most energetic flow structures.

energy injection. Larger scales are also highly linearly unstable for $R = 3 \times 10^5$ and we observe that they continue to grow.

However, in the nonlinear regime, energy transfer to smaller scales limits this growth. To show this, we take the horizontal Fourier transform of the momentum equation and extract its solenoidal part by applying the projection operator $\mathcal{P}[\boldsymbol{v}] = \boldsymbol{v} - \boldsymbol{\nabla}\Delta^{-1}\boldsymbol{\nabla}\cdot\boldsymbol{v} = \boldsymbol{v}^{\rm s}$, denoted by $\widehat{\mathcal{P}}$ when acting on horizontally Fourier-transformed fields. Taking the dot product with the complex conjugate of the solenoidal part of momentum $\widehat{(\rho \boldsymbol{v})}^{\rm s}_{\boldsymbol{k}}(z)$, integrating over depth z and angles $\Omega_{\boldsymbol{k}}$ in the horizontal spectral plane, we obtain a time-evolution equation for the solenoidal part $E^{\rm s}(k, z)$ of $E(k, z)$, integrated vertically:

$$\partial_t \int_0^1 E^{\rm s}(k, z)\, \mathrm{d}z = T(k) + F(k) + D(k), \tag{2}$$

$$T(k) = -2\,\mathrm{Re}\left[\int_0^1 \int_{\Omega_k} \widehat{(\rho \boldsymbol{v})}^{\rm s}_{\boldsymbol{k}}{}^{*} \cdot \widehat{\mathcal{P}} \left[\boldsymbol{\nabla} \cdot \widehat{(\rho \boldsymbol{v} \boldsymbol{v})}_{\boldsymbol{k}} \right] k \, \mathrm{d}\Omega_{\boldsymbol{k}} \, \mathrm{d}z \right], \tag{3}$$

$$F(k) = 2\,\mathrm{Re}\left[\int_0^1 \int_{\Omega_k} \widehat{(\rho \boldsymbol{v})}^{\rm s}_{\boldsymbol{k}}{}^{*} \cdot \widehat{\mathcal{P}} \left[\widehat{\rho \boldsymbol{g}}_{\boldsymbol{k}} \right] k \, \mathrm{d}\Omega_{\boldsymbol{k}} \, \mathrm{d}z \right]. \tag{4}$$

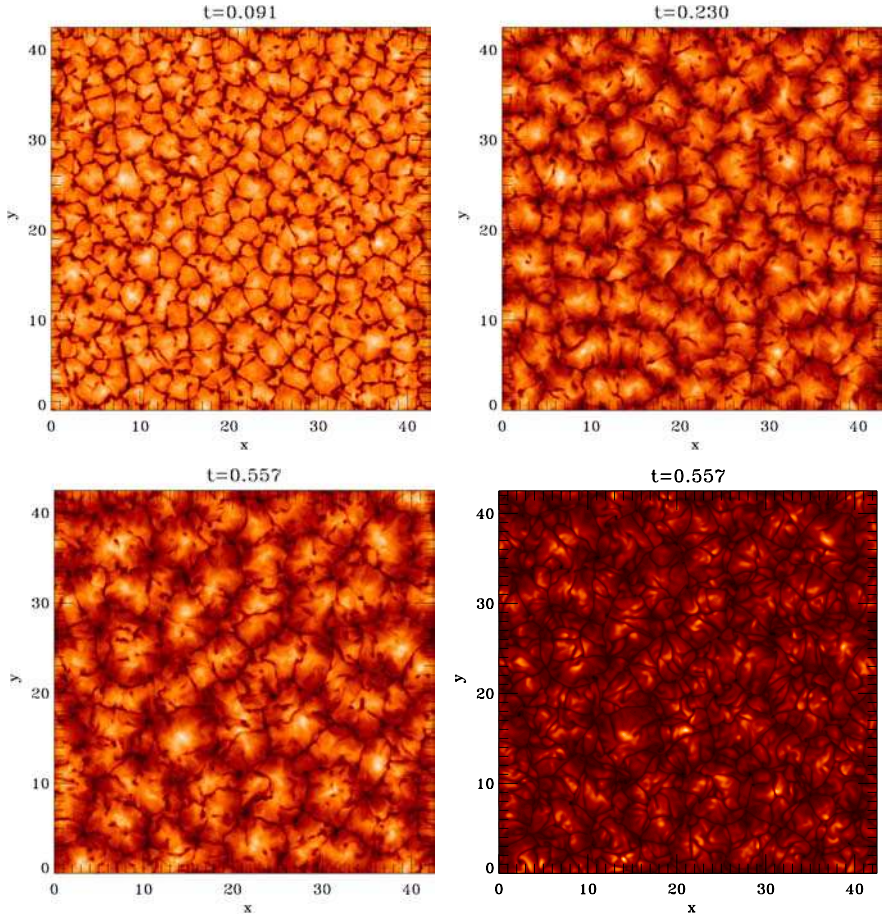

Fig. 3. From left to right and top to bottom, time-evolution of temperature maps at $z = 0.63$. The size of the visible mesoscale pattern increases until a quasi-steady state is reached (*bottom-left image*). *Bottom-right picture*: same as bottom-left image, for a surface layer ($z = 0.99$), showing the differences between in-depth mesoscale dynamics and the smaller-scale flow in the upper thermal boundary layer.

$T(k)$ represents nonlinear transfers, $F(k)$ is the forcing by buoyancy and $D(k)$, which has a similar definition, represents viscous dissipation. In Fig. 4, we plot these quantities averaged over a time interval during which $k > 12$ modes are steady, while modes with smaller k develop. We observe that $F(k)$ is the basic energy supply on large scales, as in the linear convective instability mechanism. Nonlinear transfer $T(k)$ is always negative for modes with $7 \leq k \leq 11$, which have a small but positive net energy growth. Therefore large scales do not come out of nonlinear interactions but have a *convective* origin. This effect could also be observed using the energy equation: as in linear convection, energy is injected in large scales via the advection of the horizontally averaged entropy profile, while nonlinear transfers and diffusion only remove energy from them.

Note finally that the mesoscale pattern of Fig. 3 is expected to expand slightly on a much longer time scale that can not be achieved numerically. Also, the dominant scales may depend on the Rayleigh number, as they result from a balance between buoyancy and nonlinear transfers. These mesocells are very probably the same as those observed by Cattaneo et al. (2001) in Boussinesq simulations with $A = 20$. Their size is comparable in both experiments. We therefore confirm these results for a compressible fluid, in a larger aspect ratio box with no initial symmetry, but interpret them quite differently.

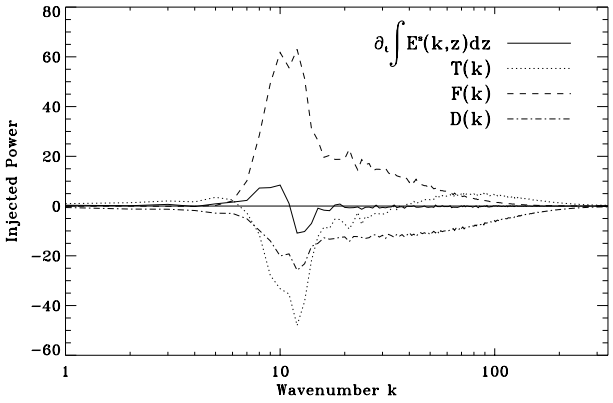

Fig. 4. Depth-integrated spectral transfer $T(k)$, buoyancy forcing $F(k)$, dissipation $D(k)$ and net power injected in $\int E^s(k,z)\,\mathrm{d}z$ following Eq. (2). An average between $t = 0.14$ and $t = 0.20$ has been taken to outline the mean growth of $k < 12$ modes during this period owing to $F(k)$ (note especially that $T(k) < 0$ for these scales). The maximum over k of the depth-integrated spectrum has been used for normalizing.

4. Discussion

4.1. Relations with solar photospheric convection

We now discuss the relevance of our results to the Sun. First, an estimate of the size (in km) of the typical structures of our

simulation can be computed to clarify the comparison with observations. Identifying the thermal boundary layer thickness with the typical vertical extent of solar granulation (~150 km), we find our mesocells to be 6000 km wide.

This numerical experiment represents a highly idealized model of photospheric convection, even though it integrates density stratification. Differences with observations or with more realistic simulations (Stein & Nordlund 1998) are therefore clearly expected. The most important one is the prominent peak at mesoscales in our power spectrum (Fig. 1), which might be due to boundary condition effects or to the absence of radiative transfer in our simulations. As noted by Cattaneo et al. (2001), granulation is directly related to the formation of a thermal boundary layer, so that changes in boundary conditions might have a strong impact on the contrast between mesogranular and granular flows. Also, in radiative convection simulations by Stein & Nordlund (2000) with an open bottom boundary, the dominant scale visually increases continuously with depth, which does not happen in our experiment. Besides, the absence of radiative transfer in our simulations makes it impossible to define a $\tau = 1$ surface. Actually, the intensity map presented by Rieutord et al. (2002) does not exhibit clear mesoscale intensity modulation whereas temperature maps at fixed depth do. Since the $\tau = 1$ surface does not correspond to a fixed depth, mesoscale convective flows may be present in the subsurface layers and be partly hidden this way.

Besides, various observations suggest some mesoscale organization. Oda (1984) has reported some clustering of granules around brighter granules distributed on mesoscales. In our simulation (Fig. 3), the imprint of mesoscales is very clear at the surface and clustering of smaller granules also occurs around bright spots corresponding to mesoscale upflows. Finally, a distribution of inter-network magnetic fields at the scale of mesogranulation has been found recently (Domínguez Cerdeña 2003; Roudier & Muller 2004), which might also be related to strong convective mesoscale plumes.

4.2. Very large scales

A final word must be said about very large-scale flows. According to the previous estimates, the horizontal size of our box is 35 000 km, which does not leave much room for supergranules. We do not obtain a second peak at small k in the spectra, so there is strictly speaking no supergranulation in our simulation. This may be because we do not have the necessary physical ingredients in the model, because our box is not large or deep enough, or because our run is too short. However, noticeable positive nonlinear transfer occurs at the smallest k (Fig. 4) and we observed weak horizontally divergent large-scale flows of still unclear origin. When subjected to horizontal strains, strong mesoscale vertical vortices resulting from angular momentum conservation in sinking plumes (Toomre et al. 1990) might help creating horizontal vorticity on large scales.

5. Conclusions

The results of our simulations of large-scale convection in a compressible polytropic atmosphere show that the dominant *convective* mode is found at mesoscales. We observe that large aspect ratio simulations are necessary to study the convective dynamics of these structures, since the integral scale is $L_{\rm int} \sim 7$ in the final quasi-steady state. A slow evolution is expected on longer time scales, which are unfortunately numerically out of reach. Some similarities with solar observations are found. If this kind of model is relevant to study the solar photosphere, our results suggest that mesoscale convection may be powerful below the Sun's surface. This would help to explain the coexistence of two apparently distinct granular and mesogranular scales. Supergranulation is not found in this experiment.

Acknowledgements. Numerical simulations have been carried out at IDRIS (Paris) and CINES (Montpellier). Both computing centers are gratefully acknowledged. F. R. would like to thank M. R. E. Proctor, N. O. Weiss, A. A. Schekochihin and B. Freytag for several helpful discussions.

References

Canuto, C., Hussaini, M. Y., Quarteroni, A., & Zang, T. A. 1988, Spectral Methods in Fluid Dynamics (Springer)
Cattaneo, F., Brummell, N. H., Toomre, J., Malagoli, A., & Hurlburt, N. E. 1991, ApJ, 370, 282
Cattaneo, F., Lenz, D., & Weiss, N. 2001, ApJ, 563, L91
DeRosa, M. L., Gilman, P. A., & Toomre, J. 2002, ApJ, 581, 1356
Domínguez Cerdeña, I. 2003, A&A, 412, L65
Duvall, T. L., & Gizon, L. 2000, Sol. Phys., 192, 177
Frigo, M., & Johnson, S. G. 1998, in Proc. 1998 IEEE Intl. Conf. Acoustics Speech and Signal Processing (IEEE), 3, 1381
Gama, S., Vergassola, M., & Frisch, U. 1994, J. Fluid Mech., 260, 95
Gough, D. O., Moore, D. R., Spiegel, E. A., & Weiss, N. O. 1976, ApJ, 206, 536
Hart, A. B. 1954, MNRAS, 114, 17
Hathaway, D. H., Beck, J. G., Bogart, R. S., et al. 2000, Sol. Phys., 193, 299
Lawrence, J. K., Cadavid, A. C., & Ruzmaikin, A. 2001, Sol. Phys., 202, 27
Lele, S. K. 1992, J. Comp. Phys., 103(1), 16
Nordlund, Å., Galsgaard, K., & Stein, R. F. 1994, in Solar Surface Magnetic Fields, ed. R. J. Rutten & C. J. Schrijver, vol. 433, NATO ASI Ser., 471
Oda, N. 1984, Sol. Phys., 93, 243
Rast, M. P. 2003, ApJ, 597, 1200
Rieutord, M., Roudier, T., Malherbe, J. M., & Rincon, F. 2000, A&A, 357, 1063
Rieutord, M., Ludwig, H.-G., Roudier, T., Nordlund, Å., & Stein, R. F. 2002, Il Nuovo Cimento C, 25, 523
Roudier, T., & Muller, R. 2004, A&A, 419, 757
Shine, R. A., Simon, G. W., & Hurlburt, N. E. 2000, Sol. Phys., 193, 313
Simon, G. W., & Leighton, R. B. 1964, ApJ, 140, 1120
Stein, R. F., & Nordlund, Å. 1998, ApJ, 499, 914
Stein, R. F., & Nordlund, Å. 2000, Sol. Phys., 192, 91
Toomre, J., Brummell, N., Cattaneo, F., & Hurlburt, N. E. 1990, Computer Phys. Commun., 59, 105

Chapitre 5

Projet de recherche

Au cours des prochaines années, l'étude des effets de la rotation, du champ magnétique et de la turbulence sur l'évolution stellaire doit bénéficier de l'exploitation des nouveaux moyens d'observation en photométrie haute précision depuis l'espace (Corot, Kepler), spectropolarimétrie (Narval, Espadons) et interférométrie (VLTI). À moyen terme (2015-2020), une nouvelle génération d'instrument (Gaïa pour l'astrométrie, Spirou pour la spectropolarimétrie et peut-être Plato pour la photométrie spatiale) prendra le relais.

Les thématiques que je souhaite développer s'inscrivent dans ce cadre puisqu'elles visent à la fois à obtenir des contraintes sur les processus magnétohydrodynamiques et à modéliser ces processus. Elles s'articulent autour de la sismologie et du magnétisme des étoiles massives et de masse intermédiaire et de la modélisation des processus de transport dans les intérieurs stellaires. Les résultats obtenus sur la théorie des oscillations des étoiles en rotation rapide lèvent un obstacle important à l'interprétation des fréquences des étoiles massives et de masse intermédiaire. Mais il n'a pas encore été montré que l'identification des fréquences est possible et c'est à cette question que nous essaierons d'apporter une réponse dans les prochaines années. Nous serons amené à la fois à améliorer la modélisation des spectres d'oscillation et probablement à obtenir des contraintes observationnelles supplémentaires sur l'identification. De même les résultats obtenus sur le magnétisme des étoiles de masse intermédiaire appellent de nouveaux programmes d'observation et de modélisation. Du point de vue observationnel, il s'agira d'une part de préciser l'étendue et les propriétés du nouveau type de magnétisme que nous avons mis en évidence avec la détection du champ de Véga et d'autre part de déterminer empiriquement la relation entre le champ minimum et la rotation dans le groupe des étoiles Ap magnétiques. Du point de vue

de la modélisation, l'origine du champ de type Véga sera considérée en étudiant la possibilité d'une dynamo dans l'enveloppe de ces étoiles (notamment la dynamo dite de Spruit) et des simulations 2D puis 3D seront effectuées pour préciser la relation champ critique-rotation et modéliser l'étendue du désert magnétique entre le magnétisme de type Véga et celui des Ap. Sur la thématique du transport turbulent des zones radiatives, je vais chercher à contraindre par des simulations numériques intensives la forme des coefficients de transport utilisés dans les modèles d'évolution stellaire. Finalement, sur une thématique plus "physique fondamentale", je chercherai des évidences observationnelles du chaos d'onde dans les étoiles en rotation rapide et éventuellement à étendre ce concept à d'autres systèmes naturels.

Ces recherches s'inscrivent parfaitement dans les objectifs de l'équipe Stellaire et Solaire du nouveau laboratoire de Toulouse qui doit voir le jour en janvier 2011.

5.1 Sismologie des étoiles en rotation rapide

À l'issue du travail présenté dans cette thèse, nous sommes capables de calculer des spectres de fréquences de modèle d'étoile en rotation rapide et nous comprenons la structure du spectre dans le régime asymptotique des modes acoustiques. Nous sommes maintenant en mesure de nous attaquer plus directement au problème de l'identification des fréquences observées et je compte le faire en développant trois axes de recherches complémentaires. Le premier consiste à utiliser des spectres théoriques pour construire des méthodes d'identification des fréquences qui seront ensuite testées sur des spectres observés (Sect. 5.1.1). Le deuxième axe de recherche vise à améliorer le réalisme des spectres théoriques en modélisant la visibilité, le mécanisme d'excitation et la saturation non-linéaire des modes (Sect. 5.1.3). Le troisième axe est de développer ou d'adapter au cas des étoiles en rotation rapide des méthodes susceptibles d'apporter des contraintes supplémentaires pour l'identification des modes, notamment par spectroscopie ou photométrie multi-couleur (Sect. 5.1.2). Par ailleurs la construction de la théorie asymptotique des modes dans une étoile en rotation rapide doit être poursuivie d'une part en approfondissant certains aspects concernant les modes acoustiques et d'autre part en développant une théorie asymptotique pour les modes gravito-inertiels (Sect. 5.1.4).

5.1.1 Construire des méthodes d'identification des fréquences observées

L'objectif est de construire, à partir de spectres théoriques, des outils d'analyse qui permettront d'identifier au moins certaines fréquences dans les spectres observés. Pour les oscillations de type solaire des étoiles à faible rotation, le diagramme échelle est un outil de ce type puisqu'il permet, au moins en principe, de déterminer le degré de l'harmonique sphérique associé aux fréquences observées. Même si une technique similaire pourraient être appliquée aux modes d'îlots de haute fréquence, l'analyse des spectres d'étoiles en rotation rapide est compliquée par plusieurs facteurs : le splitting rotationnel est suffisamment important pour mélanger les spectres acoustiques de différents m, les modes acoustiques observés se situent dans la partie basse du spectre ($n \leq n_{\max} \sim 10$) où les déviations par rapport au régime asymptotique sont plus importantes, un spectre irrégulier de modes chaotiques se superposent très probablement au spectre régulier des modes d'îlots. Dans ces conditions, les spectres théoriques serviront à construire et tester de nouvelles méthodes d'identification. La faiblesse principale des spectres théoriques est la modélisation des amplitudes intrinsèques des modes, les mécanismes non-linéaires qui les déterminent restant très mal connus. Pour cet aspect du problème, la confrontation avec les spectres observés pourrait permettre de mieux calibrer les amplitudes intrinsèques.

Nous comptons aborder cette thématique en suivant deux approches complémentaires. D'une part, nous construisons un spectre théorique valable dans le régime asymptotique. Dans ce cas, la théorie asymptotique fournit des spectres pratiquement sans calcul ce qui permet de tester des méthodes d'identification sur une gamme importante de modèles. D'autre part, nous considérons un modèle d'étoile particulier correspondant à une étoile observée et nous utilisons le code d'oscillation pour calculer un spectre théorique complet dans la gamme de fréquence observée.

Nous avons déjà commencé à tester des méthodes d'identification en nous plaçant dans le régime asymptotique. Dans ce cas, nous savons qu'au delà d'une certaine rotation le spectre de fréquence visible est la superposition de deux sous-spectres : un sous-spectre régulier décrit par une formule similaire à la formule de Tassoul et un sous-spectre irrégulier mais dont les propriétés statistiques sont connues (Lignières & Georgeot 2009, **A7**). Nous avons alors cherché dans quelle mesure la fonction d'autocorrélation du spectre permet de retrouver les propriétés de la partie régulière du spectre. Nous avons fait cette étude en faisant varier trois paramètres principaux du spectre, l'intervalle de fréquence considéré, l'angle d'inclinaison entre l'axe de rotation de l'étoile et l'observateur, et le seuil en amplitude qui permet de ne

conserver que les pics de plus hautes amplitudes du spectre. Nous avons également fait l'hypothèse que les amplitudes des pics du spectre sont déterminées par les effets d'annulation dus à l'intégration sur le disque visible. Nos résultats préliminaires indiquent que (i) la détection de patterns réguliers dépend fortement du ratio entre le nombre de modes réguliers et irréguliers (ii) les configurations où l'angle d'inclinaison est faible sont plus favorables que celles où l'étoile est vue par l'équateur (iii) en l'absence de rotation différentielle, la signature du splitting rotationnel entre les modes $m = 1$ et $m = -1$ est facilement détectable (Lignières et al. 2010). La Figure 5.1 montre les fonctions d'autocorrélation du spectres dans un cas favorable où l'angle d'inclinaison est faible. Récemment, une première détection d'un écart régulier entre fréquence dans un spectre de δ Scuti observée par Corot a été annoncée (García Hernández et al. 2009). Nous avons entamé une collaboration avec cette équipe (notamment J.C. Suarez) pour tester nos méthodes sur le spectre de cette étoile.

Le calcul d'un spectre réaliste avec le code d'oscillation est mené par D. Reese actuellement en postdoc à l'Observatoire de Meudon et avec qui je collabore notamment sur le calcul de la visibilité des modes. Le modèle d'étoile en rotation rapide réaliste dûment déformés par la force centrifuge est calculé avec le code ESTER dans le cadre d'une collaboration avec F. Espinosa et M. Rieutord. Ces calculs permettront de tester les méthodes d'identification développées dans le régime asymptotique sur des spectres plus réalistes.

5.1.2 Améliorer le réalisme des spectres théoriques

Comme cela a déjà été fait dans le cas à symétrie sphérique, le réalisme des spectres théoriques peut être amélioré en modélisant l'excitation et la visibilité des modes. Pour les étoiles qui nous concernent le principal mécanisme d'excitation est le κ mécanisme qui est lié à la présence d'un saut d'opacité dans l'étoile. Ce mécanisme est bien compris dans le cas à symétrie sphérique et il produit une gamme de modes instables que l'on peut utiliser ensuite pour définir l'intervalle de fréquences du spectre théorique. Pour faire de même avec des étoiles en rotation rapide, il faut un modèle d'étoile en rotation rapide qui prenne en compte la formation de saut d'opacité. Des modèles de ce type sont actuellement développés dans le cadre du projet ESTER. Une des questions essentielles à laquelle pourrait répondre une telle étude est la différence éventuelle entre l'excitation des modes d'îlots et des modes chaotiques. Le calcul de la visibilité des modes consiste à déterminer, pour une amplitude intrinsèque donnée, l'amplitude des perturbations de luminosité induite par le mode. Pour faire ce type de calculs, déjà réalisés pour

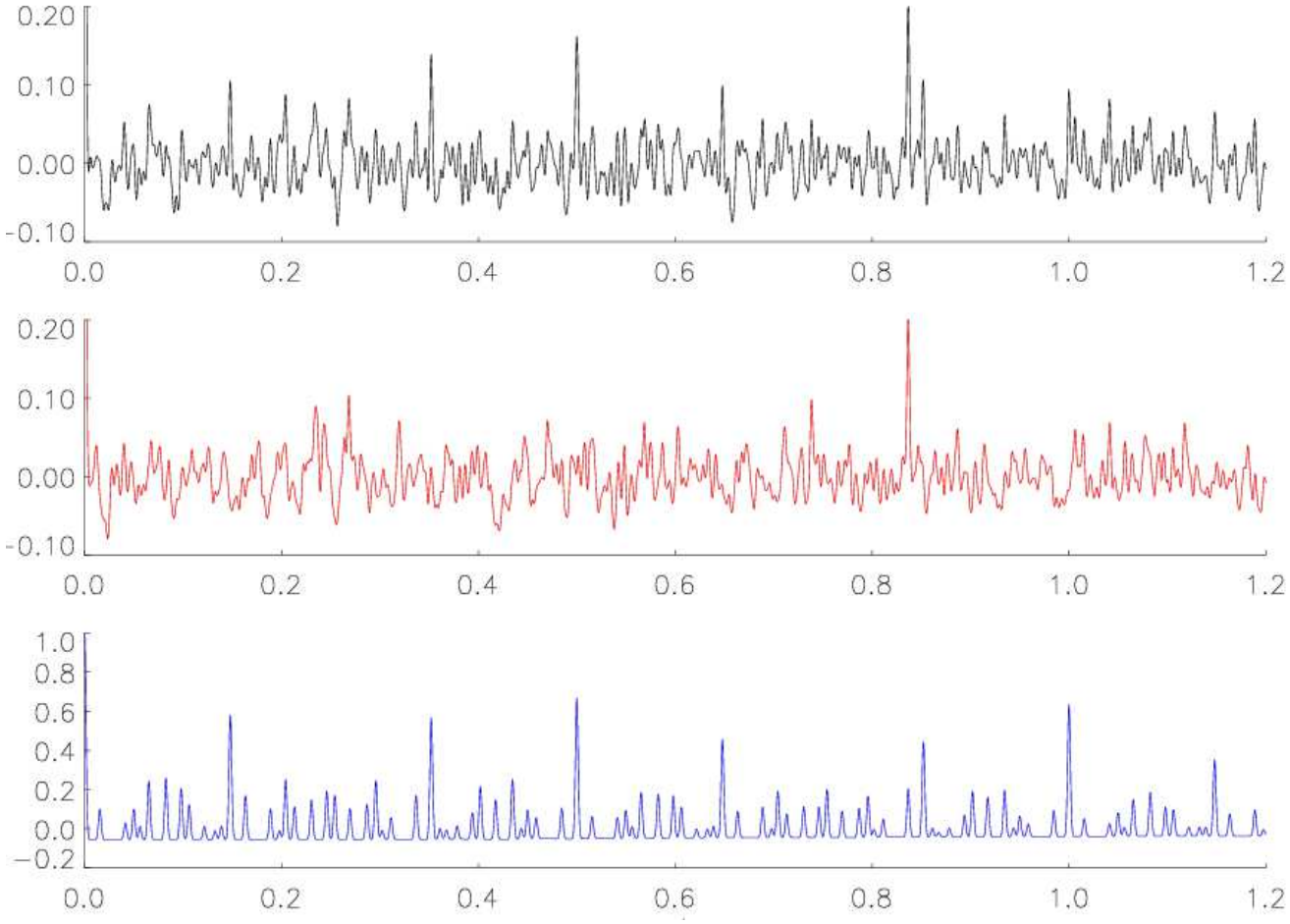

FIG. 5.1 – Autocorrélation d'un spectre asymptotique de modes-p résultant de la superposition d'un spectre de modes chaotiques et d'un spectre de modes d'îlots. La figure du haut représente l'autocorrélation du spectre entier alors que les figures du milieu et du bas montrent l'autocorrélation des spectres de modes chaotiques (en rouge) et d'îlots (en bleu). L'abscisse mesure le décalage en fréquence normalisé par l'équivalent de la grande différence Δ. Dans ce cas favorable où l'angle d'inclinaison est faible $i = 30°$, les principaux pics du spectre d'îlot (qui correspondent à des combinaisons linéaires entre δ_n et δ_ℓ - voir Eq. (2.13)) peuvent être facilement détectés dans le spectre total. On observe également un pic à 2Ω qui provient du spectre chaotique.

les étoiles à faible rotation, il faut un modèle d'étoile avec une atmosphère réaliste. Nous comptons, là encore, sur les modèles d'étoile issus du projet ESTER.

Finalement, le point dur de la modélisation des amplitudes dans le spectre théorique est la détermination des amplitudes intrinsèques des modes comme résultat d'un processus de saturation non-linéaire des modes excités par κ mécanisme. Des résultats récents obtenus dans notre équipe par T. Gastine et B. Dintrans montrent que la simulation numérique directe du κ mécanisme permet de simuler ce processus, au moins dans les conditions simples, géométrie cartésienne 1D, de ces simulations. Même si ces simulations ne sont pas réalistes pour une étoile, elles peuvent être utilisées pour tester les modèles de saturation faiblement non-linéaires (Gastine & Dintrans 2008). Ces modèles pourront alors être appliqués avec les mêmes hypothèses physiques à la saturation non-linéaire des modes non-radiaux d'étoiles.

5.1.3 Obtenir des contraintes supplémentaires sur les modes

Nous avons mentionné précédemment que la spectroscopie et la photométrie des étoiles pulsantes permettaient d'obtenir des contraintes supplémentaires sur l'identification des fréquences observées. Ces méthodes n'ont cependant été implémentées que pour le cas à symétrie sphérique et elles devront être adaptées si on veut les appliquer au cas des étoiles en rotation rapide. En particulier l'analyse des déformations des profils de raie suppose pour l'instant que la distribution de surface du mode est décrite par une seule harmonique sphérique. Dans un premier temps, il faudrait utiliser des données spectroscopiques pour montrer que cette hypothèse ne permet pas de reproduire les profils de raie observés dans le cas des étoiles en rotation rapide. Ensuite, on cherchera à améliorer la modélisation des profils de raie en utilisant, à la place des harmoniques sphériques, la distribution en surface des modes d'îlot ou des modes chaotiques. On peut d'ailleurs penser que la signature spectrale des modes chaotiques se distinguera facilement de celle des modes d'îlots, plus concentrés spatialement. La Figure 5.2 illustre un premier calcul dans cette direction effectué par D. Reese où l'on voit la déformation du profil de raie induit par un mode d'îlot ainsi que les limites de la modélisation de cette déformation par une seule harmonique sphérique.

5.1.4 Développer la théorie asymptotique des modes d'oscillation

De nombreux aspects de la théorie asymptotique restent à développer, d'une part en approfondissant la théorie asymptotique des modes acoustiques et d'autre part en construisant une théorie asymptotique

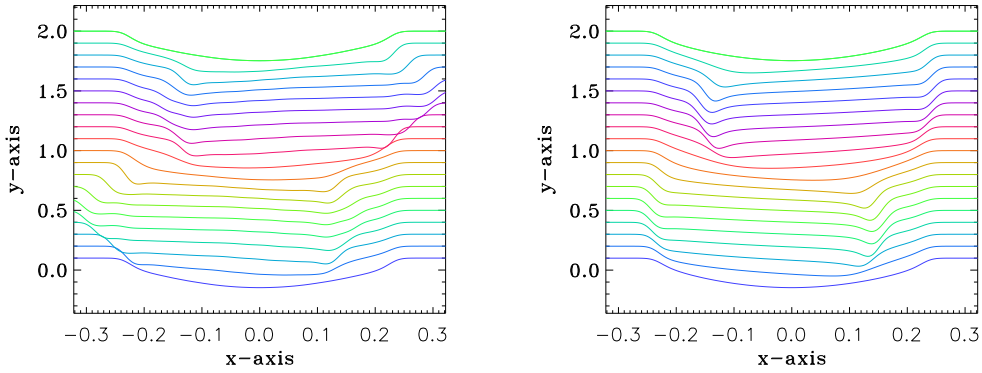

FIG. 5.2 – Variation temporelle d'un profil de raie d'absorption engendré par un mode d'îlot d'une étoile en rotation rapide (figure de gauche). L'abscisse décrit le décalage en vitesse radiale et l'évolution temporelle des profils au cours d'une période d'oscillation se lit de bas en haut. La rotation du modèle d'étoile est $\Omega = 0.3\Omega_K$ et l'angle d'inclinaison est $i = 60°$. La figure de droite montre les variations temporelles de profil que l'on obtiendrait si on cherchait à modéliser le mode d'îlot avec une seule harmonique sphérique.

pour les modes gravito-inertiels.

Dans le cadre de la thèse de Mickaël Pasek, nous étudions en détail la quantification des modes d'îlots proposée dans Lignières & Georgeot (2008, **A6**). Il s'agit de construire les solutions de type faisceau gaussien autour d'une orbite périodique stable, d'en déduire une formule de quantification de type Eq. (2.13), d'établir la façon dont les quantités potentiellement observables δ_n et δ_ℓ dépendent de la structure de l'étoile puis de confronter ces prédictions aux calculs numériques de modes. Par la suite nous chercherons également à étudier la visibilité des modes chaotiques en modélisant leur distribution spatiale par une superposition d'onde plane dont la direction du vecteur d'onde et la phase sont aléatoires (Bäcker 2007).

La première étape pour construire une théorie asymptotique des modes gravito-inertiels est de déterminer les propriétés de la dynamique des rayons associée. Les équations régissant cette dynamique ont été récemment dérivées au cours du stage de Master 2 de Vincent Prat (Prat 2010). L'équation iconale incluant les effets de la force de Coriolis, de la force centrifuge et la réfraction des ondes gravito-inertielles au voisinage de la surface de l'étoile prend la forme suivante dans le cas de modes axisymétriques dans un modèle polytropique d'étoile :

$$\omega^2 = f^2 \frac{{k_z}^2}{k^2 + {k_c}^2} + {N_0}^2 \frac{{k_\perp}^2}{k^2 + {k_c}^2} + f^2 \cos^2\Theta \frac{{k_c}^2}{k^2 + {k_c}^2} \quad \text{avec} \quad k_c^2 = \frac{\Gamma^2 \mu(\mu+2) g_0^2}{4(\mu+1)^2 c_s^4} \tag{5.1}$$

où k_z est la composante du vecteur d'onde parallèle à l'axe de rotation, $k_\perp$ est la composante perpendiculaire à la gravité effective $\vec{g}_0$, $f = 2\Omega$, Θ la pseudo-colatitude définie par $\cos\Theta = \vec{e}_z \cdot \vec{e}_{/\!/}$, où $\vec{e}_{/\!/}$ est un vecteur unitaire parallèle à gravité effective, et μ l'indice du polytrope. Le terme en k_c ne devient important que près de la surface où il provoque la réflexion des ondes. La Figure 5.3 donne l'exemple de deux rayons de gravité calculés à partir de cette équation iconale, respectivement dans le domaine super-inertiel $f < \omega < N_0$ et sub-inertiel $\omega < f$. La deuxième trajectoire correspond à une orbite périodique stable.

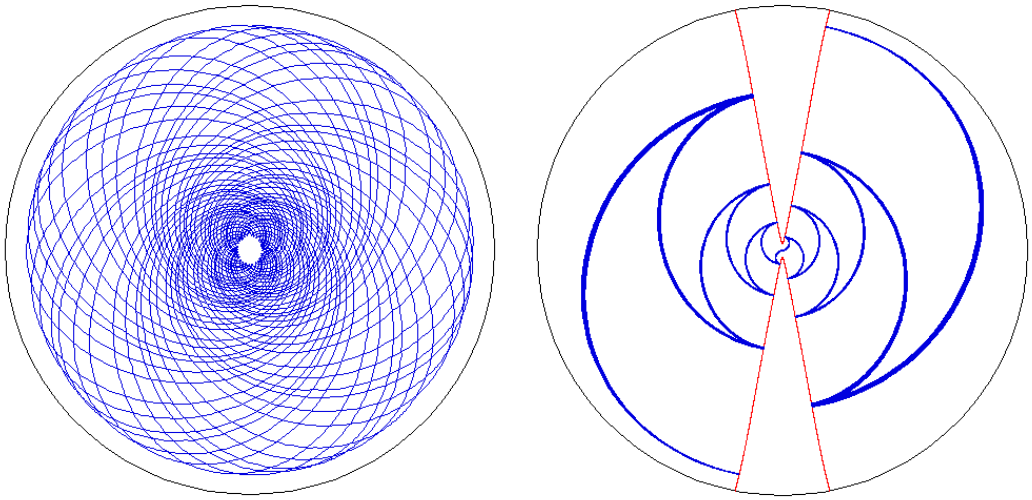

FIG. 5.3 – Trajectoires d'ondes gravito-inertielles dans le régime super-inertiel $f < \omega < N_0$ (à gauche) et sub-inertiel $\omega < f$ (à droite) décrites dans le cadre de l'approximation WKB. Les limites du domaine de propagation (en rouge) sont déterminées à partir de l'équation iconale (5.1). Les effets de l'accélération centrifuge sont négligés dans ce calcul.

À la différence de l'approche basée sur les caractéristiques (Dintrans & Rieutord 2000), la dynamique des rayons est ici Hamiltonienne ce qui interdit l'apparition d'attracteurs dans l'espace des phases. La différence entre ces deux approches est due au fait que les effets de surface assurant la réfraction des ondes gravito-inertiels ne peuvent pas être pris en compte dans le formalisme des caractéristiques. Dans Dintrans & Rieutord (2000), la réflexion des ondes à la surface de l'étoile a donc été modélisée par une réflexion sur une surface rigide, ce qui détruit le caractère Hamiltonien des équations régissant les caractéristiques.

Les premières sections de Poincaré de la dynamique des rayons gravito-inertiels indiquent de nouveau que la dynamique devient mixte avec la rotation. On constate néanmoins que la force de Coriolis tend

à la stabiliser dans le régime sub-inertiel $\omega < f$. D'après notre expérience avec les modes acoustiques, nous pouvons nous attendre à ce que les propriétés du système dynamique permettent de comprendre l'organisation du spectre de fréquences et la classification physique des modes gravito-inertiels. En collaboration avec M.A Dupret (Université de Liège), nous allons également utilisé la dynamique des rayons pour tester la validité de l'approximation dite traditionnelle pour décrire les ondes gravito-inertielles de basse fréquence.

5.2 Magnétisme stellaire

Des programmes d'observations doivent être réalisés pour caractériser d'une part le nouveau type de magnétisme mis en évidence par le champ de Véga et d'autre part le champ critique des Ap (travail en collaboration avec P. Petit, T. Böhm, M. Aurière, G. Wade). Le scénario que je propose pour expliquer le désert magnétique entre le champ critique des Ap et celui de Véga sera également confronté à une modélisation plus détaillée.

5.2.1 Programmes d'observation

Des programmes sont déjà en cours avec Narval et Espadons pour préciser les propriétés du champ magnétique de Véga (sa topologie et sa possible variabilité intrinsèque) et pour confirmer la présence d'un champ magnétique à la surface de Sirius. Au delà de ces deux objets parmi les plus brillants du ciel, le temps d'observation nécessaire à la détection d'un champ d'amplitude similaire à celui de Véga devient rapidement un facteur limitant. Dans la gamme des étoiles Am quelques cibles de magnitude ~ 2 restent encore facilement accessibles et nous avons d'ailleurs déjà fait une demande pour observer deux objets de ce type (β UMa et γ Gem). L'un deux a déjà été partiellement observé par Narval en 2010. En revanche, pour observer dans ces conditions des étoiles A normales à raie étroite du type de Véga, il faudrait de l'ordre de 45 heures de temps télescope au CFHT (39 h pour l'étoile β Psa de magnitude 4.3 et 56 h pour ν Cap dont la magnitude est 4.75). L'exploration de cette nouvelle classe d'étoile magnétique nécessitera donc des moyens dédiés comme les Large Program du TBL ou du CFHT. À plus long terme, la mise en place d'un spectropolarimètre de type Espadons/Narval sur des télescopes de plus grandes tailles (8m) permettrait un relevé spectropolarimétrique plus profond dans cette gamme de masse.

De l'autre côté du désert magnétique, le champ minimum des étoiles Ap et en particulier la façon dont il dépend des paramètres stellaires doit être précisé. Dans Aurière et al. (2007, **A8**), nous avons constaté sur quelques exemples que le champ minimum des étoiles Ap semble augmenter avec la rotation. C'est un comportement attendu dans le cadre du scénario proposé pour le champ critique des Ap et cela correspond également à l'expression du champ critique déterminée à partir d'un critère local $B_c \propto \Omega$. Mais pour confirmer cette tendance et préciser la forme de la relation entre B_c et Ω, je compte mener, en collaboration avec M. Aurière, un relevé spectropolarimétrique des étoiles Ap à fort $v \sin i$ et à champ faible (à noter que la modulation rotation du signal polarimétrique donne une accès direct à Ω). Ces nouvelles observations sont nécessaires car ces objets n'ont généralement pas été considérés dans les précédents relevés des étoiles Ap, l'élargissement Doppler des raies associé au fort $v \sin i$ augmentant le seuil de détection du champ magnétique. La relation empirique entre B_c et Ω constituera une contrainte forte pour les modèles du magnétisme des étoiles de masse intermédiaire. De même, les premières détections de champ magnétique dans les étoiles massives suggèrent l'existence d'une classe d'étoile magnétique similaire à celle des Ap/Bp puisque le champ y est fort, dominé par les grandes échelles et stable dans le temps. Une relation entre B_c et Ω est plus difficile à établir dans cette gamme de masse puisque le seuil de détection des champs par spectropolarimétrie y est plus haut (notamment parce que le nombre de raie spectrale est plus faible dans ces étoiles) et que l'on ne dispose pas d'un indicateur simple comme les anomalies d'abondance pour distinguer les étoiles magnétiques. Néanmoins, le résultat des relevés systématiques engagés dans le Large Program Mimes du CFHT permettra une première estimation de cette relation que l'on pourra éventuellement préciser avec des observations dédiées.

5.2.2 Modélisation du désert magnétique des étoiles A

Il s'agit ici d'une part de préciser le champ magnétique critique d'une étoile en deçà duquel la rotation différentielle conduit à une instabilité de la configuration magnétique et d'autre part de déterminer le champ longitudinal typique des configurations magnétiques instables. Dans un premier temps, nous réaliserons des simulations bidimensionnelles d'un champ magnétique axisymétrique initialement dipolaire en présence d'une rotation différentielle ; l'objectif de ces simulations est d'étudier la compétition entre l'advection du champ par rotation différentielle et l'établissement de la loi de Ferraro pour différentes valeurs de l'amplitude du champ et de la rotation initiales. Dans le régime à champ faible, les simulations 2D produiront des configurations dominées par un champ toroïdal et nous étudierons alors

la stabilité de ces configurations par des simulations 3D. Outre la détermination du champ critique, ce projet nous permettra de calculer le champ longitudinal à partir des simulations numériques du développement de l'instabilité de Tayler. On obtiendra ainsi un estimation théorique de l'écart entre ce champ et le champ minimum des configurations stables que l'on comparera aux observations du désert magnétique des étoiles A.

5.3 Transport turbulent dans les zones radiatives d'étoile

L'objectif est ici de tester et d'améliorer les expressions des coefficients de transport turbulents utilisés dans les modèles d'évolution stellaires (Zahn 1992). Au cours des 4 dernières années, j'ai développé différents outils pour aborder ce problème (code numérique, limite asymptotique des équations adaptée à l'étude numérique de ce problème, modèles phénoménologiques du transport) dont je compte maintenant tirer pleinement profit pour réaliser et analyser des simulations numériques intensives de ce processus. Je propose d'ailleurs un sujet de thèse sur cette thématique pour l'année 2010.

5.4 Chaos d'onde

La configuration où une étoile est vue presque depuis le pôle est favorable pour la mise en évidence des propriétés statistiques génériques des fréquences chaotiques. Cette configuration permet également de significativement simplifier l'identification des modes puisque la visibilité des modes non-axisymétriques s'annule. Je compte lancer avec T. Böhm un programme de recherche d'étoiles pulsantes en rotation rapide vue presque du pôle. Pour détecter les rotateurs rapides parmi un échantillon d'étoiles δ Scuti à faible $v \sin i$, nous comptons utiliser les signatures spectrales de l'assombrissement gravitationnel induit par la force centrifuge. L'exemple de Véga (Takeda et al. 2008) montre l'effet induit sur la forme des profils de raie. Nous comptons mettre à profit cet effet pour détecter les rotateurs rapides parmi un échantillon d'étoiles δ Scuti à faible $v \sin i$. Il faudra pour cela obtenir des spectres à très haut S/N (~ 1000) des cibles choisies.

Bibliographie

Aerts, C., Thoul, A., Daszyńska, J., et al. 2003, Science, 300, 1926

Aurière, M., Donati, J., Konstantinova-Antova, R., et al. 2010, A&A, sous presse, [arXiv :1005.4845]

Aurière, M., Wade, G. A., Konstantinova-Antova, R., et al. 2009, A&A, 504, 231

Aurière, M., Wade, G. A., Lignières, F., et al. 2010, soumis à A&A

Aurière, M., Wade, G. A., Silvester, J., et al. 2007, A&A, 475, 1053

Babcock, H. W. 1947, ApJ, 105, 105

Bäcker, A. 2007, European Physical Journal Special Topics, 145, 161

Ballot, J., Lignières, F., Reese, D. R., & Rieutord, M. 2009, in Proc. HELAS Workshop on 'New insights into the Sun', Ponte de Lima, Portugal, ed. M.S. Cunha & M.J. Thompson, [arXiv :0912.1679]

Ballot, J., Lignières, F., Reese, D. R., & Rieutord, M. 2010, A&A, sous presse, [arXiv :1005.0275]

Ballot, J., Turck-Chièze, S., & García, R. A. 2004, A&A, 423, 1051

Benomar, O., Baudin, F., Campante, T. L., et al. 2009, A&A, 507, L13

Berry, M. V. & Robnik, M. 1984, Journal of Physics A Mathematical General, 17, 2413

Bohlender, D. A. & Landstreet, J. D. 1990, MNRAS, 247, 606

Braithwaite, J. 2009, MNRAS, 397, 763

Breger, M., Lenz, P., Antoci, V., et al. 2005, A&A, 435, 955

Brown, S. F., Donati, J., Rees, D. E., & Semel, M. 1991, A&A, 250, 463

Brun, A. S. & Toomre, J. 2002, ApJ, 570, 865

Brun, A. S. & Zahn, J. 2006, A&A, 457, 665

Burke, K., Reese, D. R., & Thomspon, M. 2010, en préparation

Charpinet, S., van Grootel, V., Reese, D., et al. 2008, A&A, 489, 377

Christensen-Dalsgaard, J. 2002, Reviews of Modern Physics, 74, 1073

Christensen-Dalsgaard, J. & Mullan, D. J. 1994, MNRAS, 270, 921

Clement, M. J. 1981, ApJ, 249, 746

Clement, M. J. 1984, ApJ, 276, 724

Clement, M. J. 1986, ApJ, 301, 185

Clement, M. J. 1989, ApJ, 339, 1022

Clement, M. J. 1998, ApJS, 116, 57

Degroote, P., Aerts, C., Baglin, A., et al. 2010, Nature, 464, 259

Deheuvels, S., Bruntt, H., Michel, E., et al. 2010, A&A, sous presse, [arXiv :1003.4368]

Desmet, M., Briquet, M., Thoul, A., et al. 2009, MNRAS, 396, 1460

Dintrans, B. & Rieutord, M. 2000, A&A, 354, 86

Dintrans, B., Rieutord, M., & Valdettaro, L. 1999, Journal of Fluid Mechanics, 398, 271

Domiciano de Souza, A., Kervella, P., Jankov, S., et al. 2003, A&A, 407, L47

Donati, J. & Landstreet, J. D. 2009, ARA&A, 47, 333

Dupret, M., De Ridder, J., De Cat, P., et al. 2003, A&A, 398, 677

Dupret, M., Thoul, A., Scuflaire, R., et al. 2004, A&A, 415, 251

Font, J. A., Stergioulas, N., & Kokkotas, K. D. 2000, MNRAS, 313, 678

García Hernández, A., Moya, A., Michel, E., et al. 2009, A&A, 506, 79

Gastine, T. & Dintrans, B. 2008, A&A, 490, 743

Gough, D. O. 1990, in Progress of Seismology of the Sun and Stars, ed. Y. Osaki & H. Shibahashi (Lecture Notes in Physics, Springer), 283

Gough, D. O. 2007, Astronomische Nachrichten, 328, 273

Gutzwiller, M. C. 1990, Chaos in classical and quantum mechanics (Springer)

Haq, R. U., Pandey, A., & Bohigas, O. 1982, Physical Review Letters, 48, 1086

Ipser, J. R. & Lindblom, L. 1990, ApJ, 355, 226

Kallinger, T. & Matthews, J. M. 2010, ApJ, 711, L35

Kennelly, E. J. 1994, PhD thesis, University of British Columbia

Lebreton, Y. 2000, ARA&A, 38, 35

Lignières, F. 1999, A&A, 348, 933

Lignières, F. 2004, in SF2A-2004 : Semaine de l'Astrophysique Francaise, ed. F. Combes, D. Barret, T. Contini, F. Meynadier, & L. Pagani, 237

Lignières, F., Califano, F., & Mangeney, A. 1998, Geophysical and Astrophysical Fluid Dynamics, 88, 81

Lignières, F., Califano, F., & Mangeney, A. 1999, A&A, 349, 1027

Lignières, F., Califano, F., & Mangeney, A. 2000, Computer Physics Communications, 132, 197

Lignières, F., Catala, C., & Mangeney, A. 1996, A&A, 314, 465

Lignières, F., Catala, C., & Mangeney, A. 2000, [arXiv :0002026]

Lignières, F. & Georgeot, B. 2008, Phys. Rev. E, 78, 016215

Lignières, F. & Georgeot, B. 2009, A&A, 500, 1173

Lignières, F., Georgeot, B., & Ballot, J. 2010, IV International Helas conference proceedings, submitted to Astronomical Notes

Lignières, F., Petit, P., Böhm, T., & Aurière, M. 2009, A&A, 500, L41

Lignières, F. & Rieutord, M. 2004, in Stellar Rotation, IAU Symposium, 215, ed. A. Maeder & P. Eenens (Astronomical Society of the Pacific), 414

Lignières, F., Rieutord, M., & Reese, D. 2006, A&A, 455, 607

Lignières, F., Rieutord, M., & Valdettaro, L. 2001, in SF2A-2001 : Semaine de l'Astrophysique Francaise, ed. F. Combes, D. Barret, & F. Thévenin, 127

Lignières, F., Toqué, N., & Vincent, A. 2005, in Elements Stratification in Stars : 40 years of Atomic Diffusion, ed. G. Alecian, O. Richard, & S. Vauclair (EAS Publications Series, EDP Sciences), 209–214

Lignières, F. 2010, in Pulsations du Soleil et des étoiles, ed. J.-P. Rozelot & C. Neiner (Lecture Notes in Physics, Springer, sous presse)

MacDonald, J. & Mullan, D. J. 2004, MNRAS, 348, 702

Maeder, A. & Meynet, G. 2000, ARA&A, 38, 143

Michaud, G. 2004, in The A-Star Puzzle, IAU Symposium 224, ed. J. Zverko, J. Ziznovsky, S. J. Adelman, & W. W. Weiss (Cambridge University Press), 173–183

Michaud, G. & Zahn, J. 1998, Theoretical and Computational Fluid Dynamics, 11, 183

Nordlund, Å., Stein, R. F., & Asplund, M. 2009, Living Reviews in Solar Physics, 6, 2

Ott, E. 1993, Chaos in dynamical systems (Cambridge University Press)

Ouazzani, R., Goupil, M., Dupret, M., & Reese, D. 2009, Communications in Asteroseismology, 158, 283

Percival, I. C. 1973, Journal of Physics B Atomic Molecular Physics, 6, L229

Peterson, D. M., Hummel, C. A., Pauls, T. A., et al. 2006, Nature, 440, 896

Pinsonneault, M. 1997, ARA&A, 35, 557

Prat, V. 2010, Rapport de stage de Master 2, http ://www.ast.obs-mip.fr/users/ligniere/Rapport-Prat.pdf

Reese, D. 2006, PhD thesis, Université Toulouse III - Paul Sabatier

Reese, D., Lignières, F., & Rieutord, M. 2006, A&A, 455, 621

Reese, D., Lignières, F., & Rieutord, M. 2008, A&A, 481, 449

Reese, D. R., MacGregor, K. B., Jackson, S., Skumanich, A., & Metcalfe, T. S. 2009, A&A, 506, 189

Rieutord, M., Ludwig, H., Roudier, T., Nordlund, ., & Stein, R. 2002, Nuovo Cimento C Geophysics Space Physics C, 25, 523

Rincon, F., Lignières, F., & Rieutord, M. 2005, A&A, 430, L57

Roudier, T. 2004, Tree of Fragmenting Granules in solar observations and simulations (private communication)

Roudier, T., Lignières, F., Rieutord, M., Brandt, P. N., & Malherbe, J. M. 2003, A&A, 409, 299

Saad, Y. 1992, Numerical Methods for Large Eigenvalue Problems (Manchester University Press)

Schumacher, J. 2001, Journal of Fluid Mechanics, 441, 109

Shorlin, S. L. S., Wade, G. A., Donati, J., et al. 2002, A&A, 392, 637

Spruit, H. C. 1999, A&A, 349, 189

Spruit, H. C. 2002, A&A, 381, 923

Suàrez, J., Goupil, M., Reese, D., et al. 2010, soumis à A&A

Takeda, Y., Kawanomoto, S., & Ohishi, N. 2008, ApJ, 678, 446

Tassoul, M. 1980, ApJS, 43, 469

Thoul, A., Aerts, C., Dupret, M. A., et al. 2003, A&A, 406, 287

Toqué, N., Lignières, F., & Vincent, A. 2006, Geophysical and Astrophysical Fluid Dynamics, 100, 85

Valdettaro, L., Rieutord, M., Braconnier, T., & Fraysse, V. 2007, Journal of Computational and Applied Mathematics, 205, 382

Voller, V. R. & Porté-Agel, F. 2002, Journal of Computational Physics, 179, 698

Vorontsov, S. V. 1988, in Advances in Helio- and Asteroseismology, IAU Symposium 123, ed. J. Christensen-Dalsgaard & S. Frandsen (Reidel), 151

Wigner, E. 1932, Physical Review, 40, 749

Winget, D. E., Nather, R. E., Clemens, J. C., et al. 1991, ApJ, 378, 326

Zahn, J. 1992, A&A, 265, 115

Zima, W. 2006, A&A, 455, 227

Table des figures

Annexe A

Différentes formulations des équations d'onde dans les étoiles

On écrit ici différentes formulations possibles des équations décrivant l'évolution linéarisée de petites perturbations adiabatiques autour d'un modèle d'étoile en se restreignant au cas d'une étoile non magnétique, en rotation uniforme dont les perturbations sont adiabatiques et non affectées par la viscosité. La forme initiale de ces équations est le système d'équation (2.1), (2.2), (2.3), (2.4), présenté à la Sect. 2.1.1.

En négligeant l'accélération de Coriolis, ce système peut être réécrit de la façon suivante :

$$\partial_{tt}^2 \vec{u} \cdot \vec{g}_0 = \vec{g}_0 \cdot \vec{\nabla} \left(c_s^2 \chi + \vec{u} \cdot \vec{g}_0 - \partial_t \psi \right) - \chi \vec{g}_0 \cdot \vec{A}_0 \tag{A.1}$$

$$\partial_{tt}^2 \chi = \Delta (c_s^2 \chi + \vec{u} \cdot \vec{g}_0 - \partial_t \psi) - \vec{\nabla} \cdot (\chi \vec{A}_0) \tag{A.2}$$

$$\Delta \partial_t \psi = -4\pi G \left(\vec{u} \cdot \vec{\nabla} \rho_0 + \rho_0 \chi \right) \tag{A.3}$$

où le nombre de variables dépendantes a été réduit de six, $\vec{u}$, ρ, P, Ψ, à trois, $\vec{u} \cdot \vec{g}_0$, $\chi = \vec{\nabla} \cdot \vec{u}$, ψ et où le système peut toujours être mis sous une forme, (2.5) avec $\lambda = -\omega^2$, adaptée à la méthode de résolution du problème discrétisé que nous avons utilisée. Le vecteur $\vec{A}_0$ dépend de la structure de l'étoile et est défini par $\vec{A}_0 = (c_s^2 N_0^2 / \|\vec{g}_0\|) \vec{n}_0$, où N_0 est la fréquence de Brunt-Väisälä et $\vec{n}_0$ est un vecteur unitaire dans la direction opposée à la gravité effective $\vec{g}_0 = -\|\vec{g}_0\| \vec{n}_0$. Le détail de la dérivation peut être trouvé

dans Lignières et al. (2006, **A1**).

Si on se restreint maintenant au solution harmonique en temps $\propto \exp(-i\omega t)$ et que l'on néglige, en plus de l'accélération de Coriolis, les perturbations de potentiel gravitationnel ψ (approximation de Cowling), on peut se ramener à une équation pour une seule variable dépendante :

$$\frac{\omega_c^2-\omega^2}{c_s^2}\hat{\Psi}+\frac{N_0^2}{\omega^2}[\Delta-\frac{1}{g_0^2}(\vec{g_0}\cdot\vec{\nabla})(\vec{g_0}\cdot\vec{\nabla})]\hat{\Psi}=\Delta\hat{\Psi} \tag{A.4}$$

où $\hat{\Psi}=\hat{P}/\alpha$, $\hat{P}$ est l'amplitude complexe associée aux perturbations de pression $P=\Re\{\hat{P}\exp(-i\omega t)\}$ et α dépend de la structure de l'étoile et est donné par

$$\vec{\nabla}\alpha=\frac{B}{2c_s^2}\alpha\vec{g}_0. \tag{A.5}$$

où

$$B=1+\frac{c_s^2N_0^2}{g_0^2}-c_s^2\vec{\nabla}\cdot\left(\frac{(1-f_p)\vec{g}_0}{f_pg_0^2}\right) \tag{A.6}$$

avec

$$f_p=1-\frac{N_0^2}{\omega^2}. \tag{A.7}$$

La fréquence de coupure ω_c est donnée par

$$\omega_c^2=\frac{g_0^2B^2}{4c_s^2}+c_s^2f_p\vec{\nabla}\cdot(\frac{\vec{g}_0}{c_s^2f_p})-\frac{c_s^2}{2}\vec{\nabla}\cdot(\frac{B\vec{g}_0}{c_s^2})+\frac{(1-f_p)}{2}Bg_0^2\vec{\nabla}\cdot(\frac{\vec{g}_0}{g_0^2}), \tag{A.8}$$

Le détail de la dérivation peut être trouvé dans Lignières & Georgeot (2009, **A7**). L'équation (A.4) rend compte à la fois des ondes de gravité et des ondes sonores dans les étoiles éventuellement déformées par la force centrifuge. Pour les ondes sonores de haute fréquence, les hypothèses qui ont permis de l'obtenir sont justifiées (à l'exception de l'hypothèse d'adiabaticité dans les couches situées au voisinage de la surface). Ce n'est en revanche pas le cas pour les ondes de gravité dans les étoiles en rotation rapide notamment parce qu'elles sont affectées de façon significative par la force de Coriolis.

Récemment une équation plus générale a été obtenue au cours du stage de Master 2 de V. Prat en incluant les effets de la force de Coriolis. Son expression pour les modes axisymétriques est la suivante :

$$D\Delta\hat{\Psi} - (\omega^2 - f^2 - {N_0}^2)\vec{f}\cdot\vec{\nabla}(\vec{f}\cdot\vec{\nabla}\hat{\Psi}) + \frac{{N_0}^2\omega^2}{{g_0}^2}\vec{g_0}\cdot\vec{\nabla}(\vec{g_0}\cdot\vec{\nabla}\hat{\Psi}) \tag{A.9}$$

$$-\frac{{N_0}^2}{{g_0}^2}(\vec{f}\cdot\vec{g_0})[\vec{g_0}\cdot\vec{\nabla}(\vec{f}\cdot\vec{\nabla}\hat{\Psi}) + \vec{f}\cdot\vec{\nabla}(\vec{g_0}\cdot\vec{\nabla}\hat{\Psi})] + C\hat{\Psi} = 0 \tag{A.10}$$

où $\hat{\Psi} = \hat{P}/a$, la fonction a vérifiant

$$\vec{\nabla}a = \quad \frac{a\vec{Q}}{4G{c_s}^2 D} \tag{A.11}$$

et les termes D, C, Q et G sont définis par :

$$D = \quad \omega^4 - \omega^2(f^2 + {N_0}^2) + \frac{{N_0}^2(\vec{f}\cdot\vec{g_0})^2}{{g_0}^2} \tag{A.12}$$

$$C = \quad \frac{D}{4G}\left[\vec{\nabla}\cdot\left(\frac{\vec{Q}}{{c_s}^2 D}\right) + \frac{Q^2}{4G{c_s}^4 D^2}\right] + \frac{{N_0}^2\omega^2}{4G{g_0}^2}\left[\vec{g_0}\cdot\vec{\nabla}\left(\frac{\vec{g_0}\cdot\vec{Q}}{{c_s}^2 D}\right) + \frac{(\vec{g_0}\cdot\vec{Q})^2}{4G{c_s}^4 D^2}\right] \tag{A.13}$$

$$-\frac{\omega^2 - f^2 - {N_0}^2}{4G}\left[\vec{f}\cdot\vec{\nabla}\left(\frac{\vec{f}\cdot\vec{Q}}{{c_s}^2 D}\right) + \frac{(\vec{f}\cdot\vec{Q})^2}{4G{c_s}^4 D^2}\right] \tag{A.14}$$

$$-\frac{{N_0}^2(\vec{f}\cdot\vec{g_0})}{4G{g_0}^2}\left[\vec{f}\cdot\vec{\nabla}\left(\frac{\vec{g_0}\cdot\vec{Q}}{{c_s}^2 D}\right) + \vec{g_0}.\vec{\nabla}\left(\frac{\vec{f}\cdot\vec{Q}}{{c_s}^2 D}\right) + \frac{2(\vec{f}\cdot\vec{Q})(\vec{g_0}\cdot\vec{Q})}{4G{c_s}^4 D^2}\right] \tag{A.15}$$

$$+\frac{[(\vec{f}\cdot\vec{g_0})N + \frac{\alpha}{2}(\vec{f}\cdot\vec{\nabla}K)]}{4G{c_s}^2\omega^2}\frac{\vec{f}\cdot\vec{Q}}{{c_s}^2 D} - \frac{N}{4G{c_s}^2}\frac{\vec{g_0}\cdot\vec{Q}}{{c_s}^2 D} + \frac{M}{{c_s}^2\omega^2} \tag{A.16}$$

$$\vec{Q} = \quad \left[2ND + \alpha_0\frac{{N_0}^2}{{g_0}^2}(\vec{f}\cdot\vec{g_0})\vec{f}\cdot\vec{\nabla}K\right]\vec{g_0} - \alpha_0\omega^2(\vec{f}\cdot\vec{\nabla}K)\vec{f} \tag{A.17}$$

$$G = \quad \omega^2(\omega^2 - f^2) \tag{A.18}$$

avec

$$\alpha_0 = \quad \frac{{c_s}^2{N_0}^2}{{g_0}^2} \tag{A.19}$$

$$K = \quad (\vec{f}.\vec{g_0})^2 - \omega^2{g_0}^2 = \vec{F}.\vec{g_0} \tag{A.20}$$

$$M = \quad G\left[G + {c_s}^2 D\vec{\nabla}.\left(\frac{\vec{F}}{{c_s}^2 D}\right)\right] \tag{A.21}$$

$$N = \quad (1+\alpha_0)G + {c_s}^2 D\vec{\nabla}\left(\frac{\alpha_0\vec{F}}{{c_s}^2 D}\right) \tag{A.22}$$

$$\vec{F} = \quad (\vec{f}\cdot\vec{g_0})\vec{f} - \omega^2\vec{g_0} \tag{A.23}$$

Nous avons utilisé ces équations d'ondes réduites à une variable Ψ pour appliquer l'approximation WKB. À l'ordre dominant du développement WKB Eq. (2.9), on obtient une équation iconale qui prend une forme simplifiée lorsque l'on se place dans le domaine de fréquence $\omega = \mathcal{O}(\Lambda)$ des ondes acoustiques

Eq. (2.10) ou dans celui $\omega = \mathcal{O}(1)$ des ondes de gravité Eq. (5.1). La dynamique des rayons est alors construite comme la recherche de solutions de l'équation iconale le long d'un chemin particulier.

Annexe B

CURRICULUM VITAE

Chargé de Recherche 1ère Classe au CNRS depuis Octobre 2000

Adresse

Observatoire Midi-Pyrénées, UMR 5572, 14, Avenue Edouard Belin

31400 TOULOUSE

E-mail : Francois.Lignieres@ast.obs-mip.fr

Tel : 05.61.33.28.98

Fax : 05.61.33.28.40

Etat civil

Né le 18.10.1966 à Paris

Nationalité française

Marié, trois enfants

FORMATION

1993-1997 Thèse à l'Observatoire de Meudon obtenue le 7 juillet 1997
avec Mention TH et félicitations du jury
Titre : Distribution et évolution du moment cinétique
des étoiles pré-séquence-principale de masse intermédiaire
Co-directeurs : MM. André Mangeney et Claude Catala

1990-1991 D.E.A. Astrophysique et Techniques Spatiales de l'Université Paris 7, Juin 1991

1987-1990 Ecole Centrale Paris, Juin 1990

1984-1987 Classes préparatoires au Lycée Louis-Le-Grand (Paris)

LANGUES

Anglais (courant), Espagnol (courant)

SEJOURS À l'ETRANGER

1998-2000 Postdoc au Queen Mary and Westfield College - Londres

1991-1993 Ingénieur d'affaires dans l'entreprise Cegelec Mexico - Mexique

DOMAINES DE COMPÉTENCE

- Dynamique des fluides astrophysiques
- Astérosismologie
- Simulations numériques multi-dimensionnelles
- Observations en spectro et spectro-polarimétrie stellaire

PRINCIPAUX RÉSULTATS SCIENTIFIQUES

Mes travaux visent à mieux comprendre l'influence de la rotation, du champ magnétique et de la turbulence sur la structure et l'évolution des étoiles. Mes principaux résultats concernent :

(i) La sismologie des étoiles en rotation rapide : Calcul et théorie asymptotique des modes acoustiques.

(ii) Le magnétisme des étoiles de masse intermédiaire : découverte d'un nouveau type de magnétisme (le champ de Véga) et modélisations de la limite inférieure du champ des étoiles Ap et de l'activité des étoiles de Herbig.

(iii) La turbulence dans les intérieurs stellaires : parallélisation et évolution du code MHD Balaïtous, simulations numériques et modélisation du transport turbulent dans les atmosphères stratifiées de façon stable et les zones radiatives d'étoile, simulations numériques et analyse des données de la convection thermique à la surface du Soleil.

(iv) La physique des ondes : première mise en évidence théorique du chaos d'onde dans un système naturel à grande échelle (les étoiles en rotation rapide).

ENCADREMENT DE THESE

- N. Toqué : thèse en co-tutelle entre l'Université de Montréal (A. Vincent) et l'Université Paris 6, soutenue en 2004

- F. Rincon : thèse de l'UPS, participation à l'encadrement, soutenue en 2004

- D. Reese : thèse de l'UPS en co-encadrement avec M. Rieutord, soutenue en 2006

- M. Pasek : thèse de l'UPS en co-encadrement avec B. Georgeot, débutée en 2009

ENSEIGNEMENT, FORMATION

- Cours et T.P. de méthodes numériques en M2 Astro (11h/an depuis 2007)

- T.P. de physique statistique à Supaero (6h/an depuis 2005)

- Intérrogateur de physique-chimie en classes préparatoires (60h/an depuis 2003)

- Chargé de cours au Queen Mary and Westfield College (60h/an de 1998 à 2000)

- Intérrogateur de mathématiques en classes préparatoires (60h/an de 1988 à 1991)

- Cours sur la sismologie stellaire à l'école de St Flour, France (2008)

- Cours "Computational Stellar Fluid Dynamics" à l'école F. Lucchin, Italie (2009)

ANIMATION SCIENTIFIQUE

- Projet ANR Siroco - responsable du noeud toulousain

- Elaborations de projets de recherche (demandes de temps de calculs IDRIS/CALMIP, de temps d'observations NARVAL/ESPADONS, demandes PNPS, ANR JC, ACI, ATI, Postes Rouges, Prof. et MdC invités, BQR ...).

- Maintenance du code MHD cartésien Balaïtous.

MANAGEMENT DE LA RECHERCHE

- Membre du CS de l'Observatoire Midi-Pyrénées (depuis 2009)

- Membre du CS du PNPS (2007-2010)

- Membre du CS du PNST (2006-2009)

- Membre du Comité d'allocation de temps d'observation du CFHT (2007-2009)
- Membre du Comité d'allocation de temps de calcul du mésocentre CALMIP (2005-2008)
- Membre suppléant de la CSE 34 (2007-2008)
- Au laboratoire (membre du CL depuis 2008, correspondant Europe, commission bibliothèque).

Annexe C

Liste de publications

C.1 Publications dans des revues avec comité de lecture

1. **Lignières, F.**, Catala, C. and Mangeney, A., Angular momentum transfer in pre-main-sequence stars of intermediate mass, Astronomy and Astrophysics **314**, 465-476, 1996
2. **Lignières, F.**, Califano, F., Mangeney, A., "Stress-driven mixed layer in a stably stratified fluid", Geophys. Astrophys. Fluid Dyn. , 88, 81-113, 1998
3. **Lignières, F.**, "The small-Péclet-number approximation in radiative stellar zones", A&A, 348, 933-939, 1999
4. **Lignières, F.**, Califano, F., Mangeney, A., "Shear layer instability in a highly diffusive stably stratified atmosphere", A&A, 349, 1027-1036, 1999
5. **Lignières, F.**, Califano, F. and Mangeney, A., "A numerical study of the evolution of a mixed layer in a stably stratified fluid", Computer Physics Communication 132, 197-223, 2000.
6. Lastennet, E., **Lignières, F.**, Buser, R. Lejeune, T. Lüftinger, T. Cuisinier, F. van't Veer-Menneret, C., "Exploration of the BaSeL stellar library for 9 F-type stars COROT potential targets. Comparisons of fundamental stellar parameter determinations", A&A 365, 535-544, 2001.
7. Lastennet, E., **Lignières, F.**, F. Buser, R. Lejeune, T. Lüftinger, T. Cuisinier, F. van't Veer-Menneret, C., "Preparation of the COROT mission : fundamental stellar parameters from photometric and spectroscopic analyses of target candidates", The Journal of Astronomical Data 7, 23-37, 2001

8. Bruntt, H., Catala, C., Garrido, R., Rodriguez, E., Bouret, J.-C., Hua, T., **Lignières, F.**, Charpinet, S., Van't, Veer-menneret, C., Ballereau, D., "Abundance analysis of the gamma Dor star HD 49434", A&A, 389, 345-354, 2002.

9. Roudier, Th., **Lignières, F.**, Rieutord, M., Brandt, P.N., Malherbe ,J.M., "Families of fragmenting granules and their relation to meso and supergranular flow fields", A&A 409, 299-308, 2003.

10. Petit, P., Donati, J.-F., Oliveira, J. M., Aurière, M., Bagnulo, S., Landstreet, J. D., **Lignières, F.**, Lüftinger, T., Marsden, S., Mouillet, D., Paletou, F., Strasser, S., Toqué, N., Wade, G. A., "Photospheric magnetic field and surface differential rotation of the FK Com star HD 199178", MNRAS 351, 826-844, 2004.

11. Bruntt, H., Bikmaev, I. F., Catala, C., Solano, E., Gillon, M., Magain, P., Van't Veer-Menneret, C., Stütz, C., Weiss, W. W., Ballereau, D., Bouret, J. C., Charpinet, S., Hua, T., Katz, D., **Lignières, F.**, Lueftinger, T., "Abundance analysis of targets for the COROT/MONS asteroseismology missions. II. Abundance analysis of the COROT main targets", A&A 425, 683-695, 2004.

12. Ryabchikova, T., Wade, G. A., Aurière, M., Bagnulo, S., Donati, J.-F., Jeffers, S. V., Johnson, N., Landstreet, J. D., **Lignières, F.**, Lueftinger, T., Marsden, S., Mouillet, D., Paletou, F., Petit, P., Reegen, P., Silvester, J., Strasser, S., Toque, N., "Rotational periods of four roAp stars", A&A 429, L55-L58, 2005.

13. Rincon, F., **Lignières, F.**, Rieutord, M., "Mesoscale flows in large aspect ratio simulations of turbulent compressible convection", A&A 430, L57-L60, 2005.

14. Solano, E., Catala, C.,Garrido, R., Poretti, E., Janot-Pacheco, E., Gutiérrez, R., González, R., Mantegazza, L., Neiner, C., Fremat, Y., Charpinet, S., Weiss, W., Amado, P. J., Rainer, M., Tsymbal, V., Lyashko, D., Ballereau, D., Bouret, J. C., Hua, T., Katz, D., **Lignières, F.**, Lüftinger, T., Mittermayer, P., Nesvacil, N., Soubiran, C., van't Veer-Menneret, C., Goupil, M. J., Costa, V., Rolland, A., Antonello, E., Bossi, M., Buzzoni, A., Rodrigo, C., Aerts, C., Butler, C. J., Guenther, E., Hatzes, A. "GAUDI : A Preparatory Archive for the COROT Mission", AJ 129, 547-553, 2005.

15. Petit, P., Donati, J.-F., Aurière, M., Landstreet, J. D., **Lignières, F.**, Marsden, S., Mouillet, D., Paletou, F., Toqué, N., Wade, G. A., "Large-scale magnetic field of the G8 dwarf ξ Bootis A", MNRAS 361, 837-849, 2005

16. Wade, G. A., Aurière, M., Bagnulo, S., Donati, J.-F., Johnson, N., Landstreet, J. D., **Lignières,**

F., Marsden, S., Monin, D., Mouillet, D., Paletou, F., Petit, P., Toqué, N., Alecian, E., Folsom, C., "A search for magnetic fields in the variable HgMn star α Andromedae" A&A 451, 293, 2006

17. Toqué, N., **Lignières, F.**, Vincent, A., "Reduction of the vertical transport in two-dimensional stably stratified forced shear flows", Geophys. and Astrophys. Fluid Dynamics **100**, 85-105, 2006.

18. **Lignières F.**, Rieutord M. and Reese D., "Acoustic oscillations in rapidly rotating polytropic stars ; I. Effects of the centrifugal distortion", A&A **455**, pp. 607-620, 2006

19. Reese D., **Lignières F.** and Rieutord M., "Acoustic oscillations in rapidly rotating polytropic stars ; II. Effects of the Coriolis and centrifugal accelerations", A&A 455, 621-637, 2006

20. Aurière, M., Wade, G. A., Silvester, J., **Lignières**, F., Bagnulo, S., Bale, K., Dintrans, B., Donati, J. F., Folsom, C. P., Gruberbauer, M., Hui Bon Hoa, A., Jeffers, S., Johnson, N., Landstreet, J. D., Lèbre, A., Lueftinger, T., Marsden, S., Mouillet, D., Naseri, S., Paletou, F., Petit, P., Power, J., Rincon, F., Strasser, S., Toqué, N., "Weak magnetic fields in Ap/Bp stars. Evidence for a dipole field lower limit and a tentative interpretation of the magnetic dichotomy", A&A 475, 1053, 2007

21. **Lignières F.** and Georgeot, B., "Wave chaos in rapidly rotating stars", Phys. Rev. E. 78, 016215-016219, 2008

22. Reese D., **Lignières F.** and Rieutord M., "Regular patterns in the acoustic spectrum of rapidly rotating stars", A&A 481, 449-452, 2008

23. Aurière M., Konstantinova-Antova R., Petit P., Charbonnel C., Dintrans B., **Lignières F.**, Roudier T., Alecian E., Donati J. F., Landstreet J. D., Wade G. A., A&A 491, 499-505, 2008

24. Michel, E., Baglin, A., Auvergne, M., Catala, C., Samadi, R., Baudin, F., Appourchaux, T., Barban, C., Weiss, W. W., Berthomieu, G., Boumier, P., Dupret, M.-A., Garcia, R. A., Fridlund, M., Garrido, R., Goupil, M.-J., Kjeldsen, H., Lebreton, Y., Mosser, B., Grotsch-Noels, A., Janot-Pacheco, E., Provost, J., Roxburgh, I. W., Thoul, A., Toutain, T., Tiphène, D., Turck-Chieze, S., Vauclair, S. D., Vauclair, G. P., Aerts, C., Alecian, G., Ballot, J., Charpinet, S., Hubert, A.-M., **Lignières, F.**, Mathias, P., Monteiro, M. J. P. F. G., Neiner, C., Poretti, E., Renan de Medeiros, J., Ribas, I., Rieutord, M. L., Cortés, T. R., Zwintz, K., "CoRoT Measures Solar-Like Oscillations and Granulation in Stars Hotter Than the Sun", Science 322, 558-560, 2008

25. Morin, J., Donati, J.-F., Petit, P., Delfosse, X., Forveille, T., Albert, L., Aurière, M., Cabanac, R., Dintrans, B., Fares, R., Gastine, T., Jardine, M. M., **Lignières, F.**, Paletou, F., Ramirez Velez,

J. C., Théado, S., "Large-scale magnetic topologies of mid M dwarfs", MNRAS 390, 567-581, 2008

26. Donati, J.-F., Morin, J., Petit, P., Delfosse, X., Forveille, T., Aurière, M., Cabanac, R., Dintrans, B., Fares, R., Gastine, T., Jardine, M. M., **Lignières, F.**, Paletou, F., Velez, J. C. R., Théado, S., "Large-scale magnetic topologies of early M dwarfs", MNRAS 390, 545-560, 2008

27. Petit, P., Dintrans, B., Solanki, S. K., Donati, J.-F., Aurière, M., **Lignières, F.**, Morin, J., Paletou, F., Ramirez Velez, J., Catala, C., Fares, R., "Toroidal versus poloidal magnetic fields in Sun-like stars : a rotation threshold", MNRAS 388, 80-88, 2008

28. **Lignières F.** and Georgeot, B., "Asymptotic analysis of high-frequency acoustic modes in rapidly rotating stars", A&A 500, 1173-1192, 2009

29. **Lignières, F.**, Petit, P., Bohm, T., & Aurière, M. 2009, "First evidence of a magnetic field on Vega. Towards a new class of magnetic A-type stars", A&A 500, L41-L44, 2009

30. Ballot, J., **Lignières, F.**, Reese, D., Rieutord, M., "Gravity modes in rapidly rotating stars. Limits of perturbative methods", accepté pour publication dans A&A, 2010

31. Aurière M., Wade G. A., **Lignières F.**, Hui Bon Hoa, A. Landstreet, J. D. Iliev, I., Donati, J. F., Petit, P., Roudier, T., Théado, S., "No detection of large-scale magnetic fields at the surfaces of Am and HgMn stars", sousmis à la revue A&A

C.2 Cours dans des écoles thématiques

1. **Lignières, F.**, "Structure asymptotique du spectre de fréquences acoustiques", Cours à l'Ecole du CNRS "Les pulsations du Soleil et des Etoiles", St Flour, Octobre 2008

2. **Lignières, F.**, "Computational Fluid Dynamics of stellar interiors", Cours à the Doctoral School of Astrophysics "F. Lucchin", Abbazia di Spineto, Septembre 2009

C.3 Chapitre d'ouvrage

1. **Lignières, F.**, "Asymptotic theory of stellar oscillations based on ray dynamics" Lectures Notes in Physics, Spinger, sous presse

C.4 Proceedings avec comité de lecture

1. **Lignières, F.**, "The small-Péclet-number approximation in radiative zones and its application to shear layer instabilities", IAU Symposium No. 215 on Stellar Rotation in Cancun, eds. Eenens Ph., Maeder, A., San Francisco : Astronomical Society of the Pacific, p.346, 2004.

2. **Lignières, F.**, Rieutord, M., "Oscillations of fast rotating stars : p-modes in centrifugally flattened polytropes", IAU Symposium No. 215 on Stellar Rotation in Cancun, eds. Eenens Ph., Maeder, A., San Francisco : Astronomical Society of the Pacific, p.414, 2004.

3. Petit, P., Donati, J.-F., The MUSICOS Collaboration, Wade, G. A., Landstreet, J. D., Sigut, T. A. A., Shorlin, S. L. S., Bagnulo, S., Lüftinger, T., Strasser, S., Oliveira, J. M., Aurière, M., **Lignières, F.**, Mouillet, D., Paletou, F., "Surface Differential Rotation of Evolved Fast Rotators", IAU Symposium No. 215 on Stellar Rotation in Cancun, eds. Eenens Ph., Maeder, A., San Francisco : Astronomical Society of the Pacific, p.294, 2004.

4. Reese D., **Lignières F.** and Rieutord M., "Oscillations of rapidly rotating stars", in Communications in Asteroseismology **147**, pp. 65-68, 2006

5. **Lignières, F.**, Rieutord, M., Reese, D., "Acoustic oscillations in centrifugally distorted polytropic stars", Memorie della Societa' Astronomica Italiana **77**, 425-428, 2006

6. **Lignières F.** and Georgeot, B., "The asymptotic structure of the p-modes frequency spectrum in rapidly rotating stars", in Communications in Asteroseismology **157**, pp. 216-220, 2008

7. Petit, P. and Donati, J.-F. and The MUSICOS Collaboration et al. "Magnetic geometries of Sun-like stars : exploring the mass-rotation plane", Proc. the IAU Symposium 259, 441-442, 2009

8. Wade, G. A. and Silvester, J. and Bale, K. and Johnson, N. and Power, J. and Aurière, M. and **Lignières**, F. et al. "Why are Some A Stars Magnetic, while Most are Not ?" Proc. of the Solar Polarization 5, Astronomical Society of the Pacific, 2009

9. **Lignières F.**, Georgeot, B., Ballot, J. "P-modes in rapidly rotating stars : looking for regular patterns in synthetic asymptotic spectra", Proceedings of the 4th HELAS International Conference, Lanzarote, soumis

C.5 Proceedings sans comité de lecture

1. Catala, C. and Bouret, J.-C. and Butler, J. and Garrido, R. and **Lignières**, F. et al. "Fundamental parameters of COROT seismology targets", 2000, The Third MONS Workshop : Science Preparation and Target Selection, Proceedings of a Workshop held in Aarhus, Denmark, January 24-26, 2000, Eds. : T.C. Teixeira, and T.R. Bedding, Aarhus Universitet, 2000., p.37

2. Lastennet, E., **Lignières, F.**, Buser, R. Lejeune, T. Lüftinger, T. Cuisinier, F. van't Veer-Menneret, C., "Preparation of the COROT space mission : fundamental stellar parameters determinations from photometric and spectroscopic analyses for COROT potential target candidates", Proceedings of the COROT/MONS Workshop, Ghent, Belgium, Jan. 2001, ed. C. Sterken

3. **Lignières, F.**, Rieutord, M., Valdettaro, L., "Acoustic modes in spheroidal cavities", Proceedings of "Semaine de l'Astrophysique Française" 2001 meeting, Eds. : Société Française d'Astronomie et d'Astrophysique, EdP-Sciences, Conference Series, 2002

4. Rieutord, M., **Lignières, F.**, "On the theory of oscillations of rapidly rotating stars", 2002, in *Radial and nonradial pulsations as probes of stellar physics*, Edt Aerts C., Bedding T. and Christensen-Dalsgaard J., ASP conf. Series.

5. Roudier, Th., **Lignières, F.**, Rieutord, M., Brandt, P.N., Malherbe ,J.M., "Recurrence of fragmenting granules and their relation to meso-and supergranular flow fields", Workshop magnétisme et activité du Soleil et des étoiles en l'honneur de J.-L. Leroy, Toulouse, Septembre 2002.

6. Wade, G.A., Auriere, M., Bagnulo, S., Donati, J.F., Landstreet, J.D., **Lignières, F.**, Lüftinger, T., Petit, P., Shorlin, S.L.S., Sigut, T.A.A., Strasser, S., "Weak and Tangled Magnetic Fields in B, A and F Stars", in Modelling of Stellar Atmospheres, IAU Symposium No. 210, Eds. N.E.Piskunov, W.W. Weiss, & D.F. Gray, San Francisco : Astronomical Society of the Pacific, p. D29, 2003.

7. Lüftinger, T., Ryabchikova, T., Stütz, Ch., Weiss, W. W., Auriere, M., Donati, J.-F., **Lignières, F.**, Petit, P., Bagnulo, S., Landstreet, J. D., Shorlin, S. L. S., Sigut, T. A. A., Strasser, S., Wade, G. A., "Analysis of Stokes Profiles of the RoAp Stars HD 24712 and HD 12098", in Modelling of Stellar Atmospheres, IAU Symposium No. 210, Eds. N.E.Piskunov, W.W. Weiss, & D.F. Gray, San Francisco : Astronomical Society of the Pacific, p. D4, 2003.

8. Auriere, M., Silvester, J., Wade, G. A., Bagnulo, S., Donati, J. F., Johnson, N., Landstreet, J. D.,

Lignières, F., Lueftinger, T., Mouillet, M., Paletou, F., Petit, P., Strasser, S., "A survey of Ap stars for weak longitudinal magnetic fields", in Magnetic stars, Proceedings of the International Conference, Eds. : Yu. Glagolevskij, D. Kudryavtsev, I. Romanyuk, Nizhnij Arkhyz, p. 114-120, 2004.

9. Auriere, M., Silvester, J., Wade, G. A., Bagnulo, S., Donati, J. F., Johnson, N., Landstreet, J. D., **Lignières, F.**, Lueftinger, T., Mouillet, M., Paletou, F., Petit, P., Strasser, S., A survey of the weakest-field magnetic Ap stars : discovery of a threshold magnetic field strength ?", in The A-Star Puzzle, IAU Symposium No. 224, Eds. J. Zverko, J. Ziznovsky, S.J. Adelman, and W.W. Weiss, Cambridge University Press, p.633-636, 2004.

10. **Lignières, F.**, "The origin of early-type star magnetism : models and open questions", Semaine de l'Astrophysique Francaise, Eds. F. Combes, D. Barret, T. Contini, F. Meynadier and L. Pagani, EdP-Sciences, Conference Series, p. 237, 2004.

11. **Lignières, F.**, Toqué, N., Vincent, A., "Turbulent Transport In Stellar Radiative Zones", in Element stratification in stars :40 years of atomic diffusion, Eds. G. Alécian, O. Richard, S. Vauclair, EdP-Sciences, Conference Series, sous presse.

12. Vincent, A., **Lignières, F.**, "Diffusion of a trace element in anisotropic radiative hydrodynamics turbulence", in Element stratification in stars :40 years of atomic diffusion, Eds. G. Alécian, O. Richard, S. Vauclair, EdP-Sciences, Conference Series, sous presse.

13. Reese, D., **Lignières, F.**, Rieutord, M., "Oscillations of rapidly rotating stars", JENAM 2005 published in Communications in Asteroseismology, sous presse.

14. Michel, E., Baglin, A., Auvergne, M., Catala, C., Aerts, C. et al. "The CoRoT Mission", (Eds) M. Fridlund, A. Baglin, J. Lochard & L. Conroy, ESA Publications Division, ESA Spec.Publ. 1306 (2006), p. 39-50, 2006

15. Goupil, M. J., Moya, A., Suarez, J. C., Lochard, J., Barban, C., et al. "Why bothering to measure stellar rotation with CoRoT ?", "The CoRoT Mission", (Eds) M. Fridlund, A. Baglin, J. Lochard & L. Conroy, ESA Publications Division, ESA Spec.Publ. 1306 (2006), p. 51, 2006

16. **Lignières, F.**, Vidal, S., Georgeot, B., & Reese, D., "Wave chaos in rapidly rotating stars", SF2A-2006 : Semaine de l'Astrophysique Francaise, 479, 2006

17. Aurière, M., Wade, G. A., **Lignières, F.**, Landstreet, J. D., Donati, J.-F., et al. "Weak magnetic fields in CP stars", Contrib. Astron. Obs. Skalnate Pleso, 2008

18. Petit, P., Dintrans, B., Aurière, M., Catala, C., Donati, J.-F., et al. "Magnetic geometries of Sun-like stars : impact of rotation", SF2A-2008, 253, 2008

19. Ballot, J., **Lignières F.** et al., "Gravity modes in rapidly rotating polytropic stars", Proc. of the HELAS Workshop 'New insights into the Sun', M. S. Cunha & M. J. Thompson (eds), 2009